Measurements of differential cross sections for the production of top quark pairs in pp collisions at $\sqrt{s} = 13$ TeV with the CMS experiment

Dissertation

zur Erlangung des Doktorgrades
an der Fakultät für Mathematik, Informatik und
Naturwissenschaften
Fachbereich Physik
der Universität Hamburg

vorgelegt von
Henriette Aarup Petersen
aus Aalborg, Dänemark

Hamburg
2022

Gutachter der Dissertation:	Dr. Olaf Behnke Prof. Dr. Elisabetta Gallo
Zusammensetzung der Prüfungskommission:	Dr. Olaf Behnke Prof. Dr. Elisabetta Gallo Prof. Dr. Bernd Kniehl Prof. Dr. Dieter Horns Dr. Maria Aldaya Martin
Vorsitzender der Prüfungskommission:	Prof. Dr. Bernd Kniehl
Datum der Disputation:	24. Juni 2022
Vorsitzender des Fach-Promotionsausschusses Physik:	Prof. Dr. Wolfgang J. Parak
Leiter des Fachbereichs Physik:	Prof. Dr. Günter H. W. Sigl
Dekan der Fakultät für Mathematik, Informatik und Naturwissenschaften:	Prof. Dr. Heinrich Graener

Eidesstattliche Versicherung / Declaration on oath

Hiermit versichere ich an Eides statt, die vorliegende Dissertationsschrift selbst verfasst und keine anderen als die angegebenen Hilfsmittel und Quellen benutzt zu haben.

I hereby declare, on oath, that I have written this dissertation by myself and have not used anything other than the acknowledged resources and aids.

Hamburg, 24. April 2023 Henriette Aarup Petersen

Abstract

In this thesis, measurements of differential cross sections of top quark pair ($t\bar{t}$) production in proton-proton (pp) collisions at $\sqrt{s} = 13$ TeV are presented. The analysis is based on data obtained with the CMS experiment during 2016, 2017 and 2018 in Run 2 of the LHC, which corresponds to an integrated luminosity of 137.6 fb^{-1}. In this period of time more than 100 million $t\bar{t}$ pairs were produced in the pp collisions, facilitating an unprecedented precision in measurements of kinematic spectra and topologies in these events. The analysis is performed using the dileptonic decay channel. Differential $t\bar{t}$ production cross sections are measured in bins of the kinematic properties of the $t\bar{t}$ system, the top quarks and their visible decay products, the charged leptons and beauty flavoured jets. The cross section extraction is based on an event-counting method using reconstructed distributions, where detector effects such as resolutions, acceptances and efficiencies are corrected through a regularized unfolding procedure. The measurements are presented in the full phase-space at parton level and/or in the fiducial phase space at particle level. Both absolute and normalized cross sections are provided. All measurements are compared to alternative MC predictions based on next-to-leading order (NLO) QCD models matched to parton showers and some selected results are also compared to theoretical predictions beyond NLO precision in QCD. Most cross sections are measured single-differentially as functions of one kinematic observable, but also some double-differential cross sections are extracted as functions of two observables.

Zusammenfassung

In dieser Arbeit werden Messungen differenzieller Wirkungsquerschnitte für ($t\bar{t}$) Produktion in Proton-Proton (pp) Kollisionen bei einer Schwerpunktsenergie von $\sqrt{s} = 13$ TeV präsentiert. Die Analyse benutzt Daten die mit dem CMS Experiment in den Jahren 2016, 2017 und 2018 in dem "LHC Run 2" aufgezeichnet wurden und einer integrierten Luminosität von 137.6 fb^{-1} entsprechen. In diesem Zeitraum wurden mehr also 100 Millionen $t\bar{t}$ Paare erzeugt, was es ermöglicht kinematische Spektren und Ereignistopologien mit bislang unerreichter Präzision zu studieren. Die Analyse wird mit dem dileptonischen Zerfallskanal durchgeführt. Differenzielle Wirkungsquerschnitte werden als Funktion kinematischer Observablen des $t\bar{t}$ Systems, des Top Quarks und der sichtbaren Zerfallsprodukte, den geladenen Leptonen und "beauty flavoured jets", untersucht. Die Extrahierung der Wirkungsquerschnitte basiert auf einer Ereignis-zählmethode welche die rekonstruierten Verteilungen auf Detektoreffekte wie Akzeptanzen, Effizienzen und Verschmierungen mittels einer regularisierten Entfaltungsprozedur korrigiert. Die Messungen werden in dem vollen Phasenraum auf "Parton Level" und/oder im sichtbaren Phasenraum auf "Particle Level" präesentiert. Alle Messungen werden mit alternativen Monte Carlo Vorhersagen verglichen, die auf Modellen in nächstführender (NLO) Störungsrechnung der QCD plus Partonschauern basieren. Einige selektierte Resultate werden auch mit Rechnungen in noch höheren Ordnungen der QCD Störungsreihe verglichen. Die meisten differenziellen Wirkungsquerschnitte werden als Funktion einer kinematischen Variablen gemessen und einige auch simultan als Funktion von zwei Variablen.

Contents

Chapter 1

Introduction

A clear description of the elementary particles in the universe and the gauge bosons that mediate their interactions is provided by the Standard Model (SM) of particle physics [1] and the predictive power of this model has arguably been established in the second half of the 20th century. The bottom and top quarks were first predicted in 1973 [2] by Makoto Kobayashi and Toshihide Maskawa and were also commonly referred to as beauty and truth, respectively. Those names are a reminder of the way they elegantly completed the picture of quark mixing and helped explain the observed charge-parity violation in the kaon system. The subsequent discoveries of the quarks in 1977 (bottom [3]) and 1995 (top [4]) generated much excitement and further corroborated the emerging picture of particle physics. In the SM, the Higgs mechanism was postulated to explain how particles have mass, introducing couplings to a new type of spin 0 boson, called the Higgs. A Higgs-like particle with a mass of 125 GeV was subsequently discovered in 2012 [5, 6], confirming the last prediction of the SM. This brings us to today, where we still need answers to a number of questions that are not currently within the realm of understanding in the context of the SM, and the hope is that high-energy collisions of protons and/or heavy ions at the Large Hadron Collider (LHC) or future hadron/lepton colliders can shed light on where we're heading in terms of new physics.

The top quark is the heaviest elementary particle with a mass of 172.5 GeV [7] (average pole mass from cross section measurements) and its Yukawa coupling to the Higss boson is close to 1. Thus, its possible involvement in new production and decay modes at higher energy scales is postulated and this makes it interesting for new physics models. The name truth, the alternative moniker of the top quark, seems very beautiful in this context. Cross section measurements of the process where a top and an anti-top are produced in a pair, so-called $t\bar{t}$ production, are especially important, as they are sensitive to such new phenomena and serve as crucial tests of the validity of the SM. At the LHC, the $t\bar{t}$ production primarily happens through gluon-gluon fusion as shown in the exemplary Feynman diagram in Figure 1.1. Although the top quark pairs are not directly visible in the detector, they can be kinematically reconstructed through their daughter particles that are also shown in Figure 1.1. This is a unique feature of the top quark, as its very short lifetime means that it decays before it hadronizes, thereby facilitating access to the

bare quark.

In this work, cross sections of $t\bar{t}$ production are measured as functions of one or simultaneously two kinematic variables in the event, in a comprehensive set of differential measurements using the data collected by the Compact Muon Solenoid (CMS) experiment, situated at the LHC, in proton-proton (pp) collisions at center-of-mass energies of 13 TeV. The data used was recorded from the beginning of 2016 until the end of 2018, which corresponds to an integrated luminosity of 137.6 fb^{-1} constituting the period known as Run 2. The top quark predominantly decays to a W boson and a b quark, and the measurements are performed in the dilepton decay channel consisting of $e^{\pm}e^{\mp}$, $\mu^{\pm}\mu^{\mp}$ and $e^{\pm}\mu^{\mp}$ final states, resulting from the prompt decays of the W bosons shown in Figure 1.1. The CMS experiment is situated opposite to the ATLAS experiment on the LHC ring, and both have previously performed such measurements in the dilepton channel at center-of-mass energies of 7 (2011) [8, 9], 8 (2012) [10–12] and 13 TeV (2016) [13–15]. However, in the Run 2 period, the LHC has produced ~ 100 million $t\bar{t}$ events at just CMS alone and this makes it the largest top quark factory ever built by several orders of magnitude. The abundance of statistics facilitates unprecedented precision in the differential cross sections.

In this thesis, cross sections are measured as functions of kinematic observables of the $t\bar{t}$ system as well as the top quarks and their decay products, the charged leptons and beauty flavoured jets. Another type of cross section is also performed as a function of the total jet multiplicity in the event, which includes extra jets from the hard interaction or parton shower (see Figure 1.1), providing a direct probe of the strong interaction. The cross sections are measured in both absolute and normalized form, where the latter refers to the normalization of the former with respect to the total inclusive cross section of $t\bar{t}$ production. All distributions related to the $t\bar{t}$ system or top quarks are performed at both parton and particle level in the full and fiducial phase space, respectively, while those related to the decay observables and jet multiplicity are performed at particle level only in the fiducial phase space. A couple of high-precision SM predictions are only available for parton level measurements in the full phase space. An advantage of particle level measurements in the fiducial phase space is the minimal extrapolation uncertainties, since the selection at generator level is chosen such that it closely follows the detector acceptance and applied selection criteria at detector level. The analysis strategy follows the corresponding analyses in the dilepton channel performed at CMS using 2016 data [14, 15]. Several new single- and double-differential measurements are performed for the first time ever and the kinematic phase space of a number of observables has been extended with respect to the 2016 analysis [14]. The abundance of statistics has also made it possible to use finer binning in the differential measurements, in particular for those measured as functions of kinematic spectra of the charged leptons and b-jets. The statistically limited regions of the kinematic phase space for other observables, benefit from this as well.

The cross sections are compared to Monte Carlo (MC) simulations at next-to-leading order (NLO) and the latest set of SM predictions at next-to-next-to-leading order

(NNLO) or even higher accuracy in QCD. And for the first time in CMS, the scope of comparisons include predictions from MiNNLOPS [16–18], which interfaces NNLO matrix element calculations to parton showers. Furthermore, a selected number of measurements is compared to predictions using alternative sets of parton distribution functions (PDF), which describe the longitudinal momentum densities of quarks and gluons in the proton. The $t\bar{t}$ measurements presented in this work are expected to be particularly sensitive to the gluon-density at high proton momentum fractions, and can subsequently be used by theoreticians to constrain the PDFs. In addition, differential measurements can be used to extract the strong coupling constant and the top mass [15].

The thesis is organized as follows. In Chapter 2, a theoretical overview of the SM is given along with details on the production and decay modes of $t\bar{t}$ at the LHC. Information on the LHC itself and descriptions of the CMS experiment and its subdetectors can be found in Chapter 3. To test our understanding of the underlying phenomenology of the physics process we aim to study, MC simulations are used such that comparisons can be made directly with data. MC simulations can be factorized into a series of individual processes that are described in Chapter 4. In this thesis, MC simulations that are processed through the detector simulation are also used for subtracting background processes and correcting signal events for detector effects. The identification and reconstruction of e.g. the charged leptons and jets, including b-jets, in the detector are described in Chapter 5. In this chapter the key ingredient of the analysis is also explained, namely the kinematic reconstruction of the top and anti-top quark momentum vectors, where the visible decay products (charged leptons and b-jets) are associated with the t and $\bar{t}$ decay chains and used to determine the momentum vectors of the two neutrinos. Finally, the event selection is summarized and control plots are shown after the full section.

In Chapter 6, absolute and normalized differential cross sections are defined, along with the inclusive cross section, which is used to perform cross checks of the production rate of $t\bar{t}$ in the context of this work. This chapter also contains a complete description of the background subtraction and regularized unfolding procedure used to correct the data for detector related effects such as resolutions, efficiencies and acceptances. The data is unfolded with respect to two different definitions of the top quark at the true parton or particle level in the full or fiducial phase space, respectively, and all details pertaining to each definition are provided. As one might imagine, there are many sources of uncertainty that must be carefully evaluated and addressed when determining the precision on the cross section results. These can generally be grouped into categories of experimental, theoretical and background sources, and all are described in Chapter 7, where their overall contributions are also presented in the context of the differential measurements. Moreover, this chapter includes a description of how correlations among years for different sources of uncertainty are taken into account. The full set of results, presented in Chapter 8, are organized into two parts, where inclusive cross sections of $t\bar{t}$ production are shown in Section 8.1 and the main results, comprising differential cross sections measured as functions of one or more kinematic variables, are shown in Section 8.2. The latter set is presented in different categorises depending on the measured kinematic

spectra. Finally, the overall observations made based on the studied differential distributions are summarized in Chapter 9, where a brief outlook on the future of such measurements is also given.

The results presented in this thesis are publicly available in [19].

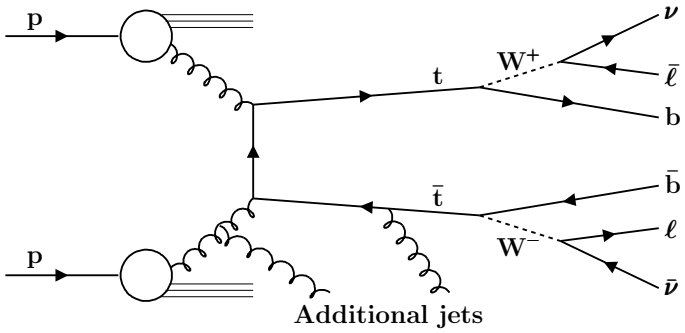

Figure 1.1: An exemplary Feynman diagram of $t\bar{t}$ plus additional jet production in pp collisions is shown for the signal process studied in this work, where the two W bosons both decay to leptons, constituting the dilepton channel.

Chapter 2

Theoretical overview

In this section a theoretical overview of the foundation for this work is given in the context of top physics. The Standard Model of particle physics is presented in Section 2.1 and Section 2.2, which describe the type of particles within the model and interactions between them, respectively. The specific characteristics of the top quark processes are outlined in Section 2.3, where the top pair and single top production modes at the Large Hadron Collider (LHC) are described in Section 2.3.1 and Section 2.3.2, respectively, while the specific top pair decay modes are outlined in Section 2.3.3. Finally, a brief discussion of new physics in relation to the top quark is given in Section 2.3.4.

2.1 Standard Model of particle physics

All matter in the universe consists of irreducible particles known as fermions that interact with each other through the exchange of other fundamental particles called bosons. The fermions and bosons constitute all known elementary particles and the underlying theory that describes their nature and interactions is called the Standard Model (SM) of particle physics [1]. Figure 2.1 shows the schema of the SM, where the fermions and bosons are distinguished by a property of their angular momentum, called spin. The former particles have spin $\frac{1}{2}$ and the latter have spin 1, however, there is an exception to this rule, namely the Higgs boson which has spin 0.

The fermion group is arranged into three generations of matter as illustrated by the first three columns in Figure 2.1. These generations are essentially successively heavier replicates of each other and one may be tempted to ask if there are more than three. However, this can be determined from the width of the Z boson resonance from which one can deduce that there are three light neutrino generations and therefore from symmetry principles one expects only three generations on the whole. The fermion group can be divided into two additional categories:

• **Leptons**: The two bottom rows show the leptons, where the first consists of the negatively-charged electron (e), muon (μ) and tau (τ) and the second comprise the electrically neutral electron-, muon- and tau-neutrino. Their dynamics are pre-

dicted by the Dirac equation which implies that each of the particles above has a corresponding anti-particle with opposite charge. Thus, the counterparts of the charged-leptons are positively charged. However, for the neutral neutrinos there is still some ambiguity and they could potentially be their own anti-particles, so-called Majorana fermions [20]. This is still an open question.

• **Quarks**: The quark family is shown in the upper two rows and consists of up (u), down (d), charm (c), strange (s), top (t) and bottom (b). Similar to leptons, each quark also has its own corresponding anti-particle. Quarks are confined into composite structures called hadrons due to the principle of colour confinement which will be explained in relation to the process of hadronization in Chapter 4. Combinations of quarks and anti-quarks are called mesons, and combinations of three quarks (anti-quarks) are called baryons (anti-baryons). Examples of the latter type include the proton and neutron, which are made up of uud and udd, respectively.

Predictions of the SM have been put to the test many times throughout roughly the last 50 years. A significant piece of the puzzle came with the discovery of the Higgs boson in 2012 [5, 6], but there are still unanswered questions that lie beyond the SM [21]. The SM has a lot of free parameters, e.g. there is no prediction about the masses of the particles themselves. Likewise, there is no explanation for the vast jump in the energy scale from the electroweak force ($\sim$ 246 GeV [22]) to that of the Planck scale ($\sim 10^{19}$ GeV [22]), where gravity starts to become dominant, which is called the gauge hierarchy problem. Along the same lines several theories have been developed to try and explain why the Higgs boson, the particle responsible for giving mass to all other particles, has a mass of only 125 GeV [22], which is also curiously smaller than the mass of the top quark. The Higgs mechanism explains how all known elementary particles gain mass according to their Yukawa coupling with the Higgs boson, which arises as a result of the electroweak spontaneous symmetry breaking of the Higgs field potential [1, 23]. However, it's not currently understood how the neutrinos acquire mass as they are predicted to be massless, in direct contradiction to experimental data. Furthermore, the visible matter in the universe only constitutes about (4.9%) of the total matter-energy content, where the rest is from dark matter (25.9%) and dark energy (69.2%) [24]. However, there is no SM particle that fits the criteria for being a dark matter candidate. The final question pertains to the observed baryon asymmetry in the universe, or in other words why there is more matter than anti-matter. One of the conditions that need to be met for this to be the case is a significant violation of charge-parity (CP) symmetry [1], but there is no sector of the SM that fulfils this criteria.

2.2 Fundamental interactions

The question of what fundamental interactions are possible between particles is answered by looking at the charges that they possess [1]. Particles that are electrically charged can interact via the photon, which is responsible for mediating the electromagnetic force described in Section 2.2.1. This includes all fermions except

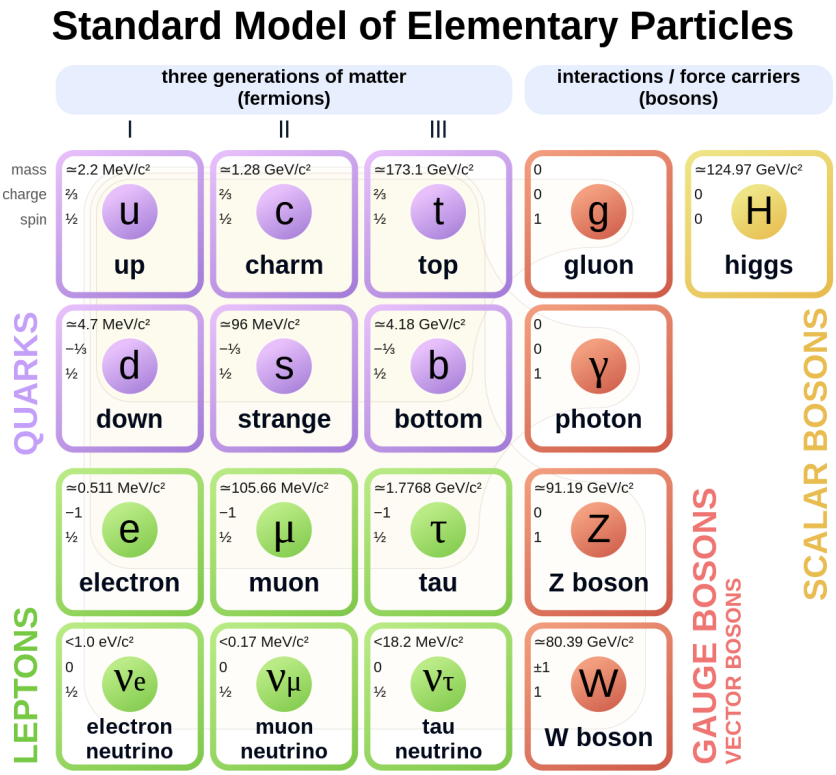

Figure 2.1: An overview of all particles within the Standard Model; the fermions and gauge bosons [25].

neutrinos, while the strong force described in Section 2.2.2 is more restrictive. Its mediator, the color-charged gluon, only couples to itself or fermions that also carry colour such as quarks. Finally, particles that posses weak hypercharge can interact via the weak force, which has both a charged and neutral current mediated by the W and Z boson, respectively, as described in Section 2.2.3. A description of the unification of the neutral current and the electromagnetic interaction is also given in this section. In Table 2.1 the fundamental forces mentioned above are ranked according to their relative strengths with respect to the strong interaction at a distance of 1 fm, which approximately corresponds to the radius of a proton. Gravity is also included in this table, but it's not described by the Standard Model as the underlying theory of general relativity must be unified with a quantum field theory description. It's speculated that the Graviton, a gauge boson with spin 2, could act as a mediator, but this has yet to be supported by experimental data. Furthermore, so far it has not been possible to formulate a renormalizable quantum field theory for spin 2 gauge bosons. The relative strength of gravity can clearly be considered negligible and is therefore not discussed further.

Table 2.1: The fundamental forces of the SM are listed according to their relative strength with respect to the strong interaction at a distance of 1 fm, which approximately corresponds to the radius of a proton. The gauge bosons responsible for each interaction are also shown alongside values of their spin and mass. The table is modified from [1].

Force	Strength	Boson	Spin	Mass/GeV
Strong	1	Gluon	1	0
Electromagnetism	10^{-3}	Photon	1	0
Weak	10^{-8}	W (Z) boson	1	80.4 (91.2)
Gravity	10^{-37}	Graviton?	2	0

2.2.1 The electromagnetic interaction

The electromagnetic force is mediated by the photon and involves interactions between two oppositely-charged fermions that are governed by the $U(1)$ gauge group theory of quantum electrodynamics (QED) [1]. Since the photon is massless, the electromagnetic force can be felt at any distance. Its coupling constant, g, can be written in terms of the dimensionless fine-structure constant, α, such that $\alpha \approx g^2$, where

$$\alpha = \frac{e_0^2}{4\pi\epsilon_0} \approx \frac{1}{137} \text{ (for } Q^2 = 0).$$

In this expression e_0 is the bare charge of the fermion participating in the interaction and ϵ_0 is the vacuum permittivity. The approximate numerical value of α is quoted at $Q^2 = 0$, where Q^2 denotes the energy scale of the interaction. Despite the term "constant", one ought to write $\alpha(Q^2)$, to signify the so-called running of the coupling constant with energy. The photon propagator cannot simply be

written as e_0^2/Q^2 since one must account for energy dependent loop corrections, or so-called vacuum polarisation corrections, which lead to a non-trivial dependence on Q^2. However, when performing matrix element calculations it's convenient to keep this simple propagator form. Thus, vacuum polarisation corrections are absorbed into the definition of the charge instead such that

$$\alpha(Q^2) = \frac{e^2(Q^2)}{4\pi\epsilon_0}.$$

Due to the fact that $\alpha \ll 1$, one can perform perturbative calculations in different orders of α.

2.2.2 The strong interaction

The strong force is mediated by the gluon and only involves interactions of particles carrying colour-charge, which excludes the leptons. Gluons themselves also carry this colour-charge and self-interactions are therefore permitted. The theory behind the strong force is quantum chromodynamics (QCD) [1], which is based on the $SU(3)$ gauge group. There are eight generators of the local $SU(3)$ gauge symmetry, which correspond to eight massless gluons. The term colour-charge refers to the three orthogonal states in the $SU(3)$ colour-space; red (r), blue (b) and green(g). Corresponding anti-colours, $\bar{r}$, $\bar{b}$ and $\bar{g}$, also exist. In QED the electrical charge must be conserved at the interaction vertex and this also applies to colour-charge in QCD. In order for this to be possible, the gluons must carry both colour and anti-colour, and have colour assignments of $r\bar{g}$, $g\bar{r}$, $r\bar{b}$, $b\bar{r}$, $g\bar{b}$, $b\bar{g}$, $\frac{1}{\sqrt{2}}(r\bar{r}-g\bar{g})$ and $\frac{1}{\sqrt{6}}(r\bar{r}+g\bar{g}-2b\bar{b})$ [1]. Due to the principle of colour confinement quarks and gluons cannot exist as free particles, instead they form bound colourless states and only hadronic states of $q\bar{q}$, qqq and $\bar{q}\bar{q}\bar{q}$ are possible for mesons, baryons and anti-baryons, respectively. Combinations of $q\bar{q}$ and qqq are also allowed but these so-called penta-quarks are much rarer and experimental data have only supported their existence in recent years [22].

Similar to QED, the strong coupling constant in QCD, denoted by α_s, depends on the energy scale, Q^2, which results in the so-called running of α_s, as shown in Figure 2.2. At low energies $\alpha_s \sim 1$, and thus perturbation theory does not apply. This is relevant for e.g. the process of hadronization. However, at large energies $\alpha_s \ll 1$, and thus one can use perturbation theory for the hard interaction (see Chapter 4).

Related to the previous discussion, the principle of colour-confinement works over large distances but at sufficiently small distances the strong force becomes relatively weak and the quarks and gluons have what is known as asymptotic freedom. This is an important concept in e.g. the study of the primordial quark-gluon plasma present in the early universe.

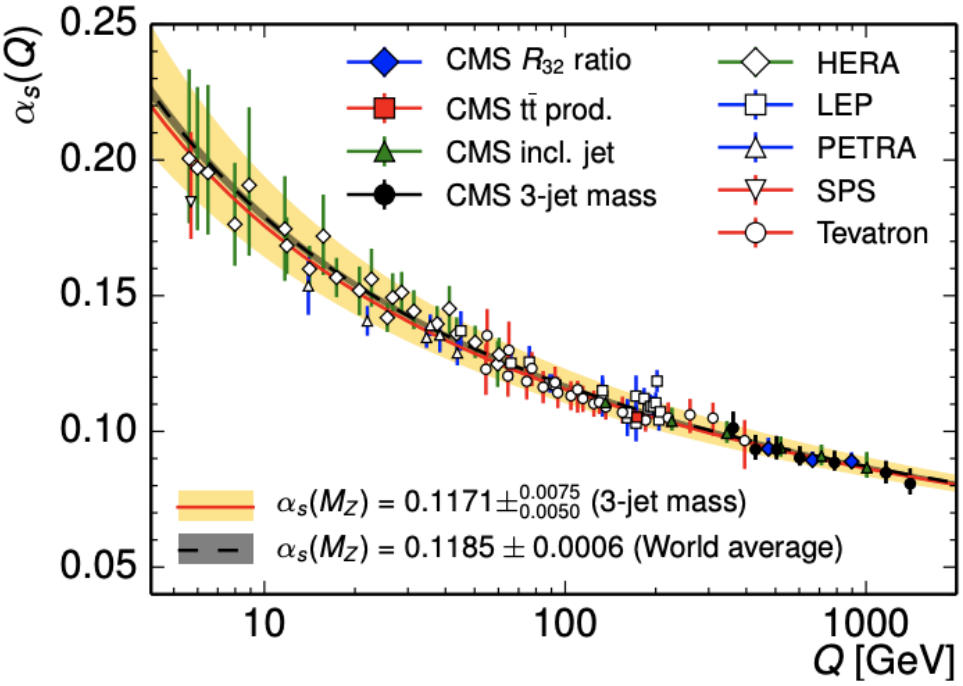

Figure 2.2: Measurements of the strong coupling constant, α_s, as a function of the energy scale, Q, performed at different experiments. The black dashed line and grey band show the world average and its corresponding uncertainty, respectively [26].

2.2.3 The weak interaction and electroweak unification

The weak interaction has both a charged and neutral current, which are mediated by the $W^{\pm}$ and Z bosons, respectively [1]. The effective coupling strength of the weak interaction is proportional to $1/m_W^2$ under the condition that the energy scale is much smaller than the mass of the W boson, $m_W = 80.4$ GeV. The range of a force is inversely proportional to the mass of the gauge boson of the interaction and hence, the weak force is restricted to relatively small distances of about 0.001 fm (10^{-18} m). At a distance of 1 fm (10^{-15} m), which approximately corresponds to the radius of a proton, the relative strength of the weak force is 10^{-8} times weaker than the strong force. The neutral current couples to both left-handed and right-handed particles/anti-particles and always conserves flavour. The charged current couples only to left-handed particles and right-handed anti-particles, and it's unique in the sense that it always violates the flavour conservation present in the electromagnetic, strong and neutral current interactions. Therefore, it's the only way in which fermions can decay to lighter ones of a different flavour. Hence, charged current processes are responsible for e.g. nuclear fusion in the sun. The $W^{\pm}$ bosons only couple to particles with non-zero values of weak isospin, denoted by I_3, which is the charge of the interaction. The charged current interactions allowed can be represented in the context of the underlying theory based on the $SU(2)$ gauge group such that

$$\begin{pmatrix}\nu_l\\ l^-\end{pmatrix}_{\rm L},\ \begin{pmatrix}q_u\\ q_d\end{pmatrix}_{\rm L},\ l^-_{\rm R},\ q_{u\rm R} \text{ and } q_{d\rm R},$$

represent the leptons and quarks that can (can't) interact weakly in terms of weak isospin doublets (singlets). The upper members of the doublets are left-handed neutrinos or up-type quarks, which all have $I_3 = 1/2$, while the bottom left-handed leptons of the same flavour or down-type quarks have $I_3 = -1/2$. The singlet states have $I_3 = 0$. The probability of an up- and down-type quark interacting weakly is given by the corresponding element in the Cabibbo, Kobayashi and Maskawa (CKM) matrix [2] defined by

$$V_{\rm CKM} = \begin{pmatrix}V_{ud} & V_{us} & V_{ub}\\ V_{cd} & V_{cs} & V_{cb}\\ V_{td} & V_{ts} & V_{tb}\end{pmatrix}.$$

The individual elements of this matrix have been determined experimentally [22] and are given by

$$V_{\rm CKM} = \begin{pmatrix}0.97446 & 0.22452 & 0.00365\\ 0.22438 & 0.97359 & 0.04214\\ 0.00896 & 0.04133 & 0.999105\end{pmatrix},$$

from which one can see that the diagonal elements are close to 1, while the off-diagonal elements are relatively small. This means that quarks belonging to the same generation are more likely to interact weakly via charged currents.

The electromagnetic and weak interaction were unified in the context of a common underlying theory based on the $U(1)_Y \times SU(2)_L$ gauge groups as described in the Glashow, Salam and Weinberg (GSW) model [1]. A requirement of $SU(2)$ gauge invariance leads to three generator transformations which correspond to three boson fields, namely W_1, W_2 and W_3. Furthermore, $SU(2)$ gauge invariance necessitates both a charged and neutral current, where the physical W bosons are responsible for the former and can be described entirely by W_1 and W_2 such that

$$W^{\pm} = \frac{1}{\sqrt{2}}(W^1_\mu \mp iW^2_\mu).$$

However, one can't simply equate the Z boson with W_3 when describing the neutral current, as this would imply that the Z boson only couples to left-handed particles which contradicts experimental data. Since the electromagnetic interaction is similar to the neutral current, it's natural to assume that both the photon and Z boson fields, denoted by A_μ and Z_μ respectively, can be expressed as mixed quantum states of two common boson fields such that

$$\begin{pmatrix}A_\mu\\ Z_\mu\end{pmatrix} = \begin{pmatrix}\cos\theta_W & \sin\theta_W\\ -\sin\theta_W & \cos\theta_W\end{pmatrix}\begin{pmatrix}B_\mu\\ W^{(3)}_\mu\end{pmatrix},$$

where θ_W denotes the weak mixing angle between $W_\mu^{(3)}$ and the new gauge field B_μ, which is invariant under $U(1)_Y$ transformations and couples to fermions with weak hypercharge, Y, including neutrinos. This charge is related to the electric charge, Q, and weak isospin as follows

$$Y = 2(Q - I_3).$$

The previous discussion of the GSW model does not explain why the photon is massless while the W and Z bosons are massive. However, this is explained within the Higgs mechanism.

2.3 Top quark physics

The top quark was first predicted in 1973 [2] by Makoto Kobayashi and Toshihide Maskawa who realized that a third generation of quarks was needed to explain the CP violation observed in the kaon system. The b quark was discovered in 1977 [3] at the E288 experiment located at the Fermi National Accelerator Laboratory (Fermilab). This only heightened expectations that its counterpart, the top quark, would also be found soon, however, there were indications that the top quark was heavy due to the size of the observed CP violation mentioned above and this would already hint at the high energy scales needed to produce it. Finally, the top quark was discovered in 1995 [4] at the CDF and DØ experiments, which were situated on the proton and anti-proton accelerator Tevatron located at Fermilab.

The top quark is special in a number of ways. It's the heaviest elementary particle with a mass of 172.5 GeV [7], and its Yukawa coupling with the Higgs boson is therefore very close to 1. In fact the top quark plays a crucial role in higher order corrections to the mass of the Higgs boson, and the masses of both the top and the Higgs have significant consequences for the vacuum stability of the universe [27]. As it turns out the universe is in a vacuum state of the Higgs potential that is close to the border of stability and metastability. If we find ourselves inside the region of metastability, it would mean that the spontaneous symmetry breaking of the Higgs potential that occurred approximately 10^{-34} s after the big bang did not result in the true ground state but in fact to a long-lived false vacuum. Depending on the nature of the vacuum, this might be rather unfortunate and lead to a possibly unstable situation. Thus, precise measurements of the top quark and Higgs boson masses are of great importance in learning about the fate of the universe.

The top quark has a very short lifetime of approximately 10^{-25} s and is the only quark to decay before it hadronizes which happens at a time scale of approximately 10^{-23} s [28]. This allows one to study the bare top quark through its decay products to which it also imparts information about e.g. its spin, thereby facilitating measurements of spin correlation in top pair production.

In Section 2.3.1 an overview is given of top pair production at the LHC and its cross section, while Section 2.3.2 contains a short summary of single top production. The different decay modes of the top pair, along with the final state of this analysis, are outlined in Section 2.3.3, and a brief discussion of new physics in relation to the top quark is provided in Section 2.3.4.

2.3.1 Top quark pair production

At leading order (LO) top pair ($t\bar{t}$) production at the LHC can happen either via quark and anti-quark annihilation ($q\bar{q}$) or gluon-gluon fusion (gg) as shown in Figure 2.3, where the latter refers to production in the s-, t- or u-channel [28]. At the LHC the colliding protons have momenta of 6.5 TeV, and the energy of the partons inside the protons, that are actually participating in the hard interaction, is typically much smaller. The proton consists of up and down valence quarks bound together by gluons which can in turn also produce intermittent quark and anti-quark pairs called sea-quarks. Further gluons can be radiated both from quarks and gluons. All of these constituents will carry a certain fraction, x, of the original energy of the proton, E_p. Thus, for e.g. top production at leading order, in a process like $gg \to t\bar{t}$, one can write

$$p(t) + p(\bar{t}) = \xi_1 p_1 + \xi_2 p_2, \tag{2.1}$$

where ξ_1 and ξ_2 denote the fractional longitudinal momenta (along the z-axis) carried by parton 1 and parton 2 participating in the interaction. Here the symbol ξ is used instead of x to emphasize that the above only applies to $t\bar{t}$ production at leading order. Finally, $p(t) = (E(t), p_x(t), p_y(t), p_z(t))$ and $p(\bar{t}) = (E(\bar{t}), p_x(\bar{t}), p_y(\bar{t}), p_z(\bar{t}))$ denote the top and anti-top momentum four-vectors respectively and $p_1 = (E_p, 0, 0, -E_p)$ and $p_2 = (E_p, 0, 0, E_p)$ denote the momentum four-vectors of the colliding protons. If the proton is assumed to have negligible mass, substituting the above into Equation 2.1 and multiplying by the p_1 or p_2 momentum four-vectors gives

$$\xi_1 = \frac{E(t) + E(\bar{t}) - p_z(t) - p_z(\bar{t})}{2E_p}$$

and

$$\xi_2 = \frac{E(t) + E(\bar{t}) + p_z(t) + p_z(\bar{t})}{2E_p}.$$

Parton distribution functions (PDFs) express the probability of finding a parton of a particular flavour and longitudinal momentum fraction, x, inside the proton. The PDFs themselves are determined from fits to experimental data, and depend on both the parton type and factorization scale, μ_f, defined as the p_{T} scale below which collinear gluon emissions are still treated as part of the non-perturbative and long distance dynamics of the parton densities within the protons. Gluon emissions with

p_{T} above μ_f are treated as part of the perturbative dynamics of the hard interaction. The μ_f scale can be chosen freely, but is usually equated with the scale of the hard interaction. The PDF dependence on the scale choice is then described by the Dokshitzer–Gribov–Lipatov–Altarelli–Parisi (DGLAP) evolution equations [29–31] and an example illustrating how different parton momentum densities within a PDF set are parameterized in x is shown in Figure 2.4, where the factorization scale is denoted by μ^2 in the plots. This particular set of PDFs is known as NNPDF3.1 [32], but there are several others including the groundbreaking PDF set from HERA [33], which was the first experiment to probe the structure of the proton in deep inelastic scattering with electrons over several orders of magnitude in x, reaching small values down to $x \sim 10^{-5}$. The ep scattering cross section measured at different energies and negative squared invariant masses, Q^2, of the exchanged gauge bosons can be used to obtain the proton structure functions from which one can then obtain the PDFs. Differential cross sections measured at the LHC can be used to further constrain these PDFs, which is particularly relevant for gluon PDFs at high x-values.

In proton-proton collisions at the LHC the most dominant production mode is gluon-gluon fusion (90% of cases) in contrast to the proton-anti-proton collisions at the Tevatron, where top pair production predominantly happened via $q\bar{q}$ annihilation. This can be explained by the differences in center-of-mass energies and the fact that energies of at least $2m_t$ are required to produce a top pair. At the LHC x must be greater than ≈ 0.03 to produce top pairs above the threshold and one can clearly see from Figure 2.4 that there are more gluons with such values than valence or sea quarks. On the other hand, at the Tevatron the center-of-mass energy was 1.96 TeV leading to a minimum of $x \approx 0.17$, above which the valence quarks dominate the proton PDFs.

The cross section, $\sigma_{pp\to t\bar{t}}$, of top pair production in proton-proton collisions, $pp \to t\bar{t}$, can be written as a convolution of the PDFs and the partonic cross section, $\hat{\sigma}_{ij\to t\bar{t}}$, for the process $x_i x_j \to t\bar{t}$, where x_i and x_j denote the proton momentum fractions carried by the two colliding partons. This is known as the factorization theorem [28] and means that $\sigma_{pp\to t\bar{t}}$ is written as the sum over all possible partons such that

$$\sigma_{pp\to t\bar{t}}(s, m_t) = \sum_{i,j=q,\bar{q},g} \int dx_i dx_j f_i(x_i, \mu_f^2) f_j(x_j, \mu_f^2) \cdot \hat{\sigma}_{ij\to t\bar{t}}(\hat{s}, m_t, \mu_f, \mu_r, \alpha_s),$$

where $f_i(x_i, \mu_f^2)$ and $f_j(x_j, \mu_f^2)$ are the corresponding PDFs. Here the partonic cross section, $\hat{\sigma}_{ij\to t\bar{t}}$, depends on the scale μ_r, which denotes the renormalization scale, usually chosen such that $\mu_f = \mu_r$. This is the scale at which the renormalized strong coupling constant, $\alpha_s(\mu_r)$, is defined and the renormalization procedure ensures that ultraviolet divergences in higher order loop diagrams are properly dealt with. This includes cases, where for example, a gluon splits into two gluons that then reunite to create a single gluon. The partonic cross section additionally depends on the top mass, m_t and the partonic center-of-mass energy, $\hat{s} = x_i x_j s$, and can be parameterized as $\hat{\sigma}_{ij\to t\bar{t}} \sim \sum_k c_k \alpha_s^k(\mu_r)$, where c_k denote the coefficients of the corresponding orders, k, of α_s. Here $k = 2$, 3 and 4, denote $t\bar{t}$ production at

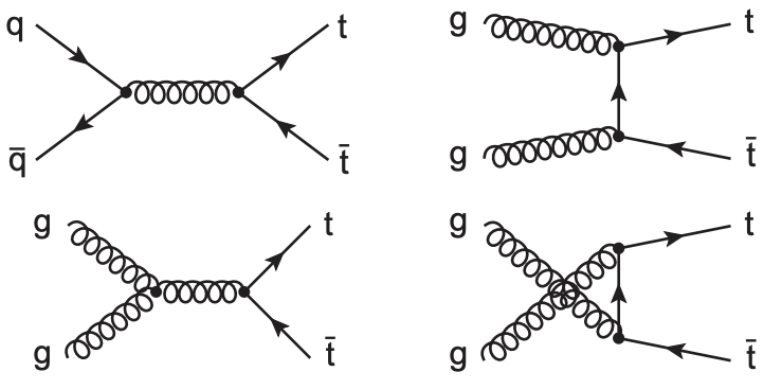

Figure 2.3: Feynman diagrams of top pair production at leading order for quark-anti-quark annihilation (top left) and gluon-gluon fusion in the s-channel (bottom left), t-channel (top right) and u-channel (bottom right) [35].

leading order (LO), next-to-leading order (NLO) and next-to-next-to-leading order (NNLO), respectively. The theoretical cross section of $t\bar{t}$ production is obtained as $\sigma_{pp\to t\bar{t}} = 830.91\ ^{+20.39}_{-29.96}$ (scale) $^{+3.92}_{-3.83}$ (PDF + α_s) pb at NNLO accuracy from the TOP++ (version 2.0) program [34], using the PDF set NNPDF3.1 (NNLO) [32] and a top mass of $m_t = 172.5$ GeV.

2.3.2 Single-top production

According to the CKM matrix single-top production predominantly proceeds via the Wtb vertex since $|V_{tb}| \gg |V_{td}|$ and $|V_{tb}| \gg |V_{ts}|$. This type of production is governed by the electroweak interaction and the leading-order processes are shown in Figure 2.5 and described below [28]:

• t-channel: in the first diagram on the left the single top quark is produced as a result of a flavour excitation of the b quark, while in the second diagram it is W-gluon fusion with $g \to b\bar{b}$ that gives rise to the top quark.

• s-channel: in the third diagram the $q\bar{q}'$ pair annihilates into a W boson that in turn produces a top and a $\bar{b}$ quark.

• tW-channel: in the fourth and final diagram a single top quark is produced together with a W boson as a gluon interacts with a b quark. Thus, this process is called associated production.

The mechanisms of single-top production described above also refer to anti-top production and Table 2.2 shows the theoretical cross sections for both top and anti-top quarks at 13 TeV in all three modes at an accuracy of NLO or NNLO in QCD, assuming a top mass of $m_t = 172.5$ GeV [36, 37]. The t-channel is the most dominant

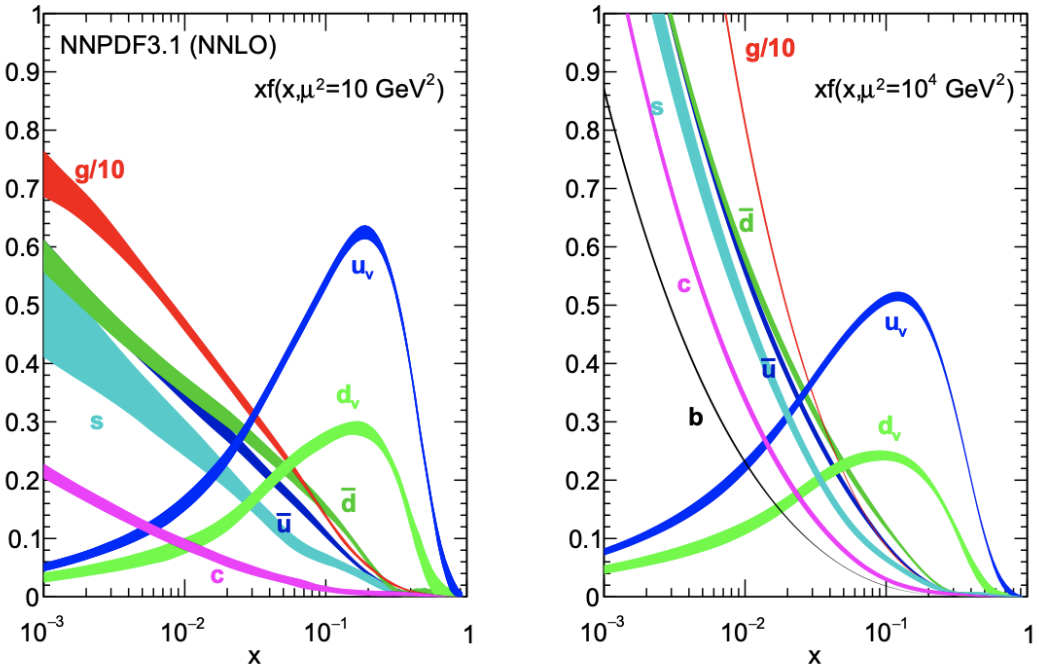

Figure 2.4: Parton distribution functions in the NNPDF3.1 set are shown for different values of the factorization scale $\mu^2 = 10\,\mathrm{GeV}^2$ (left) and $\mu^2 = 10^4\,\mathrm{GeV}^2$ (right) [32]. Valence quarks are denoted as $\mathrm{u_v}$ and $\mathrm{d_v}$. Sea quarks, which are assumed to have the same PDF for quarks and anti-quarks, are denoted as $\bar{\mathrm{u}}$, $\bar{\mathrm{d}}$, s, c and b and gluons as g.

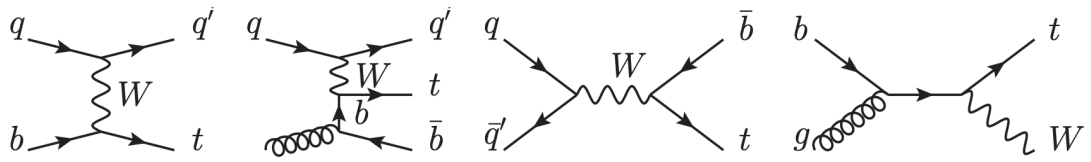

Figure 2.5: Feynman diagrams of single top production at leading order [28].

production mechanism while the s-channel is the least dominant. Top production is more likely than anti-top production in both the t- and s-channel and this stems from the simple fact that protons have two up quarks and only one down quark. It should be mentioned that although the t-channel is the most dominant single-top production mechanism, the biggest background for $t\bar{t}$ production measured in the dilepton decay channel (see Section 2.3.3) is the tW-process since this is the only mode that can give rise to two leptons.

Table 2.2: The theoretical cross sections of single-top production are shown for both top quarks in the t-, s- and tW-channel at 13 TeV for a top mass of $m_t = 172.5$ GeV. The cross section of the latter is the same for both top and anti-top and is obtained using the MSTW 2008 PDF set at approximate NNLO accuracy [36]. Cross sections of production modes via the t- and s-channel are obtained at NLO accuracy with HATHOR (version 2.1) [37].

Production mode	σ_t [pb]	$\sigma_{\bar{t}}$ [pb]
t-channel	136.02	80.95
s-channel	6.35	3.97
tW-channel	35.85	35.85

2.3.3 Top quark pair decay

As mentioned earlier in this section, the top quark decays before it hadronizes and predominantly decays to a W boson and a b quark. The W boson then subsequently decays to jets or a lepton and a neutrino as seen in Figure 2.6, which gives rise to the three decay channels of the top quark pair summarized below:

• **all-hadronic**: When both W bosons decay to $W \to q\bar{q}'$ there are only jets in the resulting final state, which is referred to as the all-hadronic channel. As seen from Figure 2.6 this occurs in 46% of cases.

• **semi-leptonic**: The lepton+jets final state constitutes the semi-leptonic decay channel and occurs in 45% of cases when one W boson decays to leptons (e.g. $W^- \to l\bar{\nu}$) and the other decays hadronically (e.g. $W^+ \to q\bar{q}'$).

• **dileptonic**: In this analysis the dileptonic channel is studied and refers to the case when both W bosons decay leptonically (e.g. $W^- \to l\bar{\nu}$ and $W^+ \to \bar{l}\nu$), which

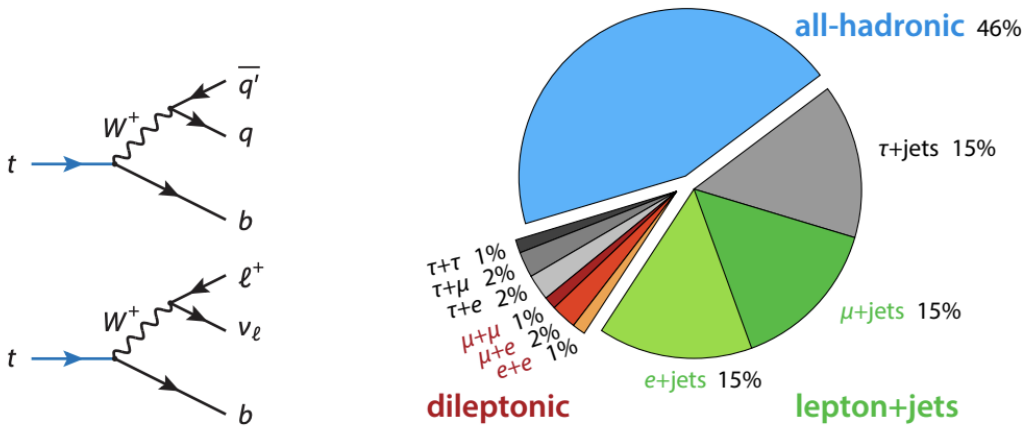

Figure 2.6: The plots on the left-hand side show the different hadronic and leptonic final states of the top quark while the plot on the right-hand side shows the branching ratios of the all-hadronic, semi-leptonic (lepton+jets) and dileptonic decay channels of the top quark pair [38].

happens in 9% of cases. In this analysis only the $e^{\pm}e^{\mp}$, $\mu^{\pm}\mu^{\mp}$ and $e^{\pm}\mu^{\mp}$ decays are selected, while decays to $\tau^{\pm}\tau^{\mp}$, $\tau^{\pm}e^{\mp}$ and $\tau^{\pm}\mu^{\mp}$ are treated as background.

Despite the fact that the all-hadronic channel might seem favourable since it has the largest branching fraction it's difficult to get a handle on due to the large background from QCD multi-jet production, mimicking the final-state event topologies of the all-hadronic $t\bar{t}$ decays. The semi-leptonic background has a similarly large branching fraction but also suffers from large backgrounds due to e.g. Z+jets production processes. However, the dileptonic channel has a significantly smaller branching ratio, but it also has a much cleaner signature, where the requirement of two leptons helps to reduce background from Z+jets in particular. Therefore, it's sometimes referred to as the golden channel and is the chosen final state in this work.

2.3.4 New top physics beyond the Standard Model

The SM of particle physics has been subject to many tests in the last 50 years but, as stated at the beginning of this section, a number of fundamental questions simply lie beyond its realm. Thus, the SM can't be the full picture and is generally thought to be a low energy approximation to a more general theory. In the previous discussion on the top quark, its unique features were explained, making it particularly interesting in the context of new physics, as it's speculated to be involved in production and decay modes of new particles at higher energy scales due to its large Yukawa coupling with the Higgs boson. Differential cross section measurements of top pair production are incredibly important as they serve as precision tests of the SM and any deviation can hint at new physics.

As previously stated, one of the biggest problems of the SM is the gauge hierarchy problem, which is also referred to as a problem of naturalness. If the SM is valid up to the Planck scale, the mass of the Higgs boson incurs quadratically divergent

terms, coming mainly from loop diagrams with top quarks, which must be added to its bare mass in addition to other higher order corrections. This "quantum field theory mass" is hard to reconcile with the experimental mass measurement of 125 GeV and many theories involving cancellations of these infinities have been suggested to address the problem. An example is the minimal supersymmetric SM (MSSM) [39], which is based on the theory of supersymmetry and attempts to bridge the gap between the electroweak scale and the Planck scale by introducing a scalar boson counterpart to every fermion within the SM. The top quark has its own supersymmetric partner, the stop quark. This so-called squark participates in loop corrections to the Higgs mass and can in theory cancel out the divergent terms coming from the top quark, which then explains the lightness of the Higgs.

Another exemplary beyond-the SM scenario is the existence of a neutral spin 1 gauge boson, called Z' [40]. This boson is thought to be produced in e.g. quark-anti-quark annihilation with a mass in the TeV range, making it a frequent character in many different new physics models [41], which attempt to explain some of the major problems of the SM, mentioned in Section 2.1. The Z' can decay to a $t\bar{t}$ pair and lead to a peak in the $t\bar{t}$ invariant mass spectrum [42].

Chapter 3

Experimental setup

The results in this work are performed using data from proton-proton (pp) collisions collected with the Compact Muon Solenoid (CMS) experiment, which is situated at the LHC and located at the "European Council for Nuclear Research" or "Conseil Européen pour la Recherche Nucléaire" (CERN) in french. Details on the LHC and the acceleration of protons can be found in Section 3.1 and further information on CMS and its sub-detectors is given in Section 3.2.

3.1 The Large Hadron Collider

The LHC [43] at CERN is a 27 km long particle accelerator located in both France and Switzerland about 100 m below ground. It takes the place of its predecessor, the Large Electron-Positron collider (LEP) [44], whose tunnel is now used for the LHC. With its ability to perform proton-proton, lead-lead or proton-lead collisions at groundbreaking centre-of-mass energies the LHC has paved the way for extraordinary discoveries and research within modern particle physics which includes the discovery of the Higgs boson in 2012 [5, 6]. The design centre-of-mass energy for proton-proton collisions is 14 TeV. In the Run 1 period of the LHC, which lasted from 2009 to 2012, proton-proton collisions reached energies of $\sqrt{s} = 7$ TeV (2009-2011) and $\sqrt{s} = 8$ TeV (2012). At the end of 2012, the LHC entered a long shutdown period needed for maintenance and upgrades of machinery in preparation for the increase to $\sqrt{s} = 13$ TeV. Operations restarted in 2015 and marked the beginning of Run 2 which lasted until 2018. The high center-of-mass energy allows for even greater insight into many existing or potentially new processes, but in the context of this analysis it also makes the LHC the ideal top quark-pair production factory, where over 100 million $t\bar{t}$ events, at CMS alone, have been produced to date, facilitating unprecedented precision in measurements of the kinematic spectra and topologies of these events.

The LHC hosts four experiments situated around the collider, namely CMS [45], ATLAS [46], ALICE [47] and LHCb [48]. ATLAS and CMS are located at opposite ends as shown in the schematic overview of the LHC in Figure 3.1. This placement is strategic and ensures that both ATLAS and CMS receive the maximum instan-

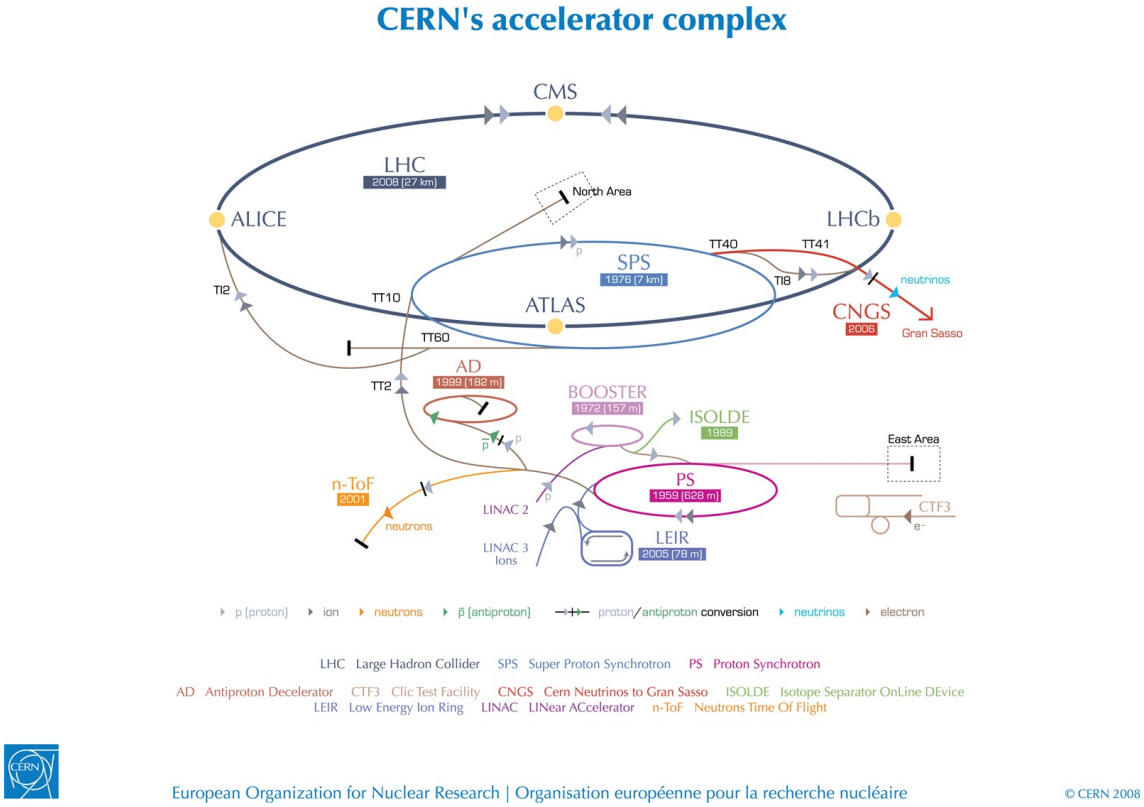

Figure 3.1: An overview of the LHC ring and the accelerator complex/booster system used to pre-accelerate protons prior to injection into the LHC [49].

taneous luminosity. Both CMS and ATLAS are general-purpose detectors, while ALICE has a focus on heavy-ion collisions with center-of-mass energies of 5.02 TeV (Run 2), in addition to pp collisions at 13 TeV, in order to study the primordial quark-gluon plasma that was present at the beginning of the universe. LHCb is dedicated to the study of the physics and interactions governing the b-quark as it's of particular interest in relation to phenomena beyond the SM like the question of the observed matter-antimatter asymmetry in the universe. The study of CP-violations in the b-quark sector at LHCb is crucial in shedding much needed light on this topic.

The protons that are injected into the LHC ring are sourced by applying an electric field to hydrogen gas. They are subsequently accelerated to 50 MeV by a linear accelerator called Linac 2 after which they are passed through a series of former particle accelerators that have been repurposed to serve as part of a booster system for the LHC in addition to delivering luminosity to a plethora of smaller experiments situated at CERN. This system consists of the Proton Synchotron Booster (PSB), the Proton Synchotron (PS) and the Super Proton Synchotron (SPS) which arrange the protons in bunches and accelerate them to energies of 1.4 GeV, 25 GeV and 450 GeV, respectively. After the SPS, protons are injected into the LHC where they reach final energies of 6.5 TeV as they go through radiofrequency cavities and special magnet configurations over several turns.

3.1.1 Luminosity at the LHC

The proton beams in the LHC are essentially trains of proton bunches with a 25 ns spacing. The number of bunches, k_b, is about 2808 and the number of protons in a bunch, N_p, is around 1.15×10^{11}. The proton beams move in opposite directions in the ring and when they are made to collide at one of the four experiments, the total number of collisions per cm^2 and per second is expressed by the instantaneous luminosity, $\mathcal{L}_{\text{inst}}$. This quantity is used to compute the number of events per second, $\dot{N}$, of a given process with cross section, σ, such that $\dot{N} = \mathcal{L}_{\text{inst}}\sigma$. The instantaneous luminosity itself is given by

$$\mathcal{L}_{\text{inst}} = \frac{\gamma f k_B N_p^2}{4\pi\epsilon_n\beta^*}F,$$

where γ is the Lorentz factor, f is the revolution frequency, ϵ_n is the normalized transverse emittance, β^* is the value of the betatron function at the nominal interaction point and F is a reduction factor based on the crossing angle of the two beams [50]. The integrated luminosity, $\mathcal{L}$, is used to express the total size of a data set collected over a given interval of time and is obtained by integrating the instantaneous luminosity such that

$$\mathcal{L} = \int \mathcal{L}_{\text{inst}}\text{dt}.$$

The total number of events of a given process in the collected sample is then given by $N = \mathcal{L}\sigma$. The design value of the instantaneous luminosity is $10^{34}\,\text{cm}^{-2}\text{s}^{-1}$ [43] and this has already been exceeded by a factor of 2. In this work Run 2 refers to the data collected between 2016 and 2018 which corresponds to an integrated luminosity of 137.6 fb^{-1}.

3.2 The Compact Muon Solenoid

The CMS detector [45, 50] is designed as a general purpose experiment for observing and reconstructing all kinds of particles produced in hard pp collisions, and consists of different sub-detectors dedicated to the identification and reconstruction of particles. These sub-detectors are organized in concentric barrel and end-cap layers around the collision/interaction point of the protons and a schematic overview is shown in Figure 3.2. The pp interaction point is located at the very center and the plethora of particles that emerge from this point first traverse through the pixel detector and silicon tracker with which one can reconstruct charged particles and their trajectories and momenta. Electrons and photons then develop electromagnetic showers as they go through the lead-tungstate electromagnetic calorimeter (ECAL), while hadrons mainly deposit their energy in the brass and scintillator hadronic calorimeter (HCAL). Very forward calorimeters are needed in order to extend the pseudo-rapidity coverage of the barrel and end-caps. All the aforementioned systems, with the exception of one HCAL component, are housed in a super-conducting solenoid that generates a field of 3.8 T. Muons are the most penetrating particles

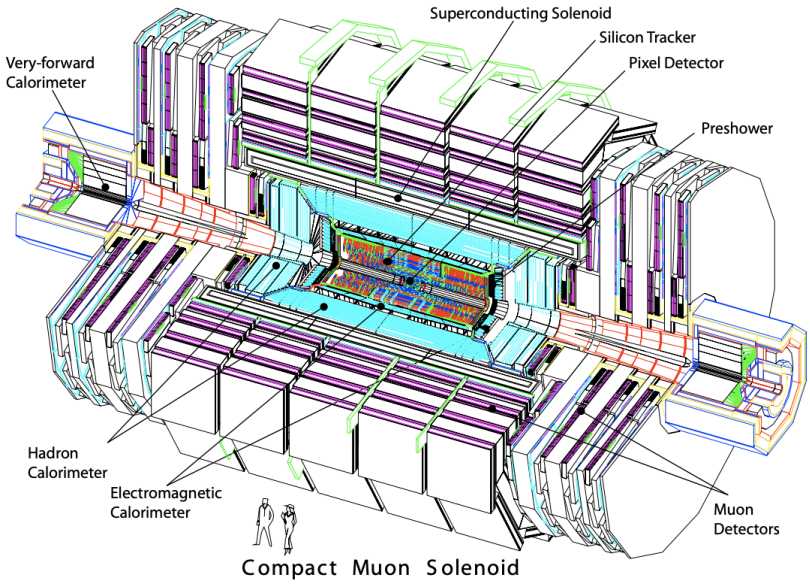

Figure 3.2: A schematic overview of the CMS experiment and its sub-detectors [50].

and traverse all sub-detectors until they reach muon stations interspersed with the iron yoke that serves as a return-flux for the magnet.

3.2.1 Coordinate systems and commonly used quantities

The coordinate system used at CMS is shown in Figure 3.3 and is arranged such that the origin is at the nominal interaction point, which is the average position of the beam crossing spot over many collisions. The positive z-axis points in the direction-of-flight of the proton beam moving in the counter-clockwise direction. The y-axis points vertically upwards, while the x-axis points towards the centre of the LHC ring. The coordinate system is also defined in terms of the polar coordinates (r, ϕ, θ), where $r = \sqrt{x^2 + y^2}$ is the radial distance from the origin, ϕ is the azimuthal angle measured from the positive x-axis in the xy-plane and θ is the polar angle measured from the positive z-axis.

Pseudorapidity and rapidity are used as alternative expressions of the polar angle θ and are given by

$$\eta = -\ln\left(\tan\frac{\theta}{2}\right) = \frac{1}{2}\ln\left(\frac{|\vec{p}| + p_z}{|\vec{p}| - p_z}\right)$$

and

$$y = \frac{1}{2}\ln\left(\frac{E + p_z}{E - p_z}\right),$$

respectively, where $|\vec{p}|$ is the magnitude of the three-momentum $\vec{p} = (p_x, p_y, p_z)$ and p_x, p_y and p_z are the momentum projections along the respective axes. The pseudorapidity depends on the polar angle only, while rapidity is dependent on the

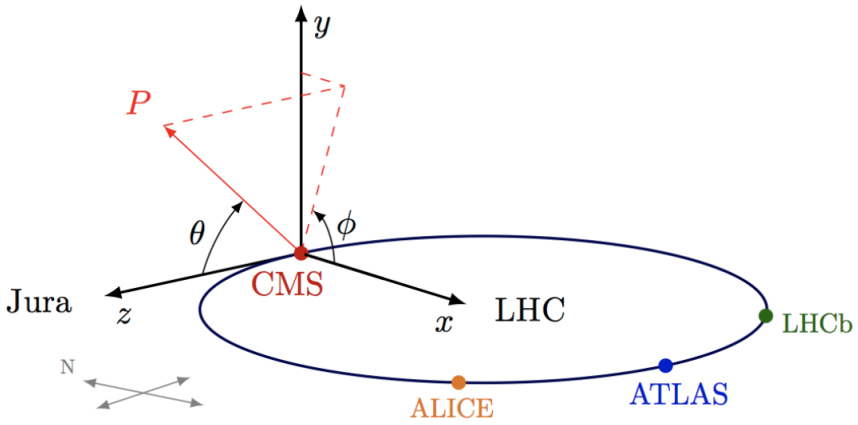

Figure 3.3: The Cartesian and polar coordinate systems used at the CMS experiment [51].

energy, E, of the particle. For particles that travel close to the speed of light or have negligible masses one can write $E \approx |\vec{p}|$ such that $\eta \approx y$. The advantage to using either pseudorapidity or rapidity instead of the polar angle is that differences between the quantities for particle 1 and particle 2 (i.e. $\Delta\eta = (\eta_1 - \eta_2)$ and $\Delta y = (y_1 - y_2)$) are invariant under a Lorentz boost along the z-axis. Other expressions used or referenced in this work include the transverse momentum and energy which are defined in terms of the x- and y-axis projections of $\vec{p}$ and $\vec{E}$, respectively, such that

$$p_{\mathrm{T}} = \sqrt{p_x^2 + p_y^2}$$

and

$$E_{\mathrm{T}} = \sqrt{E_x^2 + E_y^2}.$$

The expression "missing transverse energy" is used when talking about the p_{T} imbalance in the transverse plane which is associated with the undetectable neutrinos and is denoted by $E_{\mathrm{T}}^{\mathrm{miss}}$ (see Section 5.7.5 for further details).

3.2.2 The magnet

The magnetic field at CMS is generated by a 220 t superconducting solenoid made out of niobium-titanium (NbTi) with a length of 12.5 m and a diameter of 6 m. The solenoid houses all tracking and calorimeter sub-detectors and is designed to reach a field of 4 T inside this volume although during data-taking it operates at 3.8 T. In order to achieve a field of this strength the solenoid has been specially designed to have a 4-layer winding and is additionally surrounded by a 10000 t return-flux iron yoke. Four muon stations are interspersed with the yoke in both the barrel and

endcaps and the field strength in this region outside the solenoid is 2 T with reversed sign. One can determine the charge of a particle by the direction of its trajectory and its transverse momentum can be determined by equating the Lorentz force with the centripetal force and using the information on the curvature of the trajectory.

3.2.3 Tracking detectors

The CMS tracking system is designed to perform precise measurements of the momenta and impact parameters of charged particles from the trajectories they leave behind in the detector, so-called tracks, where the impact parameter refers to the minimum spatial distance of a track with respect to its primary point of origin, i.e. the primary vertex (see Section 5.6), in e.g. the transverse and longitudinal projections. In addition, the tracking system is vital for reconstructing primary and secondary vertices, where the former refers to the proton-proton collision point of interest and the latter refers to the decay of relatively long-lived particles like the ground states of hadrons containing b-quarks. The cylindrical tracker surrounds the interaction point with a length of 5.8 m and a diameter of 2.6 m. It consists of two sub-systems, namely the pixel detector and the silicon strip detector, which are subjected to the highest particle flux out of all sub-systems. Thus, special considerations were made in their design. For an instantaneous luminosity of 10^{34} cm^{-2}s^{-1} the tracking system is bombarded with around 1000 particles produced in more than 20 proton-proton interactions in a given bunch crossing every 25 ns. This means that the tracking modules have to be able to withstand high irradiation for years on end and further necessitates a high granularity and response time of the modules to achieve the desired resolutions. However, finely segmented modules in turn need a high electrical power which requires sufficient cooling capabilities. The latter introduces a lot of extra material which alter the tracks as the particles undergo multiple scattering, photon conversion, bremsstrahlung etc., so a compromise is made between a highly granular detector and the least obstruction to the particle flow. In order to obtain a particle occupancy of $\leq 1\%$, pixel sensors have to be used at a radius of < 10 cm from the interaction point while silicon strip detectors are sufficient at greater radii. In 2016, prior to an update of the tracker, the pixel detector consisted of 1440 modules, which correspond to 66 million pixels, spanning a total area of $1\,\mathrm{m}^2$. The silicon strip detector consists of 15148 modules with 9.3 million strips covering an area of $198\mathrm{m}^2$ [52]. This makes CMS the largest silicon tracker ever built.

A schematic overview of the tracker is shown in Figure 3.4. The pixel detector has three barrel layers (referred to as BPIX) in addition to two disks on each side of the detector (referred to as FPIX), which are situated between $4.4 < r < 10.2$ cm and $34.5 < |z| < 46.5$ cm, respectively. An upgrade was done in the end of the year shut down period in 2016/2017 where an extra layer was added in the BPIX and an extra disk was added on either side of the FPIX [53], which means that the pixel detector comprises 1856 modules in 2017 and 2018 [54]. Moreover, the inner layers and disks were moved closer to the interaction point to enhance the reconstruction of tracks in this region and the resolutions are now 1.5% in p_T and 20-75 μm in the transverse impact parameter for non-isolated particles with $1 < p_\mathrm{T} < 10$ GeV and

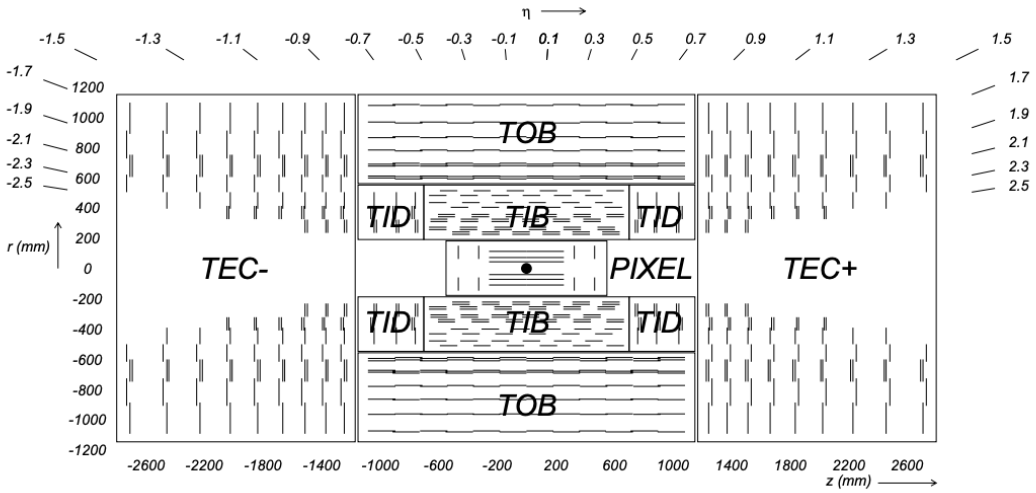

Figure 3.4: A schematic overview of the CMS tracker showing all sub-systems [45]. A detector module is indicated by a line and double lines are used to illustrate modules that are placed back-to-back in order to record stereo hits from particles. In an end-of-year upgrade in 2016/2017 an extra layer was added to the pixel barrel and an extra disk was added on either side of the forward pixel (not shown in figure).

$|\eta| < 3.0$ [54].

The silicon strip detector consists of several sub-systems [55]. The tracker inner barrel (TIB) is housed in the region between $20 < r < 55$ cm and has 4 barrel layers, while the tracker inner disks (TID) are grouped into sets of three on each side of the detector and situated at $58 < |z| < 124$ cm. The tracker outer barrel (TOB) surrounds the aforementioned systems with 6 barrel layers between $55 < r < 116$ cm, and the tracker endcaps (TEC) make up the final sub-system sitting at $124 < |z| < 282$ cm. The TEC has 9 disks on opposite ends of the detector, which brings the pseudorapidity coverage up to $|\eta| = 2.5$.

The pixels in the BPIX and FPIX have a size of $100 \times 150\ \mu\text{m}^2$ in $r\phi \times z$ and a sensor thickness of 285 μm [53], while the silicon strips in the TIB, TID and TEC (inner four rings) are 320 μm thick and the ones in the TOB and outer three TEC rings are 500 μm. The distance between adjacent strips is called the pitch and varies from 80 μm to 205 μm [55]. The tracker has a position uncertainty of $\mathcal{O}(0.1)$ mm as a result of its mechanical installation whereas the design value of the hit resolution is $\mathcal{O}(0.01)$ mm [54]. Naturally, the optimal spatial alignment is smaller than the hit resolution and corrections are therefore derived for the position, orientation and surface deformations of the modules, measuring these parameters with high precision using large sets of cosmic tracks and tracks of events in minimum bias data.

3.2.4 The electromagnetic calorimeter

The hermetic and homogeneous electromagnetic calorimeter (ECAL) is made out of lead tungstate ($PbWO_4$) crystals that act as scintillators when electrons and photons

traverse the ECAL and undergo bremsstrahlung. The choice to use $PbWO_4$ is based on the high density of the material (8.3 g/cm^3) and the short radiation length (X_0 = 8.9 mm) which also implies a small Molière-Radius of 2.2 cm. This means that the emerging shower from an incident electron or photon is contained within a reasonable volume and can be resolved with a high granularity. Furthermore, 80% of the energy of the photon or electron that initiated the shower is deposited in the ECAL within 25 ns which implies a very fast response time. Another important feature of this material is its radiation hardness which is necessary in order to withstand effects on performance from continued exposure to highly ionizing particles.

The ECAL is situated inside the magnetic solenoid and surrounds the tracking system. The calorimeter comprises a barrel component (EB) which has an end-cap (EE) on either side to cover the fiducial region. The EB is split into two half-barrels with 18 supermodules each and takes up a total volume of 8.14 m^3. A total number of 61200 crystals in the EB provide a pseudorapidity coverage in the range $0 < |\eta| < 1.479$. An individual crystal is 23 cm long (25.8 radiation lengths) and tapered such that it has a cross section of 22×22 mm^2 in the front and 26×26 mm^2 in the rear.

Each endcap has a total number of 7324 crystals which are organized into 5×5 structures called supercrystals. Similar to the EB, the crystals in the endcaps are tapered but with dimensions of 28.62×28.62 mm^2 (front), 30×30 mm^2 (rear) and a total length of 22 cm which corresponds to 24.7 radiation lengths. The EE has a total volume of 2.90 m^3 and is situated at $|z| = 314$ cm from the interaction point, however, when the magnetic field is switched on at full strength this distance decreases by 2.6 cm. The total coverage of the EE corresponds to a pseudorapidity range of $1.479 < |\eta| < 3.0$.

The electromagnetic preshower (ES) detector is situated directly before the EE and comprises a 2-layer sampling calorimeter which uses lead absorber plates and silicon strip sensors as the scintillating medium. The ES covers a pseudorapidity range of $1.653 < |\eta| < 2.6$ and the aim is to detect neutral pions and simultaneously distinguish electrons from minimum ionizing particles. Moreover, the ES has a finer granularity and this facilitates better position determination of electrons and photons.

Information from the ECAL and tracker have been combined to determine the energy scale and resolution for electrons (photons) originating from the decay process $Z \to ee$ ($Z \to \mu\mu\gamma$) using Run 2 data [56]. The measured energy resolution in the studied E_{T} range of 10 to 50 GeV was found to be 2 to 5% depending on the pseudorapidity and energy loss due to bremsstrahlung. The uncertainty on the measured electron and photon energy scale was found to be smaller than 0.1% (0.3%) in the barrel (endcaps) within the same range of energies.

3.2.5 The hadronic calorimeter

The hadronic calorimeter (HCAL) surrounds the ECAL and is not homogeneous but instead uses sampling layers of plastic scintillator tiles connected to wavelength-

shifting (WLS) fibres for read-out. Absorber plates made of brass alloy are used in between the active medium, where the material choice is based on the fact that it's non-magnetic and its short interaction length facilitates a good containment of the shower within the magnet. The hadronic barrel (HB), endcap (HE), very forward (HF) and outer (HO) sub-systems constitute all HCAL calorimetry, where the latter is the only part not situated inside the magnet. A quarter of the HCAL and its components are shown as a schematic overview in Figure 3.5.

The HB is divided into two half-barrels that each consist of 18 wedges oriented at 20° angles in ϕ. A single wedge consists of 17 scintillator layers interleaved with 15 brass absorber layers and 2 steel layers on either side which are needed for mechanical support of the structure. The first scintillator layer is situated directly next to the ECAL in order to sample showers from low-energy hadrons. The individual scintillator tiles in a layer are segmented in $\Delta\eta \times \Delta\phi = 0.087 \times 0.087$ and are connected to single WLS fibres which are then spliced with clear fibres, facilitating optical connections to tiles in different layers. The fibres that belong to the 17 scintillator tiles with the same projection are then connected to form a read-out tower. There is a total of 2304 towers in the entire HB structure which leads to a pseudorapidity coverage of $|\eta| < 1.4$. The hadron end-cap (HE) is interlocked with the HB and has a similar structure covering a pseudorapidity range of $1.3 < |\eta| < 3.0$.

The outer hadron calorimeter (HO) provides extra scintillator layers situated outside the magnet and serves as a tail-catcher for hadron showers that leak into the muon barrel system. Thus, the HO helps to reduce the tails in the energy resolution and improve measurements of $E_{\mathrm{T}}^{\mathrm{miss}}$. A total of 5 rings situated at η values of -2, -1, 0, 1 and 2 make up the HO structure. The central ring at 0 consists of two scintillator layers situated on either side of an iron absorber layer. The remaining rings have 1 scintillator layer each and the HO provides a total coverage of $|\eta| < 1.26$.

The hadron forward (HF) calorimeter is situated at $|z| = 11.2$ m from the interaction point and consists of a steel absorber with a depth of 1.65 m. Grooves parallel to the beam line are drilled in a 5 mm square grid and contain quartz fibres with a diameter of 0.6 mm. These fibres generate Cherenkov light from hadron showers in the pseudorapidity range of $3.0 < \eta < 5.0$ that is then picked up by photon multipliers.

The granularity of the different HCAL components described above has been chosen such that the sampling of hadron showers yields a similar energy resolution as a function of $E_{\mathrm{T}}^{\mathrm{miss}}$ across the entire structure. When combining information from the tracker and calorimeters, the energy resolution for hadronic jets is typically 15%, 8% and 4% given a p_{T} of 10 GeV, 100 GeV and 1 TeV, respectively. If only the ECAL and HCAL are used the corresponding energy resolutions are 40%, 12% and 5% [57].

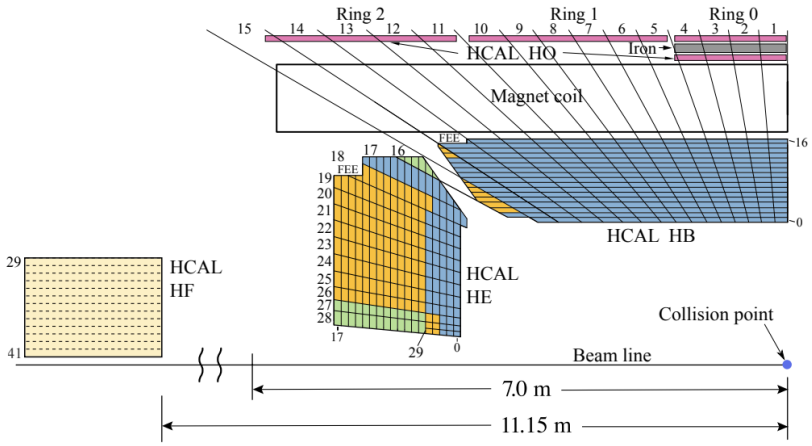

Figure 3.5: An illustrative sketch showing one quarter of the HCAL and the placement of the four components (HB, HE, HF and HO) that comprise its structure [57].

3.2.6 The muon system

The muon system at CMS serves to identify muons and reconstruct their momenta but it's also an integral part of the hardware-based L1 trigger system [58]. It comprises one barrel section and two planar end-cap regions which are all organized into structures with four muon stations interspersed with the steel flux return yoke as shown in Figure 3.6. In the barrel these stations consist of muon drift chambers (DTs) complemented by resistive plate chambers (RPCs) while the end-cap regions use cathode strip chambers (CSCs) and RPCs. The pseudorapidity coverage is $|\eta| < 1.2$ for DTs, $0.9 < |\eta| < 2.4$ for CSCs and $|\eta| < 1.9$ for RPCs. Hence, the muon system covers the full solid angle with no gaps in pseudorapidity. The different choices of muon chambers in the barrel and end-cap regions are based on the different environments. The magnetic field generated by the solenoid and saturated by the steel flux return yoke remains uniform in the barrel. Additionally, the barrel chambers are exposed to a relatively low muon rate and a low background induced by neutrons, which justifies using standard drift cells. The opposite is true for the end-caps where the environment necessitates the faster response time, finer segmentation and resistance to radiation provided by the CSCs. The RPCs are used mainly to assist in the trigger response of the DT and CSC sub-systems as they have a lower spatial resolution but are overall much faster. The muon system can operate independently from the other sub-systems but the best momentum resolution is obtained when the inner tracker is used in addition for track reconstruction. The reconstructed hit spatial resolution is typically 50 to 300 μm and the muon timing resolution is ≈ 1.4 ns.

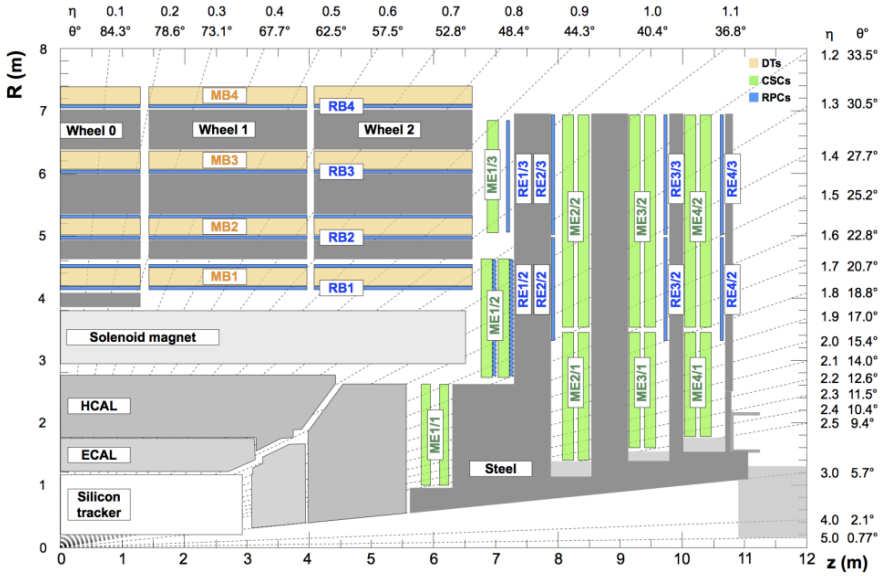

Figure 3.6: An illustrative sketch of one quadrant of the muon system, showing how its DT, CSC and RPC components are interspersed with the return yoke of the magnetic solenoid. The cross section of the system is depicted in R-z, which corresponds to the r and z coordinates introduced in this section [58].

3.2.7 Event triggering and data acquisition systems

Proton-proton collisions take place every 25 ns within the CMS detector. This corresponds to a bunch crossing frequency of 40 MHz and an expected rate of 10^9 interactions per second at design luminosity. This is far beyond what can be stored on archival media which can maximally record 10^3 interactions per second. However, not all collisions lead to interesting physical processes i.e. some may be elastic while others don't involve any considerable exchange of p_{T} but there is still an abundance of high-p_{T} interactions due to the center-of-mass energy involved. An advanced trigger system is in place to identify the most interesting processes and consists of detector electronics, Level-1 trigger processors (L1), a readout network and a processor farm for High-Level triggers (HLT).

The L1 trigger system relies on information from the calorimeters and muon chambers. The presence of primitive trigger objects such as photons, electrons, muons and jets above set E_{T} and p_{T} thresholds is required for an L1 accept decision. The word primitive refers to the fact that the objects have been reconstructed with reduced-granularity and reduced-resolution. Information on the global sums of E_{T} and $E_{\mathrm{T}}^{\mathrm{miss}}$ is also taken into account in the accept/reject decision of an event. The L1 trigger hardware was upgraded before the start of Run 2 to address the challenges of the higher center-of-mass energy and increased luminosity [59]. Existing algorithms were also improved to exploit e.g. muon isolation. By applying loose event selection criteria based on the above, the L1 trigger system reduces the trigger rate to 100 kHz with a latency of about 3.2 μs. The front-end electronics from the calorimeters and muon chambers will send signals to the services cavern where the Level-1 trigger logic is stored and the data that has been stored in a buffer in the meantime is then

either accepted or rejected in about 1 μs.

After an event has passed the L1 trigger, it is sent to the HLT processor farm through a network of front-end readout buffers. Here the event reconstruction is refined but the main goal of the HLT is not to reconstruct the whole event but rather only objects and regions that are needed. An event has to be rejected as soon as possible and therefore information is used in stages for the partial reconstruction of an event; data gathered from the muon chambers and calorimeters are used first followed by the tracker pixel and finally a full event reconstruction is performed. In this way the trigger rate is reduced to ~ 1 kHz for offline analysis.

The rate of both the L1 and HLT systems can be adjusted by using a prescale which limits the number of events. The complete sequence of L1, HLT and the trigger prescale constitutes what is known as a trigger path.

Chapter 4

Monte Carlo simulation

Monte Carlo generators play a key role in particle physics as they allow us to test and compare our understanding of the phenomenological models governing the physical processes that are being probed in the LHC experiments. They also help shed light on any remaining discrepancies between the simulations and data. The full simulation of a pp collision event and the cascade of particles associated with it is performed in a series of steps as illustrated in Figure 4.1. The hard interaction is simulated first as explained in Section 4.1, while the parton shower that models further QCD emissions at lower transverse momenta is described in Section 4.2. The shower modelling stops when the decay processes and emissions of quarks and gluons involved become non-perturbative in which case all the coloured particles start to hadronize as described in Section 4.3. Additional activity resulting from other interactions in the pp collision is referred to as the underlying event and further details are provided in Section 4.4. Information on the generators used to simulate all of the above for the purposes of this analysis is given in Section 4.5, while finally, in Section 4.6 it's explained why one must put the generated particles through a full detector simulation.

4.1 Hard interaction

As protons collide it's really their constituent partons that take part in what is known as the hard interaction. Annihilation of quarks and anti-quarks as well as gluon-gluon fusion can both facilitate the production of a top-quark pair as previously mentioned, although the latter is the most dominant at the LHC. Several pp collisions take place during one bunch crossing, with most of them being soft in nature, thus, it's only the one with the highest exchange of p_{T} that is of interest to physics and in case of $t\bar{t}$ production the partons must have momenta that sum to an invariant mass of at least $2m_t$, where m_t denotes the top mass. As stated in Chapter 2, the momenta of the two initial state partons are determined by PDFs and as the interaction takes place in the high energy regime, where $\alpha_s \ll 1$, one can compute the matrix elements (ME) for the process perturbatively. The accuracy of the calculation is determined by the order of α_s and is typically computed at either leading order (LO), next-to-leading order (NLO), next-to-next-to-leading

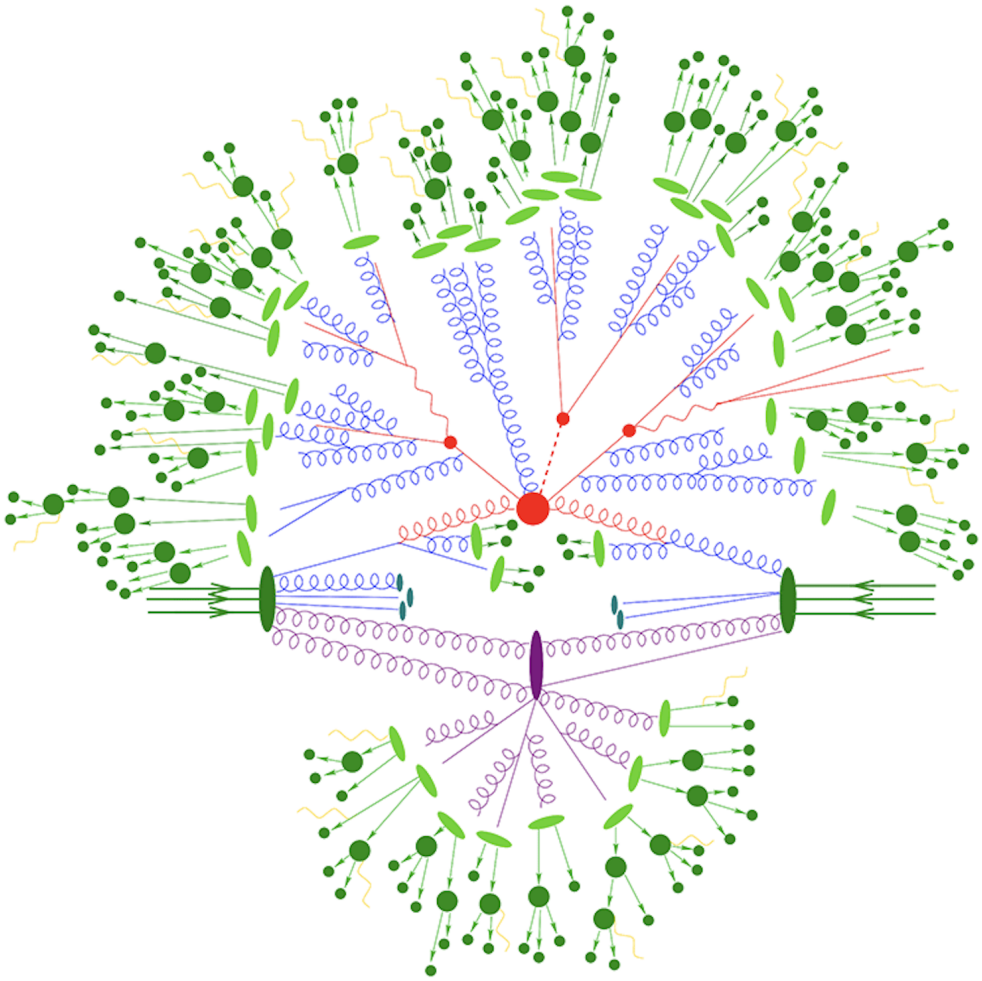

Figure 4.1: An overview of the steps involved in MC simulations [60]; the hard process is shown in red, the parton shower modelling is illustrated in blue, the hadronization process is shown in green and the underlying event is depicted in purple.

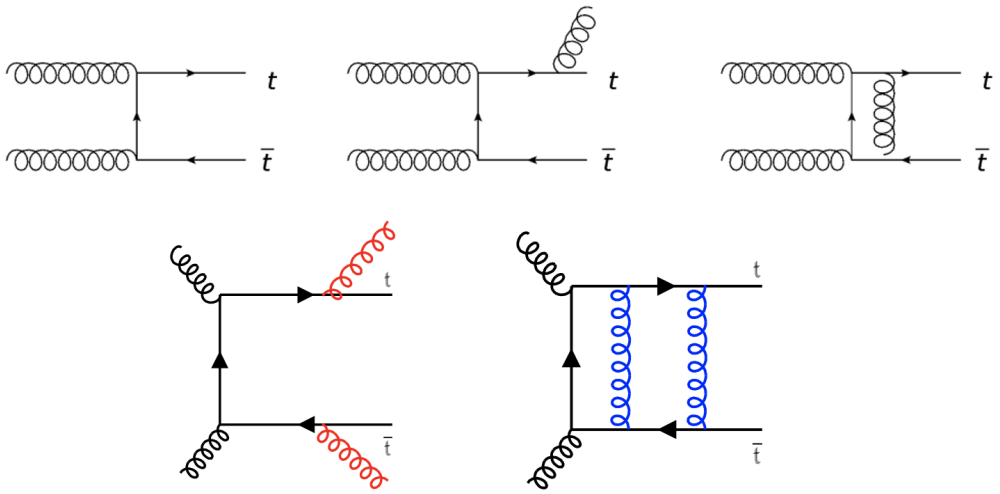

Figure 4.2: The first diagram in the upper row illustrates a leading order (LO) process of $t\bar{t}$ production in pp collisions at the LHC. The final two diagrams in the upper row depict exemplary next-to-leading order (NLO) processes, while the two diagrams in the bottom row show processes at next-to-next-to-leading order (NNLO).

order (NNLO) or next-to-next-to-leading-logarithm order (NNLL). Here LO, NLO and NNLO can also be used interchangeably with the terms first-, second- and third-order, respectively. The nth order of the ME calculation comprises both real and virtual emissions such that $n_{\text{virtual}} + n_{\text{real}} \leq n - 1$. Illustrative Feynman diagrams of the LO, NLO and NNLO processes that contribute to $t\bar{t}$ production are shown in Figure 4.2. These diagrams correspond to orders $\mathcal{O}(\alpha_s^2)$, $\mathcal{O}(\alpha_s^3)$ and $\mathcal{O}(\alpha_s^4)$, respectively, for the calculation of the partonic cross section $\hat{\sigma}_{ij\to t\bar{t}}$ (see Section 2.3.1).

4.2 Parton shower

The cross section of the partonic interaction can be computed in a fixed order model at the matrix element level, and only additional higher order effects must be simulated through so-called parton showers. Here the word shower is used as a descriptive term of the cascade of particles that develops from so-called initial and final state radiation, denoted by ISR and FSR, respectively, where initial and final refer to radiation taking place before or after the hard interaction. Emitted photons undergo pair production, while emitted gluons can split into two gluons or decay into quark pairs, which can subsequently radiate additional gluons, thereby continuing the successive splitting. The evolution of the shower depends on the scale, q, which is often defined as either $q = p_{\text{T}}$, where p_{T} is the exchanged four-momentum in the splitting, or $q \approx E^2\theta^2$, where E is the energy of the parent (before) and θ is the opening angle after the splitting [61]. The two evolution scales refer to p_{T}-based and angular-ordered splittings, respectively. The maximum value of the evolution scale,

$Q_{\max}$, is chosen in the generator settings and is set to Q, which is the scale of the hard interaction and coincides with the standard choice of the renormalization scale, $\mu_r = Q$. An iterative computation of q can then be done for successive emissions. Provided that $q_1 > q_2$ holds for parton 1 and parton 2, the Sudakov form factor [61] can be solved for q_2 given q_1, and if the former is above some defined cut-off scale, Q_0, parton 1 splits into parton 2, which now has energy q_2. The scale Q_0 marks the minimum of the evolution scale, which means that it's no longer possible to resolve emissions from their parents at this stage. It's also set as an initial parameter in the MC generator and is usually $Q_0 \sim 1$ GeV, which is where splittings become non-perturbative. The shower stops when the partons in the cascade no longer have enough energy to emit additional partons or values of q are below the cut-off, at which point hadronization occurs.

4.3 Hadronization

Hadronization describes the process of hadron formation after the parton shower stops. The coloured quarks and gluons that remain at the end of the shower cannot exist freely by themselves and must group into colour-neutral bound states called baryons and mesons. The underlying principle behind this is called colour confinement (see Chapter 2). Different methods exist for modelling hadronization in event generators but today mainly two models are used; namely the Lund string model [62] and the cluster model [63]. Both models are considered equally suitable for the purpose, but it's interesting to note that their philosophical approach to hadronization differs. The Lund string model values a good modelling of non-perturbative dynamics, whereas the cluster model is based on the idea that as long as the perturbative physics is correctly modelled any model for the hadronization will suffice. The fundamental principles behind these models are outlined in greater detail below [64]:

• **Lund string model**: In this model hadronization is governed by linear confinement. At small distances coloured objects like quarks and gluons have asymptotic freedom but as the distance between them gets larger, interactions among gluons generate a self-attracting field, which leads to a colour-flux that reassembles a tube or string, as seen in Figure 4.3. This field is what confines colour and as the quark and anti-quark in a pair continue to move away from each other, the potential energy stored in the field is increasing linearly, which can be described by $V = kr$, where $k \approx 1\,\text{GeV/fm}$ and r is the separation distance between the quarks [1]. The string analogy also applies to the dynamics of the colour-flux field between the quarks. A string that is continuously stretched will eventually break. In terms of the colour-flux picture this point is reached when there is enough energy to produce a new quark and anti-quark. As the newly formed quark and anti-quark pair up with the outer quarks, two new strings are formed that undergo the same process of stretching and breaking until the quarks in the system lose momenta and no further partitions are possible. Gluon or photon radiation from the original quark pair will lead to a kink in the colour-tube between the quarks as shown in Figure 4.3. It's important to note that the model is safe against both collinear and infrared (soft) gluon emissions, as

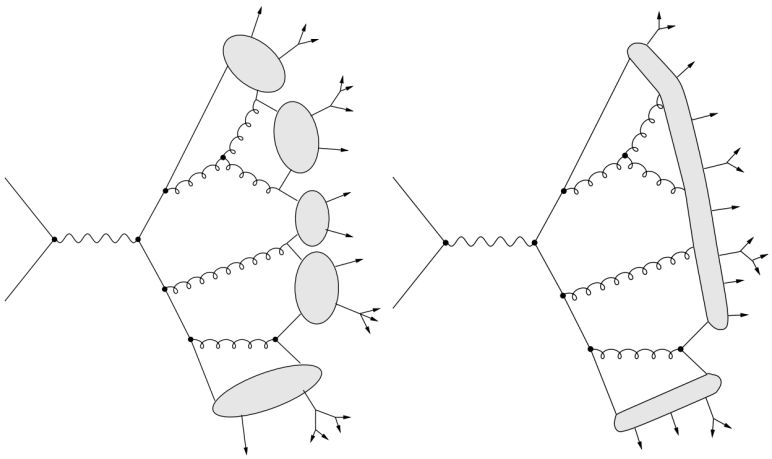

Figure 4.3: An illustration of the two hadronization models. The cluster model is shown on the left and the Lund string model is depicted on the right [66].

they will only lead to a small kink that can be neglected.

• **Cluster model**: In this model the principle of preconfinement is used to model the hadronization [65]. First, gluons present at the end of the parton shower are forced to decay into quark pairs non-perturbatively. The idea in preconfinement is then that adjacent quarks will form colour-singlet states called clusters, which implies that those quarks came from the same evolution scale, i.e. they were already preconfined to a certain part of the phase space. The unique thing about this model is that the invariant mass spectrum of the resulting clusters is independent of the energy scale of the hard interaction. However, it does depend on the cut-off scale, Q_0. The clusters are subsequently made to decay into hadrons.

4.4 Underlying event

The underlying event constitutes all activity in the simulated pp collision that is not a result of the hard interaction itself or the associated parton shower [61]. Such additional activity primarily comes from multiple parton interactions (MPI) associated with collisions of beam partons with high p_{T} exchange, that are separate from the hard interaction. Some beam partons don't exchange any significant p_{T} and are therefore known as beam-beam remnants (BBR). They make up the remainder of the additional activity, as they must undergo hadronization due to the principle of colour confinement. Therefore, BBR also contributes to the jet-activity in the event.

When modelling the non-perturbative dynamics of the underlying event one must achieve the proper colour-flow in the hadronization by using dedicated colour reconnection schemes [67]. In the Lund string model, a dipole consists of $q\bar{q}$, $q\bar{q}g$ or $q\bar{q}\gamma$ and the dipole field between colour and anti-colour form a pictorial string (with a kink if involving gluons or photons). The dipoles are viewed in terms of p_{T} as

consisting of a radiator and recoiler, and in a model based on MPI, the strings of dipoles with lower p_{T} are added to the strings of dipoles with higher p_{T}. This is done in a way that minimizes the overall string length between them. In the cluster model of hadronization, the colour reconnection is often based on the Eikonal model [68]. It's important to note that the colour reconnection model has obvious and significant consequences for the jet multiplicity and jet p_{T} in the event, which is in general due to the non-perturbative processes and complexity involved and, thus, the underlying event must be tuned to data.

4.5 Monte Carlo generators

This section contains a brief summary of each generator used to simulate the signal and background processes in this work (see Chapter 5 for a description of their final states). The **Pythia8** generator [67] is written to be a self-contained program for several types of collisions between leptons, photons, heavy ions and/or hadrons, and thus it's used to simulate e.g. pp collisions at the LHC. The event generation encompasses all steps from the hard process to hadronization, including the underlying event modelling. The hard interaction can be computed at LO or NLO accuracy in QCD depending on the process, but it's common practice to interface Pythia8 with another program for this step. A special feature of Pythia8 is precisely its modelling of ISR, FSR and MPI using a single common sequence, where the parton shower evolution follows a p_{T}-based ordering. The colour reconnection in the modelling of the underlying event is performed with the MPI-based model, and the hadronization is based on the Lund string model.

The **Herwig7** generator [69] is similar to Pythia8 in the sense that it's a multipurpose particle physics generator suited for collisions between leptons and/or hadrons, and thus, also for pp collisions. It's also frequently interfaced with other generators that perform the matrix element calculations of the hard process. However, it should be noted that in Herwig7, virtually any SM process can be simulated with LO or NLO corrections in QCD at the matrix element level, although external libraries are needed to perform the amplitude calculations for the latter. The hard process is also simulated together with parton showers, and contrary to Pythia8, these are based on both angular and p_{T}-based ordering. The cluster model is used to simulate the hadronization process and MPI colour reconnection in the underlying event is based on the Eikonal model.

The name **Powheg (version 2)** [70–72] is an abbreviation for "Positive Weight Hardest Emission Generator". It gets its name from the fact that it produces positive event weights and generates the highest p_{T} emission first when simulating the hard process of an arbitrary process. The matrix element computation is performed at NLO and takes into account spin correlations for top pair production. Contrary to Pythia8 and Herwig7 it's not self-contained and needs to be interfaced with another program for the simulation of the parton shower, hadronization and underlying event. However, Powheg (version 2) performs already a parton shower like

correction to the NLO calculation, and that is particularly relevant for emissions at low p_{T}. The strength of POWHEG (version 2) is that it can be interfaced to shower Monte Carlo (SMC) models that use either p_{T}-ordering or angular-ordering to describe the shower evolution scale as long as a p_{T} veto is in place for the latter. The p_{T} veto means that the SMC model vetoes emissions with higher p_{T} than that of the hardest emission of POWHEG (version 2). Both PYTHIA8 and HERWIG7 fulfill these requirements as do any programs compliant with "Les Houches Accord" which is the standardized interface for event generators. The parameter that regulates the damping of high p_{T} real emissions in the PYTHIA8 parton shower with respect to the first real emission in the POWHEG (version 2) matrix element is called h_{damp}.

The **MG5_aMC@NLO** [73] generator is also capable of simulating an arbitrary hard process at LO or NLO accuracy at the matrix element level. Computations at the former level of accuracy are based on tree-level processes, while the latter also accounts for one-loop amplitudes although it neglects double-loops. The hard interaction performed with MG5_aMC@NLO can be matched to parton showers, simulated with e.g. PYTHIA8. In general for the matching procedure, the parton shower approximation is first subtracted from the exact NLO calculation and the resulting events are then input to the parton shower simulation. The MG5_aMC@NLO calculation used in the analysis generates the hard matrix element separately for processes with different numbers of additional partons, at LO with up to four and at NLO with up to two. So-called jet merging is applied when sampling the parton shower. Samplings are vetoed if they alter the partonic jet configuration and create extra jets that compete with NLO processes. The jet-merging for LO (NLO) is calculated with the MLM [74, 75] (FXFX [76]) matching schemes. Finally, it should be noted that MG5_aMC@NLO also preserves off-shell effects and spin correlation for processes involving particles that can't be observed directly, but that are instead reconstructed from their daughter particles. This is the case for e.g. $t\bar{t}$ production, and unlike the other generators mentioned so far, this is done using a separate program called MADSPIN [77].

4.6 Detector simulation

The final state particles in the event generation must pass through a complete simulation of the CMS experiment in order to best describe the recorded data. This is accomplished by means of the tool kit GEANT4 [78], which is an acronym for "GEometry ANd Tracking" and aims to emulate the interaction of generated particles with the detector material as well as more technical matters such as hit and track reconstruction. Moreover, GEANT4 is capable of providing simulations of all the major LHC experiments over a wide range of energies starting from a few hundred eV in certain cases and going up to the TeV range in others. It provides a full geometrical and material description of the detector as well as the particle response to electromagnetic fields.

Chapter 5

Event reconstruction and selection

In this analysis differential cross sections of $t\bar{t}$ production are measured in the dilepton channel in which the top and anti-top quark decay as $t \to W^+(\to \bar{l}\nu)b$ and $\bar{t} \to W^-(\to l\bar{\nu})\bar{b}$, respectively. The final state is reached via intermediate decays of the W bosons, where only prompt decays to electrons or muons are considered and decays via τ are vetoed. Furthermore, the b-quarks will hadronize and form two b-jets which are not identified with 100% efficiency, while the neutrinos are invisible to the detector and can only be identified indirectly as $E_{\mathrm{T}}^{\mathrm{miss}}$ (see Section 5.7.5 for further details). Thus, the experimental signature in the detector consists of two prompt and oppositely-charged electrons and/or muons, a minimum of two jets, where at least one must be b-tagged, and the presence of $E_{\mathrm{T}}^{\mathrm{miss}}$.

Details of the data sample recorded with the CMS experiment can be found in Section 5.1, while full information on the signal definition and simulation is provided in Section 5.2. Non-negligible background contributions are described in Section 5.3 and come from other $t\bar{t}$ decays, including decays via τ, in addition to single-top, $t\bar{t}+Z/\gamma^*/W$, Z/W+jets and diboson processes. The rate of the Z+jets background must be corrected using a data-driven approach detailed in Section 5.4. As discussed in Chapter 3, not all events can be stored on tape and to select the highest number of events with the correct topology, special combinations of single lepton and dilepton triggers are used for this analysis. These combinations are described in Section 5.5.

All processing of CMS data starts with the reconstruction of vertices and particle trajectories as described in Section 5.6. Furthermore, the particle objects involved in the experimental signature, i.e. electrons, muons, jets, b-jets and missing transverse energy, are presented in Section 5.7. The reconstruction of the top and anti-top quark momentum vectors is a key ingredient in the analysis. In the kinematic reconstruction, the visible decay products (leptons and b-jets) are associated with the t and $\bar{t}$ decay chains and used to determine the momentum vectors of the two neutrinos. Two alternative methods are used, namely the full and loose kinematic reconstruction, which are described in Section 5.8.1 and 5.8.2, respectively. In both methods the neutrinos are reconstructed by applying several kinematic constraints such as transverse momentum conservation in events. Finally, in Section 5.9 the selection strategy is summarized and highlighted, and control plots for a selected number of distributions are shown at different steps of the full event selection.

5.1 Data sample

The data was recorded with the CMS detector during Run 2 of the LHC from 2016 to 2018. Only data which has been validated and deemed good for physics analysis is used and the list of good runs is shown for each year in Appendix B (see Table B.1 to B.3). The total integrated luminosity of all good runs in Run 2 corresponds to 137.6 fb^{-1}.

5.2 Signal definition and simulation

Top pair production is studied in the dilepton channel, where the signal process $t\bar{t} \to W^+bW^-\bar{b} \to l\bar{l}\nu\bar{\nu}b\bar{b}$ results from both W-bosons decaying to $W^+ \to \bar{l}\nu_l$ and $W^- \to l\bar{\nu}_l$. The experimental signature therefore consists of two oppositely-charged leptons, two b-jets and the presence of missing transverse energy in the detector. However, as the b-tagging algorithm is not 100% efficient (see Section 5.7.4) only one of these jets is required to be b-tagged. Furthermore, only prompt decays to electrons and/or muons are classified as signal and decays via τ are labelled as background and grouped together with other non-signal $t\bar{t}$ events that imitate the experimental signature. This category of background will be referred to as "$t\bar{t}$ other". The decision to veto decays via τ was made in order to simplify the kinematic reconstruction where one would otherwise have to account for two additional neutrinos.

The reference simulation of the signal process is used to scrutinize the agreement with data at detector-level and for correcting data acceptance and resolution effects in the unfolding procedure via the response matrix (see Chapter 6). Furthermore, the reference simulation is used directly in cross section measurements via a special fractional correction of the "$t\bar{t}$ other" background as described in Section 6.3. The predictions of this model at generator-level are also used in data and simulation comparisons along with two alternative models. In Chapter 4 it was described how each part of a simulation is done in a series of subsequent steps, and the specific details pertaining to the $t\bar{t}$ signal simulations used in this analysis are described below:

• **Reference simulation**: The simulation of the $t\bar{t}$ signal process is performed with the POWHEG (version 2) generator [70–72] at ME level at NLO accuracy in QCD. This is then interfaced with PYTHIA8 [67] that models the parton shower, hadronization and underlying event. The latter is tuned to data by using the CP5 tune [79] and finally, the detector simulation is performed with GEANT4 [78]. All of the above constitutes the reference simulation which will be abbreviated to POWHEG (version 2)+PYTHIA8.

• **Alternative simulation 1**: The MG5_aMC@NLO (version 2.4.2) generator [73] is used to perform ME calculations of the $t\bar{t}$ signal process at NLO accuracy in QCD. The simulation includes up to two additional partons at NLO ME precision and is interfaced to PYTHIA8 by using a matching scheme that follows the FxFx prescription [76]. The underlying event is modelled with the CP5 tune and the spin

correlation of the top quarks is preserved in the decay modelling by using MadSpin [77]. The notation MG5_aMC@NLO[FxFx] (version 2.4.2)+Pythia8 is used to denote the whole simulation.

• **Alternative simulation 2**: The $t\bar{t}$ signal process is modelled with Powheg (version 2) at ME level at NLO accuracy in QCD. The parton shower, hadronization and underlying event are simulated with Herwig7 [69], which uses the CH3 tune [80]. The whole simulation is denoted by Powheg (version 2)+Herwig7.

The proton structure is described by parton distribution functions (PDFs) which are not known a priori and must be computed to a certain accuracy. The reference and alternative simulations all use the NNPDF3.1 PDF set [32, 81] computed at NNLO accuracy. Furthermore, the top mass and the parameter that damps high p_{T} real emissions in the parton shower (see Chapter 4) are set to $m_t = 172.5$ GeV and $h_{\mathrm{damp}} = 1.379 \times m_t$ [79], respectively. Finally, the signal simulations must be normalized and this is done with the theoretical cross section of $t\bar{t}$ production which is obtained as $830.91\ ^{+20.39}_{-29.96}$ (scale) $^{+3.92}_{-3.83}$ (PDF + α_s) pb at NNLO accuracy from the TOP++ (version 2.0) program [34], where the same top mass and PDF set as stated above are used. This calculation also accounts for soft-gluon terms through a resummation at next-to-next-to-leading-logarithm (NNLL) accuracy [82–87]. The nominal reference and alternative simulations used for each year in the Run 2 period are listed in Appendix C along with dedicated samples that are used to estimate a sub-set of the theoretical systematic uncertainties. For the estimation of all other sources of uncertainty Powheg (version 2)+Pythia8 is used with the appropriate variation applied.

5.3 Background contributions

The $t\bar{t}$ dileptonic channel has smaller backgrounds than both the semi-leptonic and all hadronic channels. After the full event selection, contributions from $t\bar{t}$ other, single-top, Z+jets, W+jets, $t\bar{t}$ +Z/γ^*/W and diboson background processes still remain. The event topologies of these processes that imitate the experimental signature of the signal will be outlined below. Negligible backgrounds are not considered. This includes the QCD multijet background which is virtually non-existent due to the improbability of having double lepton misidentification.

• **$\mathbf{t\bar{t}}$ other**: Decays via τ are grouped together with other dileptonic, semi-leptonic and all-hadronic $t\bar{t}$ decays that fake the experimental signature (collectively named $t\bar{t}$ other). All are modelled with Powheg (version 2)+Pythia8 and normalized to the theoretical cross section of $t\bar{t}$ production obtained with the TOP++ (version 2.0) program. The normalization of the dileptonic, semi-leptonic and all-hadronic processes also accounts for their branching fractions (10.71 %, 44.11 % and 45.44 % [22], respectively).

• **Single-top**: The main contribution from single-top production comes from the

tW channel as described in Section 2.3.2. The tW and t-channels are divided into separate top and anti-top samples that are all simulated with POWHEG (version 2)+PYTHIA8 at NLO accuracy [88, 89], while the s-channel is simulated with MG5_aMC@NLO[MLM] +PYTHIA8 at LO accuracy, where the matching scheme follows the MLM prescription [74, 75]. The tW/$\bar{\text{t}}$W background is normalized to 35.85 pb which corresponds to the theoretical cross section obtained using the MSTW 2008 PDF set at approximate NNLO accuracy [36]. The t-channel normalization differs for the top and anti-top processes, where cross sections of 136.02 pb and 80.95 pb, respectively, are obtained at NLO accuracy with HATHOR (version 2.1) [37]. The same program is also used for the s-channel which is normalized to a cross section of 10.32 pb (NLO). All contributions described above are collectively named "Single t" in plots.

• **Z+jets**: Drell-Yan (DY) production with initial state radiation will be labelled as Z+jets. Here a quark and anti-quark annihilate to a Z boson or a photon which subsequently decays to two leptons with opposite charges. This is the most dominant background process in the $e^{\pm}e^{\mp}$ and $\mu^{\pm}\mu^{\mp}$ channels after the full event selection. The background is split into two Z boson mass ranges; 10 to 50 GeV and greater than 50 GeV. The former (latter) is simulated with MG5_aMC@NLO[MLM] +PYTHIA8 (MG5_aMC@NLO[FxFx] +PYTHIA8) at LO (NLO) accuracy and includes up to four (two) additional partons. It should be noted that the Z+jets background is overall well described in simulation but the rate must be corrected using a data-driven approach as outlined in Section 5.4.

The Z+jets background is normalized to 22635.1 (6225.4) pb in the 10 to 50 (> 50) GeV mass regime, where the theoretical cross section is obtained from FEWZ 3.1 at NNLO QCD and NLO QED [90, 91].

• **W+jets**: The W+jets process contributes to the background via the leptonic decay of the W boson and is simulated with MG5_aMC@NLO[MLM] +PYTHIA8 at LO accuracy. The simulation includes up to four additional partons at ME level and is normalized to 61526.7 pb which is the theoretical cross section obtained from FEWZ 3.1 at NNLO QCD and NLO QED [90, 91]. The simulated W+jets events are included in the category labelled as "Minor bg".

• $\mathbf{t\bar{t} + Z/\gamma^*/W}$: The process in which $t\bar{t}$ is produced in association with a Z/γ^* or W boson is modelled with MG5_aMC@NLO[FxFx] +PYTHIA8 at NLO accuracy and the simulation includes up to two extra partons per event. The associated backgrounds are included in the "Minor bg" category and normalized to 0.2529 (0.5297) pb and 0.2043 (0.4062) pb for the leptonic (all-hadronic) decays of the Z/γ^* and W boson, respectively. The cross sections are obtained at NLO accuracy from the corresponding simulations.

• **Diboson**: The diboson background is modelled with PYTHIA8 at LO accuracy. The ZZ and WZ processes are normalized to theoretical cross sections of 16.523 pb and 47.13 pb, respectively, which have been obtained at NLO accuracy with MCFM 6.6 [92, 93], while WW is normalized to 118.7 pb at NNLO accuracy [94]. The total

background due to all processes is included in the "Minor bg" category.

All backgrounds use PYTHIA8 to model the parton shower, hadronization and underlying event. The CP5 tune is used in 2017 and 2018, while the CUETP8 tune [95–97] is used in 2016 for all samples apart from $t\bar{t}$ and single-top processes. The hard interaction is modelled by either POWHEG, MG5_aMC@NLO or PYTHIA8, as described above, where the PDF set NNPDF3.1 at NNLO is used in all cases and the top mass is set to $m_t = 172.5$ GeV. Finally, the detector simulation for all background samples is performed with GEANT4, and the full list of simulated background samples for each year can be found in Appendix C.

5.4 Data-driven method for Z+jets background determination

All backgrounds described in Section 5.3 are determined from simulation, however, the normalization of the Z+jets background can be improved by using a data-driven method. The TFractionFitter class [98] in the ROOT framework [99] is used for this purpose. All simulated processes (including the $t\bar{t}$ signal) are grouped into two template categories; Z+jets and all others. The dilepton mass distributions for the two categories are then used as templates in a Poisson-based likelihood fit of the corresponding distribution in data inside the Z-peak region, with a dilepton mass between $76 \leq m_{ll} \leq 106$ GeV. The fit is performed per bin and takes statistical uncertainties on the simulations into account by using internal normalisation parameters. In this way one obtains best estimates for the fractional contributions of the input templates such that

$$\mathrm{Fit}_{\mathrm{data}} = f_{\mathrm{Z+jets}} \cdot \mathrm{T}_{\mathrm{Z+jets}} + f_{\mathrm{MC\ other}} \cdot \mathrm{T}_{\mathrm{MC\ other}},$$

where $\mathrm{Fit}_{\mathrm{data}}$ denotes the fit model. The templates (fractional contributions) for Z+jets and MC other are given by $\mathrm{T}_{\mathrm{Z+jets}}$ ($f_{\mathrm{Z+jets}}$) and $\mathrm{T}_{\mathrm{MC\ other}}$ ($f_{\mathrm{MC\ other}}$), respectively. The fit performed by TFractionFitter and the relative contributions of the two MC templates within the Z-peak region can be seen in Figure 5.1 for Run 2, in both the $e^{\pm}e^{\mp}$ and $\mu^{\pm}\mu^{\mp}$ channels. The fit procedure is performed individually for both channels and the final scale factors for the Z+jets MC simulations are computed as follows

$$SF^{e^{\pm}e^{\mp}} = \frac{f^{e^{\pm}e^{\mp}}_{\mathrm{Z+jets}} \cdot N^{e^{\pm}e^{\mp}}_{\mathrm{data,\ I}}}{N^{e^{\pm}e^{\mp}}_{\mathrm{Z+jets,\ T}}}$$

and

$$SF^{\mu^{\pm}\mu^{\mp}} = \frac{f^{\mu^{\pm}\mu^{\mp}}_{\mathrm{Z+jets}} \cdot N^{\mu^{\pm}\mu^{\mp}}_{\mathrm{data,\ I}}}{N^{\mu^{\pm}\mu^{\mp}}_{\mathrm{Z+jets,\ T}}},$$

where $N_{\text{data, I}}$ and $N_{\text{Z+jets, T}}$ are the number of events in the input data distribution and Z+jets MC template, respectively. The scale factor in the $e^{\pm}\mu^{\mp}$ channel is given by

$$SF^{e^{\pm}\mu^{\mp}} = \sqrt{SF^{e^{\pm}e^{\mp}} \times SF^{\mu^{\pm}\mu^{\mp}}}$$

and the scale factor for the combined channel is a weighted sum of the $e^{\pm}e^{\mp}$, $\mu^{\pm}\mu^{\mp}$ and $e^{\pm}\mu^{\mp}$ scale factors

$$SF^{l^{\pm}l^{\mp}} = \frac{SF^{e^{\pm}e^{\mp}} \cdot N^{e^{\pm}e^{\mp}}_{\text{data, I}} + SF^{\mu^{\pm}\mu^{\mp}} \cdot N^{\mu^{\pm}\mu^{\mp}}_{\text{data, I}} + SF^{e^{\pm}\mu^{\mp}} \cdot N^{e^{\pm}\mu^{\mp}}_{\text{data, I}}}{N^{e^{\pm}e^{\mp}}_{\text{data, I}} + N^{\mu^{\pm}\mu^{\mp}}_{\text{data, I}} + N^{e^{\pm}\mu^{\mp}}_{\text{data, I}}}.$$

The procedure has been tested for different definitions of the fitted region. The definition "in" refers to the Z-peak region, $76 \leq m_{ll} \leq 106$ GeV, whereas "out" refers to the region outside of this interval. The definition "in+out" refers to the whole m_{ll} spectrum. It was observed that the "in" definition is sufficient when computing the scale factors and "out" and "in+out" only lead to changes within $\approx 1\%$.

Table 5.1 shows scale factors computed at different selection steps (see Section 5.9) when using the "in" definition for TFractionFitter. Corresponding results are also shown for the old $R_{\text{out/in}}$-method [100] of determining the Z+jets normalization. In this method the Z+jets MC simulation is used to compute the ratio $R_{\text{out/in}}$, which is defined as the number of Z+jets events outside the Z-peak region over the number of Z+jets events inside. It is reasonable to assume that the overall normalization uncertainty of the simulation will cancel in this ratio and that $R_{\text{out/in}}$ is the same in data. Therefore, the simulation values of $R_{\text{out/in}}$ in the $e^{\pm}e^{\mp}$ and $\mu^{\pm}\mu^{\mp}$ channels are used to estimate the corresponding number of data events outside the Z-peak region by multiplying $R_{\text{out/in}}$ with the number of data events inside. Then final scale factors for the Z+jets MC simulations are derived in a similar way, as described above. A complete description of the $R_{\text{out/in}}$-method can be found in [101]. The two methods are shown to be consistent but the TFractionFitter method is preferred as the scale factors are derived based on a region that is orthogonal to the one defined by the full selection. In contrast the $R_{\text{out/in}}$-method depends on the Z+jets events outside the Z-peak in the MC simulation. Generally a good level of stability across different selection steps is observed, although scale factors for 2017 and 2018 jump at the "$E_{\text{T}}^{\text{miss}}$" selection requirement due to some residual mismodelling of this quantity but then remain stable.

In this work the scale factors will be derived with the TFractionFitter method at the "$E_{\text{T}}^{\text{miss}}$" selection requirement and applied to all subsequent steps. This step was chosen as it's closest to the final selection while still retaining enough statistics for the data and simulations used in the fit procedure.

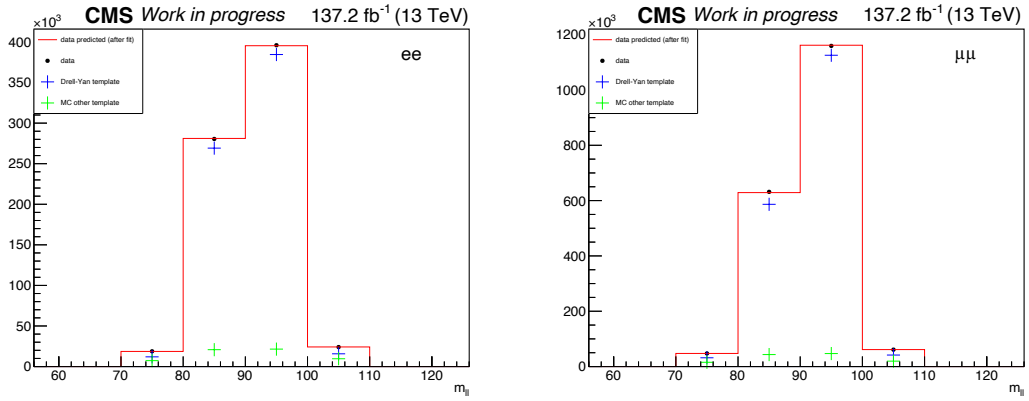

Figure 5.1: Dilepton mass distributions in the Z-peak control region, i.e. $76 \leq m_{ll} \leq 106$ GeV, are shown for the $e^{\pm}e^{\mp}$ (left) and $\mu^{\pm}\mu^{\mp}$ (right) channels for Run 2, after the event selection according to step 6 (see Section 5.9). The input data distributions are illustrated by black dots, the Z+jets templates are shown in blue and the MC other templates are depicted in green. The red histograms illustrate the results of the fits performed by TFractionFitter.

Table 5.1: Data-driven Z+jets background scale factors for different selection steps (see Section 5.9) using the TFractionFitter method (left) and $R_{\text{out/in}}$-method (right). Results are shown for all channels, years and full Run 2.

2016	ee	$\mu\mu$	μe	combined
2 jets	0.89	0.88	0.88	0.88
$E_{\text{T}}^{\text{miss}}$	0.92	0.88	0.90	0.89
b-tag	0.92	0.86	0.89	0.87
kin. fit	0.92	0.87	0.89	0.88
2017	ee	$\mu\mu$	μe	combined
2 jets	0.90	0.98	0.94	0.96
$E_{\text{T}}^{\text{miss}}$	0.94	1.02	0.98	1.00
b-tag	0.94	1.05	0.99	1.01
kin. fit	0.95	1.06	1.00	1.02
2018	ee	$\mu\mu$	μe	combined
2 jets	0.91	0.95	0.93	0.94
$E_{\text{T}}^{\text{miss}}$	1.05	1.04	1.05	1.04
b-tag	1.06	1.05	1.06	1.06
kin. fit	1.09	1.10	1.10	1.10
Run2	ee	$\mu\mu$	μe	combined
2 jets	0.90	0.94	0.92	0.93
$E_{\text{T}}^{\text{miss}}$	0.97	0.99	0.98	0.99
b-tag	0.98	1.00	0.99	0.99
kin. fit	1.00	1.03	1.01	1.02

2016	ee	$\mu\mu$	μe	combined
2 jets	0.91	0.89	0.90	0.89
$E_{\text{T}}^{\text{miss}}$	0.92	0.88	0.90	0.89
b-tag	0.89	0.85	0.87	0.86
kin. fit	0.87	0.84	0.86	0.85
2017	ee	$\mu\mu$	μe	combined
2 jets	0.91	1.00	0.95	0.97
$E_{\text{T}}^{\text{miss}}$	0.94	1.03	0.98	1.00
b-tag	0.93	1.03	0.98	1.00
kin. fit	0.93	1.03	0.98	1.00
2018	ee	$\mu\mu$	μe	combined
2 jets	0.93	0.96	0.95	0.95
$E_{\text{T}}^{\text{miss}}$	1.04	1.04	1.04	1.04
b-tag	1.02	1.05	1.04	1.04
kin. fit	1.04	1.07	1.05	1.06
Run2	ee	$\mu\mu$	μe	combined
2 jets	0.92	0.95	0.94	0.94
$E_{\text{T}}^{\text{miss}}$	0.97	0.99	0.98	0.99
b-tag	0.96	0.99	0.97	0.98
kin. fit	0.96	1.00	0.98	0.99

5.5 Trigger selection and efficiency

All events must pass a combination of single-lepton and dilepton high-level triggers. The former requires at least one electron or muon to be present, while the latter selects events that contain at least two electrons, two muons or an electron and a muon. Each year has its own set of trigger paths and these are listed in Appendix D.1 (see Table D.1 to D.3). A logical "OR" is used between the trigger paths to increase the efficiency of the selection but events passing dilepton triggers are vetoed while processing single-lepton data streams in order to avoid overlap. In 2016 the single-electron trigger has a minimum p_{T} requirement of 27 GeV, while in 2017 and 2018 this threshold is raised to 32 GeV. The single-muon trigger sets the minimum p_{T} to 24 GeV in 2016 and 2018 and to 27 GeV in 2017. In all three years, the dilepton $e^{\pm}e^{\mp}$ ($\mu^{\pm}\mu^{\mp}$) triggers require the presence of a leading electron (muon) with a threshold p_{T} of 23 (17) GeV and a trailing electron (muon) with a threshold p_{T} of 12 (8) GeV. Here leading (trailing) means that the lepton has the highest (second highest) p_{T}. The dilepton $e^{\pm}\mu^{\mp}$ triggers also have the same minimum p_{T} requirements in all three years. The leading electron or muon must have a p_{T} of at least 23 GeV and the trailing lepton must have a threshold p_{T} of 12 (or 8) GeV if it's an electron (muon). The triggers used also require some loose isolation criteria for the leptons, and the isolation variables used are defined in the discussion pertaining to electron and muon identification in Section 5.7.

The trigger selection is applied in both data and simulation and scale factors are derived and applied to the latter in order to account for discrepancies with respect to data [102]. Reference triggers, that are based on a large $E_{\mathrm{T}}^{\mathrm{miss}}$ requirement in the event and expected to be orthogonal to the dilepton triggers, are used to compute trigger efficiencies in both data and simulation by finding the number of events that pass the dilepton triggers or both sets of triggers. Scale factors are then derived differentially and independently for each year and each channel based on lepton object definitions matching those in Section 5.7. The final scale factors are shown in Appendix D.2 in bins of the leading and trailing lepton p_{T} and agree with unity within a few percent across all years. The uncertainties on the nominal scale factors are $\sim 1\%$.

5.6 Vertex and track reconstruction

Precise reconstruction of particle trajectories, referred to as tracks, is important for the momentum resolution of charged particles and accurate reconstruction of the primary vertex which in turn helps veto simultaneously occurring events within the same bunch crossing, known as pile-up. The distribution of the mean number of interactions per bunch crossing, i.e. the pile-up profile, is shown for the Run 2 data-taking period in Figure 5.2. The complexity of reconstructing vertices and tracks is emphasized by the fact that there is an average of 29 proton-proton interactions per bunch crossing throughout this period [103]. The task is two-fold; one must reconstruct tracks out of so-called hits in the silicon pixels and strips, which are

the footsteps particles leave as they traverse the tracker, and one must additionally associate the tracks to the correct vertices.

Track reconstruction is divided into four steps: namely track seeding, finding, fitting and selection [55]. In the seeding stage one aims to reconstruct small segments of the starting trajectories of charged particles. Therefore, combinations are made from two to three hits in the inner layers of the pixel detector in order to form so-called seed tracks (subject to certain constraints and selection criteria based on a weak compatibility with the primary vertex). Tracks are then found based on the Kalman filter method [104] which uses each seed track to extrapolate to the next layer of the tracker where new hits are added if they are consistent with the seed track in a χ^2 test. The track parameters are then re-estimated and an extrapolation is performed to the next layer where the procedure is repeated. This proceeds until the outer end of the tracker is reached. After all hits belonging to a candidate track are found all previous constraints are released and the hits are fitted once again using a Kalman filter and a smoother. The number of fake tracks, i.e. tracks that don't actually belong to a charged particle, are then reduced in the track selection stage by applying certain quality requirements. The procedure described above is repeated over several iterations starting with relatively strict selection criteria on candidate tracks, e.g. high p_{T} and small impact parameter (see definition in Section 3.2.3). The hits of the tracks reconstructed in the first iteration are then removed from the set of hits available for other tracks in the subsequent iterations, where tracks are reconstructed based on less and less stringent criteria.

After reconstructing all tracks, the second aim is to reconstruct the primary vertex, i.e the signal vertex, in addition to all pile-up vertices. This is done in three separate steps: track selection, track clustering and vertex position determination [55]. Tracks whose point of origin is consistent with the interaction region are selected and then clustered according to their z-coordinates at the point of closest approach to the centre of the nominal interaction region. This is done by means of a deterministic annealing algorithm [105] which takes care not to mistakenly split vertices in high pile-up conditions. Finally, the best estimate of the vertex position of a track cluster with at least two tracks is obtained by using an adaptive vertex fitting algorithm [106]. In this work selected vertices are required to have at least 4 tracks, and be within $|z| < 24$ cm and a radius of 2 cm from the average interaction point. The primary vertex is taken to be the one with the highest sum of p_{T}^2 of associated objects, including tracks and $E_{\mathrm{T}}^{\mathrm{miss}}$, and the others are labeled as pile-up vertices. The distribution of the number of vertices, N_{vtx}, is shown in Figure 5.3 for events collected in the dilepton channel that pass the single lepton and dilepton triggers, the lepton pair requirements and the dilepton mass cut of $m_{l\bar{l}} > 20$ GeV (see Section 5.9). The same distribution is shown before and after tuning the MC to match the pile-up conditions in the data, and one can see the significant improvement once such corrections are applied. The nominal MC already contains simulated additional minimum bias interactions per event but the number of these are reweighted to match the pile-up distribution in data based on an assumed value of the inelastic pp cross section of 69.2 mb and the instantaneous luminosity per

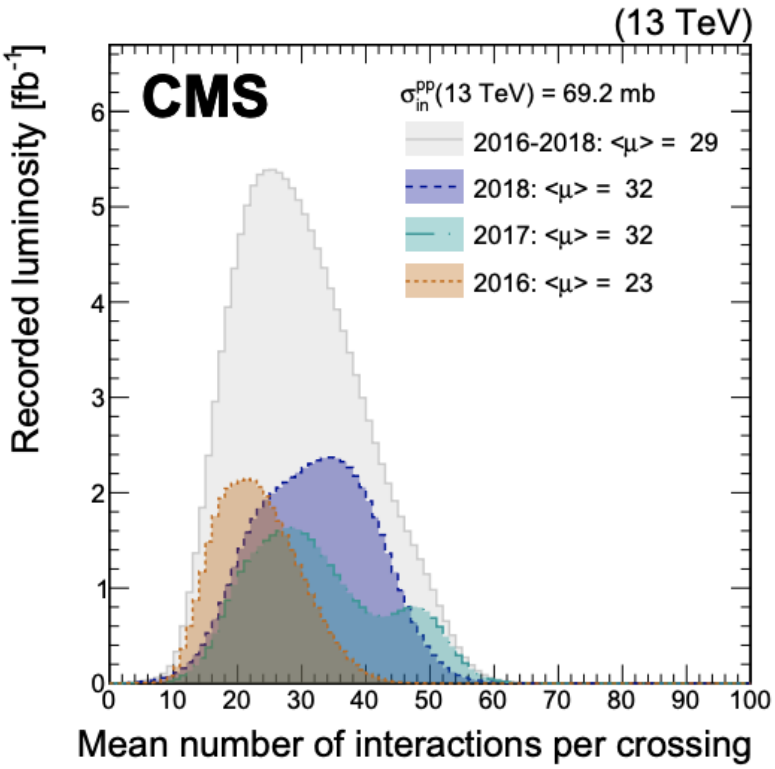

Figure 5.2: The pile-up distribution of the mean number of interactions per bunch crossing during the Run 2 data-taking period from 2016 to 2018 [103].

bunch crossing recorded for the data.

5.7 Object reconstruction

In CMS the particle-flow (PF) algorithm [107, 108] is used to combine information from all detector sub-systems in order to reconstruct and identify all stable photons, electrons and muons as well as charged and neutral hadrons in an event. The tracks and calorimeter deposits left by these particles as they traverse the CMS detector are shown in Figure 5.4. They are used as input to the PF algorithm which links them together in so-called blocks that can be interpreted as particle objects. These objects are then used in algorithms for clustering jets and identifying b-jets, and to compute the missing transverse energy referenced in previous chapters. It should be noted that all object descriptions adhere to the recommendations put forth by the LHC Top Physics Working Group [109].

5.7.1 Muon reconstruction and identification

Prompt muons originate from the hard interaction and must be distinguished from ones that come from decays of light and heavy flavour hadrons, the atmosphere (so-called cosmic muons), neutron-induced background, or misidentification due to

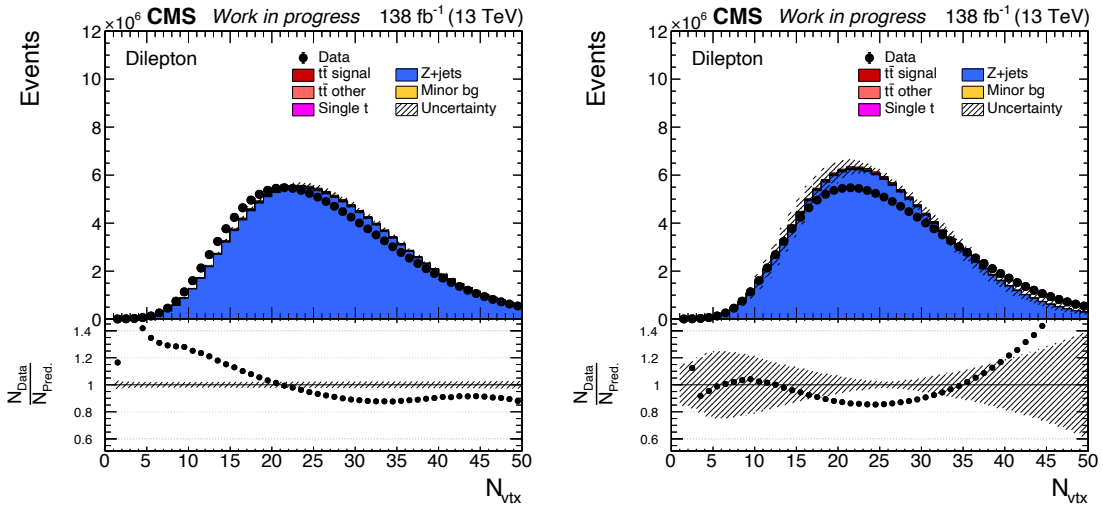

Figure 5.3: Distributions of the number of proton-proton interaction vertices, N_{vtx}, are shown for events selected in the dilepton channel before (left) and after (right) tuning the MC to match the pile-up conditions in data. Both distributions are shown after passing the single lepton and dilepton triggers, the lepton pair requirements and the dilepton mass cut of $m_{l\bar{l}} > 20$ GeV (see Section 5.9). The data (black dots) is compared to the sum of the $t\bar{t}$ signal and background processes. All simulated samples have been normalized to an integrated luminosity of 137.6 fb^{-1}and the dashed band in the ratio shows the shape uncertainties.

charged hadron shower tails that penetrate the muon-system. Muons are reconstructed and identified using the PF algorithm based on three potential track candidates [58]:

• **Standalone muons**: Muons that traverse the CSC, DT and RPC sub-systems leave traces of ionization, i.e. hits, from which one can reconstruct trajectories independently of the tracker since the whole muon system is also embedded in the steel flux return-yoke of the magnet. Standalone muon tracks are again reconstructed with a Kalman filter, but in this case the initial seed is a group of DT or CSC segments.

• **Tracker muons**: Generic tracks that are reconstructed in the tracker, as described in Section 5.6, can qualify as tracker muon candidates if they match at least one DT or CSC segment within a certain geometric region when extrapolated to the muon system. Tracker muons must additionally have $p_{\text{T}} > 0.5$ GeV and a total momentum that is greater than 2.5 GeV.

• **Global muons**: If a standalone muon track matches a generic track, a combined fit is done using a Kalman filter and the resulting track is labelled as a global muon candidate.

The reconstruction of generic tracks and muon segments have a high efficiency and

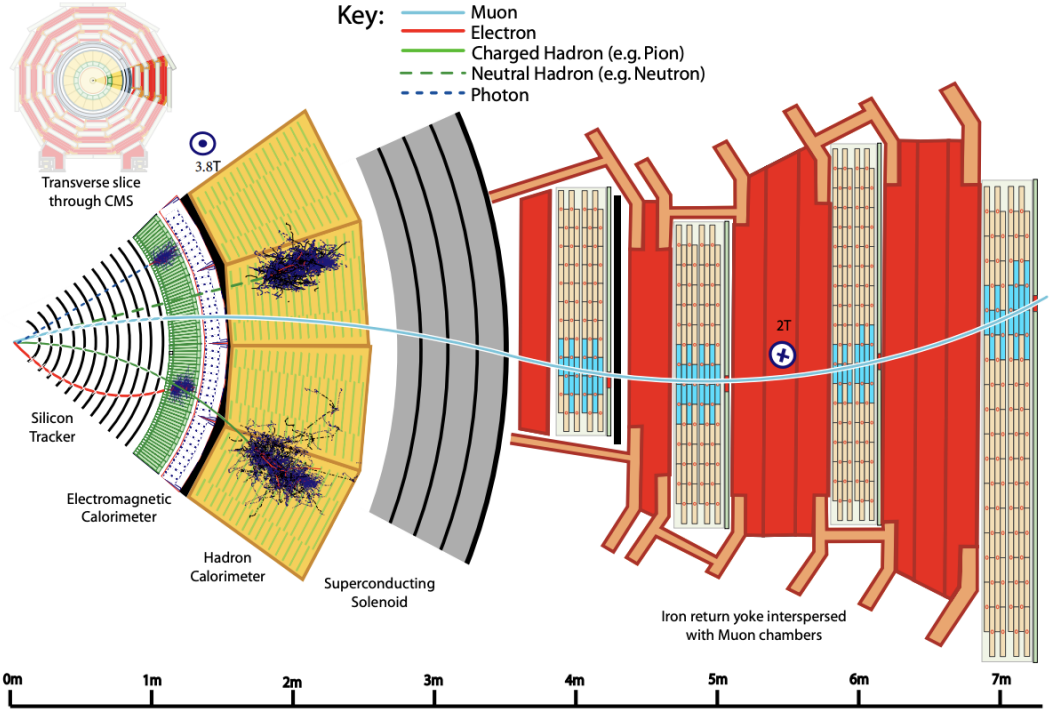

Figure 5.4: A cross section of the CMS detector that illustrates the tracks and traces left by photons, electrons and muons as well as charged and neutral hadrons [110].

a muon is reconstructed as a tracker and/or global muon in 99% of cases, provided that it is within the detector acceptance. However, global muons have the best p_{T} resolution. Finally, the standalone, tracker and global muon candidates are used as inputs in the PF algorithm, where tracks shared by both tracker and global muons enter as a single candidate track. The PF algorithm will then identify muons according to e.g. loose, medium or tight selection criteria, and in this work only muons satisfying a cut-based tight identification (tight ID) are used. A tight muon track has hits in a minimum of six layers of the inner tracker and at least one pixel hit. It must additionally be reconstructed with both the tracker and global muon algorithms. In the former the generic track must match segments from at least two muon stations, and in the latter the combined fit must have $\chi^2/\mathrm{dof} < 10$ and include a minimum of one muon system hit. Furthermore, in order for the muon to be identified as prompt it has to originate from the primary vertex. This is determined by its transverse and longitudinal impact parameters which must be smaller than 0.2 cm and 0.5 cm, respectively.

A requirement on the PF isolation of a muon relative to its p_{T} further helps to suppress muons from decays in flight. Energies of charged hadrons (from the primary vertex), neutral hadrons and photons are summed within a region around the muon defined by the cone $\Delta R = \sqrt{\Delta\eta^2 + \Delta\phi^2} = 0.4$. The energy sum of charged hadrons associated to pile-up vertices is multiplied by 0.5 and subtracted from the energy sum of neutral hadrons within the cone to mitigate pile-up contributions. The final energy sum relative to p_{T} must be smaller than 0.15, which corresponds to a tight isolation.

In this work, high precision corrections provided by the Rochester group [111] are applied to the muon momentum scale and resolution. Furthermore, muons must have a leading (trailing) p_{T} of at least 25 (20) GeV and a pseudorapidity of $|\eta| < 2.4$.

Leptonic decays of a known resonance like the Z boson are used to compute efficiencies in a data-driven technique called tag-and-probe [112]. In the current case, events with two high energy muons are considered, where strict selection requirements are imposed upon one muon (the tag) and looser requirements that don't bias the efficiency measurement are imposed on the other (the probe). The reconstructed Z boson mass from the tag and probe pair must additionally be within a certain window around the resonance for an event to be selected. Dilepton mass distributions of selected events can then be used to extract the efficiency of e.g tight ID or isolation which is defined as the ratio of the passing number of probes and the total number of probes. Scale factors that account for the differences in efficiency between data and simulation are provided centrally by the CMS collaboration. They are measured independently for each year in bins of p_{T} and η as shown in Appendix E (see Figure E.1, E.3 and E.5). The scale factors agree with unity within a few percent across all years and have uncertainties that are predominantly within 1%.

5.7.2 Electron reconstruction and identification

Electrons that are interesting for physics originate from the hard interaction and are referred to as prompt. Non-prompt electrons can arise from photon conversions and decays of light and heavy flavour hadrons. Electrons are reconstructed and identified with the PF algorithm based on information from both the ECAL and tracking system [56]. However, electrons present a particular challenge as they can interact with the material in the tracking system and electrons with $p_{\mathrm{T}} > 5$ GeV often undergo significant bremsstrahlung effects before they even reach the ECAL. On average 33% of their energy will be deposited in the material comprising the tracker [113]. Thus, the first thing the ECAL sees is the start of electromagnetic showers that have developed in the tracker. This results in several ECAL clusters in relatively close proximity, a so-called super-cluster (SC), which must be accurately identified in order to obtain the energy of the initial particle. The first step is to group crystals with a signal above a certain threshold into clusters. The cluster with the highest E_{T} in a particular region of $\eta \times \phi$ is identified as the seed cluster provided that it has $E_{\mathrm{T}}^{\mathrm{seed}} > 1$ GeV. Other clusters in close proximity are then merged with the seed cluster to form a SC.

The trajectory of an electron is also impacted by the energy loss due to bremsstrahlung and therefore an algorithm based on a Gaussian Sum filter (GSF) [114] for electron track reconstruction is used instead of the classic Kalman filter. The GSF tracking algorithm uses information on trajectory seeds in the pixel detector that can be linked with SCs in the ECAL given an electron trajectory hypothesis. Generic tracks reconstructed with a Kalman filter are also tested for compatibility with this hypothesis and track seeds from potential electron candidates are additionally used in the GSF tracking algorithm. A special algorithm is used to identify photon candidates. Finally, the ECAL clusters, SCs, GSF tracks and generic tracks are used in the PF algorithm, where they are joined into blocks representing electron and photon objects. The final list of ECAL clusters associated to such a block are joined into a refined SC and this is then used to reconstruct the electron and photon candidates. In order to identify prompt electrons and distinguish them from photons or the background electrons described above loose, medium or tight selection criteria are applied. Similar to muons, a cut-based tight ID is used in this work which, for example, only allows one missing hit for the electron track and has requirements on the noise in the HCAL relative to the electron energy in the ECAL. In case an electron/photon candidate passes both the electron and photon tight ID criteria it's labelled as an electron if it has a GSF track with at least one hit in the innermost layer of the pixel detector, otherwise it's labelled as a photon.

The electrons are also required to be isolated according to a similar definition of the PF isolation used for muons. However, there are some notable variations. The energy of photons and charged and neutral hadrons are summed within a cone of $\Delta R = 0.3$ around the electron, and pile-up effects are mitigated based on the median of the transverse energy density per unit area per event and the area of the isolation cone. Furthermore, the electron isolation depends on p_{T} since the spread in energy is greater for harder electrons. For tight electrons the final energy sum relative to p_{T} must be $< 0.0287 + 0.506\ \mathrm{GeV}/p_{\mathrm{T}}$ and $< 0.0445 + 0.963\ \mathrm{GeV}/p_{\mathrm{T}}$ in

the barrel and endcaps respectively.

Residual corrections are applied to the electron energy scale in simulation to account for the differences in resolution with respect to data. Finally, in this work leading (trailing) electrons must have a p_{T} of at least 25 (20) GeV, and a pseudorapidity of $|\eta| < 2.4$, where the region $1.44 < |\eta| < 1.57$ is excluded, as it corresponds to the gap between the ECAL barrel and endcaps and is therefore outside the detector acceptance. Similar to muons, the efficiencies in data and simulation are computed with the tag-and-probe method, and scale factors are provided centrally by the collaboration. They are again measured independently for each year in bins of p_{T} and η, as shown in Appendix E (see Figure E.2, E.4 and E.6). The scale factors agree with unity within a few percent across all years and have uncertainties that are predominantly $\sim 1\%$, ranging up to about 10% in some corners of the phase space.

5.7.3 Jet reconstruction

Jets are formed when quarks or gluons hadronize to produce collimated particles in a cone around the jet-axis, which is defined from the primary vertex and the direction-of-flight of the jet. Jet-clustering starts by grouping particles within a certain cone size, R, which defines the boundary of the jet with respect to the jet-axis. It's important to use an algorithm that is safe against infrared and collinear radiation, where the term safe means that such radiation is still contained in the jet. The anti-k_{T} algorithm [115] fulfills these requirements and clusters PF candidates with a cone size that is set to $R = 0.4$ in this work. The principle behind the anti-k_{T} algorithm is based on the distances, d_{ij}, between entities i and j, which refer to PF candidates and would-be jets. One can write

$$d_{ij} = \min(p_{\mathrm{T}i}^{-2}, p_{\mathrm{T}j}^{-2}) \frac{\Delta_{ij}^2}{R^2}$$

and

$$d_{iB} = p_{\mathrm{T}i}^{-2},$$

where $\Delta_{ij}^2 = (y_i - y_j)^2 + (\phi_i - \phi_j)^2$ is the geometric cone defined by the differences in rapidity and azimuth angle between entities i and j, and d_{iB} is the distance between entity i and the beam (parallel to the z-axis). As a first step, all distances for all combinations of entities are computed. If d_{ij} is the smallest distance overall, a new entity is formed by combining i and j. However, if d_{iB} is the smallest distance, i is removed from the list of entities and labelled a jet. Then all distances are recomputed from the new list of entities and the procedure is repeated until there are no more entities left.

Since jets are complex and composite objects that are highly dependent on the pile-up conditions in data, detector response and p_{T} resolution, the jet energy scale must be calibrated by applying corrections that depend on the jet p_{T}, η and flavour

[116, 117]. Corrections for individual jets must be derived from data and/or simulation and applied to one or both, and any differences between the two must also be taken into account by applying the appropriate set of scale factors. A factorized approach is used whereby corrections to data and simulation are derived and applied sequentially, and a schematic overview of the procedure is shown in Figure 5.5. The corrections are summarized as follows:

• **Pile-up offset corrections**: In-time pile-up (IT PU) and out-of-time pile-up (OOT PU) arise from simultaneous and consecutive bunch crossings respectively. Both contribute towards increases in jet energies and momenta and this is known as the pile-up offset. The calorimeter signal processing can help mitigate OOT PU, while tracks associated to pile-up vertices are removed to correct for IT PU (also called charged-hadron subtraction). The particle-level offset in jet p_{T}, due to pile-up from e.g. neutral hadrons and remaining OOT PU, can be estimated per event from a simulated QCD dijet sample with and without pile-up overlay. A correction factor per jet can then be obtained by using the extended hybrid jet area method [116–118]. It's applied as a multiplicative factor to the uncorrected jet transverse momentum and depends on the offset energy density, jet area, jet pseudorapidity and jet transverse momentum. Residual differences between data and simulation must also be taken into account, and scale factors for the offset are computed as a function of jet η from zero-bias data and simulation using the random cone (RC) method [117].

• **Simulated jet response corrections**: After the pile-up offset has been corrected, simulation-based corrections for the jet response are applied to both MC and data. These are derived using a QCD dijet sample which makes use of the full GEANT 4 detector simulation. The jet response is then defined as the ratio of arithmetic means of jet p_{T} with reconstructed jets in the numerator and their matched particle-level jets in the denominator. The corrections depend on the particle-level jet p_{T} and reconstructed jet η, and it should be noted that the particle-level jets do not include neutrinos in the jet-clustering in this definition.

• **Residual corrections for data**: After applying the pile-up offset and simulated jet response corrections above, residual differences in the jet response between simulation and data are taken into account by applying scale factors to the latter. The scale factors are split into two categories: relative and absolute. In the former, a dijet sample is used to calibrate jets relative to central jets with $|\eta| < 1.3$ and similar p_{T}. In the latter, a combination of $Z(\rightarrow ee)$+jets, $Z(\rightarrow \mu\mu)$+jets and γ+jets events is used to calibrate jets with $|\eta| < 1.3$ and $30 < p_{\mathrm{T}} < 800$ GeV against the Z-boson or photon momentum scale. A multijets sample is used to constrain jets with higher p_{T} and the relative and absolute corrections depend on η and p_{T}, respectively.

Once all corrections are applied, four-momenta of jets in the simulation are scaled to match the p_{T} resolution in data [116]. Furthermore, jets that overlap with the selected leptons inside $\Delta R = 0.4$ are removed, where the geometric cone between the given lepton (l) and jet (j) is defined by $\Delta R_{lj}^2 = (\eta_l - \eta_j)^2 + (\phi_l - \phi_j)^2$. Finally,

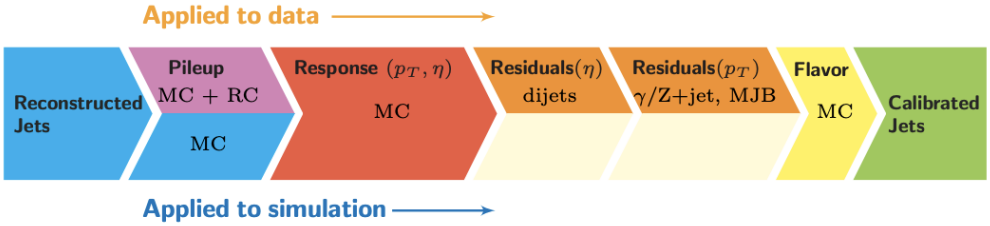

Figure 5.5: The figure shows a schematic overview of the factorized approach where corrections are derived and applied to both data and MC in sequential steps. It should be noted the optional flavour corrections (yellow) are not applied in this work [116].

all jets in this work are required to have transverse momenta of $p_{\mathrm{T}} > 30$ GeV and pseudorapidities within $|\eta| < 2.4$. At least two jets must be present in an event.

5.7.4 Identification of b-jets

Jets can contain heavy-flavour hadrons that result from b- or c-quarks undergoing hadronization and radiation. If the jet is initiated by the former it's known as a b-jet and in the latter case it's referred to as a c-jet. A jet can also be initiated by a gluon or u, d, or s-quark, in which case it's labelled as a light-jet. The b-jets are characterized by special properties that can help distinguish them from c- or light-jets and the procedure in which said properties are used to obtain discriminating variables is known as b-tagging [119]. Jets that originate from c-quarks have characteristics that are somewhat in between those of b- and light-jets and therefore c-jets have their own dedicated tagging.

The b-hadrons have a lifetime of about 1.5 ps, in comparison to c-hadrons which typically decay within 1 ps. The long lifetime means that they can travel anywhere from a few millimeters to roughly 1 cm away from the primary vertex before they decay, which leads to a secondary vertex within the jet, as illustrated in Figure 5.6 (the secondary vertex is reconstructed using two different algorithms, namely the adaptive vertex reconstruction [120] and adaptive vertex fitter [106]). Furthermore, b- and c-quarks are relatively heavy in comparison with u, d and s-quarks and are known to have a harder fragmentation, which means that the resulting heavy-flavour hadrons have a larger p_{T} with respect to the jet-axis when compared to other constituents of the jet (on average). Moreover, the b-hadron (c-hadron) can decay semi-leptonically to charged leptons and this happens in about 20% (10%) of cases. For the distinction of b- and c-jets one exploits the fact that b-hadrons have a larger mass (~ 5 GeV) compared to c-hadrons (~ 2 GeV), resulting in a larger multiplicity of decay tracks and higher invariant mass of these tracks at the decay vertex.

These features are reflected in the variables chosen as input for the b-jet tagging algorithms. One of the most important variables is the impact parameter of tracks that originate from the secondary vertex, so-called displaced tracks. When such a track is extrapolated backwards with respect to its direction-of-flight, the distance from the PV to the closest point of approach is defined as its impact parameter, and

a visual representation is shown in Figure 5.6. Here the impact parameter vector points from the primary vertex to the closest point of approach. A positive impact parameter means that the opening angle between the jet-axis and the impact parameter vector is less than $\pi/2$. In light-jets the measured impact parameters will be distributed around zero, where non-zero values are due to resolution effects or other long-lived hadrons, whereas a distinguishing feature of b-jets is that they tend to have positive values [119]. Another important variable is the flight distance of the b-hadron which is measured from the primary vertex to the secondary vertex.

In this work jets are b-tagged based on a discriminator computed using DeepCSV which is an updated version of the Combined Secondary Vertex (CSV) algorithm [119]. The information on secondary vertices and track-based variables described above constitute part of the inputs for the multi-class deep neural network used to distinguish b-jets from c- and light-jets. The resulting discriminator has three working point definitions which correspond to different thresholds, namely loose, medium and tight. Here the loose working point is chosen and this has different thresholds on the discriminator depending on the year i.e. 0.2217 (2016), 0.1522 (2017) and 0.1241 (2018). The resulting b-tagging efficiency is $\approx 80\%$ and the mistagging efficiencies for c- and light-jets are $\approx 40\%$ and $\approx 10\%$, respectively. In this analysis, only one jet (out of the at least two selected jets) is required to be b-tagged due to the algorithm not being 100% efficient. A deep neural network is also used in a multivariate regression algorithm that uses properties of reconstructed secondary vertices in addition to the composition and shape information of jets to improve b-jet energy measurements [121].

There are differences in the tagging (mistagging) efficiencies (rates) of b-jets (c- and light-jets) between data and MC. Thus flavour-dependent scale factors are provided in bins of η and p_{T} [119]. They are computed centrally by the collaboration based on a multijet reference sample. However, one must account for the different phase space in $t\bar{t}$ events. Thus, the final weight for each event includes the scale factors as well as analysis specific b-tagging (mistagging) efficiencies (rates) for all jets in the event. These efficiencies/rates are computed individually for all years from the corresponding reference simulations and are shown for b-, c- and light-jets in bins of η and p_{T} in Appendix F. Certain systematic uncertainty sources, like the ones for the jet energy scale, can impact the b-tagging efficiencies and mistag rates and in such cases they are computed from the reference simulation with the corresponding systematic variation applied.

5.7.5 Missing transverse energy reconstruction

In this chapter so far, it has been described how particles interact with the detector components and leave traces behind that facilitate measurements of their properties. Neutrinos have not been included in this discussion as they are essentially invisible to the detector due to their neutral charges, and in order to detect them, one must exploit principles of momentum conservation [122]. The longitudinal momenta of the partons participating in the hard interaction are not known as the momenta of the protons are distributed across their quark and gluon constituents. However, the

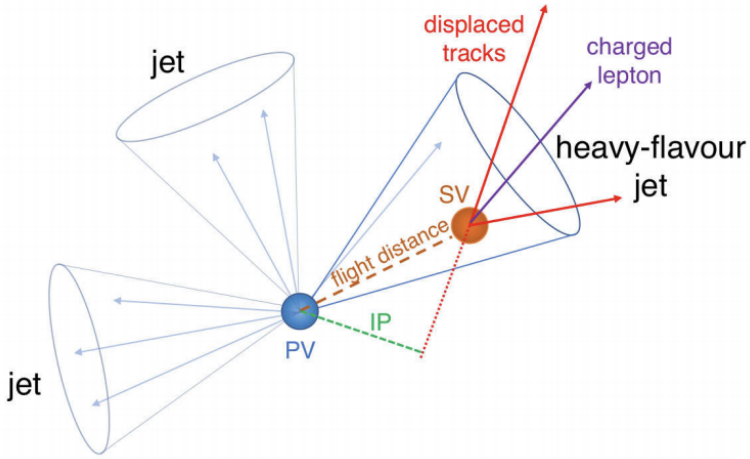

Figure 5.6: The figure shows a heavy-flavour jet that originates form a b- or c-quark. The resulting hadron decays after a certain flight distance which gives rise to tracks that are displaced from the primary vertex (PV). The displaced tracks form what is known as a secondary vertex (SV) and when such a track is extrapolated backwards with respect to its direction-of-flight the distance from the PV to the closest point of approach is defined as the impact parameter (IP) [119].

transverse momenta of all particles originating from the hard interaction must sum to 0. The transverse momenta of the neutrinos can therefore be inferred from an imbalance in the transverse plane. This is also referred to as the missing transverse energy and is given by

$$\vec{E}_{\mathrm{T}}^{\mathrm{miss}} = -\sum_{i} \vec{p}_{\mathrm{T}}(i),$$

where the sum over i runs over all PF candidates. This also includes PF candidates that can't be reconstructed as physics objects (i.e. as electrons, muons, photons, charged or neutral hadrons). Such PF candidates are collectively known as unclustered energy.

Despite the simple picture described above there are various challenges in $\vec{E}_{\mathrm{T}}^{\mathrm{miss}}$ modelling. Effects due to pile-up must be mitigated, and in this analysis, it's done by means of the PUPPI algorithm [103], which is an acronym for pileup-per-particle-identification. The probability that a particle comes from the primary vertex is assessed and a weight is assigned accordingly. Corrections to the jet/lepton energy scale and b-jet energy regression are also taken into account and propagated to the relevant objects when computing $\vec{E}_{\mathrm{T}}^{\mathrm{miss}}$. Figure 5.9 shows the $E_{\mathrm{T}}^{\mathrm{miss}}$ distributions (i.e. the magnitude of $\vec{E}_{\mathrm{T}}^{\mathrm{miss}}$) for the individual $e^{\pm}e^{\mp}$, $\mu^{\pm}\mu^{\mp}$ and $e^{\pm}\mu^{\mp}$ channels after requiring at least two jets in the event (see Section 5.9 for a summary of all selection criteria). In order to significantly reduce the background contribution from Z+jets at this stage, $E_{\mathrm{T}}^{\mathrm{miss}}$ is required to be > 40 GeV in the same-flavour channels.

5.8 Kinematic reconstruction

The top quarks can't be observed directly in the detector but one can use the kinematic spectra of their decay products to reconstruct the top and anti-top separately and/or the $t\bar{t}$ system. Two alternative methods are used in this work. In the first approach a full kinematic reconstruction of the $t\bar{t}$ system is performed using the methodology developed in [123, 124]. The full kinematic reconstruction has been used for differential cross section measurements of top pair production in the dilepton channel at 8 TeV [11, 12] and was adapted for corresponding results at 13 TeV [14]. In this work measurements of kinematic spectra of the top quarks and $t\bar{t}$ system are performed using the same adaptation of the aforementioned method, with the exception of the single-differential measurement of $m(t\bar{t})$ which is based on the loose kinematic reconstruction developed in [15]. Detailed descriptions of the full and loose kinematic reconstruction are given in Section 5.8.1 and 5.8.2, respectively.

5.8.1 Full kinematic reconstruction

The full kinematic reconstruction consists of an analytical and algebraic method performed for each event in order to reconstruct both top quarks. The momenta of the two neutrinos constitute six unknowns and therefore a system of equations is constructed based on six constraints coming from the missing transverse energy, W boson mass and top mass.

Assuming that the missing transverse energy is well modelled and can be contributed solely to the neutrinos it follows that

$$E_x^{\text{miss}} = p_{x,\nu} + p_{x,\bar{\nu}} \tag{5.1}$$

and

$$E_y^{\text{miss}} = p_{y,\nu} + p_{y,\bar{\nu}}, \tag{5.2}$$

where E_x^{miss} and E_y^{miss} are the transverse components of $\vec{E}_{\text{T}}^{\text{miss}}$, and $p_{x,\nu}$ ($p_{x,\bar{\nu}}$) and $p_{y,\nu}$ ($p_{y,\bar{\nu}}$) are the transverse components of the neutrino (anti-neutrino) momentum. Hence, the problem is reduced to 4 unknowns. One can also use the masses of the W bosons to place constraints on their decay products by assuming $m_{W^+} = m_{W^-} =$ 80.4 GeV such that

$$m_{W^+}^2 = (E_{l^+} + E_\nu)^2 - (p_{x,l^+} + p_{x,\nu})^2 - (p_{y,l^+} + p_{y,\nu})^2 - (p_{z,l^+} + p_{z,\nu})^2 \tag{5.3}$$

and

$$m_{W^-}^2 = (E_{l^-} + E_{\bar{\nu}})^2 - (p_{x,l^-} + p_{x,\bar{\nu}})^2 - (p_{y,l^-} + p_{y,\bar{\nu}})^2 - (p_{z,l^-} + p_{z,\bar{\nu}})^2, \tag{5.4}$$

where $(E_{l^-}, p_{x,l^-}, p_{y,l^-}, p_{z,l^-})/(E_\nu, p_{x,\nu}, p_{y,\nu}, p_{z,\nu})$ is the four-vector of the lepton/neutrino and $(E_{l^+}, p_{x,l^+}, p_{y,l^+}, p_{z,l^+})/(E_{\bar{\nu}}, p_{x,\bar{\nu}}, p_{y,\bar{\nu}}, p_{z,\bar{\nu}})$ is the four-vector of the

anti-lepton/anti-neutrino. The energies of the neutrinos are determined entirely by their three-momenta, assuming them to be massless. Finally, the top mass assumptions $m_t = m_{\bar{t}} = 172.5$ GeV are used to place constraints on the decay products of the top quarks and W bosons. The last two equations in the system are thus

$$m_t^2 = (E_{l^+} + E_\nu + E_b)^2 - (p_{x,l^+} + p_{x,\nu} + p_{x,b})^2 - (p_{y,l^+} + p_{y,\nu} + p_{y,b})^2 - (p_{z,l^+} + p_{z,\nu} + p_{z,b})^2 \tag{5.5}$$

and

$$m_{\bar{t}}^2 = (E_{l^-} + E_{\bar{\nu}} + E_{\bar{b}})^2 - (p_{x,l^-} + p_{x,\bar{\nu}} + p_{x,\bar{b}})^2 - (p_{y,l^-} + p_{y,\bar{\nu}} + p_{y,\bar{b}})^2 - (p_{z,l^-} + p_{z,\bar{\nu}} + p_{z,\bar{b}})^2, \tag{5.6}$$

where $(E_b, p_{x,b}, p_{y,b}, p_{z,b})/(E_{\bar{b}}, p_{x,\bar{b}}, p_{y,\bar{b}}, p_{z,\bar{b}})$ are the four-vectors of the b/anti-b-jets. The system comprising Equation 5.1 to 5.6 can be combined into a single equation which is of the 4-th order in one of the neutrino momentum components. Here, $p_{x,\nu}$ is chosen without loss of generality such that

$$0 = h_0 p_{x,\nu}^4 + h_1 p_{x,\nu}^3 + h_2 p_{x,\nu}^2 + h_3 p_{x,\nu} + h_4, \tag{5.7}$$

where the coefficients, h, depend on E_x^{miss}, E_y^{miss} and the four-vectors of the leptons and b-quarks i.e. the visible decay products. This polynomial has a maximum of four solutions. Measurement fluctuations due to imperfect detector resolutions can lead to imaginary or unphysical solutions but these can be recovered through a randomized smearing of the energies and directions of the leptons and b-jets. The smearing factors applied to the energies are obtained from the detector energy response, while the directional smearing is based on a Gaussian distribution of the angular momentum of the lepton or b-jet with respect to its nominal direction. The W-boson mass is also smeared according to its Breit–Wigner distribution. A simultaneous smearing of the leptons, b-jets and W boson mass is then performed and Equation 5.7 is solved. This is repeated 100 times which gives rise to a potential number of 100×4 solutions. The multiplicity of solutions is increased by all possible permutations of leptons and potential b-jet candidates in the event. However, solutions with two b-tagged jets are preferred. Thus, attempts at solving Equation 5.7 are first made from the list of b-tagged jets, where each possible combination with the leptons is smeared 100 times. If no solutions are found all combinations from the lists of b-tagged and non b-tagged jets are also tried in a similar way. If more than one combination yields a solution in either b-tag hierarchy, a weight is computed based on the distribution of the mass of the lepton plus b-jet, originating from a top quark decay, obtained from the reference simulation at generator level after the full selection. This is given by

$$w_s = \sum_{i=1}^{100} w_i = \sum_{i=1}^{100} w_{m(\bar{l}b)}^i \cdot w_{m(l\bar{b})}^i, \tag{5.8}$$

where $m(\bar{l}b)$ and $m(l\bar{b})$ denote the masses of one possible set of b- and anti-b-jet assignments, and if these masses are larger than 180 GeV the corresponding weights

are set to 0. These weights can be thought of as probabilities that express how likely it is to get these masses from the lepton and b-jets. Finally, the combination that gives the largest value of w_s is chosen. If a single combination results in more than one solution to Equation 5.7 the one that yields the smallest reconstructed invariant mass of the $t\bar{t}$ system is chosen, and it has been shown that this gives the correct solution in the majority of cases [125]. Finally the top and anti-top can be reconstructed from the weighted average of the smeared solutions such that the momentum of e.g. the top quark is given by

$$\langle \vec{p}(t) \rangle = \frac{1}{w_s} \sum_{i=1}^{100} w_i \vec{p}(t)_i, \tag{5.9}$$

where w_i is set to 0 if no solution was obtained for that smearing attempt. Finally, the $t\bar{t}$ system can be reconstructed by assuming that $m_t = m_{\bar{t}} = 172.5$ GeV and using the momenta of the reconstructed top and anti-top.

5.8.2 Loose kinematic reconstruction

The loose kinematic reconstruction is used as an alternative to the full kinematic reconstruction described in the previous section. An extraction of the top pole mass is outside the scope of this work but differential cross section measurements involving $m(t\bar{t})$ have been used for this purpose [15]. Hence, it's important that the $t\bar{t}$ production cross section measured in bins of $m(t\bar{t})$ does not depend on the assumed value of m_t. In the full kinematic reconstruction m_t is applied as a constraint in the procedure but this constraint is dropped in the loose kinematic reconstruction which makes an extraction of the top pole mass possible but also allows one to probe the mass onset region of $t\bar{t}$ production. However, a caveat is that one must forego reconstructing the top and anti-top separately. Only a reconstruction of the $t\bar{t}$ system can be performed in this case.

The algorithm behind the loose kinematic reconstruction starts by selecting jets and separating them into two categories; b-tagged jets and non-btagged jets. The two lists are then ordered according to p_{T} (leading first). Candidate b-jet pairs are selected from one or both lists in accordance with the following decision hierarchy:

• **Two b-tagged jets**: If there are two or more b-tagged jets present in an event the pair with highest and second-highest p_{T} are selected.

• **One b-tagged jet**: If there is only one b-tagged jet present in an event it's selected together with the highest p_{T} jet from the no b-tag category.

The candidate b-jet pairs are then tested individually to see if they pass the mass criteria $m_{lb} < 180$ GeV for at least one of the two possible sets of assignments with the selected lepton pair. Finally, the candidate b-jet pair that fulfills this criteria and has the highest rank in the hierarchy described above is selected.

In order to reconstruct the neutrino pair it is assumed that the missing transverse

energy is well-modelled and can be assigned such that

$$p_x(\nu\bar{\nu}) = E_x^{\text{miss}}$$

and

$$p_y(\nu\bar{\nu}) = E_y^{\text{miss}},$$

where $p_x(\nu\bar{\nu})$ and $p_y(\nu\bar{\nu})$ are the transverse components of the neutrino pair four-vector, and E_x^{miss} and E_y^{miss} are the corresponding components of $\vec{E}_{\text{T}}^{\text{miss}}$. It is assumed that

$$p_z(\nu\bar{\nu}) = p_z(l\bar{l})$$

and

$$E(\nu\bar{\nu}) = E(l\bar{l}),$$

where $p_z(\nu\bar{\nu})$ ($p_z(l\bar{l})$) and $E(\nu\bar{\nu})$ ($E(l\bar{l})$) are the longitudinal component and energy of the neutrino (lepton) pair four-vector, respectively. Finally, mass constraints are imposed on the neutrino pair and the $l\bar{l}\nu\bar{\nu}$ system such that $m(\nu\bar{\nu}) \geq 0$ and $m(l\bar{l}\nu\bar{\nu}) \geq 2m_W$, where the mass of the W boson is set to $m_W = 80.4$ GeV. The $t\bar{t}$ system then corresponds to the selected lepton and b-jet pairs together with the reconstructed neutrino pair. The performances of the full and loose kinematic reconstruction are similar in terms of the efficiency and kinematic resolutions, where the former is above 90% [15].

5.9 Event selection and control plots

The selection strategy in this work follows the one used in the corresponding 2016 analysis [14] and is summarized as follows:

• **Initial selection (step 1)**: The initial event selection begins by identifying the primary vertex. All good vertices must have at least 4 tracks and be within $|z| < 24$ cm and a radius of 2 cm from the nominal interaction point. If several vertices pass the criteria above, the primary vertex is taken as the one with the highest sum of p_{T}^2 of associated objects, including tracks and $E_{\text{T}}^{\text{miss}}$, and the rest are labelled as pile-up. Events that have significant noise in the hadronic calorimeter are removed. Furthermore, events are grouped into individual channels of $e^{\pm}e^{\mp}$, $\mu^{\pm}\mu^{\mp}$ and $e^{\pm}\mu^{\mp}$ by applying the corresponding trigger menus of single lepton and dilepton triggers described in Section 5.5.

• **Lepton pair (step 2)**: Exactly two oppositely charged leptons must be present in an event. The leading and trailing lepton must fulfill $p_{\text{T}} > 25$ GeV and $p_{\text{T}} > 20$ GeV, respectively, and the pseudorapidity of both leptons must satisfy $|\eta| < 2.4$.

• **Dilepton mass cut (step 3)**: In order to reduce backgrounds from low-mass Drell-Yan processes and decays of heavy-flavour resonances, the dilepton mass of the lepton pair is required to be $m_{l\bar{l}} > 20$ GeV.

• **Z-boson mass veto (step 4)**: The Z+jets background peaks within $76 < m_{l\bar{l}} < 106$ GeV and this region is therefore cut away in the same-flavour channels.

• **At least two jets (step 5)**: The jet clustering is performed with the anti-k_{T} algorithm using a cone size of 0.4. Jets that overlap with the selected leptons inside $\Delta R = 0.4$ are removed. All jets are required to have transverse momenta of $p_{\mathrm{T}} > 30$ GeV and pseudorapidities within $|\eta| < 2.4$. At least two jets must be present in an event.

• $\boldsymbol{E_{\mathrm{T}}^{\mathrm{miss}}}$ **(step 6)**: The missing transverse energy is required to be $E_{\mathrm{T}}^{\mathrm{miss}} > 40$ GeV in the same-flavour channels.

• **At least one b-tagged jet (step 7)**: At least one selected jet is required to be b-tagged according to the loose working point definition of the DeepCSV algorithm.

• **Kinematic reconstruction (step 8)**: Finally, the event must have a solution when using either the full or loose kinematic reconstruction to reconstruct the top, anti-top and/or $t\bar{t}$ system. The $t\bar{t}$ production cross section measured as function of the invariant mass of the $t\bar{t}$ system, $m(t\bar{t})$, is performed with the loose kinematic reconstruction (see Section 8.2.2), while the full kinematic reconstruction is used for all other measurements.

Table 5.2 shows the total number of expected events for the signal, background and observed number of events in data for each selection step (after step 4) and channel ($\mu^{\pm}\mu^{\mp}$, $e^{\pm}\mu^{\mp}$, $e^{\pm}e^{\mp}$ and the combined channel). The simulation has been normalized to a total integrated luminosity of 137.6 fb^{-1}, which corresponds to the Run 2 data-taking period and separate tables for individual years can be found in Appendix G.

Figures 5.7 to 5.14 show control plots for a selected number of distributions from step 3 and up. Generally a good agreement between data and the reference simulation is observed within uncertainties. It's immediately clear that the dileptonic channel is a very clean signature upon looking at Figure 5.13, which shows distributions of the transverse momentum and rapidity of the top quark (denoted by $p_{\mathrm{T}}(t)$ and $y(t)$, respectively), as well as the transverse momentum of the $t\bar{t}$ system and jet multiplicity (denoted by $p_{\mathrm{T}}(t\bar{t})$ and N_{jet}, respectively) after the full selection. The distribution of $y(t)$ is slightly more central in simulation compared to data, while the $p_{\mathrm{T}}(t)$ spectrum illustrates that data is softer than in simulation. This is known as the top p_{T} problem and has also been observed in previous ATLAS and CMS measurements in other channels and at different energies [11, 13, 14]. The $p_{\mathrm{T}}(t\bar{t})$ spectrum exhibits a slight modulation in the ratio of data and simulation, while N_{jet} is well described within uncertainties.

The full and loose kinematic reconstructions are compared in Figure 5.14 which shows distributions of the rapidity and invariant mass of the $t\bar{t}$ system ($y(t\bar{t})$ and $m(t\bar{t})$, respectively). The two types of kinematic reconstruction are found to have a consistent and good agreement between data and simulation. Furthermore, it's evident from the distributions of $m(t\bar{t})$ that dropping the requirement on m_t in the loose kinematic reconstruction allows one to probe the threshold region.

Table 5.2: The table shows the total number of expected events for signal and background processes compared to the number of events observed in Run 2 data for each selection step and channel ($\mu^{\pm}\mu^{\mp}$, $e^{\pm}\mu^{\mp}$, $e^{\pm}e^{\mp}$ and the combined channel). The simulation has been normalized to a total integrated luminosity of 137.6 fb^{-1}, which corresponds to the Run 2 data-taking period.

$\mu^{\pm}\mu^{\mp}$ sample	Z-veto	≥ 2 jets	$E_{\mathrm{T}}^{\mathrm{miss}}$	≥ 1 b-tag	kin. reco	loose. kin. reco
$t\bar{t}$ signal	444855.9	355495.3	298368.2	282649.9	253742.1	270402.6
$t\bar{t}$ other	79962.5	63990.1	52861.7	49395.8	45740.4	47084.6
$t\bar{t} + Z/W$	1340.1	1272.0	1093.8	1042.1	849.6	921.4
Single top	51821.6	23943.4	20183.8	17946.9	12569.9	14020.2
diboson	70605.2	9496.5	5915.2	2125.0	1221.5	1364.8
W+jets	7964.7	1487.6	1284.1	621.8	360.5	364.4
Z+jets	7423415.1	590204.4	227674.6	82410.8	52847.3	56849.7
Sum MC	8079965.1	1045889.2	607381.3	436192.3	367331.3	391007.6
Data	8089847.0	1019665.0	601963.0	428294.0	360945.0	381792.0
$e^{\pm}\mu^{\mp}$ sample	Z-veto	≥ 2 jets	$E_{\mathrm{T}}^{\mathrm{miss}}$	≥ 1 b-tag	kin. reco	loose. kin. reco
$t\bar{t}$ signal	807429.9	646894.4	646894.4	613361.4	563073.5	588473.3
$t\bar{t}$ other	143899.9	115370.0	115370.0	108215.4	101679.7	103698.6
$t\bar{t} + Z/W$	2191.6	2071.6	2071.6	1958.6	1676.9	1774.9
Single top	93452.7	43161.4	43161.4	38445.7	28163.3	30528.2
diboson	110821.1	9591.8	9591.8	3183.9	1998.2	2161.2
W+jets	22723.9	3299.5	3299.5	947.8	676.9	696.7
Z+jets	281184.0	25594.6	25594.6	8942.2	7136.2	7282.5
Sum MC	1461703.1	845983.3	845983.3	775055.0	704404.8	734615.4
Data	1424701.0	803181.0	803181.0	730465.0	663856.0	689489.0
$e^{\pm}e^{\mp}$ sample	Z-veto	≥ 2 jets	$E_{\mathrm{T}}^{\mathrm{miss}}$	≥ 1 b-tag	kin. reco	loose. kin. reco
$t\bar{t}$ signal	229181.8	183585.9	151039.8	143001.8	129703.4	136411.9
$t\bar{t}$ other	37047.0	29710.4	24440.2	23026.2	21516.4	22069.8
$t\bar{t} + Z/W$	730.3	693.4	578.1	548.4	444.6	480.6
Single top	26264.2	12375.5	10192.1	9131.2	6331.5	6951.6
diboson	35380.7	4947.9	2741.8	1029.3	581.9	651.8
W+jets	7465.3	899.7	623.8	231.5	114.7	116.2
Z+jets	3284703.0	271230.6	80952.9	29045.8	19274.4	20836.9
Sum MC	3620772.3	503443.4	270568.7	206014.0	177966.9	187518.8
Data	3436947.0	472229.0	258627.0	193868.0	167443.0	174818.0
combined sample	Z-veto	≥ 2 jets	$E_{\mathrm{T}}^{\mathrm{miss}}$	≥ 1 b-tag	kin. reco	loose. kin. reco
$t\bar{t}$ signal	1481467.6	1185975.6	1096302.3	1039013.1	946519.0	995287.8
$t\bar{t}$ other	260909.4	209070.4	192671.9	180637.4	168936.5	172853.0
$t\bar{t} + Z/W$	4262.0	4037.1	3743.5	3549.0	2971.1	3176.9
Single top	171538.5	79480.2	73537.2	65523.8	47064.8	51500.0
diboson	216807.0	24036.2	18248.9	6338.2	3801.6	4177.8
W+jets	38153.8	5686.8	5207.4	1801.1	1152.2	1177.3
Z+jets	10989302.1	887550.6	334195.3	120384.8	79261.8	84973.0
Sum MC	13162440.4	2395837.0	1723906.6	1417247.4	1249706.8	1313145.8
Data	12951495.0	2295075.0	1663771.0	1352627.0	1192244.0	1246099.0

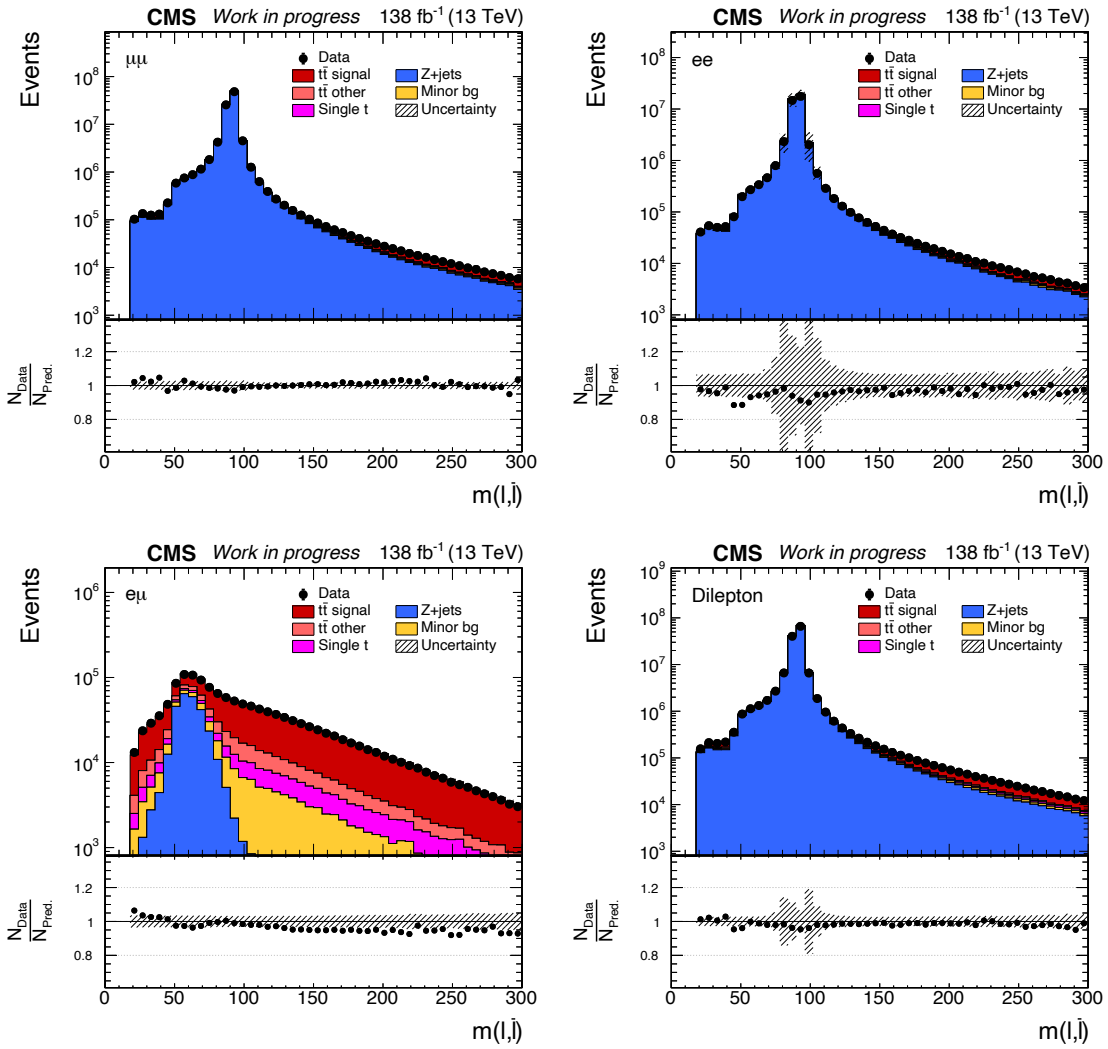

Figure 5.7: Distributions of the dilepton mass, $m(l\bar{l})$, are shown separately for the $\mu^{\pm}\mu^{\mp}$ (top left), $e^{\pm}e^{\mp}$ (top right), $e^{\pm}\mu^{\mp}$ (bottom left) and combined channels (bottom right) at step 3 in the selection cutflow, after passing the single lepton and dilepton triggers, the lepton pair requirements and the dilepton mass cut of $m_{l\bar{l}} > 20$ GeV. The data (black dots) is compared to the summed $t\bar{t}$ signal and backgrounds, where the former is simulated with POWHEG (version 2)+PYTHIA8. All simulated samples have been normalized to an integrated luminosity of 137.6 fb^{-1}and the dashed band in the ratio shows the shape uncertainties (see Chapter 7).

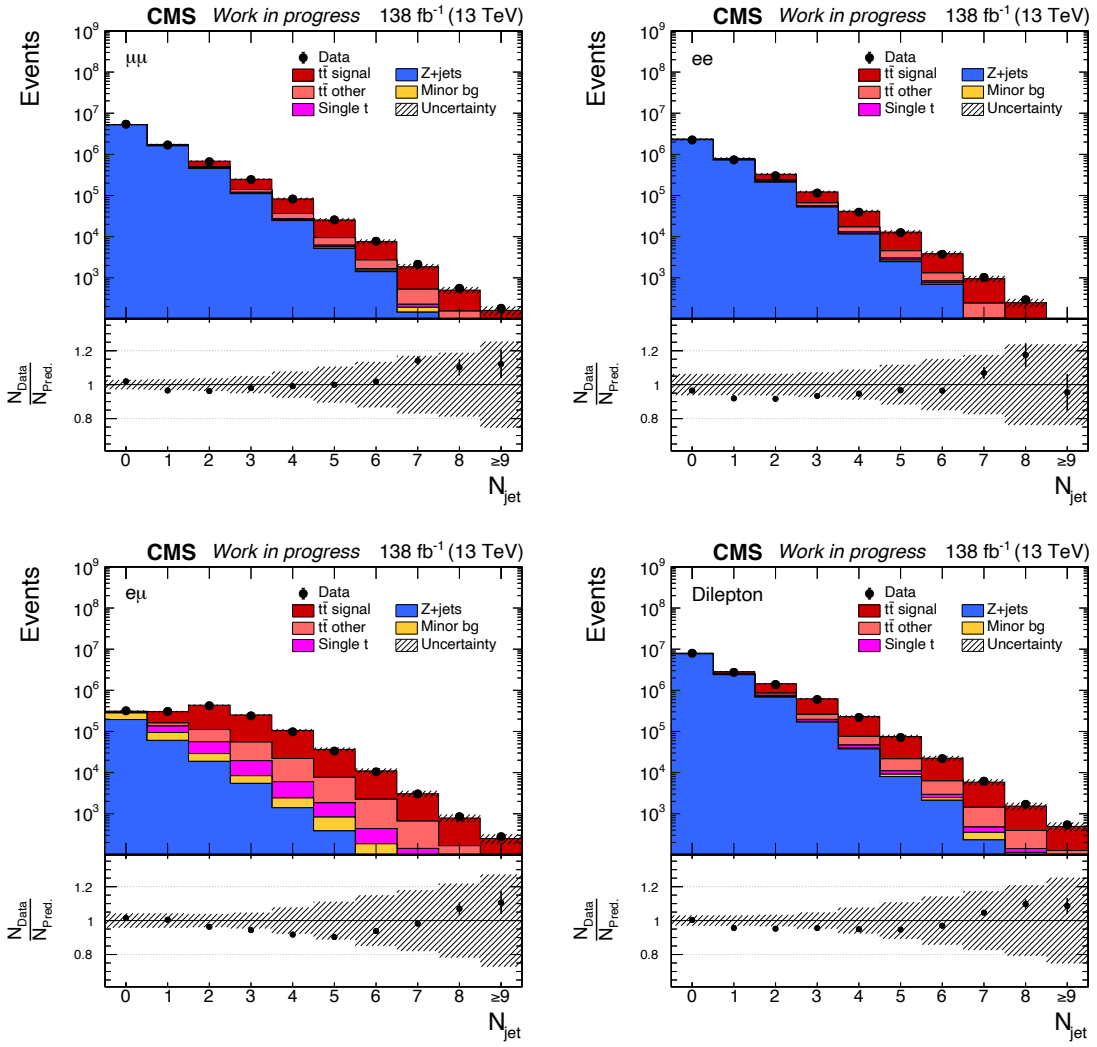

Figure 5.8: Distributions of the jet multiplicity, N_{jet}, are shown separately for the $\mu^{\pm}\mu^{\mp}$ (top left), $e^{\pm}e^{\mp}$ (top right), $e^{\pm}\mu^{\mp}$ (bottom left) and combined channels (bottom right) at step 4 in the selection cutflow, after excluding the Z boson mass window of $76 < m_{l\bar{l}} < 106$ GeV. See Figure 5.7 for further details.

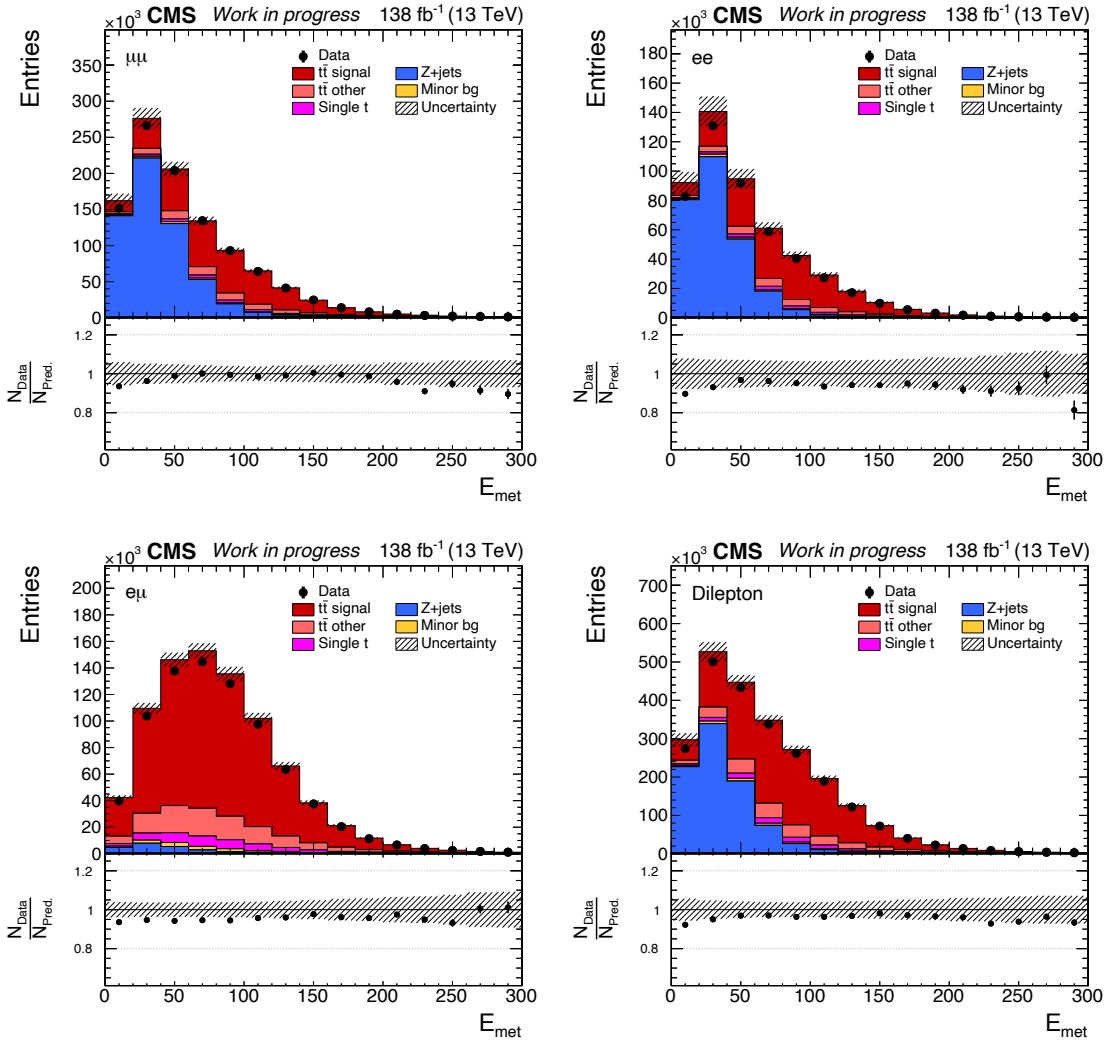

Figure 5.9: Distributions of the missing transverse energy energy, $E_{\mathrm{T}}^{\mathrm{miss}}$, are shown separately for the $\mu^{\pm}\mu^{\mp}$ (top left), $e^{\pm}e^{\mp}$ (top right), $e^{\pm}\mu^{\mp}$ (bottom left) and combined channels (bottom right) at step 5 in the selection cutflow, after requiring at least two jets. See Figure 5.7 for further details.

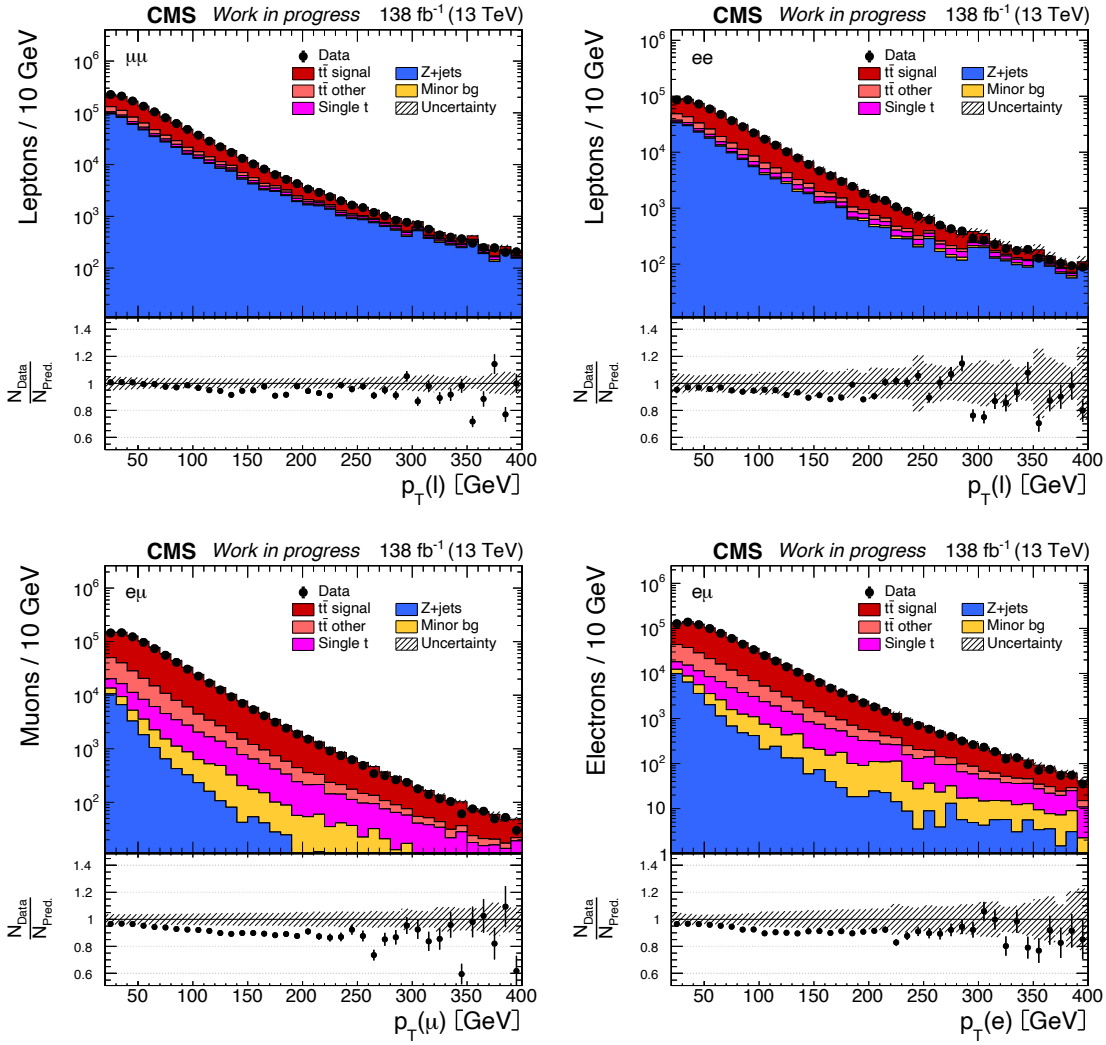

Figure 5.10: Distributions of the transverse momenta of both leptons, $p_{\mathrm{T}}(\ell)$, are shown separately for the $\mu^{\pm}\mu^{\mp}$ (top left), $e^{\pm}e^{\mp}$ (top right) and $e^{\pm}\mu^{\mp}$ channels, where the bottom left (right) plot shows $p_{\mathrm{T}}(\ell)$ for the muon (electron) at step 6 in the selection cutflow, after applying the cut $E_{\mathrm{T}}^{\mathrm{miss}} > 40$ GeV in the same-flavour channels. See Figure 5.7 for further details.

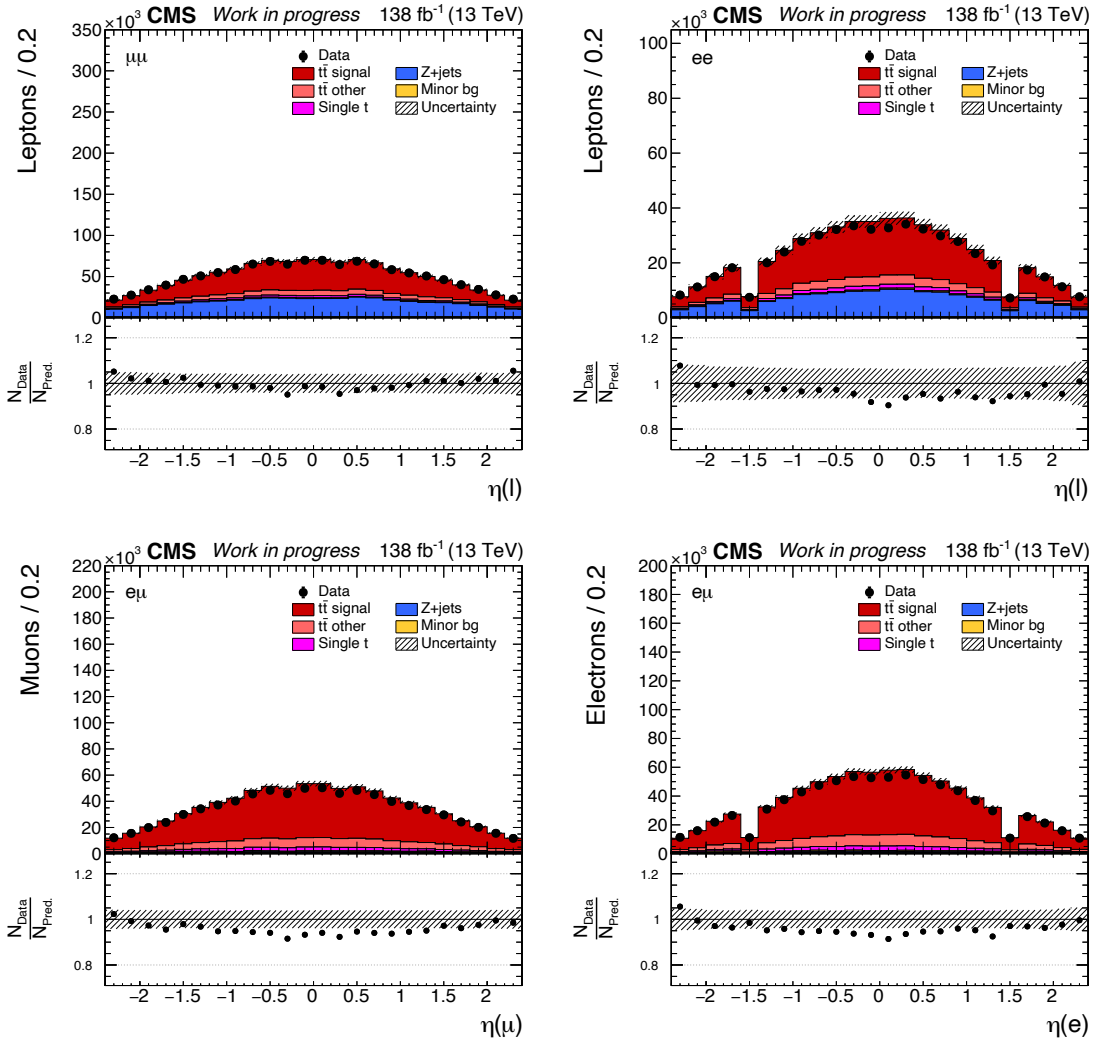

Figure 5.11: Distributions of the pseudorapidity of both leptons, $\eta(l)$, are shown separately for the $\mu^{\pm}\mu^{\mp}$ (top left), $e^{\pm}e^{\mp}$ (top right) and $e^{\pm}\mu^{\mp}$ channels, where the bottom left (right) plot shows $\eta(l)$ for the muon (electron) at step 6 in the selection cutflow, after applying the cut $E_{\mathrm{T}}^{\mathrm{miss}} > 40$ GeV in the same-flavour channels. See Figure 5.7 for further details.

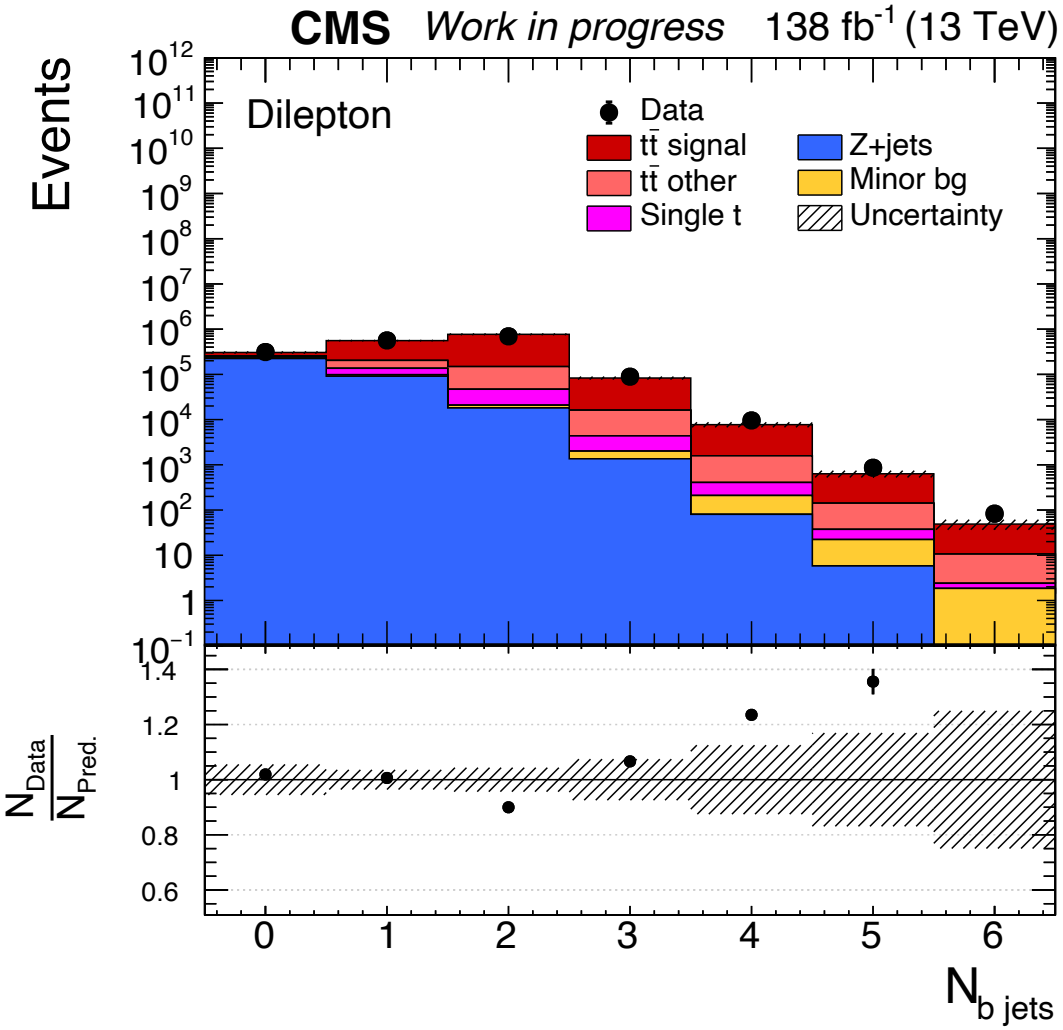

Figure 5.12: The distribution of the b-jet multiplicity, $N_{b\,\text{jets}}$, is shown in the combined channel at step 6 in the selection cutflow, after applying the cut $E_{\text{T}}^{\text{miss}} > 40$ GeV in the same-flavour channels. See Figure 5.7 for further details.

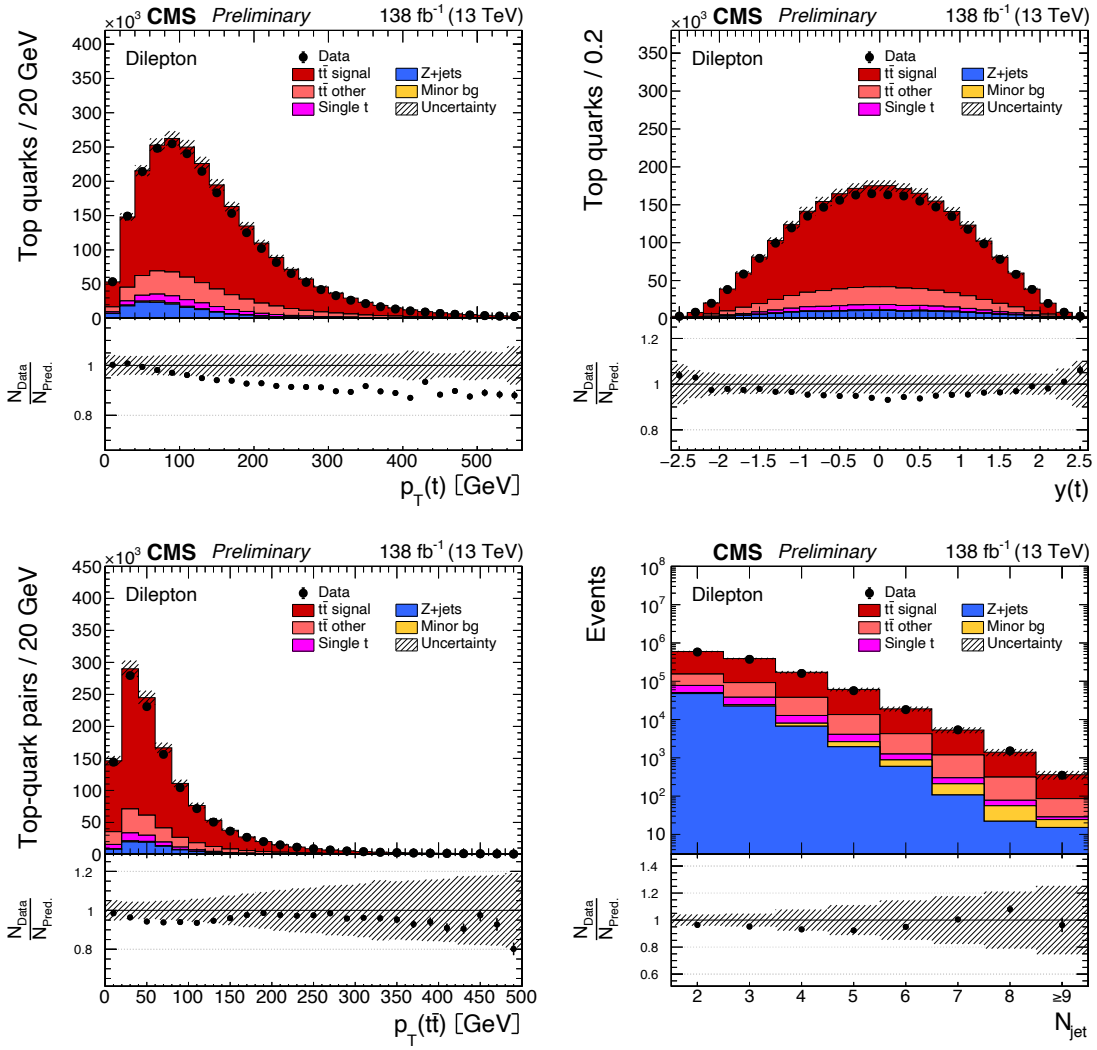

Figure 5.13: The top left and right plots show distributions of the transverse momentum, $p_{\mathrm{T}}(t)$, and rapidity, $y(t)$, of the top quark, respectively, while the bottom left and right plots show distributions of the transverse momentum of the $t\bar{t}$ system, $p_{\mathrm{T}}(t\bar{t})$, and jet multiplicity, N_{jet}, respectively. The top and $t\bar{t}$ system have been reconstructed with the full kinematic reconstruction and all distributions are shown after the full selection in the dilepton channel for Run 2. See Figure 5.7 for further details.

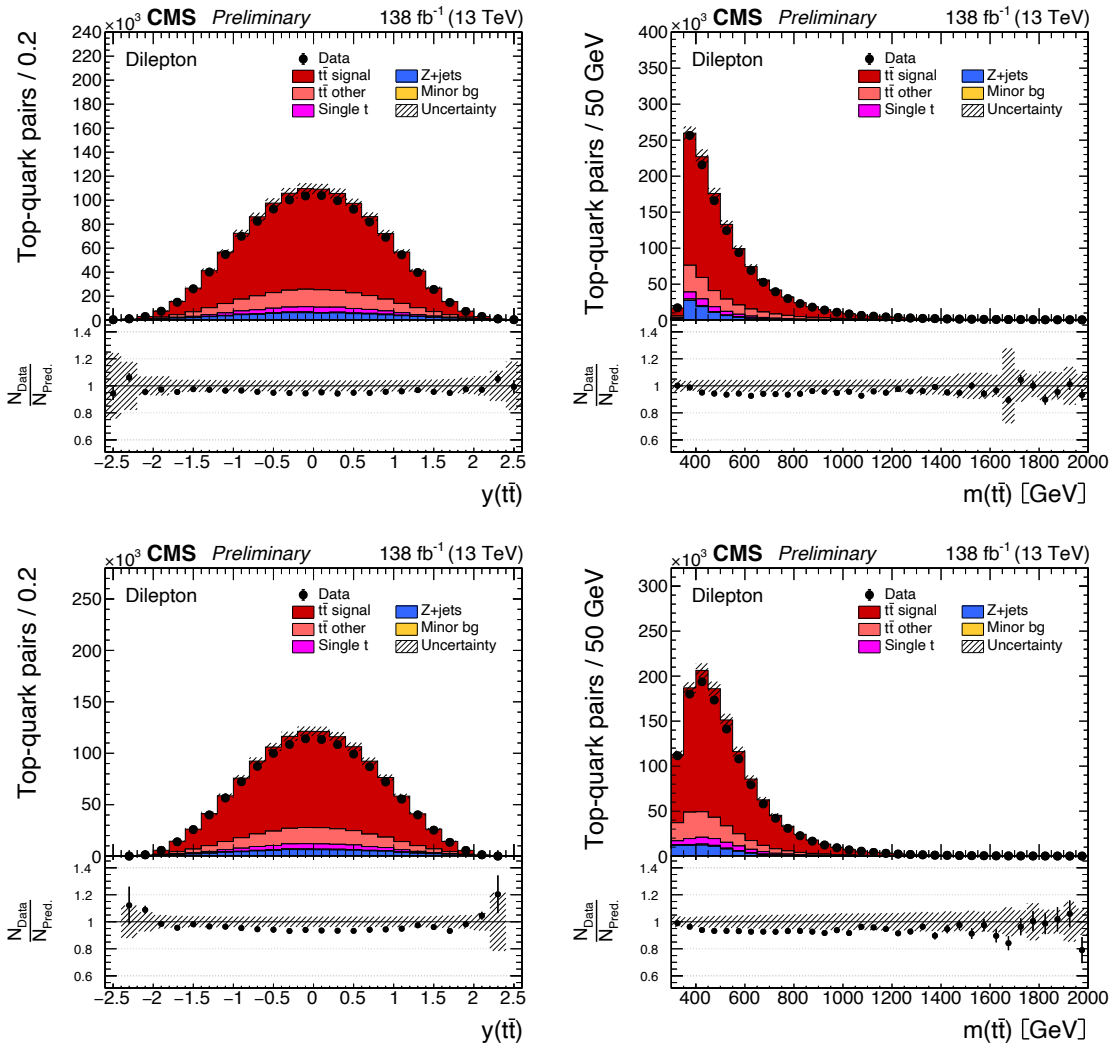

Figure 5.14: The plots in the left and right columns show distributions of the rapidity, $y(t\bar{t})$, and invariant mass, $m(t\bar{t})$, of the $t\bar{t}$ system, respectively. Distributions in the top (bottom) row are shown after the full selection using the full (loose) kinematic reconstruction. See Figure 5.7 for further details.

Chapter 6

Top quark pair production

Cross section measurements of top pair production can be performed inclusively or differentially. The latter is the subject of this work but the former is also performed as a cross check of the total production rate. The inclusive measurement provides the total absolute $t\bar{t}$ production rate in the full phase space as explained in Section 6.1, while the differential cross sections are functions of one or more kinematic variables, where the variable X or combination [Y, X] refer to single- and double-differential measurements, respectively. The super-bin is listed first in this notation, hence [Y, X] means that the differential cross section is measured as a function of X in ranges of Y. In this work, the focus is solely on single- and double-differential distributions for which both absolute and normalized cross sections are provided with exact definitions given in Section 6.2.

Prior to performing any of the measurements described above, one must subtract the background from the total number of events in data after applying all selection criteria. This procedure is outlined in Section 6.3. Section 6.4 then proceeds to describe how detector effects such as resolutions, efficiencies and acceptances are corrected in differential measurements via an unfolding procedure with the TUnfold software [126]. Moreover, two different definitions are used for the true spectrum in this procedure. One can unfold to either parton or particle level, which differ in their definitions of the top quark, its visible decay products and the covered phase space. Measurements at parton (particle) level are performed in the full (fiducial) phase space and further details are given in Section 6.6.

Finally, it is crucial to choose a good binning for the measured spectra and this can be achieved by monitoring the purity, stability and efficiency as explained in Section 6.7. Consistency checks of the unfolding setup are performed for each cross section, where the chosen example in Section 6.8 serves to highlight the main features of different types of tests, assessing the validity of the unfolding procedure, the statistical properties of the estimator of the true level spectrum and the sensitivity to a potential bias in the truth of the unfolded spectra.

6.1 Inclusive cross sections

The inclusive cross section is computed by counting $t\bar{t}$ events that pass the full selection criteria and is given by

$$\sigma_{t\bar{t}}^{\text{incl.}} = \frac{N_{\text{data}}^{\text{signal}}}{\epsilon^{\text{det}} \mathcal{A} \mathcal{B} \mathcal{L}}, \tag{6.1}$$

where the total number of signal-like events in data is denoted by $N_{\text{data}}^{\text{signal}}$ (after background subtraction, see Section 6.3). Moreover, one must also account for the selection and reconstruction efficiencies, hence $N_{\text{data}}^{\text{signal}}$ is divided by the detector efficiency, ϵ_{det}, and the result is extrapolated to the full phase space by, additionally, correcting for the acceptance, $\mathcal{A}$ (see Section 6.6 for further details on the phase space extrapolation). Finally, the result is divided by the branching ratio in the $t\bar{t}$ dileptonic decay channel, $\mathcal{B}$, and the integrated luminosity, $\mathcal{L}$.

6.2 Absolute and normalized differential cross sections

Measurements of differential cross sections can be either absolute or normalized. In this work, both are performed for each measurement of the $t\bar{t}$ production cross section as a function of kinematic spectra of the studied objects.

The absolute differential cross section of an observable X at parton level in the full phase space is given by the following expression

$$\frac{d\sigma_i}{dX} = \frac{1}{\mathcal{B}\mathcal{L}} \frac{x_i}{\Delta_i^X}, \tag{6.2}$$

where x_i is the number of events in bin i of X after the full event selection, background subtraction and unfolding, as described later in this chapter. Here x_i also accounts for the efficiency corrections and phase space extrapolation, which are handled via the normalization of the response matrix in the unfolding procedure (see Section 6.4). The term Δ_i^X is the width of bin i of X, $\mathcal{L}$ is the integrated luminosity and $\mathcal{B}$ is the branching ratio of the $t\bar{t}$ dileptonic decay channel. Equation 6.2 also holds true for measurements at particle level in the fiducial phase space, except here $\mathcal{B}$ is not applied. Furthermore, in the case of double-differential measurements it should be noted that the division by bin width is done with respect to the variable on the x-axis in the result figures.

Both $\mathcal{B}$ and $\mathcal{L}$ cancel out for the normalized cross section measurement, which is given by

$$\frac{1}{\sigma}\frac{d\sigma_i}{dX} = \frac{1}{\Delta_i^X} \frac{x_i}{\sum_i x_i}. \tag{6.3}$$

While absolute cross sections are sensitive to both the rate and shape of the measured spectra, the corresponding normalized measurements are only sensitive to

the latter. However, as seen in Equation 6.3, this has the advantage that rate-based uncertainties cancel out, facilitating better precision overall.

6.3 Background subtraction

To perform either differential or inclusive cross section measurements of $t\bar{t}$ production, background must be subtracted from data after the full event selection. The non-$t\bar{t}$ background can simply be subtracted as follows

$$N_{\text{data}}^{\text{all } t\bar{t}} = N_{\text{data}}^{\text{selected}} - N_{\text{MC}}^{\text{bkg}},$$

where $N_{\text{data}}^{\text{all } t\bar{t}}$ gives the total number of $t\bar{t}$ events in data, $N_{\text{data}}^{\text{selected}}$ is the total number of selected events in data and $N_{\text{MC}}^{\text{bkg}}$ is the corresponding number of events for all non-$t\bar{t}$ backgrounds. The background processes arising from $t\bar{t}$ are subtracted though a fractional correction of $N_{\text{data}}^{\text{all } t\bar{t}}$ defined by

$$f^{signal} = \frac{N_{\text{MC}}^{\text{signal}}}{N_{\text{MC}}^{\text{signal}} + N_{\text{MC}}^{t\bar{t}\,\text{other}}},$$

where $N_{\text{MC}}^{\text{signal}}$ is the total number of signal events in the reference MC and $N_{\text{MC}}^{t\bar{t}\,\text{other}}$ is the total number of background events arising from $t\bar{t}$. Here the latter includes $t\bar{t}$ decays via τ, as well as backgrounds from the $t\bar{t}$ lepton+jets and all-hadronic decay channels. However, it's important to note that for measurements performed at particle level in the fiducial phase space, $N_{\text{MC}}^{t\bar{t}\,\text{other}}$ also includes a special out-of-space background, coming from events that are reconstructed and selected at detector level but generated outside the fiducial phase space. The fractional correction of the type of events listed above ensures that the measured cross section doesn't depend on the theoretical cross section of $t\bar{t}$ production used in the normalization of these samples (see Chapter 5). Finally, one can write

$$N_{\text{data}}^{\text{signal}} = N_{\text{data}}^{\text{all } t\bar{t}} \cdot f^{\text{signal}},$$

where $N_{\text{data}}^{\text{signal}}$ is the total number of signal-like events in data, i.e. the number referred to as y later in the text (see discussion pertaining to Equation 6.4).

6.4 Unfolding with TUnfold

The unfolding is performed with the TUnfold software package [126], developed at Deutsches Elektronen-Synchrotron (DESY). The process of unfolding can be thought of as correcting for blurring detector effects in order to unveil the spectrum of a given observable that is as close to the truth as possible.

When a particle is detected, the subsequent reconstruction of its kinematic spectra is limited by the finite precision of the detector itself. This is due to the finite spatial resolution of e.g. pixels in the tracking system, limited time resolution of read-out systems, statistical fluctuations when sampling energies in the calorimeters

etc. It's also due to problems incurred by the detector systems along the way such as the accumulation of irradiation effects in detector components and dead modules. In MC, these effects are accounted for by putting the prediction through the detector simulation and using dedicated scale factors or corrections applied to kinematic spectra of the reconstructed particles in order to match the MC to resolutions and efficiencies in data. The detector efficiency can then be extracted from the MC, and for inclusive cross sections, it's sufficient to apply this as a correction that includes the impact from distorted kinematic distributions on the selected number of signal events in data, but for differential measurements, where one must know the event counts in data within small windows of the phase space, the procedure has an added level of complexity. Now the signal events in data must be corrected based on how the reconstructed MC signal events at detector level behave with respect to their predictions at generator level for different bins of the measured spectra. The method of correcting for reconstructed events that migrate away from their predictions and end up in different bins of the phase space, so-called bin-to-bin migrations, is called unfolding.

The task of unfolding is stated explicitly in Equation 6.4 as follows

$$\tilde{y}_i = \sum_{j=1}^{m} A_{ij}\tilde{x}_j,\ 1 \leq i \leq n. \tag{6.4}$$

Here A denotes the response matrix of a given observable, where the true distribution is compared to the reconstructed distribution at detector level. This can also be thought of as a probability matrix, expressing how likely it is that a generated event in bin j will be reconstructed in bin i. Thus, the response matrix emulates the detector effects which manifest in the form of bin-to-bin migrations, and an example of it is depicted in Figure 6.1, which shows the response matrix for the transverse momentum of the top, $p_{\mathrm{T}}(t)$, at parton level in the full phase space. Upon applying the response matrix to the true spectrum, $\tilde{x}$, one obtains the expected yields at detector level, $\tilde{y}$. However, it's important to emphasize that the observed event counts at detector level after background subtraction, y, differ from $\tilde{y}$ due to the presence of statistical fluctuations, described by the Poisson distribution. Therefore, when applying the inverse response matrix on y one actually obtains an estimator, x, of the true spectrum as visualized by the schematic overview in Figure 6.2. In practice, however, the problem of unfolding cannot be reduced to a trivial matrix inversion of Equation 6.4 with $\tilde{y}$ and $\tilde{x}$ substituted for y and x, respectively. If the response matrix is not diagonal, the statistical fluctuations of y will be amplified in such a procedure and lead to high frequency oscillations of the estimator x. To tackle the problem of unfolding, while simultaneously dampening such oscillations, TUnfold employs least square minimization with Tikhonov regularisation [127]. In this type of approach it's important that the number of bins, n, at detector level is larger than the number of bins, m, at generator level.

The Lagrangian used in TUnfold is written as

$$\mathcal{L}(x, \lambda) = \mathcal{L}_1 + \mathcal{L}_2 + \mathcal{L}_3, \tag{6.5}$$

where

$$\mathcal{L}_1 = (y - Ax)^T V_{yy}^{-1}(y - Ax),$$
$$\mathcal{L}_2 = \tau^2(x - f_b x_0)(L^T L)(x - f_b x_0),$$
$$\mathcal{L}_3 = \lambda(Y - e^T x),$$
$$Y = \sum_i y_i,$$

and

$$e_j = \sum_i A_{ij}.$$

The term $\mathcal{L}_1$ in Equation 6.5 describes the least square minimization, where x has dimension m, y has dimension n and V_{yy} is the covariance matrix of y at detector level. It's important to note that the response matrix is normalized according to

$$A_{ij} = \frac{M_{ij}}{s_j} \; (i > 0) \tag{6.6}$$

where

$$s_j = \sum_{i=0}^{n} M_{ij}.$$

The matrix M_{ij} is constructed in the same manner as explained previously for A_{ij} in Equation 6.4, but includes an extra row with indices 0j. This row contains events that are generated within the given phase space but not reconstructed in any bin at detector level, and is included in the normalization to ensure proper corrections of detector efficiencies and acceptance.

The term $\mathcal{L}_2$ in Equation 6.5 introduces the regularization into the unfolding procedure with a strength governed by the parameter τ. The matrix L has n rows and m-2 columns and represents a set of regularization conditions. It's initialized with $L_{i,i} = 1$, $L_{i,i+1} = -2$ and $L_{i,i+2} = 1$, which means that the regularization is performed with respect to the second derivative of x. The component $f_b x_0$ is known as the bias vector, where

$$(x_0)_j = s_j$$

and f_b is the corresponding normalization factor, which is set to 1 within the context of this work. Like the response matrix, the bias vector is obtained purely from the simulated $t\bar{t}$ signal reference sample. This means that a choice of $f_b = 1$

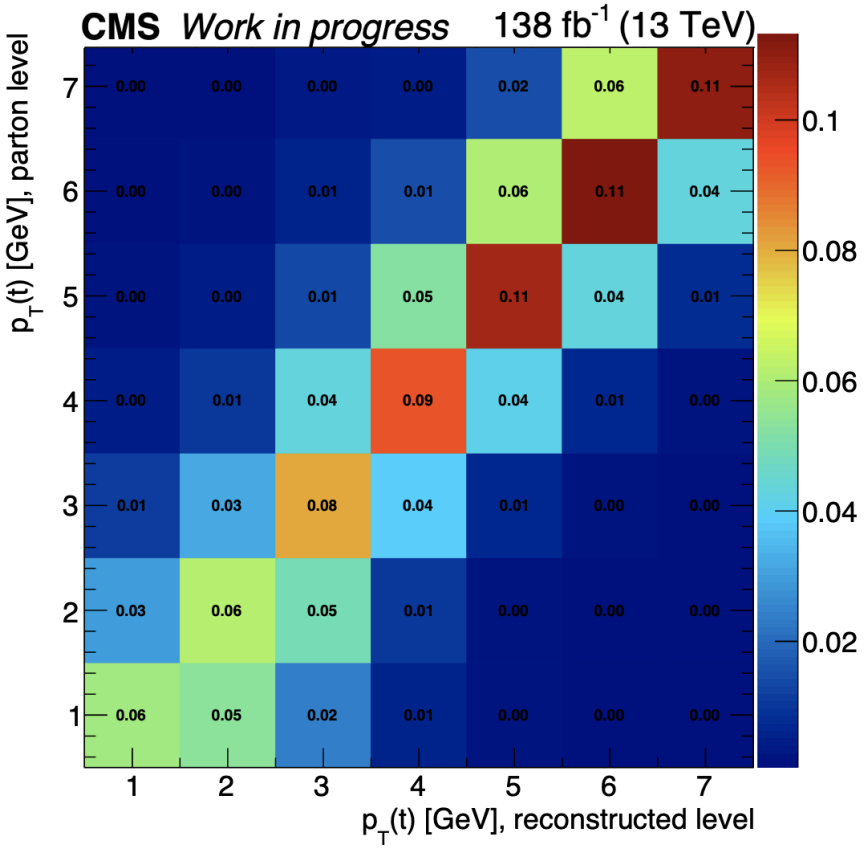

Figure 6.1: The response matrix used for the single-differential measurement of the transverse momentum of the top, $p_{\mathrm{T}}(t)$, in the full phase space at parton level.

helps to suppress deviations of the second derivative of x with respect to the second derivative of the true values of the signal simulation at generator level, but a balance must be struck with the regularization strength. If τ is too small, the solution of x will inherit the amplified statistical fluctuations of y at detector level, resulting in strong anti-correlations between neighboring bins. However, if τ is too large, the solution x will be biased towards having the same second derivative as the vector $f_b x_0$, hence the name bias vector.

The final term $\mathcal{L}_3$ in Equation 6.5 represents an area constraint with λ as the Lagrangian parameter. The total event count of x, corrected for efficiencies given by the vector e, is normalized with respect to the total event count at detector level, denoted by Y. This is done in order to ensure the validity of the procedure if the data follows Poisson statistics, as the minimization of least squares is otherwise only applicable for normally distributed data. Finally, the vector x satisfying the stationary point of the Lagrangian $\mathcal{L}(x, \lambda)$ is taken as the solution.

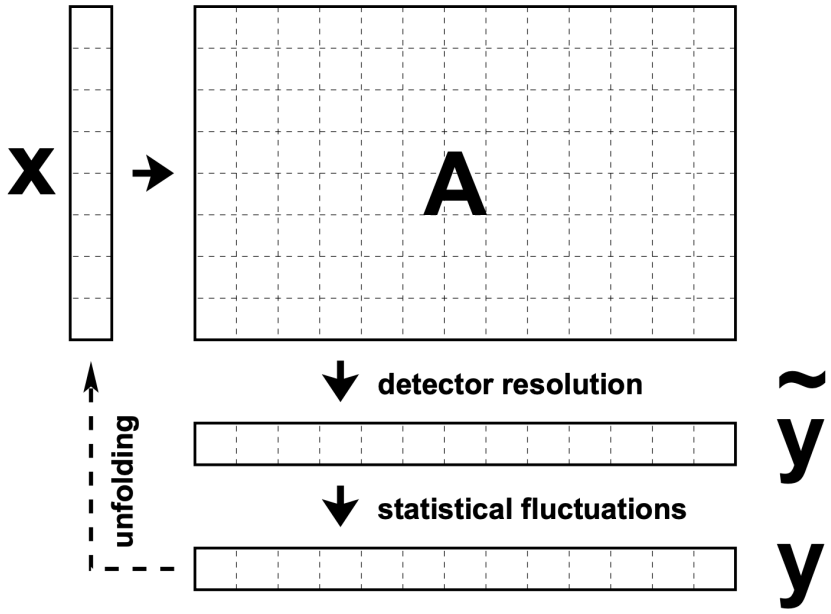

Figure 6.2: A schematic overview illustrating the problem of unfolding for a given observable [126]. Here y represents the observed number of events at detector level, including statistical fluctuations, $\tilde{y}$ is the expected number of events at detector level, A is the response matrix and x is the estimator of the true spectrum.

6.5 Regularization strength

It's of critical importance to find the value of τ that balances the two terms $\mathcal{L}_1$ and $\mathcal{L}_2$, and in this work, the method of minimizing the average global correlation coefficient is employed [126]. Thus, to find the best value of τ one must minimize

$$\sum_i \frac{\rho_i}{n}, \tag{6.7}$$

where n is the dimension of x and the global correlation coefficients, ρ_i, are defined as follows

$$\rho_i = \sqrt{1 - \frac{1}{(V_{xx}^{-1})_{ii}(V_{xx})_{ii}}}. \tag{6.8}$$

In Equation 6.8 the covariance matrix of x is given by V_{xx}, which can be obtained from the covariance matrix at detector level, V_{yy}, through the propagator matrix, D_{xy}, as follows

$$V_{xx} = D^{xy} V_{yy} (D^{xy})^T, \; (D^{xy})_{ki} = \frac{\partial x_k}{\partial y_i},$$

using error propagation. To obtain the best value of τ, the term in Equation 6.7 is scanned for different points of $\log \tau$ and the minimum is chosen, as exemplified

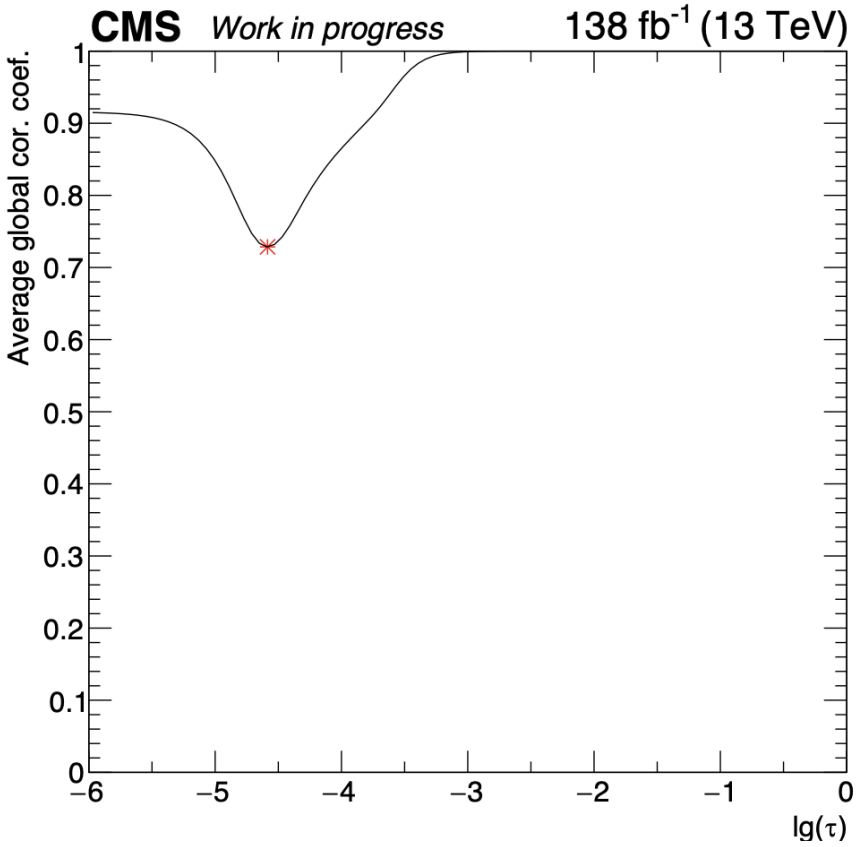

Figure 6.3: The optimal choice of τ is shown (red star) for the single-differential measurement of the transverse momentum of the top, $p_{\mathrm{T}}(t)$, at parton level in the full phase space. The average global correlation coefficients are also computed for different points of $\log \tau$.

by Figure 6.3, which shows the optimal choice of τ for the single-differential measurement of the transverse momentum of the top, $p_{\mathrm{T}}(t)$, at parton level in the full phase space. For the differential cross section measurements of this analysis, the chosen τ parameter is usually quite small, resulting in an $\mathcal{L}_2$ term that is typically within 1% of the total Lagrangian, which indicates that the regularization strength is reasonably small.

6.6 Truth level and phase space definitions

The true level that one unfolds to in measurements of the $t\bar{t}$ production cross section depends on how the top quark is defined and the scope of the phase space. The measured spectra can be defined either at parton or particle level and the exact definitions of both will be outlined in the following section in the context of the full and fiducial phase space, respectively. Technically, these definitions are encoded in the response matrix, defined in Equation 6.6.

6.6.1 Parton level

Measurements performed at parton level are based on the generator model of the bare top quark. This means that in the decay chain of the given generator, top quarks are chosen right before they decay but after they undergo initial and final state radiation.

At parton level, cross sections are measured as functions of kinematic spectra of the top quarks and $t\bar{t}$ system and extrapolated to the full phase space. This is done to allow for comparisons with several predictions at NNLO or even higher order accuracy in QCD that are only available for this cross section definition. Moreover, differential measurements at parton level are used for extractions of properties such as the spin correlation and charge asymmetry of the top quark pair in addition to the top pole mass, m_t, and strong coupling constant, α_s [15, 22, 128]. Theoreticians also use these measurements for improved PDF fits.

6.6.2 Particle level

Measurements performed at particle level use information further down in the decay chain of the given generator to reconstruct the top quarks. The particle level is defined from the stable particles produced in the $t\bar{t}$ decay, that are used to reconstruct proxies of the top and anti-top, prior to being passed through the GEANT 4 detector simulation.

At particle level, cross sections are measured as functions of kinematic spectra of not only the top quarks and $t\bar{t}$-system but also the leptons and beauty-flavoured jets from the decay chain in which the top and anti-top quark decay to $t \to W^+(\to \bar{l}\nu)b$ and $\bar{t} \to W^-(\to l\bar{\nu})\bar{b}$, respectively. Cross sections at particle level are also measured as functions of the total jet multiplicity in the event, which in addition to the two b-jets, comprise jets that arise in the hard interaction or from initial- or final-state radiation. The measurements are performed in a fiducial phase space that is very close to the detector level phase space in terms of selection criteria applied to the particle level objects. Hence, the nature of particle level cross sections leads to a reduction in extrapolation uncertainties. An additional advantage is that the top quark proxy definition is less dependent on the choice of MC generator and underlying event tune, as no model assumptions have to be made about the bare top. The exact prescriptions for the particle level objects used to define the top quark proxies in the context of the fiducial phase space follow [14, 129] and are detailed below:

• The leptons in the experimental signature are reconstructed as **dressed leptons**. This means that photon radiation within the vicinity of a prompt electron or muon is included in the momenta of these particles by clustering them with their associated photons using the anti-k_T algorithm with a cone size of 0.1. Both leptons are required to fulfill $p_{\mathrm{T}} > 20$ GeV and $\eta > 2.4$.

• The **neutrinos** are required to be prompt, excluding neutrinos from hadronic decays.

• The **jets** are clustered with the anti-k_T algorithm using a cone size of 0.4. All stable particles with a lifetime of $\tau > 0.3 \cdot 10^{-10}$ s are included in the clustering with the exception of the dressed leptons and prompt neutrinos. Note that neutrinos from hadronic decays are included in the clustering, which is a change in definition with respect to [14]. This is done to increase congruence with definitions used in the NNLO predictions from M. Czakon et al. [130–133]. All jets in the event are required to have $p_{\mathrm{T}} > 30$ GeV and $\eta > 2.4$.

• The two candidate **b-jets** are identified using the ghost b-hadron technique. A copy or so-called ghost is made from the b-hadron, with all the same properties as the original with the exception of its momentum, which is scaled down to a negligible value. In this way, when the original b-hadron decays, information is kept about its trajectory, thereby helping to tag the jet as a b-jet. The ghost is included in the clustering as it has no effect on the resulting jet momentum.

The fiducial phase space consists of exactly two oppositely-charged dressed leptons (electrons or muons) as defined above, where decays via τ are vetoed. The invariant mass of the selected lepton pair is required to be $m_{ll} > 20$ GeV and two particle jets in the event must be associated with b-hadrons as described above.

Finally, proxies for the W bosons are obtained by finding lepton-neutrino assignments according to the principle where

$$\Delta m = |m(l_1, v_1) - m_W| + |m(l_2, v_2) - m_W|$$

is minimized for a W boson mass of $m_W = 80.4$ GeV. Here e.g. $m(l_1, v_1)$ denotes the mass of an assigned lepton and neutrino. Similarly, proxies for the top quarks are found via the W-b-jet assignments that minimize

$$\Delta m = |m(W_1, b_1) - m_t| + |m(W_2, b_2) - m_t|,$$

where the top mass is set to $m_t = 172.5$ GeV, and e.g. $m(W_1, b_1)$ denotes the mass of an assigned W boson and b-jet.

6.6.3 Phase space extrapolation

The overall efficiency that is corrected for, explicitly in Equation 6.1 for inclusive measurements and implicitly in Equations 6.2 and 6.3 for differential measurements, differs depending on whether a full or fiducial phase space definition is used.

In the full phase space the efficiency correction is actually a product of the detector acceptance, $\mathcal{A}$, and corresponding efficiency, ϵ^{det}, i.e.

$$\epsilon = \mathcal{A}\epsilon^{\mathrm{det}}. \tag{6.9}$$

The acceptance is defined by

$$\mathcal{A} = \frac{N_{\text{gen}}^{\text{PS selection}}}{N_{\text{gen}}^{\text{total}}}, \tag{6.10}$$

where $N_{\text{gen}}^{\text{PS selection}}$ is the total number of events generated within the selected phase space and $N_{\text{gen}}^{\text{total}}$ is the total number of generated events. Thus, by correcting for the acceptance, one extrapolates results to the full phase space. The detector efficiency is denoted by

$$\epsilon^{\text{det}} = \frac{N_{\text{reco}}^{\text{selected}}}{N_{\text{gen}}^{\text{PS selection}}}, \tag{6.11}$$

where $N_{\text{reco}}^{\text{selected}}$ is the selected number of reconstructed events and $N_{\text{gen}}^{\text{PS selection}}$ is defined above. Finally, when substituting Equation 6.10 and 6.11 into Equation 6.9 one obtains

$$\epsilon = \frac{N_{\text{reco}}^{\text{selected}}}{N_{\text{gen}}^{\text{total}}}.$$

In the fiducial phase space no extrapolation is performed, provided that the selection of particle level objects perfectly matches the criteria applied at detector level, in which case

$$\epsilon = \epsilon^{\text{det}} = \frac{N_{\text{reco}}^{\text{selected}}}{N_{\text{gen}}^{\text{PS selection}}}.$$

However, in this work the selection of particle level objects differs very slightly from detector level, as the cut of $p_{\text{T}} > 25$ GeV, that is applied for the leading lepton at detector level, is not applied at particle level, where instead a cut of $p_{\text{T}} > 20$ GeV is applied for both dressed leptons. This means that extrapolation effects are not completely absent in the fiducial phase space but heavily reduced.

6.7 Purity, stability and efficiency

Differential measurements are performed in a binning that has been carefully considered according to a specific set of principles, which will be outlined in the following section.

The three main quantitative measures of the quality of a certain binning scheme are the efficiency, purity and stability, evaluated for each bin of the unfolded distribution. The efficiency is defined as follows

$$\epsilon_j = \frac{N_j^{\text{gen in bin \& rec}}}{N_j^{\text{gen in bin}}}$$

where the numerator denotes all reconstructed events, originally generated within bin j, and the denominator is the total number of generated events within

said bin. Hence, the maximal value of ϵ is 1 and $1 - \epsilon$ quantifies the fraction of events that were generated but not reconstructed in any bin.

The purity is given by

$$p_j = \frac{N_j^{\text{both gen \& rec in bin}}}{N_j^{\text{rec in bin}}},$$

where the numerator refers to the number of events that are generated and reconstructed within the same bin and the denominator is the total number of events that are reconstructed but not necessarily generated within this bin. Thus, 1-p is an expression of the fraction of reconstructed events migrating into the bin at generator level, where a high value of p indicates few incoming bin-to-bin migrations with the maximal value being 1.

Finally, the stability is given by

$$s_j = \frac{N_j^{\text{both gen \& rec in bin}}}{N_j^{\text{gen in bin \& rec}}},$$

where the numerator again refers to the number of events that are generated and reconstructed within the same bin and the denominator is the total number of events that are generated but not necessarily reconstructed within this bin, or in other words, that migrate out of the bin. Thus, contrary to purity, 1-s is an expression of migrations out of a given bin, and the stability can again maximally be 1.

When choosing the binning scheme one is faced with a compromise between probing the $t\bar{t}$ production cross section within finely-binned and interesting regions of the kinematic phase space versus the detector resolution. The latter is always the limiting factor and physically it does not make sense to have a finer binning than the resolution allows. The purity and stability innately reflect this restriction. If the binning scheme is too fine it will cause a surge in bin-to-bin migrations and hence lead to very low values of these quantities. The purity and stability can also reveal something about the physical process itself.

Figure 6.4 shows an example of the purity, stability and efficiency, computed for the single-differential measurement of the transverse momentum of the top, $p_{\mathrm{T}}(t)$, in the full phase space at parton level, and highlights some of the considerations made about these quantities. The binning scheme is generally chosen such that the purity and stability remain above a 30% threshold with very few exceptions in the extreme ends of the spectra for certain distributions, as seen here for the top p_{T}, where the purity dips to around 20% in the outer bin.

6.8 Closure tests

Three different types of tests were performed to validate the setup of TUnfold. Pseudo data is generated from the reference MC by folding the nominal (reweighted) prediction using the nominal (reweighted) response matrix depending on the type of

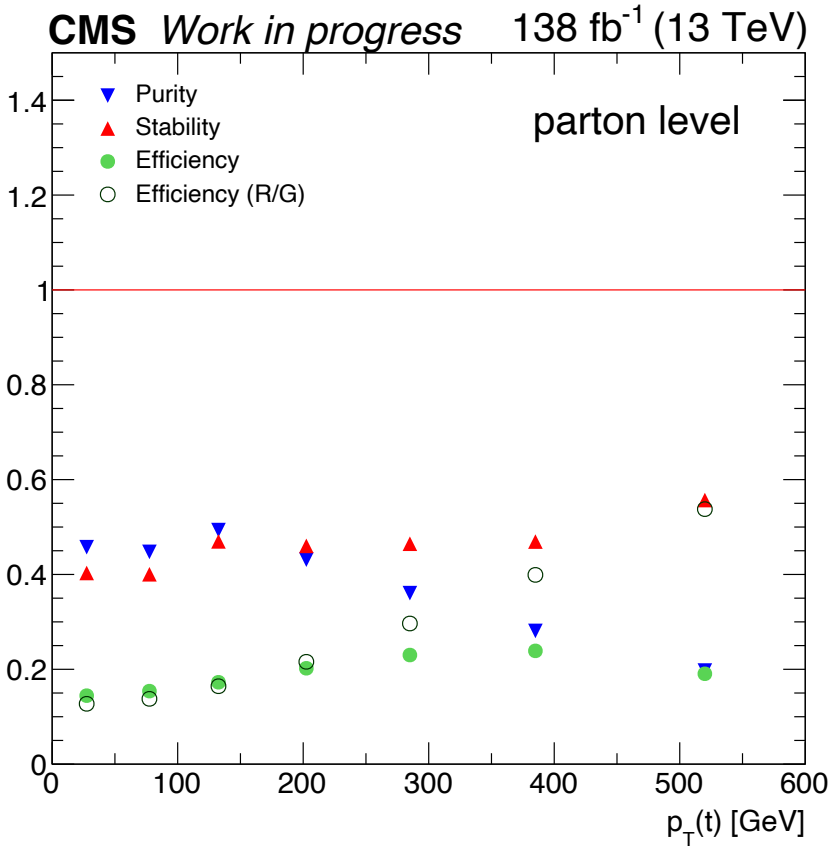

Figure 6.4: The purity, stability and efficiency for the single-differential measurement of the transverse momentum of the top, $p_{\mathrm{T}}(t)$, in the full phase space at parton level.

test. The resulting pseudo data is subsequently unfolded using the nominal response matrix and compared to the original prediction. The closure tests consist of

1. A truth test to make sure the setup of the unfolding procedure is sound.

2. Toy experiments to test the statistical properties of the estimator of the true spectrum in the unfolding procedure.

3. Four different types of reweighting tests with varying degrees of distortions of the truth, which help assess the sensitivity to a potential bias impacting the unfolded result through the response matrix and bias vector.

Each test is performed for each individual cross section and two different choices of unfolding, namely regularized unfolding and unregularized unfolding with $\tau = 0$. Further details along with examples are given in the following sections.

6.8.1 Truth test

The truth test is used as a sanity check. The prediction from the reference MC is folded using the nominal response matrix to generate pseudo data, which is subsequently unfolded in the standard way. Figure 6.5 shows the transverse momentum of the top, $p_{\mathrm{T}}(t)$, measured in the full phase space at parton level and illustrated for the two choices of unfolding, where the ratio is taken with respect to the original prediction (see Appendix H.1 for additional examples). One would expect perfect agreement here and this is exactly what is observed.

6.8.2 Toy test

The toy test serves to validate the statistical properties of the estimator of the true spectrum in the unfolding procedure. The expected yields at detector level, computed from the folded MC reference prediction, were fluctuated according to Poisson statistics. This procedure was repeated to generate 1000 toy experiments, which were subsequently unfolded using the nominal response matrix. The average unfolded result, computed over all toy experiments, is denoted by

$$\hat{M}^{unf}_{avg} = \langle \hat{M}^{unf} \rangle$$

and the sample covariance is found by averaging over all toys as follows

$$(Cov_{\hat{M}^{unf}_{avg}\hat{M}^{unf}_{avg}})_{ij} = \langle (\hat{M}^{unf}_{i} - \hat{M}^{unf}_{avg,i})(\hat{M}^{unf}_{j} - \hat{M}^{unf}_{avg,j}) \rangle.$$

Figure 6.6 shows plots of the relative $\hat{M}^{unf}_{avg}$ residuals and pulls, given as the residuals over their respective uncertainties, as well as the χ^2 of $\hat{M}^{unf}_{avg}$ with respect to the true MC reference prediction in all bins. In each case the given distribution is depicted for the two choices of unfolding and shown for the transverse momentum of the top, $p_{\mathrm{T}}(t)$, measured in the full phase space at parton level (see Appendix H.2

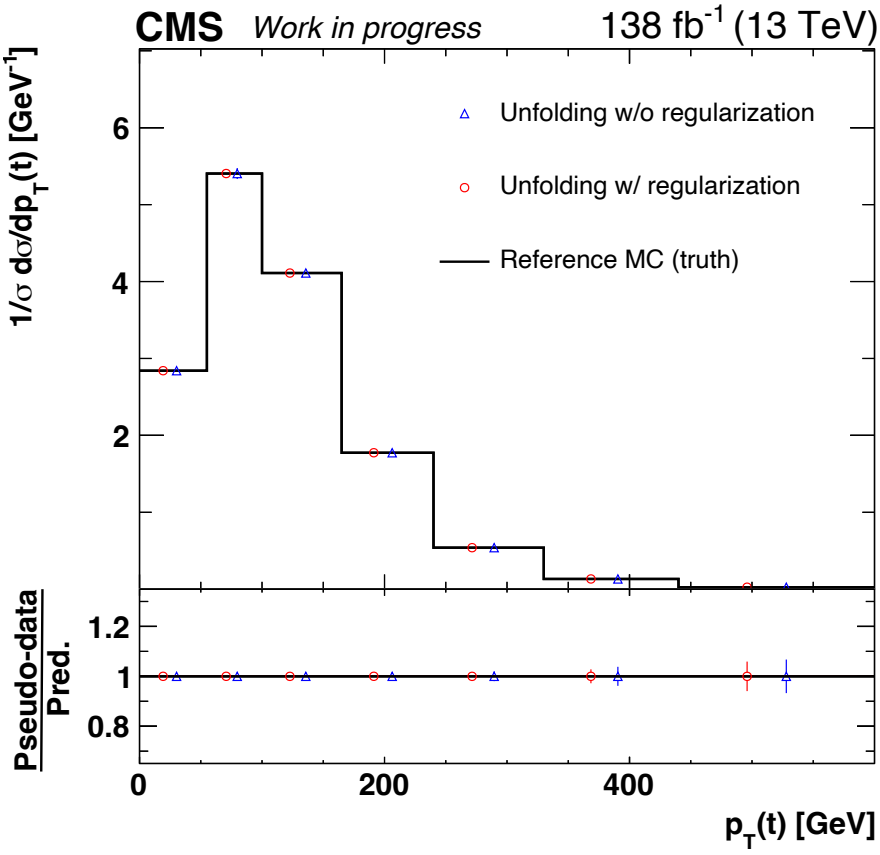

Figure 6.5: Absolute differential $t\bar{t}$ production cross section for the transverse momentum of the top, $p_{\mathrm{T}}(t)$, measured in the full phase space at parton level and performed with pseudo data for regularized and unregularized unfolding. The ratio is shown with respect to the original truth (black).

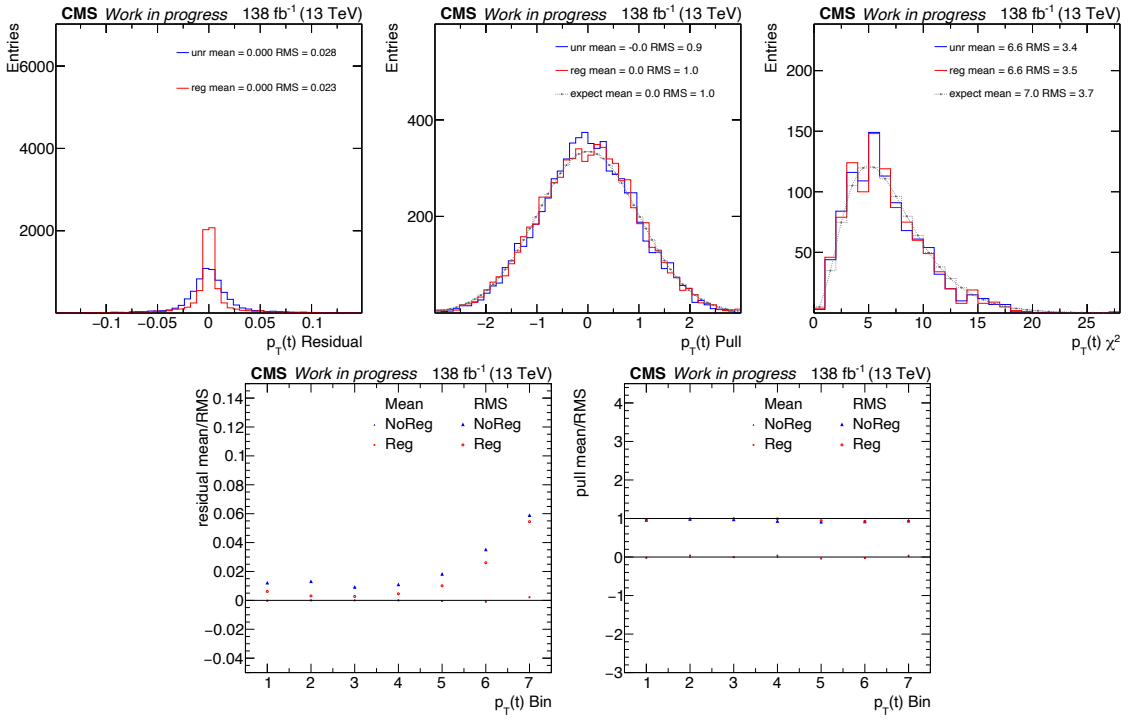

Figure 6.6: Residual (relative), pull and χ^2 distributions are shown for the transverse momentum of the top, $p_{\mathrm{T}}(t)$, measured in the full phase space at parton level and performed with pseudo data for regularized and unregularized unfolding. The pull and χ^2 distributions are also shown alongside the expectation. The top row shows plots of the residuals (relative), pulls and χ^2 of $\hat{M}_{avg}^{unf}$ with respect to the true MC reference prediction in all bins. The bottom row shows plots of the mean and RMS of the residuals and pulls per bin (see Chapter 8).

for additional examples). The pull and χ^2 distributions are also shown alongside the expectation. Both regularized and unregularized unfolding are in agreement with the expectation and are similar in terms of χ^2. Figure 6.6 also shows plots of the mean and RMS of the relative residuals and the pulls per bin. The RMS of the relative residuals shows the statistical uncertainty of the measurement, which increases towards higher p_{T}. The mean values of the relative residuals and of the pulls are both very close to 0, while the RMS values of the pulls are close to unity, as expected. The RMS of the relative residuals are smaller for regularized unfolding than for the unregularized case, as one also expects. The larger uncertainties of the latter are at least partially compensated by larger negative correlations between neighboring bins (not shown).

Figure 6.7 shows the sample correlation matrix for the $p_{\mathrm{T}}(t)$ distribution (red), computed from $(Cov_{\hat{M}_{avg}^{unf}\hat{M}_{avg}^{unf}})_{ij}$, alongside the estimated correlation matrix (black), which is obtained from the direct average of the covariance matrix returned by the given unfolding algorithm for each toy. The comparison is again performed for the two choices of unfolding and the sample and estimated correlation matrices show good agreement in each case.

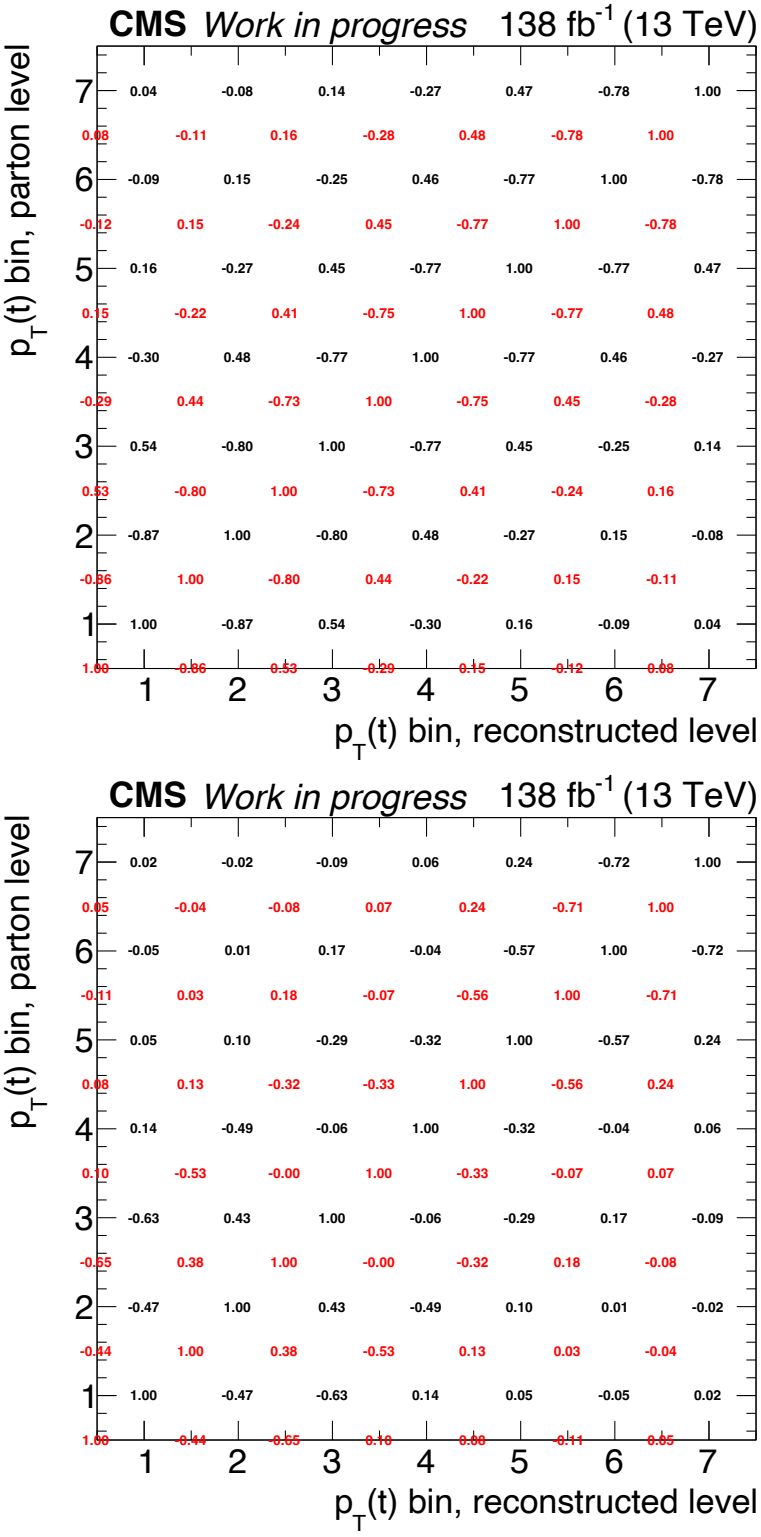

Figure 6.7: Correlation matrices are shown for the transverse momentum of the top, $p_{\mathrm{T}}(t)$, measured in the full phase space at parton level. The sample correlation matrix (red), computed from $(Cov_{\hat{M}^{unf}_{avg}\hat{M}^{unf}_{avg}})_{ij}$, is shown alongside the estimated correlation matrix (black), which is obtained from the direct average of the covariance matrix returned by the unfolding algorithm for each toy. The comparison is performed for unregularized unfolding (top) and regularized unfolding (bottom).

6.8.3 Reweighting test

In order to assess the effects on the unfolding procedure due to a potential bias in the truth, which will affect both the response matrix and the bias vector used in the unfolding, the MC reference prediction was reweighted and pseudo data was generated in the same manner as previously described but now using the weighted response matrix to fold the data. The computation of the weights is performed using the following expression

$$w = Az^B(1-z)^C(1+Dz+Ez^2),\ z = \frac{x - x_{min}}{x_{max} - x_{min}},$$

where A ensures the correct normalization with respect to the original prediction prior to reweighting. The values x_{min} and x_{max} are the minimum and maximum values of the kinematic variables studied in the cross section, while the parameters B, C, D and E are chosen in order to produce distortions of the truth in the range 5% to 100%. The pseudo data is subsequently unfolded using the nominal response matrix. Figure 6.8 shows the unfolded cross sections for the transverse momentum of the top, $p_{\mathrm{T}}(t)$, measured in the full phase space at parton level (see Appendix H.3 for additional examples). The figures depict four different reweighting scenarios for each cross section, where the ratio is shown with respect to the reweighted MC (truth) in black. The distortions can be judged with respect to the red curve, which shows the original reference MC. Regularized unfolding is observed to recover well from any introduced bias even for very large distortions of the truth with the exception of the first bin of the $p_{\mathrm{T}}(t)$ spectrum. There is a small effect of the bias visible in this bin, which is present also for smaller distortions. This is the case for both regularized and unregularized unfolding, which would suggest that the effect stems from the response matrix primarily. However, for reweighting scenario 2 with distortions of the order of 20%, the effect of the bias is small and within the statistical uncertainties.

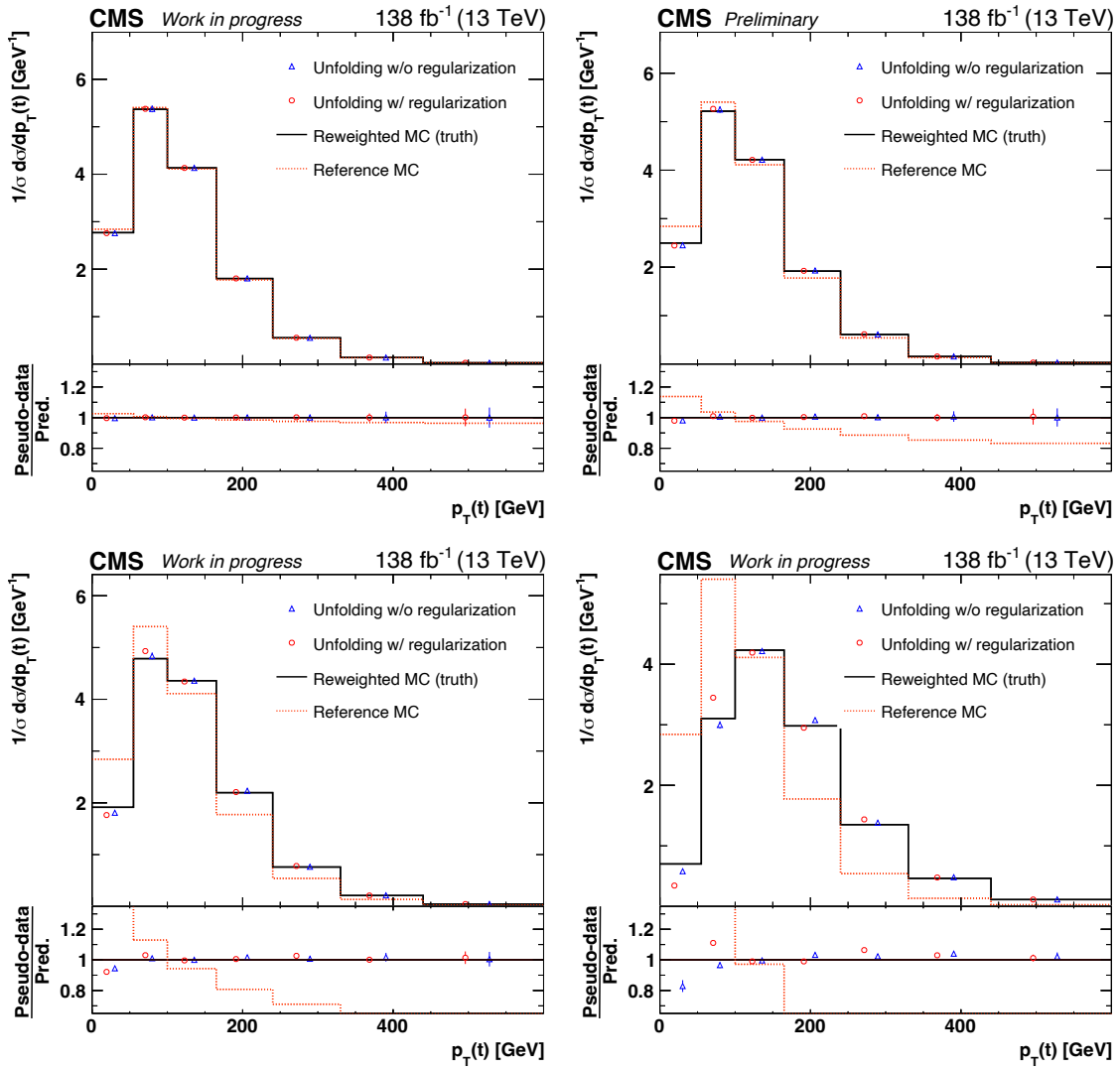

Figure 6.8: Absolute differential $t\bar{t}$ production cross sections, performed with pseudo data for regularized and unregularized unfolding, are shown for the transverse momentum of the top, $p_{\mathrm{T}}(t)$, measured in the full phase space at parton level. Four reweighting scenarios are shown with distortions within 5% to 100%. The ratio is shown with respect to the reweighted MC (truth) in black. The distortions can be judged with respect to the red curve which shows the original reference MC.

Chapter 7

Systematic Uncertainties

To obtain the most precise differential measurements of the $t\bar{t}$ production cross section, each source of uncertainty must be assessed and evaluated carefully. All sources of uncertainty belong to one of the following groups:

• The **statistical uncertainties** comprise both statistical errors on the input data sample and simulated signal and background samples.

• The **experimental uncertainties** are obtained by varying the scale factors that account for detector effects such as misidentification of particles, inefficiencies and limited resolutions of detector sub-systems within their respective uncertainties.

• The **theoretical uncertainties** consist of uncertainties on the assumptions made in the Monte Carlo simulations.

• The **background uncertainties** affect the normalization of background samples.

The entire analysis procedure, i.e. event selection, kinematic reconstruction and unfolding, is repeated for each cross section and each source of uncertainty and for both the up and down variation of said source. It should be mentioned that the event selection and kinematic reconstruction are only repeated when necessary, i.e. when varying a given source results in changes to kinematic spectra that impact the selection. Finally, the difference with respect to the nominal cross section per bin constitutes the corresponding uncertainty on the given differential measurement.

In this section all considered sources will be outlined in accordance with the groupings above. The statistical uncertainty is described in Section 7.1, and the experimental, theoretical and background uncertainties are summarized in Section 7.2, 7.3 and 7.4, respectively.

The differential measurements in this work are performed using the full Run 2 dataset, therefore, one must consider how uncertainty sources correlate among 2016, 2017 and 2018 data samples. A detailed description of the treatment of uncorrelated, fully correlated and partially correlated sources is given in Section 7.5. Finally, a review is given of the most dominant sources of uncertainty for the inclusive cross

section and different types of differential measurements in Section 7.6.

7.1 Statistical uncertainties

The data distribution used in the unfolding procedure performed with TUnfold [126] is corrected for $t\bar{t}$ and non-$t\bar{t}$ background by means of a fractional correction and a direct subtraction, respectively, as described in Section 6.3. The statistical error on this input distribution is given by

$$\mathrm{err}^{\mathrm{stat}} = f^{\mathrm{signal}} \cdot \sqrt{(\mathrm{err}^{\mathrm{selected}}_{\mathrm{data}})^2 + (\mathrm{err}^{\mathrm{bkg}}_{\mathrm{MC}})^2},$$

where $\mathrm{err}^{\mathrm{selected}}_{\mathrm{data}}$ and $\mathrm{err}^{\mathrm{bkg}}_{\mathrm{MC}}$ are the statistical errors on the total number of selected data events prior to background subtraction, $N^{\mathrm{selected}}_{\mathrm{data}}$, and the total number of non-$t\bar{t}$ background events, $N^{\mathrm{bkg}}_{\mathrm{MC}}$, respectively. The fraction f^{signal} then accounts for the actual number of signal events by correcting the resulting statistical error for the $t\bar{t}$ background events. These errors originate from the finite statistics of the data and simulated samples.

7.2 Experimental uncertainties

Detector effects such as the misidentification of particles, inefficiencies and limited resolutions of detector sub-systems are corrected for by applying appropriate scale factors to the simulations to match the data. The scale factors are derived by dedicated groups within the CMS collaboration known as Physics Object/Working Groups, which study electrons, muons, luminosity, missing transverse energy, jets and b-jets independently of each other and utilize different methods specific to their task. The derivations of the different types of scale factors, although accurate, carry with them a certain level of systematic uncertainty. The following outlines all the experimental sources considered in the uncertainty assessment of the differential cross sections.

7.2.1 Luminosity

The integrated luminosities for 2016, 2017 and 2018 are 36.33 fb^{-1} [134], 41.53 fb^{-1} [135] and 59.74 fb^{-1} [136], respectively. The precision on the luminosity measurement for 2016 was recently improved from 2.5% to 1.2% by using advanced techniques to evaluate the beam position monitoring and other beam properties [134], and in 2017 (2018) the luminosity is measured with an uncertainty of 2.3% [135] (2.5% [136]). The uncertainties for all three years are treated as 30% correlated among years and corresponding variations are applied as weights to all simulated samples prior to unfolding.

7.2.2 Pile-up

The uncertainty on pile-up is evaluated by varying the total proton-proton inelastic cross section, which is set to 69.2 mb, within its uncertainties. This is the same cross section used in Figure 5.2 in Section 5.6, which shows the mean number of interactions per bunch crossing during the Run 2 data-taking period from 2016 to 2018. Up and down variations of 4.6% of this cross section are performed separately for each year and applied as event weights to the simulated signal and background samples both at generator and detector level [137]. Prior to unfolding, the resulting differences in data and MC were scrutinized and found to have consistent features for each year. Thus, the uncertainties due to pile-up are treated as fully correlated among years.

Pile-up also impacts the jet energy scale and the lepton isolation in addition to the evaluation of missing transverse energy, however, these effects are accounted for in the respective uncertainty assessments of these sources.

7.2.3 Trigger efficiency

Trigger efficiencies are determined by means of the orthogonal method detailed in Chapter 5, where a set of baseline triggers for the missing transverse energy are used to compute efficiencies in data for dilepton triggers that are approximately uncorrelated with the former set. The efficiencies are determined in bins of leading p_{T} and trailing p_{T} when triggering on same-flavour leptons or in bins of p_{T}^{e} and p_{T}^{μ} when using the dilepton trigger for $e\mu$. Typically the resulting scale factors are within 1% of unity (up to 5% in few bins) and are applied to simulations to match the conditions in data. The uncertainty due to the trigger efficiency is determined by varying the scale factors within their uncertainties and applying the corresponding event weights to the simulated signal and background samples.

The uncertainties are primarily statistical in nature but also include an evaluation of the dependency on the defined phase space by considering different regions based on

- the number of reconstructed jets: $N_{\mathrm{jets}} < 3$ and $N_{\mathrm{jets}} \geq 3$,
- the number of primary vertices: $N_{\mathrm{vertex}} < 30$ and $N_{\mathrm{vertex}} \geq 30$, and
- the missing transverse momentum: $p_{\mathrm{T}}^{\mathrm{miss}} < 150$ GeV and $p_{\mathrm{T}}^{\mathrm{miss}} \geq 150$ GeV.

Other contributions to the overall trigger efficiency uncertainty come from residual correlations between the baseline and dilepton triggers. The trigger efficiencies are computed separately for each year, and given that the baseline and dilepton triggers can be considered approximately orthogonal, the resulting uncertainties for all years are treated as uncorrelated.

7.2.4 L1 trigger prefiring

An issue occurred with the L1 trigger prefiring where high η trigger primitives were wrongly associated with the previous bunch crossing as a gradual timing shift in

the ECAL was not properly taken into account [19]. When a significant amount of energy was present in the ECAL region within $2.4 < |\eta| < 3.0$, the effected events began to self veto as two consecutive bunch crossings are not allowed to fire in the L1 trigger system. This is of particular consequence for events containing e.g. high p_{T} jets. The issue was fixed in 2018 but was present in both 2016 and 2017. The resulting systematic uncertainties in those years are estimated by varying the L1 prefiring probabilities up and down within their respective uncertainties and applying the corresponding event weights to the simulated signal and background samples. The L1 trigger prefiring issue is treated as fully correlated for 2016 and 2017.

7.2.5 Lepton selection

Uncertainties on muons and electrons are evaluated separately. Combined scale factors are computed for the identification and reconstruction of muons and for the identification and isolation of electrons. Individual scale factors for isolation and reconstruction are applied for muons and electrons, respectively. The aforementioned scale factors are all computed based on a Drell-Yan sample using the "tag and probe" method as described in Chapter 5. In the uncertainty assessment the combined and individual scale factors are varied up or down within their respective uncertainties independently of each other and separately for electrons and muons as stated. Since the scale factors are computed for a Drell-Yan sample one must apply an additional uncertainty that accounts for the extrapolation to the $t\bar{t}$ phase space. This is of particular relevance to the isolation efficiency which can be affected by the higher number of jets in the $t\bar{t}$ signal sample. Therefore, an extra variation per lepton of 1% (0.5%) is applied on top of the isolation efficiency of electrons (muons) when computing the event weights. All the lepton uncertainties described above are treated as uncorrelated with each other but fully correlated across the years.

7.2.6 Jet energy scale

The jet energy scale uncertainty is made up of seven sources that are relevant for this analysis, i.e. that pertain to jets within $|\eta| < 2.4$, and that correspond to a reduced set based on the full set of 19 sources, which have been grouped according to different detector regions. The seven sources take into account e.g. uncertainties on the pile-up offset, simulated jet response and jet p_{T} resolution, as well as those uncertainties associated with the methods and samples used for the determination of the corrections mentioned in Section 5.7.3, such as the impact from initial and final state radiation. The estimated uncertainties from using either the complete set or the reduced set are similar in the central bins of the differential cross sections but the latter set is preferred as the smaller number of sources leads to less statistical fluctuations in the extreme ends of the spectra.

The uncertainty of each individual source is assessed by applying η- and p_{T} dependent scale factor corrections to the jet four-momenta in simulated signal and background samples. The corrected jets are then used to recompute the missing

transverse energy after which the entire analysis procedure is repeated as normal. The individual sources are treated as uncorrelated with each other and recommendations from the relevant Physics Object Groups are followed with respect to the correlations among years.

7.2.7 Jet energy resolution

Uncertainties due to the jet energy resolution are evaluated separately for two different regions defined as follows

$$\text{Region I: } |\eta| < 1.93 \text{ and } \text{Region II: } 1.93 < |\eta| < 2.5,$$

for which the η resolution scale factors are varied by $\pm 1\sigma$ and used in the hybrid method (see Section 5.7.3) to obtain corresponding variations of the p_{T} resolution scale factors. These are then applied as multiplicative factors to the jet four-momenta. All changes are propagated to the missing transverse energy and the whole analysis procedure is performed again. The resulting jet energy resolution uncertainties from the two regions are treated as uncorrelated with each other and among years.

7.2.8 Unclustered missing transverse energy

To determine the uncertainty on the estimation of the missing transverse energy, one must consider the impact from leptons, jets and the so-called unclustered energy, i.e. isolated or low-energy particles that are identified as pile-up or noise in the calorimeters and therefore not clustered into jets. The impact from leptons and jets are accounted for in their respective uncertainty assessments by propagating changes in p_{T} and η to the corresponding particle collections used for recomputing $E_{\mathrm{T}}^{\mathrm{miss}}$. However, the uncertainty due to the unclustered energy is determined separately by only considering photons in addition to charged and neutral hadrons that fall into the unclustered category defined above and varying their energies in accordance with the corresponding resolution. The missing transverse energy is then recomputed and the analysis procedure is repeated. The resulting unclustered uncertainties are treated as uncorrelated across the years due to the random nature of the source.

7.2.9 B-tagging

The term b-tag identification efficiency refers to the probability to tag a jet of any flavour as a b-jet. A certain fraction of b-tagged jets are wrongly identified as such and are instead associated with c-jets or light-jets, where the light jet category constitutes jets originating from gluons or u, d or s quarks. This is known as the mistag rate. Both the b-tag efficiency and the mistag rate differ in data and MC and the discrepancy is accounted for by applying event weights to the simulated signal and background samples, as described in Section 5.7.4. This weight includes scale factor corrections, SF_{b-tag}, for all jets in the event, where SF_{b-tag} depends on the jet flavour, p_{T} and $|\eta|$, and is computed for a QCD-enriched sample that is orthogonal

to the signal region. Moreover, the aforementioned event weight accounts for the dependency on the phase space by also correcting for b-tagging efficiencies and mistag rates (both labelled ϵ_{b-tag}^{MC}) computed for the $t\bar{t}$ signal sample in corresponding bins of p_{T} and $|\eta|$.

Independent computations of ϵ_{b-tag}^{MC} are performed for every systematic source that directly impacts the jet topology in the $t\bar{t}$ signal sample. In these cases SF_{b-tag} is unchanged.

The uncertainty assessment of the b-tag identification efficiency is split into sources that are correlated and uncorrelated among years. Here the uncorrelated sources arise from statistics and light jets while the additional sources are treated as fully correlated among years. Each of the correlated sources has both an up and down contribution where SF_{b-tag} is varied in the same direction simultaneously for b and c-jets. The scale factors for light jets are varied up and down independently as they are uncorrelated with the aforementioned jets. The total uncertainty on the b-tag identification efficiency is then found by adding up all the resulting uncertainties from the correlated and uncorrelated sources in quadrature.

7.3 Theoretical sources

The fundamental steps involved in Monte Carlo simulations were outlined in Chapter 4. These constitute the simulation of the hard interaction of a process, where matrix elements are computed at fixed-order, generating the parton shower from initial and final state radiation and forming hadrons out of the remaining quarks and gluons as well as modelling the underlying event and properly accounting for colour assignments by using special colour reconnection schemes. Naturally, some theoretical assumptions have to be made in relation to the above and the corresponding uncertainties on these assumptions have to be assessed, as they affect the generated event and by extension the response matrix and acceptance corrections in the unfolding procedure. The theoretical sources of uncertainty contributing to the overall precision of the differential measurements are detailed below. It should be noted that all theoretical sources are treated as fully correlated among the years. All variations discussed below are simultaneously applied to the $t\bar{t}$ signal and "$t\bar{t}$ other" background simulations.

7.3.1 Hard interaction

The uncertainty on the matrix element computation of the hard interaction comes from missing higher order terms and is estimated by scale variations. The factorization (μ_F) and renormalization (μ_R) scales were explained in Section 2.3, and the estimated uncertainty on the nominal scale choice $\mu_F = \mu_R$ consists of an envelope of individual uncertainties arising from variations of the μ_F and μ_R scales. Three types of variations of these scales are performed in both the up and down direction totaling a number of six uncertainties to be included in the envelope of which the resulting maximum of the cross section measurement variation is chosen in each bin. The contribution from the uncertainty on the choice of the μ_R scale is found by

keeping the μ_F scale fixed while varying the μ_R scale up (down) by factors of 2 (0.5). Similarly, the contribution from the μ_F scale is found by keeping the μ_R scale fixed and varying the μ_F scale up (down) by factors of 2 (0.5). The final contribution comes from a simultaneous up (down) variation of both scales by factors of 2 (0.5).

7.3.2 Matching

The matching and merging of parton showers to matrix element calculations was described in Chapter 4. The parameter that controls this step is h_{damp} and in the reference simulation its nominal value is set to $1.379 \times m_t$ [79]. The up and down variations are $0.926 \times m_t$ and $0.505 \times m_t$, respectively. The resulting uncertainties on the differential measurements are computed by replacing the nominal signal and $t\bar{t}$ background samples by dedicated samples with the matching variations already applied and repeating the analysis procedure as normal.

7.3.3 Initial and final state radiation of the parton shower

The process of simulating the parton shower was described in Section 4.2. The QCD renormalization scales of the initial and final state radiation are varied up (down) by factors of 2 (0.5).

7.3.4 Branching ratios

The semi-leptonic branching ratios of b-hadrons and their corresponding uncertainties are taken from the Particle Data Group (PDG) (2020) [22] and compared with the corresponding values from the Pythia 8 decay tables used for the reference simulation. Envelopes are constructed for both neutral and charged b-hadrons and cover the differences between corresponding Pythia 8 and PDG branching ratios and uncertainties. These envelopes are then used to re-weight the populations of b-jets with and without semi-leptonic b-hadron decays at generator level. Accounting for such an uncertainty is important, as semi-leptonic decays of b-hadrons give rise to neutrinos in jets, thereby impacting the b-jet energy response.

The branching ratios and corresponding uncertainties of the signal process, denoted by $\mathcal{BR}\left(t\bar{t} \to \ell\ell + X\right)$, are taken from the PDG (2020) [22]. The values for the ee, $\mu\mu$, $e\mu$ and combined channels are 0.01147, 0.01130, 0.02277 and 0.04554, respectively, and the uncertainty in each case is quoted as $\pm 1.5\%$.

7.3.5 Top quark mass assumption

The top quark mass is assumed to be $m_t = 172.5$ GeV in the reference simulation. The uncertainty on the mass is set to 1 GeV which is in line with the precision of the latest experimental measurement of the top quark MC mass [22], albeit slightly more on the conservative side. In this work the analysis is repeated with dedicated signal and $t\bar{t}$ background samples with $m_t = 169.5$ GeV and $m_t = 175.5$ GeV. The

resulting differences with respect to the corresponding nominal cross section are then scaled by 1/3 such that the top mass variation effectively corresponds to 1 GeV.

7.3.6 Parton distribution functions

The parton distribution functions (PDFs) are described by NNPDF3.1 [32, 81] at NNLO accuracy in the reference simulation and all background samples. This set assumes values of $m_t = 172.5$ GeV and $\alpha_s = 0.0018$ for the top mass and strong coupling constant, respectively. The set comes with the nominal PDF and weights representing $\pm 1\sigma$ variations along the 100 uncorrelated eigenvectors of the PDF covariance matrix. The analysis procedure is repeated individually for each of these variations. The resulting differences with respect to the corresponding nominal cross section are then added in quadrature. The effect from the uncertainty on α_s is estimated separately by varying the parameter up and down by ± 0.0001. The resulting uncertainty contribution is referred to as PDF α_s and treated as uncorrelated with all other PDF uncertainties.

7.3.7 Colour reconnection

The colour reconnection scheme was described in Section 4.4. The reference simulation uses an MPI based colour reconnection model (CR0) with early resonance decays (ERD) switched off. Three uncertainties on the colour reconnection are considered. First the CR0 model is used again with ERD switched on. The two other uncertainties evolve from the MPI based model and are known as the QCD based model (CR1) and the Gluon-move model (CR2). The variations are performed by using independent samples for the $t\bar{t}$ signal process and "$t\bar{t}$ other" backgrounds for which the entire analysis procedure is repeated. Finally, envelopes are constructed out of the maximal uncertainty of the three sources in each measurement bin.

7.3.8 Underlying event tune

The underlying event tune was described in Section 4.4. The event generators are tuned by adjusting a set of parameters that control the event modelling such that simulations match underlying event data from both the CDF and CMS experiments [79]. The uncertainty on the tune is found by simultaneously varying these parameters in the same direction (up or down) within their respective uncertainties.

7.4 Background uncertainties

The background uncertainties are split into two categories, namely Drell-Yan and other non-$t\bar{t}$ backgrounds. The scale factors needed to account for the data and MC discrepancy of the former are computed as described in Section 5.4. The $m_{l\bar{l}}$ distribution is fitted using TFractionFitter in the Z boson peak window of $76 \leq m_{l\bar{l}} \leq 106$ GeV, at the selection stage where the requirement of $E_T^{miss} > 40$ GeV is enforced for

the same-flavour channels (step 6), and the scale factors are then derived from the fit (all selection steps are listed in Section 5.9). The uncertainty on the Drell-Yan normalization is also calculated using this method by starting at step 6 and then switching on the subsequent cuts one by one after recomputing the scale factors. Thus, first the requirement of at least one b-tagged jet is switched on (step 7) and then finally a solution from the given kinematic reconstruction is required (step 8), as described for the full and loose variants in Section 5.8. This is done independently for 2016, 2017, 2018 and full Run 2 and, moreover, repeated separately for the corresponding ee and $\mu\mu$ channels. The largest difference between all scale factors computed at step 6, step 7 and step 8 for any channel and any year including full Run 2 is then assigned as the systematic uncertainty. Referring back to Table 5.1 in Section 5.4, this is found to be 20%.

The uncertainty on the normalization of the other non-$t\bar{t}$ background processes is estimated to be 30% [14]. A study was performed to validate this value for the dominant process among these backgrounds, single top tW production. One expects the number of events with 1 b-tagged jet to be higher than the number of events with 2 b-tagged jets for this background as opposed to the signal process. Therefore, a way to study its normalization is to observe how the MC/data ratio behaves in the bins with 1 and 2 b-tagged jets. One would expect data and MC to be in good agreement in both bins. This means that there is also no slope in the MC/data ratio between the two bins. A variation in the normalization that produces a steeper slope or a generally worse agreement with data is not meaningful and therefore a cut-off can be set on the normalization uncertainty.

The single top tW production cross section was varied up and down by 10%, 15%, 20%, 25%, 30%, 50%, and 100%. The resulting effects on the distribution of the number of b-tagged jets were studied after the full event selection for the ee, $\mu\mu$ and $e\mu$ channels individually (see Appendix I.1, Appendix I.2 and Appendix I.3, respectively). The agreement with data after varying the contribution from the tW process is expressed by Pearson's χ^2-test and is shown for each plot. The increasing trend in χ^2 for upwards variations of the tW normalization justifies assigning a one-sided uncertainty on the single top tW process, however, this is not done, as a symmetric uncertainty assessment is favoured. Moreover, as stated above it is reasonable to assign an uncertainty according to the variation that gives the smallest MC/data slope. The clearest picture can be obtained by looking at the $e\mu$ channel as effects due to the Drell-Yan process are suppressed. The smallest slope is observed when varying the tW contribution down by no more than the current uncertainty of 30%.

7.5 Correlations of systematic sources among years

It's important to account for the correlations among years when computing the systematic uncertainties. In order to evaluate whether a given source is fully correlated, uncorrelated or partially correlated among years one must consider the origin of the source and the methodology used to estimate the nominal corrections and their cor-

responding uncertainties for each year. The Physics Object Groups themselves are therefore responsible for estimating the degree of correlation and their recommendations were outlined in Section 7.2 and 7.3 for the experimental and theoretical uncertainties, respectively, together with the descriptions of the different sources.

A description of the general treatment of correlations among years is given in this section. The following procedure is performed for all full Run 2 distributions and results, which includes control distributions as well as inclusive and differential cross section measurements. It should be noted that the subsequent discussion applies to the step prior to unfolding in case of differential measurements.

For a given source the corresponding Run 2 uncertainty is split into contributions of uncorrelated and fully correlated terms added in quadrature. This means that one can collect relative contributions δ such that the sum of δ^2 is equal to unity i.e.:

$$\delta_a^2 = 1 = \delta_{a,\,\text{uncorr}}^2 + \delta_{ab}^2 + \delta_{ac}^2 + \delta_{abc}^2,$$

$$\delta_b^2 = 1 = \delta_{b,\,\text{uncorr}}^2 + \delta_{ab}^2 + \delta_{bc}^2 + \delta_{abc}^2,$$

and

$$\delta_c^2 = 1 = \delta_{c,\,\text{uncorr}}^2 + \delta_{ac}^2 + \delta_{bc}^2 + \delta_{abc}^2,$$

where a, b and c denote 2016, 2017 and 2018, respectively, and the subscript "uncorr" denotes uncorrelated sub-sources given by

$$\delta_{a,\,\text{uncorr}} = \sqrt{1 - \delta_{ab}^2 - \delta_{ac}^2 - \delta_{abc}^2}, \tag{7.1}$$

$$\delta_{b,\,\text{uncorr}} = \sqrt{1 - \delta_{ab}^2 - \delta_{bc}^2 - \delta_{abc}^2}, \tag{7.2}$$

and

$$\delta_{c,\,\text{uncorr}} = \sqrt{1 - \delta_{ac}^2 - \delta_{bc}^2 - \delta_{abc}^2}. \tag{7.3}$$

The following is a general prescription and in practice not all relative contributions are considered. This is evaluated on a source-by-source basis as previously described.

As a first step uncorrelated and fully correlated sub-sources are constructed out of the corresponding varied and nominal simulations. In the following description the notation "MC" is used to denote a simulation and the subscript "nom" is used to indicate when the sample in question is nominal, whereas the subscript "var" is used to exemplify when the given simulation is varied with respect to the nominal sample. Thus at detector-level one can construct sub-sources as follows:

$$\text{MC}_{a,\,\text{uncorr, var}} = \text{MC}_{a,\,\text{var}} + \text{MC}_{b,\,\text{nom}} + \text{MC}_{c,\,\text{nom}},$$

$$\mathrm{MC}_{b,\,\mathrm{uncorr},\,\mathrm{var}} = \mathrm{MC}_{a,\,\mathrm{nom}} + \mathrm{MC}_{b,\,\mathrm{var}} + \mathrm{MC}_{c,\,\mathrm{nom}},$$

$$\mathrm{MC}_{c,\,\mathrm{uncorr},\,\mathrm{var}} = \mathrm{MC}_{a,\,\mathrm{nom}} + \mathrm{MC}_{b,\,\mathrm{nom}} + \mathrm{MC}_{c,\,\mathrm{var}},$$

$$\mathrm{MC}_{ab,\,\mathrm{var}} = \mathrm{MC}_{a,\,\mathrm{var}} + \mathrm{MC}_{b,\,\mathrm{var}} + \mathrm{MC}_{c,\,\mathrm{nom}},$$

$$\mathrm{MC}_{bc,\,\mathrm{var}} = \mathrm{MC}_{a,\,\mathrm{nom}} + \mathrm{MC}_{b,\,\mathrm{var}} + \mathrm{MC}_{c,\,\mathrm{var}},$$

$$\mathrm{MC}_{ac,\,\mathrm{var}} = \mathrm{MC}_{a,\,\mathrm{var}} + \mathrm{MC}_{b,\,\mathrm{nom}} + \mathrm{MC}_{c,\,\mathrm{var}},$$

and

$$\mathrm{MC}_{abc,\,\mathrm{var}} = \mathrm{MC}_{a,\,\mathrm{var}} + \mathrm{MC}_{b,\,\mathrm{var}} + \mathrm{MC}_{c,\,\mathrm{var}}.$$

The difference with respect to the nominal is then scaled by the appropriate δ as given by Equation 7.1 to 7.3. Hence,

$$\begin{aligned} \mathrm{MC}_{a,\,\mathrm{var}} \rightarrow \\ \delta_{a,\,\mathrm{uncorr}} * (\mathrm{MC}_{a,\,\mathrm{uncorr},\,\mathrm{var}} - \mathrm{MC}_{\mathrm{nom}}) + \mathrm{MC}_{\mathrm{nom}}, \\ \delta_{ab} * (\mathrm{MC}_{ab,\,\mathrm{var}} - \mathrm{MC}_{\mathrm{nom}}) + \mathrm{MC}_{\mathrm{nom}}, \\ \delta_{ac} * (\mathrm{MC}_{ac,\,\mathrm{var}} - \mathrm{MC}_{\mathrm{nom}}) + \mathrm{MC}_{\mathrm{nom}}, \\ \delta_{abc} * (\mathrm{MC}_{abc,\,\mathrm{var}} - \mathrm{MC}_{\mathrm{nom}}) + \mathrm{MC}_{\mathrm{nom}}, \end{aligned} \tag{7.4}$$

$$\begin{aligned} \mathrm{MC}_{b,\,\mathrm{var}} \rightarrow \\ \delta_{b,\,\mathrm{uncorr}} * (\mathrm{MC}_{b,\,\mathrm{uncorr},\,\mathrm{var}} - \mathrm{MC}_{\mathrm{nom}}) + \mathrm{MC}_{\mathrm{nom}}, \\ \delta_{ab} * (\mathrm{MC}_{ab,\,\mathrm{var}} - \mathrm{MC}_{\mathrm{nom}}) + \mathrm{MC}_{\mathrm{nom}}, \\ \delta_{bc} * (\mathrm{MC}_{bc,\,\mathrm{var}} - \mathrm{MC}_{\mathrm{nom}}) + \mathrm{MC}_{\mathrm{nom}} \\ \delta_{abc} * (\mathrm{MC}_{abc,\,\mathrm{var}} - \mathrm{MC}_{\mathrm{nom}}) + \mathrm{MC}_{\mathrm{nom}}, \end{aligned} \tag{7.5}$$

and

$$\begin{aligned} \mathrm{MC}_{c,\,\mathrm{var}} \rightarrow \\ \delta_{c,\,\mathrm{uncorr}} * (\mathrm{MC}_{c,\,\mathrm{uncorr},\,\mathrm{var}} - \mathrm{MC}_{\mathrm{nom}}) + \mathrm{MC}_{\mathrm{nom}}, \\ \delta_{ac} * (\mathrm{MC}_{ac,\,\mathrm{var}} - \mathrm{MC}_{\mathrm{nom}}) + \mathrm{MC}_{\mathrm{nom}}, \\ \delta_{bc} * (\mathrm{MC}_{bc,\,\mathrm{var}} - \mathrm{MC}_{\mathrm{nom}}) + \mathrm{MC}_{\mathrm{nom}} \\ \delta_{abc} * (\mathrm{MC}_{abc,\,\mathrm{var}} - \mathrm{MC}_{\mathrm{nom}}) + \mathrm{MC}_{\mathrm{nom}}. \end{aligned} \tag{7.6}$$

The total Run 2 uncertainty for a given systematic source can then be computed as the quadratic sum of independent terms from $\mathrm{MC}_{a,\,\mathrm{var}}$, $\mathrm{MC}_{b,\,\mathrm{var}}$ and $\mathrm{MC}_{c,\,\mathrm{var}}$. In the case of differential measurements this refers to the final uncertainty for each of the terms after unfolding. If the source is uncorrelated $\delta_{a,\,\mathrm{uncorr}} = \delta_{b,\,\mathrm{uncorr}} = \delta_{c,\,\mathrm{uncorr}} = 1$ and $\delta = 0$ for all other terms. If the source is fully correlated $\delta_{abc} = 1$ and $\delta = 0$ for all other terms. In this work the only source that is partially correlated among years is luminosity for which the measurements are all 30% correlated. This results in $\delta_{a,\,\mathrm{uncorr}} = \delta_{b,\,\mathrm{uncorr}} = \delta_{c,\,\mathrm{uncorr}} = \sqrt{1-0.3}$ and $\delta_{abc} = \sqrt{0.3}$. Since the correlation is the same between the different years it follows that $\delta_{ab} = \delta_{bc} = \delta_{ac} = 0$.

7.6 Summary of uncertainties and their impact

The systematic uncertainties are evaluated by computing the difference of the varied and nominal results. The definition of the total uncertainty computed from the up and down variations of all the sources vary for inclusive and differential measurements. This section contains a summary of the uncertainty computation and impact for both types of results.

7.6.1 Uncertainties on the inclusive cross section measurements

The systematic uncertainties on the $t\bar{t}$ inclusive cross section measurements are symmetrized such that the total uncertainty is given by

$$\Delta^{\mathrm{total\ incl.}} = \sqrt{(\Delta^{\mathrm{stat.}})^2 + \sum_s (\Delta^{\mathrm{s,\ incl.}})^2},$$

where

$$\Delta^{\mathrm{s,\ incl.}} = (|\sigma^{\mathrm{nom}}_{\mathrm{incl.}} - \sigma^{\mathrm{up}}_{\mathrm{incl.}}| + |\sigma^{\mathrm{nom}}_{\mathrm{incl.}} - \sigma^{\mathrm{down}}_{\mathrm{incl.}}|) * 0.5$$

denotes the systematic uncertainty of an individual source s for which $\sigma^{\mathrm{nom}}_{\mathrm{incl.}}$ is the nominal inclusive cross section while $\sigma^{\mathrm{up}}_{\mathrm{incl.}}$ and $\sigma^{\mathrm{down}}_{\mathrm{incl.}}$ denote the inclusive cross section measurements corresponding to the up and down variations of s, respectively.

A summary of the individual uncertainty contributions of the $t\bar{t}$ inclusive cross section measured in the ee, $\mu\mu$, $e\mu$ and combined channels for full Run 2 is shown in Table 7.1. The corresponding results measured in the combined channels of the individual years are shown in Table 7.2. As stated in Chapter 8 all combinations are performed with BLUE [138] [139], using only the results for the individual years. It is immediately evident from these tables that the analysis is limited by the systematic uncertainties which yield a total uncertainty of 3.7% when added in quadrature for full Run 2 in the combined channel whereas the statistical uncertainty only accounts for 0.4%. The experimental sources are dominant and the largest uncertainties come

from the luminosity, lepton efficiencies, jet energy scale and background normalization. The largest theoretical uncertainties come from the branching ratio of the signal process, $\mathcal{BR}\,(t\bar{t} \to \ell\ell + X)$, the parton shower final state radiation, PS α_S^{FSR}, and the top quark mass.

7.6.2 Uncertainties on the differential cross section measurements

The systematic uncertainties of the $t\bar{t}$ differential cross section measurements are added in quadrature while preserving any asymmetry in up and down variations such that the total positive and negative uncertainties are given by

$$\Delta_i^{\mathrm{s,\,+}} = \sqrt{(\Delta_i^{\mathrm{stat.}})^2 + \sum_s (\Delta_i^{\mathrm{s,\,+}})^2},$$

$$\Delta_i^{\mathrm{s,\,-}} = \sqrt{(\Delta_i^{\mathrm{stat.}})^2 + \sum_s (\Delta_i^{\mathrm{s,\,-}})^2},$$

where the bins of the differential spectra are denoted by i, and $\Delta_i^{\mathrm{s,\,+}}$ and $\Delta_i^{\mathrm{s,\,-}}$ refer to the positive and negative values of either the up or down variation of source s in bin i. If the up and down variations are both positive (negative) the largest (smallest) uncertainty is chosen and the other is set to 0.

Figure 7.1 shows the uncertainty contributions of the differential $t\bar{t}$ cross sections measured as functions of the transverse momentum of the top, $p_{\mathrm{T}}(t)$, for both normalized (top) and absolute (bottom) measurements performed at parton level in the full phase space. This example is chosen as it demonstrates several of the points relating to the impact of the systematic uncertainties in the discussion below. Corresponding uncertainty contribution plots for all remaining differential measurements are shown in Appendix J where Figures J.2 to J.13 in Appendix J.1.1 and Figures J.14 to J.40 in Appendix J.1.2 show single-differential measurements performed at parton and particle level, respectively, while Figures J.41 to J.46 in Appendix J.2.1 show the double-differential measurements performed at particle level.

One can see from Figure 7.1 that the differential measurements are limited by the systematic uncertainties in each bin. The total uncertainty on the jet energy scale (denoted by JES in the plot) is one of the most dominating sources. This is true for the majority of measurements, most noticeably so in the extreme ends of the spectra, although for several spectra the dominant uncertainty in the first bin tend to come from the background normalization which is due to the relatively higher fraction of background events in this bin. Another dominant source of uncertainty comes from the lepton efficiencies (labelled Lepton) and is generally largest relative to others for cross sections measured as functions of the lepton kinematic spectra. The luminosity uncertainty tends to be of comparable size to that of the lepton efficiencies for the absolute measurements. Other experimental sources (denoted

Table 7.1: Summary of the systematic uncertainties for the measurement of the inclusive $t\bar{t}$ cross section. Results are shown for Run 2 in all channels. All combinations are performed with BLUE [138] [139]. The labels "Muon reconstruction" and "Electron reconstruction" refer to all corresponding id, reconstruction, isolation and extrapolation uncertainties added in quadrature. Likewise, the label "b-tagging heavy flavours" covers all sub-sources pertaining to the heavy flavour uncertainty and similar applies to the label "Jet energy scale sources" where the set of 7 individual sources are added in quadrature. The contribution of backgrounds other than Drell-Yan and the single top tW process is referred to as "Background cross sections".

Source	**Uncertainty (%)**			
	ee	$\mu\mu$	$e\mu$	combined
Trigger efficiency	1.8	1.5	1.0	0.6
L1 ECAL prefiring	0.2	0.3	0.3	0.3
Electron reconstruction	4.0	0.0	2.3	0.7
Muon reconstruction	0.0	2.0	0.9	1.6
Background cross sections	0.3	0.3	0.2	0.2
Single-top tw-process cross sections	1.4	1.4	1.4	1.4
Drell-Yan cross sections	2.5	4.8	0.3	0.4
Jet energy scale sources	2.0	2.1	1.3	1.1
Jet energy resolution	1.1	1.1	0.5	0.5
Pile-up	0.4	0.1	0.3	0.1
b-tagging heavy flavours	1.4	1.4	1.1	1.0
b-tagging light flavours	0.6	0.6	0.1	0.2
Unclustered met	2.1	1.0	0.1	0.2
Top quark mass	0.9	0.7	0.7	0.7
Total scale uncertainty	0.1	0.1	0.2	0.2
PS α_S^{FSR}	1.5	1.1	1.2	1.1
PS α_S^{ISR}	0.0	0.1	0.0	0.0
ME-PS matching	0.5	0.2	0.3	0.2
Underlying event tune	0.5	0.3	0.3	0.2
PDF α_S	0.1	0.1	0.1	0.1
PDF replicas	0.5	-	-	-
Colour reconnection	0.6	0.4	0.5	0.4
B semi-leptonic BR	0.3	0.3	0.3	0.3
$\mathcal{BR}\,(t\bar{t} \to \ell\ell + X)$	1.5	1.5	1.5	1.5
Luminosity	2.0	1.6	1.3	1.2
Total systematic error	7.1	6.9	4.4	3.7
Statistical error	0.9	0.6	0.3	0.4

Table 7.2: Summary of the systematic uncertainties for the measurement of the inclusive $t\bar{t}$ cross section. Results for Run 2 are compared with 2016, 2017 and 2018 in the combined channel. All combinations are performed with BLUE [138] [139]. The labels "Muon reconstruction" and "Electron reconstruction" refer to all corresponding id, reconstruction, isolation and extrapolation uncertainties added in quadrature. Likewise, the label "b-tagging heavy flavours" covers all sub-sources pertaining to the heavy flavour uncertainty and similar applies to the label "Jet energy scale sources" where the set of 7 individual sources are added in quadrature. The contribution of backgrounds other than Drell-Yan and the single top tW process is referred to as "Background cross sections".

Source	**Uncertainty (%)**			
	2016	2017	2018	Run 2
Trigger efficiency	0.7	1.6	0.8	0.6
L1 ECAL prefiring	0.4	0.5	0.0	0.3
Electron reconstruction	0.7	1.2	0.7	0.7
Muon reconstruction	1.6	1.8	1.1	1.6
Background cross sections	0.2	0.2	0.2	0.2
Single-top tw-process cross sections	1.4	1.3	1.3	1.4
Drell-Yan cross sections	0.3	0.8	0.8	0.4
Jet energy scale sources	1.2	1.2	1.6	1.1
Jet energy resolution	0.4	0.4	0.2	0.5
Pile-up	0.3	0.1	0.3	0.1
b-tagging heavy flavours	1.0	0.9	1.4	1.0
b-tagging light flavours	0.0	0.0	0.0	0.2
Unclustered met	0.3	0.4	0.2	0.2
Top quark mass	0.7	0.6	0.7	0.7
Total scale uncertainty	0.2	0.3	0.2	0.2
PS α_S^{FSR}	1.1	1.2	1.2	1.1
PS α_S^{ISR}	0.0	0.0	0.0	0.0
ME-PS matching	0.3	0.2	0.3	0.2
Underlying event tune	0.2	0.2	0.2	0.2
PDF α_S	0.1	0.1	0.1	0.1
PDF replicas	0.5	-	-	-
Colour reconnection	0.4	0.3	0.2	0.4
B semi-leptonic BR	0.3	0.3	0.3	0.3
$\mathcal{BR}\,(t\bar{t} \to \ell\ell + X)$	1.5	1.5	1.5	1.5
Luminosity	1.2	2.3	2.5	1.2
Total systematic error	3.8	4.7	4.5	3.7
Statistical error	0.4	0.4	0.3	0.4

by "Other exp syst") also contribute significantly to the overall uncertainty when added in quadrature.

Some of the aforementioned uncertainties tend to increase significantly in the extreme ends of p_{T} and mass spectra due to limited statistics. This is particularly true for the JES uncertainty and is explained by the fact that it consists of several sub-sources that are varied independently and in a way that affects the selection. Thus, the varied simulations associated with these sub-sources will naturally incur some fluctuations in the statistically limited outer ends of the spectra that are enhanced by the quadratic sum.

The theoretical uncertainties are overall smaller than the experimental uncertainties but the parton shower final state radiation (PS FSR), matrix element scales (ME scales), matching (h_{damp}), top quark mass (m_t) and underlying event tune (UE tune) constitute the largest contributions amongst the theoretical sources depending on the spectra. Sometimes large fluctuations also occur for the theoretical sources in the outer bins. This is the case for h_{damp} and UE tune in particular and mainly comes from the fact that both are computed from independent samples of a smaller size than the simulation of the nominal signal process.

Comparable distributions at parton and particle level have similar uncertainty contributions both in terms of trends and overall impact. One would expect the theoretical uncertainties to be slightly reduced at particle level with respect to parton level, as the extrapolation uncertainties are reduced. However, this is not observed. A possible reason is that the fiducial selection at particle level deviates slightly from the selection at detector level, as the former has a softer cut on the p_{T} of the leading lepton, which means that some level of extrapolation uncertainty is still present, but the most likely reason is that the fiducial measurement is performed with a smaller amount of statistics as implied by its very definition.

Normalized cross section measurements are more precise with respect to their absolute counterpart as the rate components of the systematic uncertainties cancel. An excellent level of precision is achieved overall and in particular for normalized cross sections measured as functions of the lepton kinematic spectra. Here the achieved level of precision goes down to 2%. The maximal uncertainty varies up to 25% depending on the bin and type of spectra.

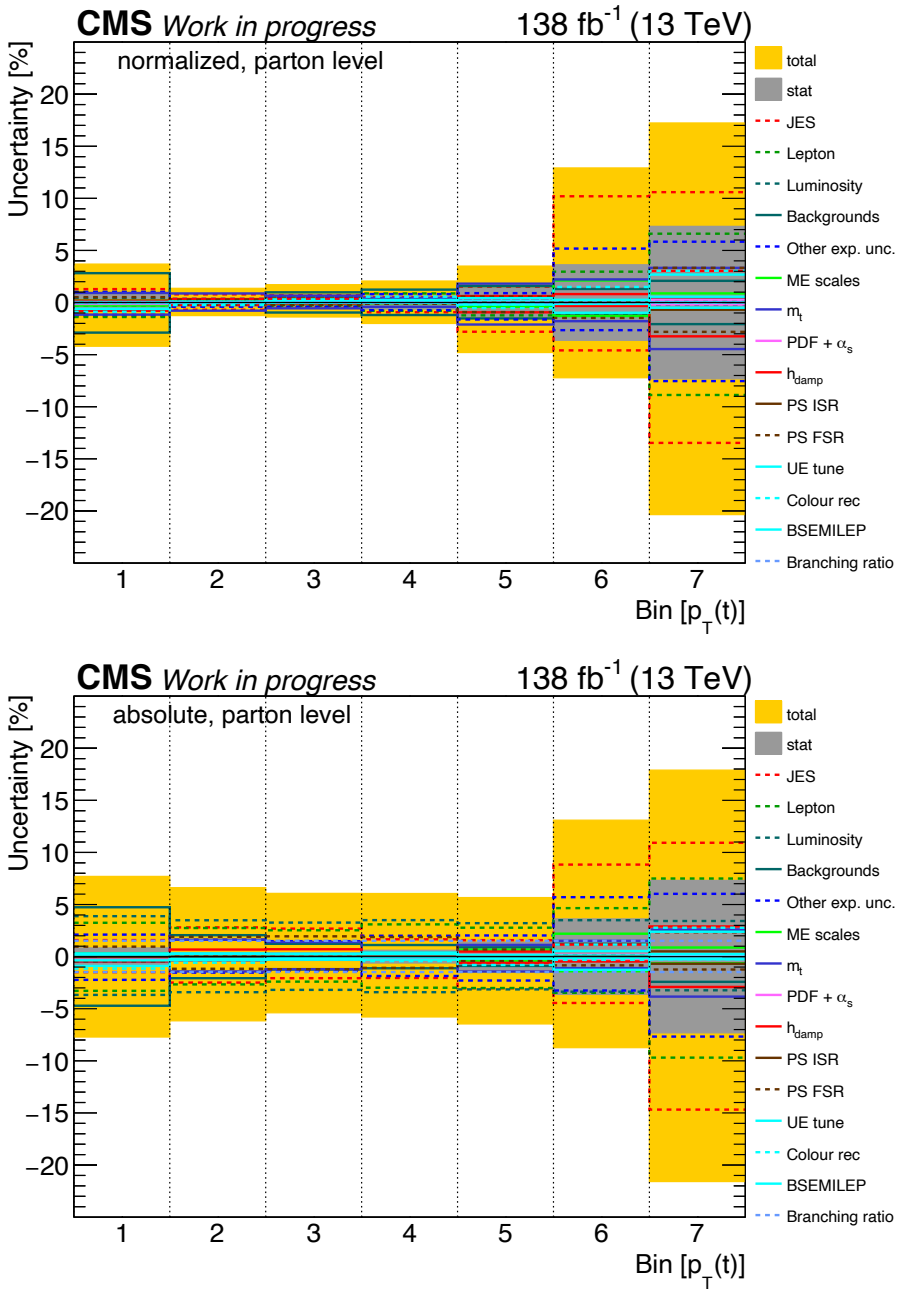

Figure 7.1: The figure shows the uncertainty contributions of the differential $t\bar{t}$ cross section measured as a function of the transverse momentum of the top, $p_{\mathrm{T}}(t)$, for both normalized (top) and absolute (bottom) measurements performed in the full phase space at parton level.

Chapter 8

Results

Two types of measurements are performed in this work, namely inclusive and differential cross sections of $t\bar{t}$ production. The former are done as a cross check of the analysis procedure, and the latter make up the main results. All measurements are performed in the dilepton channel with the CMS experiment using the full Run 2 data, which corresponds to an integrated luminosity of 137.6 fb^{-1}. The results are presented in the combined channel, which refers to the combination of individual channels of oppositely charged lepton pairs, i.e. $e^{\pm}e^{\mp}$, $\mu^{\pm}\mu^{\mp}$ and $e^{\pm}\mu^{\mp}$, originating from prompt decays of the W bosons. Decays via τ are vetoed and labelled as background (see Chapter 5 for further details).

8.1 Inclusive cross sections of $t\bar{t}$ production

The inclusive cross section of $t\bar{t}$ production is computed as described in Chapter 6. The parts of the analysis procedure that comprise the event selection and kinematic reconstruction are the same for inclusive and differential cross sections. It's in the combination of data that the two types of results differ in their approach. Run 2 data for all years and channels are added directly when performing differential measurements in the combined channel, while inclusive cross sections are first measured individually for each year and each channel. The BLUE software [138] [139] is then used for the combination of results. The algorithm calculates a weighted average of the input measurements by performing a χ^2 minimization with respect to the combined result. A total of 9 measurements are combined to obtain the result for the inclusive cross section of $t\bar{t}$ production in the combined channel for Run 2. The nominal measurements for all years and all channels are used with their full covariance matrices, including the appropriate systematic uncertainty correlations between the measurements obtained in different years.

Table 8.1 lists the number of events, total efficiency and acceptance, branching ratio etc. which are used to compute the inclusive cross sections in all channels for Run 2 (see Equation 6.1 in Section 6.1). Here the result for each channel is obtained by performing the BLUE combination of the corresponding cross sections measured in the three different years. The corresponding numbers and results in the combined channel for all years are shown in Table 8.2, where the result for

each year is obtained by performing the BLUE combination of the cross sections measured in the three different channels. The final result for the inclusive cross section of $t\bar{t}$ production in the combined channel for Run 2 is found to be $786.4 \pm 2.9\,(\text{stat.}) \pm 29.3\,(\text{syst.})$ pb, which demonstrates an excellent level of precision. The corresponding results in the $e^{\pm}e^{\mp}$, $\mu^{\pm}\mu^{\mp}$ and $e^{\pm}\mu^{\mp}$ channels are consistent with this result within the uncertainties and the same remark applies to the results obtained in the combined channel for different years.

Table 8.1: Inclusive cross sections are shown for Run 2 in the individual and combined dilepton channels. The result for each channel is obtained by combining the corresponding cross sections measured in the three different years. All combinations are performed with BLUE [138] [139].

Channel	$e^{\pm}e^{\mp}$	$\mu^{\pm}\mu^{\mp}$	$e^{\pm}\mu^{\mp}$	combined
Events in data	167443	360945	663856	1192240
$t\bar{t}$ signal	129703	253742	563074	946519
$t\bar{t}$ other background	21516	45740	101680	168936
Non-$t\bar{t}$ background	26744	67833	39650	134231
Total efficiency and acceptance	9.539	18.653	20.698	17.398
Branching ratio [%]	1.147	1.130	2.277	4.554
Cross section [pb]	788.5	773.8	783.1	786.3
Statistical error [pb]	7.2	4.3	2.2	2.9
Systematic error [pb]	55.9	53.2	34.3	29.5
Total error [pb]	56.4	53.4	34.4	29.6

Table 8.2: Inclusive cross sections are shown for each year in the combined dilepton channel alongside the Run 2 result from Table 8.1. The result for each year is obtained by combining the cross sections measured in the three different channels. All combinations are performed with BLUE [138] [139].

Year	2016	2017	2018	Run 2
Events in data	291502	367464	533278	1192240
$t\bar{t}$ signal	243116	283144	420259	946519
$t\bar{t}$ other background	42444	51426	75066	168936
Non-$t\bar{t}$ background	31900	44162	58446	134231
Total efficiency and acceptance	16.924	17.242	17.794	17.398
Branching ratio [%]	4.554	4.554	4.554	4.554
Cross section [pb]	786.9	847.5	835.1	786.3
Statistical error [pb]	3.5	3.1	2.9	2.9
Systematic error [pb]	30.0	40.0	37.7	29.5
Total error [pb]	30.2	40.1	37.8	29.6

8.2 Differential cross sections

In this work both normalized and absolute differential $t\bar{t}$ production cross sections are studied as functions of one or more kinematic variables. Measurements of the top quarks and $t\bar{t}$ system are performed both at parton level in the full phase space and at particle level in the fiducial phase space, while measurements of the charged leptons and beauty flavoured jets as well as the total jet multiplicity are performed at particle level only in the fiducial phase space. A full overview of all variables and combinations of variables is given below:

List of figures showing absolute and normalized single-differential cross sections performed at both parton and particle level:

• **Figure 8.1**: the transverse momentum of the top, $p_{\mathrm{T}}(t)$.
• **Figure 8.2**: the transverse momentum of the anti-top, $p_{\mathrm{T}}(\bar{t})$.
• **Figure 8.3**: the rapidity of the top, $y(t)$.
• **Figure 8.4**: the rapidity of the anti-top, $y(\bar{t})$.
• **Figure 8.5**: the difference in absolute value of rapidity of the top and absolute value of rapidity of the anti-top, $|y(t)| - |y(\bar{t})|$.
• **Figure 8.6**: the absolute value of the azimuthal angle (ϕ) between the top and the anti-top, $|\Delta\phi(t,\bar{t})|$.
• **Figure 8.7**: the transverse momentum of the $t\bar{t}$ system, $p_{\mathrm{T}}(t\bar{t})$.
• **Figure 8.8**: the rapidity of the $t\bar{t}$ system, $y(t\bar{t})$.
• **Figure 8.9**: the invariant mass of the $t\bar{t}$ system, $m(t\bar{t})$.
• **Figure 8.10**: the ratio of the transverse momentum of the top quark over the invariant mass of the $t\bar{t}$ system, $p_{\mathrm{T}}(t)/m(t\bar{t})$.
• **Figure 8.11**: the ratio of the transverse momentum of the $t\bar{t}$ system over the invariant mass of the $t\bar{t}$ system, $p_{\mathrm{T}}(t\bar{t})/m(t\bar{t})$.
• **Figure 8.12**: the log10 of the proton momentum fraction from the incoming parton (leading order QCD), $\log(\xi_1)$.
• **Figure 8.13**: the log10 of the proton momentum fraction from the incoming anti-parton (leading order QCD), $\log(\xi_2)$.

List of figures showing absolute and normalized single-differential cross sections performed at particle level only:

• **Figure 8.14**: the transverse momentum of the lepton, $p_{\mathrm{T}}(\ell)$, and
the ratio of the transverse momentum of the trailing lepton over the transverse momentum of the leading lepton, $p_{\mathrm{T}}(\ell)$ trailing/$p_{\mathrm{T}}(\ell)$ leading.
• **Figure 8.15**: the ratio of the transverse momentum of the lepton over the transverse momentum of the anti-top quark, $p_{\mathrm{T}}(\ell)/\mathrm{p_T}(\bar{\mathrm{t}})$, and
the ratio of the scalar sum of p_{T} of b and p_{T} of anti-b over the scalar sum of p_{T} of top and p_{T} of anti-top, $(p_{\mathrm{T}}(\mathrm{b}) + \mathrm{p_T}(\bar{\mathrm{b}}))/(\mathrm{p_T(t)} + \mathrm{p_T}(\bar{\mathrm{t}}))$.
• **Figure 8.16**: the transverse momentum of the leading b quark, $p_{\mathrm{T}}(\mathrm{b})$ leading, and

the transverse momentum of the trailing b quark, p_{T}(b) trailing.
• **Figure 8.17**: the transverse momentum of the $\ell\bar{\ell}$ system, $p_{\mathrm{T}}(\ell\bar{\ell})$, and
the absolute pseudorapidity of the $\ell\bar{\ell}$ system, $|\eta(\ell\bar{\ell})|$.
• **Figure 8.18**: the difference in absolute pseudorapidity of the lepton and absolute pseudorapidity of the anti-lepton, $|\eta(\ell)| - |\eta(\bar{\ell})|$, and
the absolute value of the azimuthal angle (ϕ) between the lepton and the anti-lepton, $|\Delta\phi(\ell,\bar{\ell})|$.
• **Figure 8.19**: the invariant mass of the $\ell\bar{\ell}$ system, $m(\ell\bar{\ell})$, and
the invariant mass of the $b\bar{b}$ system, $m(b\bar{b})$.
• **Figure 8.20**: the invariant mass of the $l\bar{l}b\bar{b}$ system, $m(\ell\bar{\ell}\mathrm{b}\bar{\mathrm{b}})$.
• **Figure 8.27**: the total jet multiplicity, N_{jet} (the last bin is inclusive for ≥ 7).

List of figures showing absolute and normalized double-differential cross sections performed at particle level only:

• **Figure 8.21**: the absolute value of the azimuthal angle between the lepton and the anti-lepton, $|\Delta\phi(\ell,\bar{\ell})|$, in ranges of the invariant mass of the $t\bar{t}$ system, $m(t\bar{t})$. Shorthand notation: $[m(t\bar{t}), |\Delta\phi(\ell,\bar{\ell})|]$.
• **Figure 8.22**: the absolute value of the azimuthal angle between the lepton and the anti-lepton, $|\Delta\phi(\ell,\bar{\ell})|$, in ranges of the transverse momentum of the top, $p_{\mathrm{T}}(t)$. Shorthand notation: $[p_{\mathrm{T}}(t), |\Delta\phi(\ell,\bar{\ell})|]$.
• **Figure 8.23**: the absolute value of the azimuthal angle between the lepton and the anti-lepton, $|\Delta\phi(\ell,\bar{\ell})|$, in ranges of the difference in absolute value of pseudorapidity of the lepton and absolute value of pseudorapidity of the anti-lepton, $|\eta(\ell)| - |\eta(\bar{\ell})|$. Shorthand notation: $[|\eta(\ell)| - |\eta(\bar{\ell})|, |\Delta\phi(\ell,\bar{\ell})|]$.
• **Figure 8.24**: the invariant mass of the $\ell\bar{\ell}$ system, $m(\ell\bar{\ell})$, in ranges of the absolute pseudorapidity of the $\ell\bar{\ell}$ system, $|\eta(\ell\bar{\ell})|$. Shorthand notation: $[|\eta(\ell\bar{\ell})|, \mathrm{m}(\ell\bar{\ell})]$.
• **Figure 8.25**: the transverse momentum of the $\ell\bar{\ell}$ system, $p_{\mathrm{T}}(\ell\bar{\ell})$, in ranges of the absolute pseudorapidity of the $\ell\bar{\ell}$ system, $|\eta(\ell\bar{\ell})|$. Shorthand notation: $[|\eta(\ell\bar{\ell})|, \mathrm{p_T}(\ell\bar{\ell})]$.
• **Figure 8.26**: the invariant mass of the $\ell\bar{\ell}$ system, $m(\ell\bar{\ell})$, in ranges of the transverse momentum of the $\ell\bar{\ell}$ system, $p_{\mathrm{T}}(\ell\bar{\ell})$. Shorthand notation: $[p_{\mathrm{T}}(\ell\bar{\ell}), \mathrm{m}(\ell\bar{\ell})]$.

Three different types of data to theory comparisons are done to either alternative MC generators, predictions beyond-NLO in QCD, or alternative PDFs. The alternative MC models consist of MG5_aMC@NLO[FxFx] (version 2.4.2)+Pythia8 and Powheg (version 2)+Herwig7, which are abbreviated to FXFX+PYT and POW+HER, respectively. This applies to figures and tables and when the models are referenced in the rest of this section. In the first set of comparisons, predictions from the two alternative models are plotted together with the reference simulation, i.e. Powheg (version 2)+Pythia8, which will be abbreviated to POW+PYT. The differential measurements are divided into several categories and presented in Sections 8.2.1 to 8.2.4, while numerical values of the results can be found in Appendix K. A summary on the description of data by the MC models along with tables listing χ^2 values for all models can be found in Section 8.2.5, and the corresponding χ^2 definition is given in Appendix A.

A second set of plots showing comparisons of data to predictions from $a\text{N}^3\text{LO}$ [140], Stripper [130–133], Matrix [141–148] and MiNNLOPS [16–18] at beyond-NLO in QCD is discussed in Section 8.2.6, while the third and final set of plots, comparing the data to POW+PYT using different PDF models, is shown in Section 8.2.7. Here the reference simulation, with the PDF set NNPDF3.1 at NNLO accuracy [32], is compared to POW+PYT simulations, where the PDF sets NNPDF3.1 [32], CT14 [149], ABMP16 [150], MMHT2014 [151] and HERAPDF2.0 [33] at NLO accuracy are used instead.

Contrary to the control plots and closure tests presented earlier, agreement between the prediction and data is now expressed as the ratio of the two with the prediction in the numerator. This choice reflects the shift in focus to how different predictions compare with data as opposed to how well the reference simulation agrees with data.

8.2.1 Cross sections measured as functions of kinematic spectra of the top quarks at parton and particle level

In this section the discussion pertains to Figures 8.1 to 8.4. Differential $t\bar{t}$ cross sections are presented as functions of kinematic spectra of the top quarks at parton level in the full phase space and particle level in the fiducial phase space.

The two independent quantities characterizing the dynamics of the top quarks are the transverse momentum, p_{T}, and rapidity, y. Figure 8.1 and 8.2 show cross sections of $p_{\text{T}}(t)$ and $p_{\text{T}}(\bar{t})$, respectively, where the kinematic phase space has been slightly extended to 600 GeV in comparison to the previous result in the dileptonic channel, where $p_{\text{T}}(t)$ was measured up to 550 GeV [14]. One expects the measurements of $p_{\text{T}}(t)$ and $p_{\text{T}}(\bar{t})$ to mirror each other as the top and anti-top are governed by the same principles of physics, and indeed this is the case. The small differences in precision observed in the outer bins are artefacts of statistical fluctuations. The same holds true for $y(t)$ and $y(\bar{t})$, as shown in Figure 8.3 and Figure 8.4, respectively. The $p_{\text{T}}(t)$ and $p_{\text{T}}(\bar{t})$ spectra are not well described by POW+PYT and FXFX+PYT. Both models give rise to a positive slope as a function of p_{T} when comparing the predictions to data, which favours a softer spectrum. This is a known effect and has been observed at both CMS and ATLAS, as previously mentioned in Section 5.9. The discrepancy has been shown to decrease for predictions at NNLO [14], however, the cause of the so-called "top-p_{T} slope" is not fully understood and therefore remains an open question. The POW+HER prediction describes the data well and exhibits no slope, however, this particular model fails to describe other distributions as evident from the following discussion. Finally, all models predict $y(t)$ and $y(\bar{t})$ to be slightly more central than is observed in data.

The observations made above apply to the distributions at both parton and particle level, and as this is generally the case, the following discussion will focus on the former for measurements performed in both phase spaces. Furthermore, from the figures described above one can see that the normalized differential measurements

have smaller uncertainties when compared to the absolute ones. This was also stated in Chapter 7 and is due to the cancellation of the luminosity and background uncertainties in normalized distributions, which will be the focus of the subsequent discussion.

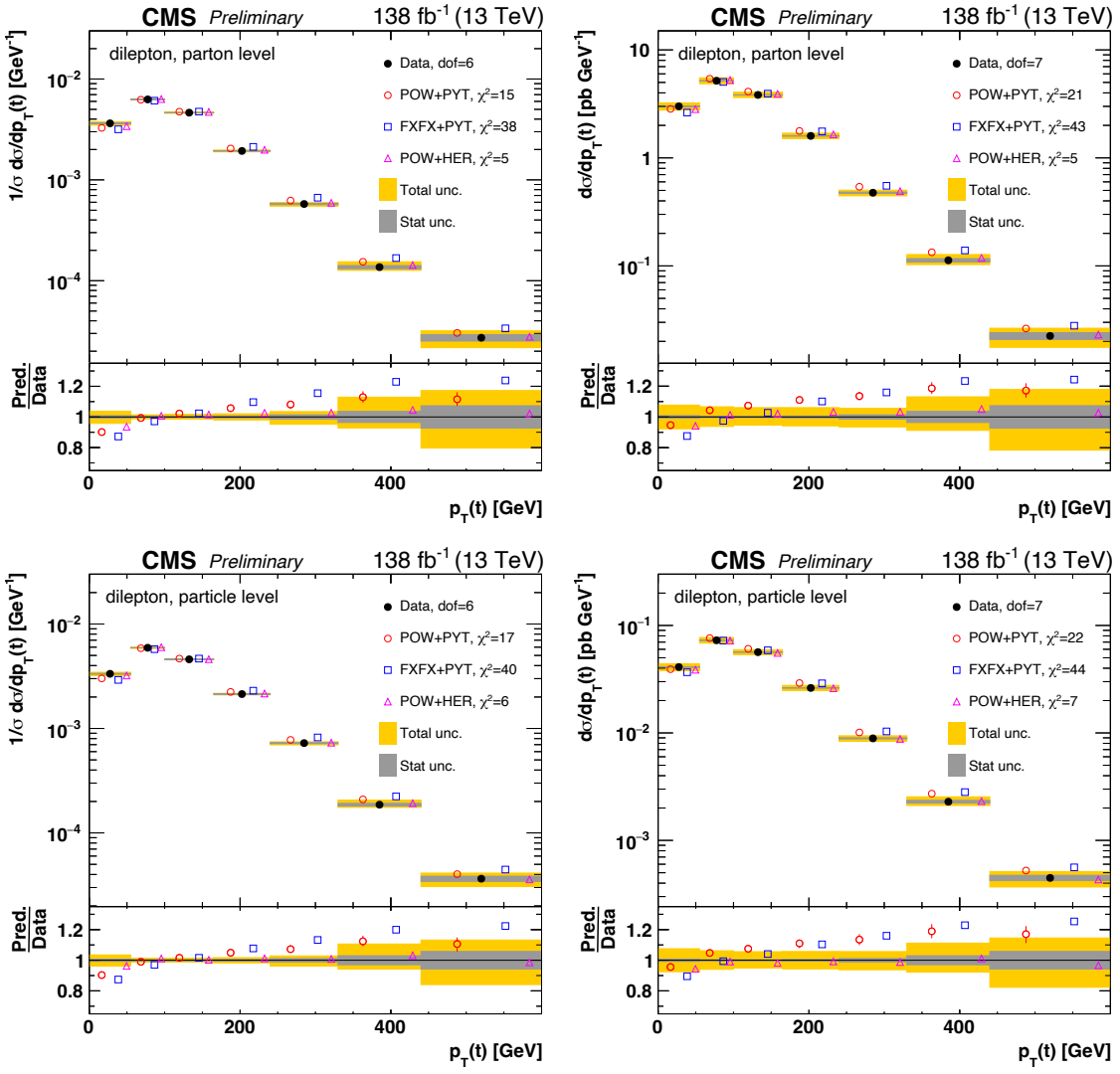

Figure 8.1: Differential $t\bar{t}$ cross sections measured as functions of the transverse momentum of the top, $p_{\mathrm{T}}(t)$, in the full phase space at parton level (top row) and in the fiducial phase space at particle level (bottom row). The left and right columns show normalized and absolute cross sections, respectively. The data (black dots) is shown together with the reference simulation, depicted in red and abbreviated to POW+PYT, and two alternative simulation models, FXFX+PYT (blue) and POW+HER (magenta). The statistical and total uncertainties on the data are illustrated by the grey and yellow bands, respectively, where the latter corresponds to systematic and statistical uncertainties added in quadrature. The uncertainty on the POW+PYT prediction is indicated by error bars. Furthermore, a χ^2 value that takes all measurement uncertainties into account is reported for each MC model, and the ratios with respect to data are shown in the bottom panel of each plot.

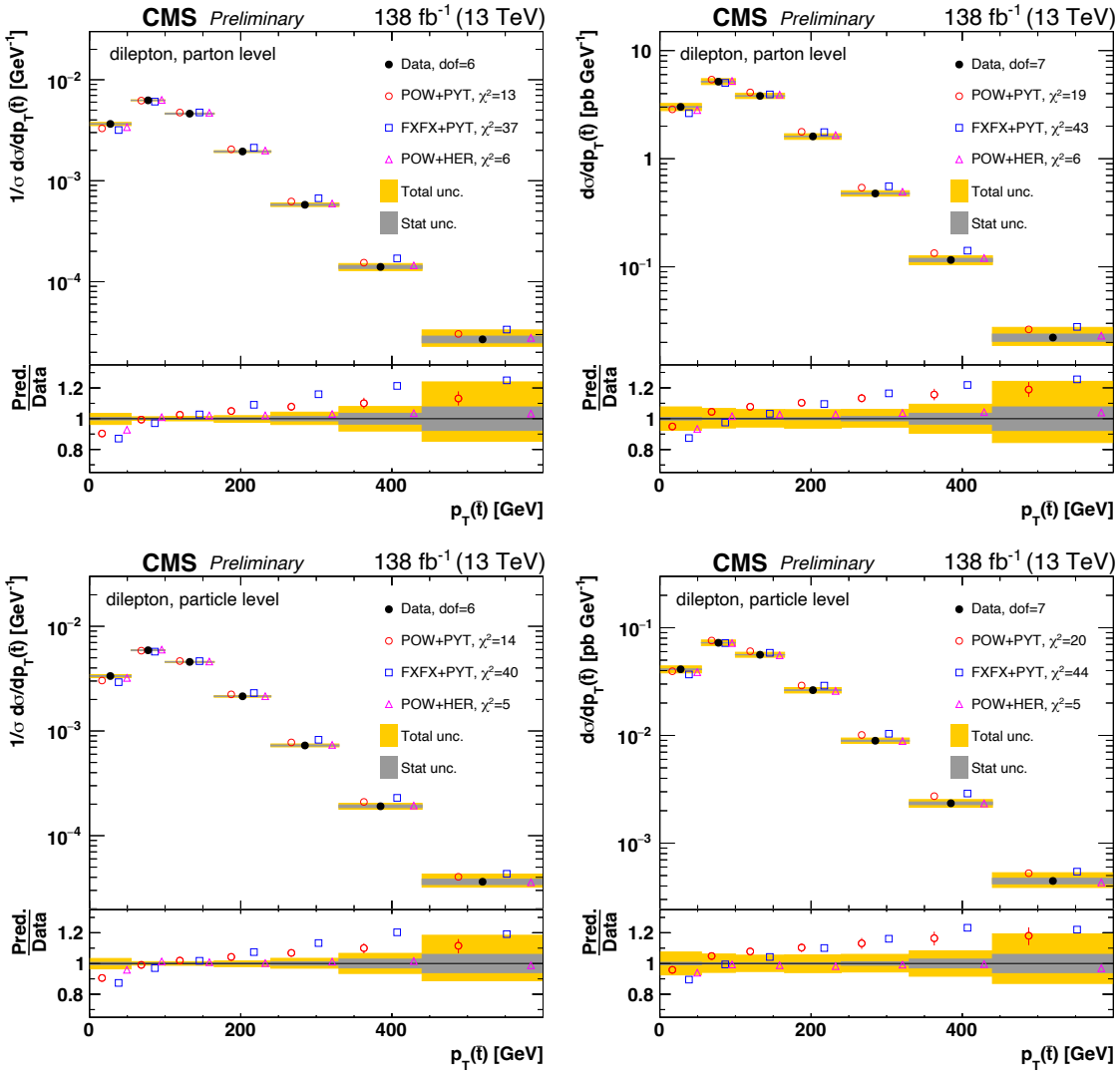

Figure 8.2: Differential $t\bar{t}$ cross sections measured as functions of the transverse momentum of the anti-top, $p_{\mathrm{T}}(\bar{t})$, in the full phase space at parton level (top row) and in the fiducial phase space at particle level (bottom row). The left and right columns show normalized and absolute cross sections, respectively. For further details see Figure 8.1.

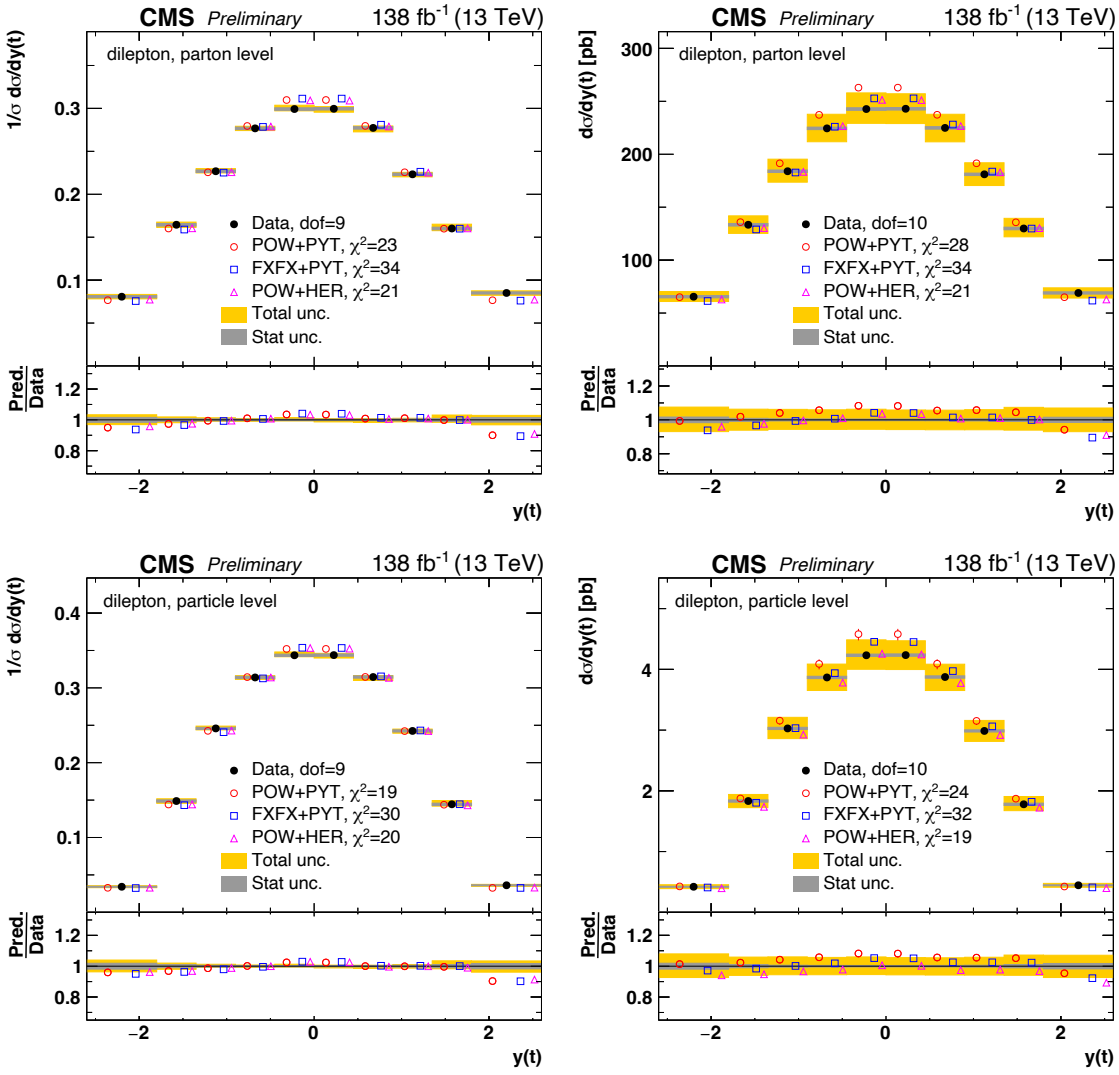

Figure 8.3: Differential $t\bar{t}$ cross sections measured as functions of the rapidity of the top, $y(t)$, in the full phase space at parton level (top row) and in the fiducial phase space at particle level (bottom row). The left and right columns show normalized and absolute cross sections, respectively. For further details see Figure 8.1.

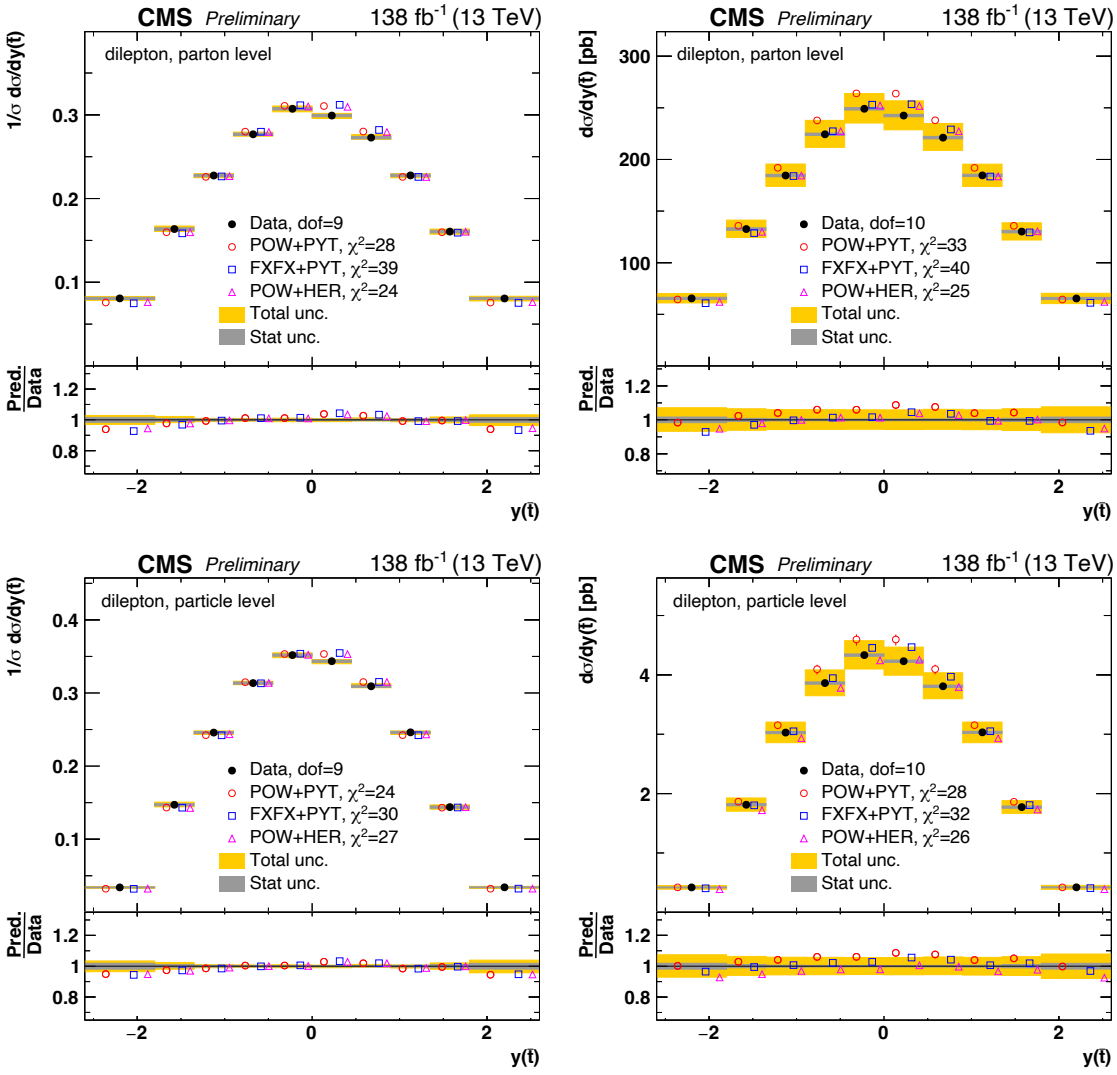

Figure 8.4: Differential $t\bar{t}$ cross sections measured as functions of the rapidity of the anti-top, $y(\bar{t})$, in the full phase space at parton level (top row) and in the fiducial phase space at particle level (bottom row). The left and right columns show normalized and absolute cross sections, respectively. For further details see Figure 8.1.

8.2.2 Cross sections measured as functions of kinematic spectra of the $t\bar{t}$ system including correlations of the top and anti-top quark at parton and particle level

The following discussion centers on Figures 8.5 to 8.13 which show differential $t\bar{t}$ cross sections measured as functions of kinematic spectra of the $t\bar{t}$ system at parton level in the full phase space and particle level in the fiducial phase space. The spectra also include several variables representing kinematic correlations of the top and anti-top quark.

Figure 8.5 shows the cross sections measured as functions of $|y(t)| - |y(\bar{t})|$, which is sensitive to $t\bar{t}$ dynamics and additional gluon radiation. All models give rise to distributions that are more central than data, underestimating the data in the outer regions where $|y(t)| - |y(\bar{t})| < -2$ or $|y(t)| - |y(\bar{t})| > 2$.

The $|\Delta\phi(t,\bar{t})|$ and $p_{\mathrm{T}}(t\bar{t})$ cross sections are shown in Figure 8.6 and Figure 8.7, respectively. The distributions are useful for probing the effects of QCD radiation. At leading order, the top and anti-top will be created back-to-back, resulting in an azimuthal angle of π between the top and anti-top and zero net p_T of the $t\bar{t}$ system. However, at higher order, real emissions will cause the parent top quark to recoil leading to distributions with tails away from 0 and π. The $|\Delta\phi(t,\bar{t})|$ distribution is described well by POW+PYT with a small χ^2 of 1 (normalized). The other models FXFX+PYT and POW+HER also show good agreement between the prediction and data within data uncertainties. The description of the prediction versus data for $p_{\mathrm{T}}(t\bar{t})$ appears to have a slight modulation for all models. The reference generator POW+PYT has the best modelling at low p_{T}, leading to the best χ^2 overall despite the overestimation of data at high p_{T}. In the intermediate p_{T} bins, the alternative models FXFX+PYT and POW+HER generally over- and undershoot the data, respectively, which results in higher values of χ^2. However, the latter has a noticeably better description in the high p_{T} bins than both POW+PYT and FXFX+PYT, suggesting a better modelling of higher order and high p_{T} QCD radiation. It should be noted that the $p_{\mathrm{T}}(t\bar{t})$ binning has been extended from 570 GeV to 1 TeV in comparison with [14]. A good precision within 20% is still obtained for the extended phase space.

Figure 8.8 shows the $y(t\bar{t})$ distribution, where the central binning has been made slightly finer in comparison with the previous measurement [14]. Among other things this observable is expected to be sensitive to the proton PDFs, since $y(t\bar{t})$ depends on the ratio of the momenta of the two partons initiating the hard interaction in e.g. gluon-gluon fusion. Both POW+PYT and FXFX+PYT predict the spectra to be a little more central than is observed in data. This is a common feature for the rapidity distributions, and appears to be more pronounced for the latter, which has a higher χ^2 as a result. The best χ^2 is reported for POW+HER, which has a good description of the data overall.

The measurement of $m(t\bar{t})$ shown in Figure 8.9 is performed with the loose kinematic

reconstruction. Two POW+PYT models using different top masses of $m_t = 175.5$ GeV (green) and $m_t = 169.5$ GeV (cyan) are shown in addition to the reference simulation and the two alternative models, which are all based on the assumption that $m_t = 172.5$ GeV. However, the loose kinematic reconstruction doesn't constrain m_t, thereby allowing an unbiased view of the threshold region. All models with $m_t = 172.5$ GeV describe the data well within the uncertainties with an exception of the first bin, i.e. the threshold region, where the models underestimate the data. The model with $m_t = 169.5$ GeV also provides a good description of the data. A good distinction is seen with respect to the model with $m_t = 175.5$, which significantly underestimates the data in the first bin and is slightly harder than the data in the intermediate bins. Among other things $m(t\bar{t})$ is also sensitive to the proton PDFs, since $m(t\bar{t})^2$ is proportional to the product of the momenta of the two partons initiating the hard interaction in e.g. gluon-gluon fusion.

Figures 8.10 and 8.11 show cross sections measured for the first time as functions of $p_{\mathrm{T}}(t)/m(t\bar{t})$ and $p_{\mathrm{T}}(t\bar{t})/m(t\bar{t})$, respectively. The measurement of $p_{\mathrm{T}}(t)/m(t\bar{t})$ was performed in order to shed light on the top p_{T} problem inspired by [15], which suggests that this problem is more pronounced when $m(t\bar{t})$ is large. The measurement of $p_{\mathrm{T}}(t\bar{t})/m(t\bar{t})$ is expected to be sensitive to p_{T} re-summation effects instead. As can be seen from the measured distributions in Figure 8.10, the statement made above for $p_{\mathrm{T}}(t)/m(t\bar{t})$ clearly holds true for both POW+PYT and FXFX+PYT, which predict much harder distributions than is observed in data, but it's worth noting that this is not the case for POW+HER for which a reasonable agreement between the prediction and data is observed. This is in line with the previous observations made for the POW+HER modelling of the $p_{\mathrm{T}}(t)$ spectra. A modulation in pred./data was observed for all three models when looking at the $p_{\mathrm{T}}(t\bar{t})$ spectra and, as can be seen from Figure 8.11, this is also present for $p_{\mathrm{T}}(t\bar{t})/m(t\bar{t})$ and appears to be enhanced.

The measurements of $\log(\xi_1)$ and $\log(\xi_2)$ are shown in Figures 8.12 and 8.13, respectively. Here the definition $\xi_1 = (E(t\bar{t}) - p_z(t\bar{t}))/2E_p$ ($\xi_2 = (E(t\bar{t}) + p_z(t\bar{t}))/2E_p$) is used, as previously described in Section 2.3.1, where it was stated that ξ_1 (ξ_2) is equivalent to the momentum fraction of the incoming parton from the proton (other proton) at leading order in QCD. All models provide a reasonably good description of the data within the associated uncertainties but exhibit a slight overestimation in the central region. The measurements in the highest ξ_1 and ξ_2 bins are, in the leading order QCD picture, expected to be sensitive to the gluon density at proton momentum fractions of ~ 0.2.

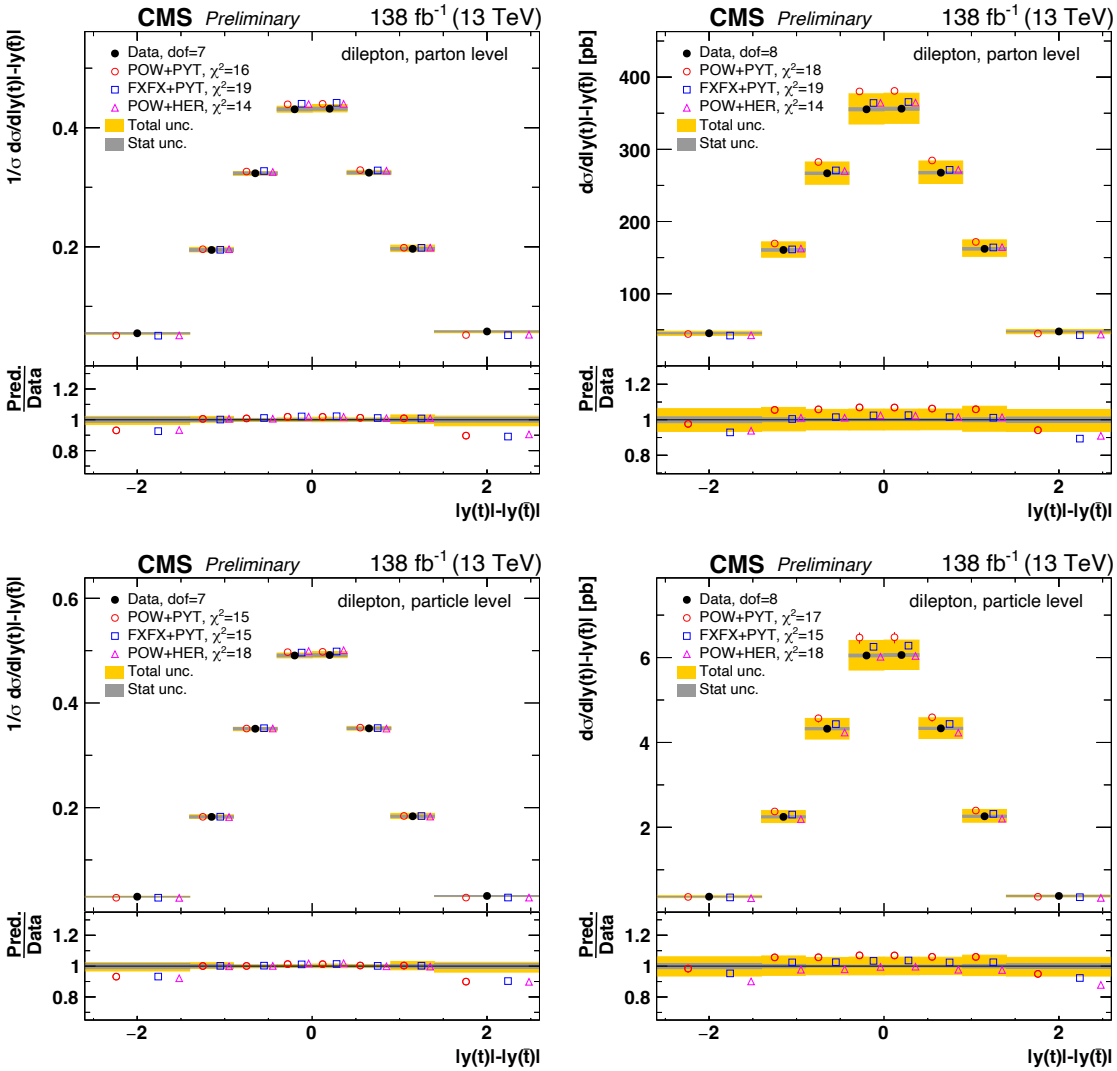

Figure 8.5: Differential $t\bar{t}$ cross sections measured as functions of the difference in absolute value of rapidity of the top and absolute value of rapidity of the anti-top, $|y(t)| - |y(\bar{t})|$, in the full phase space at parton level (top row) and in the fiducial phase space at particle level (bottom row). The left and right columns show normalized and absolute cross sections, respectively. For further details see Figure 8.1.

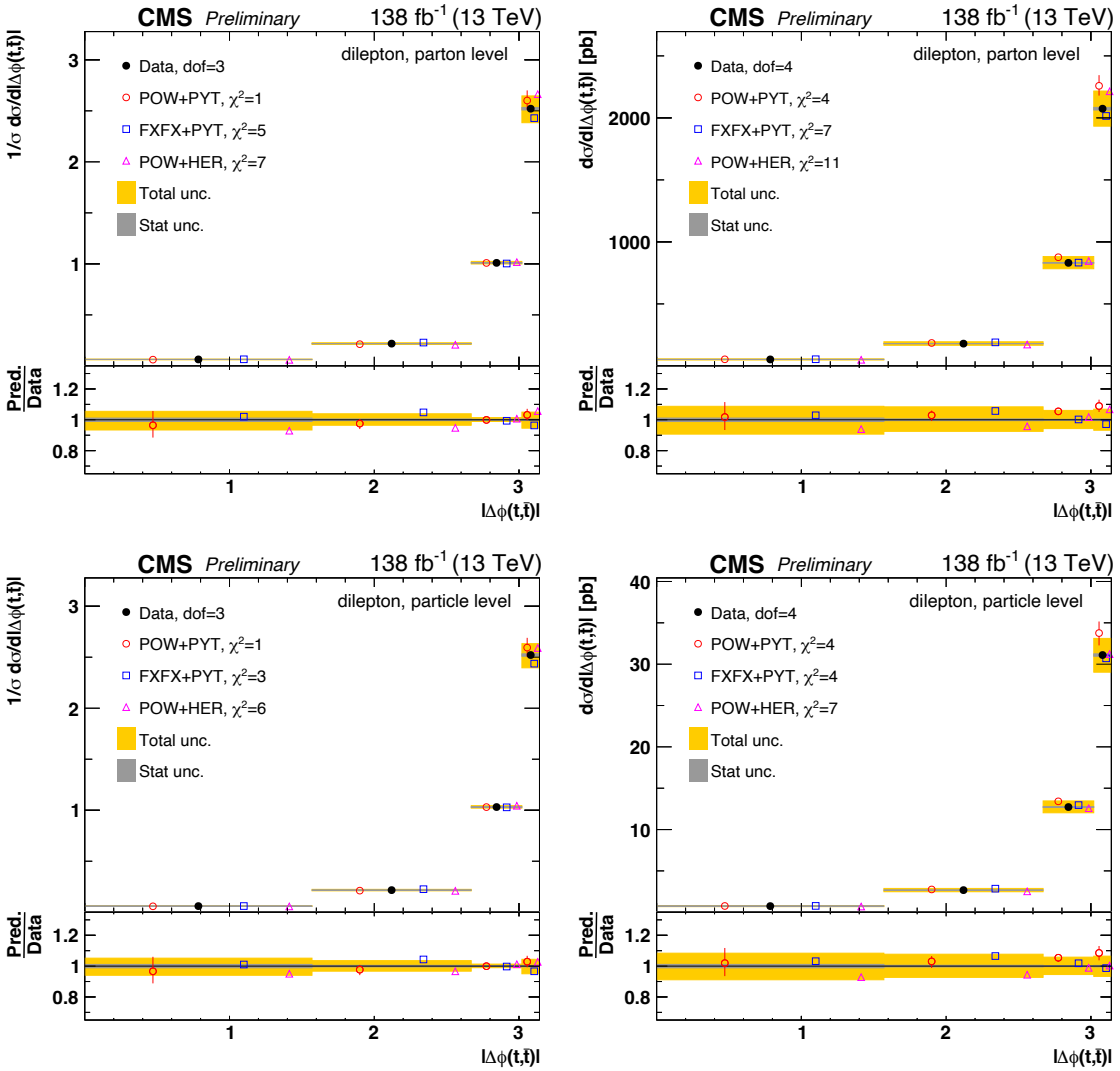

Figure 8.6: Differential $t\bar{t}$ cross sections measured as functions of the absolute value of the azimuthal angle (ϕ) between the top and the anti-top, $|\Delta\phi(t,\bar{t})|$, in the full phase space at parton level (top row) and in the fiducial phase space at particle level (bottom row). The left and right columns show normalized and absolute cross sections, respectively. For further details see Figure 8.1.

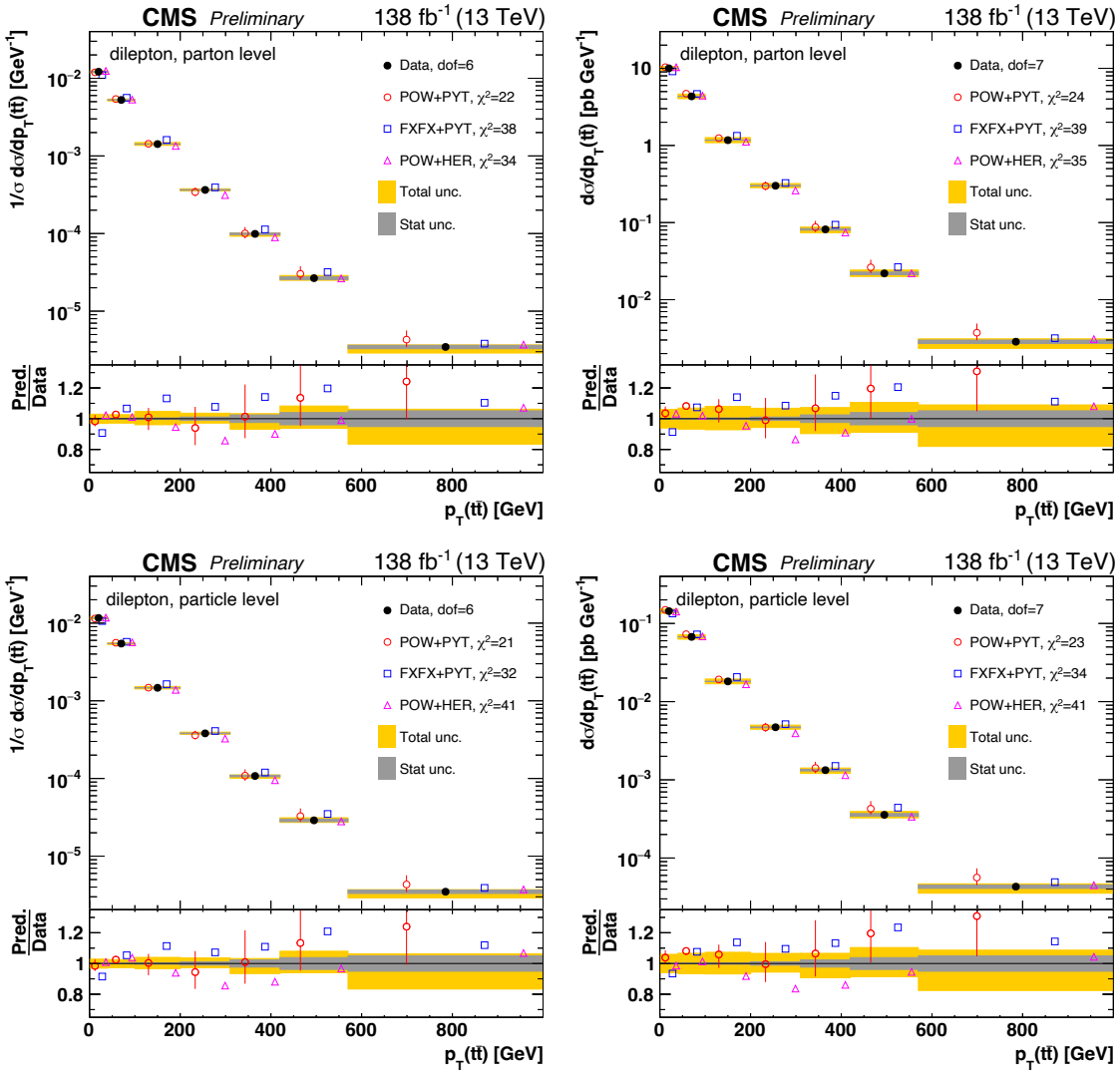

Figure 8.7: Differential $t\bar{t}$ cross sections measured as functions of the transverse momentum of the $t\bar{t}$ system, $p_{\mathrm{T}}(t\bar{t})$, in the full phase space at parton level (top row) and in the fiducial phase space at particle level (bottom row). The left and right columns show normalized and absolute cross sections, respectively. For further details see Figure 8.1.

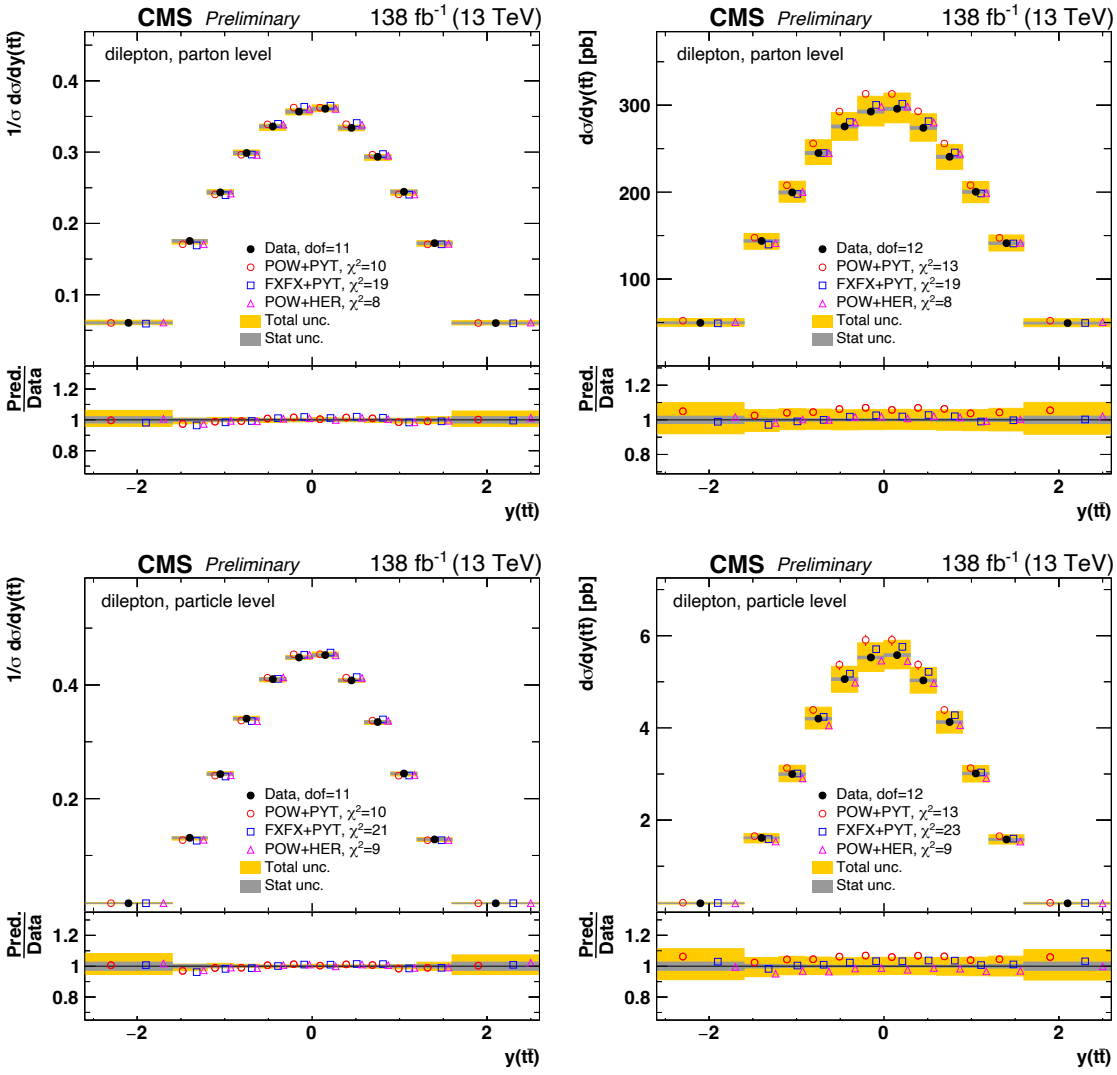

Figure 8.8: Differential $t\bar{t}$ cross sections measured as functions of the rapidity of the $t\bar{t}$ system, $y(t\bar{t})$, in the full phase space at parton level (top row) and in the fiducial phase space at particle level (bottom row). The left and right columns show normalized and absolute cross sections, respectively. For further details see Figure 8.1.

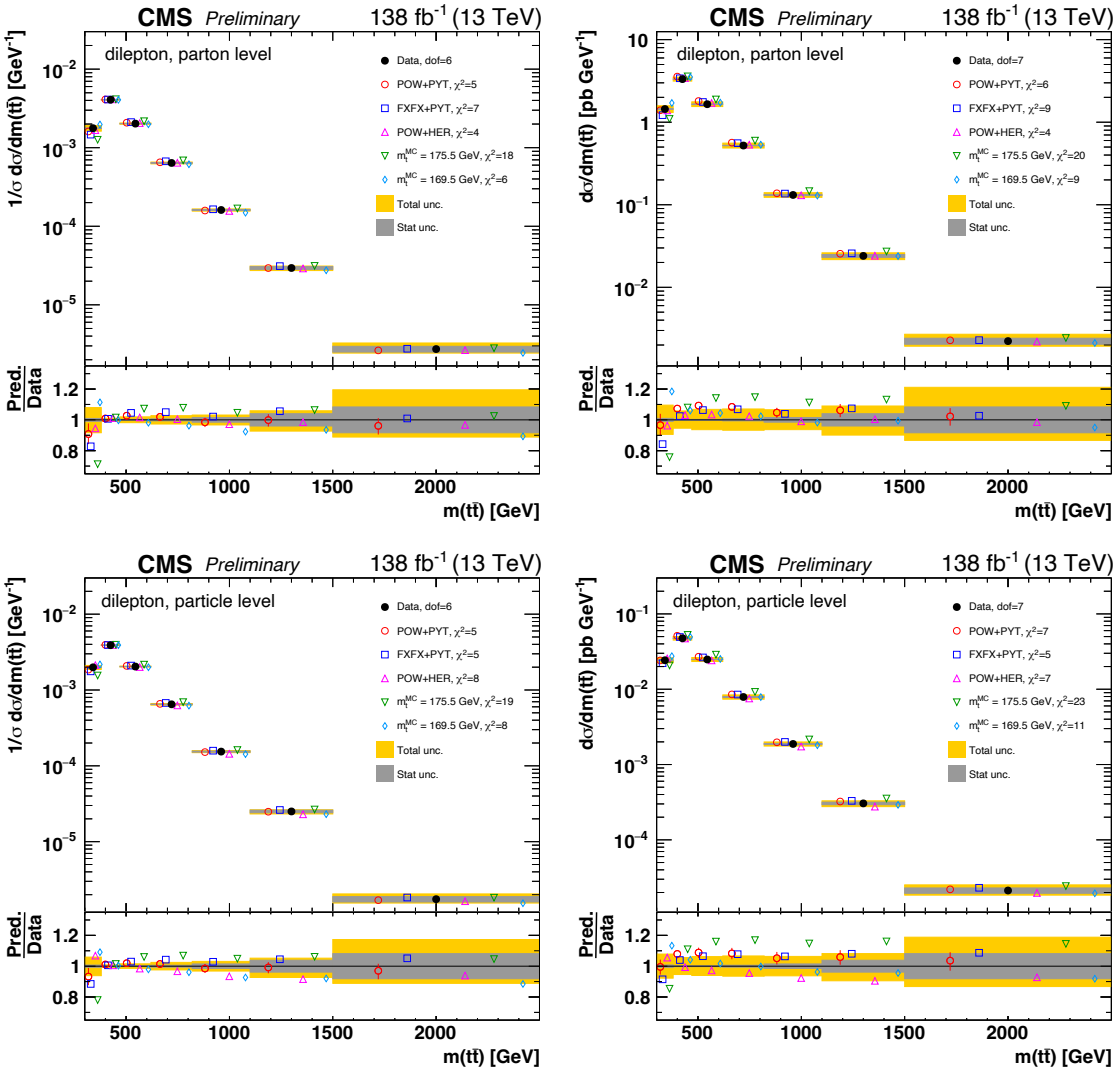

Figure 8.9: Differential $t\bar{t}$ cross sections measured as functions of the invariant mass of the $t\bar{t}$ system, $m(t\bar{t})$, in the full phase space at parton level (top row) and in the fiducial phase space at particle level (bottom row). The left and right columns show normalized and absolute cross sections, respectively. For further details see Figure 8.1.

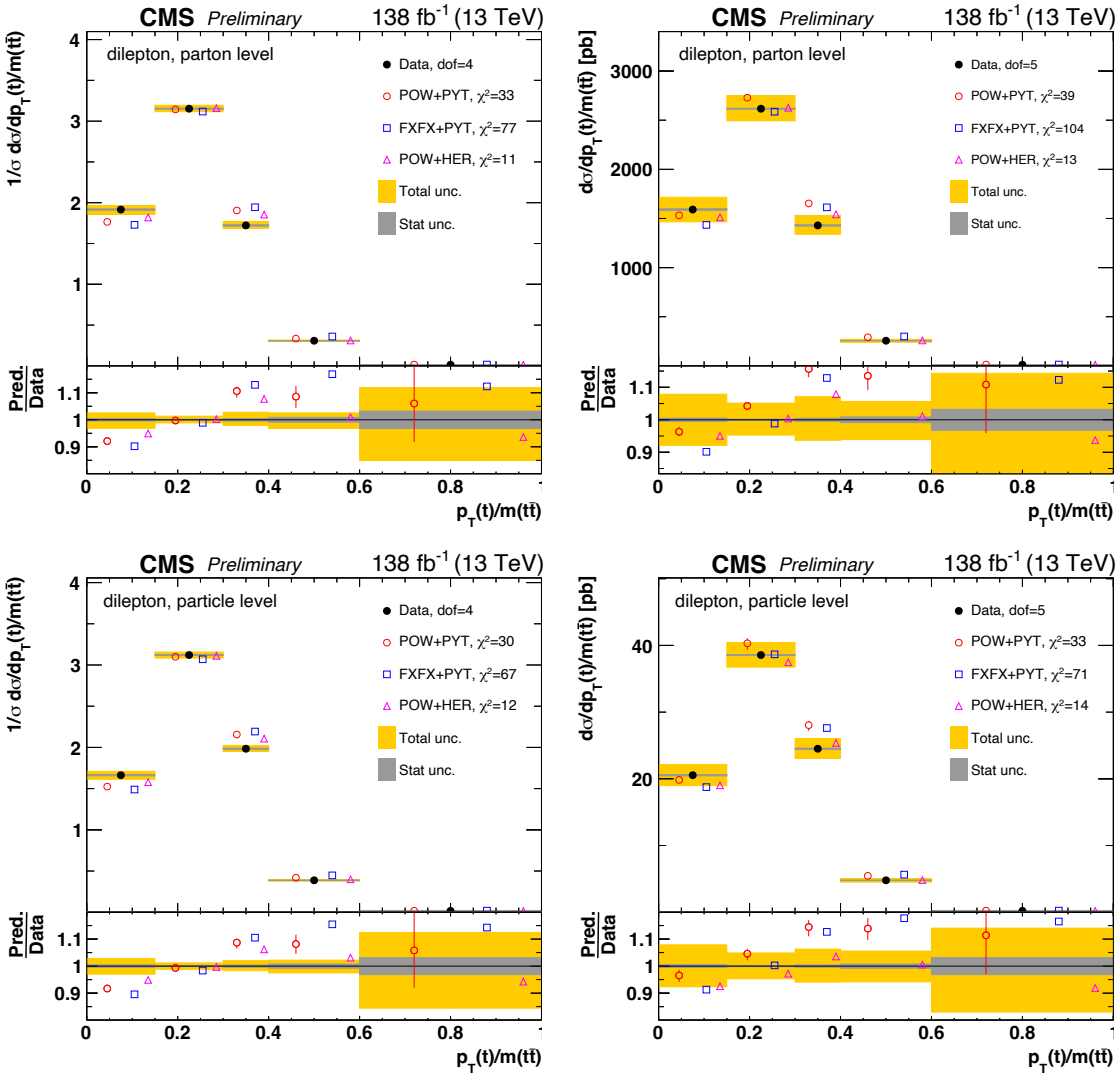

Figure 8.10: Differential $t\bar{t}$ cross sections measured as functions of the ratio of the transverse momentum of the top quark over the invariant mass of the $t\bar{t}$ system, $p_{\mathrm{T}}(t)/m(t\bar{t})$, in the full phase space at parton level (top row) and in the fiducial phase space at particle level (bottom row). The left and right columns show normalized and absolute cross sections, respectively. For further details see Figure 8.1.

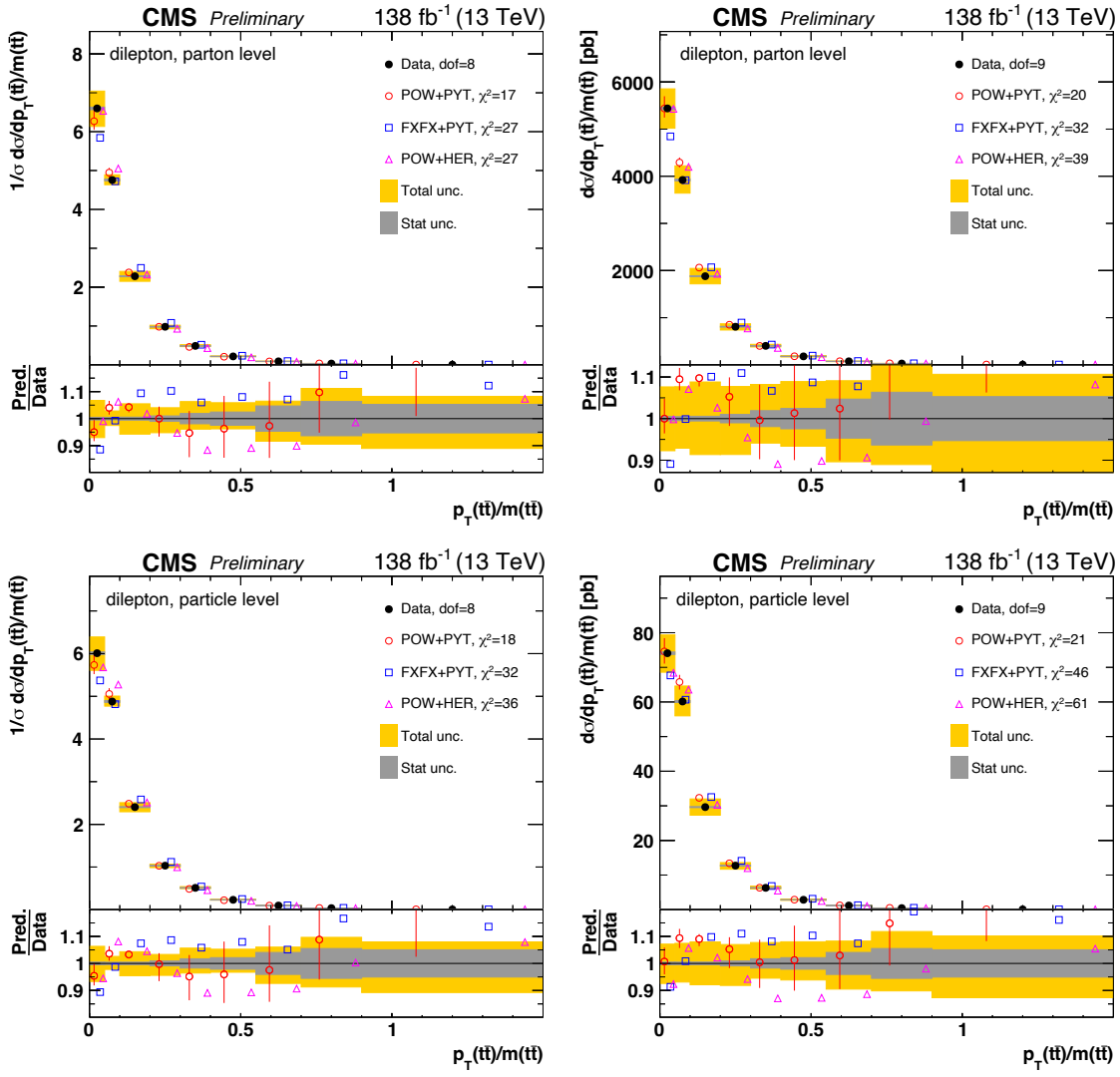

Figure 8.11: Differential $t\bar{t}$ cross sections measured as functions of the ratio of the transverse momentum of the $t\bar{t}$ system over the invariant mass of the $t\bar{t}$ system, $p_{\mathrm{T}}(t\bar{t})/m(t\bar{t})$, in the full phase space at parton level (top row) and in the fiducial phase space at particle level (bottom row). The left and right columns show normalized and absolute cross sections, respectively. For further details see Figure 8.1.

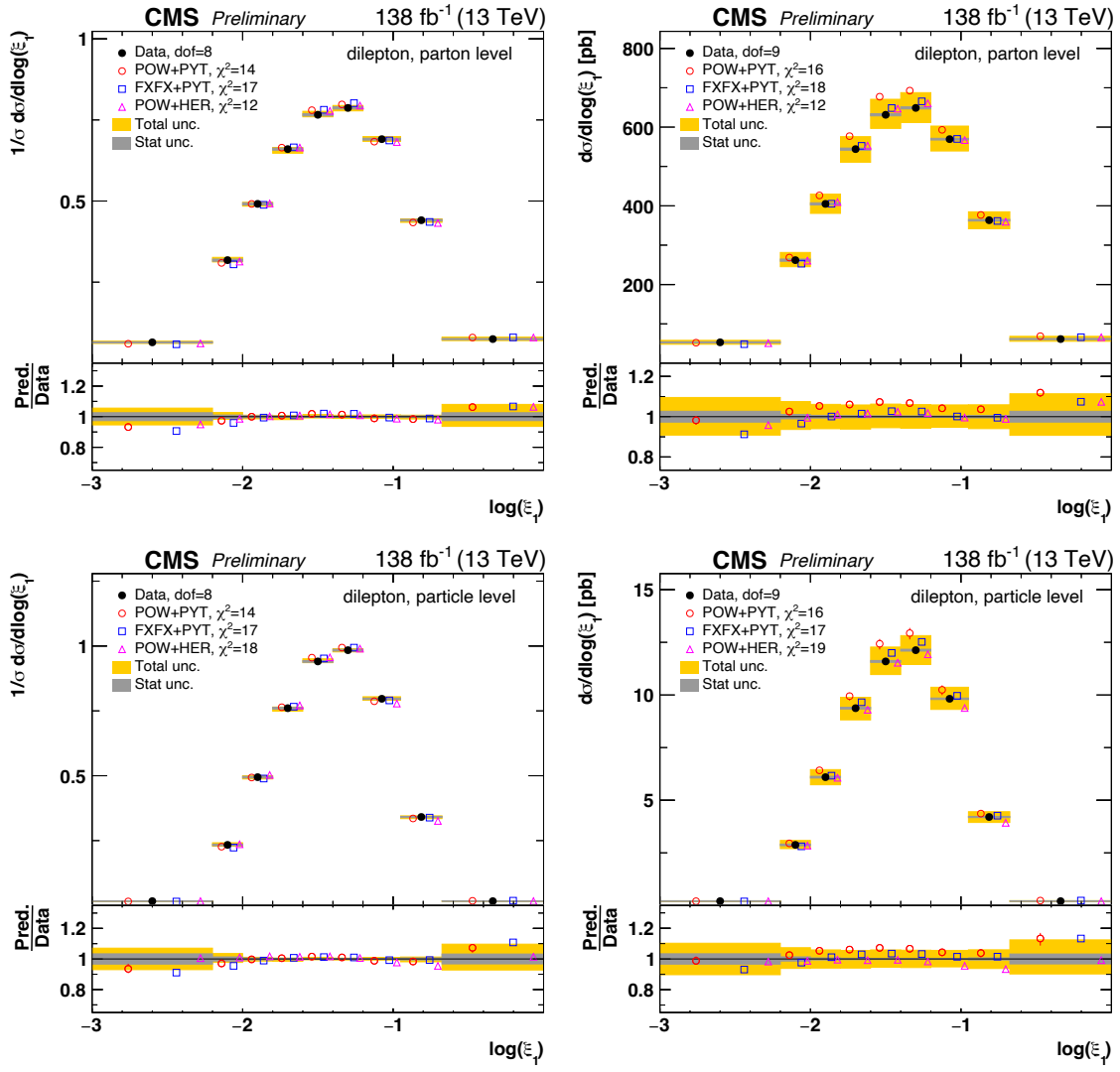

Figure 8.12: Differential $t\bar{t}$ cross sections measured as functions of $\log(\xi_1)$, which is equivalent to the momentum fraction of the incoming parton from one of the protons in the leading order QCD picture, in the full phase space at parton level (top row) and in the fiducial phase space at particle level (bottom row). The left and right columns show normalized and absolute cross sections, respectively. For further details see Figure 8.1.

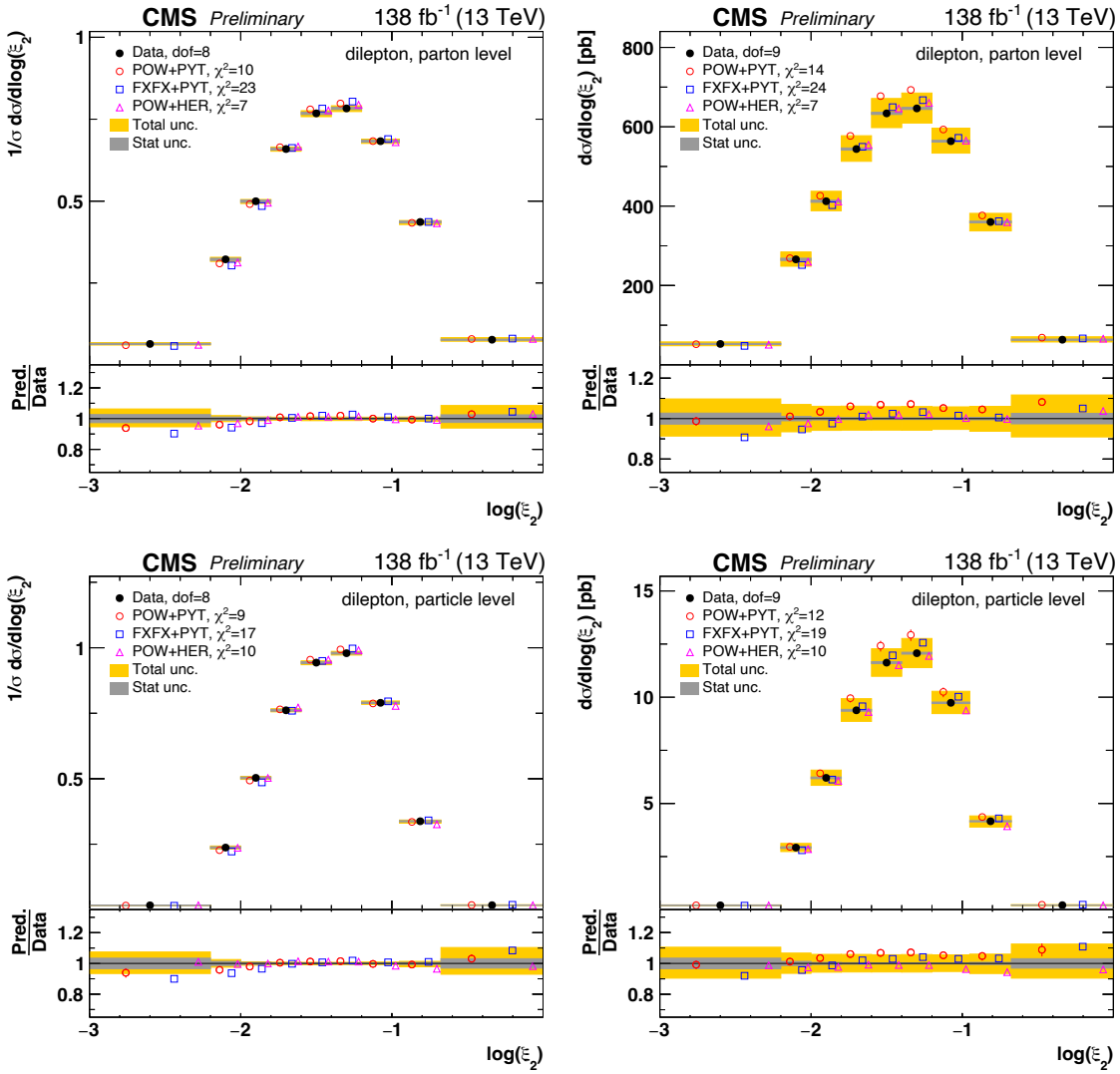

Figure 8.13: Differential $t\bar{t}$ cross sections measured as functions of $\log(\xi_2)$, which is equivalent to the momentum fraction of the incoming parton from one of the protons in the leading order QCD picture, in the full phase space at parton level (top row) and in the fiducial phase space at particle level (bottom row). The left and right columns show normalized and absolute cross sections, respectively. For further details see Figure 8.1.

8.2.3 Cross sections measured as functions of kinematic spectra of the charged leptons and beauty flavored jets at particle level

Figures 8.14 to 8.26 show differential $t\bar{t}$ cross sections measured as functions of kinematic spectra of the leptons and beauty flavored jets at particle level in the fiducial phase space. These distributions are especially interesting as a way to study the top quark decay but also correlations with the kinematics of the $t\bar{t}$ system. Furthermore, the precision of these types of measurements benefit greatly from the excellent identification and resolutions of the objects in the CMS experiment.

Figure 8.14 shows distributions of both $p_{\mathrm{T}}(\ell)$ and $p_{\mathrm{T}}(\ell)$ trailing/$p_{\mathrm{T}}(\ell)$ leading. Since the lepton is a daughter particle of the top quark, the $p_{\mathrm{T}}(\ell)$ spectra is correlated with that of $p_{\mathrm{T}}(t)$ and therefore one may expect to see similar trends in the description of data. Both POW+PYT and FXFX+PYT exhibit the same type of slope in Pred./Data as seen for $p_{\mathrm{T}}(t)$ while POW+HER retains a good agreement with data for both distributions and performs the best in terms of χ^2. The latter model also provides the best prediction for $p_{\mathrm{T}}(\ell)$ trailing/$p_{\mathrm{T}}(\ell)$ leading, where POW+PYT and FXFX+PYT both overestimate the data for smaller values of this observable.

Figure 8.15 shows distributions of $p_{\mathrm{T}}(\ell)/\mathrm{p_T}(\bar{\mathrm{t}})$ and $(p_{\mathrm{T}}(\mathrm{b}) + \mathrm{p_T}(\bar{\mathrm{b}}))/(\mathrm{p_T}(\mathrm{t}) + \mathrm{p_T}(\bar{\mathrm{t}}))$. These observables directly probe the momentum transfer of the mother top quarks to the daughter particles. Both POW+PYT and POW+HER provide predictions that agree reasonably well with the data for smaller values of $p_{\mathrm{T}}(\ell)/\mathrm{p_T}(\bar{\mathrm{t}})$, but the same cannot be said for $(p_{\mathrm{T}}(\mathrm{b}) + \mathrm{p_T}(\bar{\mathrm{b}}))/(\mathrm{p_T}(\mathrm{t}) + \mathrm{p_T}(\bar{\mathrm{t}}))$. Here the description is particularly bad in the second bin, where the prediction lies above the data. The worst performance overall is seen for FXFX+PYT.

Measurements of the leading and trailing $p_{\mathrm{T}}(\mathrm{b})$ spectra are also performed and shown in Figure 8.16. The data is generally well described by both POW+PYT and POW+HER within uncertainties. However, POW+PYT has a general tendency to be slightly harder than the data while POW+HER is slightly softer. FXFX+PYT also gives rise to a harder spectra than observed in data but the discrepancy is more pronounced than for POW+PYT.

Now moving from single particles to spectra of particle systems, measurements of $p_{\mathrm{T}}(\ell\bar{\ell})$ and $|\eta(\ell\bar{\ell})|$ are shown in Figure 8.17. The $\ell\bar{\ell}$ system is expected to be kinematically correlated with the mother $t\bar{t}$ system, despite the fact that it's carrying only a fraction of its four-momentum. A very good agreement with data is obtained for all models although POW+PYT and FXFX+PYT give rise to slightly harder p_{T} spectra and more central $|\eta(\ell\bar{\ell})|$ distributions. Cross sections measured as functions of $|\eta(\ell)| - |\eta(\bar{\ell})|$ and $|\Delta\phi(\ell,\bar{\ell})|$ are shown in Figure 8.18. All three models predict $|\eta(\ell)| - |\eta(\bar{\ell})|$ to be more central than is observed in data, but otherwise describe the data reasonably well. The number of back-to-back leptons in ϕ are overestimated with respect to data and all models have considerably high χ^2 values for $|\Delta\phi(\ell,\bar{\ell})|$. This distribution is sensitive to effects from the spin correlation of the parent top

quarks and is therefore of particular interest [152].

Figure 8.19 shows measurements of $m(\ell\bar{\ell})$ and $m(b\bar{b})$, while $m(\ell\bar{\ell}\mathrm{b}\bar{\mathrm{b}})$ is shown in Figure 8.20. A prime motivation here is to assess the sensitivity of the masses of the partial $t\bar{t}$ decay systems to the top quark mass. Both POW+PYT and FXFX+PYT predict $m(\ell\bar{\ell})$ to be harder than is observed in data. However, these models undershoot the data in the outer ends of the spectra when looking at $m(b\bar{b})$ and $m(\ell\bar{\ell}\mathrm{b}\bar{\mathrm{b}})$. The POW+HER model exhibits a clear tendency towards softer spectra for these two distributions. Alternative POW+PYT models using masses of $m_t = 175.5$ GeV (green) and $m_t = 169.5$ GeV (cyan) are again shown alongside the other MC models which use the nominal value of $m_t = 172.5$ GeV. One can conclude from $m(\ell\bar{\ell})$, $m(b\bar{b})$ and $m(\ell\bar{\ell}\mathrm{b}\bar{\mathrm{b}})$ that the MC models exhibit a shift towards a harder description of the data for higher values of m_t. A reduced level of sensitivity to m_t is seen for $m(\ell\bar{\ell})$ and $m(b\bar{b})$ with respect to the corresponding $m(t\bar{t})$ distribution at low invariant mass. The $m(\ell\bar{\ell}\mathrm{b}\bar{\mathrm{b}})$ distribution demonstrates the highest sensitivity in this region.

Double-differential cross section measurements of $t\bar{t}$ production are performed as functions of kinematic spectra of the leptons in bins of other kinematic variables of the top quarks, $t\bar{t}$ or $\ell\bar{\ell}$ system. Figures 8.21, 8.22 and 8.23 show distributions of $[m(t\bar{t}), |\Delta\phi(\ell,\bar{\ell})|]$, $[p_{\mathrm{T}}(t), |\Delta\phi(\ell,\bar{\ell})|]$ and $[|\eta(\ell)| - |\eta(\bar{\ell})|, |\Delta\phi(\ell,\bar{\ell})|]$, respectively, which illustrate how the absolute value of the opening angle between the lepton and anti-lepton, $|\Delta\phi(\ell,\bar{\ell})|$, behaves in different ranges of $m(t\bar{t})$, $p_{\mathrm{T}}(t)$ or $|\eta(\ell)| - |\eta(\bar{\ell})|$, referred to as super-bins. A positive slope in the ratio of prediction and data as a function of $|\Delta\phi(\ell,\bar{\ell})|$ is generally present for all three of the aforementioned distributions. The effect is especially enhanced in the last super-bin of $[m(t\bar{t}), |\Delta\phi(\ell,\bar{\ell})|]$ and $[p_{\mathrm{T}}(t), |\Delta\phi(\ell,\bar{\ell})|]$ where all three models fail to describe the data for larger values of $m(t\bar{t})$ or $p_{\mathrm{T}}(t)$. This is particularly true when the corresponding opening angle is small, where the predictions clearly underestimate the data. For $[|\eta(\ell)| - |\eta(\bar{\ell})|, |\Delta\phi(\ell,\bar{\ell})|]$ there is a tendency to consistently underestimate the data for small values of $|\Delta\phi(\ell,\bar{\ell})|$ while overestimating the data for large values of $|\Delta\phi(\ell,\bar{\ell})|$ irrespective of the $|\eta(\ell)| - |\eta(\bar{\ell})|$ range. Generally, POW+PYT and POW+HER exhibit a similar level of performance while FXFX+PYT is worse in comparison.

Figures 8.24, 8.25 and 8.26 show measurements of $[|\eta(\ell\bar{\ell})|, \mathrm{m}(\ell\bar{\ell})]$, $[|\eta(\ell\bar{\ell})|, \mathrm{p_T}(\ell\bar{\ell})]$ and $[p_{\mathrm{T}}(\ell\bar{\ell}), \mathrm{m}(\ell\bar{\ell})]$ respectively, where the excellent kinematic resolution of leptons is further exploited to obtain very precise and finely-binned double-differential cross sections. This study provides a survey of the full set of independent kinematic variables of the $\ell\bar{\ell}$ system, $|\eta(\ell\bar{\ell})|$, $m(\ell\bar{\ell})$ and $p_{\mathrm{T}}(\ell\bar{\ell})$, and their correlations. All models generally provide a reasonably good description of the data although the trend noted above, where POW+PYT and POW+HER outperform FXFX+PYT, still holds. The observations made for the 1D measurements of $m(\ell\bar{\ell})$ and $p_{\mathrm{T}}(\ell\bar{\ell})$ are also visible for $[|\eta(\ell\bar{\ell})|, \mathrm{m}(\ell\bar{\ell})]$ and $[|\eta(\ell\bar{\ell})|, \mathrm{p_T}(\ell\bar{\ell})]$. All models underestimate the data for low values of $m(\ell\bar{\ell})$ and this effect is more pronounced for larger values of $|\eta(\ell\bar{\ell})|$. POW+PYT and FXFX+PYT predict slightly harder $p_{\mathrm{T}}(\ell\bar{\ell})$ spectra and

this is seemingly enhanced at small values of $|\eta(\ell\bar{\ell})|$ in particular for the latter. When looking at $[p_{\mathrm{T}}(\ell\bar{\ell}), \mathrm{m}(\ell\bar{\ell})]$ one can see that POW+PYT and FXFX+PYT begin to overestimate the data when $p_{\mathrm{T}}(\ell\bar{\ell})$ increases. This observation is again most pronounced for the latter.

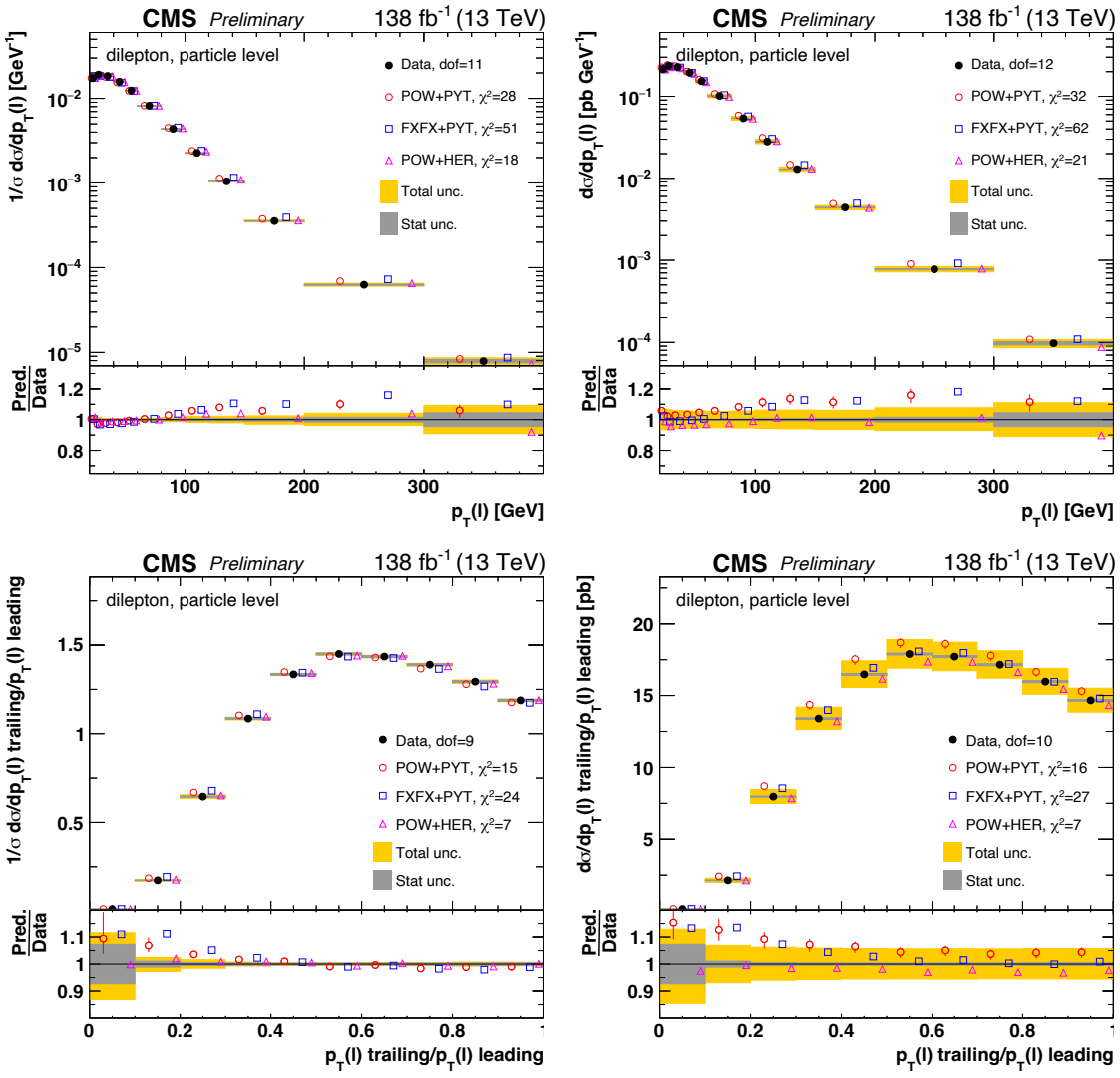

Figure 8.14: Differential $t\bar{t}$ cross sections measured as functions of the transverse momentum of the lepton, $p_{\mathrm{T}}(\ell)$, in the top row and the ratio of the transverse momentum of the trailing lepton over the transverse momentum of the leading lepton, $p_{\mathrm{T}}(\ell)$ trailing/$p_{\mathrm{T}}(\ell)$ leading, in the bottom row. The measurements are performed in the fiducial phase space at particle level. The left and right columns show normalized and absolute cross sections, respectively. For further details see Figure 8.1.

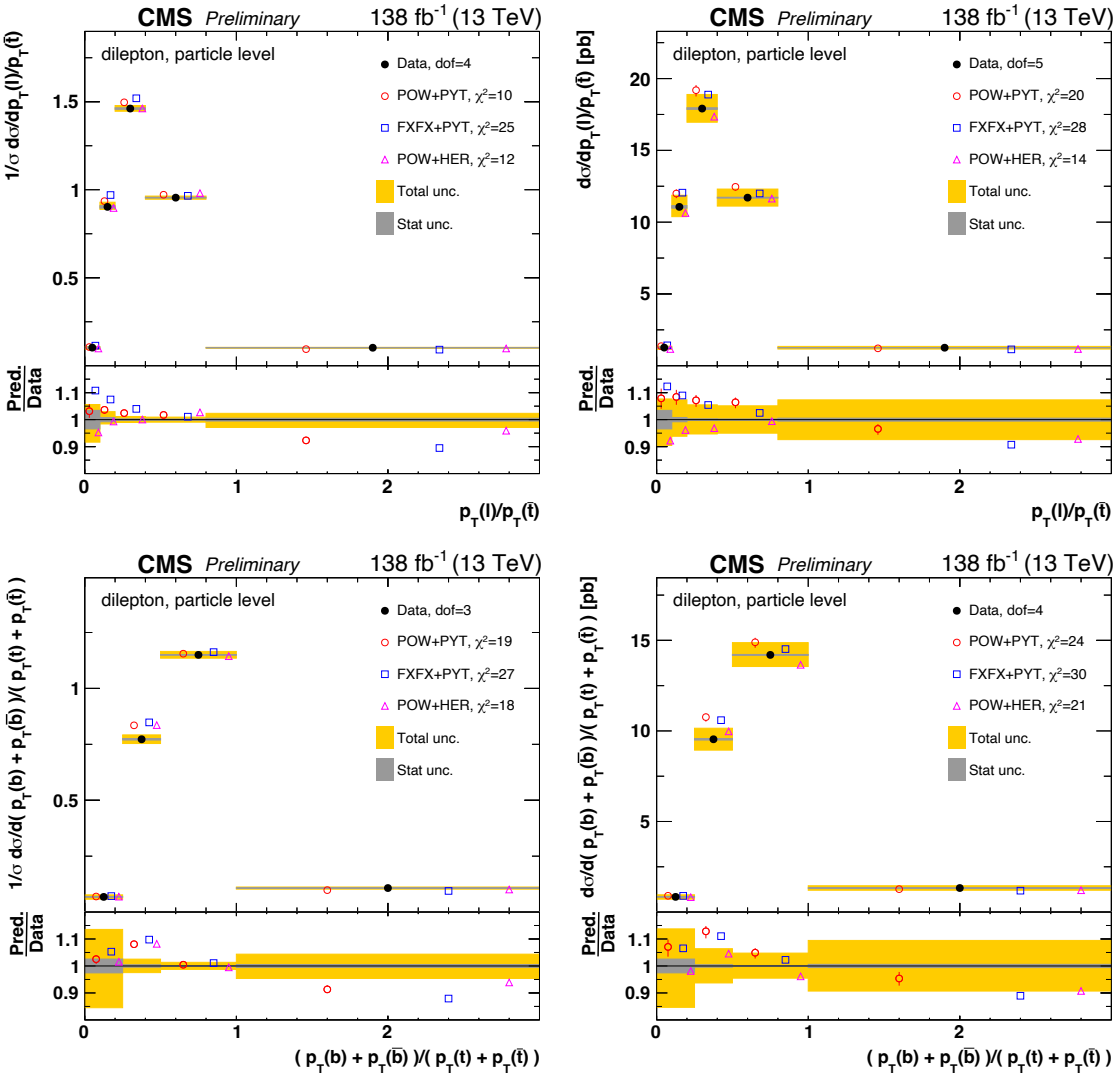

Figure 8.15: Differential $t\bar{t}$ cross sections measured as functions of the ratio of the transverse momentum of the lepton over the transverse momentum of the anti-top quark, $p_{\mathrm{T}}(\ell)/\mathrm{p_T}(\bar{\mathrm{t}})$, in the top row and the ratio of the scalar sum of p_{T} of b and p_{T} of anti-b over the scalar sum of p_{T} of top and p_{T} of anti-top, $(p_{\mathrm{T}}(\mathrm{b}) + \mathrm{p_T}(\bar{\mathrm{b}}))/(\mathrm{p_T}(\mathrm{t}) + \mathrm{p_T}(\bar{\mathrm{t}}))$, in the bottom row. The measurements are performed in the fiducial phase space at particle level. The left and right columns show normalized and absolute cross sections, respectively. For further details see Figure 8.1.

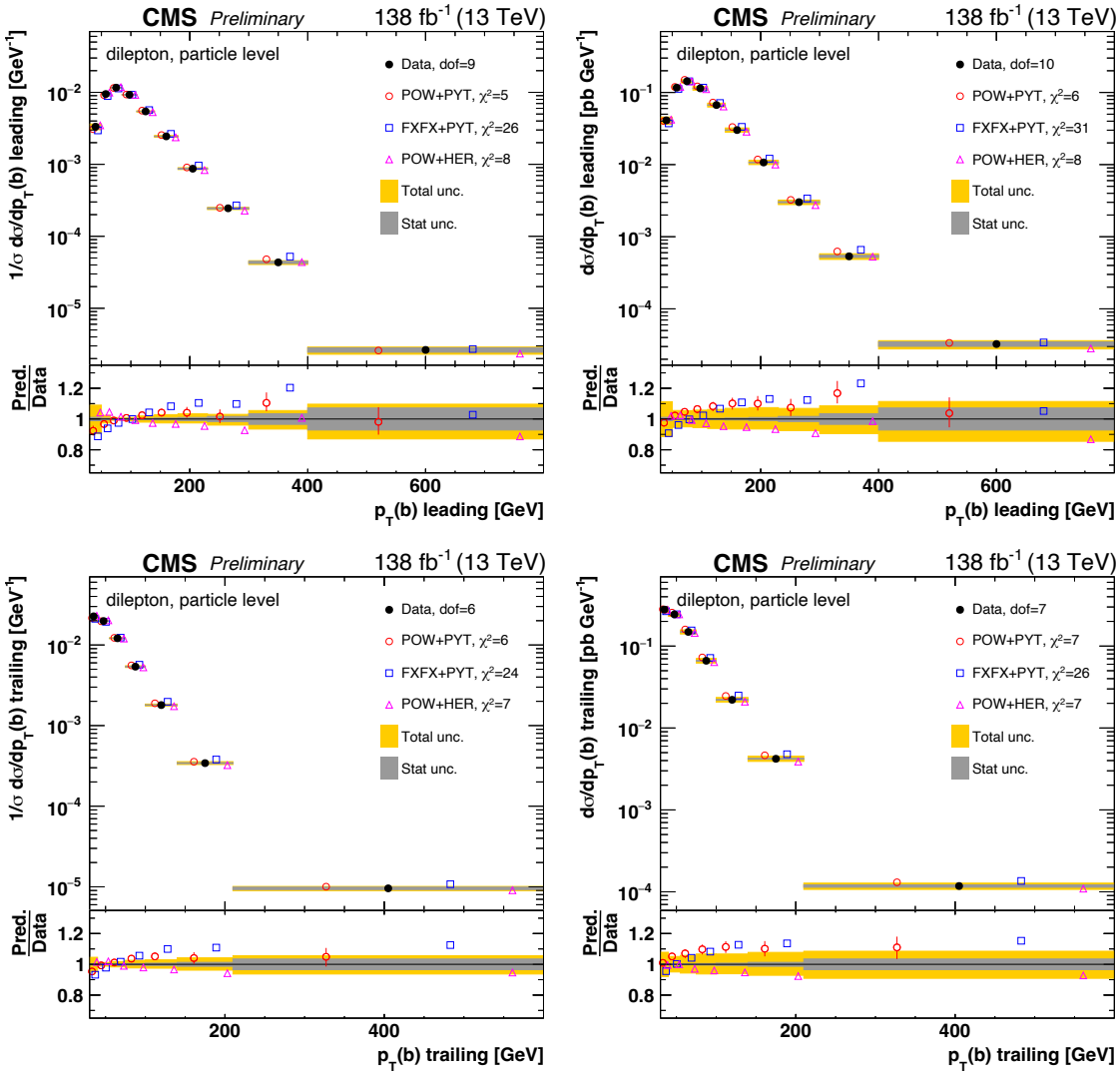

Figure 8.16: Differential $t\bar{t}$ cross sections measured as functions of the transverse momentum of the leading b quark, p_{T}(b) leading, in the top row and the transverse momentum of the trailing b quark, p_{T}(b) trailing, in the bottom row. The measurements are performed in the fiducial phase space at particle level. The left and right columns show normalized and absolute cross sections, respectively. For further details see Figure 8.1.

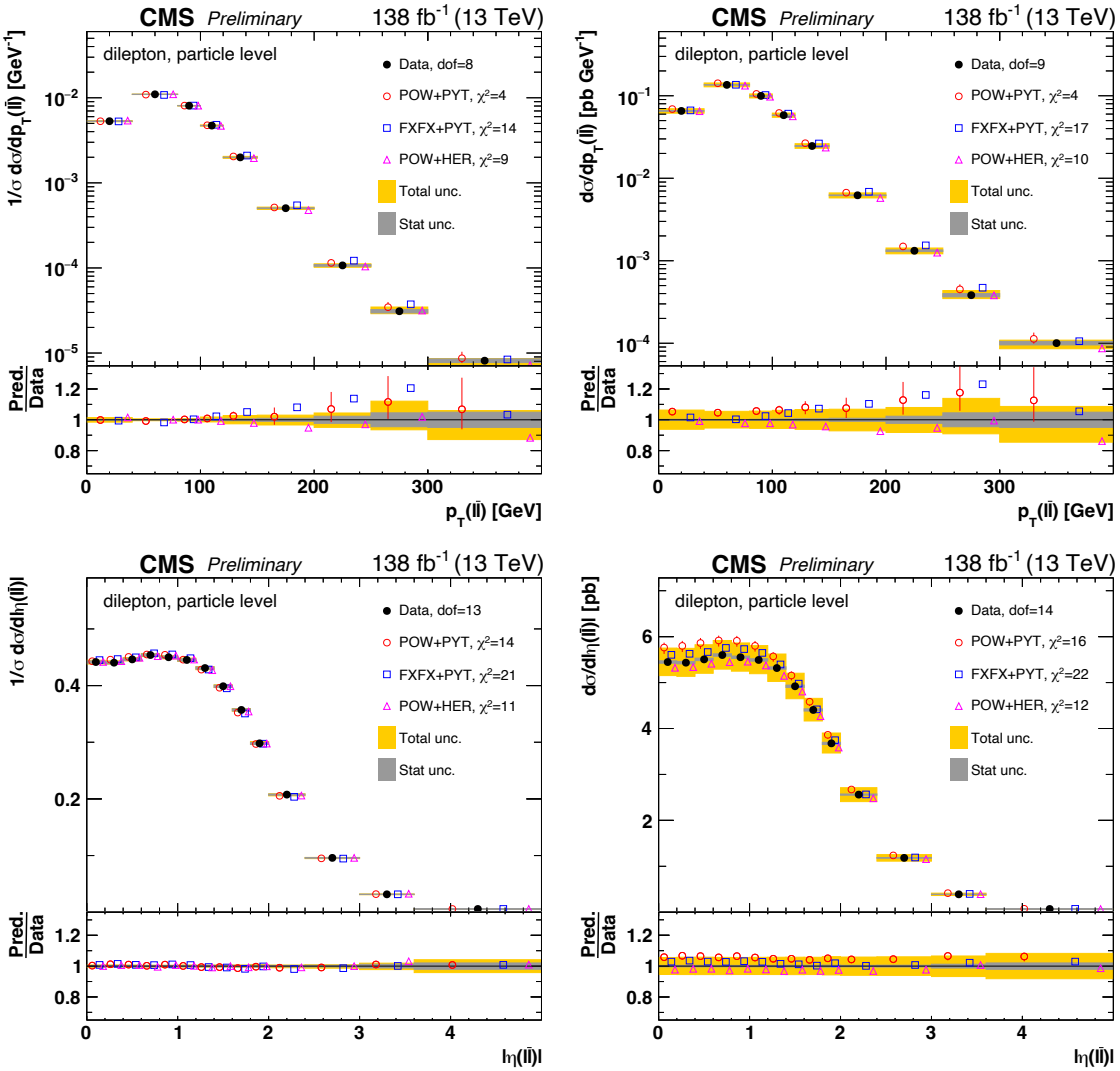

Figure 8.17: Differential $t\bar{t}$ cross sections measured as functions of the transverse momentum of the $\ell\bar{\ell}$ system, $p_{\mathrm{T}}(\ell\bar{\ell})$, in the top row and the absolute pseudorapidity of the $\ell\bar{\ell}$ system, $|\eta(\ell\bar{\ell})|$, in the bottom row. The measurements are performed in the fiducial phase space at particle level. The left and right columns show normalized and absolute cross sections, respectively. For further details see Figure 8.1.

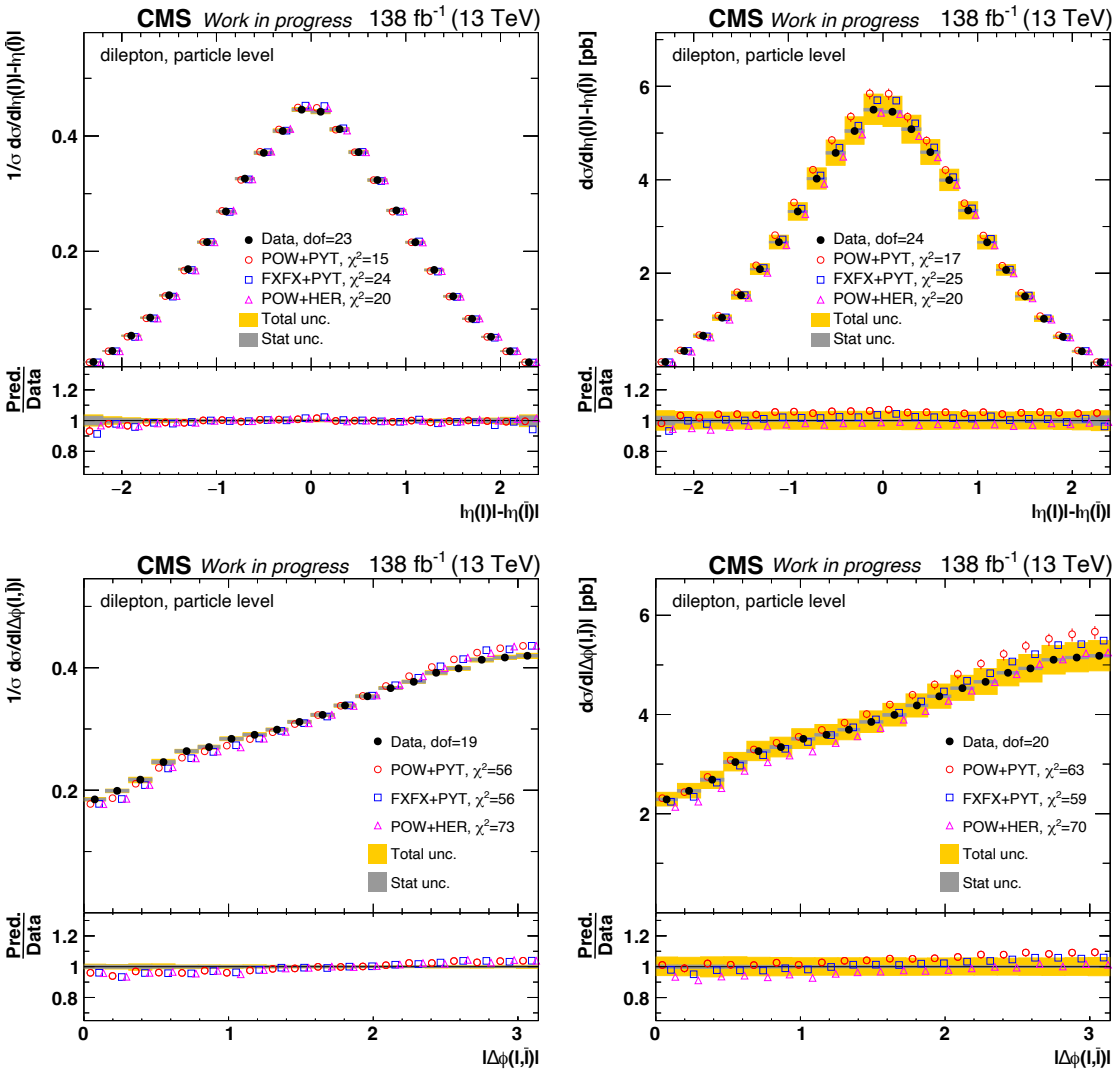

Figure 8.18: Differential $t\bar{t}$ cross sections measured as functions of the difference in absolute pseudorapidity of the lepton and absolute pseudorapidity of the anti-lepton, $|\eta(\ell)| - |\eta(\bar{\ell})|$, in the top row and the absolute value of the azimuthal angle between the lepton and the anti-lepton, $|\Delta\phi(\ell, \bar{\ell})|$, in the bottom row. The measurements are performed in the fiducial phase space at particle level. The left and right columns show normalized and absolute cross sections, respectively. For further details see Figure 8.1.

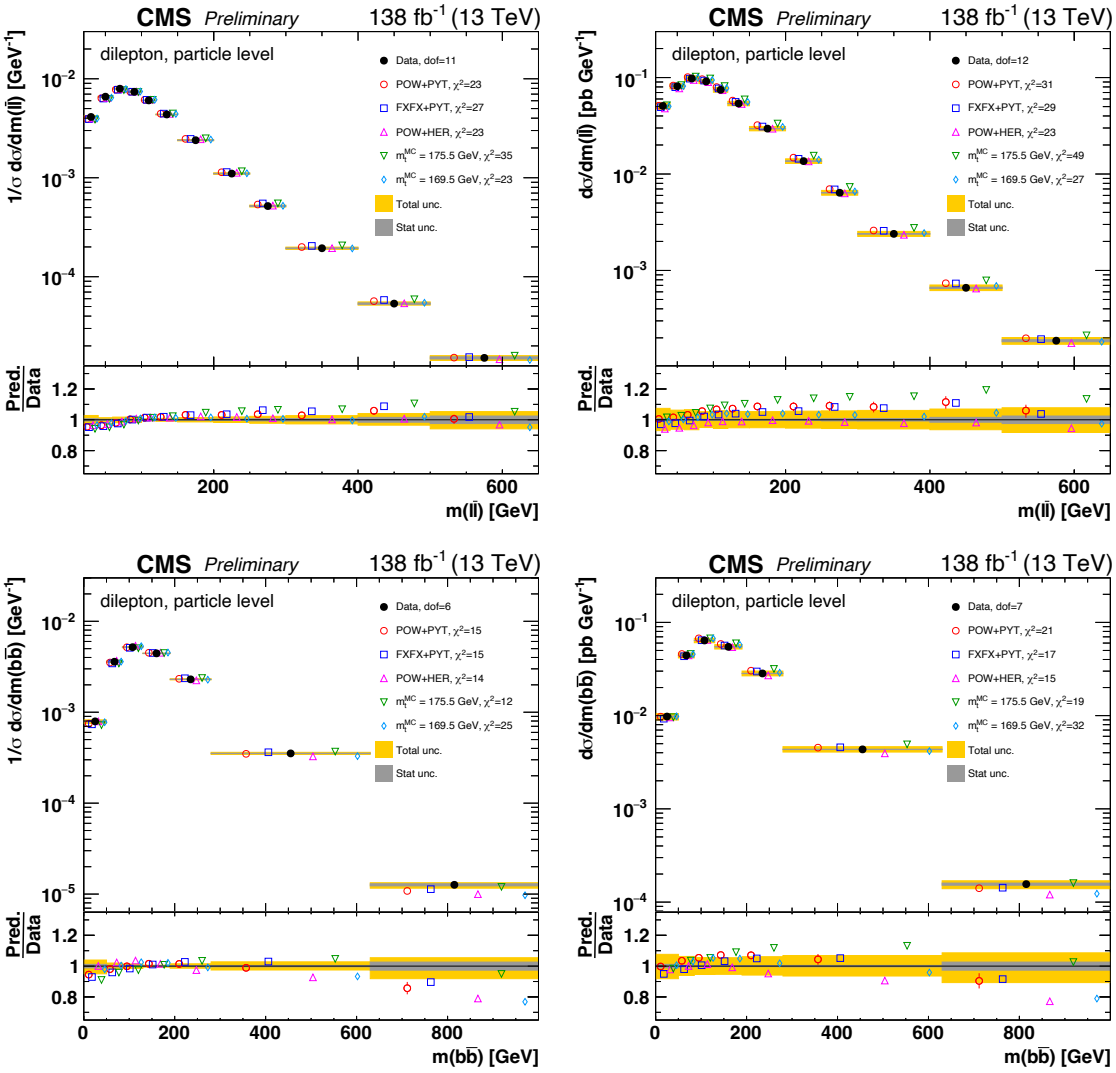

Figure 8.19: Differential $t\bar{t}$ cross sections measured as functions of the invariant mass of the $\ell\bar{\ell}$ system, $m(\ell\bar{\ell})$, in the top row and the invariant mass of the $b\bar{b}$ system, $m(b\bar{b})$, in the bottom row. The measurements are performed in the fiducial phase space at particle level. The left and right columns show normalized and absolute cross sections, respectively. For further details see Figure 8.1.

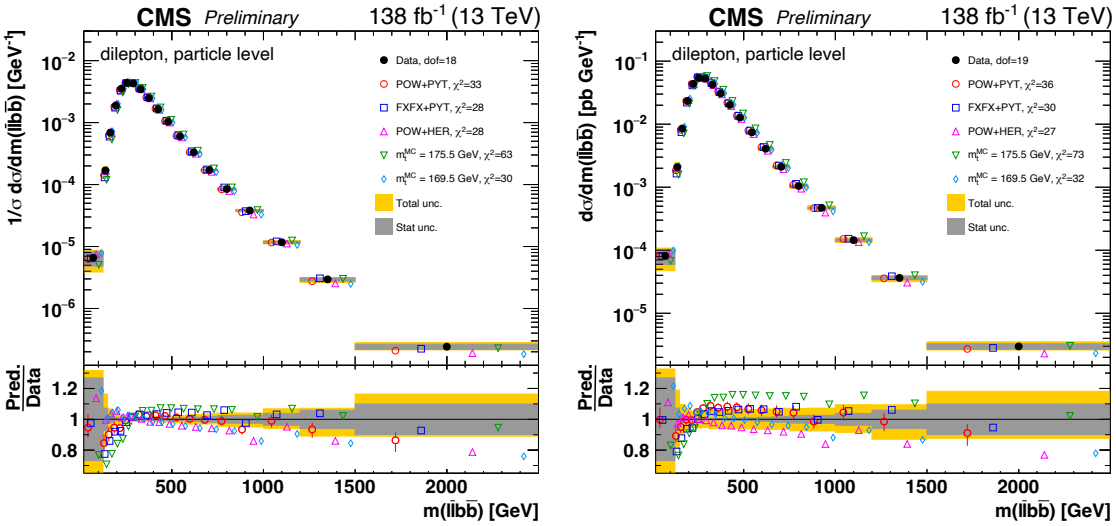

Figure 8.20: Differential $t\bar{t}$ cross sections measured as functions of the invariant mass of the $l\bar{l}b\bar{b}$ system, $m(\ell\bar{\ell}\mathrm{b}\bar{\mathrm{b}})$, in the fiducial phase space at particle level for normalized (left) and absolute (right) distributions. For further details see Figure 8.1.

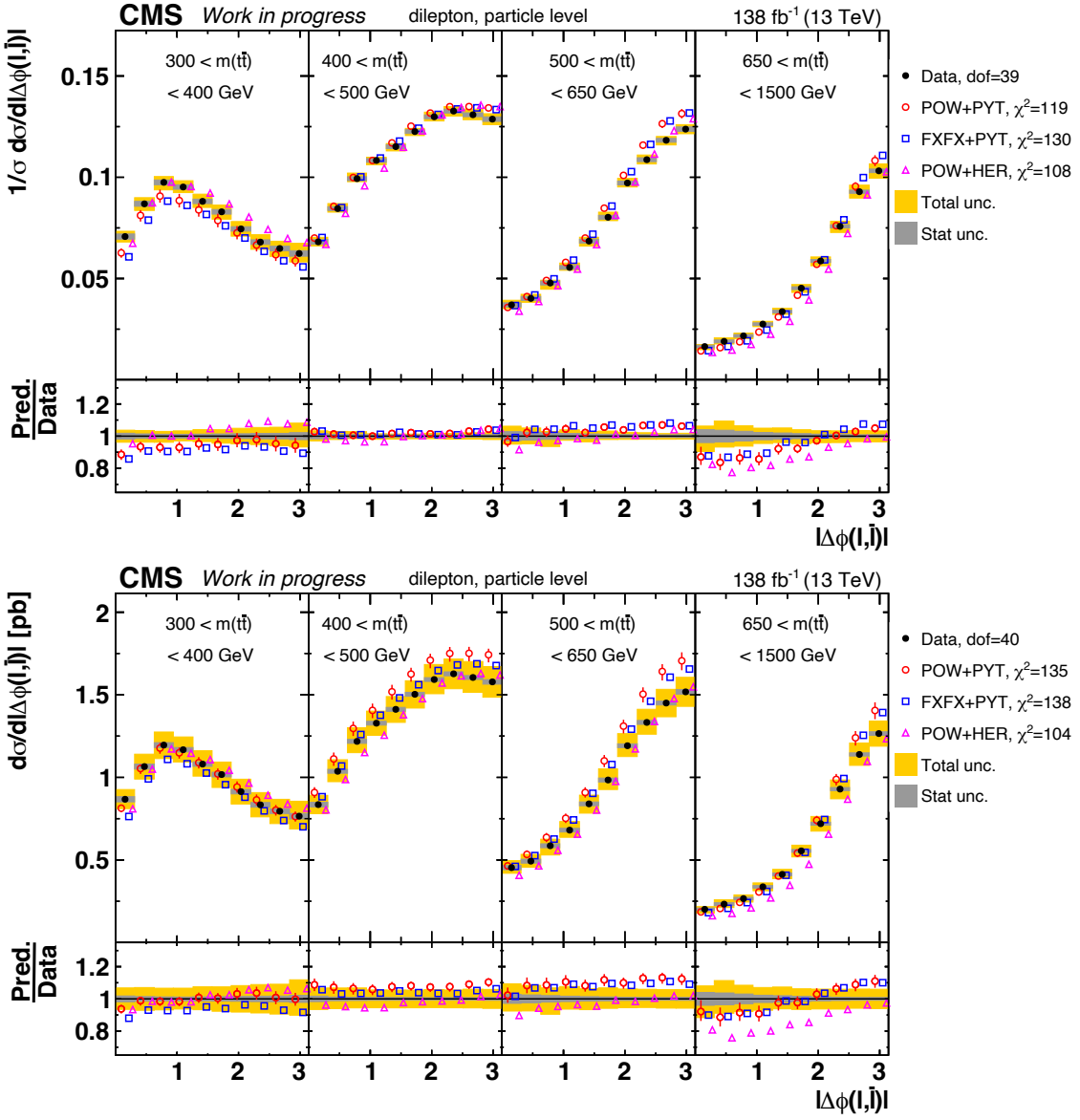

Figure 8.21: Differential $t\bar{t}$ cross sections measured as functions of the absolute value of the azimuthal angle between the lepton and the anti-lepton, $|\Delta\phi(\ell,\bar{\ell})|$, in ranges of the invariant mass of the $t\bar{t}$ system, $m(t\bar{t})$, for both normalized (top) and absolute (bottom) measurements performed in the fiducial phase space at particle level. For further details see Figure 8.1.

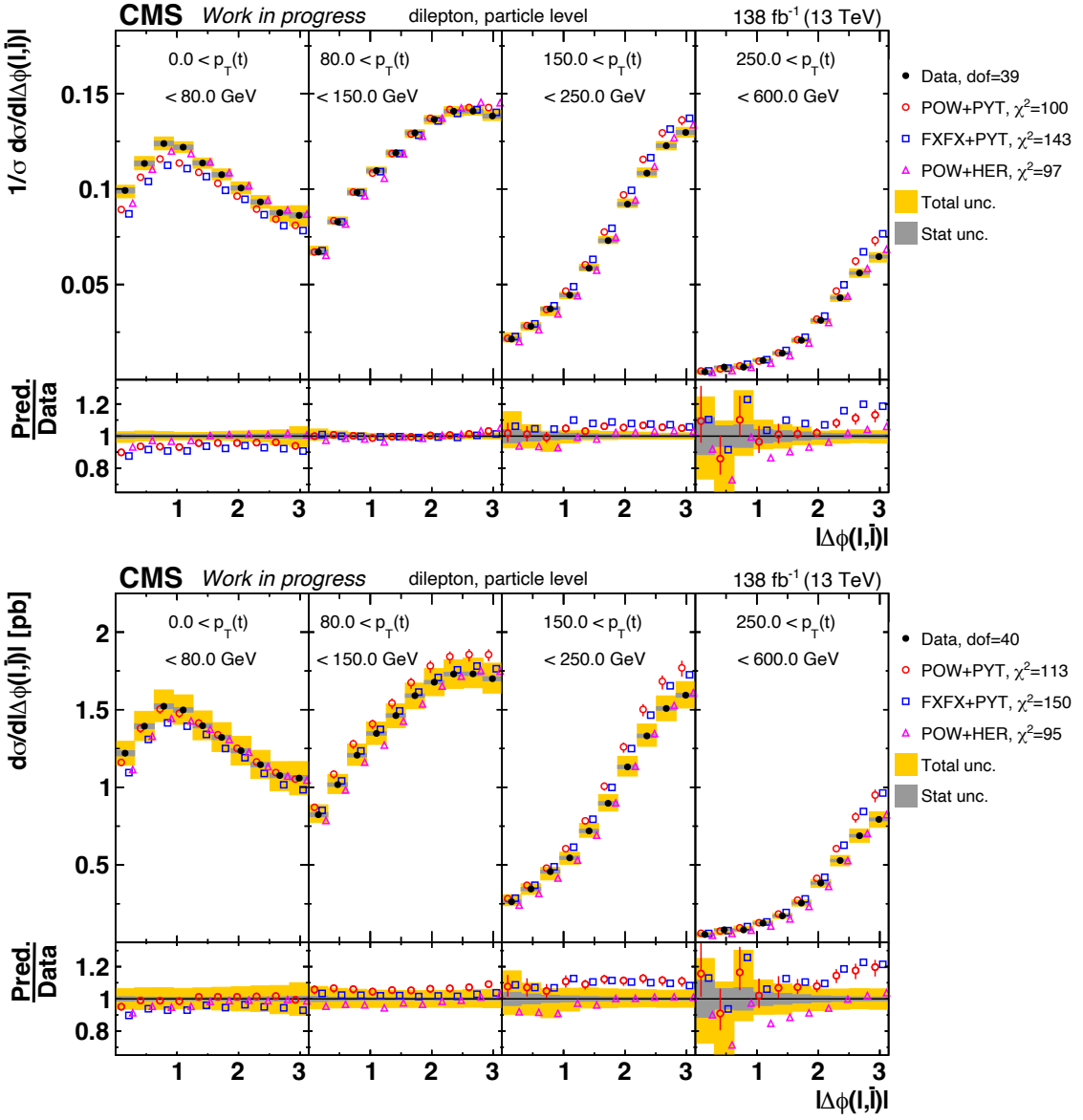

Figure 8.22: Differential $t\bar{t}$ cross sections measured as functions of the absolute value of the azimuthal angle between the lepton and the anti-lepton, $|\Delta\phi(\ell,\bar{\ell})|$, in ranges of the transverse momentum of the top, $p_{\mathrm{T}}(t)$, for both normalized (top) and absolute (bottom) measurements performed in the fiducial phase space at particle level. For further details see Figure 8.1.

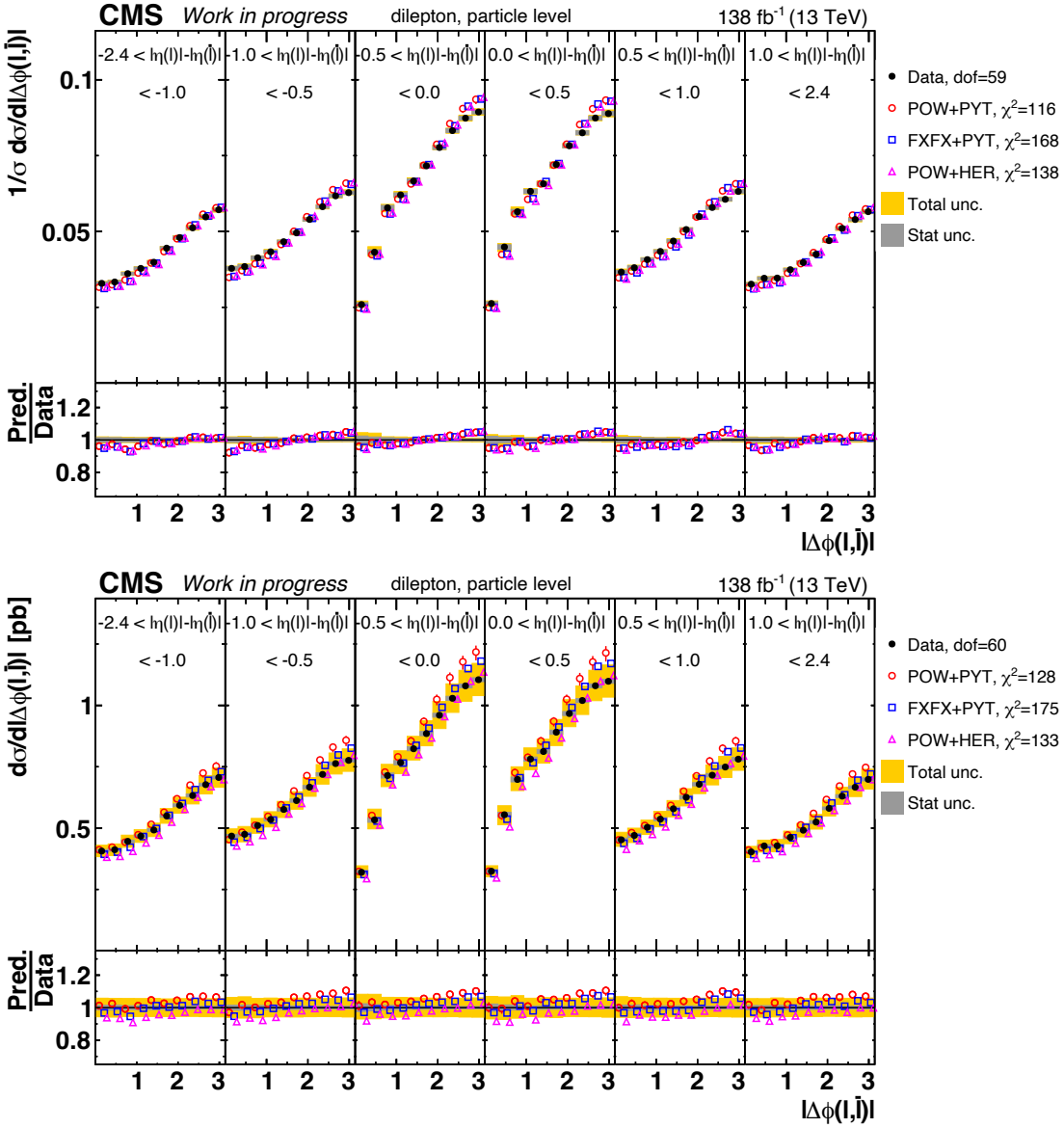

Figure 8.23: Differential $t\bar{t}$ cross sections measured as functions of the absolute value of the azimuthal angle between the lepton and the anti-lepton, $|\Delta\phi(\ell,\bar{\ell})|$, in ranges of the difference in absolute value of pseudorapidity of the lepton and absolute value of pseudorapidity of the anti-lepton, $|\eta(\ell)| - |\eta(\bar{\ell})|$, for both normalized (top) and absolute (bottom) measurements performed in the fiducial phase space at particle level. For further details see Figure 8.1.

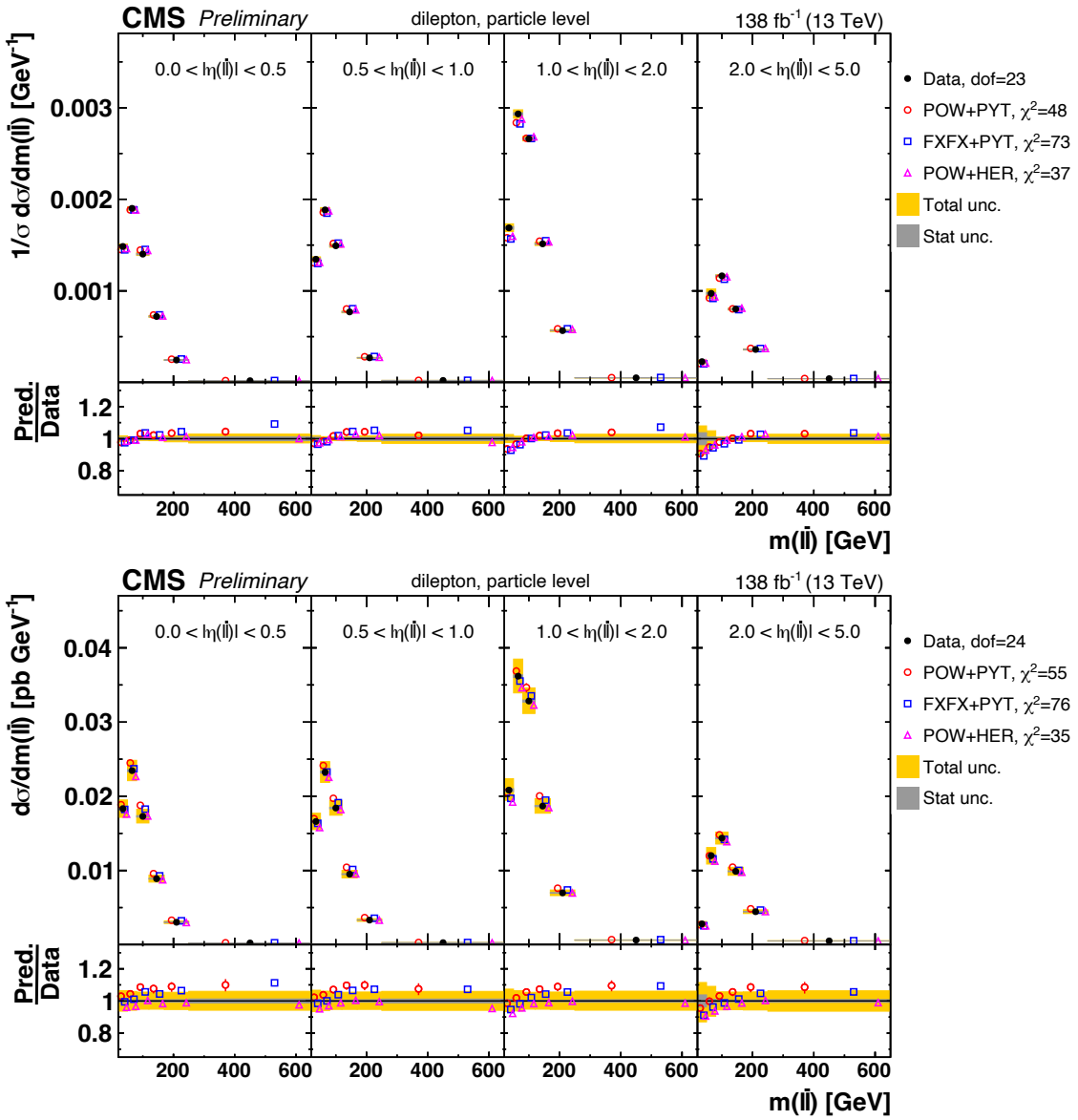

Figure 8.24: Differential $t\bar{t}$ cross sections measured as functions of the invariant mass of the $\ell\bar{\ell}$ system, $m(\ell\bar{\ell})$, in ranges of the absolute pseudorapidity of the $\ell\bar{\ell}$ system, $|\eta(\ell\bar{\ell})|$, for both normalized (top) and absolute (bottom) measurements performed in the fiducial phase space at particle level. For further details see Figure 8.1.

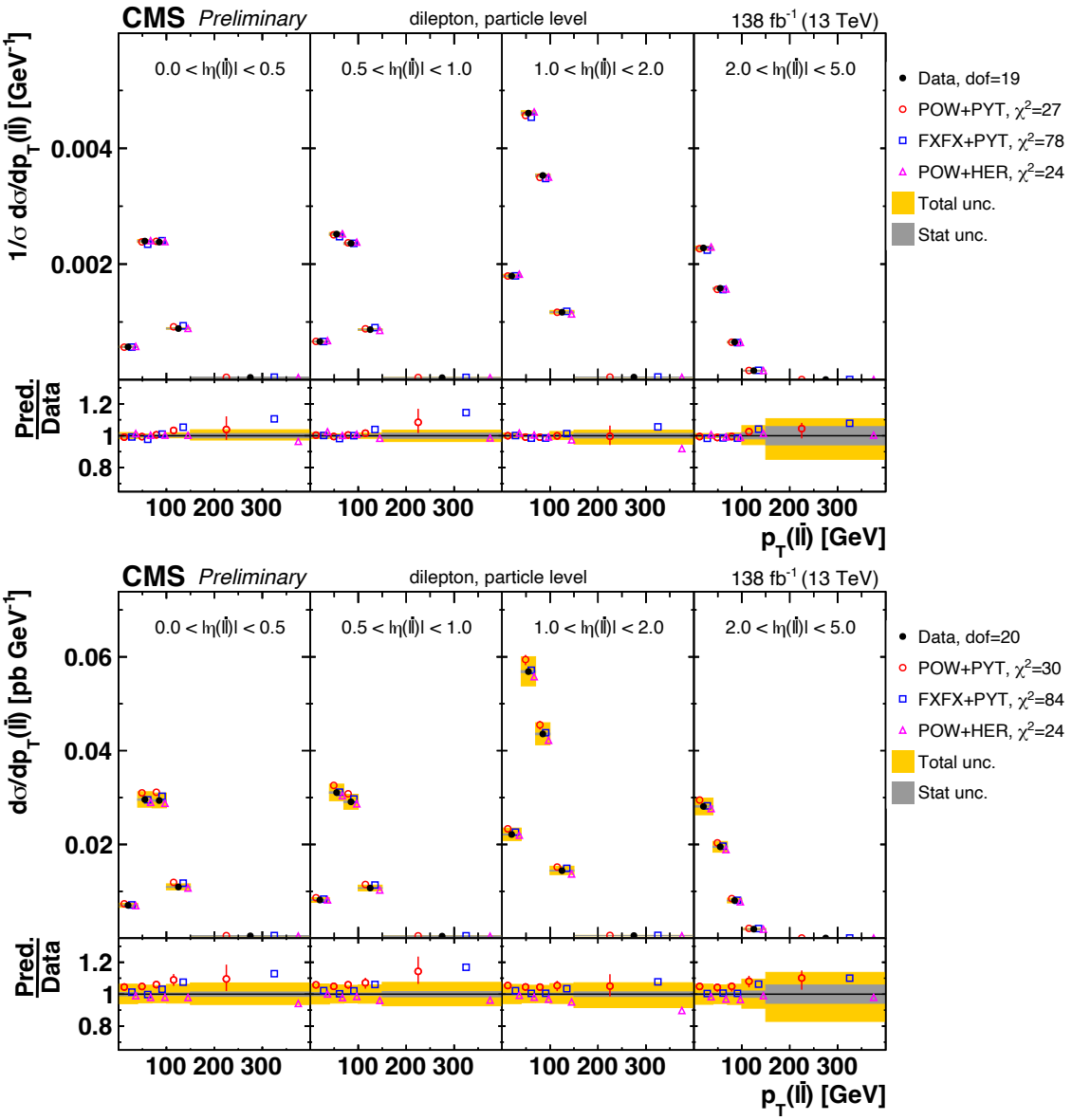

Figure 8.25: Differential $t\bar{t}$ cross sections measured as functions of the transverse momentum of the $\ell\bar{\ell}$ system, $p_{\mathrm{T}}(\ell\bar{\ell})$, in ranges of the absolute pseudorapidity of the $\ell\bar{\ell}$ system, $|\eta(\ell\bar{\ell})|$, for both normalized (top) and absolute (bottom) measurements performed in the fiducial phase space at particle level. For further details see Figure 8.1.

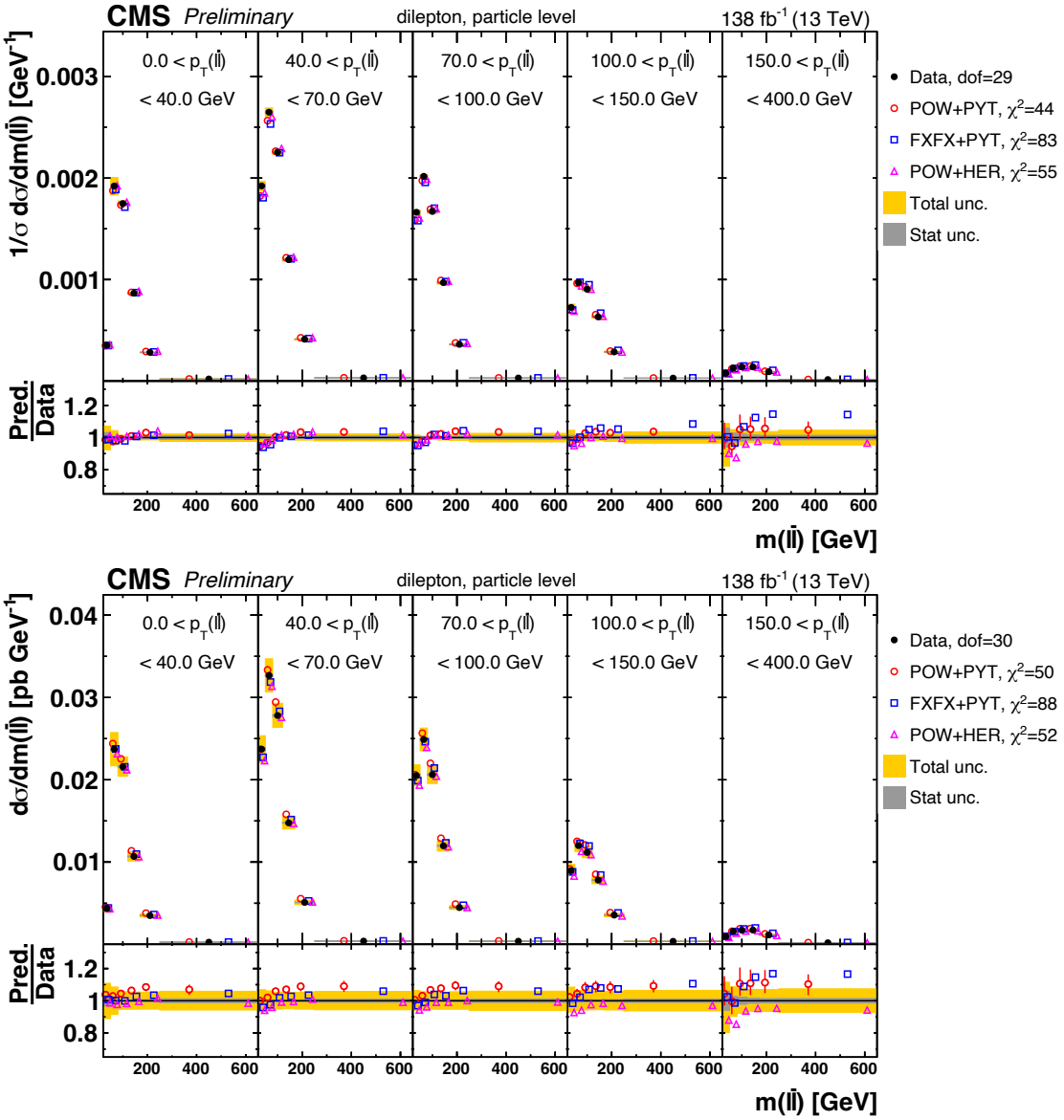

Figure 8.26: Differential $t\bar{t}$ cross sections measured as functions of the invariant mass of the $\ell\bar{\ell}$ system, $m(\ell\bar{\ell})$, in ranges of the transverse momentum of the $\ell\bar{\ell}$ system, $p_{\mathrm{T}}(\ell\bar{\ell})$, for both normalized (top) and absolute (bottom) measurements performed in the fiducial phase space at particle level. For further details see Figure 8.1.

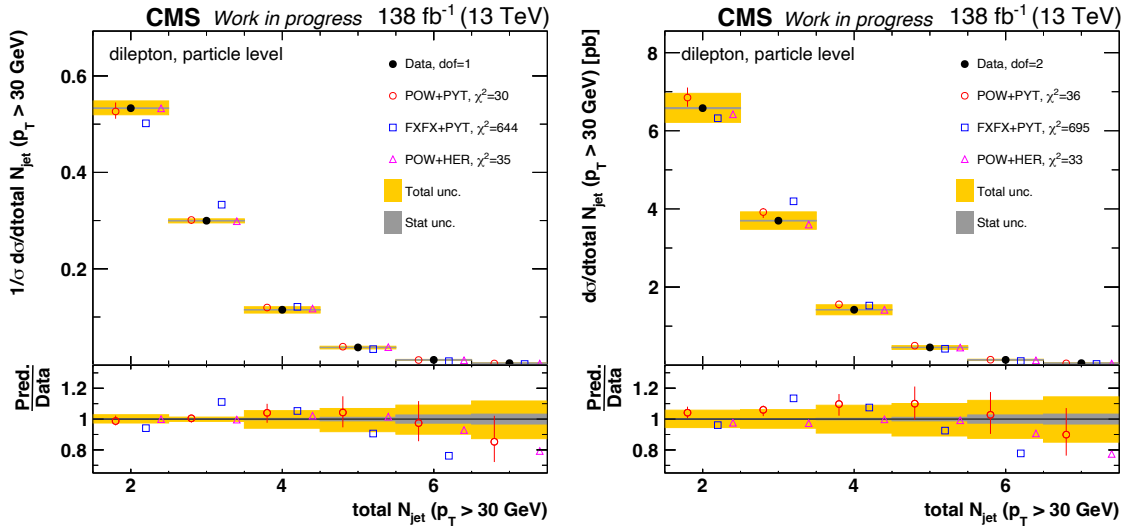

Figure 8.27: Differential $t\bar{t}$ cross sections measured as functions of the total jet multiplicity, N_{jet} (the last bin is inclusive for ≥ 7), in the fiducial phase space at particle level for normalized (left) and absolute (right) distributions. For further details see Figure 8.1.

8.2.4 Cross sections measured as functions of kinematic spectra of the jet multiplicity at particle level

The total jet multiplicity, N_{jet}, is measured at particle level in the fiducial phase space and is shown in Figure 8.27. The last bin is inclusive for $N_{\text{jet}} \geq 7$. The models POW+PYT and POW+HER provide predictions that agree reasonably well with the data within uncertainties, but FXFX+PYT completely fails to describe the data for multiplicities of $N_{\text{jet}} = 3$ ($N_{\text{jet}} > 4$) for which it predicts too many (few) events. The $N_{\text{jet}} = 3$ multiplicity corresponds to an NLO process for $t\bar{t}$ production with one real jet emission (see the NLO Feynman diagram in Figure 4.2 in Chapter 4). The $N_{\text{jet}} = 4, 5, 6, 7+$ cross sections probe processes with $\sigma(\alpha_s^4)$ or up to $\sigma(\alpha_s^7)$ for $t\bar{t}$ production. The description of these processes by the MC models relies on the parton shower approximation, which seems to work quite well overall.

8.2.5 Summary on the description of data by the MC models

The χ^2 values of all MC models are summarized in Tables 8.3 to 8.8. The best description of data overall is generally provided by POW+PYT, however, this model also tends to predict harder p_{T} spectra of the top quark and lepton than is observed in data. Predictions by FXFX+PYT also tend to be too hard, but the effect is much more pronounced than for the latter. In contrast, POW+HER has a very good description of these spectra, but the same cannot be said for the p_{T} spectra of particle systems, where this model has a tendency to be too soft. On the whole all models predict more central rapidity spectra. Cross sections measured as functions of the invariant masses $m(t\bar{t})$, $m(\ell\bar{\ell})$, $m(b\bar{b})$ and $m(\ell\bar{\ell}\mathrm{b}\bar{\mathrm{b}})$ are also studied in comparisons of the MC models along with alternative POW+PYT models using different top masses, i.e $m_t = 175.5$ GeV and $m_t = 169.5$ GeV, in order to gauge the sensitivity to the top mass. The MC models use $m_t = 172.5$ GeV and have a reasonably good description of all mass distributions except at the threshold, where they generally undershoot the data. A higher value of m_t is shown to result in a harder description of the data and $m(\ell\bar{\ell}\mathrm{b}\bar{\mathrm{b}})$ in particular shows a high degree of sensitivity to the different top masses.

Differential cross sections are also performed as functions of several new ratios of observables. One such ratio is $p_{\mathrm{T}}(t)/m(t\bar{t})$, which sheds light on the top p_{T} problem, while another measurement, $p_{\mathrm{T}}(t\bar{t})/m(t\bar{t})$, is sensitive to the p_{T} re-summation effects instead. In the former, POW+PYT and FXFX+PYT predict much harder spectra than is observed in data, lending support to the idea that the top p_{T} problem is more pronounced when $m(t\bar{t})$ is large. However, the POW+HER model retains a reasonable description, as is also observed for the single-differential measurement of $p_{\mathrm{T}}(t)$. Furthermore, the modulation in the prediction and data agreement observed in the single-differential measurement of $p_{\mathrm{T}}(t)$ is more enhanced in $p_{\mathrm{T}}(t\bar{t})/m(t\bar{t})$.

Finally, the POW+PYT and POW+HER models have a similar description of the data in the double-differential measurements, where a worse performance is seen for FXFX+PYT. A positive slope in the ratio of prediction and data as a function of $|\Delta\phi(\ell,\bar{\ell})|$ is seen for all models when correlating this observable with $m(t\bar{t})$, $p_{\mathrm{T}}(t)$ and $|\eta(\ell\bar{\ell})|$. Reasonably good descriptions of the data is observed for all MC models when correlating spectra of the $\ell\bar{\ell}$ system, i.e. $|\eta(\ell\bar{\ell})|$, $m(\ell\bar{\ell})$ and $p_{\mathrm{T}}(\ell\bar{\ell})$, and the high-level precision in such measurements are a result of the excellent resolution of leptons in the CMS experiment. However, the general observation that POW+PYT and POW+HER outperform FXFX+PYT still holds.

Table 8.3: The χ^2 values and degrees of freedom for normalized differential cross sections measured as functions of kinematic spectra of the top quarks and $t\bar{t}$ system are listed for the different NLO MC models. The values are shown for the parton level definition in the full phase space. Uncertainties on the measurement are taken into account when computing the χ^2 but uncertainties on the predictions are not included.

Cross section variables	dof	χ^2		
		POW+PYT	POW+HER	FXFX+PYT
$p_{\mathrm{T}}(t)$	6	15	5	38
$p_{\mathrm{T}}(\bar{t})$	6	13	6	37
$y(t)$	9	23	21	34
$y(\bar{t})$	9	28	24	39
$p_{\mathrm{T}}(t\bar{t})$	6	22	34	38
$y(t\bar{t})$	11	10	8	19
$m(t\bar{t})$	6	5	4	7
$\lvert\Delta\phi(t,\bar{t})\rvert$	3	1	7	5
$\lvert y(t)\rvert - \lvert y(\bar{t})\rvert$	7	16	14	19
$p_{\mathrm{T}}(t)/m(t\bar{t})$	4	33	11	77
$p_{\mathrm{T}}(t\bar{t})/m(t\bar{t})$	8	17	27	27
$\log(\xi_1)$	8	14	12	17
$\log(\xi_2)$	8	10	7	23

Table 8.4: The χ^2 values and degrees of freedom for absolute differential cross sections measured as functions of kinematic spectra of the top quarks and $t\bar{t}$ system are listed for the different NLO MC models. The values are shown for the parton level definition in the full phase space. Uncertainties on the measurement are taken into account when computing the χ^2 but uncertainties on the predictions are not included.

Cross section variables	dof	χ^2		
		POW+PYT	POW+HER	FXFX+PYT
$p_{\mathrm{T}}(t)$	7	21	5	43
$p_{\mathrm{T}}(\bar{t})$	7	19	6	43
$y(t)$	10	28	21	34
$y(\bar{t})$	10	33	25	40
$p_{\mathrm{T}}(t\bar{t})$	7	24	35	39
$y(t\bar{t})$	12	13	8	19
$m(t\bar{t})$	7	6	4	9
$\lvert\Delta\phi(t,\bar{t})\rvert$	4	4	11	7
$\lvert y(t)\rvert - \lvert y(\bar{t})\rvert$	8	18	14	19
$p_{\mathrm{T}}(t)/m(t\bar{t})$	5	39	13	104
$p_{\mathrm{T}}(t\bar{t})/m(t\bar{t})$	9	20	39	32
$\log(\xi_1)$	9	16	12	18
$\log(\xi_2)$	9	14	7	24

Table 8.5: The χ^2 values and degrees of freedom for normalized differential cross sections measured as functions of kinematic spectra of the top quarks and $t\bar{t}$ system are listed for the different NLO MC models. The values are shown for the particle level definition in the fiducial phase space. Uncertainties on the measurement are taken into account when computing the χ^2 but uncertainties on the predictions are not included.

Cross section variables	dof	χ^2		
		POW+PYT	POW+HER	FXFX+PYT
$p_{\mathrm{T}}(t)$	6	17	6	40
$p_{\mathrm{T}}(\bar{t})$	6	14	5	40
$y(t)$	9	19	20	30
$y(\bar{t})$	9	24	27	30
$p_{\mathrm{T}}(t\bar{t})$	6	21	41	32
$y(t\bar{t})$	11	10	9	21
$m(t\bar{t})$	6	5	8	5
$\lvert\Delta\phi(t,\bar{t})\rvert$	3	1	6	3
$\lvert y(t)\rvert - \lvert y(\bar{t})\rvert$	7	15	18	15
$p_{\mathrm{T}}(t)/m(t\bar{t})$	4	30	12	67
$p_{\mathrm{T}}(t\bar{t})/m(t\bar{t})$	8	18	36	32
$\log(\xi_1)$	8	14	18	17
$\log(\xi_2)$	8	9	10	17

Table 8.6: The χ^2 values and degrees of freedom for absolute differential cross sections measured as functions of kinematic spectra of the top quarks and $t\bar{t}$ system are listed for the different NLO MC models. The values are shown for the particle level definition in the fiducial phase space. Uncertainties on the measurement are taken into account when computing the χ^2 but uncertainties on the predictions are not included.

Cross section variables	dof	χ^2		
		POW+PYT	POW+HER	FXFX+PYT
$p_{\mathrm{T}}(t)$	7	22	7	44
$p_{\mathrm{T}}(\bar{t})$	7	20	5	44
$y(t)$	10	24	19	32
$y(\bar{t})$	10	28	26	32
$p_{\mathrm{T}}(t\bar{t})$	7	23	41	34
$y(t\bar{t})$	12	13	9	23
$m(t\bar{t})$	7	7	7	5
$\lvert\Delta\phi(t,\bar{t})\rvert$	4	4	7	4
$\lvert y(t)\rvert - \lvert y(\bar{t})\rvert$	8	17	18	15
$p_{\mathrm{T}}(t)/m(t\bar{t})$	5	33	14	71
$p_{\mathrm{T}}(t\bar{t})/m(t\bar{t})$	9	21	61	46
$\log(\xi_1)$	9	16	19	17
$\log(\xi_2)$	9	12	10	19

Table 8.7: The χ^2 values and degrees of freedom for normalized differential cross sections measured as functions of kinematic spectra of the charged leptons and beauty flavoured jets are listed for the different NLO MC models. The values are shown for the particle level definition in the fiducial phase space. Uncertainties on the measurement are taken into account when computing the χ^2 but uncertainties on the predictions are not included.

Cross section variables	dof	χ^2		
		POW+PYT	POW+HER	FXFX+PYT
$p_{\mathrm{T}}(\ell)$	11	28	18	51
$p_{\mathrm{T}}(\ell)$ trailing/$p_{\mathrm{T}}(\ell)$ leading	9	15	7	24
$p_{\mathrm{T}}(\ell)/p_{\mathrm{T}}(\bar{t})$	4	10	12	25
p_{T}(b) leading	9	5	8	26
p_{T}(b) trailing	6	6	7	24
$(p_{\mathrm{T}}(\mathrm{b}) + \mathrm{p_T}(\bar{\mathrm{b}}))/(\mathrm{p_T(t)} + \mathrm{p_T}(\bar{\mathrm{t}}))$	3	19	18	27
$m(\ell\bar{\ell})$	11	23	23	27
$m(b\bar{b})$	6	15	14	15
$m(\ell\bar{\ell}\mathrm{b}\bar{\mathrm{b}})$	18	33	28	28
$p_{\mathrm{T}}(\ell\bar{\ell})$	8	4	9	14
$\lvert\eta(\ell\bar{\ell})\rvert$	13	14	11	21
$[m(t\bar{t}), \lvert\Delta\phi(\ell,\bar{\ell})\rvert]$	39	119	108	130
$[p_{\mathrm{T}}(t), \lvert\Delta\phi(\ell,\bar{\ell})\rvert]$	39	100	97	143
$[\lvert\eta(\ell)\rvert - \lvert\eta(\bar{\ell})\rvert, \lvert\Delta\phi(\ell,\bar{\ell})\rvert]$	59	116	138	168
$[\lvert\eta(\ell\bar{\ell})\rvert, \mathrm{m}(\ell\bar{\ell})]$	23	48	37	73
$[\lvert\eta(\ell\bar{\ell})\rvert, \mathrm{p_T}(\ell\bar{\ell})]$	19	27	24	78
$[p_{\mathrm{T}}(\ell\bar{\ell}), \mathrm{m}(\ell\bar{\ell})]$	29	44	55	83

Table 8.8: The χ^2 values and degrees of freedom for absolute differential cross sections measured as functions of kinematic spectra of the charged leptons and beauty flavoured jets are listed for the different NLO MC models. The values are shown for the particle level definition in the fiducial phase space. Uncertainties on the measurement are taken into account when computing the χ^2 but uncertainties on the predictions are not included.

Cross section variables	dof	χ^2		
		POW+PYT	POW+HER	FXFX+PYT
$p_{\mathrm{T}}(\ell)$	12	32	21	62
$p_{\mathrm{T}}(\ell)$ trailing/$p_{\mathrm{T}}(\ell)$ leading	10	16	7	27
$p_{\mathrm{T}}(\ell)/p_{\mathrm{T}}(\bar{t})$	5	20	14	28
p_{T}(b) leading	10	6	8	31
p_{T}(b) trailing	7	7	7	26
$(p_{\mathrm{T}}(\mathrm{b}) + \mathrm{p_T}(\bar{\mathrm{b}}))/(\mathrm{p_T(t)} + \mathrm{p_T}(\bar{\mathrm{t}}))$	4	24	21	30
$m(\ell\bar{\ell})$	12	31	23	29
$m(b\bar{b})$	7	21	15	17
$m(\ell\bar{\ell}\mathrm{b}\bar{\mathrm{b}})$	19	36	27	30
$p_{\mathrm{T}}(\ell\bar{\ell})$	9	4	10	17
$\lvert\eta(\ell\bar{\ell})\rvert$	14	16	12	22
$[m(t\bar{t}), \lvert\Delta\phi(\ell,\bar{\ell})\rvert]$	40	135	104	138
$[p_{\mathrm{T}}(t), \lvert\Delta\phi(\ell,\bar{\ell})\rvert]$	40	113	95	150
$[\lvert\eta(\ell)\rvert - \lvert\eta(\bar{\ell})\rvert, \lvert\Delta\phi(\ell,\bar{\ell})\rvert]$	60	128	133	175
$[\lvert\eta(\ell\bar{\ell})\rvert, \mathrm{m}(\ell\bar{\ell})]$	24	55	35	76
$[\lvert\eta(\ell\bar{\ell})\rvert, \mathrm{p_T}(\ell\bar{\ell})]$	20	30	24	84
$[p_{\mathrm{T}}(\ell\bar{\ell}), \mathrm{m}(\ell\bar{\ell})]$	30	50	52	88

8.2.6 Comparisons to theoretical predictions at beyond-NLO accuracy

The measured cross sections are also compared to the following theoretical predictions at beyond-NLO accuracy in QCD:

• Cross sections measured as functions of $p_{\mathrm{T}}(t)$ and $y(t)$ are compared to theoretical predictions at approximate next-to-next-to-next-leading-order (aN^{3}LO) accuracy, which is achieved by resumming soft-gluon contributions at next-to-next-to-leading-logarithm (NNLL) accuracy [140]. The renormalization and factorization scales are set to the transverse mass, $m_{\mathrm{T}} = \sqrt{m_t^2 + p_{\mathrm{T}}(t)^2}$, for the $p_{\mathrm{T}}(t)$ spectra and the top mass, m_t, for the $y(t)$ spectra.

• All cross sections at parton level are compared to theoretical predictions computed with the MATRIX package [141–148] at full NNLO accuracy in QCD (apart from $\log(\xi_1)$ and $\log(\xi_2)$). The renormalization and factorization scales are set to $H_{\mathrm{T}}/4$, where H_{T} is given as the sum of m_{T} of the top quark and anti-top quark.

• All cross sections at parton and particle level are compared to theoretical predictions from the STRIPPER framework [130–133], which provides fixed-order predictions at full NNLO accuracy in QCD (N_{jet} is not included in the set of comparisons). The renormalization and factorization scales are again set to $H_{\mathrm{T}}/4$. It should be noted that STRIPPER provides the first calculation for top-quark pair production and decay to dilepton final states, performed in the narrow width approximation at NNLO QCD.

• The MINNLOPS method [16–18] is used together with the MiNLO prescription [153, 154] to compute and integrate fixed-order predictions at full NNLO accuracy in QCD with parton showers in the POWHEG-V2-BOX [72] interfaced with PYTHIA 8. The underlying event and hadronization are taken into account when simulating the parton shower. The renormalization scale used for the two powers of α_s and the scale used for the modified logarithms are set to $H_{\mathrm{T}}/4$ and $H_{\mathrm{T}}/8$, respectively.

All predictions described above use the PDF set NNPDF3.1 [32] at NNLO accuracy and assume a value of $m_t = 172.5$ GeV for the top mass. In all the following theory to data comparisons, the POW+PYT predictions are also shown, as a reference model for the NLO MC generators. The uncertainties on the reference model and fixed-order predictions are represented by their respective error bars, but the latter only include scale uncertainties obtained by varying the renormalization and factorization scales up (down) by factors of 2 (0.5). Cross sections measured as functions of kinematic spectra of the top quarks at parton level in the full phase space and particle level in the fiducial phase space are shown in Figures 8.28 to 8.31. The spectra for $p_{\mathrm{T}}(t)$ and $p_{\mathrm{T}}(\bar{t})$ are shown in Figures 8.28 and 8.29, respectively. The comparisons to different MC generators showed that predictions at NLO give rise to harder spectra with respect to data but one can see that this is not true for predictions at fixed-order which all describe the data remarkably well. The prediction

from $a\text{N}^3\text{LO}$ has a higher value of χ^2 than POW+PYT and this seems to be due to the slightly worse agreement with data in the second and third bin in particular, where the data is measured with very high precision. All predictions follow the same trend as POW+PYT for $y(t\bar{t})$ (Figure 8.30) and $y(\bar{t})$ (Figure 8.31) which are more central at both NLO and beyond-NLO accuracy than data.

Cross sections measured as functions of kinematic spectra of the $t\bar{t}$ system, including correlations of the top and anti-top quark, at parton and particle level are shown in Figures 8.32 to 8.40. Figure 8.32 shows $|y(t)| - |y(\bar{t})|$, which is overall well described by MATRIX, STRIPPER and MINNLOPS in both central and outer bins. The problem that $|y(t)| - |y(\bar{t})|$ is more central than data at NLO accuracy is exemplified by POW+PYT but this is not the case for predictions at beyond-NLO accuracy.

The $|\Delta\phi(t,\bar{t})|$ and $p_{\text{T}}(t\bar{t})$ measurements are shown in Figure 8.33 and 8.34, respectively. Both MATRIX and STRIPPER have large uncertainties in all bins of the $|\Delta\phi(t,\bar{t})|$ distribution. These predictions have a good description at small opening angles but clearly predict too steep a rise near π, contrary to POW+PYT, which has an excellent description overall. The closely related $p_{\text{T}}(t\bar{t})$ spectra show that MATRIX, STRIPPER and MINNLOPS have the same type of modulation in the agreement with data as the reference simulation. Here MATRIX and STRIPPER perform better than both POW+PYT and MINNLOPS. The latter has the worst description at intermediate $p_{\text{T}}(t\bar{t})$, where it underestimates the data.

The $y(t\bar{t})$ distribution in Figure 8.35 is well described by MATRIX, STRIPPER and MINNLOPS but all three underestimate $m(t\bar{t})$ in Figure 8.36 at threshold along with POW+PYT. However, the predictions still give a good description of data overall.

Distributions of $p_{\text{T}}(t)/m(t\bar{t})$ and $p_{\text{T}}(t\bar{t})/m(t\bar{t})$ are shown in Figures 8.37 and 8.38, respectively. All predictions describe the $p_{\text{T}}(t)/m(t\bar{t})$ spectra well, especially compared to POW+PYT which fails to describe the data. However, $p_{\text{T}}(t\bar{t})/m(t\bar{t})$ is not well described by any prediction. This cross section exhibits a more pronounced modulation in the agreement with data than observed for $p_{\text{T}}(t\bar{t})$. The prediction from POW+PYT performs the best overall in this case.

The $\log(\xi_1)$ and $\log(\xi_2)$ measurements are shown in Figures 8.39 and 8.40, respectively, and are well described by both STRIPPER and MINNLOPS in the central bins. The latter performs the best overall. Some differences in prediction versus data are observed in the extreme ends of the spectra, primarily for STRIPPER at large values of ξ.

Cross sections measured as functions of kinematic spectra of the leptons and beauty flavoured jets at particle level in the fiducial phase space are shown in Figures 8.41 to 8.45. The $p_{\text{T}}(\ell)$ and $p_{\text{T}}(\ell)$ trailing/$p_{\text{T}}(\ell)$ leading spectra are shown in Figure 8.41, while $p_{\text{T}}(\ell)/\text{p}_{\text{T}}(\bar{\text{t}})$ and $(p_{\text{T}}(\text{b}) + \text{p}_{\text{T}}(\bar{\text{b}}))/(\text{p}_{\text{T}}(\text{t}) + \text{p}_{\text{T}}(\bar{\text{t}}))$ are shown in Figure 8.42. As previously stated, POW+PYT exhibits a slope in $p_{\text{T}}(\ell)$ which is correlated with

the slope seen for $p_{\mathrm{T}}(t)$. As Stripper had no visible slope for $p_{\mathrm{T}}(t)$ one expects to see the same for $p_{\mathrm{T}}(\ell)$ and this is indeed the case. POW+PYT still performs best in terms of the χ^2 but this is due to a slightly better description at low p_{T}. POW+PYT similarly performs best for $p_{\mathrm{T}}(\ell)$ trailing/$p_{\mathrm{T}}(\ell)$ leading although it is closely matched by Stripper with the exception of the first bin, whereas Stripper has the best description of both $p_{\mathrm{T}}(\ell)/\mathrm{p_T(\bar{t})}$ and $(p_{\mathrm{T}}(\mathrm{b})+\mathrm{p_T(\bar{b})})/(\mathrm{p_T(t)}+\mathrm{p_T(\bar{t})})$.

The $p_{\mathrm{T}}(\mathrm{b})$ leading and $p_{\mathrm{T}}(\mathrm{b})$ trailing distributions in Figure 8.43 are overall well described across the whole spectra within the corresponding data uncertainties.

The $m(\ell\bar{\ell})$ and $m(b\bar{b})$ distributions in Figure 8.44 are better modelled by POW+PYT as opposed to Stripper. This also applies to $m(\ell\bar{\ell}\mathrm{b\bar{b}})$ in Figure 8.45. Here Stripper provides predictions that are mostly within the data uncertainties in all three cases. An exception to this is seen for $m(b\bar{b})$ at threshold, where Stripper significantly overshoots the data.

Double-differential measurements are shown at particle level in the fiducial phase space in Figures 8.46 to 8.51. Distributions of $[m(t\bar{t}), |\Delta\phi(\ell,\bar{\ell})|]$, $[p_{\mathrm{T}}(t), |\Delta\phi(\ell,\bar{\ell})|]$ and $[|\eta(\ell)| - |\eta(\bar{\ell})|, |\Delta\phi(\ell,\bar{\ell})|]$ are shown in Figures 8.46, 8.47 and 8.48, respectively. POW+PYT performs better than Stripper in terms of χ^2 but neither are describing the data within data uncertainties. Typically Stripper and POW+PYT agree in that they either both undershoot or overshoot the data but the extent of the disagreement with data can vary significantly between the two predictions and Stripper tends to fluctuate more than POW+PYT. The reference simulation POW+PYT also performs better than Stripper for the measurements of $[|\eta(\ell\bar{\ell})|, \mathrm{m}(\ell\bar{\ell})]$, $[|\eta(\ell\bar{\ell})|, \mathrm{p_T}(\ell\bar{\ell})]$ and $[p_{\mathrm{T}}(\ell\bar{\ell}), \mathrm{m}(\ell\bar{\ell})]$ as shown in Figures 8.49, 8.50 and 8.51, respectively.

In summary, the predictions at NNLO or even higher order accuracy in QCD have a better description of the data when compared to the reference model POW+PYT for all differential cross sections measured as functions of kinematic spectra of the top and anti-top as well as the $t\bar{t}$ system, including correlations of the top quarks. However, exceptions are $|\Delta\phi(t,\bar{t})|$, $p_{\mathrm{T}}(t\bar{t})$ and $p_{\mathrm{T}}(t\bar{t})/m(t\bar{t})$ where the fixed-order predictions generally exhibit a relatively poor data description. In the differential cross sections measured as functions of kinematic spectra of the leptons and beauty flavoured jets, Stripper tends to perform worse than POW+PYT overall. The worst description of data is mainly seen for the lepton and $\ell\bar{\ell}$ system, although the new ratio observable, $p_{\mathrm{T}}(\ell)/\mathrm{p_T(\bar{t})}$, is an exception to this. Here a good description of the $p_{\mathrm{T}}(t)$ spectrum seems to outweigh the relatively worse description of the $p_{\mathrm{T}}(\ell)$ spectrum. The b-jet p_{T} spectra show that Stripper provides a good description of data, similar to POW+PYT, and Stripper is even shown to perform better for $(p_{\mathrm{T}}(\mathrm{b}) + \mathrm{p_T(\bar{b})})/(\mathrm{p_T(t)} + \mathrm{p_T(\bar{t})})$, which is again likely related to its good description of $p_{\mathrm{T}}(t)$. Relatively high χ^2-values are seen for the invariant mass distributions, $m(\ell\bar{\ell})$, $m(b\bar{b})$ and $m(\ell\bar{\ell}\mathrm{b\bar{b}})$, where the latter two show the same poor description of data primarily in the first bin. Finally, in the double differential distributions, where $|\Delta\phi(\ell,\bar{\ell})|$ is studied in ranges of $m(t\bar{t})$, $p_{\mathrm{T}}(t)$ and $|\eta(\ell)| - |\eta(\bar{\ell})|$, the predictions from

STRIPPER exhibit small distortions around the data distributions, and the same can be said for the distributions showing correlations of $|\eta(\ell\bar{\ell})|$, $m(\ell\bar{\ell})$ and $p_{\mathrm{T}}(\ell\bar{\ell})$. This behaviour then results in very large χ^2 values in comparison to POW+PYT.

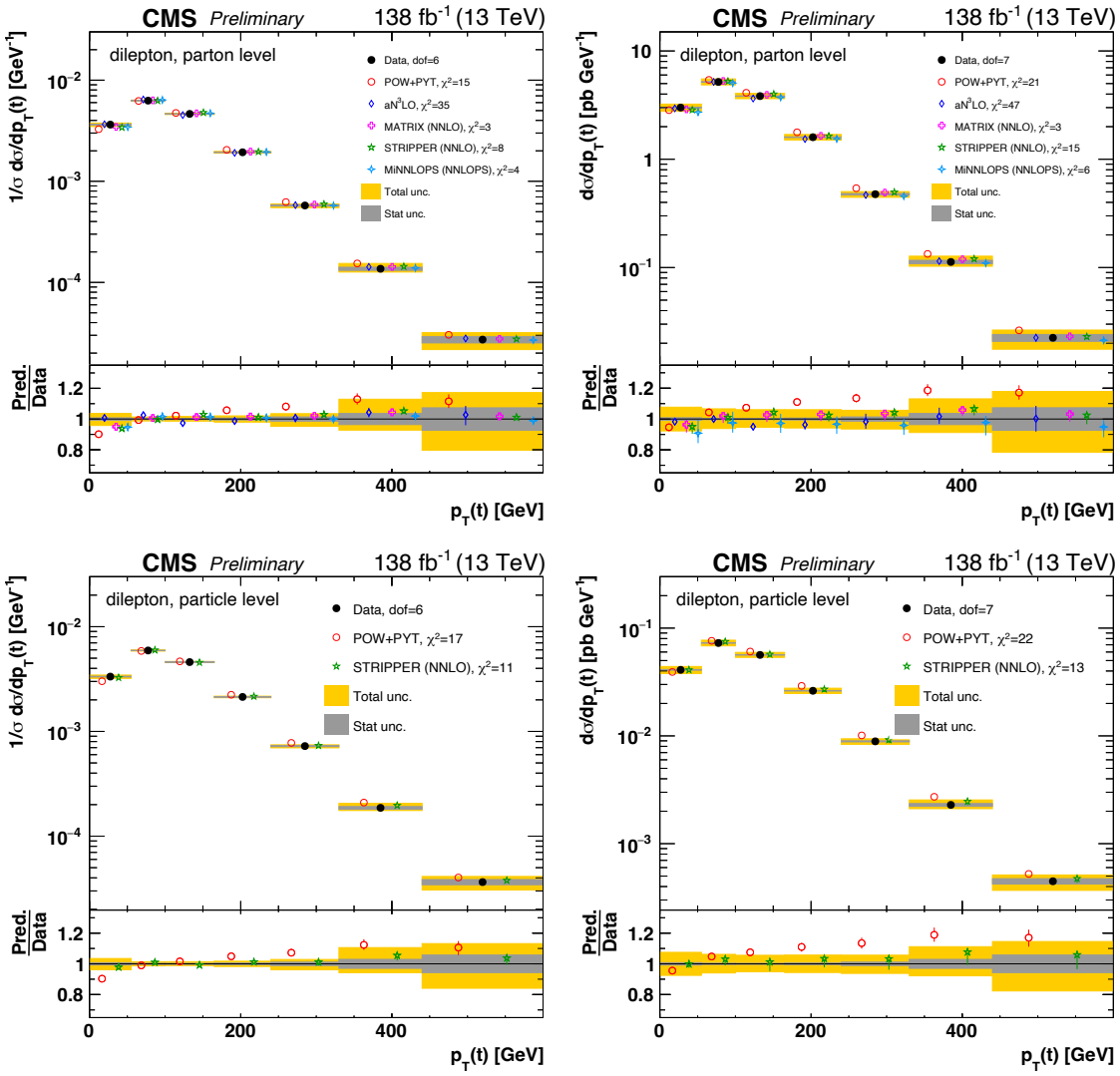

Figure 8.28: Differential $t\bar{t}$ cross sections measured as functions of the transverse momentum of the top, $p_{\mathrm{T}}(t)$, in the full phase space at parton level (top row) and in the fiducial phase space at particle level (bottom row). The left and right columns show normalized and absolute cross sections, respectively. The data (black dots) is shown together with the reference simulation, depicted in red and abbreviated to POW+PYT, and predictions from $a\mathrm{N}^3\mathrm{LO}$ (blue), MATRIX (magenta), MiNNLOPS (cyan) and STRIPPER (green), computed at beyond-NLO accuracy in QCD. The statistical and total uncertainties on the data are illustrated by the grey and yellow bands, respectively, where the latter corresponds to systematic and statistical uncertainties added in quadrature. The uncertainties on POW+PYT and all fixed-order predictions are indicated by error bars, but the latter only account for scale uncertainties. Furthermore, a χ^2 value that takes all measurement uncertainties into account is reported for POW+PYT and all fixed-order predictions, and the ratios with respect to data are shown in the bottom panel of each plot.

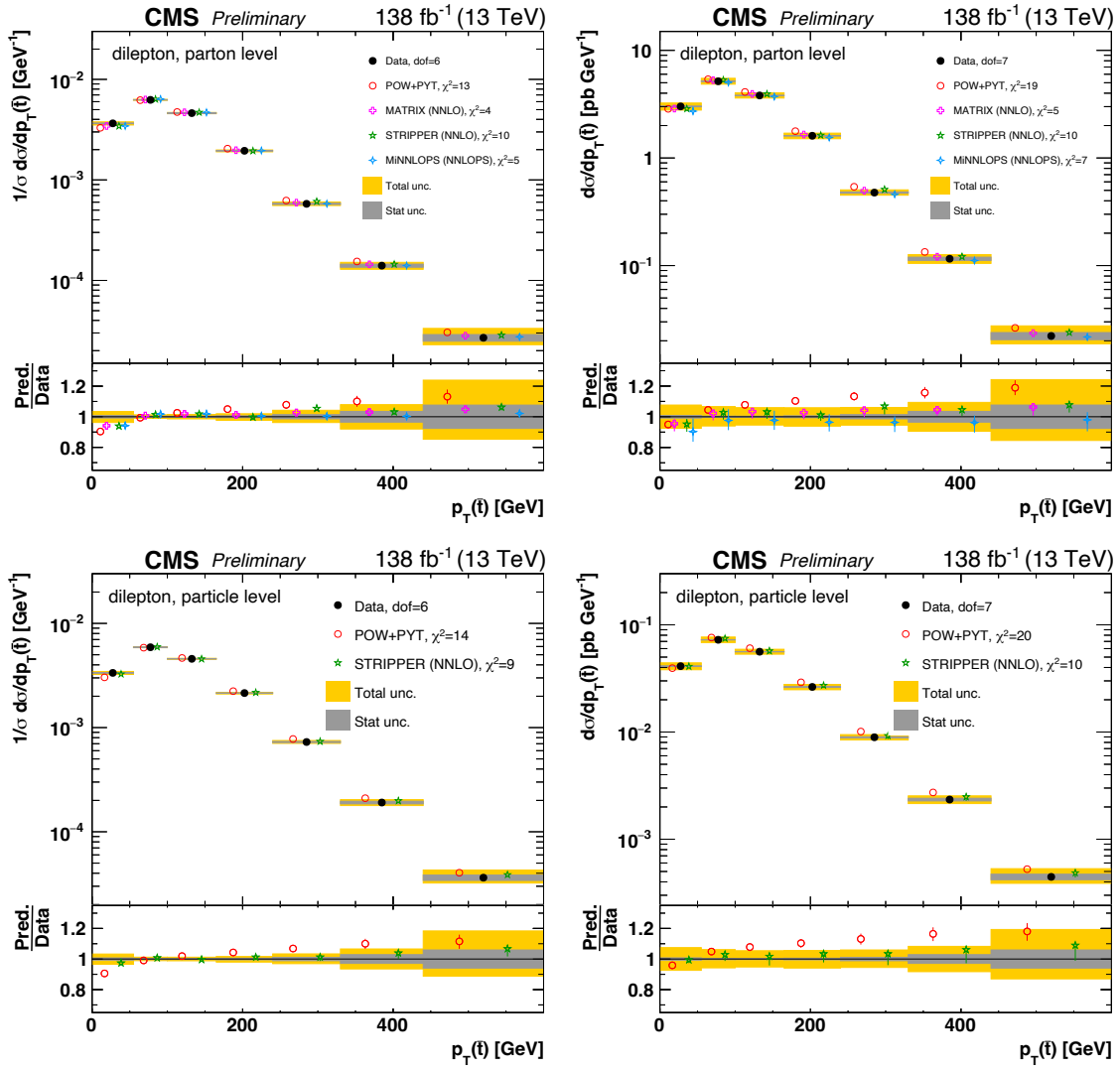

Figure 8.29: Differential $t\bar{t}$ cross sections measured as functions of the transverse momentum of the anti-top, $p_{\mathrm{T}}(\bar{t})$, in the full phase space at parton level (top row) and in the fiducial phase space at particle level (bottom row). The left and right columns show normalized and absolute cross sections, respectively. For further details see Figure 8.28.

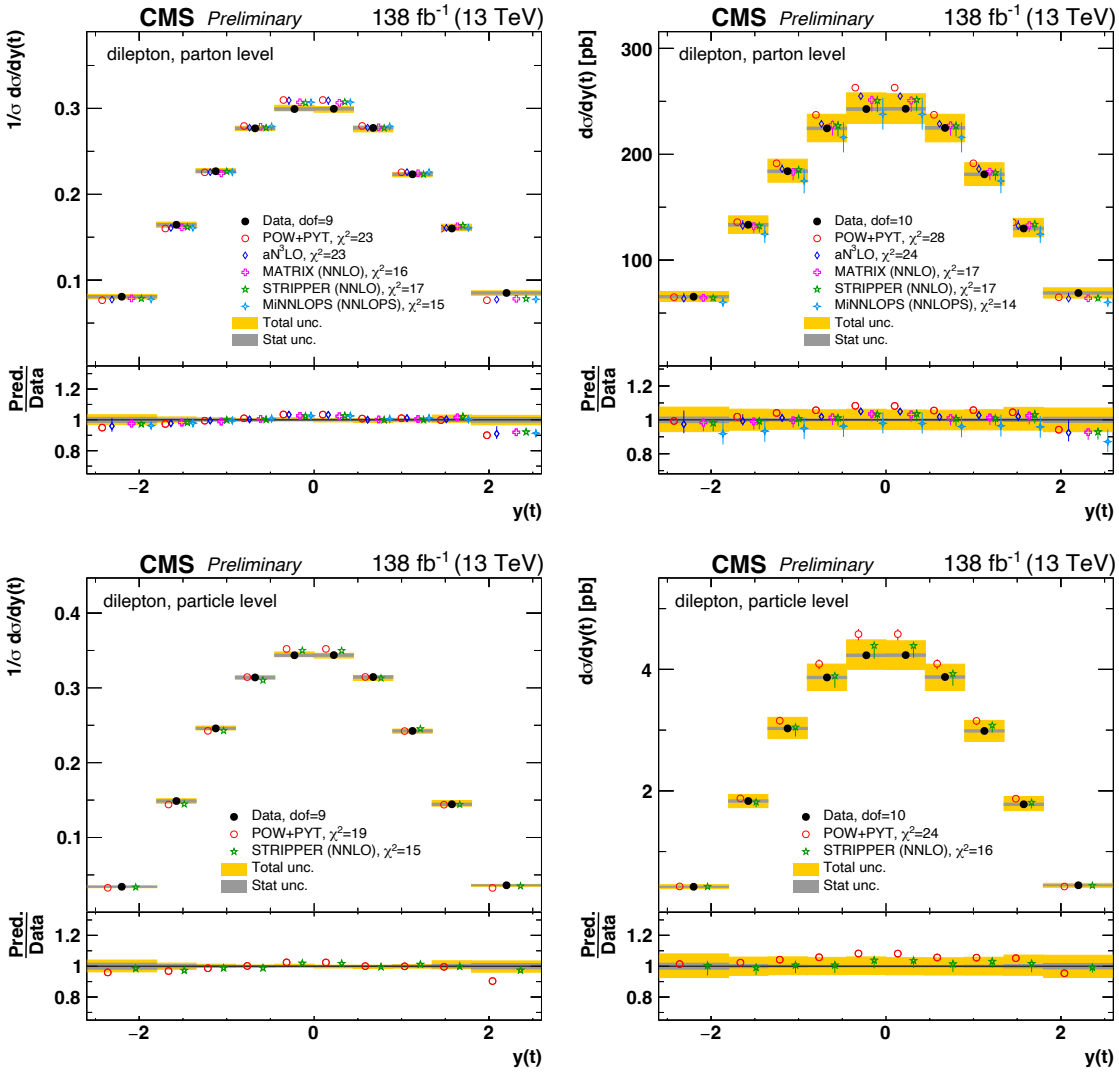

Figure 8.30: Differential $t\bar{t}$ cross sections measured as functions of the rapidity of the top, $y(t)$, in the full phase space at parton level (top row) and in the fiducial phase space at particle level (bottom row). The left and right columns show normalized and absolute cross sections, respectively. For further details see Figure 8.28.

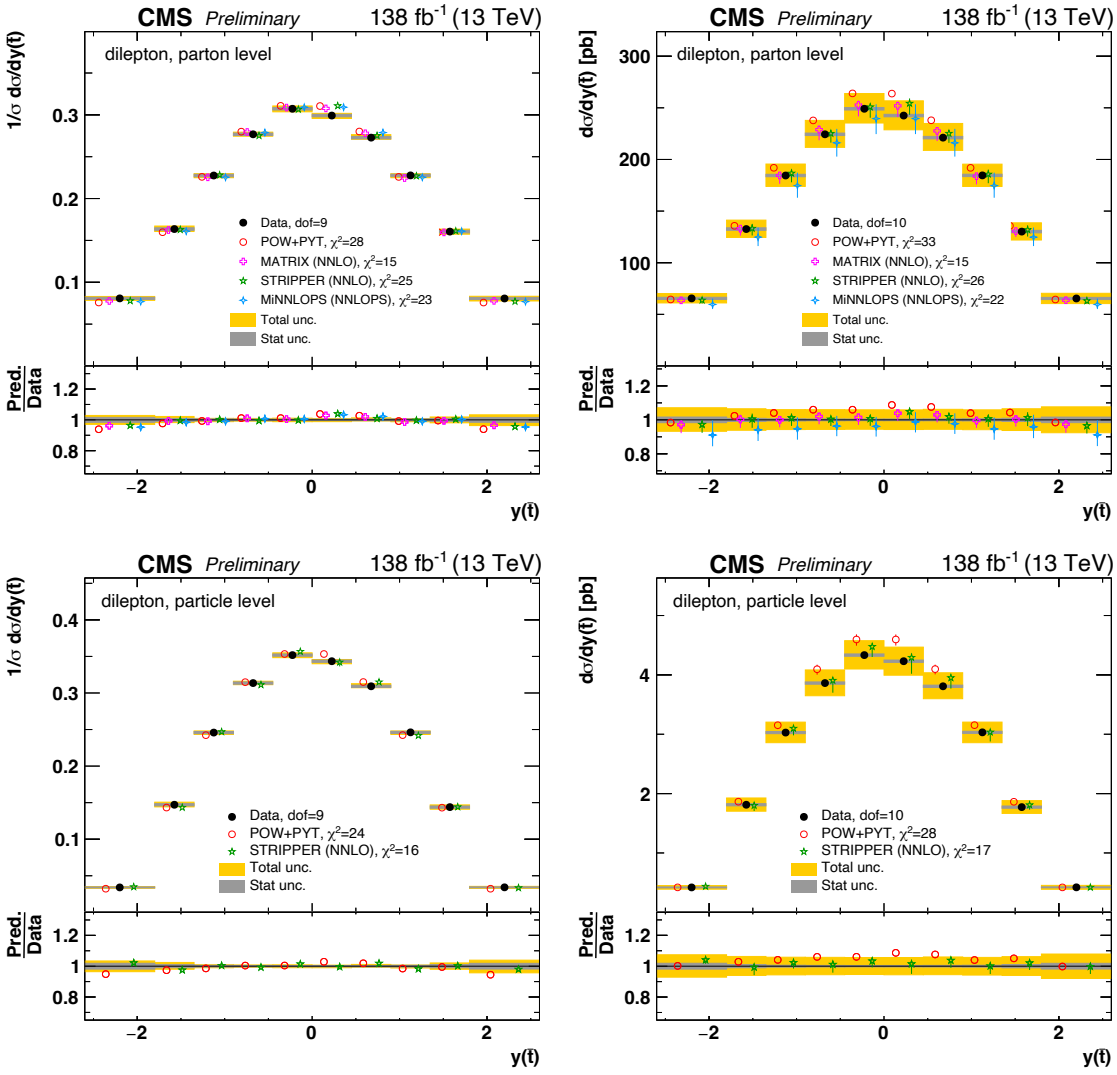

Figure 8.31: Differential $t\bar{t}$ cross sections measured as functions of the rapidity of the anti-top, $y(\bar{t})$, in the full phase space at parton level (top row) and in the fiducial phase space at particle level (bottom row). The left and right columns show normalized and absolute cross sections, respectively. For further details see Figure 8.28.

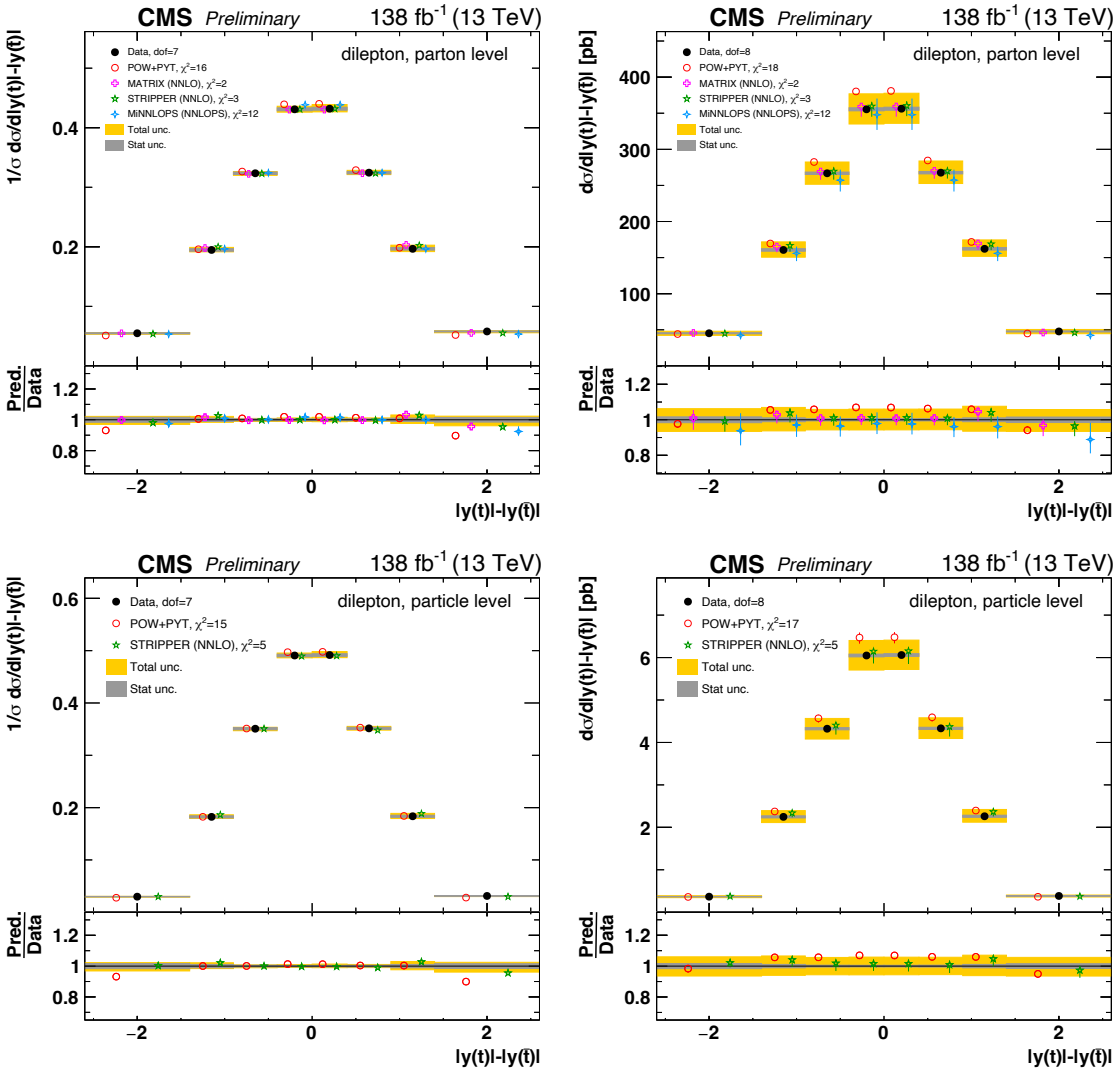

Figure 8.32: Differential $t\bar{t}$ cross sections measured as functions of the difference in absolute value of rapidity of the top and absolute value of rapidity of the anti-top, $|y(t)|-|y(\bar{t})|$, in the full phase space at parton level (top row) and in the fiducial phase space at particle level (bottom row). The left and right columns show normalized and absolute cross sections, respectively. For further details see Figure 8.28.

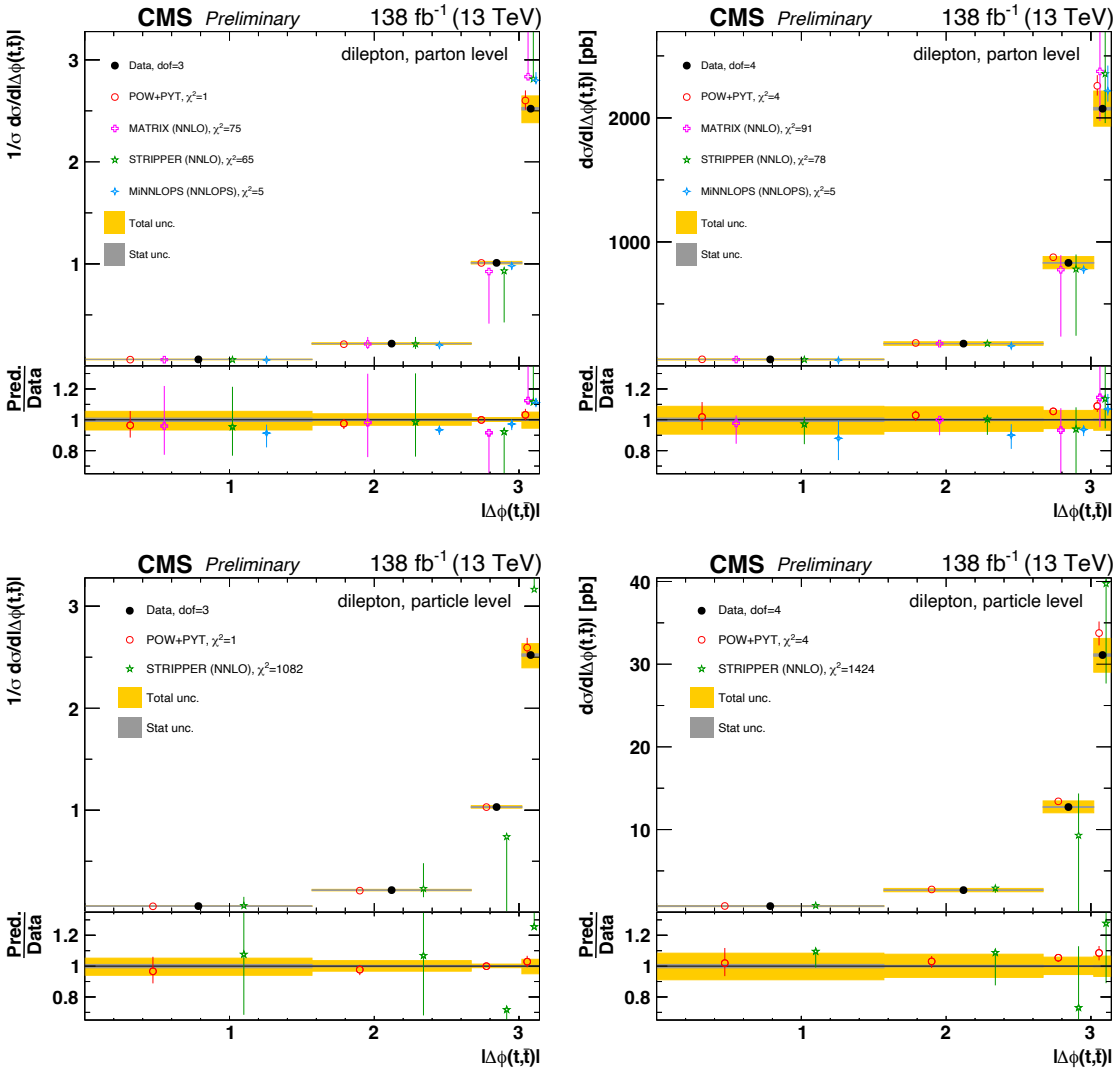

Figure 8.33: Differential $t\bar{t}$ cross sections measured as functions of the absolute value of the azimuthal angle (ϕ) between the top and the anti-top, $|\Delta\phi(t,\bar{t})|$, in the full phase space at parton level (top row) and in the fiducial phase space at particle level (bottom row). The left and right columns show normalized and absolute cross sections, respectively. For further details see Figure 8.28.

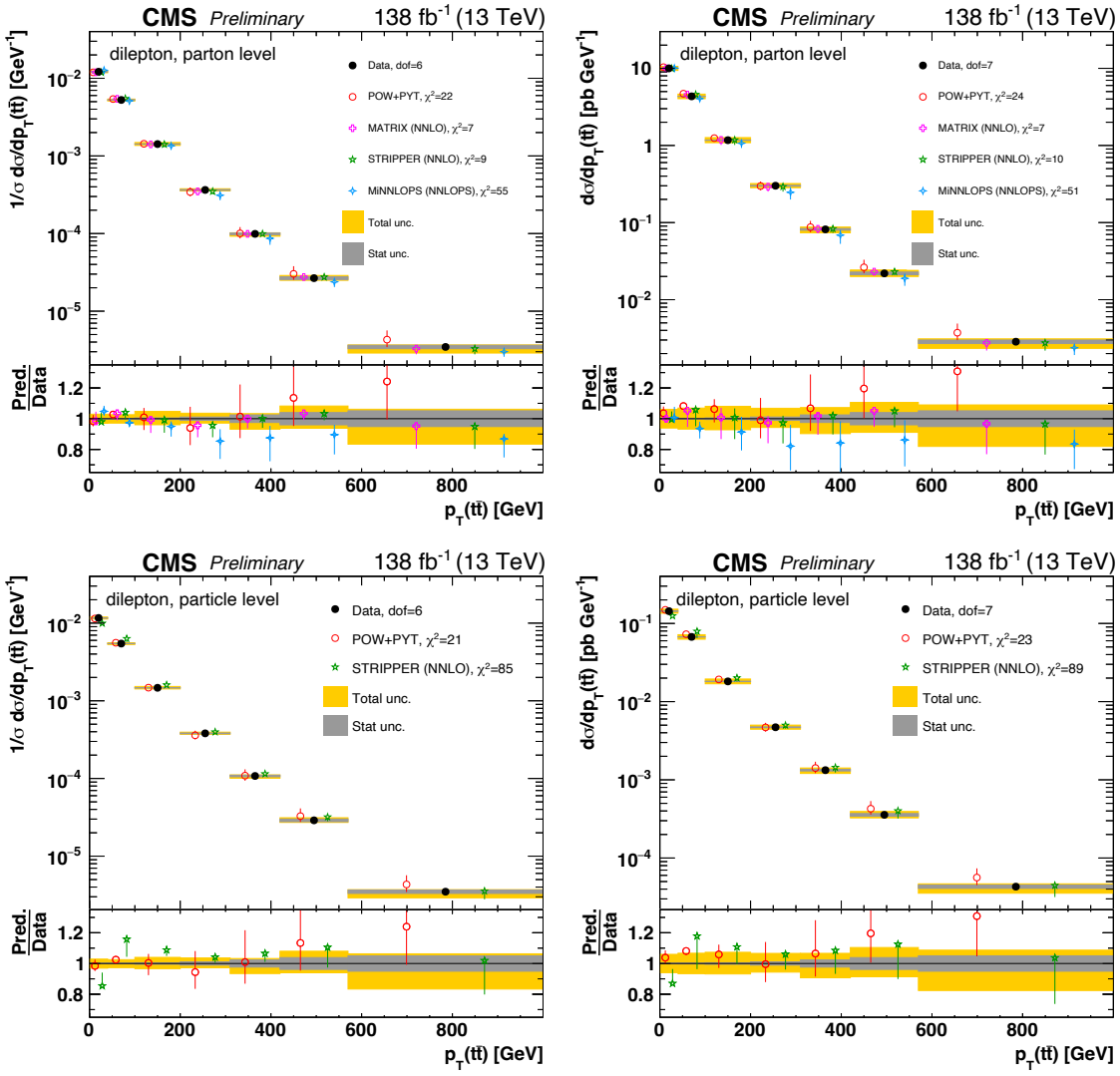

Figure 8.34: Differential $t\bar{t}$ cross sections measured as functions of the transverse momentum of the $t\bar{t}$ system, $p_{\mathrm{T}}(t\bar{t})$, in the full phase space at parton level (top row) and in the fiducial phase space at particle level (bottom row). The left and right columns show normalized and absolute cross sections, respectively. For further details see Figure 8.28.

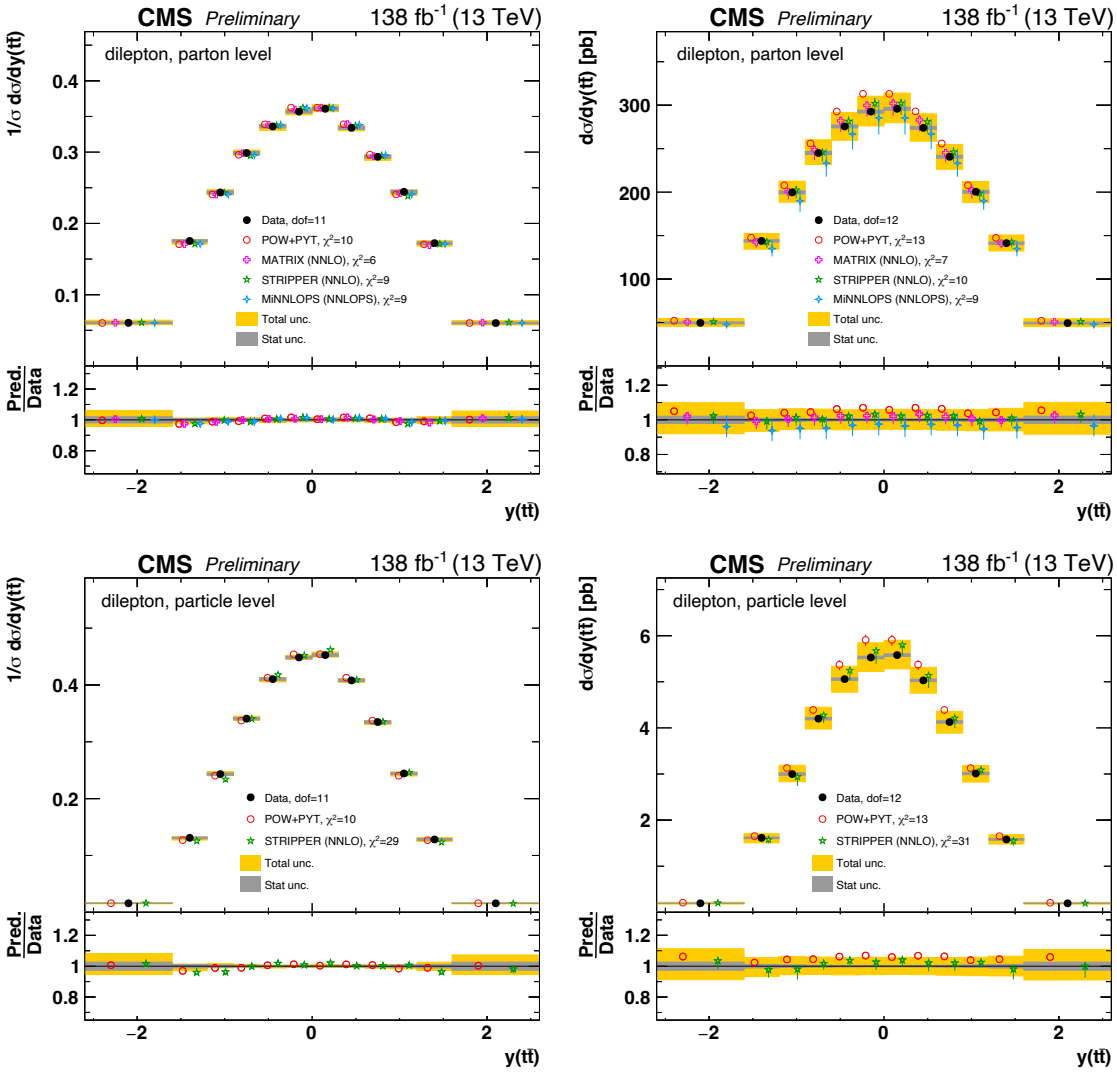

Figure 8.35: Differential $t\bar{t}$ cross sections measured as functions of the rapidity of the $t\bar{t}$ system, $y(t\bar{t})$, in the full phase space at parton level (top row) and in the fiducial phase space at particle level (bottom row). The left and right columns show normalized and absolute cross sections, respectively. For further details see Figure 8.28.

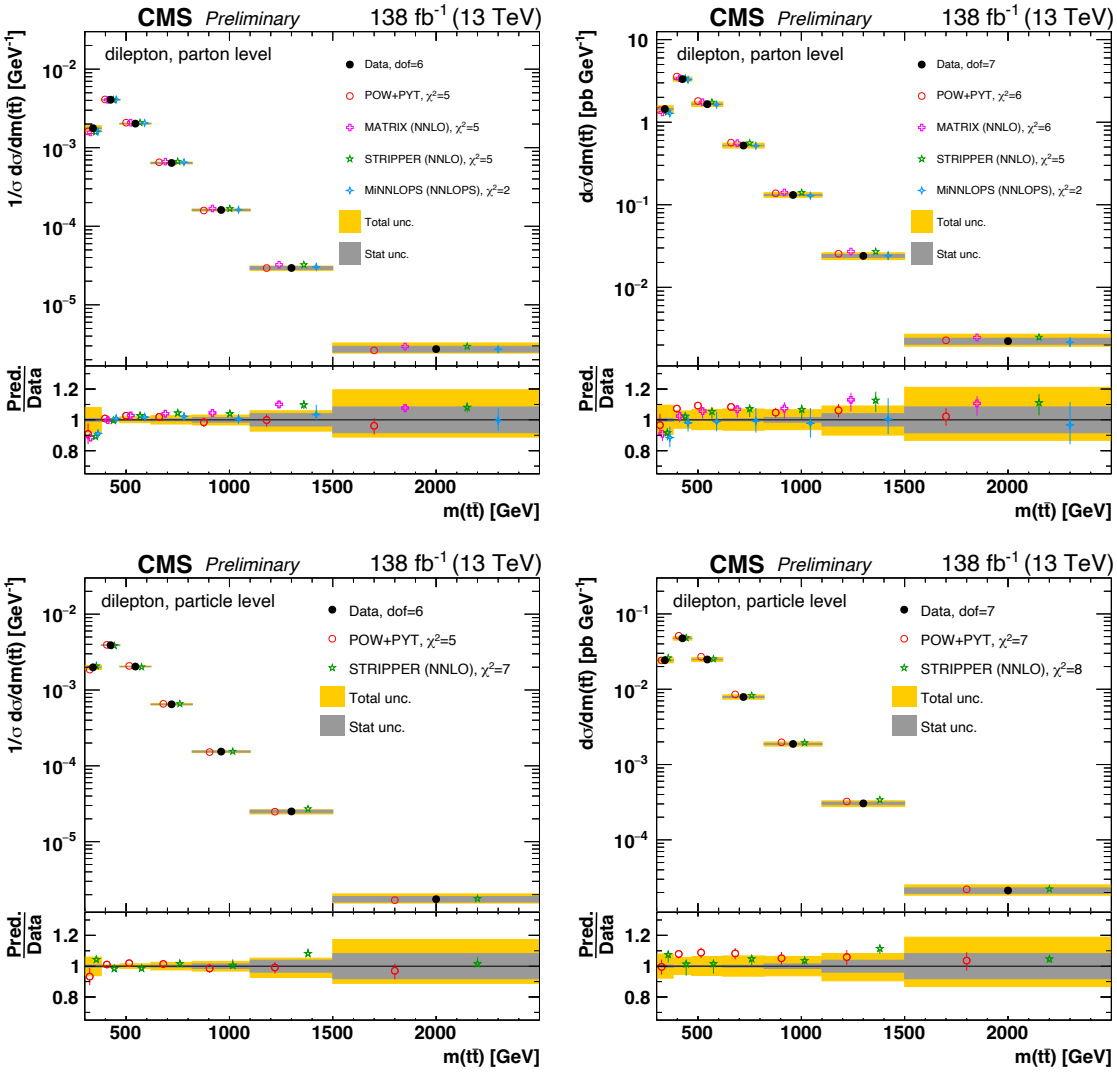

Figure 8.36: Differential $t\bar{t}$ cross sections measured as functions of the invariant mass of the $t\bar{t}$ system, $m(t\bar{t})$, in the full phase space at parton level (top row) and in the fiducial phase space at particle level (bottom row). The left and right columns show normalized and absolute cross sections, respectively. For further details see Figure 8.28.

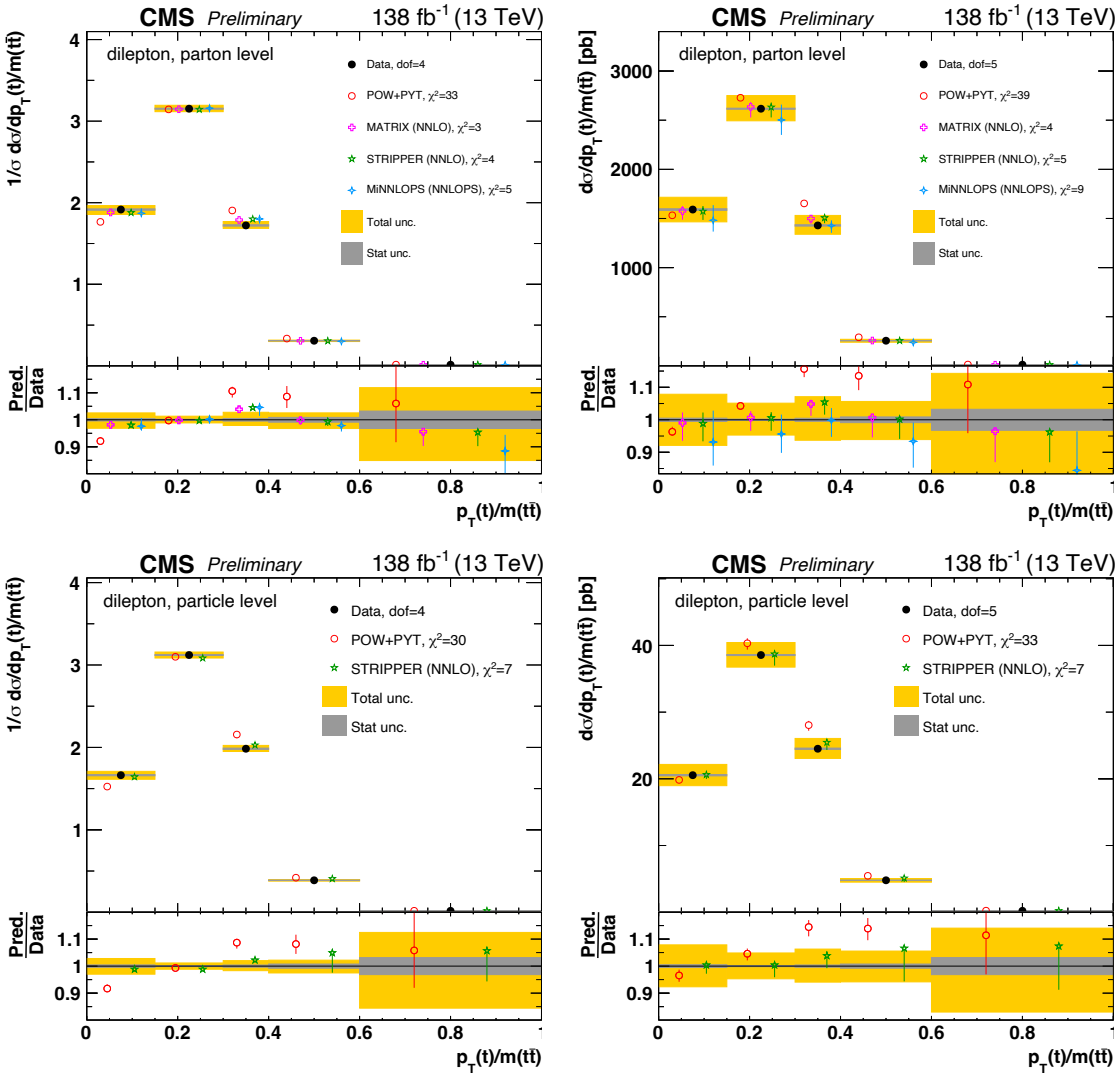

Figure 8.37: Differential $t\bar{t}$ cross sections measured as functions of the ratio of the transverse momentum of the top quark over the invariant mass of the $t\bar{t}$ system, $p_{\mathrm{T}}(t)/m(t\bar{t})$, in the full phase space at parton level (top row) and in the fiducial phase space at particle level (bottom row). The left and right columns show normalized and absolute cross sections, respectively. For further details see Figure 8.28.

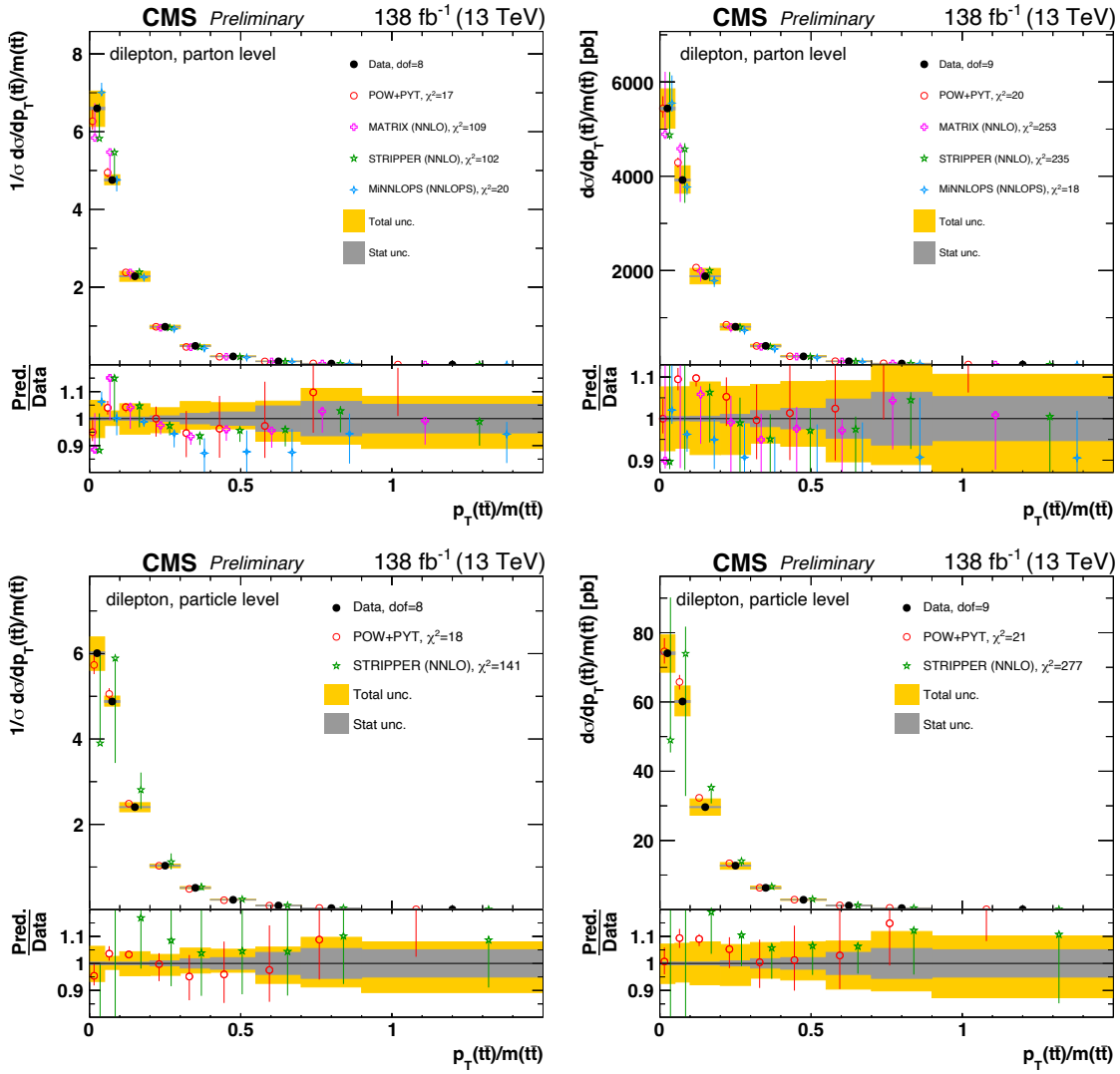

Figure 8.38: Differential $t\bar{t}$ cross sections measured as functions of the ratio of the transverse momentum of the $t\bar{t}$ system over the invariant mass of the $t\bar{t}$ system, $p_{\mathrm{T}}(t\bar{t})/m(t\bar{t})$, in the full phase space at parton level (top row) and in the fiducial phase space at particle level (bottom row). The left and right columns show normalized and absolute cross sections, respectively. For further details see Figure 8.28.

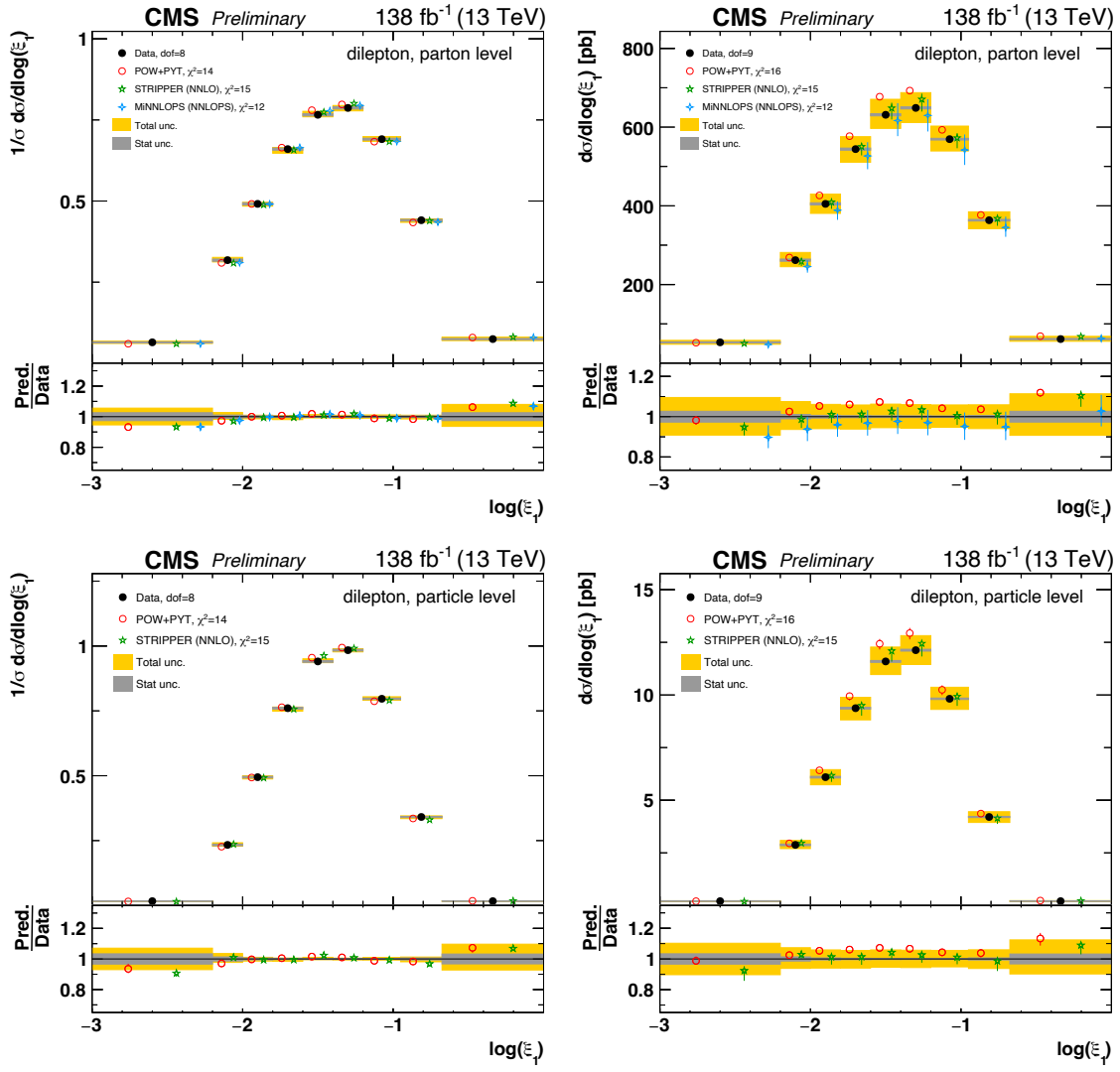

Figure 8.39: Differential $t\bar{t}$ cross sections measured as functions of $\log(\xi_1)$, which is equivalent to the momentum fraction of the incoming parton from one of the protons in the leading order QCD picture, in the full phase space at parton level (top row) and in the fiducial phase space at particle level (bottom row). The left and right columns show normalized and absolute cross sections, respectively. For further details see Figure 8.28.

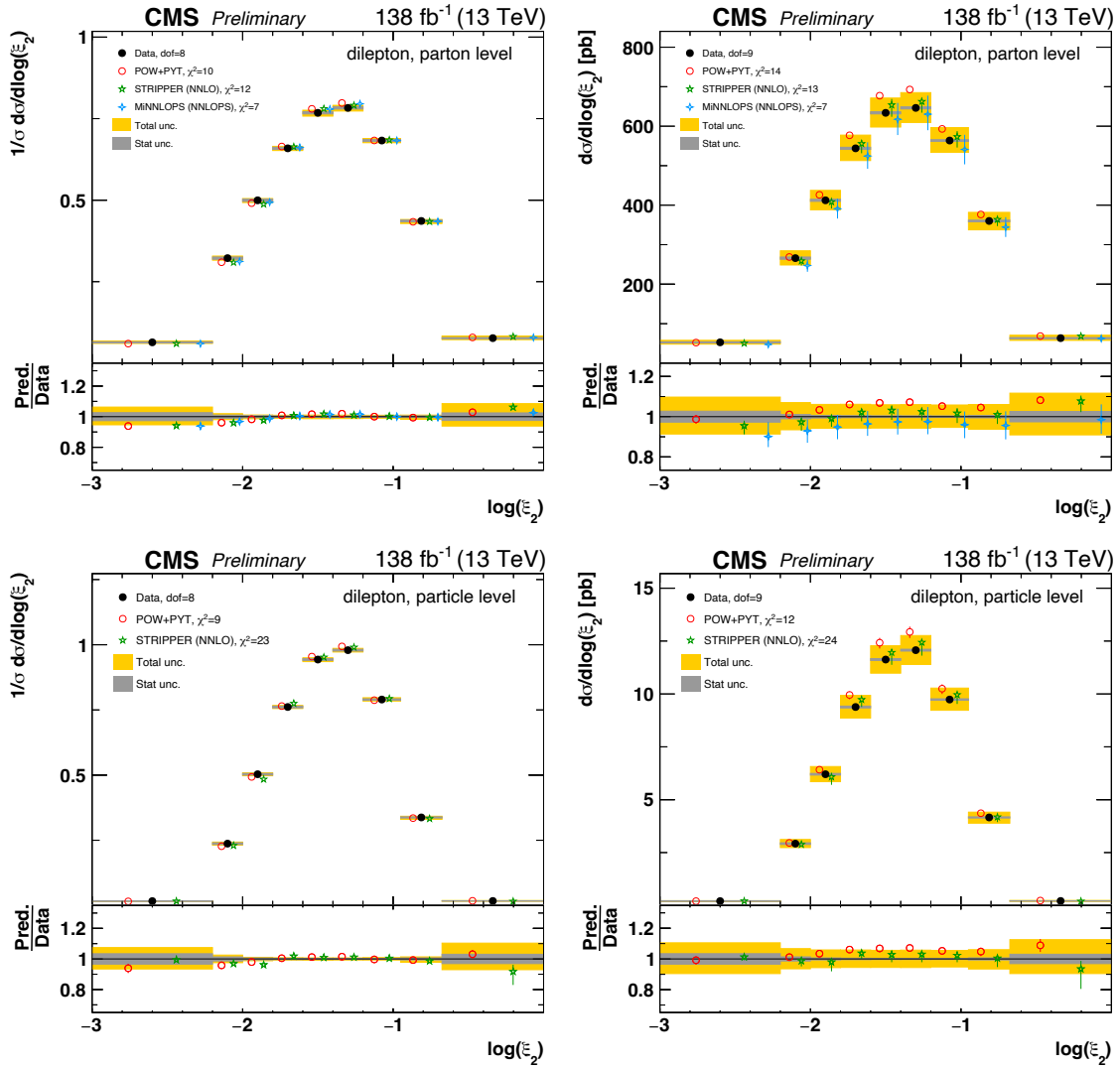

Figure 8.40: Differential $t\bar{t}$ cross sections measured as functions of $\log(\xi_2)$, which is equivalent to the momentum fraction of the incoming parton from one of the protons in the leading order QCD picture, in the full phase space at parton level (top row) and in the fiducial phase space at particle level (bottom row). The left and right columns show normalized and absolute cross sections, respectively. For further details see Figure 8.28.

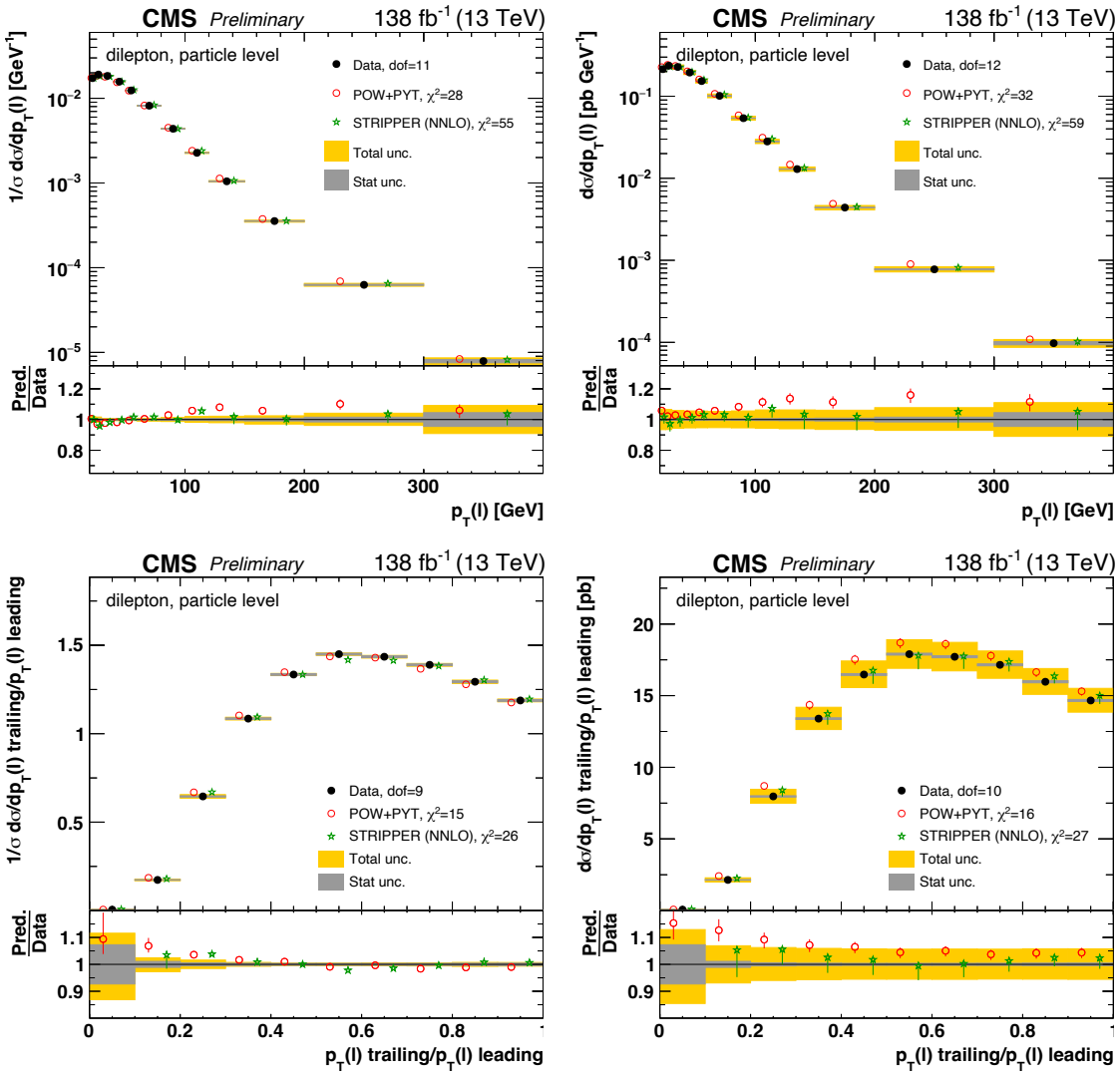

Figure 8.41: Differential $t\bar{t}$ cross sections measured as functions of the transverse momentum of the lepton, $p_{\mathrm{T}}(\ell)$, in the top row and the ratio of the transverse momentum of the trailing lepton over the transverse momentum of the leading lepton, $p_{\mathrm{T}}(\ell)$ trailing/$p_{\mathrm{T}}(\ell)$ leading, in the bottom row. The measurements are performed in the fiducial phase space at particle level. The left and right columns show normalized and absolute cross sections, respectively. For further details see Figure 8.28.

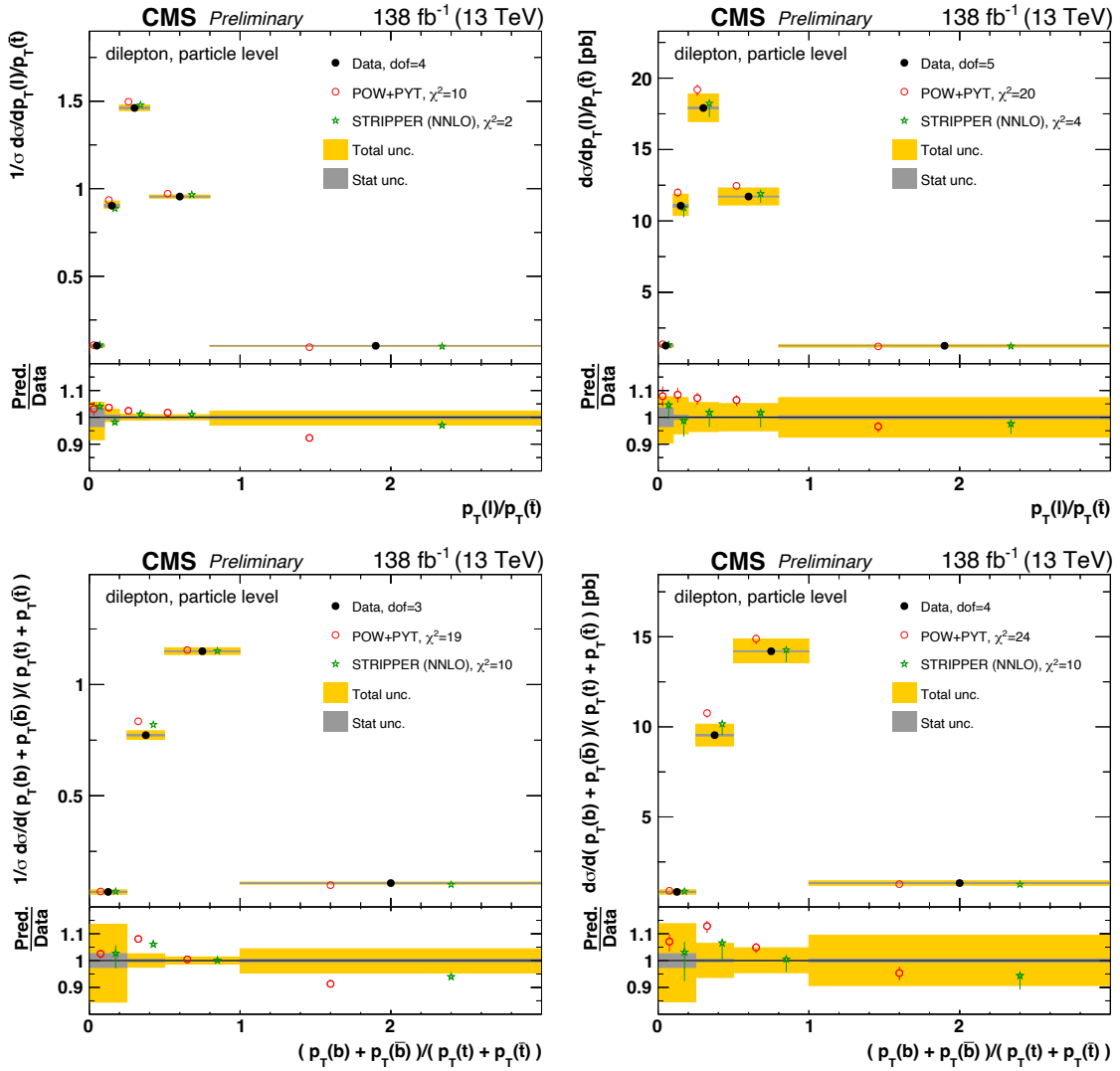

Figure 8.42: Differential $t\bar{t}$ cross sections measured as functions of the ratio of the transverse momentum of the lepton over the transverse momentum of the anti-top quark, $p_{\mathrm{T}}(\ell)/\mathrm{p_T}(\bar{\mathrm{t}})$, in the top row and the ratio of the scalar sum of p_{T} of b and p_{T} of anti-b over the scalar sum of p_{T} of top and p_{T} of anti-top, $(p_{\mathrm{T}}(\mathrm{b}) + \mathrm{p_T}(\bar{\mathrm{b}}))/(\mathrm{p_T}(\mathrm{t}) + \mathrm{p_T}(\bar{\mathrm{t}}))$, in the bottom row. The measurements are performed in the fiducial phase space at particle level. The left and right columns show normalized and absolute cross sections, respectively. For further details see Figure 8.28.

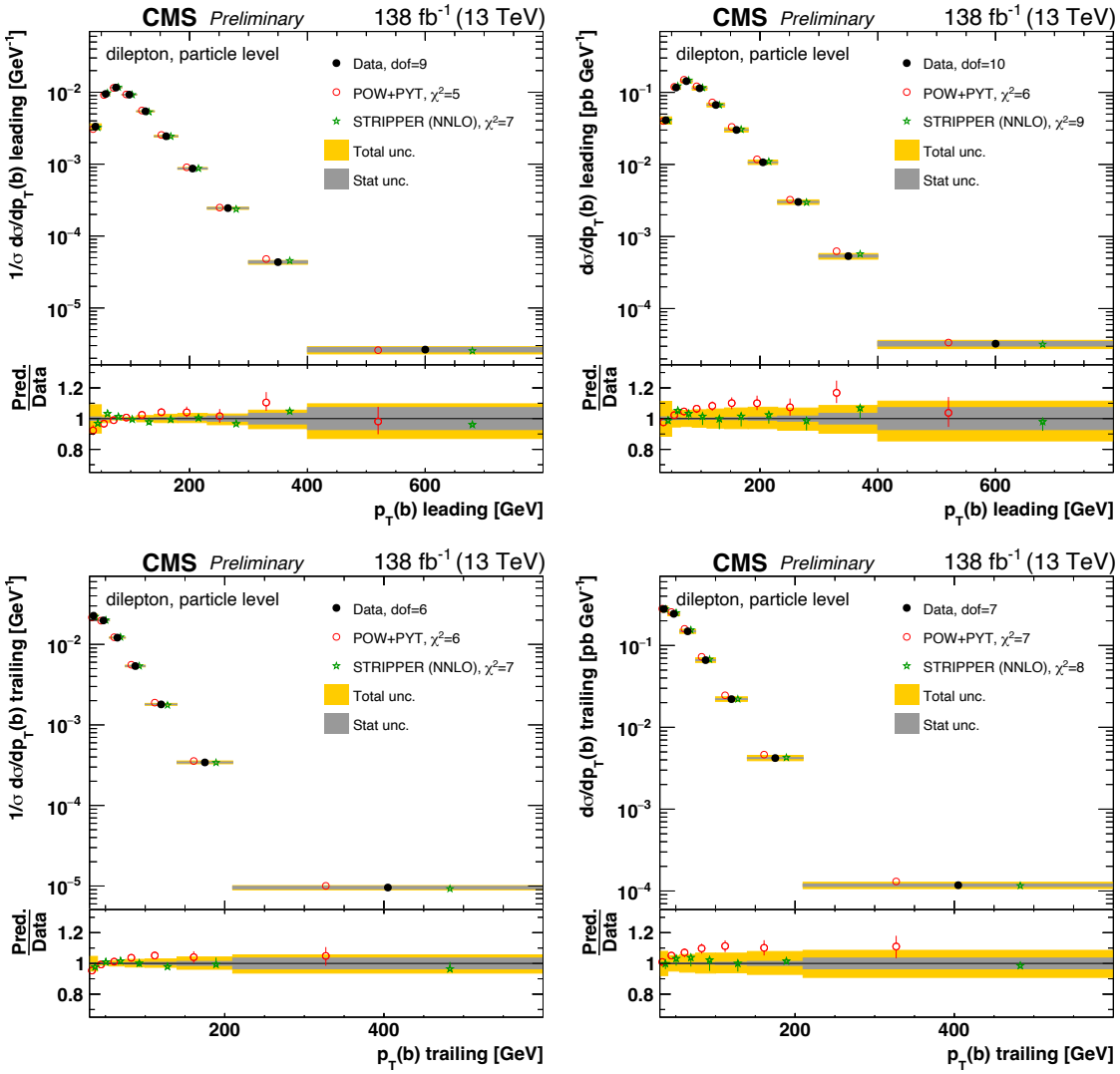

Figure 8.43: Differential $t\bar{t}$ cross sections measured as functions of the transverse momentum of the leading b quark, p_{T}(b) leading, in the top row and the transverse momentum of the trailing b quark, p_{T}(b) trailing, in the bottom row. The measurements are performed in the fiducial phase space at particle level. The left and right columns show normalized and absolute cross sections, respectively. For further details see Figure 8.28.

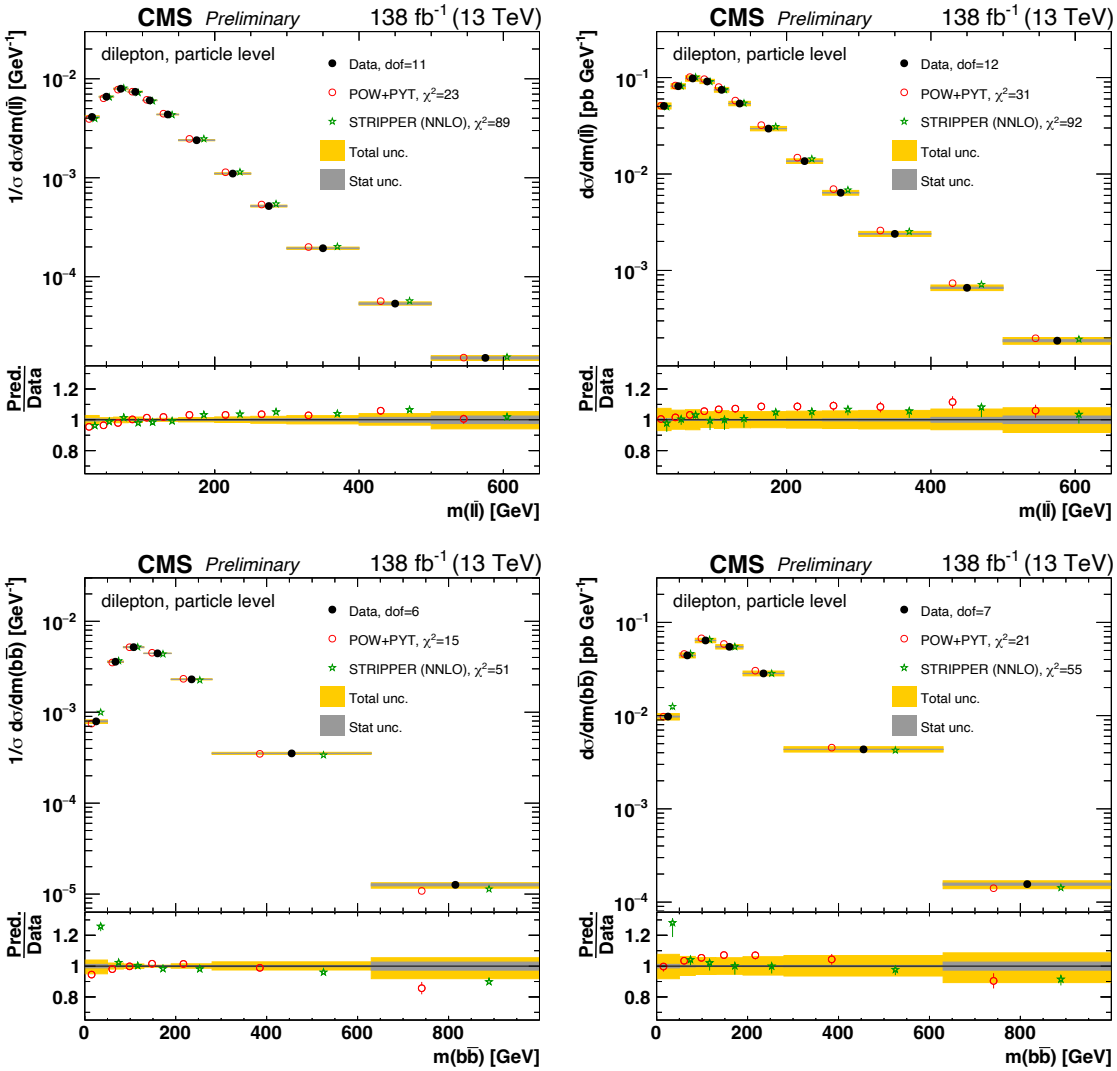

Figure 8.44: Differential $t\bar{t}$ cross sections measured as functions of the invariant mass of the $\ell\bar{\ell}$ system, $m(\ell\bar{\ell})$, in the top row and the invariant mass of the $b\bar{b}$ system, $m(b\bar{b})$, in the bottom row. The measurements are performed in the fiducial phase space at particle level. The left and right columns show normalized and absolute cross sections, respectively. For further details see Figure 8.28.

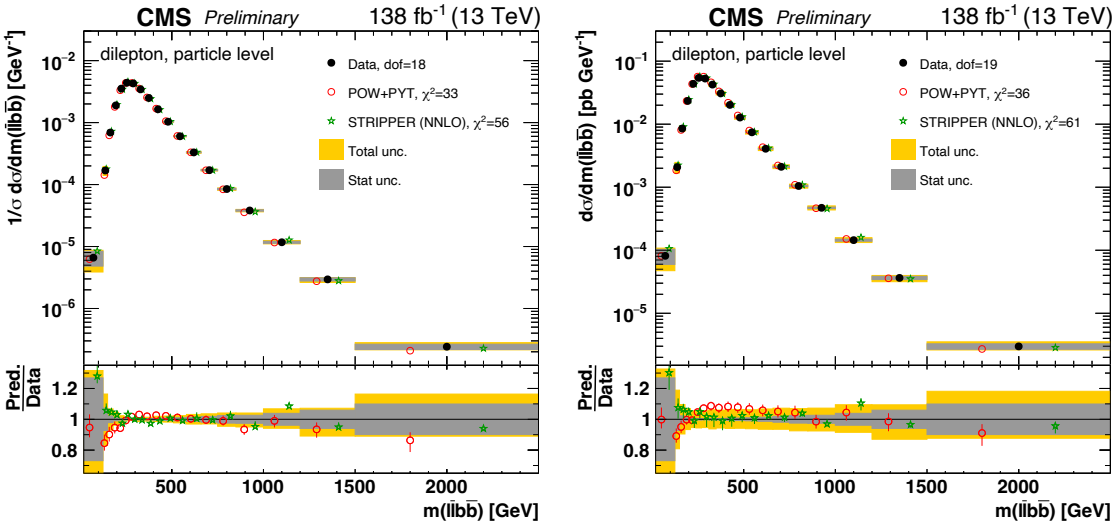

Figure 8.45: Differential $t\bar{t}$ cross sections measured as functions of the invariant mass of the $l\bar{l}b\bar{b}$ system, $m(\ell\bar{\ell}\mathrm{b}\bar{\mathrm{b}})$, in the fiducial phase space at particle level for normalized (left) and absolute (right) distributions. For further details see Figure 8.28.

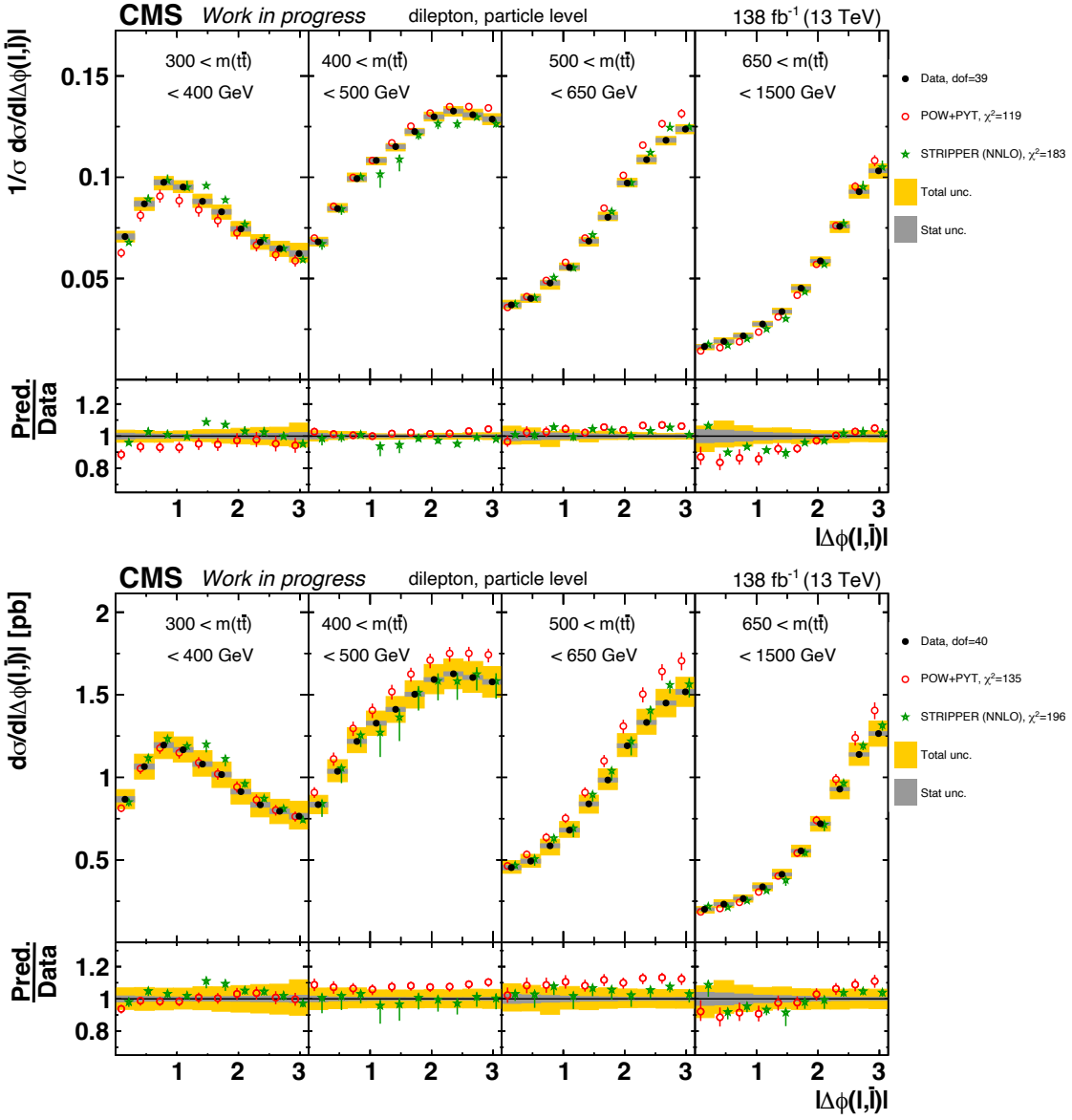

Figure 8.46: Differential $t\bar{t}$ cross sections measured as functions of the absolute value of the azimuthal angle between the lepton and the anti-lepton, $|\Delta\phi(\ell,\bar{\ell})|$, in ranges of the invariant mass of the $t\bar{t}$ system, $m(t\bar{t})$, for both normalized (top) and absolute (bottom) measurements performed in the fiducial phase space at particle level. For further details see Figure 8.28.

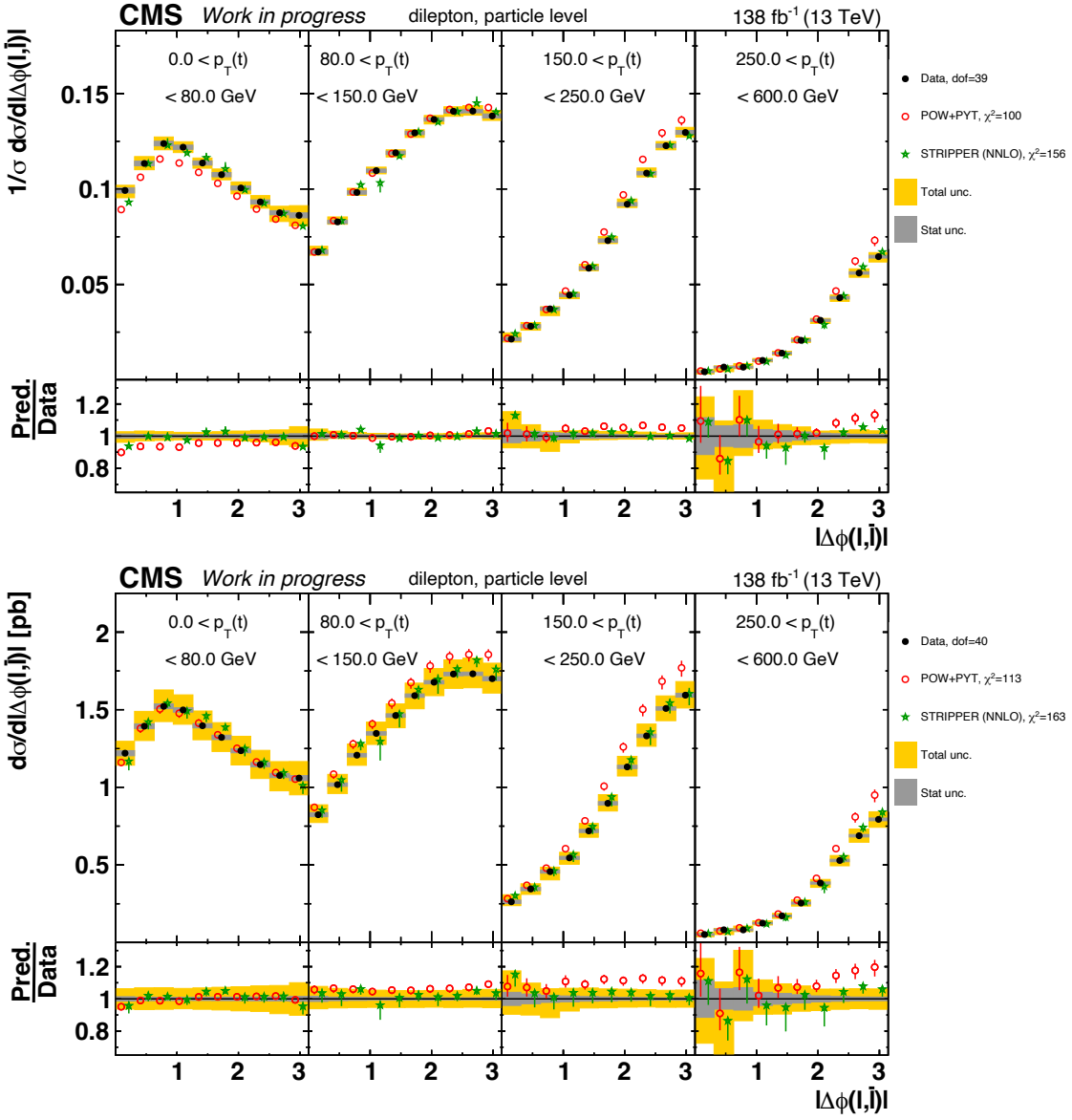

Figure 8.47: Differential $t\bar{t}$ cross sections measured as functions of the absolute value of the azimuthal angle between the lepton and the anti-lepton, $|\Delta\phi(\ell,\bar{\ell})|$, in ranges of the transverse momentum of the top, $p_{\mathrm{T}}(t)$, for both normalized (top) and absolute (bottom) measurements performed in the fiducial phase space at particle level. For further details see Figure 8.28.

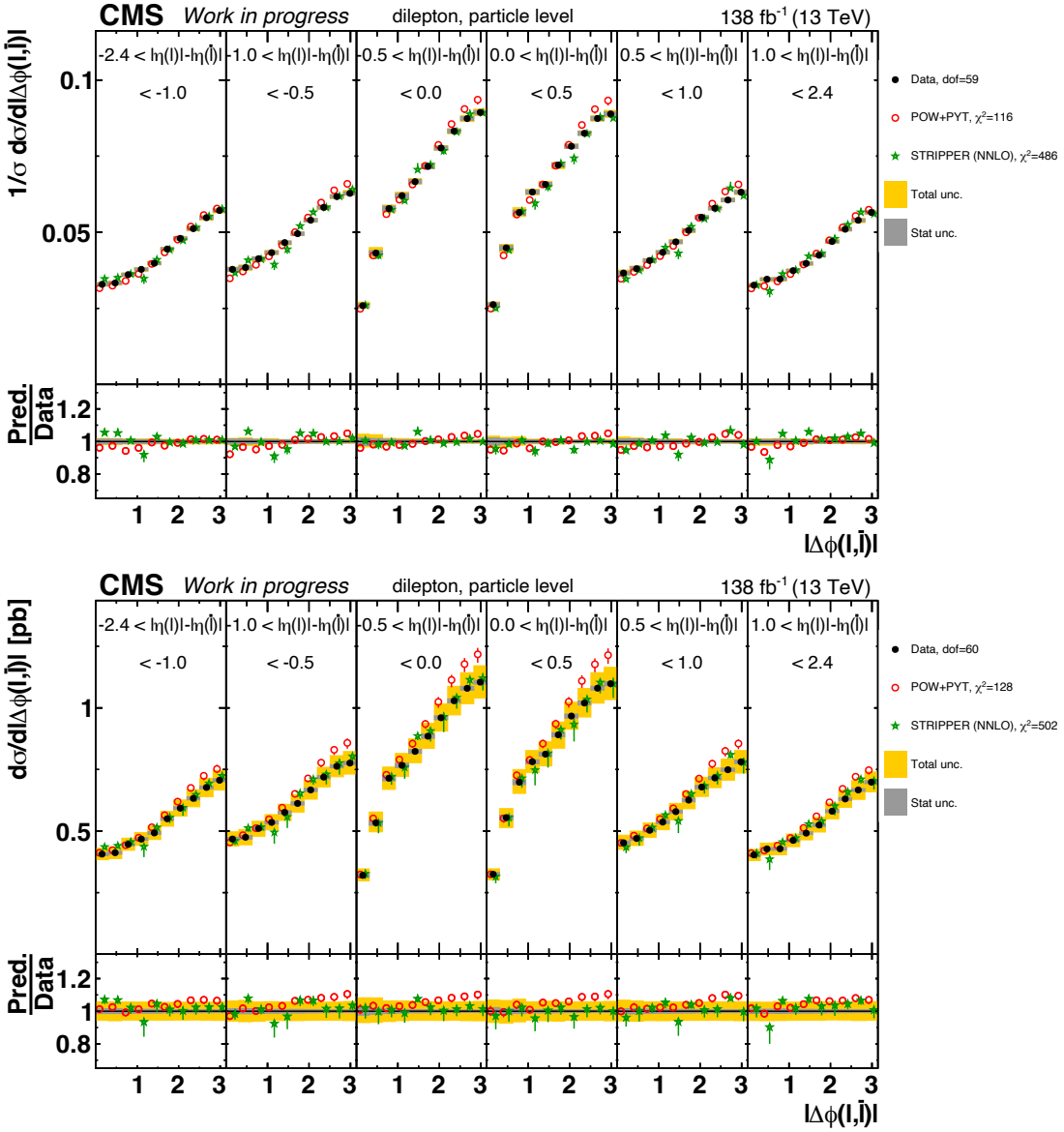

Figure 8.48: Differential $t\bar{t}$ cross sections measured as functions of the absolute value of the azimuthal angle between the lepton and the anti-lepton, $|\Delta\phi(\ell,\bar{\ell})|$, in ranges of the difference in absolute value of pseudorapidity of the lepton and absolute value of pseudorapidity of the anti-lepton, $|\eta(\ell)| - |\eta(\bar{\ell})|$, for both normalized (top) and absolute (bottom) measurements performed in the fiducial phase space at particle level. For further details see Figure 8.28.

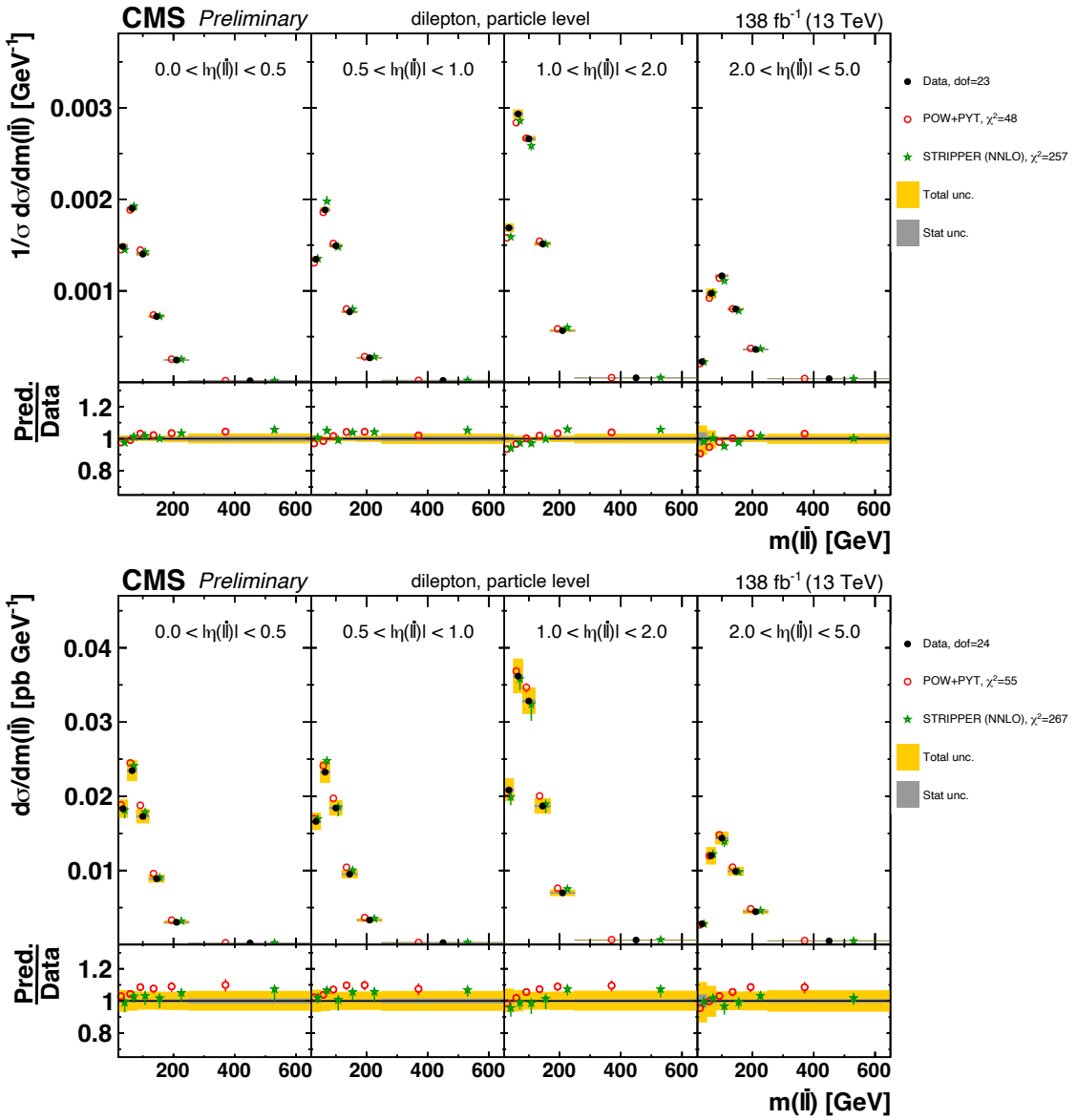

Figure 8.49: Differential $t\bar{t}$ cross sections measured as functions of the invariant mass of the $\ell\bar{\ell}$ system, $m(\ell\bar{\ell})$, in ranges of the absolute pseudorapidity of the $\ell\bar{\ell}$ system, $|\eta(\ell\bar{\ell})|$, for both normalized (top) and absolute (bottom) measurements performed in the fiducial phase space at particle level. For further details see Figure 8.28.

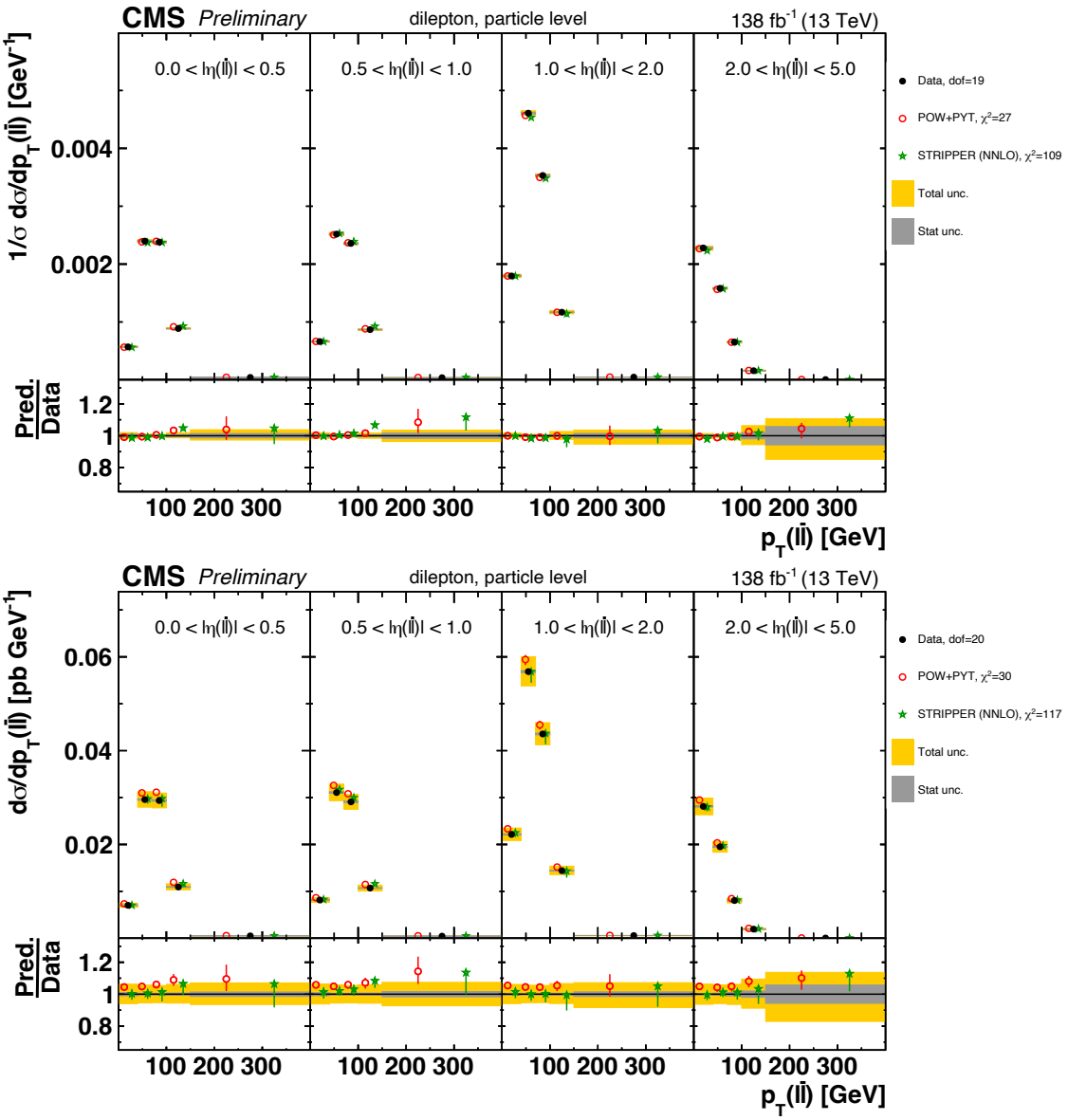

Figure 8.50: Differential $t\bar{t}$ cross sections measured as functions of the transverse momentum of the $\ell\bar{\ell}$ system, $p_{\mathrm{T}}(\ell\bar{\ell})$, in ranges of the absolute pseudorapidity of the $\ell\bar{\ell}$ system, $|\eta(\ell\bar{\ell})|$, for both normalized (top) and absolute (bottom) measurements performed in the fiducial phase space at particle level. For further details see Figure 8.28.

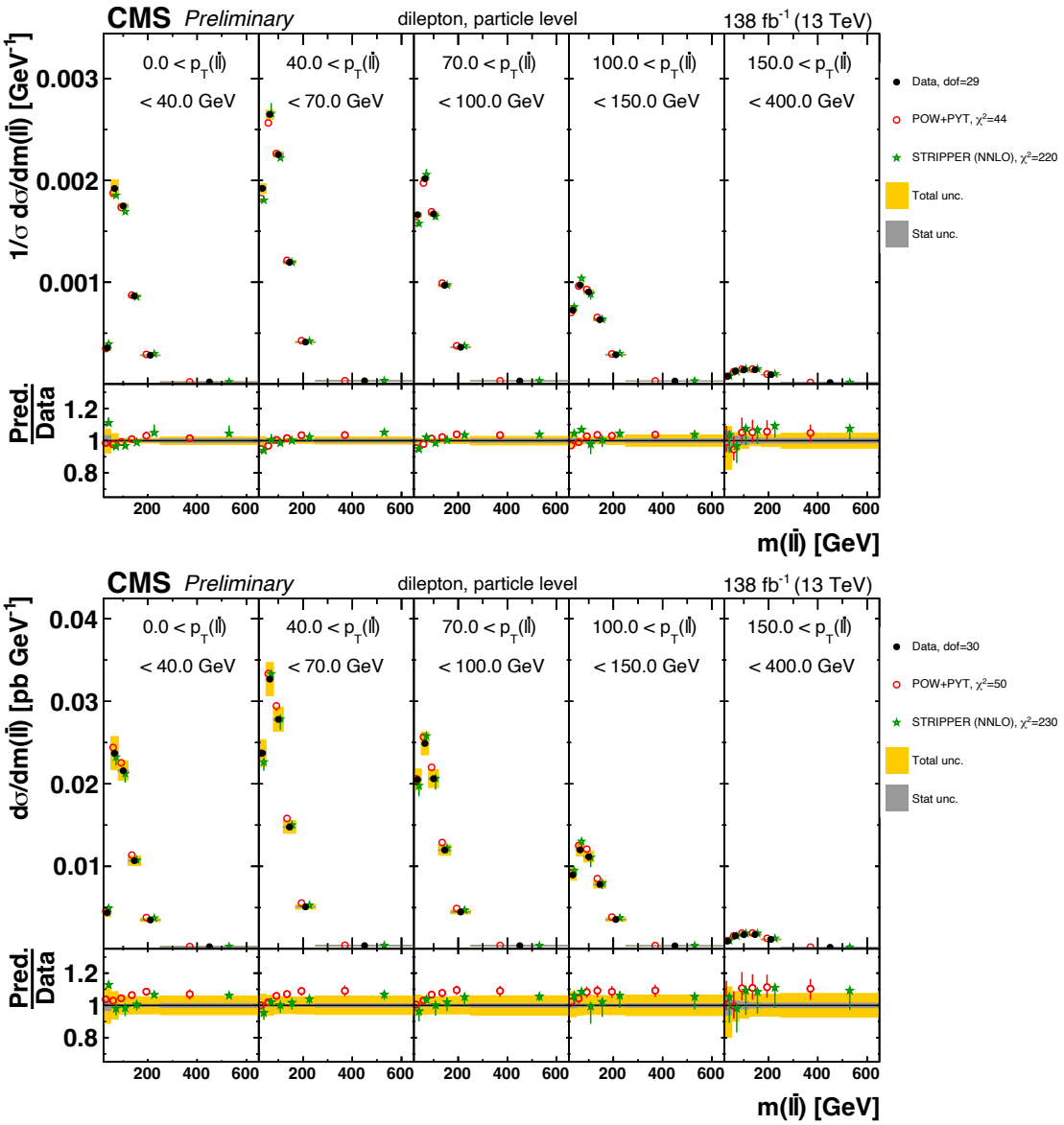

Figure 8.51: Differential $t\bar{t}$ cross sections measured as functions of the invariant mass of the $\ell\bar{\ell}$ system, $m(\ell\bar{\ell})$, in ranges of the transverse momentum of the $\ell\bar{\ell}$ system, $p_{\mathrm{T}}(\ell\bar{\ell})$, for both normalized (top) and absolute (bottom) measurements performed in the fiducial phase space at particle level. For further details see Figure 8.28.

8.2.7 Comparisons to alternative PDF models

Top pair production at the LHC predominantly happens via gluon-gluon fusion, as explained in Chapter 2. This means that certain differential cross sections show a particular sensitivity to the gluon density in PDF sets for large values of x. A selected number of the differential cross sections, which exhibit such sensitivity to the choice of PDF, are shown in Figures 8.52 to 8.54. The POW+PYT reference simulation is performed with the PDF set NNPDF3.1 at NNLO accuracy as previously stated and is shown in the figures as "NNPDF3.1 NNLO". For comparison these figures additionally show POW+PYT simulations performed with different PDF sets, namely NNPDF3.1 [32], CT14 [149], ABMP16 [150], MMHT2014 [151] and HERAPDF2.0 [33] at NLO accuracy. They differ in the input data they use and how they are extracted and modelled [155, 156].

Cross sections measured as functions of $p_{\mathrm{T}}(t)$ and $y(t)$ are shown in Figure 8.52. From the p_{T} spectra one can see that the data is well described by HERAPDF2.0, while other PDF sets exhibit the same positive slope in p_{T} as observed for the reference PDF. The $y(t)$ spectra illustrate the fact that all PDF sets are slightly more central than data, however, this effect is most pronounced for HERAPDF2.0, which also underestimates the data significantly in the outer bins giving rise to a considerably higher χ^2 value. Figure 8.53 shows measurements of $y(t\bar{t})$ and $m(t\bar{t})$, whose χ^2 values also indicate that HERAPDF2.0 performs worse than other PDFs. In the latter distribution, HERAPDF2.0 follows the same trend in $m(t\bar{t})$ as the other PDFs but begins to significantly underestimate the data according to a negative slope when $m(t\bar{t}) > 1000$ GeV.

Cross sections measured as functions of $\log(\xi_1)$ and $\log(\xi_2)$ are shown in Figure 8.54. As previously mentioned, ξ is equivalent to the proton momentum fractions of the incoming partons at leading order in QCD. Neither PDF set describes the data well in the highest bin but HERAPDF2.0 also underestimates the data in the lowest bin, which could possibly mean that the gluon density in this PDF is not entirely accurate in the extreme ends of the spectra, corresponding to small and large proton momentum fractions.

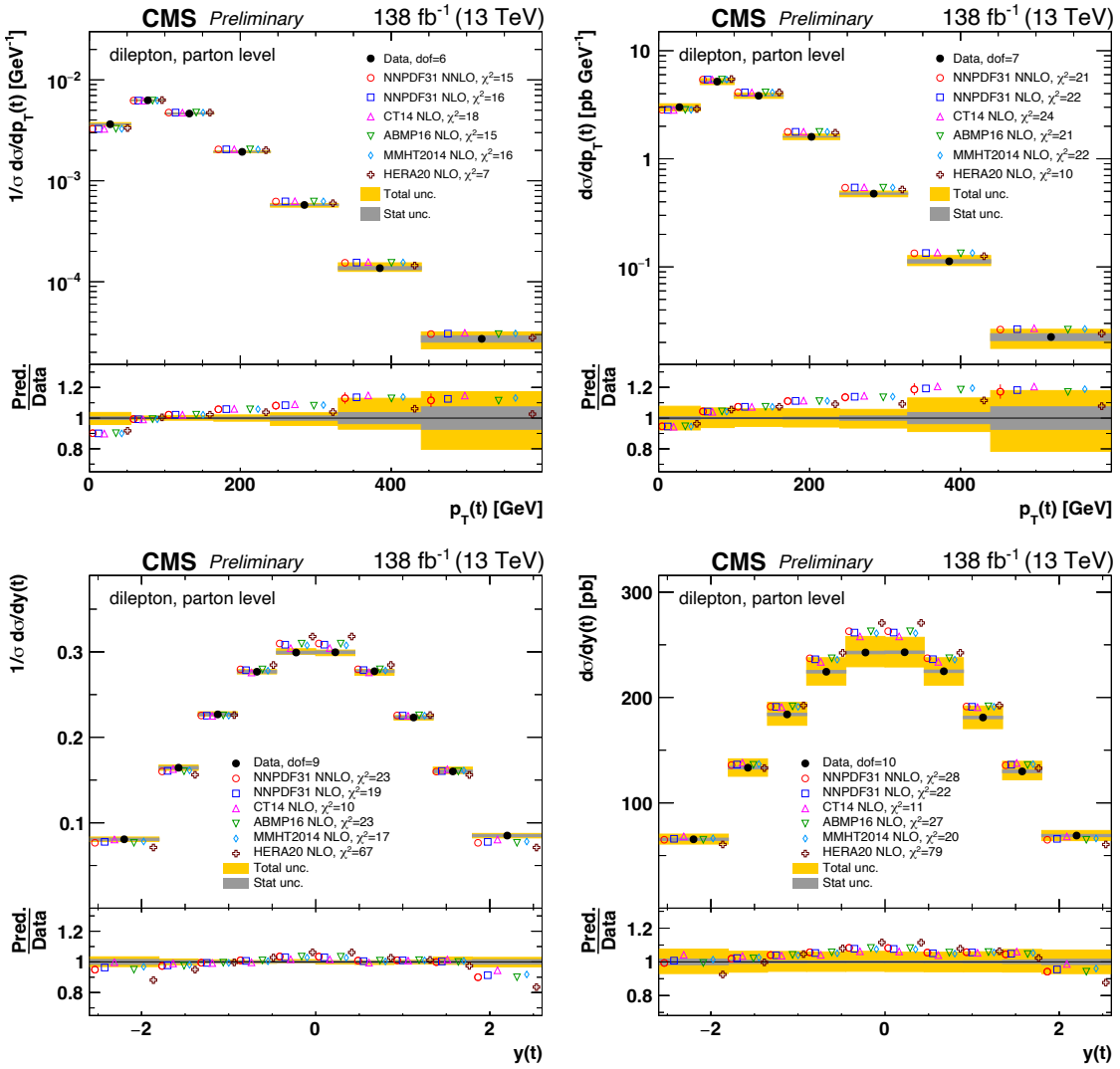

Figure 8.52: Differential $t\bar{t}$ cross sections measured as functions of the transverse momentum of the top, $p_{\mathrm{T}}(t)$, in the top row, and the rapidity of the top, $y(t)$, in the bottom row. Both cross sections are measured in the full phase space at parton level, and the left and right columns show normalized and absolute cross sections, respectively. The data (black dots) is shown together with the POW+PYT reference simulation, depicted in red and denoted by the corresponding reference PDF set NNPDF3.1 at NNLO accuracy. POW+PYT simulations, where the PDF sets NNPDF3.1 (blue), CT14 (magenta), ABMP16 (green), MMHT2014 (cyan) and HERAPDF2.0 (dark red) at NLO accuracy are used instead, are also shown. The statistical and total uncertainties on the data are illustrated by the grey and yellow bands, respectively, where the latter corresponds to systematic and statistical uncertainties added in quadrature. The uncertainties on the reference simulation are indicated by error bars. Furthermore, a χ^2 value that takes all measurement uncertainties into account is reported for the reference simulation and all alternative simulations with different PDF sets, and the ratios with respect to data are shown in the bottom panel of each plot.

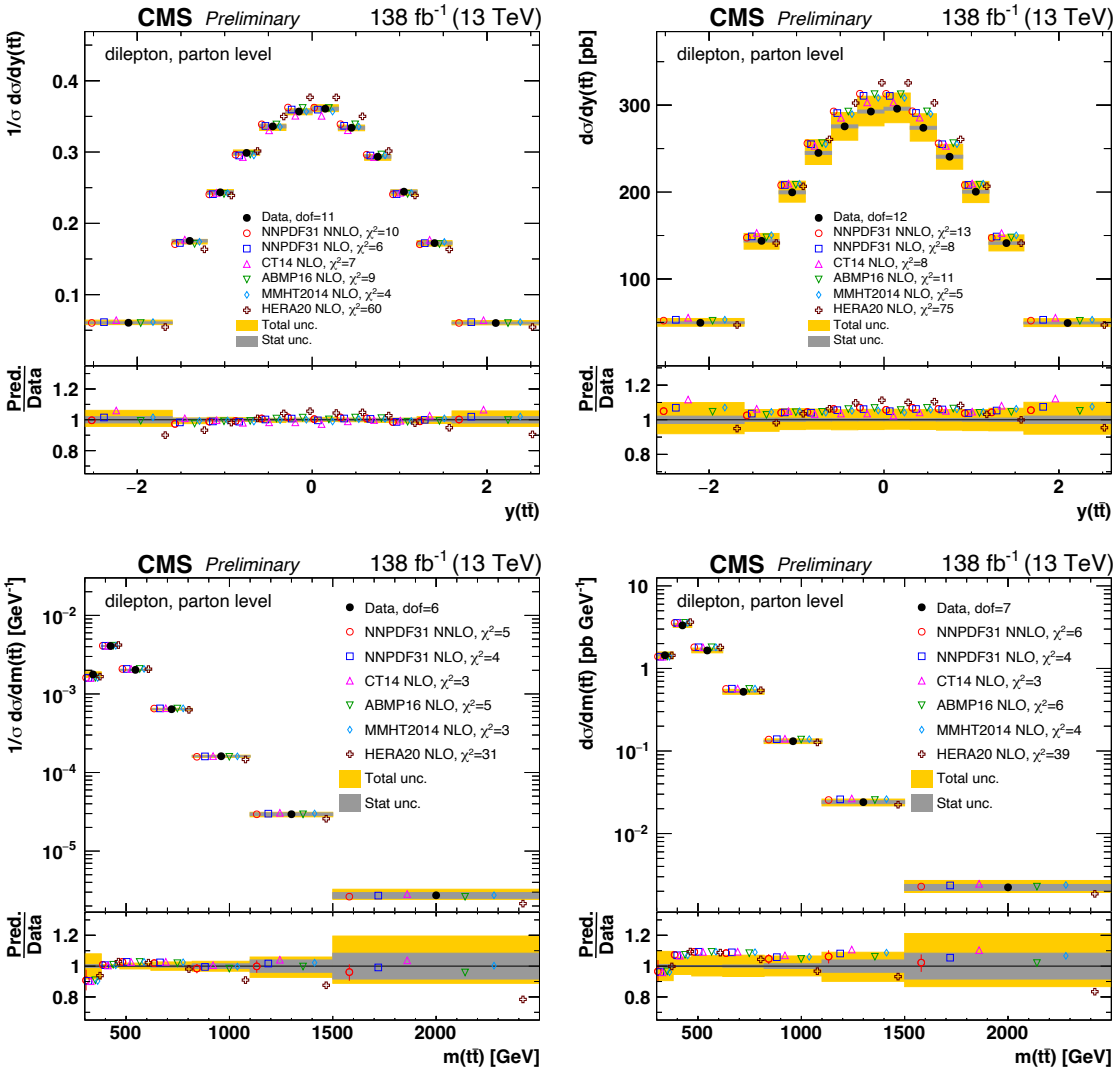

Figure 8.53: Differential $t\bar{t}$ cross sections measured as functions of the rapidity of the $t\bar{t}$ system, $y(t\bar{t})$, in the top row, and the invariant mass of the $t\bar{t}$ system, $m(t\bar{t})$, in the bottom row. Both cross sections are measured in the full phase space at parton level, and the left and right columns show normalized and absolute cross sections, respectively. For further details see Figure 8.52.

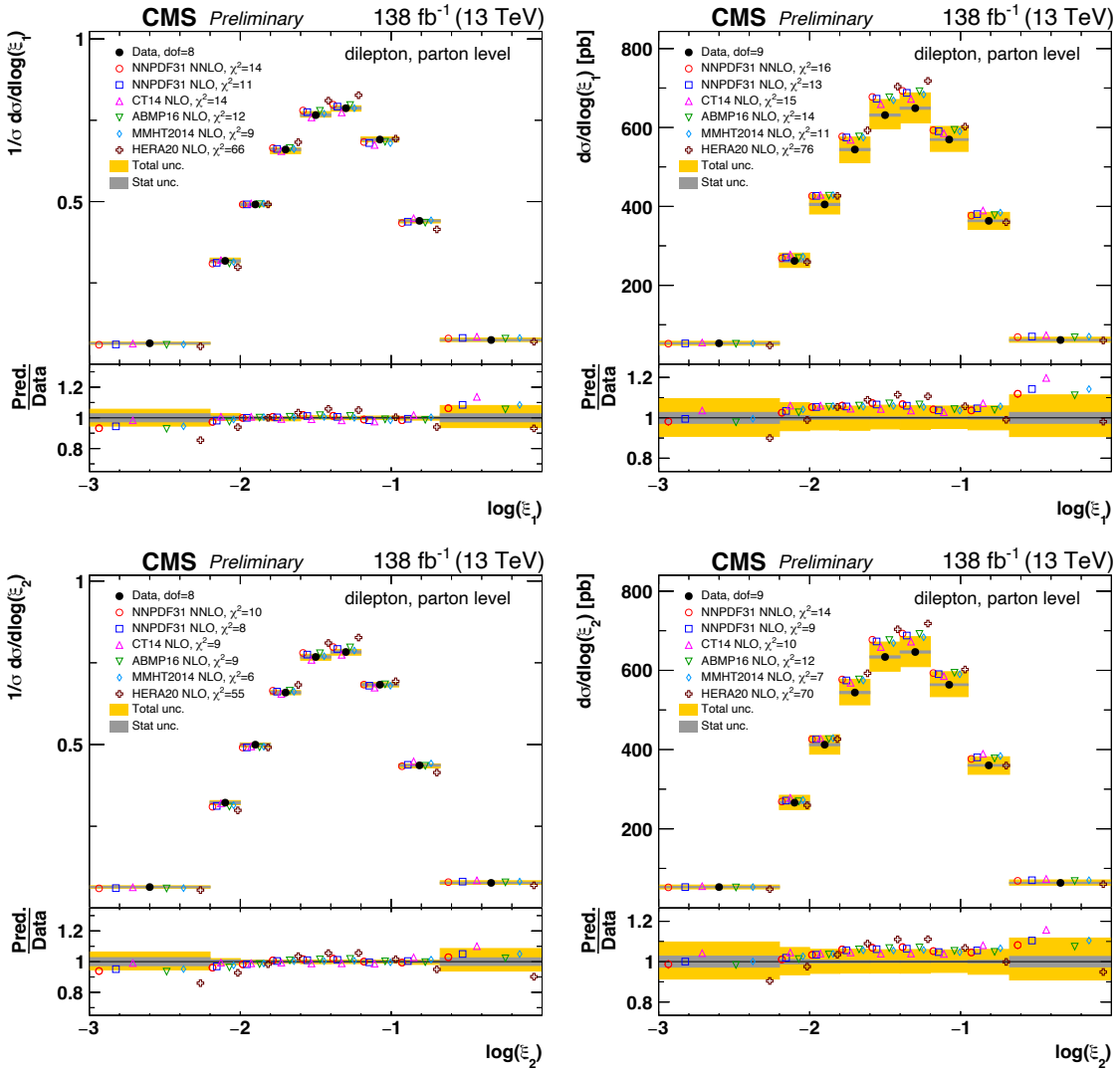

Figure 8.54: Differential $t\bar{t}$ cross sections measured as functions of $\log(\xi_1)$ (top row) and $\log(\xi_2)$ (bottom row), which are equivalent to the proton momentum fractions of the incoming partons in the leading order QCD picture. Both cross sections are measured in the full phase space at parton level, and the left and right columns show normalized and absolute cross sections, respectively. For further details see Figure 8.52.

Chapter 9

Conclusion

In this work, differential cross section measurements of $t\bar{t}$ production in pp collisions at center-of-mass energies of 13 TeV were presented. The data used was recorded with the CMS experiment at the LHC in the period from the beginning of 2016 until the end of 2018, which is known as Run 2, corresponding to an integrated luminosity of 137.6 fb^{-1}. The measurements were performed in the dilepton channel, which constitutes final states of oppositely charged lepton pairs, i.e. $e^{\pm}e^{\mp}$, $\mu^{\pm}\mu^{\mp}$ and $e^{\pm}\mu^{\mp}$, arising as a result of the prompt decays of the W bosons in the top and anti-top decay chains. Both absolute and normalized cross section measurements were presented as functions of one or more kinematic observables of the $t\bar{t}$ system, the top and anti-top quarks and their decay products, the charged leptons and beauty flavoured jets, as well as the total jet multiplicity in the event, which includes extra jets from the hard interaction or parton shower. All measurements related to the $t\bar{t}$ system or top quarks were performed at both parton and particle level in the full and fiducial phases, respectively, while those related to the charged leptons and beauty flavoured jets were performed at particle level in the fiducial phase space only. The differential cross sections were extracted by subtracting simulated background contributions from the data and applying a regularized unfolding procedure to correct measurements of the signal process for the finite detector acceptance, efficiency and resolution.

The differential cross sections are measured with a precision that is between 2 and 25%, including all statistical and systematic uncertainties. This corresponds to a reduction by a factor of ≈ 2 with respect to the previous analysis, where differential $t\bar{t}$ production cross sections in pp collisions at 13 TeV were measured in the dilepton channel using 2016 data only [14]. This improvement is in part due to the abundance of statistics for both data and MC but also due to the following reasons: the algorithms and methods for identifying and reconstructing the physics objects have been improved for e.g. b-jets, separate calibrations have been applied for each year of data-taking, e.g. for the jet energy scale, and finally the estimation of the Z+jets background contribution has been improved.

Different theory to data comparisons are performed. First, all measurements are compared to NLO plus parton shower MC models. The reference generator is Powheg (version 2)+Pythia8 [67, 70–72] and two alternative models are also

studied: MG5_aMC@NLO[FxFx] (version 2.4.2)+Pythia8 [67, 73, 76, 77] and Powheg (version 2)+Herwig7 [69–72]. The predicted top $p_{\mathrm{T}}(t)$ spectra is observed to be harder than data for all models except Powheg (version 2)+Herwig7, which shows no positive slope in its predictions with respect to data. The presence of a slope is known as the top p_{T} problem and has previously been observed at both ATLAS and CMS in the semi-leptonic and dileptonic decay modes of the $t\bar{t}$ pair [11, 13, 14]. All models predict the top rapidity to be more central than is observed in data although they still give a reasonable description of the spectrum on the whole. A reasonable description of data by the MC models is also seen for the rapidity and invariant mass of the $t\bar{t}$ system but its transverse momentum is not well described by any model. Cross sections are studied as functions of several new ratio observables and, for example, distributions of the $p_{\mathrm{T}}(t)$ over the $t\bar{t}$ invariant mass, $p_{\mathrm{T}}(t)/m(t\bar{t})$, indicate that the top p_{T} problem is enhanced when $m(t\bar{t})$ is large. Similarly, the mismodelling of the $p_{\mathrm{T}}(t\bar{t})$ spectra appears to be significantly enhanced in distributions of this observable over the $t\bar{t}$ invariant mass, $p_{\mathrm{T}}(t\bar{t})/m(t\bar{t})$.

The distributions of the charged leptons and b-jets clearly benefit from the excellent resolution of these objects at the CMS experiment and are among the results measured with the greatest precision. This further facilitates measurements of highly resolved and precise double differential cross sections of $t\bar{t}$ production, measured as functions of kinematic spectra of the leptons in bins of other kinematic variables of the top quarks, $t\bar{t}$ or $\ell\bar{\ell}$ system, as well as a survey of the full set of independent kinematic variables of the $\ell\bar{\ell}$ system, $|\eta(\ell\bar{\ell})|$, $m(\ell\bar{\ell})$ and $p_{\mathrm{T}}(\ell\bar{\ell})$, and their correlations. The single-differential measurement of $p_{\mathrm{T}}(\ell)$ exhibits a similar positive slope in p_{T} as is seen for $p_{\mathrm{T}}(t)$ and in general all models, except Powheg (version 2)+Herwig7, tend to predict harder p_{T} spectra than is observed in data. Out of the measured invariant mass distributions of partial decay systems originating from the $t\bar{t}$ pair, i.e. $m(\ell\bar{\ell})$, $m(b\bar{b})$ and $m(\ell\bar{\ell}\mathrm{b}\bar{\mathrm{b}})$, that of the $l\bar{l}b\bar{b}$ system is shown to provide a very good sensitivity to the top mass, especially at threshold. A particularly good distinction between the different MC models is seen for the double-differential measurements performed as a function of $|\Delta\phi(\ell,\bar{\ell})|$, e.g. $[p_{\mathrm{T}}(t), |\Delta\phi(\ell,\bar{\ell})|]$. No single MC model provides a good description of the data in all measured cross sections, but the reference generator Powheg (version 2)+Pythia8 generally performs the best, while the poorest performance is seen for MG5_aMC@NLO[FxFx] (version 2.4.2)+Pythia8.

A second set of theory to data comparisons is performed, showing different SM predictions at NNLO or even higher order accuracy in QCD. Differential $t\bar{t}$ production cross sections measured as functions of kinematic spectra of the top quarks and $t\bar{t}$ system are shown to be better described by predictions at beyond-NLO accuracy in comparison to the NLO MC reference model Powheg (version 2)+Pythia8. However, exceptions are $|\Delta\phi(t,\bar{t})|$, $p_{\mathrm{T}}(t\bar{t})$ and $p_{\mathrm{T}}(t\bar{t})/m(t\bar{t})$, where the fixed-order predictions generally exhibit a relatively poor data description accompanied by large theory scale uncertainties.

Cross sections measured as functions of kinematic spectra of the charged leptons and beauty flavoured jets, generally show a worse or similar performance with respect to the NLO MC model. Predictions provided by Stripper [130–133], which

are also available at particle level at NNLO, are shown to result in particularly high χ^2 values for the measured double differential cross sections, which can be attributed to small distortions around the data distributions exhibited by STRIPPER.

In the third and final set of theory to data comparisons the POWHEG (version 2)+PYTHIA8 predictions are shown using alternative PDF sets. The cross sections measured as functions of $\log(\xi_1)$ and $\log(\xi_2)$, which are equivalent to the proton momentum fractions of the incoming partons in the leading order QCD picture, are shown to be sensitive to the gluon density at proton momentum fractions ranging from ~ 0.03 to ~ 0.2. These distributions also show that the predictions with the HERAPDF2.0 set [33] underestimate the data in the lowest and highest regions, corresponding to small and large proton momentum fractions, respectively, which could possibly mean that the gluon density in this PDF is not entirely accurate in the extreme ends of the spectra.

ATLAS has performed differential cross section measurements of $t\bar{t}$ production in, for example, the lepton+jets [13] and dilepton [157] channels in pp collisions at center-of-mass energies of 13 TeV, using the 2015 and 2016 data, corresponding to an integrated luminosity of 36 fb^{-1}. The lepton+jets paper, in particular, includes a wealth of interesting measurements of kinematic spectra, and in the dilepton channel, an excellent precision was obtained for cross sections measured as functions of kinematic spectra of the charged leptons, which is also the case for such distributions in this analysis. In the first complete CMS Run 2 paper [158], differential cross sections of $t\bar{t}$ production were measured in pp collisions at center-of-mass energies of 13 TeV for the full kinematic range in the lepton+jets channel, including the boosted region. The common conclusion based on these results, support the remarks made on the differential cross sections presented in this work. No single model at NLO or beyond-NLO precision provides a good description of the data in all measured cross sections and the discrepancies between the predictions and data are enhanced in the double-differential measurements.

9.1 Outlook

The overall precision achieved for the differential $t\bar{t}$ cross section measurements presented in this work is expected to improve with pp collision data at center-of-mass energies of 13.6 TeV in the imminent Run 3 data-taking period of the LHC [159], where data recorded with the CMS experiment is projected to reach a total integrated luminosity of 400 fb^{-1} by the end of the run, resulting in a tripling of the available statistics. However, perhaps the most significant improvements will be seen for the High-Luminosity Large Hadron Collider (HL-LHC) project [160] following Run 3. Here pp collisions at center-of-mass energies of 14 TeV, i.e. the design value, will take place at very high instantaneous luminosities, amounting to a total integrated luminosity of 3000 fb^{-1} by the end of the project. Measurements based on either of these data-taking periods, but in particular the latter, will face challenges in terms of pile-up, which must be addressed by implementing the proper

treatment and propagation of pile-up corrections in the analysis. However, outer bins of the differential cross sections in statistically limited regions of the kinematic phase space are expected to benefit from the increased statistics.

It should be noted that it's also possible to improve the current precision by using a wide bin aggregation approach for the unfolding procedure. Unfolding in very fine bins should, in theory, result in a reduced dependence of the response matrix on model uncertainties but is hampered by the large statistical fluctuations that occur with the surge in bin-to-bin migrations in the matrix. If the fine bins are aggregated into wider bins after unfolding, these fluctuations should cancel out. Thus, in this sense one ends up with reduced model uncertainties without having to pay the price. Preliminary studies on wide bin aggregation were performed in the context of this analysis but no clear conclusion could be drawn as to the true effect of the procedure, in part, due to the limited statistics of the independent MC samples available for some of the model uncertainties. Therefore, for Run 3 and HL-LHC it would be of great value to have all systematic model variations stored as weights in the simulated $t\bar{t}$ signal samples, as weight-based variations are less affected by statistical fluctuations.

The top quarks and $t\bar{t}$ system are reconstructed using two different methods in this work, based on applying kinematic constraints. In [102], a multivariate analysis was developed to improve the kinematic reconstruction for $t\bar{t}$ plus one additional jet events. A regression neural network was trained on these events, based on kinematic spectra of the decay objects like the charged leptons and beauty flavoured jets, as well as the solutions obtained using both $t\bar{t}$ kinematic reconstructions. This was observed to significantly improve the kinematic reconstruction, and this analysis could possibly benefit from a similar approach. A deep neural network or multivariate approach could also be used to fit signal and background simultaneously, based on discriminating variables like e.g. the b-jet multiplicity.

In this analysis, the normalization of the Z+jets background was improved by using a data-driven method, and fitting the data and simulated samples in the region corresponding to the Z boson resonance in the dilepton mass distribution. The TFractionFitter class [98] in the ROOT framework [99] was used for this purpose, and in future measurements, the method presented in this work can be improved by performing the fit of the Z peak in differential bins of the kinematic phase space, e.g. at low and high rapidity of the top in the $y(t)$ measurement, and applying the obtained scale factors to the corresponding rapidity regions of the Z+jets background contribution outside the Z peak region. This differential estimation of the normalization of the Z+jets background contribution will lead to reduced systematic uncertainties on the corresponding background subtraction in the differential measurement bins.

The aforementioned improvements in statistics, kinematic reconstruction and background estimation will pave the way for a plethora of new differential $t\bar{t}$ production cross section measurements with even greater precision than achieved so far.

Bibliography

[1] M. Thomson. *Modern particle physics*. New York: Cambridge University Press, 2013. ISBN: 978-1-107-03426-6.

[2] M. Kobayashi and T. Maskawa. "CP Violation in the Renormalizable Theory of Weak Interaction". In: *Prog. Theor. Phys.* 49 (1973), pp. 652–657. DOI: 10.1143/PTP.49.652.

[3] S. W. Herb et al. "Observation of a Dimuon Resonance at 9.5-GeV in 400-GeV Proton-Nucleus Collisions". In: *Phys. Rev. Lett.* 39 (1977), pp. 252–255. DOI: 10.1103/PhysRevLett.39.252.

[4] CDF Collaboration. "Observation of top quark production in $\bar{p}p$ collisions". In: *Phys. Rev. Lett.* 74 (1995), pp. 2626–2631. DOI: 10.1103/PhysRevLett.74.2626. arXiv: hep-ex/9503002.

[5] ATLAS Collaboration. "Observation of a new particle in the search for the Standard Model Higgs boson with the ATLAS detector at the LHC". In: *Phys. Lett. B* 716 (2012), pp. 1–29. DOI: 10.1016/j.physletb.2012.08.020. arXiv: 1207.7214 [hep-ex].

[6] CMS Collaboration. "Observation of a New Boson at a Mass of 125 GeV with the CMS Experiment at the LHC". In: *Phys. Lett. B* 716 (2012), pp. 30–61. DOI: 10.1016/j.physletb.2012.08.021. arXiv: 1207.7235 [hep-ex].

[7] P. A. Zyla et al. (Particle Data Group). "Review of Particle Physics". In: *Prog. Theor. Exp. Phys.* 2020.083C01 (2020). and 2021 update. DOI: 10.1093/ptep/ptaa104.

[8] ATLAS Collaboration. "Measurements of top quark pair relative differential cross-sections with ATLAS in pp collisions at $\sqrt{s} = 7$ TeV". In: *Eur. Phys. J. C* 73.1 (2013), p. 2261. DOI: 10.1140/epjc/s10052-012-2261-1. arXiv: 1207.5644 [hep-ex].

[9] CMS Collaboration. "Measurement of Differential Top-Quark Pair Production Cross Sections in pp collisions at $\sqrt{s} = 7$ TeV". In: *Eur. Phys. J. C* 73.3 (2013), p. 2339. DOI: 10.1140/epjc/s10052-013-2339-4. arXiv: 1211.2220 [hep-ex].

[10] ATLAS Collaboration. "Measurements of top-quark pair differential cross-sections in the lepton+jets channel in pp collisions at $\sqrt{s} = 8$ TeV using the ATLAS detector". In: *Eur. Phys. J. C* 76.10 (2016), p. 538. DOI: 10.1140/epjc/s10052-016-4366-4. arXiv: 1511.04716 [hep-ex].

[11] CMS Collaboration. "Measurement of the differential cross section for top quark pair production in pp collisions at $\sqrt{s} = 8\,\text{TeV}$". In: *Eur. Phys. J. C* 75.11 (2015), p. 542. DOI: 10.1140/epjc/s10052-015-3709-x. arXiv: 1505.04480 [hep-ex].

[12] CMS Collaboration. "Measurement of double-differential cross sections for top quark pair production in pp collisions at $\sqrt{s} = 8$ TeV and impact on parton distribution functions". In: *Eur. Phys. J. C* 77.7 (2017), p. 459. DOI: 10.1140/epjc/s10052-017-4984-5. arXiv: 1703.01630 [hep-ex].

[13] ATLAS Collaboration. "Measurements of top-quark pair differential and double-differential cross-sections in the ℓ+jets channel with pp collisions at $\sqrt{s} = 13$ TeV using the ATLAS detector". In: *Eur. Phys. J. C* 79.12 (2019). [Erratum: Eur. Phys. J. C 80, 1092 (2020)], p. 1028. DOI: 10.1140/epjc/s10052-019-7525-6. arXiv: 1908.07305 [hep-ex].

[14] CMS Collaboration. "Measurements of $\mathrm{t\bar{t}}$ differential cross sections in proton-proton collisions at $\sqrt{s} = 13$ TeV using events containing two leptons". In: *JHEP* 02 (2019), p. 149. DOI: 10.1007/JHEP02(2019)149. arXiv: 1811.06625 [hep-ex].

[15] CMS Collaboration. "Measurement of $\mathrm{t\bar{t}}$ normalised multi-differential cross sections in pp collisions at $\sqrt{s} = 13$ TeV, and simultaneous determination of the strong coupling strength, top quark pole mass, and parton distribution functions". In: *Eur. Phys. J. C* 80.7 (2020), p. 658. DOI: 10.1140/epjc/s10052-020-7917-7. arXiv: 1904.05237 [hep-ex].

[16] P. F. Monni et al. "MiNNLO$_{PS}$: a new method to match NNLO QCD to parton showers". In: *JHEP* 05 (2020), p. 143. DOI: 10.1007/JHEP05(2020)143. arXiv: 1908.06987 [hep-ph].

[17] P. F. Monni, E. Re, and M. Wiesemann. "MiNNLO$_{\text{PS}}$: optimizing $2 \to 1$ hadronic processes". In: *Eur. Phys. J. C* 80.11 (2020), p. 1075. DOI: 10.1140/epjc/s10052-020-08658-5. arXiv: 2006.04133 [hep-ph].

[18] J. Mazzitelli et al. "Top-pair production at the LHC with MINNLO$_{PS}$". In: *JHEP* 04 (2022), p. 079. DOI: 10.1007/JHEP04(2022)079. arXiv: 2112.12135 [hep-ph].

[19] CMS Collaboration. *Measurement of differential cross sections for the production of top quark pairs and of additional jets in pp collisions at* $\sqrt{s} = 13$ TeV. CMS Physics Analysis Summary CMS-PAS-TOP-20-006. 2022. URL: http://cds.cern.ch/record/2803771.

[20] E. Akhmedov. *Majorana neutrinos and other Majorana particles:Theory and experiment*. Dec. 2014. arXiv: 1412.3320 [hep-ph].

[21] H. Murayama. "Physics Beyond the Standard Model and Dark Matter". In: *Les Houches Summer School - Session 86: Particle Physics and Cosmology: The Fabric of Spacetime*. Apr. 2007. arXiv: 0704.2276 [hep-ph].

[22] P. A. Zyla et al. (Particle Data Group). "Review of Particle Physics". In: *Prog. Theor. Exp. Phys.* 2020.083C01 (2020). DOI: 10.1093/ptep/ptaa104.

[23] P. W. Higgs. "Broken Symmetries and the Masses of Gauge Bosons". In: *Phys. Rev. Lett.* 13 (1964). Ed. by J. C. Taylor, pp. 508–509. DOI: 10.1103/PhysRevLett.13.508.

[24] Planck Collaboration. "Planck 2015 results. XIII. Cosmological parameters". In: *Astron. Astrophys.* 594 (2016), A13. DOI: 10.1051/0004-6361/201525830. arXiv: 1502.01589 [astro-ph.CO].

[25] Wikipedia. *Standard Model*. URL: https://en.wikipedia.org/wiki/Standard_Model (visited on 05/10/2022).

[26] CMS Collaboration. "Measurement of the inclusive 3-jet production differential cross section in proton–proton collisions at 7 TeV and determination of the strong coupling constant in the TeV range". In: *Eur. Phys. J. C* 75.5 (2015), p. 186. DOI: 10.1140/epjc/s10052-015-3376-y. arXiv: 1412.1633 [hep-ex].

[27] T. Markkanen, A. Rajantie, and S. Stopyra. "Cosmological Aspects of Higgs Vacuum Metastability". In: *Front. Astron. Space Sci.* 5 (2018), p. 40. DOI: 10.3389/fspas.2018.00040. arXiv: 1809.06923 [astro-ph.CO].

[28] F. Schilling. "Top Quark Physics at the LHC: A Review of the First Two Years". In: *Int. J. Mod. Phys. A* 27 (2012), p. 1230016. DOI: 10.1142/S0217751X12300165. arXiv: 1206.4484 [hep-ex].

[29] G. Altarelli and G. Parisi. "Asymptotic freedom in parton language". In: *Nuclear Physics B* 126.2 (1977), pp. 298–318. ISSN: 0550-3213. DOI: https://doi.org/10.1016/0550-3213(77)90384-4.

[30] Y. L. Dokshitzer. "Calculation of the Structure Functions for Deep Inelastic Scattering and e+ e- Annihilation by Perturbation Theory in Quantum Chromodynamics." In: *Sov. Phys. JETP* 46 (1977), pp. 641–653.

[31] V. N. Gribov and L. N. Lipatov. "Deep inelastic e p scattering in perturbation theory". In: *Sov. J. Nucl. Phys.* 15 (1972), pp. 438–450.

[32] R. D. Ball et al. "Parton distributions from high-precision collider data". In: *Eur. Phys. J. C* 77.10 (2017), p. 663. DOI: 10.1140/epjc/s10052-017-5199-5. arXiv: 1706.00428 [hep-ph].

[33] H. Abramowicz et al. "Combination of measurements of inclusive deep inelastic $e^{\pm}p$ scattering cross sections and QCD analysis of HERA data". In: *Eur. Phys. J. C* 75.12 (2015), p. 580. DOI: 10.1140/epjc/s10052-015-3710-4. arXiv: 1506.06042 [hep-ex].

[34] M. Czakon and A. Mitov. "Top++: A Program for the Calculation of the Top-Pair Cross-Section at Hadron Colliders". In: *Comput. Phys. Commun.* 185 (2014), p. 2930. DOI: 10.1016/j.cpc.2014.06.021. arXiv: 1112.5675 [hep-ph].

[35] U. Husemann. "Top-Quark Physics: Status and Prospects". In: *Prog. Part. Nucl. Phys.* 95 (2017), pp. 48–97. DOI: 10.1016/j.ppnp.2017.03.002. arXiv: 1704.01356 [hep-ex].

[36] N. Kidonakis. "Two-loop soft anomalous dimensions for single top quark associated production with a W^- or H^-". In: *Phys. Rev. D* 82 (2010), p. 054018. DOI: 10.1103/PhysRevD.82.054018. arXiv: 1005.4451 [hep-ph].

[37] P. Kant et al. "HatHor for single top-quark production: Updated predictions and uncertainty estimates for single top-quark production in hadronic collisions". In: *Comput. Phys. Commun.* 191 (2015), pp. 74–89. DOI: 10.1016/j.cpc.2015.02.001. arXiv: 1406.4403 [hep-ph].

[38] K. Zoch. "Cross-section measurements of top-quark pair production in association with a hard photon at 13 TeV with the ATLAS detector". PhD thesis. Gottingen U., 2020. arXiv: 2007.14701 [hep-ex].

[39] C. Csaki. "The Minimal supersymmetric standard model (MSSM)". In: *Mod. Phys. Lett. A* 11 (1996), p. 599. DOI: 10.1142/S021773239600062X. arXiv: hep-ph/9606414.

[40] C. Helsens et al. "Heavy resonances at energy-frontier hadron colliders". In: *Eur. Phys. J. C* 79 (2019), p. 569. DOI: 10.1140/epjc/s10052-019-7062-3. arXiv: 1902.11217 [hep-ph].

[41] P. Langacker. "The Physics of Heavy Z' Gauge Bosons". In: *Rev. Mod. Phys.* 81 (2009), pp. 1199–1228. DOI: 10.1103/RevModPhys.81.1199. arXiv: 0801.1345 [hep-ph].

[42] CMS Collaboration. "Search for resonant $\mathrm{t\bar{t}}$ production in proton-proton collisions at $\sqrt{s} = 13$ TeV". In: *JHEP* 04 (2019), p. 031. DOI: 10.1007/JHEP04(2019)031. arXiv: 1810.05905 [hep-ex].

[43] L. Evans and P. Bryant. "LHC Machine". In: *JINST* 3 (2008), S08001. DOI: 10.1088/1748-0221/3/08/S08001.

[44] CERN. *LEP Design Report: Vol.2. The LEP Main Ring*. CERN-LEP-84-01. Copies shelved as reports in LEP, PS and SPS libraries. Geneva: CERN, 1984. URL: https://cds.cern.ch/record/102083.

[45] CMS Collaboration. "The CMS Experiment at the CERN LHC". In: *JINST* 3 (2008), S08004. DOI: 10.1088/1748-0221/3/08/S08004.

[46] ATLAS Collaboration. "The ATLAS Experiment at the CERN Large Hadron Collider". In: *JINST* 3 (2008), S08003. DOI: 10.1088/1748-0221/3/08/S08003.

[47] ALICE Collaboration. "The ALICE experiment at the CERN LHC". In: *JINST* 3 (2008), S08002. DOI: 10.1088/1748-0221/3/08/S08002.

[48] LHCb Collaboration. "The LHCb Detector at the LHC". In: *JINST* 3 (2008), S08005. DOI: 10.1088/1748-0221/3/08/S08005.

[49] C. Lefvre. *The CERN accelerator complex*. DOI: 10.2172/1151650. URL: https://cds.cern.ch/record/1260465.

[50] CMS Collaboration. "CMS Physics: Technical Design Report Volume 1: Detector Performance and Software". In: CERN-LHCC-2006-001, CMS-TDR-8-1 (2006). URL: http://cds.cern.ch/record/922757.

[51] I. Neutelings. *The coordinate system used at CMS*. URL: https://wiki.physik.uzh.ch/cms/latex:example_spherical_coordinates (visited on 05/10/2022).

[52] CMS Collaboration. "Commissioning of the CMS experiment and the cosmic run at four tesla". In: *Journal of Instrumentation* 5.03 (2010), T03001–T03001. DOI: 10.1088/1748-0221/5/03/t03001.

[53] A. Dominguez et al. *CMS Technical Design Report for the Pixel Detector Upgrade*. Tech. rep. CERN-LHCC-2012-016, CMS-TDR-11. 2012. DOI: 10.2172/1151650. URL: https://cds.cern.ch/record/1481838.

[54] CMS Collaboration. "Strategies and performance of the CMS silicon tracker alignment during LHC Run 2". In: *Nucl. Instrum. Methods A 1037 166795* (2022). arXiv: 2111.08757 [physics.ins-det].

[55] CMS Collaboration. "Description and performance of track and primary-vertex reconstruction with the CMS tracker". In: *JINST* 9.10 (2014), P10009. DOI: 10.1088/1748-0221/9/10/P10009. arXiv: 1405.6569 [physics.ins-det].

[56] CMS Collaboration. "Electron and photon reconstruction and identification with the CMS experiment at the CERN LHC". In: *JINST* 16.05 (2021), P05014. DOI: 10.1088/1748-0221/16/05/P05014. arXiv: 2012.06888 [hep-ex].

[57] CMS Collaboration. "Calibration of the CMS hadron calorimeters using proton-proton collision data at $\sqrt{s} = 13$ TeV". In: *JINST* 15.05 (2020), P05002. DOI: 10.1088/1748-0221/15/05/P05002. arXiv: 1910.00079 [physics.ins-det].

[58] CMS Collaboration. "Performance of the CMS muon detector and muon reconstruction with proton-proton collisions at $\sqrt{s} = 13$ TeV". In: *JINST* 13.06 (2018), P06015. DOI: 10.1088/1748-0221/13/06/P06015. arXiv: 1804.04528 [physics.ins-det].

[59] A. Tapper and D. Acosta. *CMS Technical Design Report for the Level-1 Trigger Upgrade*. Tech. rep. CERN-LHCC-2013-011, CMS-TDR-12. 2013. URL: https://cds.cern.ch/record/1556311.

[60] SLAC National Accelerator Laboratory. *Theoretical Physics: Simulations*. URL: https://theory.slac.stanford.edu/our-research/simulations (visited on 05/10/2022).

[61] A. Buckley et al. "General-purpose event generators for LHC physics". In: *Phys. Rept.* 504 (2011), pp. 145–233. DOI: 10.1016/j.physrep.2011.03.005. arXiv: 1101.2599 [hep-ph].

[62] B. Andersson et al. "Parton fragmentation and string dynamics". In: *Physics Reports* 97.2 (1983), pp. 31–145. ISSN: 0370-1573. DOI: https://doi.org/10.1016/0370-1573(83)90080-7. URL: https://www.sciencedirect.com/science/article/pii/0370157383900807.

[63] B. R. Webber. "A QCD Model for Jet Fragmentation Including Soft Gluon Interference". In: *Nucl. Phys. B* 238 (1984), pp. 492–528. DOI: 10.1016/0550-3213(84)90333-X.

[64] M. H. Seymour and M. Marx. "Monte Carlo Event Generators". In: *69th Scottish Universities Summer School in Physics: LHC Physics*. Apr. 2013, pp. 287–319. DOI: 10.1007/978-3-319-05362-2_8. arXiv: 1304.6677 [hep-ph].

[65] S. Höche. "Introduction to parton-shower event generators". In: *Theoretical Advanced Study Institute in Elementary Particle Physics: Journeys Through the Precision Frontier: Amplitudes for Colliders*. 2015, pp. 235–295. DOI: 10.1142/9789814678766_0005. arXiv: 1411.4085 [hep-ph].

[66] B. R. Webber. "Fragmentation and hadronization". In: *Int. J. Mod. Phys. A* 15S1 (2000). Ed. by J. Jaros and M. E. Peskin, pp. 577–606. DOI: 10.1142/S0217751X00005334. arXiv: hep-ph/9912292.

[67] T. Sjöstrand et al. "An introduction to PYTHIA 8.2". In: *Comput. Phys. Commun.* 191 (2015), pp. 159–177. DOI: 10.1016/j.cpc.2015.01.024. arXiv: 1410.3012 [hep-ph].

[68] I. Borozan and M. H. Seymour. "An Eikonal model for multiparticle production in hadron hadron interactions". In: *JHEP* 09 (2002), p. 015. DOI: 10.1088/1126-6708/2002/09/015. arXiv: hep-ph/0207283.

[69] J. Bellm et al. "Herwig 7.0/Herwig++ 3.0 release note". In: *Eur. Phys. J. C* 76.4 (2016), p. 196. DOI: 10.1140/epjc/s10052-016-4018-8. arXiv: 1512.01178 [hep-ph].

[70] S. Frixione, P. Nason, and C. Oleari. "Matching NLO QCD computations with Parton Shower simulations: the POWHEG method". In: *JHEP* 11 (2007), p. 070. DOI: 10.1088/1126-6708/2007/11/070. arXiv: 0709.2092 [hep-ph].

[71] S. Frixione, P. Nason, and G. Ridolfi. "A Positive-weight next-to-leading-order Monte Carlo for heavy flavour hadroproduction". In: *JHEP* 09 (2007), p. 126. DOI: 10.1088/1126-6708/2007/09/126. arXiv: 0707.3088 [hep-ph].

[72] S. Alioli et al. "A general framework for implementing NLO calculations in shower Monte Carlo programs: the POWHEG BOX". In: *JHEP* 06 (2010), p. 043. DOI: 10.1007/JHEP06(2010)043. arXiv: 1002.2581 [hep-ph].

[73] J. Alwall et al. "The automated computation of tree-level and next-to-leading order differential cross sections, and their matching to parton shower simulations". In: *JHEP* 07 (2014), p. 079. DOI: 10.1007/JHEP07(2014)079. arXiv: 1405.0301 [hep-ph].

[74] M. L. Mangano et al. "Matching matrix elements and shower evolution for top-quark production in hadronic collisions". In: *JHEP* 01 (2007), p. 013. DOI: 10.1088/1126-6708/2007/01/013. arXiv: hep-ph/0611129.

[75] S. Mrenna and P. Richardson. "Matching matrix elements and parton showers with HERWIG and PYTHIA". In: *JHEP* 05 (2004), p. 040. DOI: 10.1088/1126-6708/2004/05/040. arXiv: hep-ph/0312274.

[76] R. Frederix and S. Frixione. "Merging meets matching in MC@NLO". In: *JHEP* 12 (2012), p. 061. DOI: 10.1007/JHEP12(2012)061. arXiv: 1209.6215 [hep-ph].

[77] P. Artoisenet et al. "Automatic spin-entangled decays of heavy resonances in Monte Carlo simulations". In: *JHEP* 03 (2013), p. 015. DOI: 10.1007/JHEP03(2013)015. arXiv: 1212.3460 [hep-ph].

[78] S. Agostinelli et al. "GEANT4–a simulation toolkit". In: *Nucl. Instrum. Meth. A* 506 (2003), pp. 250–303. DOI: 10.1016/S0168-9002(03)01368-8.

[79] CMS Collaboration. "Extraction and validation of a new set of CMS PYTHIA8 tunes from underlying-event measurements". In: *Eur. Phys. J. C* 80.1 (2020), p. 4. DOI: 10.1140/epjc/s10052-019-7499-4. arXiv: 1903.12179 [hep-ex].

[80] CMS Collaboration. "Development and validation of HERWIG 7 tunes from CMS underlying-event measurements". In: *Eur. Phys. J. C* 81.4 (2021), p. 312. DOI: 10.1140/epjc/s10052-021-08949-5. arXiv: 2011.03422 [hep-ex].

[81] R. D. Ball et al. "Unbiased global determination of parton distributions and their uncertainties at NNLO and at LO". In: *Nucl. Phys. B* 855 (2012), pp. 153–221. DOI: 10.1016/j.nuclphysb.2011.09.024. arXiv: 1107.2652 [hep-ph].

[82] M. Cacciari et al. "Top-pair production at hadron colliders with next-to-next-to-leading logarithmic soft-gluon resummation". In: *Phys. Lett. B* 710 (2012), pp. 612–622. DOI: 10.1016/j.physletb.2012.03.013. arXiv: 1111.5869 [hep-ph].

[83] P. Bärnreuther, M. Czakon, and A. Mitov. "Percent Level Precision Physics at the Tevatron: First Genuine NNLO QCD Corrections to $q\bar{q} \to t\bar{t} + X$". In: *Phys. Rev. Lett.* 109 (2012), p. 132001. DOI: 10.1103/PhysRevLett.109.132001. arXiv: 1204.5201 [hep-ph].

[84] M. Czakon and A. Mitov. "NNLO corrections to top-pair production at hadron colliders: the all-fermionic scattering channels". In: *JHEP* 12 (2012), p. 054. DOI: 10.1007/JHEP12(2012)054. arXiv: 1207.0236 [hep-ph].

[85] M. Czakon and A. Mitov. "NNLO corrections to top pair production at hadron colliders: the quark-gluon reaction". In: *JHEP* 01 (2013), p. 080. DOI: 10.1007/JHEP01(2013)080. arXiv: 1210.6832 [hep-ph].

[86] M. Beneke et al. "Hadronic top-quark pair production with NNLL threshold resummation". In: *Nucl. Phys. B* 855 (2012), pp. 695–741. DOI: 10.1016/j.nuclphysb.2011.10.021. arXiv: 1109.1536 [hep-ph].

[87] M. Czakon, P. Fiedler, and A. Mitov. "Total Top-Quark Pair-Production Cross Section at Hadron Colliders Through $O(\alpha_S^4)$". In: *Phys. Rev. Lett.* 110 (2013), p. 252004. DOI: 10.1103/PhysRevLett.110.252004. arXiv: 1303.6254 [hep-ph].

[88] E. Re. "Single-top Wt-channel production matched with parton showers using the POWHEG method". In: *Eur. Phys. J. C* 71 (2011), p. 1547. DOI: 10.1140/epjc/s10052-011-1547-z. arXiv: 1009.2450 [hep-ph].

[89] S. Alioli et al. "NLO single-top production matched with shower in POWHEG: s- and t-channel contributions". In: *JHEP* 09 (2009). [Erratum: JHEP 02, 011 (2010)], p. 111. DOI: 10.1088/1126-6708/2009/09/111. arXiv: 0907.4076 [hep-ph].

[90] R. Gavin et al. "FEWZ 2.0: A code for hadronic Z production at next-to-next-to-leading order". In: *Comput. Phys. Commun.* 182 (2011), pp. 2388–2403. DOI: 10.1016/j.cpc.2011.06.008. arXiv: 1011.3540 [hep-ph].

[91] Y. Li and F. Petriello. "Combining QCD and electroweak corrections to dilepton production in FEWZ". In: *Phys. Rev. D* 86 (2012), p. 094034. DOI: 10.1103/PhysRevD.86.094034. arXiv: 1208.5967 [hep-ph].

[92] J. M. Campbell, R. K. Ellis, and C. Williams. "Vector boson pair production at the LHC". In: *JHEP* 07 (2011), p. 018. DOI: 10.1007/JHEP07(2011)018. arXiv: 1105.0020 [hep-ph].

[93] J. M. Campbell, R. K. Ellis, and W. T. Giele. "A Multi-Threaded Version of MCFM". In: *Eur. Phys. J. C* 75.6 (2015), p. 246. DOI: 10.1140/epjc/s10052-015-3461-2. arXiv: 1503.06182 [physics.comp-ph].

[94] T. Gehrmann et al. "W^+W^- Production at Hadron Colliders in Next to Next to Leading Order QCD". In: *Phys. Rev. Lett.* 113.21 (2014), p. 212001. DOI: 10.1103/PhysRevLett.113.212001. arXiv: 1408.5243 [hep-ph].

[95] P. Skands, S. Carrazza, and J. Rojo. "Tuning PYTHIA 8.1: the Monash 2013 Tune". In: *Eur. Phys. J. C* 74.8 (2014), p. 3024. DOI: 10.1140/epjc/s10052-014-3024-y. arXiv: 1404.5630 [hep-ph].

[96] CMS Collaboration. "Event generator tunes obtained from underlying event and multiparton scattering measurements". In: *Eur. Phys. J. C* 76.3 (2016), p. 155. DOI: 10.1140/epjc/s10052-016-3988-x. arXiv: 1512.00815 [hep-ex].

[97] CMS Collaboration. *Investigations of the impact of the parton shower tuning in Pythia 8 in the modelling of* $\mathrm{t\bar{t}}$ *at* $\sqrt{s} = 8$ *and 13 TeV*. CMS Physics Analysis Summary CMS-PAS-TOP-16-021. 2016. URL: https://cds.cern.ch/record/2235192.

[98] R. J. Barlow and C. Beeston. "Fitting using finite Monte Carlo samples". In: *Comput. Phys. Commun.* 77 (1993), pp. 219–228. DOI: 10.1016/0010-4655(93)90005-W.

[99] I. Antcheva et al. "ROOT: A C++ framework for petabyte data storage, statistical analysis and visualization". In: *Comput. Phys. Commun.* 180 (2009), pp. 2499–2512. DOI: 10.1016/j.cpc.2009.08.005. arXiv: 1508.07749 [physics.data-an].

[100] CMS Collaboration. "Measurement of the $t\bar{t}$ production cross section and the top quark mass in the dilepton channel in pp collisions at $\sqrt{s} = 7$ TeV". In: *JHEP* 07 (2011), p. 049. DOI: 10.1007/JHEP07(2011)049. arXiv: 1105.5661 [hep-ex].

[101] M. Savitskyi. "Measurements of differential cross sections for $t\bar{t}$ production in proton-proton collisions at $\sqrt{s} = 13$ TeV using events containing two leptons with the CMS experiment". PhD thesis. Hamburg: Hamburg U., 2018. DOI: 10.3204/PUBDB-2018-02408.

[102] CMS Collaboration. *Measurement of the top quark pole mass using $t\bar{t}$ +jet events in the dilepton final state in proton-proton collisions at $\sqrt{s} = 13$ TeV*. CMS Physics Analysis Summary CMS-PAS-TOP-21-008. 2022. URL: https://cds.cern.ch/record/2814956.

[103] CMS Collaboration. "Pileup mitigation at CMS in 13 TeV data". In: *JINST* 15.09 (2020), P09018. DOI: 10.1088/1748-0221/15/09/P09018. arXiv: 2003.00503 [hep-ex].

[104] R. Fruhwirth. "Application of Kalman filtering to track and vertex fitting". In: *Nucl. Instrum. Meth. A* 262 (1987), pp. 444–450. DOI: 10.1016/0168-9002(87)90887-4.

[105] K. Rose. "Deterministic annealing for clustering, compression, classification, regression, and related optimization problems". In: *IEEE Proc.* 86.11 (1998), pp. 2210–2239. DOI: 10.1109/5.726788.

[106] R. Fruhwirth, W. Waltenberger, and P. Vanlaer. "Adaptive vertex fitting". In: *J. Phys. G* 34 (2007), N343. DOI: 10.1088/0954-3899/34/12/N01.

[107] CMS Collaboration. *Particle-Flow Event Reconstruction in CMS and Performance for Jets, Taus, and MET*. CMS Physics Analysis Summary CMS-PAS-PFT-09-001. 2009. URL: https://cds.cern.ch/record/1194487.

[108] CMS Collaboration. *Commissioning of the Particle-flow Event Reconstruction with the first LHC collisions recorded in the CMS detector*. CMS Physics Analysis Summary CMS-PAS-PFT-10-001. 2010. URL: https://cds.cern.ch/record/1247373.

[109] LHCTopWG. *LHC Top Physics Working Group*. URL: https://twiki.cern.ch/twiki/bin/view/LHCPhysics/LHCTopWG (visited on 05/10/2022).

[110] CMS Collaboration. "Particle-flow reconstruction and global event description with the CMS detector". In: *JINST* 12.10 (2017), P10003. DOI: 10.1088/1748-0221/12/10/P10003. arXiv: 1706.04965 [physics.ins-det].

[111] A. Bodek et al. "Extracting Muon Momentum Scale Corrections for Hadron Collider Experiments". In: *Eur. Phys. J. C* 72 (2012), p. 2194. DOI: 10.1140/epjc/s10052-012-2194-8. arXiv: 1208.3710 [hep-ex].

[112] CMS Collaboration. "Performance of CMS Muon Reconstruction in pp Collision Events at $\sqrt{s} = 7$ TeV". In: *JINST* 7 (2012), P10002. DOI: 10.1088/1748-0221/7/10/P10002. arXiv: 1206.4071 [physics.ins-det].

[113] CMS Collaboration. "Performance of Electron Reconstruction and Selection with the CMS Detector in Proton-Proton Collisions at $\sqrt{s} = 8$ TeV". In: *JINST* 10.06 (2015), P06005. DOI: 10.1088/1748-0221/10/06/P06005. arXiv: 1502.02701 [physics.ins-det].

[114] W. Adam, R. Frühwirth, A. Strandlie and T. Todorov. "Reconstruction of electrons with the Gaussian-sum filter in the CMS tracker at the LHC". In: *Journal of Physics G: Nuclear and Particle Physics* 31.9 (July 2005), N9–N20. DOI: 10.1088/0954-3899/31/9/n01.

[115] M. Cacciari, G. P. Salam, and G. Soyez. "The anti-k_t jet clustering algorithm". In: *JHEP* 04 (2008), p. 063. DOI: 10.1088/1126-6708/2008/04/063. arXiv: 0802.1189 [hep-ph].

[116] CMS Collaboration. "Jet energy scale and resolution in the CMS experiment in pp collisions at 8 TeV". In: *JINST* 12.02 (2017), P02014. DOI: 10.1088/1748-0221/12/02/P02014. arXiv: 1607.03663 [hep-ex].

[117] CMS Collaboration. "Determination of Jet Energy Calibration and Transverse Momentum Resolution in CMS". In: *JINST* 6 (2011), P11002. DOI: 10.1088/1748-0221/6/11/P11002. arXiv: 1107.4277 [physics.ins-det].

[118] M. Cacciari, G. P. Salam, and G. Soyez. "FastJet User Manual". In: *Eur. Phys. J. C* 72 (2012), p. 1896. DOI: 10.1140/epjc/s10052-012-1896-2. arXiv: 1111.6097 [hep-ph].

[119] CMS Collaboration. "Identification of heavy-flavour jets with the CMS detector in pp collisions at 13 TeV". In: *JINST* 13.05 (2018), P05011. DOI: 10.1088/1748-0221/13/05/P05011. arXiv: 1712.07158 [physics.ins-det].

[120] W. Waltenberger. *Adaptive vertex reconstruction*. CMS Note CERN-CMS-NOTE-2008-033. 2008. URL: https://cds.cern.ch/record/1166320.

[121] CMS Collaboration. "A Deep Neural Network for Simultaneous Estimation of b Jet Energy and Resolution". In: *Comput. Softw. Big Sci.* 4.1 (2020), p. 10. DOI: 10.1007/s41781-020-00041-z. arXiv: 1912.06046 [hep-ex].

[122] CMS Collaboration. "Performance of missing transverse momentum reconstruction in proton-proton collisions at $\sqrt{s} = 13$ TeV using the CMS detector". In: *JINST* 14.07 (2019), P07004. DOI: 10.1088/1748-0221/14/07/P07004. arXiv: 1903.06078 [hep-ex].

[123] L. Sonnenschein. "Algebraic approach to solve $t\bar{t}$ dilepton equations". In: *Phys. Rev. D* 72 (2005), p. 095020. DOI: 10.1103/PhysRevD.72.095020. arXiv: hep-ph/0510100.

[124] L. Sonnenschein. "Analytical solution of ttbar dilepton equations". In: *Phys. Rev. D* 73 (2006). [Erratum: Phys.Rev.D 78, 079902 (2008)], p. 054015. DOI: 10.1103/PhysRevD.78.079902. arXiv: hep-ph/0603011.

[125] I. Korol. "Measurement of Double Differential $t\bar{t}$ Production Cross Sections with the CMS Detector". PhD thesis. 2016. URL: https://cds.cern.ch/record/2162903.

[126] S. Schmitt. "TUnfold: an algorithm for correcting migration effects in high energy physics". In: *JINST* 7 (2012), T10003. DOI: 10.1088/1748-0221/7/10/T10003. arXiv: 1205.6201 [physics.data-an].

[127] A. N. Tikhonov. "Solution of incorrectly formulated problems and the regularization method". In: *Sov. Math. Dokl.* 4 (1963), p. 1035.

[128] A. A. Anuar. "Top Quark Spin and Polarization Properties in Searches for New Phenomena with the CMS Detector at the LHC". PhD thesis. Hamburg U., 2019. DOI: 10.3204/PUBDB-2020-00203.

[129] CMS Collaboration. *Object definitions for top quark analyses at the particle level*. CMS Note CERN-CMS-NOTE-2017-004. 2017. URL: https://cds.cern.ch/record/2267573.

[130] M. Czakon. "A novel subtraction scheme for double-real radiation at NNLO". In: *Phys. Lett. B* 693 (2010), pp. 259–268. DOI: 10.1016/j.physletb.2010.08.036. arXiv: 1005.0274 [hep-ph].

[131] M. Czakon and D. Heymes. "Four-dimensional formulation of the sector-improved residue subtraction scheme". In: *Nucl. Phys. B* 890 (2014), pp. 152–227. DOI: 10.1016/j.nuclphysb.2014.11.006. arXiv: 1408.2500 [hep-ph].

[132] M. Czakon. "Double-real radiation in hadronic top quark pair production as a proof of a certain concept". In: *Nucl. Phys. B* 849 (2011), pp. 250–295. DOI: 10.1016/j.nuclphysb.2011.03.020. arXiv: 1101.0642 [hep-ph].

[133] M. Czakon et al. "Top-pair production at the LHC through NNLO QCD and NLO EW". In: *JHEP* 10 (2017), p. 186. DOI: 10.1007/JHEP10(2017)186. arXiv: 1705.04105 [hep-ph].

[134] CMS Collaboration. "Precision luminosity measurement in proton-proton collisions at $\sqrt{s} = 13$ TeV in 2015 and 2016 at CMS". In: *Eur. Phys. J. C* 81.9 (2021), p. 800. DOI: 10.1140/epjc/s10052-021-09538-2. arXiv: 2104.01927 [hep-ex].

[135] CMS Collaboration. *CMS luminosity measurement for the 2017 data-taking period at* $\sqrt{s} = 13$ TeV. CMS Physics Analysis Summary CMS-PAS-LUM-17-004. 2018. URL: https://cds.cern.ch/record/2621960.

[136] CMS Collaboration. *CMS luminosity measurement for the 2018 data-taking period at* $\sqrt{s} = 13$ TeV. CMS Physics Analysis Summary CMS-PAS-LUM-18-002. 2019. URL: https://cds.cern.ch/record/2676164.

[137] ATLAS Collaboration. "Measurement of the Inelastic Proton-Proton Cross Section at $\sqrt{s} = 13$ TeV with the ATLAS Detector at the LHC". In: *Phys. Rev. Lett.* 117.18 (2016), p. 182002. DOI: 10.1103/PhysRevLett.117.182002. arXiv: 1606.02625 [hep-ex].

[138] R. Nisius. "BLUE: combining correlated estimates of physics observables within ROOT using the Best Linear Unbiased Estimate method". In: *SoftwareX 11 100468* (2020). DOI: 10.1016/j.softx.2020.100468. arXiv: 2001.10310 [physics.data-an].

[139] R. Nisius. "On the combination of correlated estimates of a physics observable". In: *Eur. Phys. J. C* 74.8 (2014), p. 3004. DOI: 10.1140/epjc/s10052-014-3004-2. arXiv: 1402.4016 [physics.data-an].

[140] N. Kidonakis. "NNNLO soft-gluon corrections for the top-quark p_T and rapidity distributions". In: *Phys. Rev. D* 91.3 (2015), p. 031501. DOI: 10.1103/PhysRevD.91.031501. arXiv: 1411.2633 [hep-ph].

[141] S. Catani et al. "Top-quark pair production at the LHC: Fully differential QCD predictions at NNLO". In: *JHEP* 07 (2019), p. 100. DOI: 10.1007/JHEP07(2019)100. arXiv: 1906.06535 [hep-ph].

[142] M. Grazzini, S. Kallweit, and M. Wiesemann. "Fully differential NNLO computations with MATRIX". In: *Eur. Phys. J. C* 78.7 (2018), p. 537. DOI: 10.1140/epjc/s10052-018-5771-7. arXiv: 1711.06631 [hep-ph].

[143] S. Catani et al. "Top-quark pair hadroproduction at next-to-next-to-leading order in QCD". In: *Phys. Rev. D* 99.5 (2019), p. 051501. DOI: 10.1103/PhysRevD.99.051501. arXiv: 1901.04005 [hep-ph].

[144] F. Buccioni et al. "OpenLoops 2". In: *Eur. Phys. J. C* 79.10 (2019), p. 866. DOI: 10.1140/epjc/s10052-019-7306-2. arXiv: 1907.13071 [hep-ph].

[145] F. Cascioli, P. Maierhofer, and S. Pozzorini. "Scattering Amplitudes with Open Loops". In: *Phys. Rev. Lett.* 108 (2012), p. 111601. DOI: 10.1103/PhysRevLett.108.111601. arXiv: 1111.5206 [hep-ph].

[146] A. Denner, S. Dittmaier, and L. Hofer. "Collier: a fortran-based Complex One-Loop LIbrary in Extended Regularizations". In: *Comput. Phys. Commun.* 212 (2017), pp. 220–238. DOI: 10.1016/j.cpc.2016.10.013. arXiv: 1604.06792 [hep-ph].

[147] S. Catani et al. "Vector boson production at hadron colliders: hard-collinear coefficients at the NNLO". In: *Eur. Phys. J. C* 72 (2012), p. 2195. DOI: 10.1140/epjc/s10052-012-2195-7. arXiv: 1209.0158 [hep-ph].

[148] S. Catani and M. Grazzini. "An NNLO subtraction formalism in hadron collisions and its application to Higgs boson production at the LHC". In: *Phys. Rev. Lett.* 98 (2007), p. 222002. DOI: 10.1103/PhysRevLett.98.222002. arXiv: hep-ph/0703012.

[149] S. Dulat et al. "New parton distribution functions from a global analysis of quantum chromodynamics". In: *Phys. Rev. D* 93.3 (2016), p. 033006. DOI: 10.1103/PhysRevD.93.033006. arXiv: 1506.07443 [hep-ph].

[150] S. Alekhin, J. Blümlein, and S. Moch. "NLO PDFs from the ABMP16 fit". In: *Eur. Phys. J. C* 78.6 (2018), p. 477. DOI: 10.1140/epjc/s10052-018-5947-1. arXiv: 1803.07537 [hep-ph].

[151] L. A. Harland-Lang et al. "Parton distributions in the LHC era: MMHT 2014 PDFs". In: *Eur. Phys. J. C* 75.5 (2015), p. 204. DOI: 10.1140/epjc/s10052-015-3397-6. arXiv: 1412.3989 [hep-ph].

[152] CMS Collaboration. "Measurement of the top quark polarization and $t\bar{t}$ spin correlations using dilepton final states in proton-proton collisions at $\sqrt{s} = 13$ TeV". In: *Phys. Rev. D* 100.7 (2019), p. 072002. DOI: 10.1103/PhysRevD.100.072002. arXiv: 1907.03729 [hep-ex].

[153] K. Hamilton, P. Nason, and G. Zanderighi. "MINLO: Multi-Scale Improved NLO". In: *JHEP* 10 (2012), p. 155. DOI: 10.1007/JHEP10(2012)155. arXiv: 1206.3572 [hep-ph].

[154] K. Hamilton et al. "Merging H/W/Z + 0 and 1 jet at NLO with no merging scale: a path to parton shower + NNLO matching". In: *JHEP* 05 (2013), p. 082. DOI: 10.1007/JHEP05(2013)082. arXiv: 1212.4504 [hep-ph].

[155] J. Butterworth et al. "PDF4LHC recommendations for LHC Run II". In: *J. Phys. G* 43 (2016), p. 023001. DOI: 10.1088/0954-3899/43/2/023001. arXiv: 1510.03865 [hep-ph].

[156] A. Accardi et al. "A Critical Appraisal and Evaluation of Modern PDFs". In: *Eur. Phys. J. C* 76.8 (2016), p. 471. DOI: 10.1140/epjc/s10052-016-4285-4. arXiv: 1603.08906 [hep-ph].

[157] ATLAS Collaboration. "Measurement of the $t\bar{t}$ production cross-section and lepton differential distributions in $e\mu$ dilepton events from pp collisions at $\sqrt{s} = 13\,\text{TeV}$ with the ATLAS detector". In: *Eur. Phys. J. C* 80.6 (2020), p. 528. DOI: 10.1140/epjc/s10052-020-7907-9. arXiv: 1910.08819 [hep-ex].

[158] CMS Collaboration. "Measurement of differential $t\bar{t}$ production cross sections in the full kinematic range using lepton+jets events from proton-proton collisions at $\sqrt{s} = 13$ TeV". In: *Phys. Rev. D* 104.9 (2021), p. 092013. DOI: 10.1103/PhysRevD.104.092013. arXiv: 2108.02803 [hep-ex].

[159] S. Fartoukh et al. *LHC Configuration and Operational Scenario for Run 3*. Tech. rep. CERN-ACC-2021-0007. 2021. URL: https://cds.cern.ch/record/2790409.

[160] I. Zurbano Fernandez et al. *High-Luminosity Large Hadron Collider (HL-LHC): Technical design report*. Tech. rep. CERN-2020-010. 2020. DOI: 10.23731/CYRM-2020-0010.

Acknowledgements

I have absolutely loved my time as a PhD student at DESY and that is in no small part due to the fantastic people in the DESY CMS top group, all of whom I would like to mention here but then these acknowledgements would be several pages long.

First and foremost, I would like to express my gratitude to my supervisors Dr. Olaf Behnke and Prof. Dr. Elisabetta Gallo for their guidance. A special thank you to you Olaf, for all your feedback and advice and not least your invaluable support. I would also like to thank Dr. Maria Aldaya Martin for her support and advice. And last, but certainly not least, I would like to say thank you to Dr. Mykola Savitskyi for his brilliant oversight of the analysis, and from whom I have learned a lot.

A special mention for the people in the tracker alignment group, both at DESY and CMS, for making the service task an exciting part of my PhD.

And finally, thank you to my family, friends and Joel.

Appendix A

Definitions of covariance matrices and χ^2 for theory to data comparisons

In this work, the theory to data comparisons in Chapter 8 are shown together with χ^2 values, which are defined as

$$\chi^2 = \mathbf{R}_N^{\mathrm{T}} \mathbf{Cov}_N^{-1} \mathbf{R}_N, \tag{A.1}$$

where $\mathbf{R}_N$ is a vector of differences between the measured cross sections and the corresponding predictions in all bins N of the measurement. The covariance matrix in Equation A.1 is given by

$$\mathbf{Cov_N} = \mathbf{Cov}^{\mathrm{unf}} + \mathbf{Cov}^{\mathrm{syst}}, \tag{A.2}$$

which is the sum of the individual covariance matrices for the statistical uncertainties from the unfolding procedure and systematic uncertainties, denoted by $\mathbf{Cov}^{\mathrm{unf}}$ and $\mathbf{Cov}^{\mathrm{syst}}$, respectively. The latter is defined as

$$\mathbf{Cov}_{ij}^{\mathrm{syst}} = \sum_{k,l} \frac{1}{N_k} C_{j,k,l} C_{i,k,l}, \quad 1 \leq i \leq N, \quad 1 \leq j \leq N, \tag{A.3}$$

where all data uncertainties are taken into account but uncertainties on the prediction are not considered. The term $C_{j,k,l}$ denotes a variation, l, for the systematic uncertainty source, k, in a specific bin of the measurement, i. The sum in Equation A.3 includes all systematic uncertainties and their variations, where the term N_k denotes the total number of variations of source k, which is typically 2 (i.e. up and down variations). An exception is the colour reconnection source, which has more variations.

Appendix B

Good runs

Table B.1: The list of good runs for data collected with the CMS experiment in 2016 which corresponds to an integrated luminosity of 36.3 fb^{-1}.

Sample	Run range
/MuonEG/Run2016B-17Jul2018_ver2-v1	273150–275376
/MuonEG/Run2016C-17Jul2018-v1	275656–276283
/MuonEG/Run2016D-17Jul2018-v1	276315–276811
/MuonEG/Run2016E-17Jul2018-v2	276831–277305
/MuonEG/Run2016F-17Jul2018-v1	277932–278808
/MuonEG/Run2016G-17Jul2018-v1	278923–280385
/MuonEG/Run2016H-17Jul2018-v1	281613–284044
/DoubleEG/Run2016B-17Jul2018_ver2-v1	273150–275376
/DoubleEG/Run2016C-17Jul2018-v1	275656–276283
/DoubleEG/Run2016D-17Jul2018-v1	276315–276811
/DoubleEG/Run2016E-17Jul2018-v1	276831–277305
/DoubleEG/Run2016F-17Jul2018-v1	277932–278808
/DoubleEG/Run2016G-17Jul2018-v1	278923–280385
/DoubleEG/Run2016H-17Jul2018-v1	281613–284044
/DoubleMuon/Run2016B-17Jul2018_ver2-v1	273150–275376
/DoubleMuon/Run2016C-17Jul2018-v1	275656–276283
/DoubleMuon/Run2016D-17Jul2018-v1	276315–276811
/DoubleMuon/Run2016E-17Jul2018-v1	276831–277305
/DoubleMuon/Run2016F-17Jul2018-v1	277932–278808
/DoubleMuon/Run2016G-17Jul2018-v1	278923–280385
/DoubleMuon/Run2016H-17Jul2018-v1	281613–284044
/SingleMuon/Run2016B-17Jul2018_ver2-v1	273150–275376
/SingleMuon/Run2016C-17Jul2018-v1	275656–276283
/SingleMuon/Run2016D-17Jul2018-v1	276315–276811
/SingleMuon/Run2016E-17Jul2018-v1	276831–277305
/SingleMuon/Run2016F-17Jul2018-v1	277932–278808
/SingleMuon/Run2016G-17Jul2018-v1	278923–280385
/SingleMuon/Run2016H-17Jul2018-v1	281613–284044
/SingleElectron/Run2016B-17Jul2018_ver2-v1	273150–275376
/SingleElectron/Run2016C-17Jul2018-v1	275656–276283
/SingleElectron/Run2016D-17Jul2018-v1	276315–276811
/SingleElectron/Run2016E-17Jul2018-v1	276831–277305
/SingleElectron/Run2016F-17Jul2018-v1	277932–278808
/SingleElectron/Run2016G-17Jul2018-v1	278923–280385
/SingleElectron/Run2016H-17Jul2018-v1	281613–284044

Table B.2: The list of good runs for data collected with the CMS experiment in 2017 which corresponds to an integrated luminosity of 41.5 fb^{-1}.

Sample	Run range
/MuonEG/Run2017B-31Mar2018-v1	297046–299329
/MuonEG/Run2017C-31Mar2018-v1	299368–302029
/MuonEG/Run2017D-31Mar2018-v1	302030–303434
/MuonEG/Run2017E-31Mar2018-v1	303824–304797
/MuonEG/Run2017F-31Mar2018-v1	305040–306462
/DoubleEG/Run2017B-31Mar2018-v1	297046–299329
/DoubleEG/Run2017C-31Mar2018-v1	299368–302029
/DoubleEG/Run2017D-31Mar2018-v1	302030–303434
/DoubleEG/Run2017E-31Mar2018-v1	303824–304797
/DoubleEG/Run2017F-31Mar2018-v1	305040–306462
/DoubleMuon/Run2017B-31Mar2018-v1	297046–299329
/DoubleMuon/Run2017C-31Mar2018-v1	299368–302029
/DoubleMuon/Run2017D-31Mar2018-v1	302030–303434
/DoubleMuon/Run2017E-31Mar2018-v1	303824–304797
/DoubleMuon/Run2017F-31Mar2018-v1	305040–306462
/SingleMuon/Run2017B-31Mar2018-v1	297046–299329
/SingleMuon/Run2017C-31Mar2018-v1	299368–302029
/SingleMuon/Run2017D-31Mar2018-v1	302030–303434
/SingleMuon/Run2017E-31Mar2018-v1	303824–304797
/SingleMuon/Run2017F-31Mar2018-v1	305040–306462
/SingleElectron/Run2017B-31Mar2018-v1	297046–299329
/SingleElectron/Run2017C-31Mar2018-v1	299368–302029
/SingleElectron/Run2017D-31Mar2018-v1	302030–303434
/SingleElectron/Run2017E-31Mar2018-v1	303824–304797
/SingleElectron/Run2017F-31Mar2018-v1	305040–306462

Table B.3: The list of good runs for data collected with the CMS experiment in 2018 which corresponds to an integrated luminosity of 59.7 fb^{-1}.

Sample	Run range
/MuonEG/Run2018A-17Sep2018-v1	315257–316995
/MuonEG/Run2018B-17Sep2018-v1	317080–319310
/MuonEG/Run2018C-17Sep2018-v1	319337–320065
/MuonEG/Run2018D-PromptReco-v2	320500–325175
/EGamma/Run2018A-17Sep2018-v2	315257–316995
/EGamma/Run2018B-17Sep2018-v1	317080–319310
/EGamma/Run2018C-17Sep2018-v1	319337–320065
/EGamma/Run2018D-22Jan2019-v2	320500–325175
/DoubleMuon/Run2018A-17Sep2018-v2	315257–316995
/DoubleMuon/Run2018B-17Sep2018-v1	317080–319310
/DoubleMuon/Run2018C-17Sep2018-v1	319337–320065
/DoubleMuon/Run2018D-PromptReco-v2	320500–325175
/SingleMuon/Run2018A-17Sep2018-v2	315257–316995
/SingleMuon/Run2018B-17Sep2018-v1	317080–319310
/SingleMuon/Run2018C-17Sep2018-v1	319337–320065
/SingleMuon/Run2018D-22Jan2019-v2	320500–325175

Appendix C

Simulated samples

C.1 Nominal signal

Table C.1: The list of simulated $t\bar{t}$ signal and background samples (nominal) used in the analysis of the 2016 data are shown together with their corresponding cross sections.

sample	σ [pb]
/TTTo2L2Nu_TuneCP5_PSweights_13TeV-powheg-pythia8/ RunIISummer16MiniAODv3-PUMoriond17_94X_mcRun2_asymptotic_v3-v1	830.91×0.10706
/TTToSemiLeptonic_TuneCP5_PSweights_13TeV-powheg-pythia8/ RunIISummer16MiniAODv3-PUMoriond17_94X_mcRun2_asymptotic_v3-v1	830.91×0.44113
/TTToHadronic_TuneCP5_PSweights_13TeV-powheg-pythia8/ RunIISummer16MiniAODv3-PUMoriond17_94X_mcRun2_asymptotic_v3-v1	830.91×0.45441
/ST_s-channel_4f_leptonDecays_TuneCP5_PSweights_13TeV-amcatnlo-pythia8/ RunIISummer16MiniAODv3-PUMoriond17_94X_mcRun2_asymptotic_v3-v1	10.32
/ST_tW_top_5f_NoFullyHadronicDecays_TuneCP5_PSweights_13TeV-powheg-pythia8/ RunIISummer16MiniAODv3-94X_mcRun2_asymptotic_v3-v1	35.85×0.54559
/ST_tW_antitop_5f_NoFullyHadronicDecays_TuneCP5_PSweights_13TeV-powheg-pythia8/ RunIISummer16MiniAODv3-94X_mcRun2_asymptotic_v3-v1	35.85×0.54559
/ST_t-channel_top_4f_InclusiveDecays_TuneCP5_PSweights_13TeV-powheg-pythia8/ RunIISummer16MiniAODv3-PUMoriond17_94X_mcRun2_asymptotic_v3-v1	136.02
/ST_t-channel_antitop_4f_InclusiveDecays_TuneCP5_PSweights_13TeV-powheg-pythia8/ RunIISummer16MiniAODv3-PUMoriond17_94X_mcRun2_asymptotic_v3-v1	80.95
/DYJetsToLL_M-10to50_TuneCUETP8M1_13TeV-madgraphMLM-pythia8/ RunIISummer16MiniAODv3-PUMoriond17_94X_mcRun2_asymptotic_v3-v2	22635.1
/DYJetsToLL_M-50_TuneCUETP8M1_13TeV-amcatnloFXFX-pythia8/ RunIISummer16MiniAODv3-PUMoriond17_94X_mcRun2_asymptotic_v3_ext2-v1	6225.4
/WJetsToLNu_TuneCUETP8M1_13TeV-madgraphMLM-pythia8/ RunIISummer16MiniAODv3-PUMoriond17_94X_mcRun2_asymptotic_v3-v2	61526.7
/WJetsToLNu_TuneCUETP8M1_13TeV-madgraphMLM-pythia8/ RunIISummer16MiniAODv3-PUMoriond17_94X_mcRun2_asymptotic_v3_ext2-v2	61526.7
/WW_TuneCUETP8M1_13TeV-pythia8/ RunIISummer16MiniAODv3-PUMoriond17_94X_mcRun2_asymptotic_v3-v2	118.7
/WW_TuneCUETP8M1_13TeV-pythia8/ RunIISummer16MiniAODv3-PUMoriond17_94X_mcRun2_asymptotic_v3_ext1-v21	118.7
/WZ_TuneCUETP8M1_13TeV-pythia8/ RunIISummer16MiniAODv3-PUMoriond17_94X_mcRun2_asymptotic_v3-v2	47.13
/WZ_TuneCUETP8M1_13TeV-pythia8/ RunIISummer16MiniAODv3-PUMoriond17_94X_mcRun2_asymptotic_v3_ext1-v2	47.13
/ZZ_TuneCUETP8M1_13TeV-pythia8/ RunIISummer16MiniAODv3-PUMoriond17_94X_mcRun2_asymptotic_v3-v2	16.523
/ZZ_TuneCUETP8M1_13TeV-pythia8/ RunIISummer16MiniAODv3-PUMoriond17_94X_mcRun2_asymptotic_v3_ext1-v2	16.523
/TTWJetsToLNu_TuneCUETP8M1_13TeV-amcatnloFXFX-madspin-pythia8/ RunIISummer16MiniAODv3-PUMoriond17_94X_mcRun2_asymptotic_v3_ext1-v2	0.2043
/TTWJetsToLNu_TuneCUETP8M1_13TeV-amcatnloFXFX-madspin-pythia8/ RunIISummer16MiniAODv3-PUMoriond17_94X_mcRun2_asymptotic_v3_ext2-v1	0.2043
/TTWJetsToQQ_TuneCUETP8M1_13TeV-amcatnloFXFX-madspin-pythia8/ RunIISummer16MiniAODv3-PUMoriond17_94X_mcRun2_asymptotic_v3-v2	0.4062
/TTZToLLNuNu_M-10_TuneCUETP8M1_13TeV-amcatnlo-pythia8/ RunIISummer16MiniAODv3-PUMoriond17_94X_mcRun2_asymptotic_v3_ext1-v2	0.2529
/TTZToLLNuNu_M-10_TuneCUETP8M1_13TeV-amcatnlo-pythia8/ RunIISummer16MiniAODv3-PUMoriond17_94X_mcRun2_asymptotic_v3_ext2-v1	0.2529
/TTZToLLNuNu_M-10_TuneCUETP8M1_13TeV-amcatnlo-pythia8/ RunIISummer16MiniAODv3-PUMoriond17_94X_mcRun2_asymptotic_v3_ext3-v1	0.2529
/TTZToQQ_TuneCUETP8M1_13TeV-amcatnlo-pythia8/ RunIISummer16MiniAODv3-PUMoriond17_94X_mcRun2_asymptotic_v3-v2	0.5297

Table C.2: The list of simulated $t\bar{t}$ signal and background samples (nominal) used in the analysis of the 2017 data are shown together with their corresponding cross sections.

sample	σ [pb]
/TTTo2L2Nu_TuneCP5_PSweights_13TeV-powheg-pythia8/ RunIIFall17MiniAODv2-PU2017_12Apr2018_new_pmx_94X_mc2017_realistic_v14-v2	830.91×0.10706
/TTToSemiLeptonic_TuneCP5_PSweights_13TeV-powheg-pythia8/ RunIIFall17MiniAODv2-PU2017_12Apr2018_94X_mc2017_realistic_v14-v2	830.91×0.44113
/TTToHadronic_TuneCP5_PSweights_13TeV-powheg-pythia8/ RunIIFall17MiniAODv2-PU2017_12Apr2018_new_pmx_94X_mc2017_realistic_v14-v1	830.91×0.45441
/ST_s-channel_4f_leptonDecays_TuneCP5_PSweights_13TeV-amcatnlo-pythia8 ... _correctnPartonsInBorn/RunIIFall17MiniAODv2-PU2017_12Apr2018_94X_mc2017_realistic_v14-v1	10.32
/ST_tW_top_5f_NoFullyHadronicDecays_TuneCP5_PSweights_13TeV-powheg-pythia8/ RunIIFall17MiniAODv2-PU2017_12Apr2018_new_pmx_94X_mc2017_realistic_v14-v1	35.85×0.54559
/ST_tW_antitop_5f_NoFullyHadronicDecays_TuneCP5_PSweights_13TeV-powheg-pythia8/ RunIIFall17MiniAODv2-PU2017_12Apr2018_94X_mc2017_realistic_v14-v2	35.85×0.54559
/ST_t-channel_top_4f_InclusiveDecays_TuneCP5_PSweights_13TeV-powheg-pythia8/ RunIIFall17MiniAODv2-PU2017_12Apr2018_94X_mc2017_realistic_v14-v1	136.02
/ST_t-channel_antitop_4f_InclusiveDecays_TuneCP5_PSweights_13TeV-powheg-pythia8/ RunIIFall17MiniAODv2-PU2017_12Apr2018_94X_mc2017_realistic_v14-v1	80.95
/DYJetsToLL_M-10to50_TuneCP5_13TeV-madgraphMLM-pythia8/ RunIIFall17MiniAODv2-PU2017_12Apr2018_94X_mc2017_realistic_v14_ext1-v2	22635.1
/DYJetsToLL_M-50_TuneCP5_13TeV-amcatnloFXFX-pythia8/ RunIIFall17MiniAODv2-PU2017_12Apr2018_new_pmx_94X_mc2017_realistic_v14-v1	6225.4
/DYJetsToLL_M-50_TuneCP5_13TeV-amcatnloFXFX-pythia8/ RunIIFall17MiniAODv2-PU2017_12Apr2018_new_pmx_94X_mc2017_realistic_v14_ext1-v1	6225.4
/DYJetsToLL_M-50_TuneCP5_13TeV-amcatnloFXFX-pythia8/ RunIIFall17MiniAODv2-PU2017_12Apr2018_94X_mc2017_realistic_v14_ext3-v1	6225.4
/WJetsToLNu_TuneCP5_13TeV-madgraphMLM-pythia8/ RunIIFall17MiniAODv2-PU2017_12Apr2018_94X_mc2017_realistic_v14-v2	61526.7
/WJetsToLNu_TuneCP5_13TeV-madgraphMLM-pythia8/ RunIIFall17MiniAODv2-PU2017_12Apr2018_94X_mc2017_realistic_v14_ext1-v2	61526.7
/WW_TuneCP5_13TeV-pythia8/ RunIIFall17MiniAODv2-PU2017_12Apr2018_94X_mc2017_realistic_v14-v1	118.7
/WZ_TuneCP5_13TeV-pythia8/ RunIIFall17MiniAODv2-PU2017_12Apr2018_94X_mc2017_realistic_v14-v1	47.13
/ZZ_TuneCP5_13TeV-pythia8/ RunIIFall17MiniAODv2-PU2017_12Apr2018_new_pmx_94X_mc2017_realistic_v14-v2	16.523
/TTWJetsToLNu_TuneCP5_PSweights_13TeV-amcatnloFXFX-madspin-pythia8/ RunIIFall17MiniAODv2-PU2017_12Apr2018_new_pmx_94X_mc2017_realistic_v14-v1	0.2043
/TTWJetsToQQ_TuneCP5_13TeV-amcatnloFXFX-madspin-pythia8/ RunIIFall17MiniAODv2-PU2017_12Apr2018_94X_mc2017_realistic_v14-v2	0.4062
/TTZToLLNuNu_M-10_TuneCP5_PSweights_13TeV-amcatnlo-pythia8/ RunIIFall17MiniAODv2-PU2017_12Apr2018_94X_mc2017_realistic_v14-v1	0.2529
/TTZToQQ_TuneCP5_13TeV-amcatnlo-pythia8/ RunIIFall17MiniAODv2-PU2017_12Apr2018_94X_mc2017_realistic_v14-v2	0.5297

Table C.3: The list of simulated $t\bar{t}$ signal and background samples (nominal) used in the analysis of the 2018 data are shown together with their corresponding cross sections.

sample	σ [pb]
/TTTo2L2Nu_TuneCP5_13TeV-powheg-pythia8/ RunIIAutumn18MiniAOD-102X_upgrade2018_realistic_v15-v1	830.91×0.10706
/TTToSemiLeptonic_TuneCP5_13TeV-powheg-pythia8/ RunIIAutumn18MiniAOD-102X_upgrade2018_realistic_v15-v1	830.91×0.44113
/TTToHadronic_TuneCP5_13TeV-powheg-pythia8/ RunIIAutumn18MiniAOD-102X_upgrade2018_realistic_v15-v1	830.91×0.45441
/ST_s-channel_4f_leptonDecays_TuneCP5_13TeV-amcatnlo-pythia8/ RunIIAutumn18MiniAOD-102X_upgrade2018_realistic_v15-v1	10.32
/ST_tW_top_5f_NoFullyHadronicDecays_TuneCP5_13TeV-powheg-pythia8/ RunIIAutumn18MiniAOD-102X_upgrade2018_realistic_v15_ext1-v2	35.85×0.54559
/ST_tW_top_5f_NoFullyHadronicDecays_TuneCP5_13TeV-powheg-pythia8/ RunIIAutumn18MiniAOD-102X_upgrade2018_realistic_v15_ext1-v3	35.85×0.54559
/ST_tW_antitop_5f_NoFullyHadronicDecays_TuneCP5_13TeV-powheg-pythia8/ RunIIAutumn18MiniAOD-102X_upgrade2018_realistic_v15_ext1-v2	35.85×0.54559
/ST_tW_antitop_5f_NoFullyHadronicDecays_TuneCP5_13TeV-powheg-pythia8/ RunIIAutumn18MiniAOD-102X_upgrade2018_realistic_v15_ext1-v3	35.85×0.54559
/ST_t-channel_top_4f_InclusiveDecays_TuneCP5_13TeV-powheg-madspin-pythia8/ RunIIAutumn18MiniAOD-102X_upgrade2018_realistic_v15-v1	136.02
/ST_t-channel_antitop_5f_TuneCP5_13TeV-powheg-pythia8/ RunIIAutumn18MiniAOD-102X_upgrade2018_realistic_v15-v1	80.95
/DYJetsToLL_M-10to50_TuneCP5_13TeV-madgraphMLM-pythia8/ RunIIAutumn18MiniAOD-102X_upgrade2018_realistic_v15-v2	22635.1
/DYJetsToLL_M-10to50_TuneCP5_13TeV-madgraphMLM-pythia8/ RunIIAutumn18MiniAOD-102X_upgrade2018_realistic_v15_ext1-v1	22635.1
/DYJetsToLL_M-50_TuneCP5_13TeV-amcatnloFXFX-pythia8/ RunIIAutumn18MiniAOD-102X_upgrade2018_realistic_v15-v1	6225.4
/DYJetsToLL_M-50_TuneCP5_13TeV-amcatnloFXFX-pythia8/ RunIIAutumn18MiniAOD-102X_upgrade2018_realistic_v15_ext2-v1	6225.4
/WJetsToLNu_TuneCP5_13TeV-madgraphMLM-pythia8/ RunIIAutumn18MiniAOD-102X_upgrade2018_realistic_v15-v2	61526.7
/WW_TuneCP5_PSweights_13TeV-pythia8/ RunIIAutumn18MiniAOD-102X_upgrade2018_realistic_v15-v1	118.7
/WZ_TuneCP5_PSweights_13TeV-pythia8/ RunIIAutumn18MiniAOD-102X_upgrade2018_realistic_v15-v1	47.13
/ZZ_TuneCP5_13TeV-pythia8/ RunIIAutumn18MiniAOD-102X_upgrade2018_realistic_v15-v2	16.523
/TTWJetsToLNu_TuneCP5_13TeV-amcatnloFXFX-madspin-pythia8/ RunIIAutumn18MiniAOD-102X_upgrade2018_realistic_v15_ext1-v2	0.2043
/TTWJetsToQQ_TuneCP5_13TeV-amcatnloFXFX-madspin-pythia8/ RunIIAutumn18MiniAOD-102X_upgrade2018_realistic_v15-v1	0.4062
/TTZToLLNuNu_M-10_TuneCP5_13TeV-amcatnlo-pythia8/ RunIIAutumn18MiniAOD-102X_upgrade2018_realistic_v15_ext1-v2	0.2529
/TTZToQQ_TuneCP5_13TeV-amcatnlo-pythia8/ RunIIAutumn18MiniAOD-102X_upgrade2018_realistic_v15-v1	0.5297

C.2 Independent systematic uncertainties

Table C.4: The list of simulated signal $t\bar{t}$ samples used for estimating the systematic uncertainties on the top mass, underlying event tune, colour reconnection and h_{damp} in the analysis of the 2016 data are shown together with their corresponding cross sections.

sample	σ [pb]
/TTTo2L2Nu_hdampDOWN_TuneCP5_PSweights_13TeV-powheg-pythia8/ RunIISummer16MiniAODv3-PUMoriond17_94X_mcRun2_asymptotic_v3-v1	830.91×0.10706
/TTTo2L2Nu_hdampDOWN_TuneCP5_PSweights_13TeV-powheg-pythia8/ RunIISummer16MiniAODv3-PUMoriond17_94X_mcRun2_asymptotic_v3_ext1-v1	830.91×0.10706
/TTTo2L2Nu_hdampDOWN_TuneCP5_PSweights_13TeV-powheg-pythia8/ RunIISummer16MiniAODv3-PUMoriond17_94X_mcRun2_asymptotic_v3_ext2-v1	830.91×0.10706
/TTTo2L2Nu_hdampUP_TuneCP5_PSweights_13TeV-powheg-pythia8/ RunIISummer16MiniAODv3-PUMoriond17_94X_mcRun2_asymptotic_v3-v1	830.91×0.10706
/TTTo2L2Nu_hdampUP_TuneCP5_PSweights_13TeV-powheg-pythia8/ RunIISummer16MiniAODv3-PUMoriond17_94X_mcRun2_asymptotic_v3_ext1-v1	830.91×0.10706
/TTTo2L2Nu_hdampUP_TuneCP5_PSweights_13TeV-powheg-pythia8/ RunIISummer16MiniAODv3-PUMoriond17_94X_mcRun2_asymptotic_v3_ext2-v1	830.91×0.10706
/TTTo2L2Nu_TuneCP5down_PSweights_13TeV-powheg-pythia8/ RunIISummer16MiniAODv3-PUMoriond17_94X_mcRun2_asymptotic_v3-v1	830.91×0.10706
/TTTo2L2Nu_TuneCP5down_PSweights_13TeV-powheg-pythia8/ RunIISummer16MiniAODv3-PUMoriond17_94X_mcRun2_asymptotic_v3_ext1-v1	830.91×0.10706
/TTTo2L2Nu_TuneCP5down_PSweights_13TeV-powheg-pythia8/ RunIISummer16MiniAODv3-PUMoriond17_94X_mcRun2_asymptotic_v3_ext2-v1	830.91×0.10706
/TTTo2L2Nu_TuneCP5up_PSweights_13TeV-powheg-pythia8/ RunIISummer16MiniAODv3-PUMoriond17_94X_mcRun2_asymptotic_v3-v1	830.91×0.10706
/TTTo2L2Nu_TuneCP5up_PSweights_13TeV-powheg-pythia8/ RunIISummer16MiniAODv3-PUMoriond17_94X_mcRun2_asymptotic_v3_ext1-v1	830.91×0.10706
/TTTo2L2Nu_TuneCP5up_PSweights_13TeV-powheg-pythia8/ RunIISummer16MiniAODv3-PUMoriond17_94X_mcRun2_asymptotic_v3_ext2-v1	830.91×0.10706
/TTTo2L2Nu_TuneCP5_PSweights_erdON_13TeV-powheg-pythia8/ RunIISummer16MiniAODv3-PUMoriond17_94X_mcRun2_asymptotic_v3-v1	830.91×0.10706
/TTTo2L2Nu_TuneCP5_PSweights_erdON_13TeV-powheg-pythia8/ RunIISummer16MiniAODv3-PUMoriond17_94X_mcRun2_asymptotic_v3_ext1-v1	830.91×0.10706
/TTTo2L2Nu_TuneCP5_PSweights_erdON_13TeV-powheg-pythia8/ RunIISummer16MiniAODv3-PUMoriond17_94X_mcRun2_asymptotic_v3_ext2-v1	830.91×0.10706
/TTTo2L2Nu_TuneCP5CR1_QCDbased_PSweights_13TeV-powheg-pythia8/ RunIISummer16MiniAODv3-PUMoriond17_94X_mcRun2_asymptotic_v3-v1	830.91×0.10706
/TTTo2L2Nu_TuneCP5CR1_QCDbased_PSweights_13TeV-powheg-pythia8/ RunIISummer16MiniAODv3-PUMoriond17_94X_mcRun2_asymptotic_v3_ext1-v1	830.91×0.10706
/TTTo2L2Nu_TuneCP5CR2_GluonMove_PSweights_13TeV-powheg-pythia8/ RunIISummer16MiniAODv3-PUMoriond17_94X_mcRun2_asymptotic_v3-v1	830.91×0.10706
/TTTo2L2Nu_TuneCP5CR2_GluonMove_PSweights_13TeV-powheg-pythia8/ RunIISummer16MiniAODv3-PUMoriond17_94X_mcRun2_asymptotic_v3_ext1-v1	830.91×0.10706
/TTTo2L2Nu_TuneCP5_PSweights_mtop1695_13TeV-powheg-pythia8/ RunIISummer16MiniAODv3-PUMoriond17_backup_94X_mcRun2_asymptotic_v3-v1	830.91×0.10706
/TTTo2L2Nu_TuneCP5_PSweights_mtop1695_13TeV-powheg-pythia8/ RunIISummer16MiniAODv3-PUMoriond17_backup_94X_mcRun2_asymptotic_v3_ext1-v1	830.91×0.10706
/TTTo2L2Nu_TuneCP5_PSweights_mtop1755_13TeV-powheg-pythia8/ RunIISummer16MiniAODv3-PUMoriond17_backup_94X_mcRun2_asymptotic_v3-v1	830.91×0.10706
/TTTo2L2Nu_TuneCP5_PSweights_mtop1755_13TeV-powheg-pythia8/ RunIISummer16MiniAODv3-PUMoriond17_backup_94X_mcRun2_asymptotic_v3_ext1-v1	830.91×0.10706

Table C.5: The list of alternative simulated $t\bar{t}$ signal samples used in the analysis of the 2016 data are shown together with their corresponding cross sections.

sample	σ [pb]
/TTJets_TuneCP5_PSweights_13TeV-amcatnloFXFX-pythia8/ RunIISummer16MiniAODv3-PUMoriond17_94X_mcRun2_asymptotic_v3-v1	830.91
/TT_TuneEE5C_13TeV-powheg-herwigpp/ RunIISummer16MiniAODv3-PUMoriond17_94X_mcRun2_asymptotic_v3_ext3-v2	830.91

Table C.6: The list of simulated semi-leptonic $t\bar{t}$ samples used for estimating the systematic uncertainties on the top mass, underlying event tune, colour reconnection and h_{damp} in the analysis of the 2016 data are shown together with their corresponding cross sections.

sample	σ [pb]
/TTToSemiLeptonic_hdampDOWN_TuneCP5_PSweights_13TeV-powheg-pythia8/ RunIISummer16MiniAODv3-PUMoriond17_94X_mcRun2_asymptotic_v3-v1	830.91×0.44113
/TTToSemiLeptonic_hdampUP_TuneCP5_PSweights_13TeV-powheg-pythia8/ RunIISummer16MiniAODv3-PUMoriond17_94X_mcRun2_asymptotic_v3-v1	830.91×0.44113
/TTToSemiLeptonic_TuneCP5down_PSweights_13TeV-powheg-pythia8/ RunIISummer16MiniAODv3-PUMoriond17_94X_mcRun2_asymptotic_v3-v1	830.91×0.44113
/TTToSemiLeptonic_TuneCP5up_PSweights_13TeV-powheg-pythia8/ RunIISummer16MiniAODv3-PUMoriond17_94X_mcRun2_asymptotic_v3-v1	830.91×0.44113
/TTToSemiLeptonic_TuneCP5_PSweights_erdON_13TeV-powheg-pythia8/ RunIISummer16MiniAODv3-PUMoriond17_94X_mcRun2_asymptotic_v3-v1	830.91×0.44113
/TTToSemiLeptonic_TuneCP5CR1_QCDbased_PSweights_13TeV-powheg-pythia8/ RunIISummer16MiniAODv3-PUMoriond17_94X_mcRun2_asymptotic_v3-v1	830.91×0.44113
/TTToSemiLeptonic_TuneCP5CR2_GluonMove_PSweights_13TeV-powheg-pythia8/ RunIISummer16MiniAODv3-PUMoriond17_94X_mcRun2_asymptotic_v3-v1	830.91×0.44113
/TTToSemiLeptonic_TuneCP5_PSweights_mtop1695_13TeV-powheg-pythia8/ RunIISummer16MiniAODv3-PUMoriond17_backup_94X_mcRun2_asymptotic_v3-v1	830.91×0.44113
/TTToSemiLeptonic_TuneCP5_PSweights_mtop1755_13TeV-powheg-pythia8/ RunIISummer16MiniAODv3-PUMoriond17_backup_94X_mcRun2_asymptotic_v3-v1	830.91×0.44113

Table C.7: The list of simulated all-hadronic $t\bar{t}$ samples used for estimating the systematic uncertainties on the top mass, underlying event tune, colour reconnection and h_{damp} in the analysis of the 2016 data are shown together with their corresponding cross sections.

sample	σ [pb]
/TTToHadronic_hdampDOWN_TuneCP5_PSweights_13TeV-powheg-pythia8/ RunIISummer16MiniAODv3-PUMoriond17_94X_mcRun2_asymptotic_v3-v2	830.91×0.45441
/TTToHadronic_hdampUP_TuneCP5_PSweights_13TeV-powheg-pythia8/ RunIISummer16MiniAODv3-PUMoriond17_94X_mcRun2_asymptotic_v3-v1	830.91×0.45441
/TTToHadronic_TuneCP5down_PSweights_13TeV-powheg-pythia8/ RunIISummer16MiniAODv3-PUMoriond17_94X_mcRun2_asymptotic_v3-v1	830.91×0.45441
/TTToHadronic_TuneCP5up_PSweights_13TeV-powheg-pythia8/ RunIISummer16MiniAODv3-PUMoriond17_94X_mcRun2_asymptotic_v3-v1	830.91×0.45441
/TTToHadronic_TuneCP5_PSweights_erdON_13TeV-powheg-pythia8/ RunIISummer16MiniAODv3-PUMoriond17_94X_mcRun2_asymptotic_v3-v1	830.91×0.45441
/TTToHadronic_TuneCP5CR1_QCDbased_PSweights_13TeV-powheg-pythia8/ RunIISummer16MiniAODv3-PUMoriond17_94X_mcRun2_asymptotic_v3-v1	830.91×0.45441
/TTToHadronic_TuneCP5CR2_GluonMove_PSweights_13TeV-powheg-pythia8/ RunIISummer16MiniAODv3-PUMoriond17_94X_mcRun2_asymptotic_v3-v1	830.91×0.45441
/TTToHadronic_TuneCP5_PSweights_mtop1695_13TeV-powheg-pythia8/ RunIISummer16MiniAODv3-PUMoriond17_backup_94X_mcRun2_asymptotic_v3-v1	830.91×0.45441
/TTToHadronic_TuneCP5_PSweights_mtop1755_13TeV-powheg-pythia8/ RunIISummer16MiniAODv3-PUMoriond17_backup_94X_mcRun2_asymptotic_v3-v1	830.91×0.45441

Table C.8: The list of simulated signal $t\bar{t}$ samples used for estimating the systematic uncertainties on the top mass, underlying event tune, colour reconnection and h_{damp} in the analysis of the 2017 data are shown together with their corresponding cross sections.

sample	σ [pb]
/TTTo2L2Nu_hdampDOWN_TuneCP5_PSweights_13TeV-powheg-pythia8/ RunIIFall17MiniAODv2-PU2017_12Apr2018_new_pmx_94X_mc2017_realistic_v14-v1	830.91×0.10706
/TTTo2L2Nu_hdampDOWN_TuneCP5_PSweights_13TeV-powheg-pythia8/ RunIIFall17MiniAODv2-PU2017_12Apr2018_94X_mc2017_realistic_v14_ext1-v1	830.91×0.10706
/TTTo2L2Nu_hdampDOWN_TuneCP5_PSweights_13TeV-powheg-pythia8/ RunIIFall17MiniAODv2-PU2017_12Apr2018_94X_mc2017_realistic_v14_ext2-v2	830.91×0.10706
/TTTo2L2Nu_hdampUP_TuneCP5_PSweights_13TeV-powheg-pythia8/ RunIIFall17MiniAODv2-PU2017_12Apr2018_new_pmx_94X_mc2017_realistic_v14-v1	830.91×0.10706
/TTTo2L2Nu_hdampUP_TuneCP5_PSweights_13TeV-powheg-pythia8/ RunIIFall17MiniAODv2-PU2017_12Apr2018_94X_mc2017_realistic_v14_ext1-v1	830.91×0.10706
/TTTo2L2Nu_hdampUP_TuneCP5_PSweights_13TeV-powheg-pythia8/ RunIIFall17MiniAODv2-PU2017_12Apr2018_94X_mc2017_realistic_v14_ext2-v2	830.91×0.10706
/TTTo2L2Nu_TuneCP5down_PSweights_13TeV-powheg-pythia8/ RunIIFall17MiniAODv2-PU2017_12Apr2018_new_pmx_94X_mc2017_realistic_v14-v1	830.91×0.10706
/TTTo2L2Nu_TuneCP5down_PSweights_13TeV-powheg-pythia8/ RunIIFall17MiniAODv2-PU2017_12Apr2018_94X_mc2017_realistic_v14_ext1-v1	830.91×0.10706
/TTTo2L2Nu_TuneCP5down_PSweights_13TeV-powheg-pythia8/ RunIIFall17MiniAODv2-PU2017_12Apr2018_94X_mc2017_realistic_v14_ext2-v2	830.91×0.10706
/TTTo2L2Nu_TuneCP5up_PSweights_13TeV-powheg-pythia8/ RunIIFall17MiniAODv2-PU2017_12Apr2018_new_pmx_94X_mc2017_realistic_v14-v1	830.91×0.10706
/TTTo2L2Nu_TuneCP5up_PSweights_13TeV-powheg-pythia8/ RunIIFall17MiniAODv2-PU2017_12Apr2018_94X_mc2017_realistic_v14_ext1-v1	830.91×0.10706
/TTTo2L2Nu_TuneCP5up_PSweights_13TeV-powheg-pythia8/ RunIIFall17MiniAODv2-PU2017_12Apr2018_94X_mc2017_realistic_v14_ext2-v2	830.91×0.10706
/TTTo2L2Nu_TuneCP5_erdON_13TeV-powheg-pythia8/ RunIIFall17MiniAODv2-PU2017_12Apr2018_94X_mc2017_realistic_v14-v1	830.91×0.10706
/TTTo2L2Nu_TuneCP5_erdON_13TeV-powheg-pythia8/ RunIIFall17MiniAODv2-PU2017_12Apr2018_94X_mc2017_realistic_v14_ext2-v2	830.91×0.10706
/TTTo2L2Nu_TuneCP5CR1_QCDbased_PSweights_13TeV-powheg-pythia8/ RunIIFall17MiniAODv2-PU2017_12Apr2018_94X_mc2017_realistic_v14-v1	830.91×0.10706
/TTTo2L2Nu_TuneCP5CR1_QCDbased_PSweights_13TeV-powheg-pythia8/ RunIIFall17MiniAODv2-PU2017_12Apr2018_94X_mc2017_realistic_v14_ext1-v1	830.91×0.10706
/TTTo2L2Nu_TuneCP5CR1_QCDbased_PSweights_13TeV-powheg-pythia8/ RunIIFall17MiniAODv2-PU2017_12Apr2018_94X_mc2017_realistic_v14_ext2-v2	830.91×0.10706
/TTTo2L2Nu_TuneCP5CR2_GluonMove_PSweights_13TeV-powheg-pythia8/ RunIIFall17MiniAODv2-PU2017_12Apr2018_94X_mc2017_realistic_v14-v1	830.91×0.10706
/TTTo2L2Nu_TuneCP5CR2_GluonMove_PSweights_13TeV-powheg-pythia8/ RunIIFall17MiniAODv2-PU2017_12Apr2018_94X_mc2017_realistic_v14_ext1-v1	830.91×0.10706
/TTTo2L2Nu_TuneCP5CR2_GluonMove_PSweights_13TeV-powheg-pythia8/ RunIIFall17MiniAODv2-PU2017_12Apr2018_94X_mc2017_realistic_v14_ext2-v2	830.91×0.10706
/TTTo2L2Nu_mtop169p5_TuneCP5_PSweights_13TeV-powheg-pythia8/ RunIIFall17MiniAODv2-PU2017_12Apr2018_new_pmx_94X_mc2017_realistic_v14-v1	830.91×0.10706
/TTTo2L2Nu_mtop169p5_TuneCP5_PSweights_13TeV-powheg-pythia8/ RunIIFall17MiniAODv2-PU2017_12Apr2018_94X_mc2017_realistic_v14_ext1-v1	830.91×0.10706
/TTTo2L2Nu_mtop169p5_TuneCP5_PSweights_13TeV-powheg-pythia8/ RunIIFall17MiniAODv2-PU2017_12Apr2018_94X_mc2017_realistic_v14_ext2-v2	830.91×0.10706
/TTTo2L2Nu_mtop175p5_TuneCP5_PSweights_13TeV-powheg-pythia8/ RunIIFall17MiniAODv2-PU2017_12Apr2018_new_pmx_94X_mc2017_realistic_v14-v1	830.91×0.10706
/TTTo2L2Nu_mtop175p5_TuneCP5_PSweights_13TeV-powheg-pythia8/ RunIIFall17MiniAODv2-PU2017_12Apr2018_94X_mc2017_realistic_v14_ext1-v1	830.91×0.10706
/TTTo2L2Nu_mtop175p5_TuneCP5_PSweights_13TeV-powheg-pythia8/ RunIIFall17MiniAODv2-PU2017_12Apr2018_94X_mc2017_realistic_v14_ext2-v2	830.91×0.10706

Table C.9: The list of alternative simulated $t\bar{t}$ signal samples used in the analysis of the 2017 data are shown together with their corresponding cross sections.

sample	σ [pb]
/TTJets_TuneCP5_13TeV-amcatnloFXFX-pythia8/ RunIIFall17MiniAODv2-PU2017_12Apr2018_new_pmx_94X_mc2017_realistic_v14-v1	830.91
/TT_TuneCH3_13TeV-powheg-herwig7/ RunIIFall17MiniAODv2-PU2017_12Apr2018_94X_mc2017_realistic_v14-v2	830.91

Table C.10: The list of simulated semi-leptonic $t\bar{t}$ samples used for estimating the systematic uncertainties on the top mass, underlying event tune, colour reconnection and h_{damp} in the analysis of the 2017 data are shown together with their corresponding cross sections.

sample	σ [pb]
/TTToSemiLeptonic_hdampDOWN_TuneCP5_PSweights_13TeV-powheg-pythia8/ RunIIFall17MiniAODv2-PU2017_12Apr2018_94X_mc2017_realistic_v14-v1	830.91×0.44113
/TTToSemiLeptonic_hdampUP_TuneCP5_PSweights_13TeV-powheg-pythia8/ RunIIFall17MiniAODv2-PU2017_12Apr2018_new_pmx_94X_mc2017_realistic_v14-v2	830.91×0.44113
/TTToSemiLeptonic_TuneCP5down_PSweights_13TeV-powheg-pythia8/ RunIIFall17MiniAODv2-PU2017_12Apr2018_94X_mc2017_realistic_v14-v1	830.91×0.44113
/TTToSemiLeptonic_TuneCP5up_PSweights_13TeV-powheg-pythia8/ RunIIFall17MiniAODv2-PU2017_12Apr2018_new_pmx_94X_mc2017_realistic_v14-v2	830.91×0.44113
/TTToSemiLeptonic_TuneCP5_erdON_13TeV-powheg-pythia8/ RunIIFall17MiniAODv2-PU2017_12Apr2018_94X_mc2017_realistic_v14-v1	830.91×0.44113
/TTToSemiLeptonic_TuneCP5CR1_QCDbased_PSweights_13TeV-powheg-pythia8/ RunIIFall17MiniAODv2-PU2017_12Apr2018_94X_mc2017_realistic_v14-v1	830.91×0.44113
/TTToSemiLeptonic_TuneCP5CR2_GluonMove_PSweights_13TeV-powheg-pythia8/ RunIIFall17MiniAODv2-PU2017_12Apr2018_94X_mc2017_realistic_v14-v1	830.91×0.44113
/TTToSemiLeptonic_mtop169p5_TuneCP5_PSweights_13TeV-powheg-pythia8/ RunIIFall17MiniAODv2-PU2017_12Apr2018_new_pmx_94X_mc2017_realistic_v14-v1	830.91×0.44113
/TTToSemiLeptonic_mtop169p5_TuneCP5_PSweights_13TeV-powheg-pythia8/ RunIIFall17MiniAODv2-PU2017_12Apr2018_94X_mc2017_realistic_v14_ext1-v1	830.91×0.44113
/TTToSemiLeptonic_mtop175p5_TuneCP5_PSweights_13TeV-powheg-pythia8/ RunIIFall17MiniAODv2-PU2017_12Apr2018_new_pmx_94X_mc2017_realistic_v14-v2	830.91×0.44113
/TTToSemiLeptonic_mtop175p5_TuneCP5_PSweights_13TeV-powheg-pythia8/ RunIIFall17MiniAODv2-PU2017_12Apr2018_94X_mc2017_realistic_v14_ext1-v1	830.91×0.44113

Table C.11: The list of simulated all-hadronic $t\bar{t}$ samples used for estimating the systematic uncertainties on the top mass, underlying event tune, colour reconnection and h_{damp} in the analysis of the 2017 data are shown together with their corresponding cross sections.

sample	σ [pb]
/TTToHadronic_hdampDOWN_TuneCP5_PSweights_13TeV-powheg-pythia8/ RunIIFall17MiniAODv2-PU2017_12Apr2018_new_pmx_94X_mc2017_realistic_v14-v1	830.91×0.45441
/TTToHadronic_hdampUP_TuneCP5_PSweights_13TeV-powheg-pythia8/ RunIIFall17MiniAODv2-PU2017_12Apr2018_94X_mc2017_realistic_v14-v2	830.91×0.45441
/TTToHadronic_TuneCP5down_PSweights_13TeV-powheg-pythia8/ RunIIFall17MiniAODv2-PU2017_12Apr2018_new_pmx_94X_mc2017_realistic_v14-v2	830.91×0.45441
/TTToHadronic_TuneCP5up_PSweights_13TeV-powheg-pythia8/ RunIIFall17MiniAODv2-PU2017_12Apr2018_new_pmx_94X_mc2017_realistic_v14-v1	830.91×0.45441
/TTToHadronic_TuneCP5_erdON_13TeV-powheg-pythia8/ RunIIFall17MiniAODv2-PU2017_12Apr2018_94X_mc2017_realistic_v14-v3	830.91×0.45441
/TTToHadronic_TuneCP5CR1_QCDbased_PSweights_13TeV-powheg-pythia8/ RunIIFall17MiniAODv2-PU2017_12Apr2018_94X_mc2017_realistic_v14-v1	830.91×0.45441
/TTToHadronic_TuneCP5CR2_GluonMove_PSweights_13TeV-powheg-pythia8/ RunIIFall17MiniAODv2-PU2017_12Apr2018_94X_mc2017_realistic_v14-v1	830.91×0.45441
/TTToHadronic_mtop169p5_TuneCP5_PSweights_13TeV-powheg-pythia8/ RunIIFall17MiniAODv2-PU2017_12Apr2018_94X_mc2017_realistic_v14-v3	830.91×0.45441
/TTToHadronic_mtop175p5_TuneCP5_PSweights_13TeV-powheg-pythia8/ RunIIFall17MiniAODv2-PU2017_12Apr2018_new_pmx_94X_mc2017_realistic_v14-v2	830.91×0.45441

Table C.12: The list of simulated signal $t\bar{t}$ samples used for estimating the systematic uncertainties on the top mass, underlying event tune, colour reconnection and h_{damp} in the analysis of the 2018 data are shown together with their corresponding cross sections.

sample	σ [pb]
/TTTo2L2Nu_hdampDOWN_TuneCP5_13TeV-powheg-pythia8/ RunIIAutumn18MiniAOD-102X_upgrade2018_realistic_v15-v1	830.91 × 0.10706
/TTTo2L2Nu_hdampDOWN_TuneCP5_13TeV-powheg-pythia8/ RunIIAutumn18MiniAOD-102X_upgrade2018_realistic_v15_ext1-v1	830.91 × 0.10706
/TTTo2L2Nu_hdampDOWN_TuneCP5_13TeV-powheg-pythia8/ RunIIAutumn18MiniAOD-102X_upgrade2018_realistic_v15_ext2-v2	830.91 × 0.10706
/TTTo2L2Nu_hdampUP_TuneCP5_13TeV-powheg-pythia8/ RunIIAutumn18MiniAOD-102X_upgrade2018_realistic_v15-v1	830.91 × 0.10706
/TTTo2L2Nu_hdampUP_TuneCP5_13TeV-powheg-pythia8/ RunIIAutumn18MiniAOD-102X_upgrade2018_realistic_v15_ext1-v1	830.91 × 0.10706
/TTTo2L2Nu_hdampUP_TuneCP5_13TeV-powheg-pythia8/ RunIIAutumn18MiniAOD-102X_upgrade2018_realistic_v15_ext2-v2	830.91 × 0.10706
/TTTo2L2Nu_TuneCP5down_13TeV-powheg-pythia8/ RunIIAutumn18MiniAOD-102X_upgrade2018_realistic_v15-v1	830.91 × 0.10706
/TTTo2L2Nu_TuneCP5down_13TeV-powheg-pythia8/ RunIIAutumn18MiniAOD-102X_upgrade2018_realistic_v15_ext1-v1	830.91 × 0.10706
/TTTo2L2Nu_TuneCP5down_13TeV-powheg-pythia8/ RunIIAutumn18MiniAOD-102X_upgrade2018_realistic_v15_ext2-v3	830.91 × 0.10706
/TTTo2L2Nu_TuneCP5up_13TeV-powheg-pythia8/ RunIIAutumn18MiniAOD-102X_upgrade2018_realistic_v15-v1	830.91 × 0.10706
/TTTo2L2Nu_TuneCP5up_13TeV-powheg-pythia8/ RunIIAutumn18MiniAOD-102X_upgrade2018_realistic_v15_ext1-v1	830.91 × 0.10706
/TTTo2L2Nu_TuneCP5up_13TeV-powheg-pythia8/ RunIIAutumn18MiniAOD-102X_upgrade2018_realistic_v15_ext2-v3	830.91 × 0.10706
/TTTo2L2Nu_TuneCP5_erdON_13TeV-powheg-pythia8/ RunIIAutumn18MiniAOD-102X_upgrade2018_realistic_v15-v1	830.91 × 0.10706
/TTTo2L2Nu_TuneCP5_erdON_13TeV-powheg-pythia8/ RunIIAutumn18MiniAOD-102X_upgrade2018_realistic_v15_ext1-v1	830.91 × 0.10706
/TTTo2L2Nu_TuneCP5_erdON_13TeV-powheg-pythia8/ RunIIAutumn18MiniAOD-102X_upgrade2018_realistic_v15_ext2-v2	830.91 × 0.10706
/TTTo2L2Nu_TuneCP5CR1_QCDbased_13TeV-powheg-pythia8/ RunIIAutumn18MiniAOD-102X_upgrade2018_realistic_v15-v1	830.91 × 0.10706
/TTTo2L2Nu_TuneCP5CR1_QCDbased_13TeV-powheg-pythia8/ RunIIAutumn18MiniAOD-102X_upgrade2018_realistic_v15_ext1-v2	830.91 × 0.10706
/TTTo2L2Nu_TuneCP5CR2_GluonMove_13TeV-powheg-pythia8/ RunIIAutumn18MiniAOD-102X_upgrade2018_realistic_v15-v1	830.91 × 0.10706
/TTTo2L2Nu_TuneCP5CR2_GluonMove_13TeV-powheg-pythia8/ RunIIAutumn18MiniAOD-102X_upgrade2018_realistic_v15_ext1-v2	830.91 × 0.10706
/TTTo2L2Nu_mtop169p5_TuneCP5_13TeV-powheg-pythia8/ RunIIAutumn18MiniAOD-102X_upgrade2018_realistic_v15-v1	830.91 × 0.10706
/TTTo2L2Nu_mtop169p5_TuneCP5_13TeV-powheg-pythia8/ RunIIAutumn18MiniAOD-102X_upgrade2018_realistic_v15_ext1-v1	830.91 × 0.10706
/TTTo2L2Nu_mtop169p5_TuneCP5_13TeV-powheg-pythia8/ RunIIAutumn18MiniAOD-102X_upgrade2018_realistic_v15_ext2-v2	830.91 × 0.10706
/TTTo2L2Nu_mtop175p5_TuneCP5_13TeV-powheg-pythia8/ RunIIAutumn18MiniAOD-102X_upgrade2018_realistic_v15-v1	830.91 × 0.10706
/TTTo2L2Nu_mtop175p5_TuneCP5_13TeV-powheg-pythia8/ RunIIAutumn18MiniAOD-102X_upgrade2018_realistic_v15_ext1-v1	830.91 × 0.10706
/TTTo2L2Nu_mtop175p5_TuneCP5_13TeV-powheg-pythia8/ RunIIAutumn18MiniAOD-102X_upgrade2018_realistic_v15_ext1-v2	830.91 × 0.10706

Table C.13: The list of alternative simulated $t\bar{t}$ signal samples used in the analysis of the 2018 data are shown together with their corresponding cross sections.

sample	σ [pb]
/TTJets_TuneCP5_13TeV-amcatnloFXFX-pythia8/ RunIIAutumn18MiniAOD-102X_upgrade2018_realistic_v15_ext1-v2	830.91
/TT_TuneCH3_13TeV-powheg-herwig7/ RunIIAutumn18MiniAOD-102X_upgrade2018_realistic_v15-v2	830.91

Table C.14: The list of simulated semi-leptonic $t\bar{t}$ samples used for estimating the systematic uncertainties on the top mass, underlying event tune, colour reconnection and h_{damp} in the analysis of the 2018 data are shown together with their corresponding cross sections.

sample	σ [pb]
/TTToSemiLeptonic_hdampDOWN_TuneCP5_13TeV-powheg-pythia8/ RunIIAutumn18MiniAOD-102X_upgrade2018_realistic_v15-v1	830.91×0.44113
/TTToSemiLeptonic_hdampUP_TuneCP5_13TeV-powheg-pythia8/ RunIIAutumn18MiniAOD-102X_upgrade2018_realistic_v15-v1	830.91×0.44113
/TTToSemiLeptonic_TuneCP5down_13TeV-powheg-pythia8/ RunIIAutumn18MiniAOD-102X_upgrade2018_realistic_v15-v1	830.91×0.44113
/TTToSemiLeptonic_TuneCP5up_13TeV-powheg-pythia8/ RunIIAutumn18MiniAOD-102X_upgrade2018_realistic_v15-v1	830.91×0.44113
/TTToSemiLeptonic_TuneCP5_erdON_13TeV-powheg-pythia8/ RunIIAutumn18MiniAOD-102X_upgrade2018_realistic_v15-v1	830.91×0.44113
/TTToSemiLeptonic_TuneCP5CR1_QCDbased_13TeV-powheg-pythia8/ RunIIAutumn18MiniAOD-102X_upgrade2018_realistic_v15-v1	830.91×0.44113
/TTToSemiLeptonic_TuneCP5CR2_GluonMove_13TeV-powheg-pythia8/ RunIIAutumn18MiniAOD-102X_upgrade2018_realistic_v15-v1	830.91×0.44113
/TTToSemiLeptonic_mtop169p5_TuneCP5_13TeV-powheg-pythia8/ RunIIAutumn18MiniAOD-102X_upgrade2018_realistic_v15-v1	830.91×0.44113
/TTToSemiLeptonic_mtop169p5_TuneCP5_13TeV-powheg-pythia8/ RunIIAutumn18MiniAOD-102X_upgrade2018_realistic_v15_ext1-v1	830.91×0.44113
/TTToSemiLeptonic_mtop175p5_TuneCP5_13TeV-powheg-pythia8/ RunIIAutumn18MiniAOD-102X_upgrade2018_realistic_v15-v1	830.91×0.44113
/TTToSemiLeptonic_mtop175p5_TuneCP5_13TeV-powheg-pythia8/ RunIIAutumn18MiniAOD-102X_upgrade2018_realistic_v15_ext1-v1	830.91×0.44113

Table C.15: The list of simulated all-hadronic $t\bar{t}$ samples used for estimating the systematic uncertainties on the top mass, underlying event tune, colour reconnection and h_{damp} in the analysis of the 2018 data are shown together with their corresponding cross sections.

sample	σ [pb]
/TTToHadronic_hdampDOWN_TuneCP5_13TeV-powheg-pythia8/ RunIIAutumn18MiniAOD-102X_upgrade2018_realistic_v15-v1	830.91×0.45441
/TTToHadronic_hdampUP_TuneCP5_13TeV-powheg-pythia8/ RunIIAutumn18MiniAOD-102X_upgrade2018_realistic_v15-v1	830.91×0.45441
/TTToHadronic_TuneCP5down_13TeV-powheg-pythia8/ RunIIAutumn18MiniAOD-102X_upgrade2018_realistic_v15-v1	830.91×0.45441
/TTToHadronic_TuneCP5up_13TeV-powheg-pythia8/ RunIIAutumn18MiniAOD-102X_upgrade2018_realistic_v15-v1	830.91×0.45441
/TTToHadronic_TuneCP5_erdON_13TeV-powheg-pythia8/ RunIIAutumn18MiniAOD-102X_upgrade2018_realistic_v15-v1	830.91×0.45441
/TTToHadronic_TuneCP5CR1_QCDbased_13TeV-powheg-pythia8/ RunIIAutumn18MiniAOD-102X_upgrade2018_realistic_v15-v1	830.91×0.45441
/TTToHadronic_TuneCP5CR2_GluonMove_13TeV-powheg-pythia8/ RunIIAutumn18MiniAOD-102X_upgrade2018_realistic_v15-v1	830.91×0.45441
/TTToHadronic_mtop169p5_TuneCP5_13TeV-powheg-pythia8/ RunIIAutumn18MiniAOD-102X_upgrade2018_realistic_v15-v1	830.91×0.45441
/TTToHadronic_mtop175p5_TuneCP5_13TeV-powheg-pythia8/ RunIIAutumn18MiniAOD-102X_upgrade2018_realistic_v15-v1	830.91×0.45441

Appendix D

Triggers

D.1 Trigger paths

Table D.1: The same trigger menu is used in both data and simulation and the combinations of single and dilepton triggers in 2016 are shown separately for the individual channels.

channel	run	trigger
$\mu^{\pm}\mu^{\mp}$	B-H	HLT_Mu17_TrkIsoVVL_TkMu8_TrkIsoVVL_DZ_v*
	B-H	HLT_Mu17_TrkIsoVVL_Mu8_TrkIsoVVL_DZ_v*
	B-G	HLT_Mu17_TrkIsoVVL_TkMu8_TrkIsoVVL_v*
	B-G	HLT_Mu17_TrkIsoVVL_Mu8_TrkIsoVVL_v*
	B-H	HLT_IsoMu24_v*
	B-H	HLT_IsoTkMu24_v*
$e^{\pm}e^{\mp}$	B-H	HLT_Ele23_Ele12_CaloIdL_TrackIdL_IsoVL_DZ_v*
	B-H	HLT_Ele27_WPTight_Gsf_v*
$e^{\pm}\mu^{\mp}$	B-G	HLT_Mu23_TrkIsoVVL_Ele12_CaloIdL_TrackIdL_IsoVL_v*
	B-G	HLT_Mu8_TrkIsoVVL_Ele23_CaloIdL_TrackIdL_IsoVL_v*
	B-H	HLT_Mu23_TrkIsoVVL_Ele12_CaloIdL_TrackIdL_IsoVL_DZ_v*
	B-H	HLT_Mu8_TrkIsoVVL_Ele23_CaloIdL_TrackIdL_IsoVL_DZ_v*
	B-H	HLT_Ele27_WPTight_Gsf_v*
	B-H	HLT_IsoMu24_v*
	B-H	HLT_IsoTkMu24_v*

Table D.2: The same trigger menu is used in both data and simulation and the combinations of single and dilepton triggers in 2017 are shown separately for the individual channels.

channel	run	trigger
$\mu^{\pm}\mu^{\mp}$	A-B	HLT_Mu17_TrkIsoVVL_Mu8_TrkIsoVVL_DZ_v*
	C-F	HLT_Mu17_TrkIsoVVL_Mu8_TrkIsoVVL_DZ_Mass3p8_v*
	A-F	HLT_IsoMu27_v*
$e^{\pm}e^{\mp}$	A-F	HLT_Ele23_Ele12_CaloIdL_TrackIdL_IsoVL_DZ_v*
	A-F	HLT_Ele23_Ele12_CaloIdL_TrackIdL_IsoVL_v*
	A-F	HLT_Ele32_WPTight_Gsf_L1DoubleEG_v*
$e^{\pm}\mu^{\mp}$	A-F	HLT_Mu23_TrkIsoVVL_Ele12_CaloIdL_TrackIdL_IsoVL_v*
	A-F	HLT_Mu23_TrkIsoVVL_Ele12_CaloIdL_TrackIdL_IsoVL_DZ_v*
	A-F	HLT_Mu12_TrkIsoVVL_Ele23_CaloIdL_TrackIdL_IsoVL_DZ_v*
	A-F	HLT_Mu8_TrkIsoVVL_Ele23_CaloIdL_TrackIdL_IsoVL_DZ_v*
	A-F	HLT_Ele32_WPTight_Gsf_L1DoubleEG_v*
	E-F	HLT_IsoMu27_v*

Table D.3: The same trigger menu is used in both data and simulation and the combinations of single and dilepton triggers in 2018 are shown separately for the individual channels.

channel	run	trigger
$\mu^{\pm}\mu^{\mp}$	A-D	HLT_Mu17_TrkIsoVVL_Mu8_TrkIsoVVL_DZ_Mass3p8_v*
	A-D	HLT_IsoMu24_v*
$e^{\pm}e^{\mp}$	A-D	HLT_Ele23_Ele12_CaloIdL_TrackIdL_IsoVL_DZ_v*
	A-D	HLT_Ele23_Ele12_CaloIdL_TrackIdL_IsoVL_v*
	A-D	HLT_Ele32_WPTight_Gsf_v*
$e^{\pm}\mu^{\mp}$	A-D	HLT_Mu23_TrkIsoVVL_Ele12_CaloIdL_TrackIdL_IsoVL_v*
	A-D	HLT_Mu23_TrkIsoVVL_Ele12_CaloIdL_TrackIdL_IsoVL_DZ_v*
	A-D	HLT_Mu12_TrkIsoVVL_Ele23_CaloIdL_TrackIdL_IsoVL_DZ_v*
	A-D	HLT_Mu8_TrkIsoVVL_Ele23_CaloIdL_TrackIdL_IsoVL_DZ_v*
	A-D	HLT_Ele32_WPTight_Gsf_v*
	A-D	HLT_IsoMu24_v*

D.2 Trigger scale factors

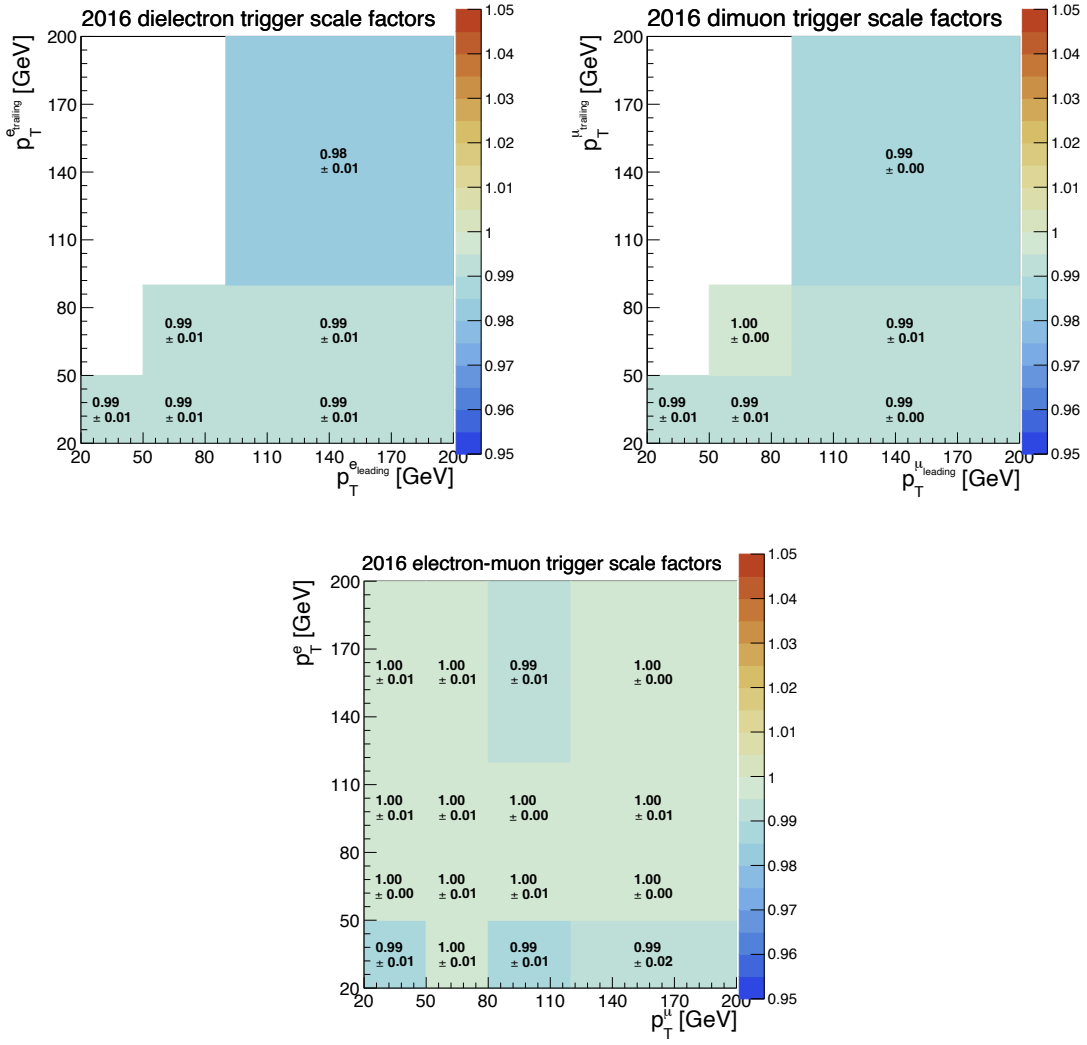

Figure D.1: The trigger scale factors in 2016 are shown separately for the $e^{\pm}e^{\mp}$ (top left), $\mu^{\pm}\mu^{\mp}$ (top right) and $e^{\pm}\mu^{\mp}$ (bottom) channels and are provided in bins of the leading and trailing lepton p_{T}. The systematic and statistical uncertainties on the scale factors are added in quadrature.

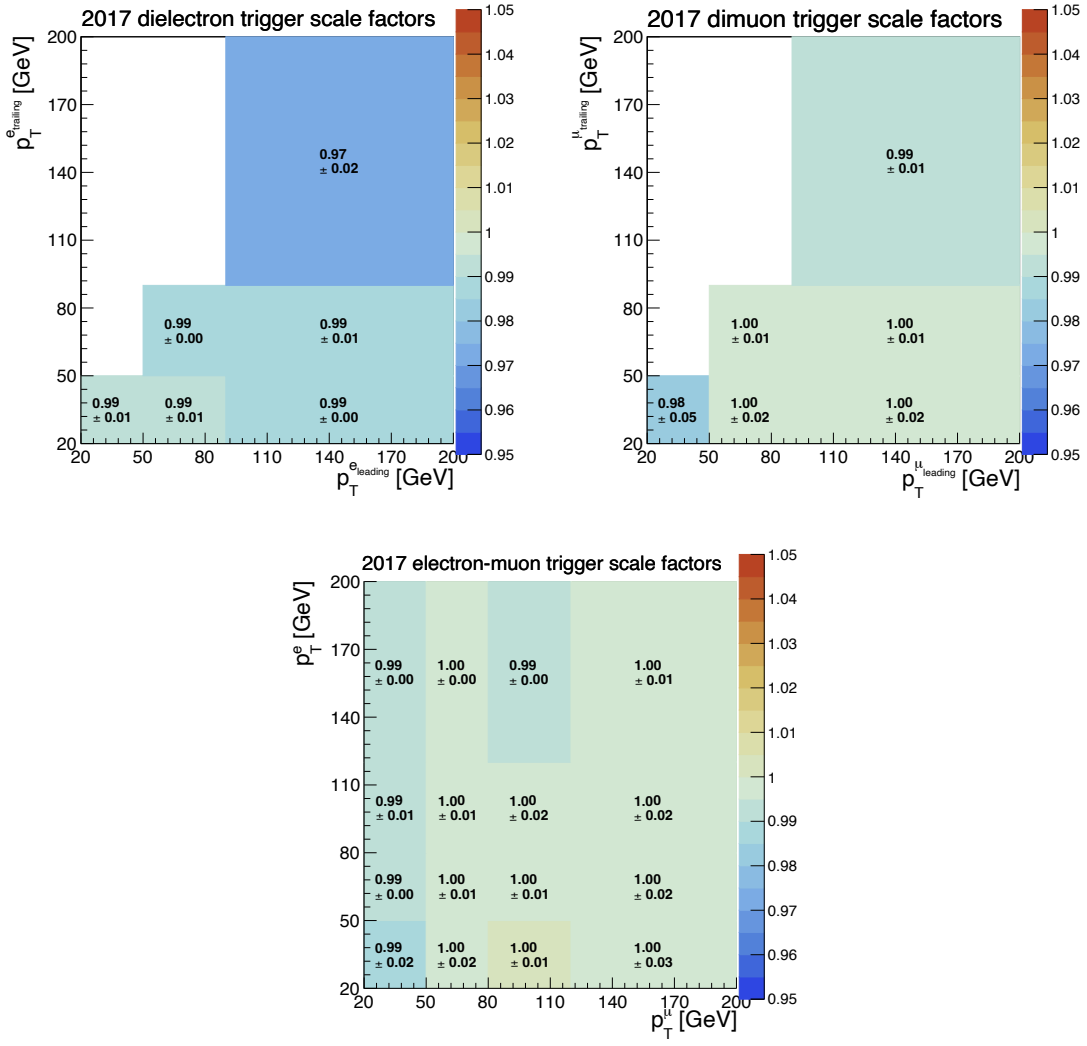

Figure D.2: The trigger scale factors in 2017 are shown separately for the $e^{\pm}e^{\mp}$ (top left), $\mu^{\pm}\mu^{\mp}$ (top right) and $e^{\pm}\mu^{\mp}$ (bottom) channels and are provided in bins of the leading and trailing lepton p_{T}. The systematic and statistical uncertainties on the scale factors are added in quadrature.

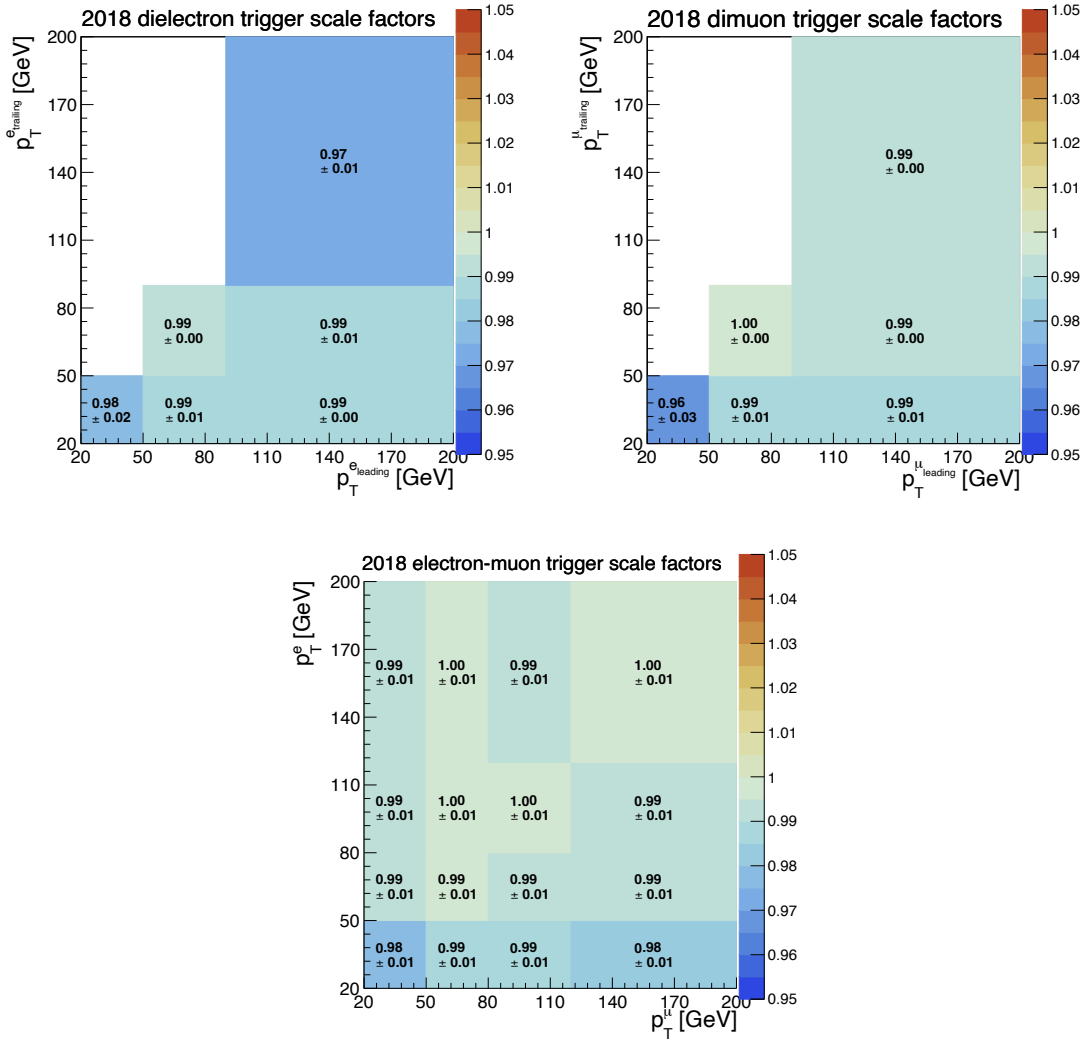

Figure D.3: The trigger scale factors in 2018 are shown separately for the $e^{\pm}e^{\mp}$ (top left), $\mu^{\pm}\mu^{\mp}$ (top right) and $e^{\pm}\mu^{\mp}$ (bottom) channels and are provided in bins of the leading and trailing lepton p_{T}. The systematic and statistical uncertainties on the scale factors are added in quadrature.

Appendix E

Lepton reconstruction and identification scale factors

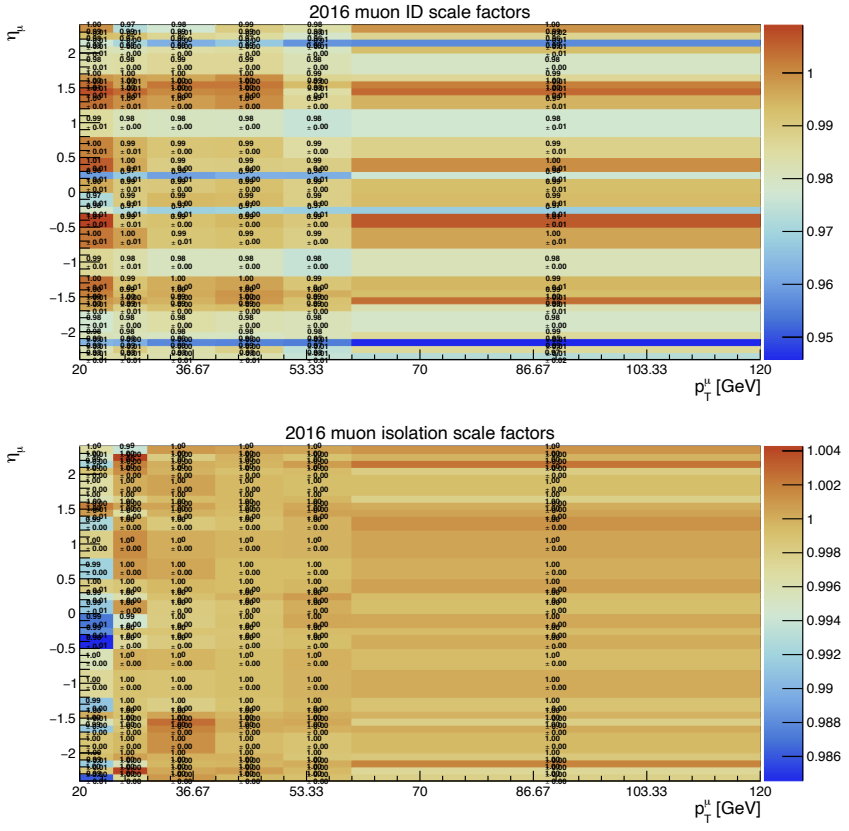

Figure E.1: The figure shows the ratio of muon efficiencies in 2016 data and simulation. The resulting scale factors for both the identification (top) and isolation (bottom) efficiencies are applied per muon in simulation in bins of p_{T} and η.

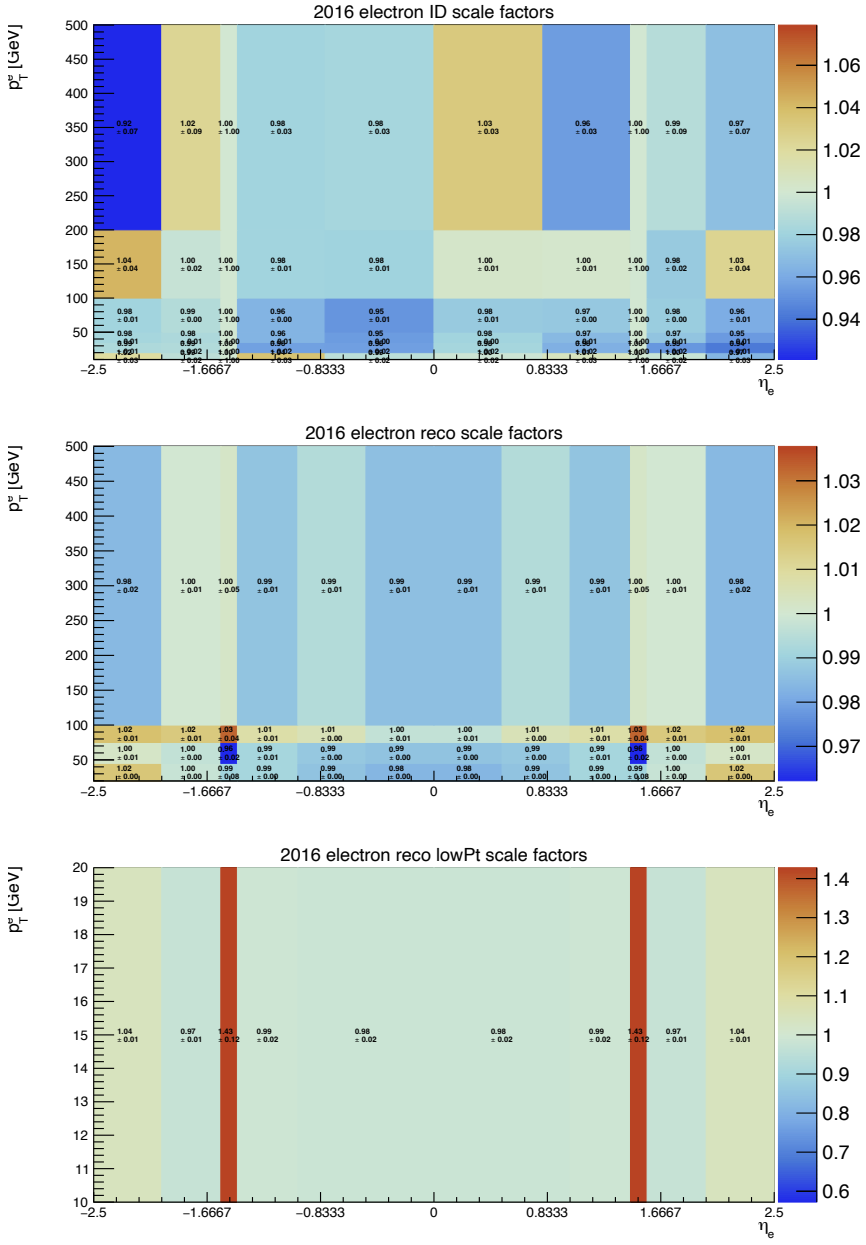

Figure E.2: The figure shows the ratio of electron efficiencies in 2016 data and simulation. The resulting scale factors for the identification (top) and reconstruction (middle and bottom for high and low electron p_{T}, respectively) efficiencies are applied per electron in simulation in bins of p_{T} and η.

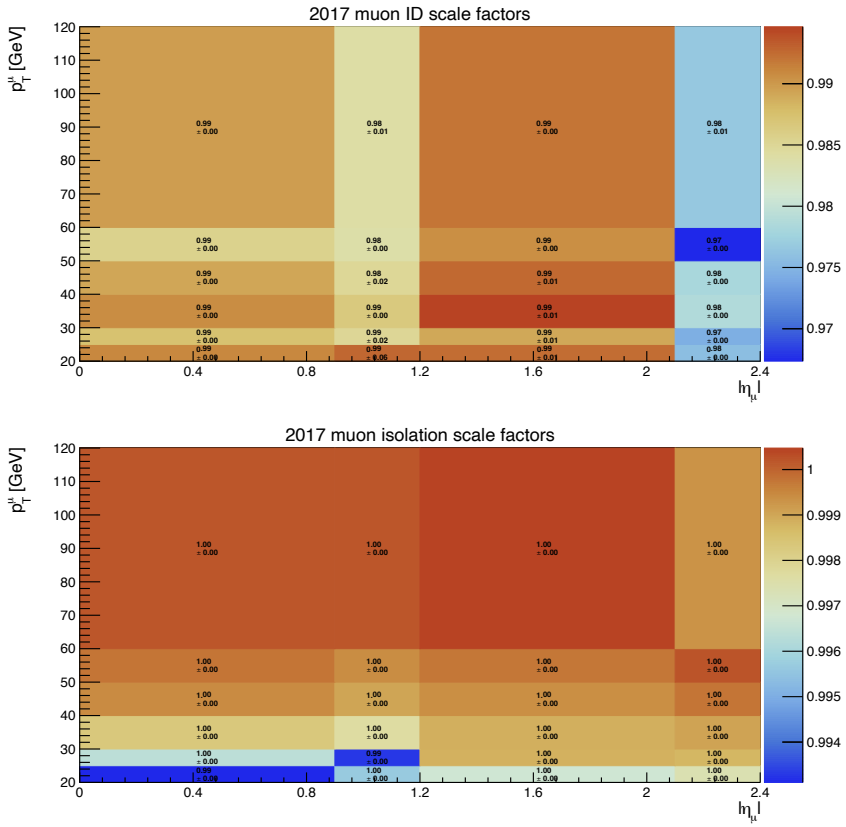

Figure E.3: The figure shows the ratio of muon efficiencies in 2017 data and simulation. The resulting scale factors for both the identification (top) and isolation (bottom) efficiencies are applied per muon in simulation in bins of p_{T} and absolute η.

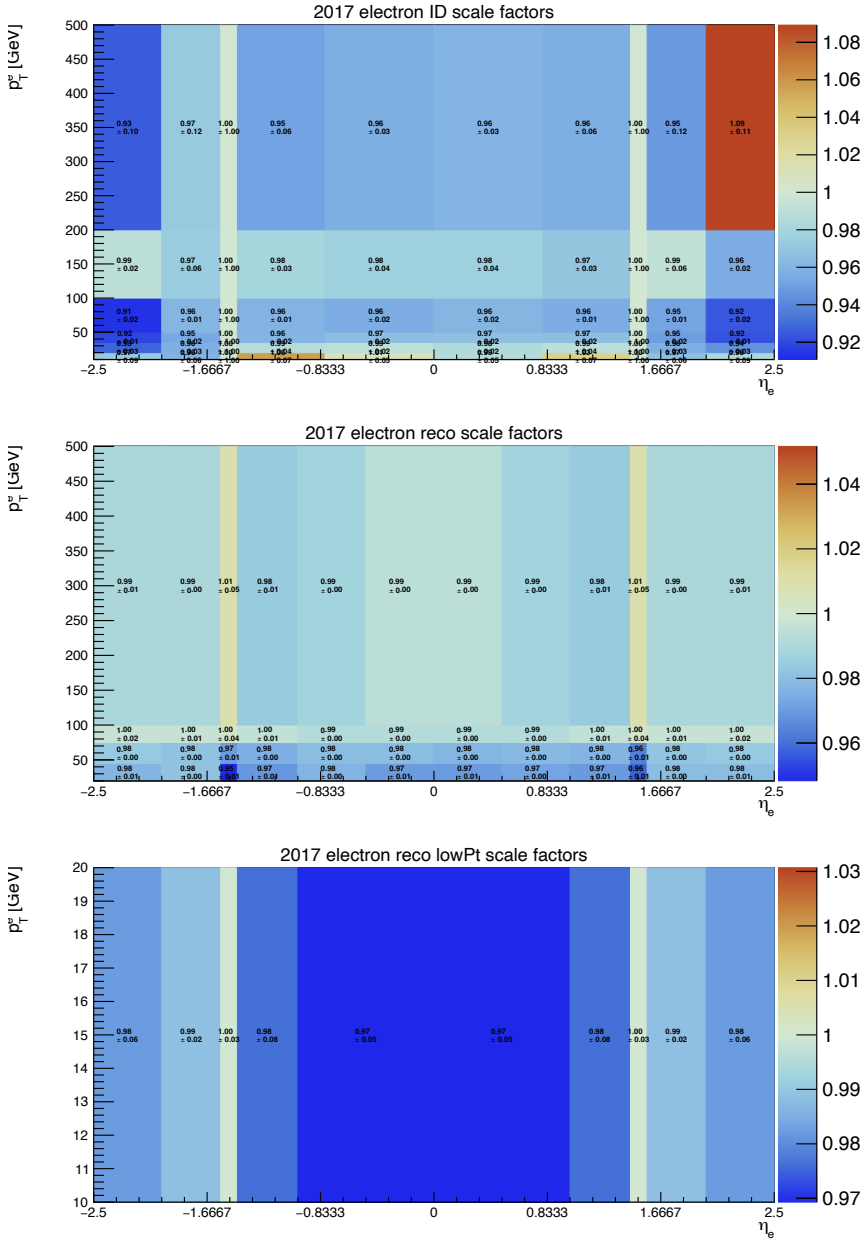

Figure E.4: The figure shows the ratio of electron efficiencies in 2017 data and simulation. The resulting scale factors for the identification (top) and reconstruction (middle and bottom for high and low electron p_{T}, respectively) efficiencies are applied per electron in simulation in bins of p_{T} and η.

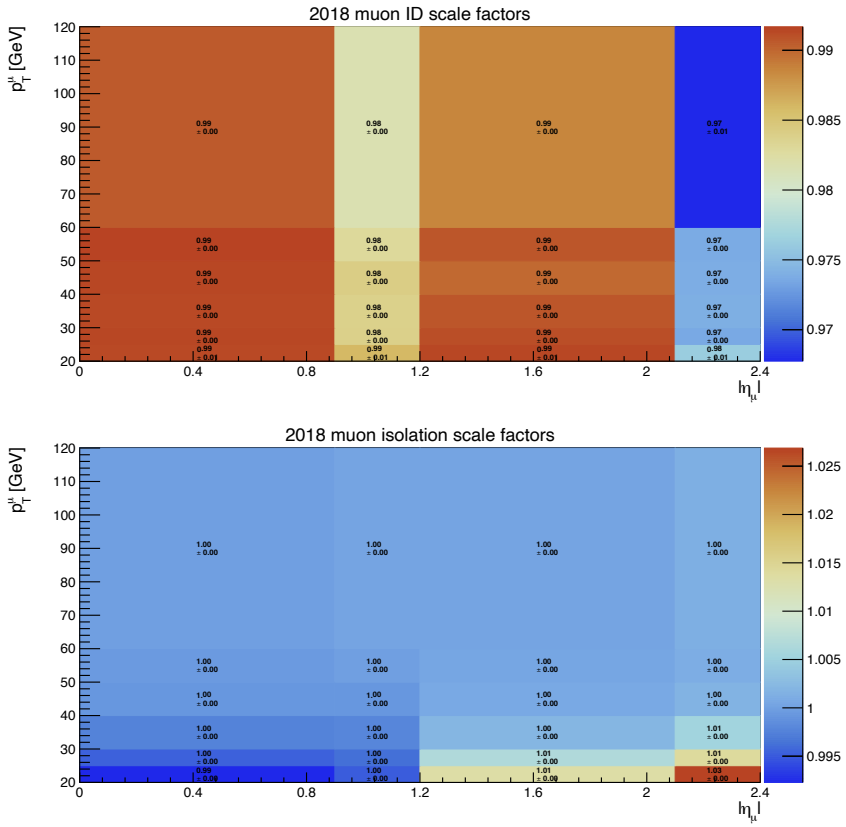

Figure E.5: The figure shows the ratio of muon efficiencies in 2018 data and simulation. The resulting scale factors for both the identification (top) and isolation (bottom) efficiencies are applied per muon in simulation in bins of p_{T} and absolute η.

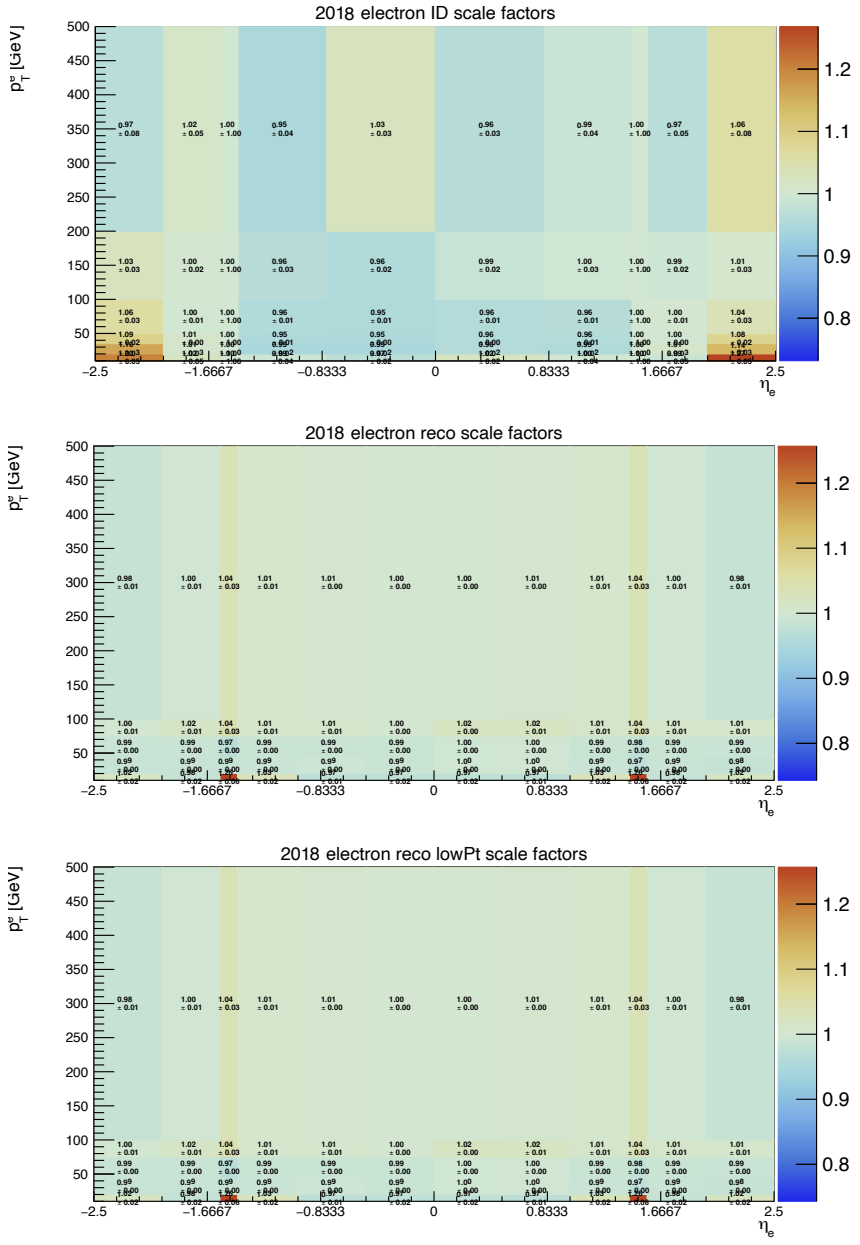

Figure E.6: The figure shows the ratio of electron efficiencies in 2018 data and simulation. The resulting scale factors for the identification (top) and reconstruction (middle and bottom for high and low electron p_{T}, respectively) efficiencies are applied per electron in simulation in bins of p_{T} and η.

Appendix F

B-tagging efficiencies and mistag rates for c- and light-jets

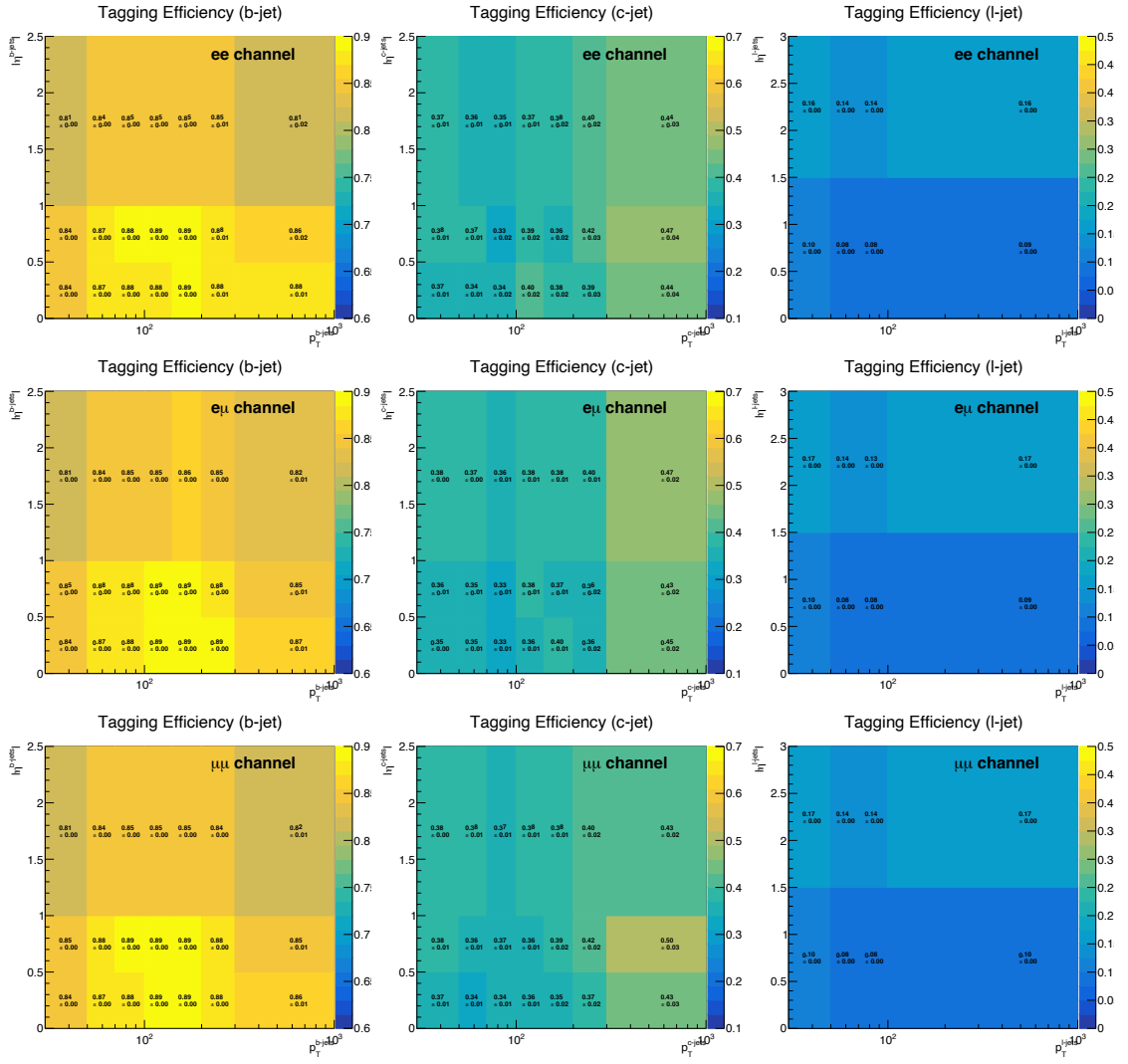

Figure F.1: The b-tag efficiency and mistag rates are computed in bins of jet p_{T} and η and are shown for 2016 in the $e^{\pm}e^{\mp}$ (top row), $e^{\pm}\mu^{\mp}$ (middle row) and $\mu^{\pm}\mu^{\mp}$ (third row) channels. The b-tagging efficiency is shown in the first column while the mistag rates for c- and light-jets are shown in the second and third column, respectively.

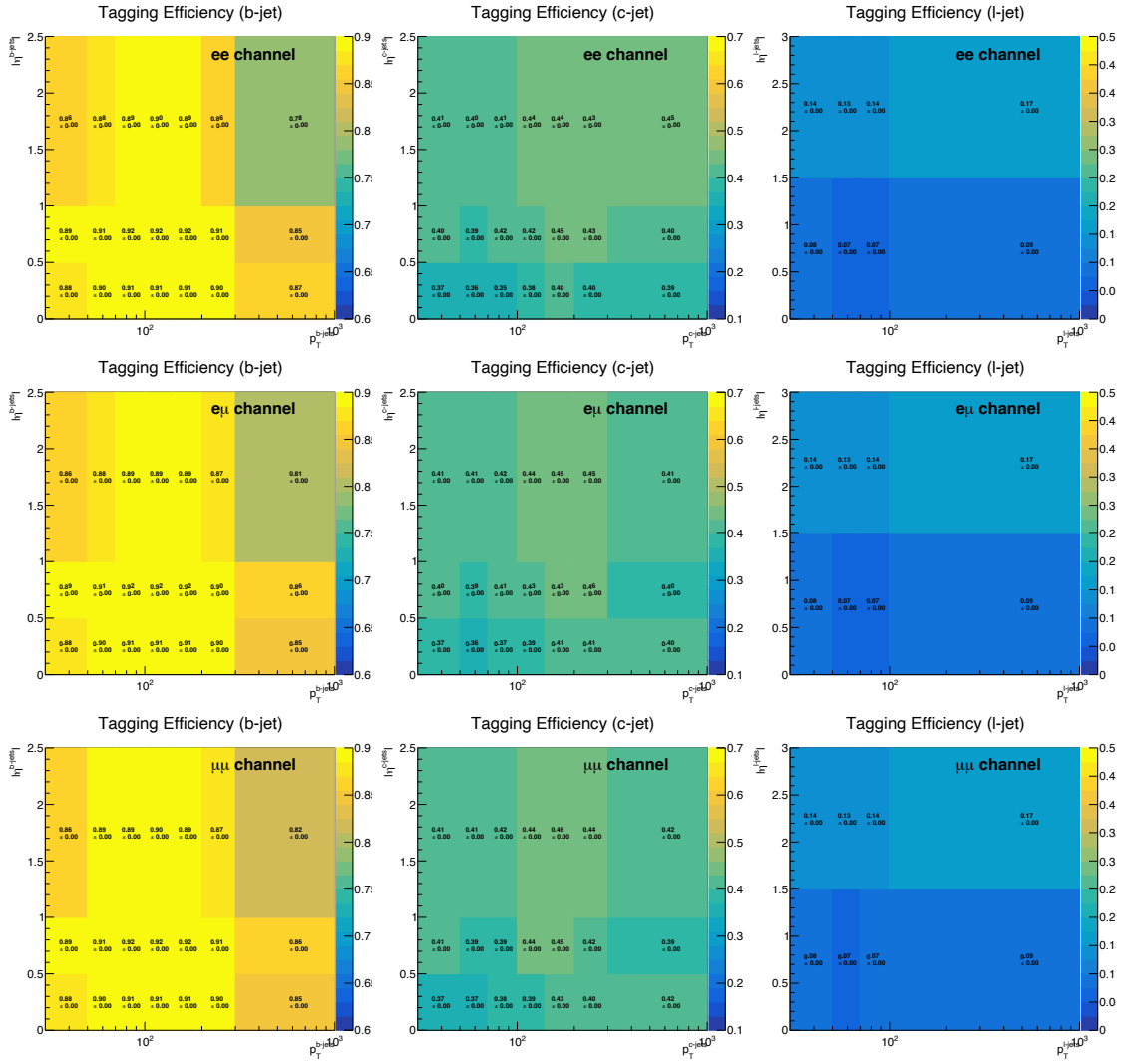

Figure F.2: The b-tag efficiency and mistag rates are computed in bins of jet p_{T} and η and are shown for 2017 in the $e^{\pm}e^{\mp}$ (top row), $e^{\pm}\mu^{\mp}$ (middle row) and $\mu^{\pm}\mu^{\mp}$ (third row) channels. The b-tagging efficiency is shown in the first column while the mistag rates for c- and light-jets are shown in the second and third column, respectively.

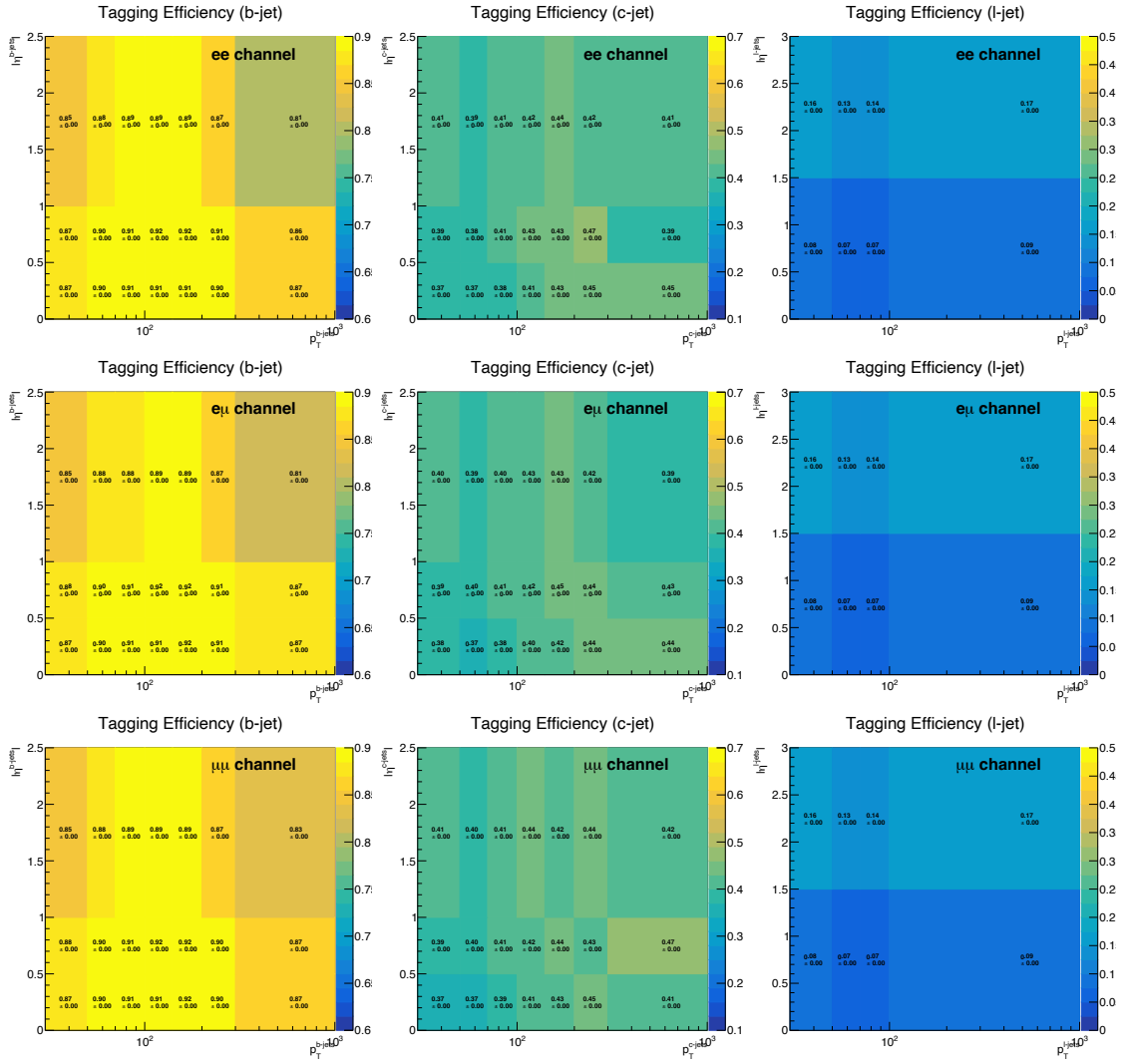

Figure F.3: The b-tag efficiency and mistag rates are computed in bins of jet p_{T} and η and are shown for 2018 in the $e^{\pm}e^{\mp}$ (top row), $e^{\pm}\mu^{\mp}$ (middle row) and $\mu^{\pm}\mu^{\mp}$ (third row) channels. The b-tagging efficiency is shown in the first column while the mistag rates for c- and light-jets are shown in the second and third column, respectively.

Appendix G

Event count tables for individual years

Table G.1: The table shows the total number of expected events for signal and background processes compared to the number of events observed in 2016 data for each selection step and channel ($\mu^{\pm}\mu^{\mp}$, $e^{\pm}\mu^{\mp}$, $e^{\pm}e^{\mp}$ and the combined channel). The simulation has been normalized to a total integrated luminosity of 36.3 fb^{-1}, which corresponds to the 2016 data-taking period.

$\mu^{\pm}\mu^{\mp}$ sample	Z-veto	$\geq$ 2 jets	$E_{\mathrm{T}}^{\mathrm{miss}}$	$\geq$ 1 b-tag	kin. reco	loose. kin. reco
$t\bar{t}$ signal	117779.0	94150.4	79536.3	75305.9	66763.1	72105.1
$t\bar{t}$ other	20307.5	16284.6	13514.5	12635.5	11693.7	12084.6
$t\bar{t} + Z/W$	344.2	328.5	285.0	269.0	216.4	238.6
Single top	13477.0	6218.6	5283.8	4691.7	3217.9	3656.5
diboson	18259.1	2585.4	1674.9	598.8	331.3	380.0
W+jets	1611.5	259.2	259.2	145.7	18.2	18.5
Z+jets	1972077.9	133453.1	54174.8	19888.1	12368.4	13462.3
Sum MC	2143856.3	253279.8	154728.5	113534.8	94609.0	101945.5
Data	2049279.0	247639.0	149265.0	104955.0	87636.0	93753.0
$e^{\pm}\mu^{\mp}$ sample	Z-veto	$\geq$ 2 jets	$E_{\mathrm{T}}^{\mathrm{miss}}$	$\geq$ 1 b-tag	kin. reco	loose. kin. reco
$t\bar{t}$ signal	206886.5	165837.8	165837.8	157159.1	143844.5	150928.2
$t\bar{t}$ other	35814.6	28723.7	28723.7	26943.8	25403.0	25881.4
$t\bar{t} + Z/W$	546.3	519.0	519.0	486.5	419.1	444.1
Single top	23859.9	11036.2	11036.2	9832.8	7180.8	7810.1
diboson	27391.4	2679.9	2679.9	883.7	555.0	604.0
W+jets	4677.7	642.4	642.4	227.8	179.2	195.4
Z+jets	71255.2	5914.1	5914.1	1957.1	1572.1	1585.9
Sum MC	370431.5	215353.0	215353.0	197490.8	179153.7	187449.1
Data	355116.0	199639.0	199639.0	180048.0	163299.0	170357.0
$e^{\pm}e^{\mp}$ sample	Z-veto	$\geq$ 2 jets	$E_{\mathrm{T}}^{\mathrm{miss}}$	$\geq$ 1 b-tag	kin. reco	loose. kin. reco
$t\bar{t}$ signal	57284.9	45953.3	37668.8	35660.7	32508.1	34061.6
$t\bar{t}$ other	9179.5	7373.3	6034.4	5681.7	5347.5	5456.1
$t\bar{t} + Z/W$	175.8	167.8	138.7	130.9	107.2	114.9
Single top	6579.0	3079.7	2517.1	2250.2	1575.0	1720.1
diboson	8572.5	1328.8	744.7	278.0	165.4	184.6
W+jets	1907.3	229.1	152.3	28.2	28.0	28.2
Z+jets	819102.9	63537.8	17499.0	6226.0	3966.9	4408.0
Sum MC	902801.9	121669.8	64754.9	50255.8	43698.1	45973.5
Data	885409.0	115642.0	61430.0	46650.0	40567.0	42306.0
combined sample	Z-veto	$\geq$ 2 jets	$E_{\mathrm{T}}^{\mathrm{miss}}$	$\geq$ 1 b-tag	kin. reco	loose. kin. reco
$t\bar{t}$ signal	381950.4	305941.5	283042.9	268125.7	243115.7	257094.9
$t\bar{t}$ other	65301.6	52381.5	48272.5	45261.0	42444.2	43422.1
$t\bar{t} + Z/W$	1066.3	1015.2	942.6	886.4	742.7	797.6
Single top	43915.9	20334.6	18837.1	16774.7	11973.7	13186.7
diboson	54223.1	6594.1	5099.5	1760.6	1051.7	1168.6
W+jets	8196.5	1130.6	1053.9	401.7	225.4	242.1
Z+jets	2862435.9	202388.6	77611.8	28088.7	17911.4	19459.0
Sum MC	3417089.7	589786.2	434860.4	361298.8	317464.8	335370.8
Data	3289804.0	562920.0	410334.0	331653.0	291502.0	306416.0

Table G.2: The table shows the total number of expected events for signal and background processes compared to the number of events observed in 2017 data for each selection step and channel ($\mu^{\pm}\mu^{\mp}$, $e^{\pm}\mu^{\mp}$, $e^{\pm}e^{\mp}$ and the combined channel). The simulation has been normalized to a total integrated luminosity of 41.5 fb^{-1}, which corresponds to the 2017 data-taking period.

$\mu^{\pm}\mu^{\mp}$ sample	Z-veto	$\geq$ 2 jets	$E_{\mathrm{T}}^{\mathrm{miss}}$	$\geq$ 1 b-tag	kin. reco	loose. kin. reco
$t\bar{t}$ signal	131352.2	104857.9	88566.7	83612.1	75591.5	79979.1
$t\bar{t}$ other	24307.6	19420.2	16200.9	15026.1	13930.5	14300.4
$t\bar{t} + Z/W$	402.6	381.8	331.0	312.5	256.2	276.3
Single top	15504.8	7086.7	6014.5	5311.8	3761.3	4149.0
diboson	20729.7	2721.6	1773.7	593.5	344.8	380.1
W+jets	3118.6	481.2	407.9	156.0	115.6	116.5
Z+jets	2199162.7	186368.4	83742.9	27411.1	18878.6	20043.3
Sum MC	2394578.1	321317.7	197037.5	132423.0	112878.6	119244.7
Data	2477872.0	318845.0	199501.0	133916.0	114124.0	119794.0
$e^{\pm}\mu^{\mp}$ sample	Z-veto	$\geq$ 2 jets	$E_{\mathrm{T}}^{\mathrm{miss}}$	$\geq$ 1 b-tag	kin. reco	loose. kin. reco
$t\bar{t}$ signal	241340.0	193247.2	193247.2	182663.6	168061.9	175316.8
$t\bar{t}$ other	43991.1	35229.3	35229.3	32828.6	30841.5	31430.7
$t\bar{t} + Z/W$	655.1	618.4	618.4	578.8	498.7	526.6
Single top	28141.4	12869.1	12869.1	11365.1	8346.5	9032.7
diboson	32754.0	2715.4	2715.4	786.2	473.7	514.7
W+jets	7579.3	981.8	981.8	372.8	223.7	225.0
Z+jets	84764.1	7771.3	7771.3	2337.8	1868.4	1919.4
Sum MC	439225.0	253432.4	253432.4	230932.9	210314.5	218965.8
Data	429428.0	243923.0	243923.0	220852.0	201114.0	208631.0
$e^{\pm}e^{\mp}$ sample	Z-veto	$\geq$ 2 jets	$E_{\mathrm{T}}^{\mathrm{miss}}$	$\geq$ 1 b-tag	kin. reco	loose. kin. reco
$t\bar{t}$ signal	68986.9	55254.5	46061.0	43464.0	39490.6	41486.0
$t\bar{t}$ other	11299.4	9050.9	7562.4	7111.9	6653.8	6813.5
$t\bar{t} + Z/W$	216.0	204.8	174.9	164.2	134.0	144.7
Single top	7916.2	3727.5	3106.9	2756.2	1917.5	2110.1
diboson	10490.1	1460.0	887.2	307.4	175.8	194.8
W+jets	2291.7	479.6	333.6	101.5	30.6	30.9
Z+jets	998591.5	79230.9	31619.6	10148.1	7126.5	7472.2
Sum MC	1099791.9	149408.4	89745.6	64053.3	55528.8	58252.3
Data	1014434.0	142953.0	86176.0	60249.0	52226.0	54505.0
combined sample	Z-veto	$\geq$ 2 jets	$E_{\mathrm{T}}^{\mathrm{miss}}$	$\geq$ 1 b-tag	kin. reco	loose. kin. reco
$t\bar{t}$ signal	441679.1	353359.6	327874.8	309739.7	283144.1	296781.9
$t\bar{t}$ other	79598.1	63700.3	58992.6	54966.6	51425.8	52544.6
$t\bar{t} + Z/W$	1273.7	1205.0	1124.3	1055.4	888.9	947.6
Single top	51562.4	23683.3	21990.5	19433.1	14025.4	15291.8
diboson	63973.8	6897.0	5376.4	1687.1	994.3	1089.6
W+jets	12989.6	1942.6	1723.3	630.3	369.9	372.4
Z+jets	3282518.3	273919.3	123198.8	39901.1	27890.4	29445.2
Sum MC	3933595.0	724707.3	540280.6	427413.3	378738.7	396473.2
Data	3921734.0	705721.0	529600.0	415017.0	367464.0	382930.0

Table G.3: The table shows the total number of expected events for signal and background processes compared to the number of events observed in 2018 data for each selection step and channel ($\mu^{\pm}\mu^{\mp}$, $e^{\pm}\mu^{\mp}$, $e^{\pm}e^{\mp}$ and the combined channel). The simulation has been normalized to a total integrated luminosity of 59.7 fb^{-1}, which corresponds to the 2018 data-taking period.

$\mu^{\pm}\mu^{\mp}$ sample	Z-veto	$\geq$ 2 jets	$E_{\mathrm{T}}^{\mathrm{miss}}$	$\geq$ 1 b-tag	kin. reco	loose. kin. reco
$t\bar{t}$ signal	195724.7	156487.1	130265.2	123731.9	111387.5	118318.4
$t\bar{t}$ other	35347.4	28285.2	23146.3	21734.2	20116.1	20699.7
$t\bar{t} + Z/W$	593.3	561.7	477.8	460.6	377.0	406.5
Single top	22839.8	10638.1	8885.5	7943.4	5590.7	6214.7
diboson	31616.4	4189.5	2466.6	932.7	545.4	604.7
W+jets	3234.6	747.2	617.0	320.1	226.7	229.4
Z+jets	3252174.6	272514.5	89918.1	35162.1	21683.3	23408.8
Sum MC	3541530.8	473423.3	255776.5	190285.1	159926.7	169882.1
Data	3562696.0	453181.0	253197.0	189423.0	159185.0	168245.0
$e^{\pm}\mu^{\mp}$ sample	Z-veto	$\geq$ 2 jets	$E_{\mathrm{T}}^{\mathrm{miss}}$	$\geq$ 1 b-tag	kin. reco	loose. kin. reco
$t\bar{t}$ signal	359203.5	287809.4	287809.4	273538.6	251167.1	262228.4
$t\bar{t}$ other	64094.2	51417.1	51417.1	48443.0	45435.2	46386.4
$t\bar{t} + Z/W$	990.2	934.3	934.3	893.3	759.1	804.3
Single top	41451.5	19256.0	19256.0	17247.8	12636.0	13685.4
diboson	50675.7	4196.5	4196.5	1514.1	969.5	1042.6
W+jets	10466.8	1675.3	1675.3	347.2	274.0	276.3
Z+jets	125164.7	12080.2	12080.2	4750.6	3776.3	3861.5
Sum MC	652046.5	377368.9	377368.9	346734.6	315017.1	328284.8
Data	640157.0	359619.0	359619.0	329565.0	299443.0	310501.0
$e^{\pm}e^{\mp}$ sample	Z-veto	$\geq$ 2 jets	$E_{\mathrm{T}}^{\mathrm{miss}}$	$\geq$ 1 b-tag	kin. reco	loose. kin. reco
$t\bar{t}$ signal	102910.0	82378.1	67310.0	63877.1	57704.7	60864.4
$t\bar{t}$ other	16568.2	13286.2	10843.4	10232.5	9515.1	9800.2
$t\bar{t} + Z/W$	338.4	320.8	264.5	253.3	203.4	220.9
Single top	11768.9	5568.2	4568.1	4124.8	2839.1	3121.4
diboson	16318.0	2159.1	1109.9	443.8	240.7	272.4
W+jets	3266.3	191.0	137.9	101.7	56.1	57.1
Z+jets	1467008.6	131377.6	31917.8	12858.8	8279.7	9075.4
Sum MC	1618178.5	235281.0	116151.7	91892.1	78838.8	83411.7
Data	1537104.0	213634.0	111021.0	86969.0	74650.0	78007.0
combined sample	Z-veto	$\geq$ 2 jets	$E_{\mathrm{T}}^{\mathrm{miss}}$	$\geq$ 1 b-tag	kin. reco	loose. kin. reco
$t\bar{t}$ signal	657838.1	526674.6	485384.6	461147.6	420259.2	441411.1
$t\bar{t}$ other	116009.7	92988.6	85406.8	80409.7	75066.4	76886.3
$t\bar{t} + Z/W$	1921.9	1816.8	1676.6	1607.2	1339.5	1431.7
Single top	76060.2	35462.3	32709.6	29316.0	21065.7	23021.5
diboson	98610.1	10545.0	7773.0	2890.6	1755.6	1919.6
W+jets	16967.7	2613.5	2430.3	769.1	556.9	562.8
Z+jets	4844347.9	415781.4	133936.8	52776.0	33736.6	36342.1
Sum MC	5811755.7	1085882.2	749317.8	628916.3	553779.9	581575.1
Data	5739957.0	1026434.0	723837.0	605957.0	533278.0	556753.0

Appendix H

Closure tests

H.1 Truth test

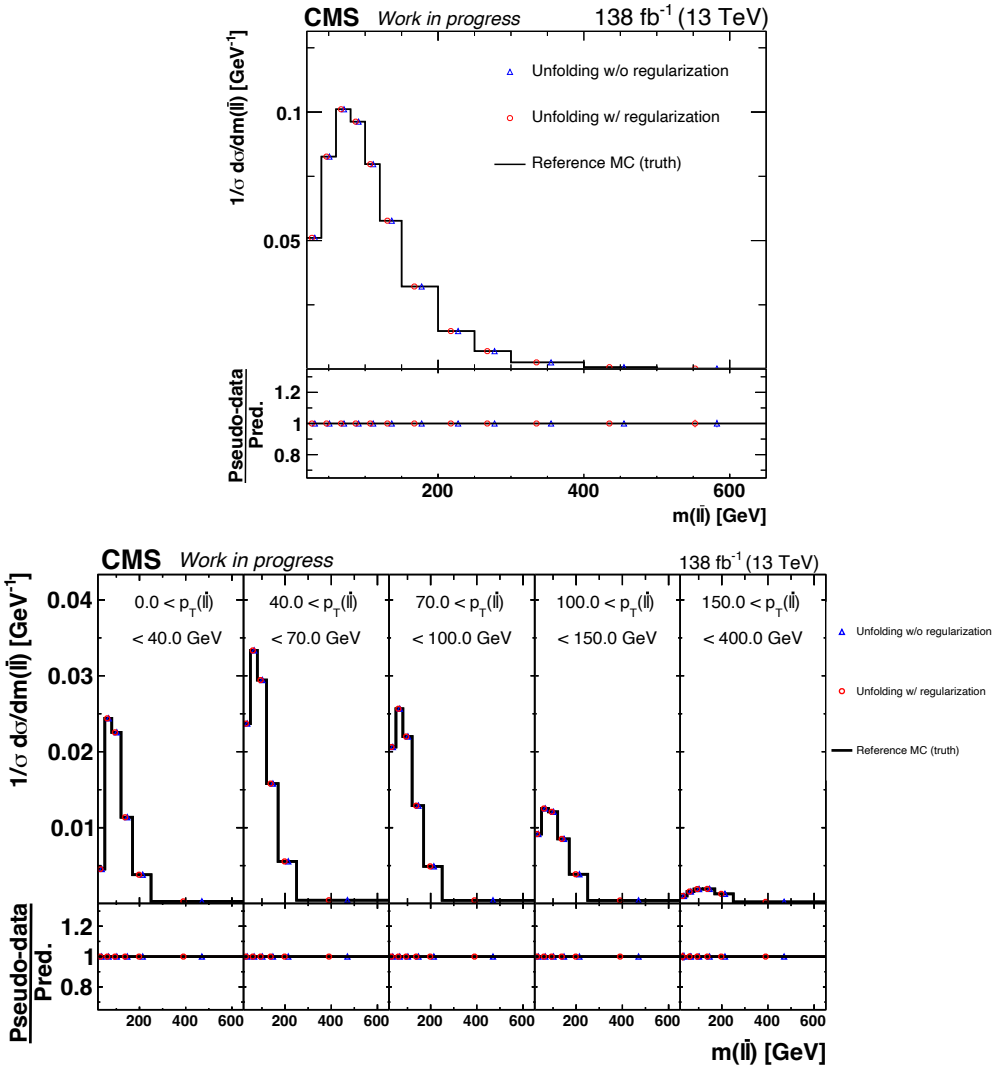

Figure H.1: Absolute differential $t\bar{t}$ production cross sections, performed with pseudo data for regularized and unregularized unfolding. The top plot shows the invariant mass of the dilepton system, $m(\ell\bar{\ell})$, measured in the fiducial phase space at particle level, while the bottom plot shows the invariant mass of the dilepton system in bins of the transverse momentum of the dilepton system, $[p_{\mathrm{T}}(\ell\bar{\ell}), \mathrm{m}(\ell\bar{\ell})]$, measured in the fiducial phase space at particle level. The ratio is shown with respect to the original truth (black).

H.2 Toy test

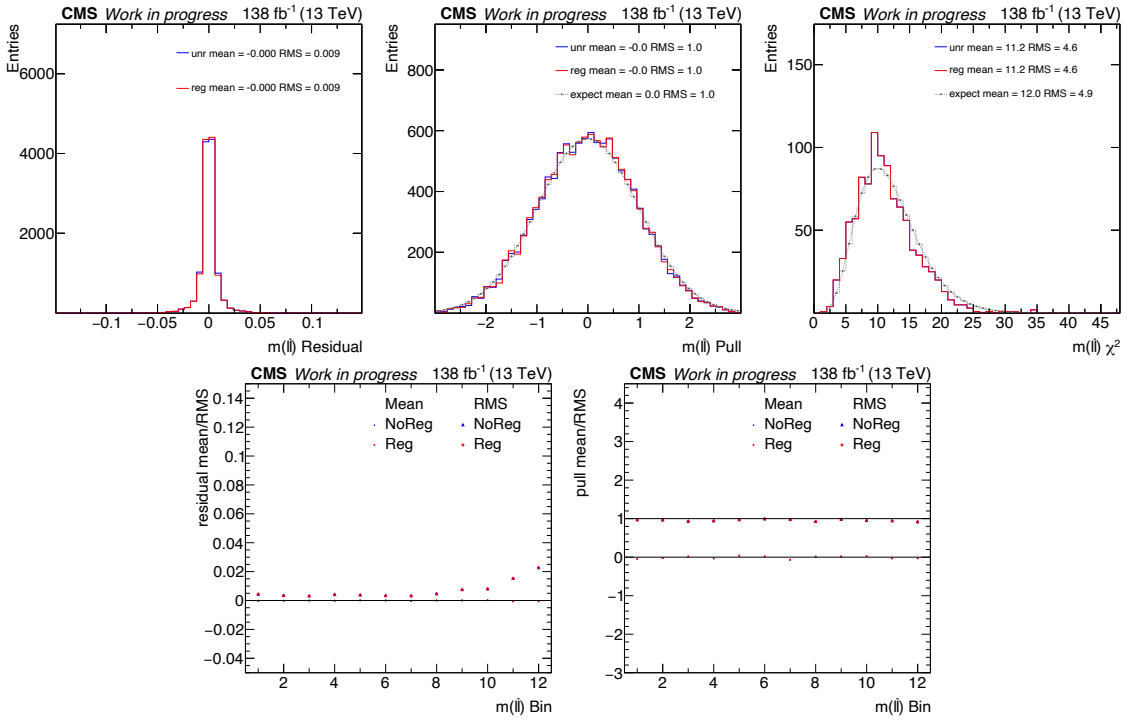

Figure H.2: Residual (relative), pull and $\chi 2$ distributions are shown for the invariant mass of the dilepton system, $m(\ell\bar{\ell})$, measured in the fiducial phase space at particle level, and performed with pseudo data for regularized and unregularized unfolding. The pull and χ^2 distributions are also shown alongside the expectation. The top row shows plots of the residuals (relative), pulls and χ^2 of $\hat{M}_{avg}^{unf}$ with respect to the true MC reference prediction in all bins. The bottom row shows plots of the mean and RMS of the residuals and pulls per bin (see Chapter 8).

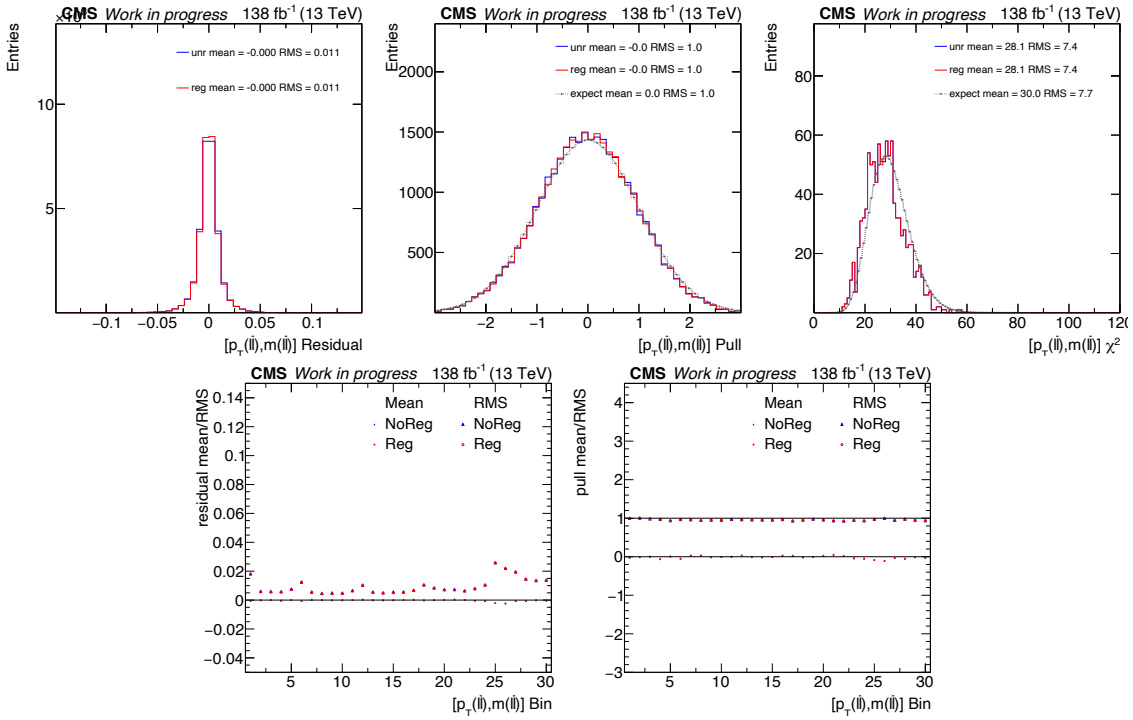

Figure H.3: Residual (relative), pull and $\chi 2$ distributions are shown for the invariant mass of the dilepton system in bins of the transverse momentum of the dilepton system, $[p_{\mathrm{T}}(\ell\bar{\ell}), \mathrm{m}(\ell\bar{\ell})]$, measured in the fiducial phase space at particle level, and performed with pseudo data for regularized and unregularized unfolding. The pull and χ^2 distributions are also shown alongside the expectation. The top row shows plots of the residuals (relative), pulls and χ^2 of $\hat{M}^{unf}_{avg}$ with respect to the true MC reference prediction in all bins. The bottom row shows plots of the mean and RMS of the residuals and pulls per bin (see Chapter 8).

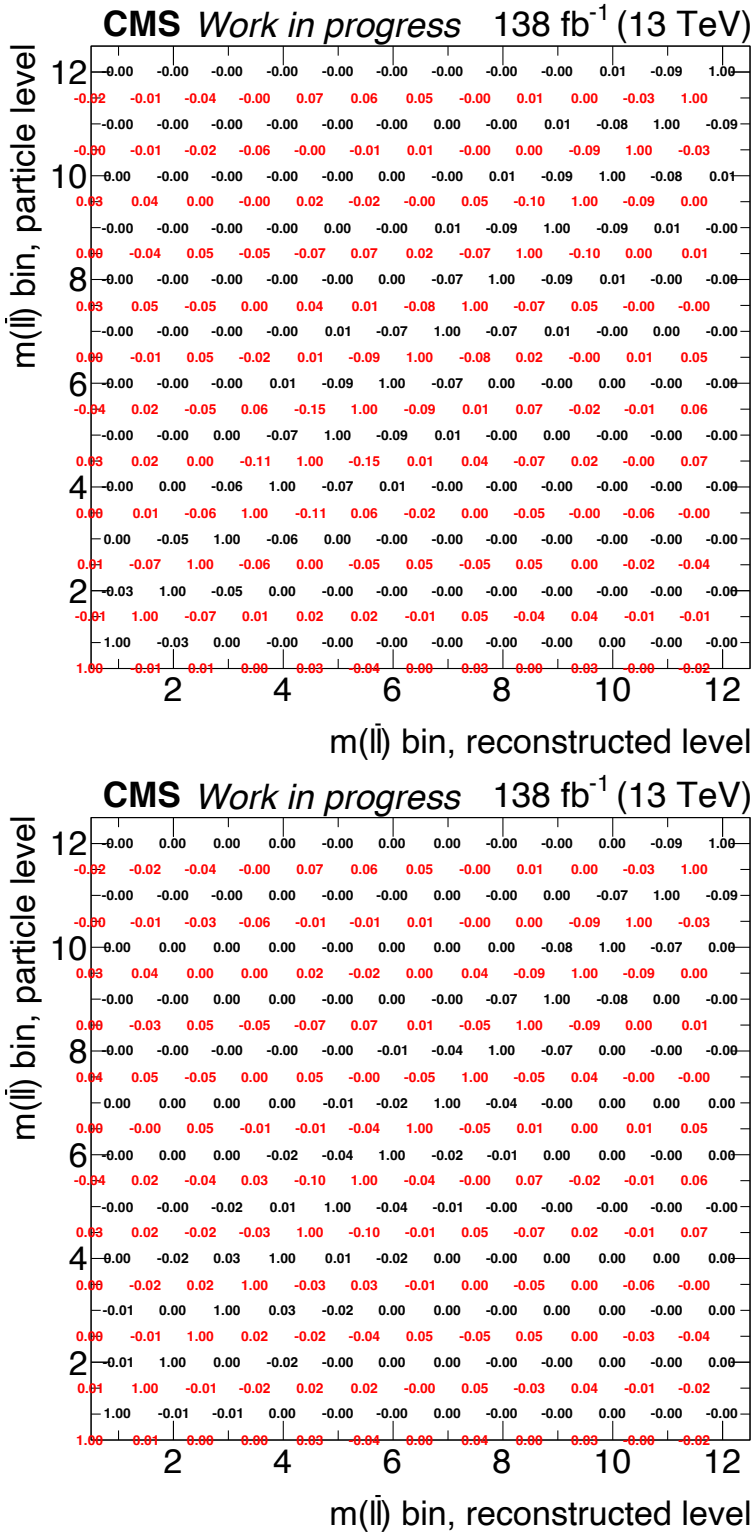

Figure H.4: Correlation matrices are shown for the invariant mass of the dilepton system, $m(\ell\bar{\ell})$, measured in the fiducial phase space at particle level. The sample correlation matrix (red), computed from $(Cov_{\hat{M}^{unf}_{avg}\hat{M}^{unf}_{avg}})_{ij}$, is shown alongside the estimated correlation matrix (black), which is obtained from the direct average of the covariance matrix returned by the unfolding algorithm for each toy. The comparison is performed for unregularized unfolding (top) and regularized unfolding (bottom).

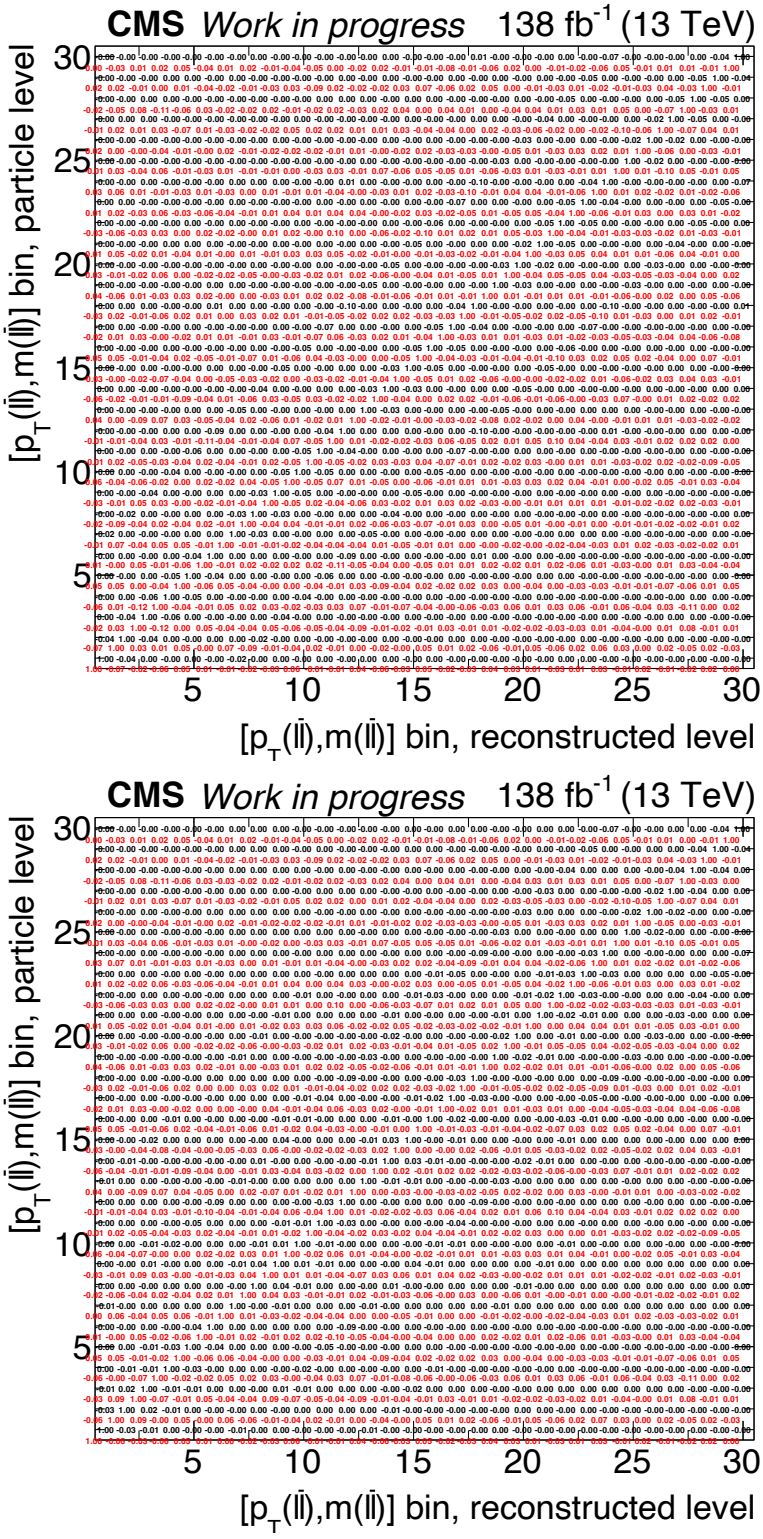

Figure H.5: Correlation matrices are shown for the invariant mass of the dilepton system in bins of the transverse momentum of the dilepton system, $[p_{\mathrm{T}}(\ell\bar{\ell}), \mathrm{m}(\ell\bar{\ell})]$, measured in the fiducial phase space at particle level. The sample correlation matrix (red), computed from $(Cov_{\hat{M}^{unf}_{avg}\hat{M}^{unf}_{avg}})_{ij}$, is shown alongside the estimated correlation matrix (black), which is obtained from the direct average of the covariance matrix returned by the unfolding algorithm for each toy. The comparison is performed for unregularized unfolding (top) and regularized unfolding (bottom).

H.3 Reweighting test

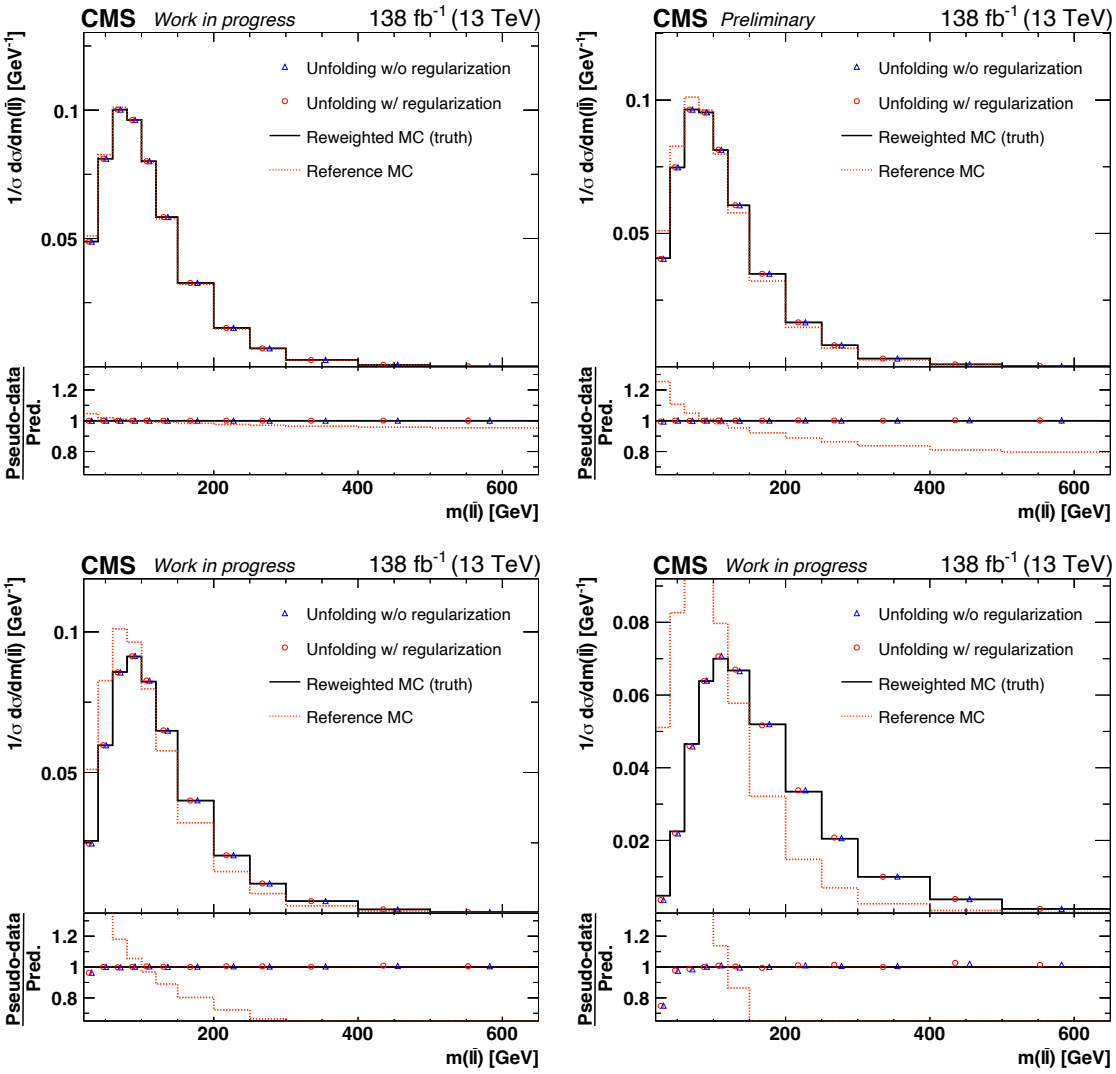

Figure H.6: Absolute differential $t\bar{t}$ production cross sections, performed with pseudo data for regularized and unregularized unfolding, are shown for the invariant mass of the dilepton system, $m(\ell\bar{\ell})$, measured in the fiducial phase space at particle level. Four reweighting scenarios are shown with distortions within 5% to 100%. The ratio is shown with respect to the reweighted MC (truth) in black. The distortions can be judged with respect to the red curve which shows the original reference MC.

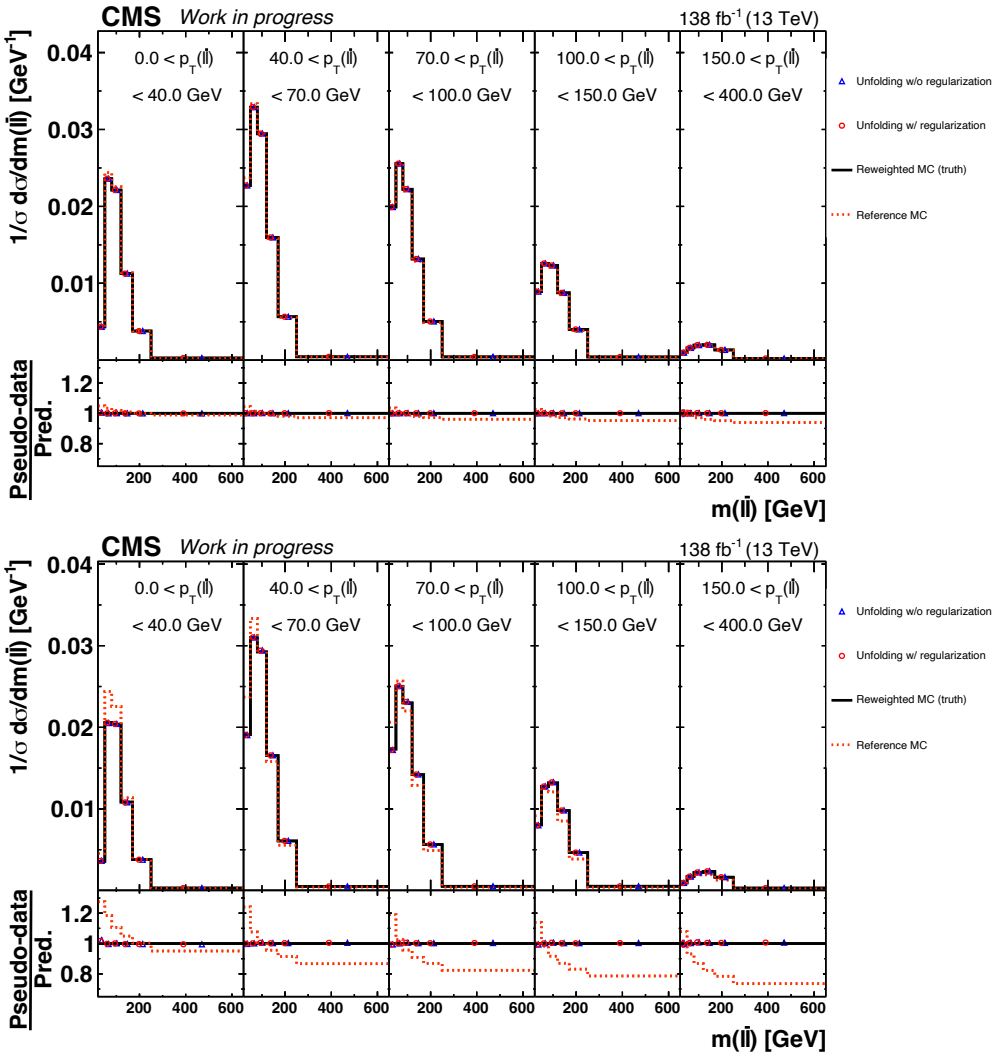

Figure H.7: Absolute differential $t\bar{t}$ production cross sections, performed with pseudo data for regularized and unregularized unfolding, are shown for the invariant mass of the dilepton system in bins of the transverse momentum of the dilepton system, $[p_{\mathrm{T}}(\ell\bar{\ell}), \mathrm{m}(\ell\bar{\ell})]$, measured in the fiducial phase space at particle level. The first two reweighting scenarios are shown with distortions within 5% to 100%. The ratio is shown with respect to the reweighted MC (truth) in black. The distortions can be judged with respect to the red curve which shows the original reference MC.

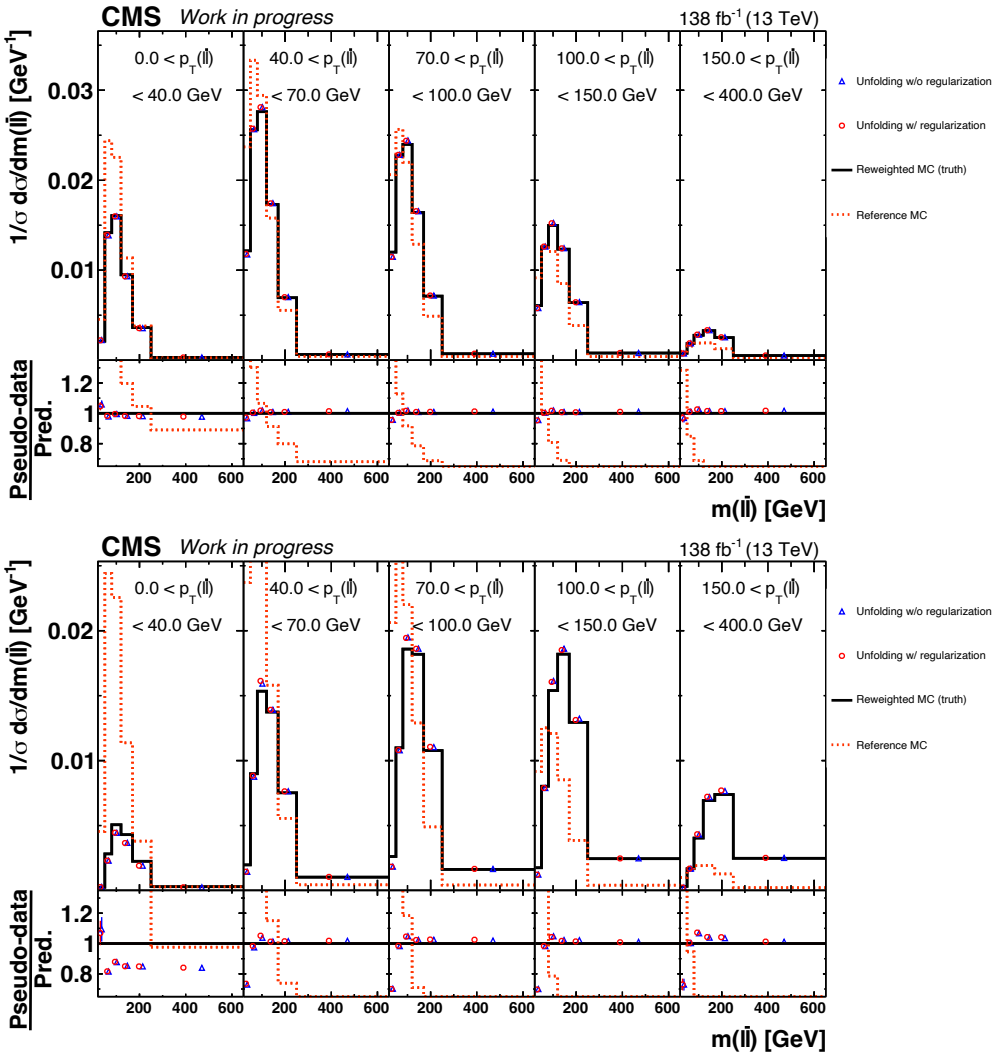

Figure H.8: Absolute differential $t\bar{t}$ production cross sections, performed with pseudo data for regularized and unregularized unfolding, are shown for the invariant mass of the dilepton system in bins of the transverse momentum of the dilepton system, $[p_{\mathrm{T}}(\ell\bar{\ell}), \mathrm{m}(\ell\bar{\ell})]$, measured in the fiducial phase space at particle level. The last two reweighting scenarios are shown with distortions within 5% to 100%. The ratio is shown with respect to the reweighted MC (truth) in black. The distortions can be judged with respect to the red curve which shows the original reference MC.

Appendix I

Estimation of the uncertainty on the tW normalization

I.1 ee channel

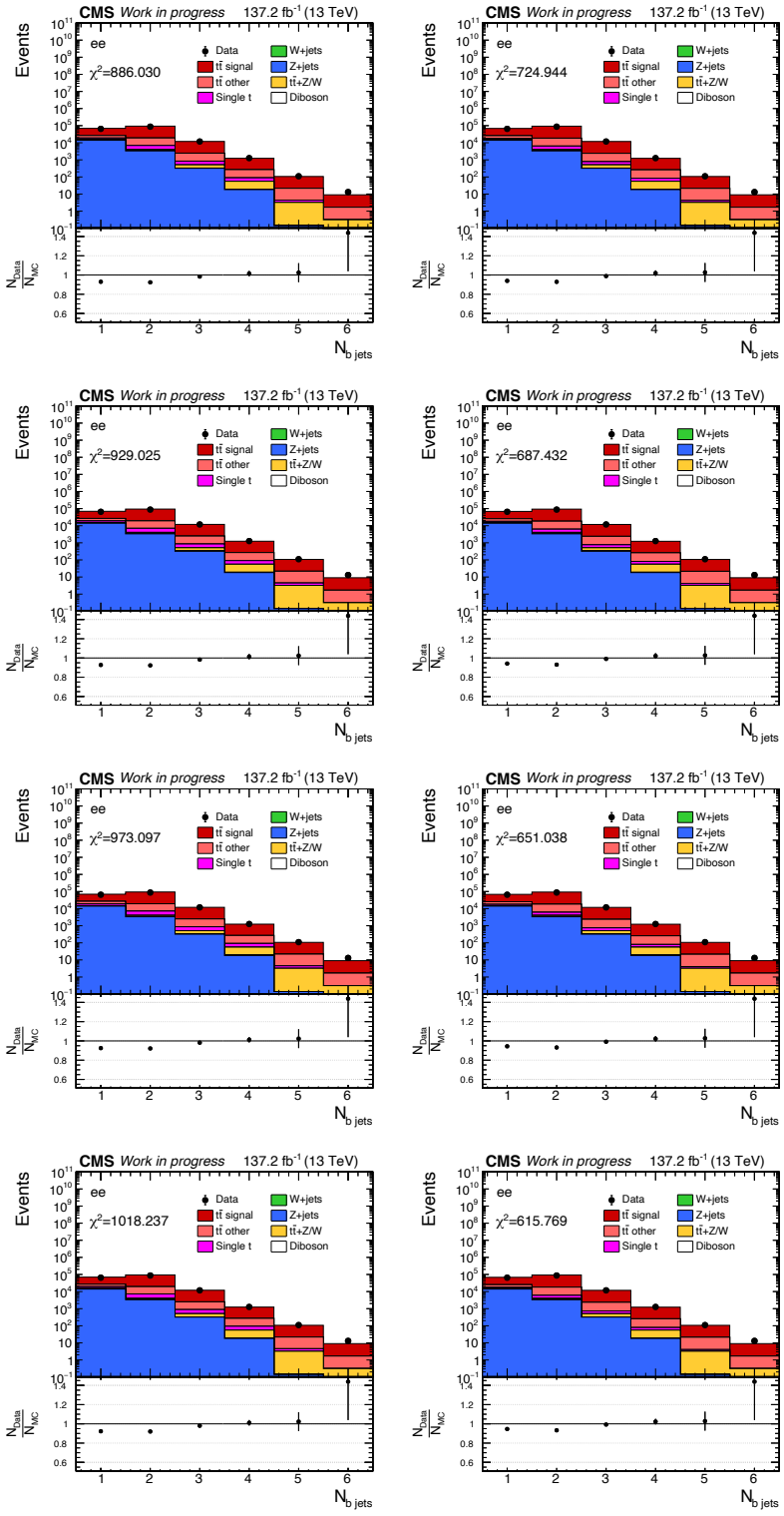

Figure I.1: The figure shows the number of b-tagged jets for the *ee* channel after the full event selection. The normalization of the contribution from the single top tW production is varied up (first column) and down (second column) by 10% (first row), 15% (second row), 20% (third row) and 25% (fourth row). The simulated samples are normalized to an integrated luminosity of 137.6 fb^{-1}. The Z+jets sample (blue area) is scaled to account for the discrepancy in the normalization of this background for data and MC (see Section 5). The systematic uncertainties are not included for the purposes of illustration.

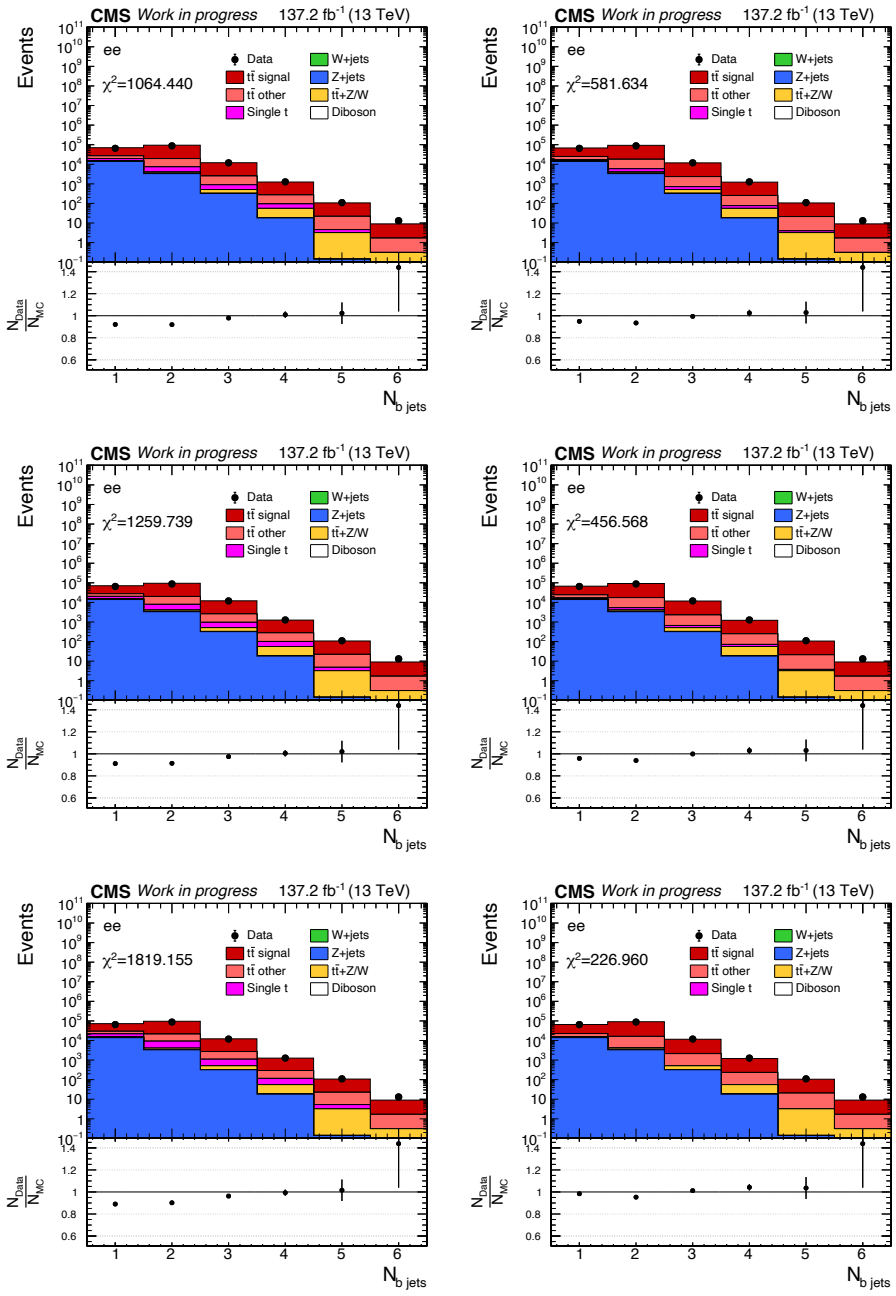

Figure I.2: The figure shows the number of b-tagged jets for the *ee* channel after the full event selection. The normalization of the contribution from the single top tW production is varied up (first column) and down (second column) by 30% (first row), 50% (second row) and 100% (third row). The simulated samples are normalized to an integrated luminosity of 137.6 fb^{-1}. The Z+jets sample (blue area) is scaled to account for the discrepancy in the normalization of this background for data and MC (see Section 5. The systematic uncertainties are not included for the purposes of illustration.

I.2 $\mu\mu$ channel

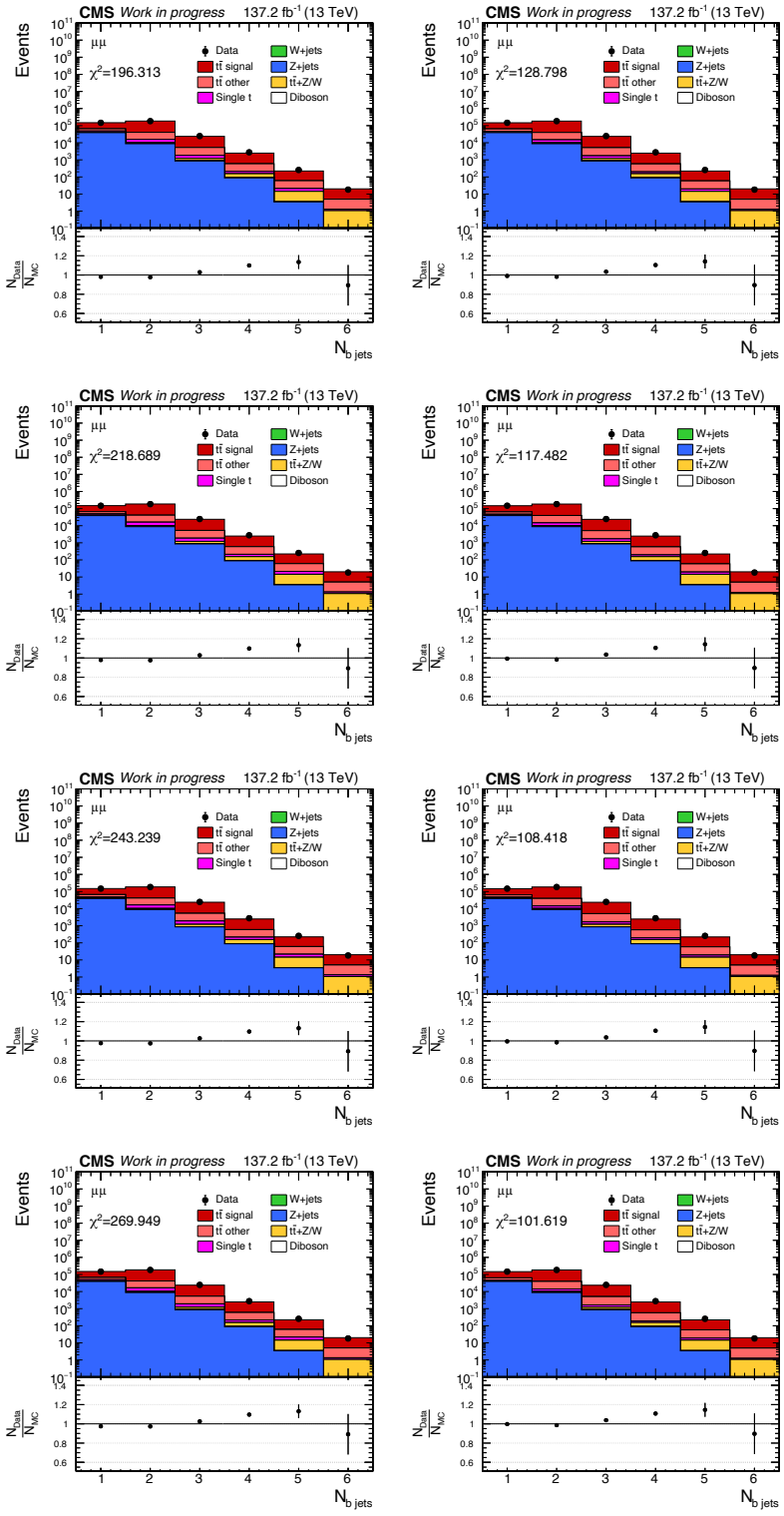

Figure I.3: The figure shows the number of b-tagged jets for the $\mu\mu$ channel after the full event selection. The normalization of the contribution from the single top tW production is varied up (first column) and down (second column) by 10% (first row), 15% (second row), 20% (third row) and 25% (fourth row). The simulated samples are normalized to an integrated luminosity of 137.6 fb^{-1}. The Z+jets sample (blue area) is scaled to account for the discrepancy in the normalization of this background for data and MC (see Section 5). The systematic uncertainties are not included for the purposes of illustration.

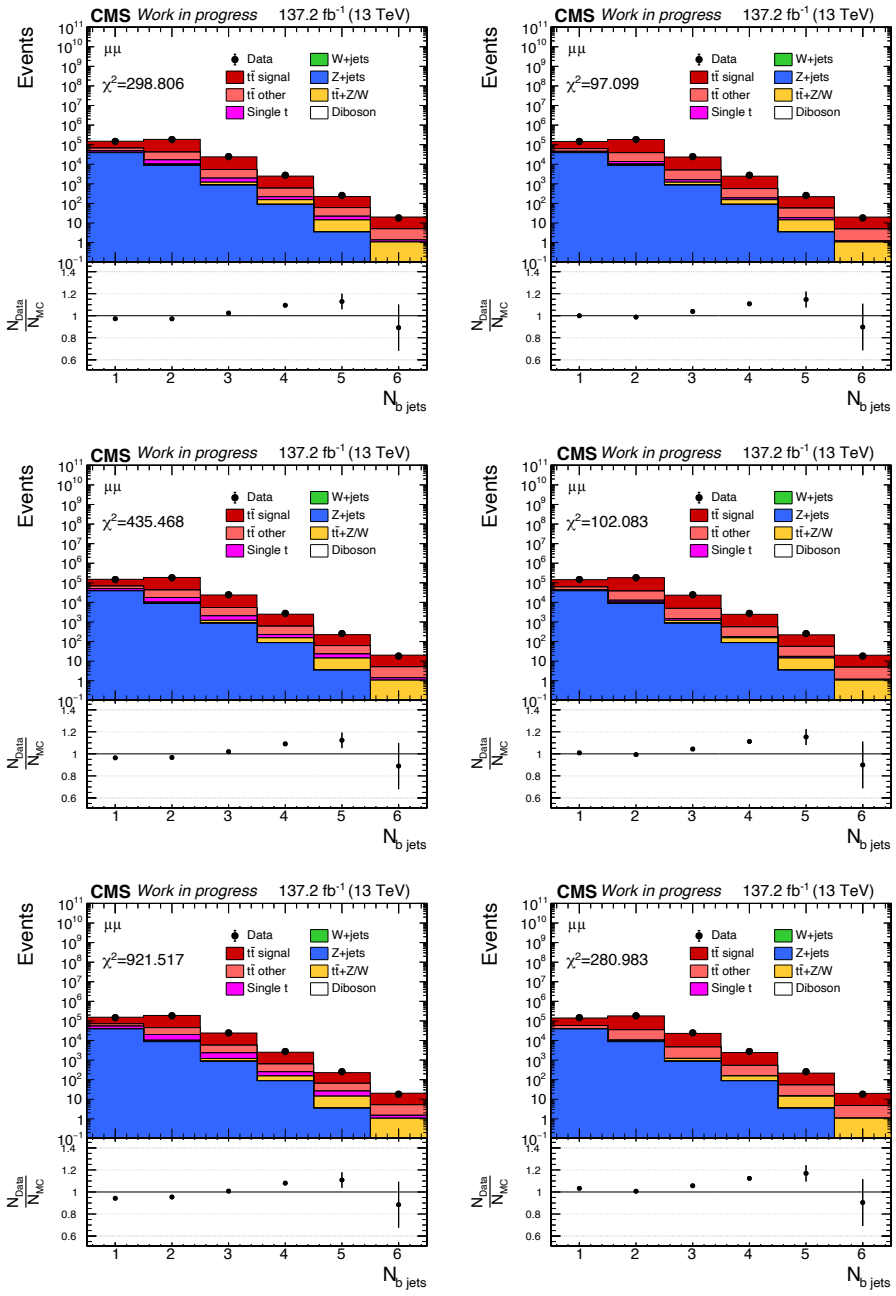

Figure I.4: The figure shows the number of b-tagged jets for the $\mu\mu$ channel after the full event selection. The normalization of the contribution from the single top tW production is varied up (first column) and down (second column) by 30% (first row), 50% (second row) and 100% (third row). The simulated samples are normalized to an integrated luminosity of 137.6 fb^{-1}. The Z+jets sample (blue area) is scaled to account for the discrepancy in the normalization of this background for data and MC (see Section 5. The systematic uncertainties are not included for the purposes of illustration.

I.3 $e\mu$ channel

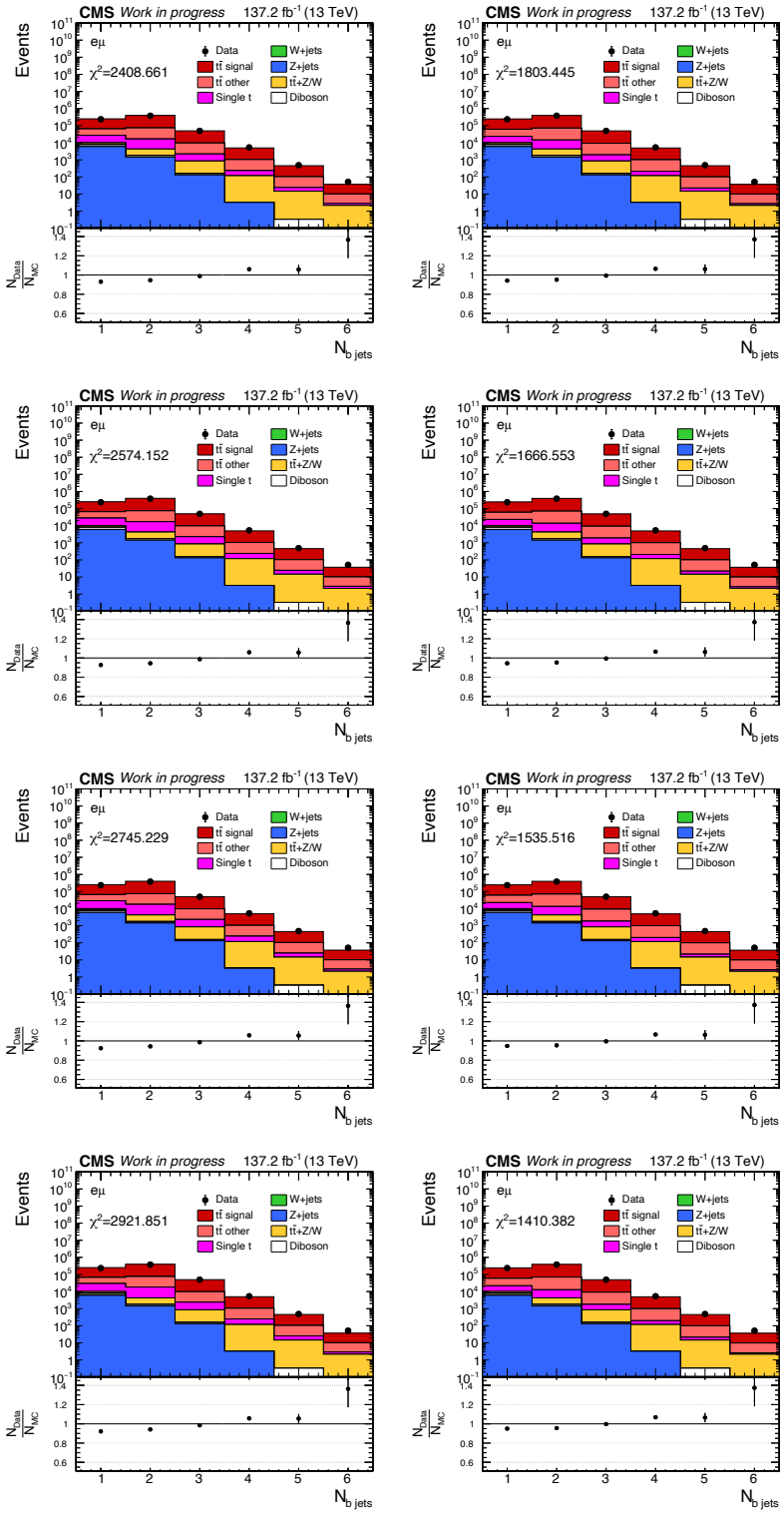

Figure I.5: The figure shows the number of b-tagged jets for the $e\mu$ channel after the full event selection. The normalization of the contribution from the single top tW production is varied up (first column) and down (second column) by 10% (first row), 15% (second row), 20% (third row) and 25% (fourth row). The simulated samples are normalized to an integrated luminosity of 137.6 fb^{-1}. The Z+jets sample (blue area) is scaled to account for the discrepancy in the normalization of this background for data and MC (see Section 5). The systematic uncertainties are not included for the purposes of illustration.

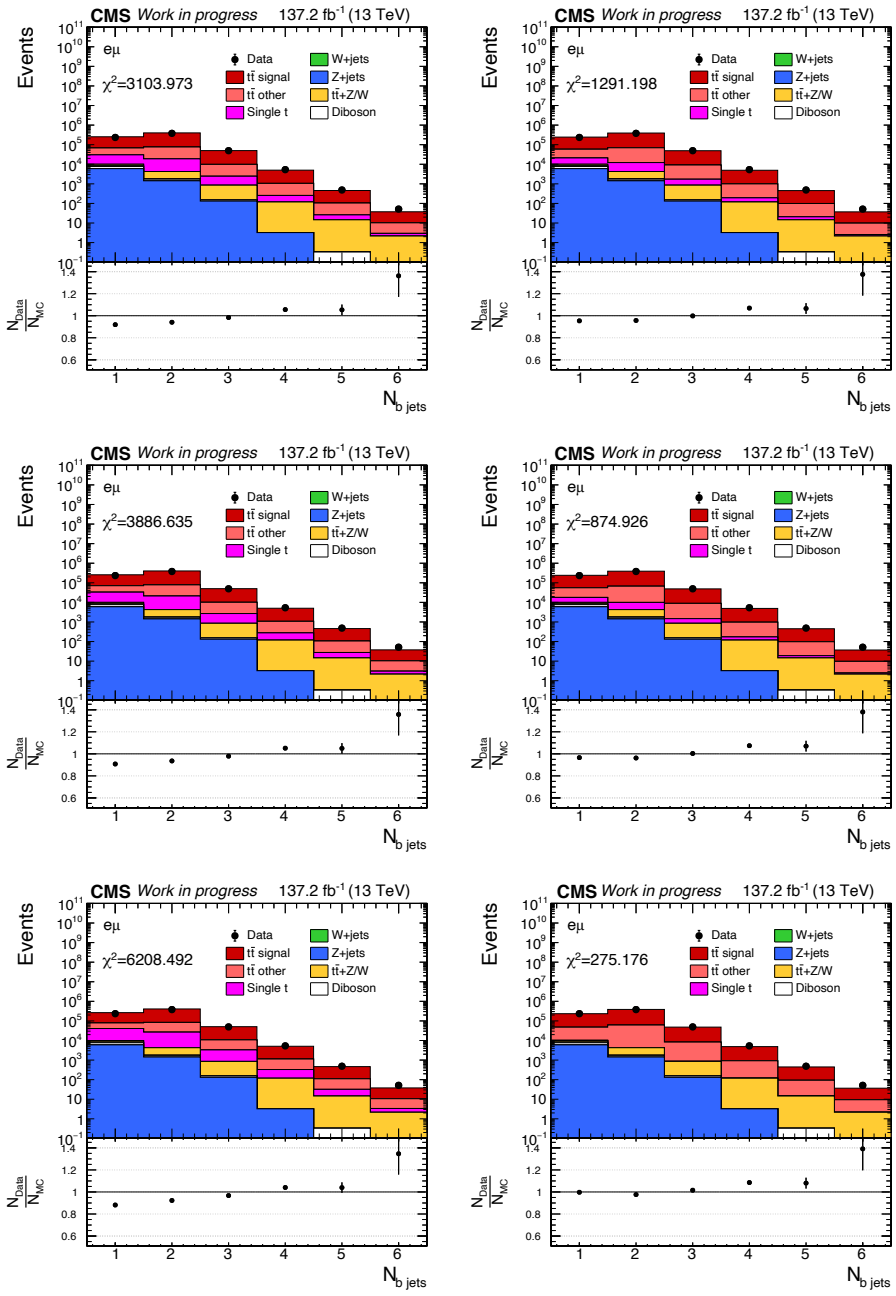

Figure I.6: The figure shows the number of b-tagged jets for the $e\mu$ channel after the full event selection. The normalization of the contribution from the single top tW production is varied up (first column) and down (second column) by 30% (first row), 50% (second row) and 100% (third row). The simulated samples are normalized to an integrated luminosity of 137.6 fb^{-1}. The Z+jets sample (blue area) is scaled to account for the discrepancy in the normalization of this background for data and MC (see Section 5. The systematic uncertainties are not included for the purposes of illustration.

Appendix J

Systematic uncertainty contributions

J.1 Single-differential measurements

J.1.1 Parton level

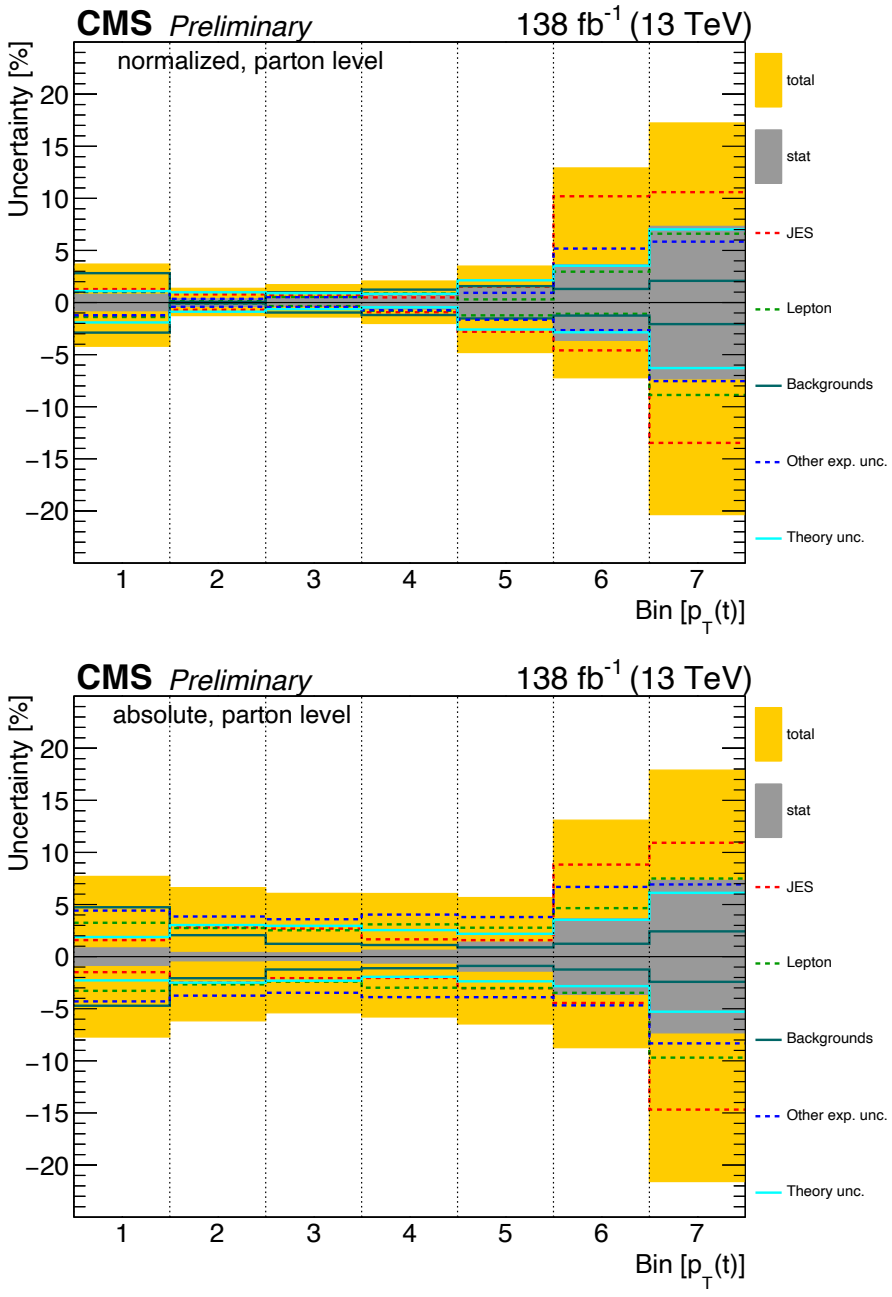

Figure J.1: The figure shows the uncertainty contributions of the differential $t\bar{t}$ cross section measured as a function of the transverse momentum of the top, $p_{\mathrm{T}}(t)$, for both normalized (top) and absolute (bottom) measurements performed in the full phase space at parton level.

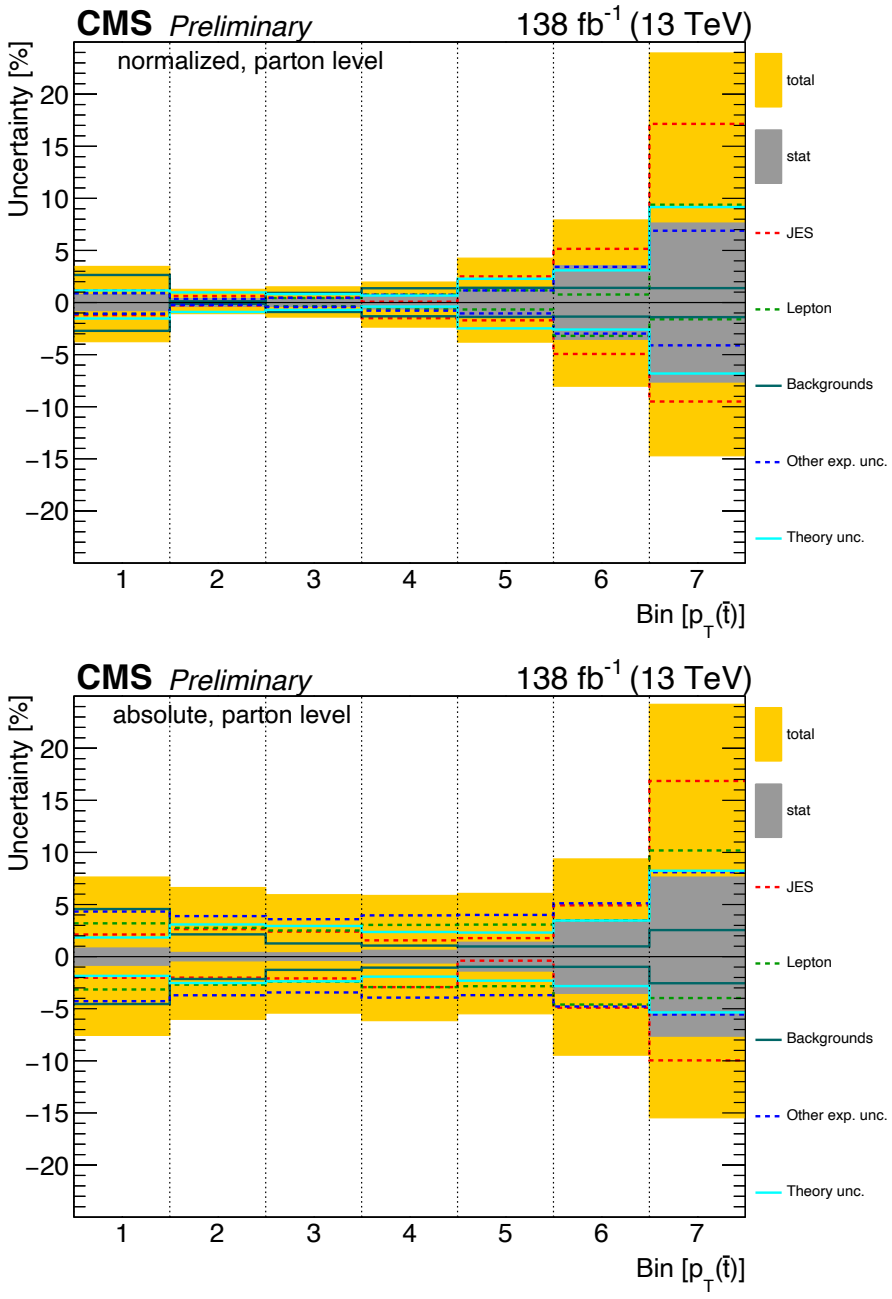

Figure J.2: The figure shows the uncertainty contributions of the differential $t\bar{t}$ cross section measured as a function of the transverse momentum of the anti-top, $p_{\mathrm{T}}(\bar{t})$, for both normalized (top) and absolute (bottom) measurements performed in the full phase space at parton level.

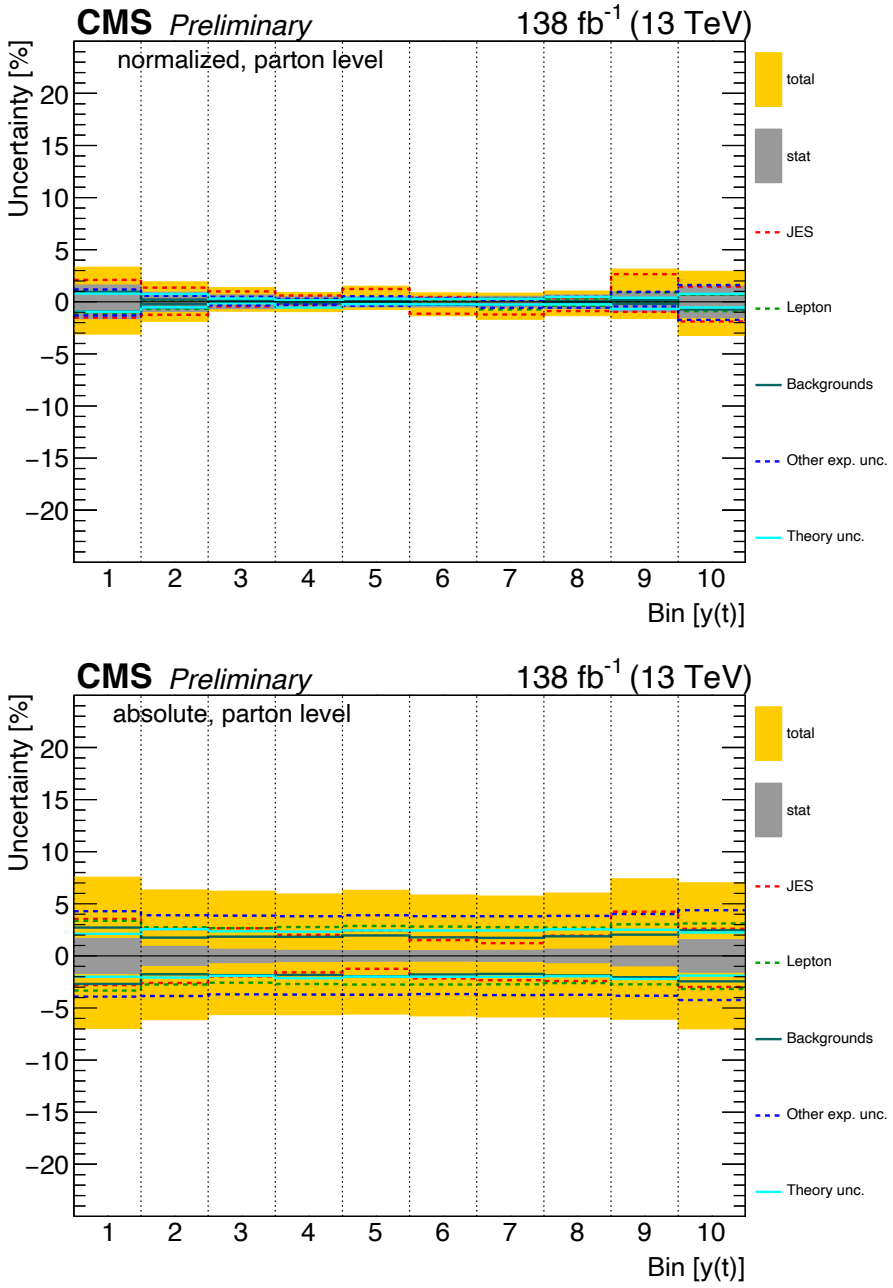

Figure J.3: The figure shows the uncertainty contributions of the differential $t\bar{t}$ cross section measured as a function of the rapidity of the top, $y(t)$, for both normalized (top) and absolute (bottom) measurements performed in the full phase space at parton level.

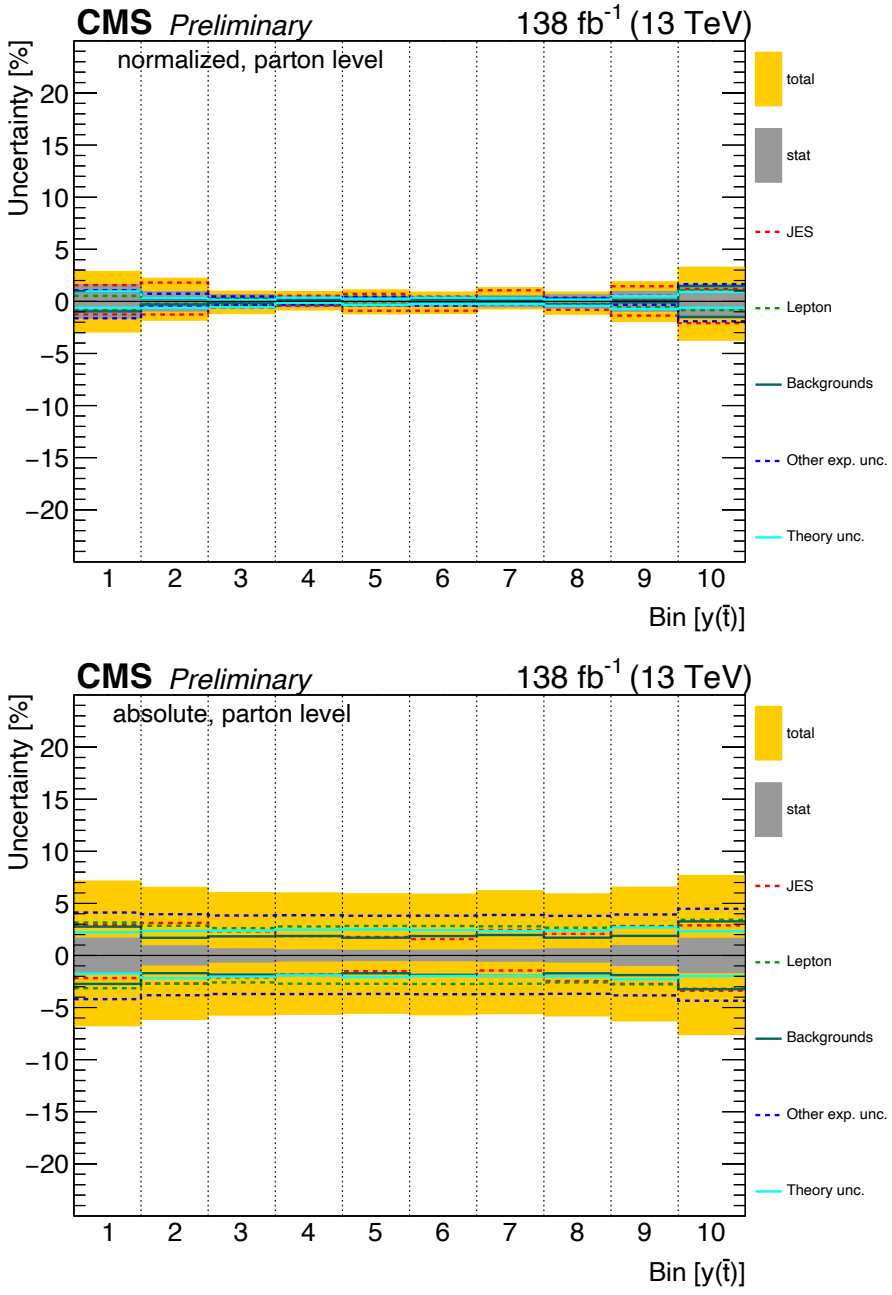

Figure J.4: The figure shows the uncertainty contributions of the differential $t\bar{t}$ cross section measured as a function of the rapidity of the anti-top, $y(\bar{t})$, for both normalized (top) and absolute (bottom) measurements performed in the full phase space at parton level.

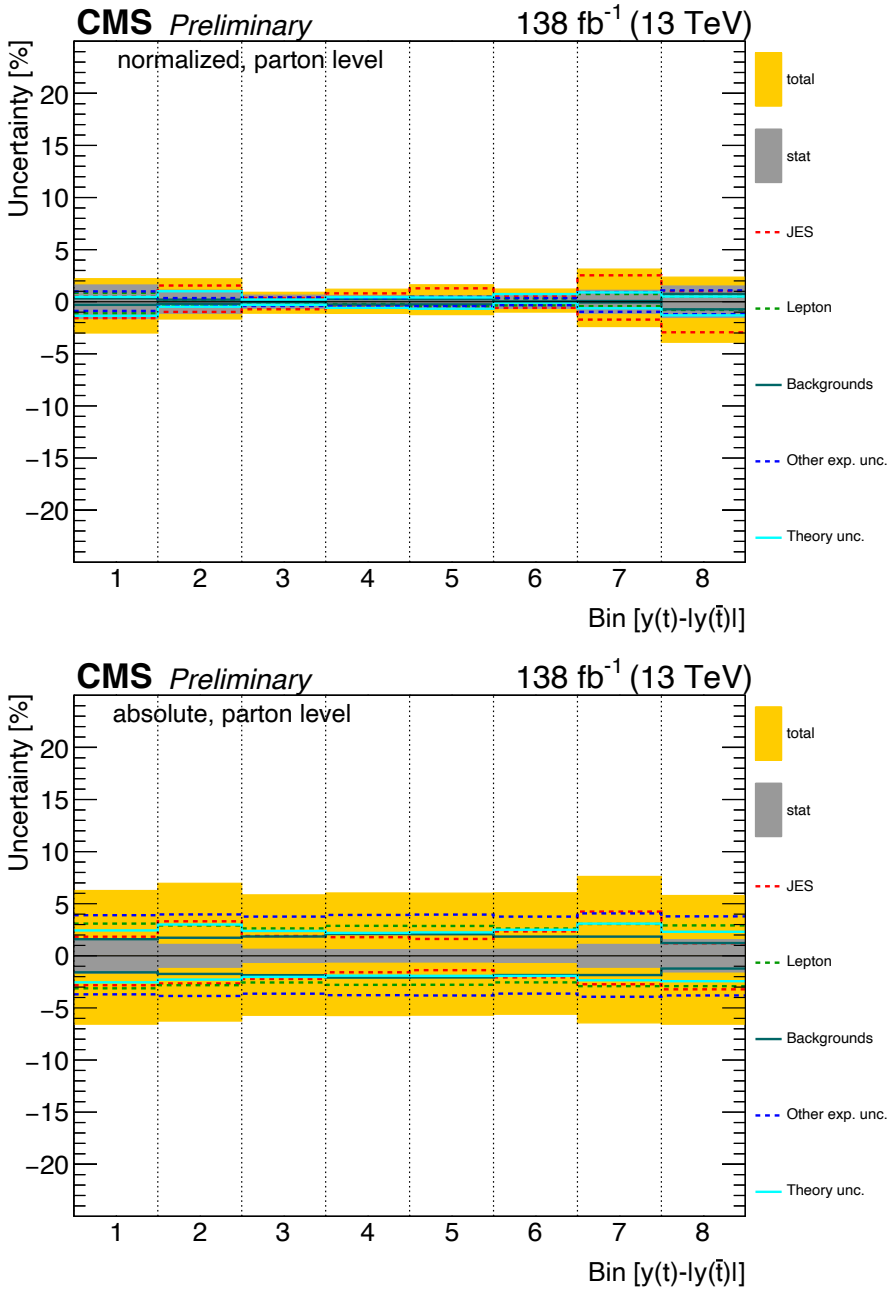

Figure J.5: The figure shows the uncertainty contributions of the differential $t\bar{t}$ cross section measured as a function of the difference in absolute value of rapidity of the top and absolute value of rapidity of the anti-top, $|y(t)| - |y(\bar{t})|$, for both normalized (top) and absolute (bottom) measurements performed in the full phase space at parton level.

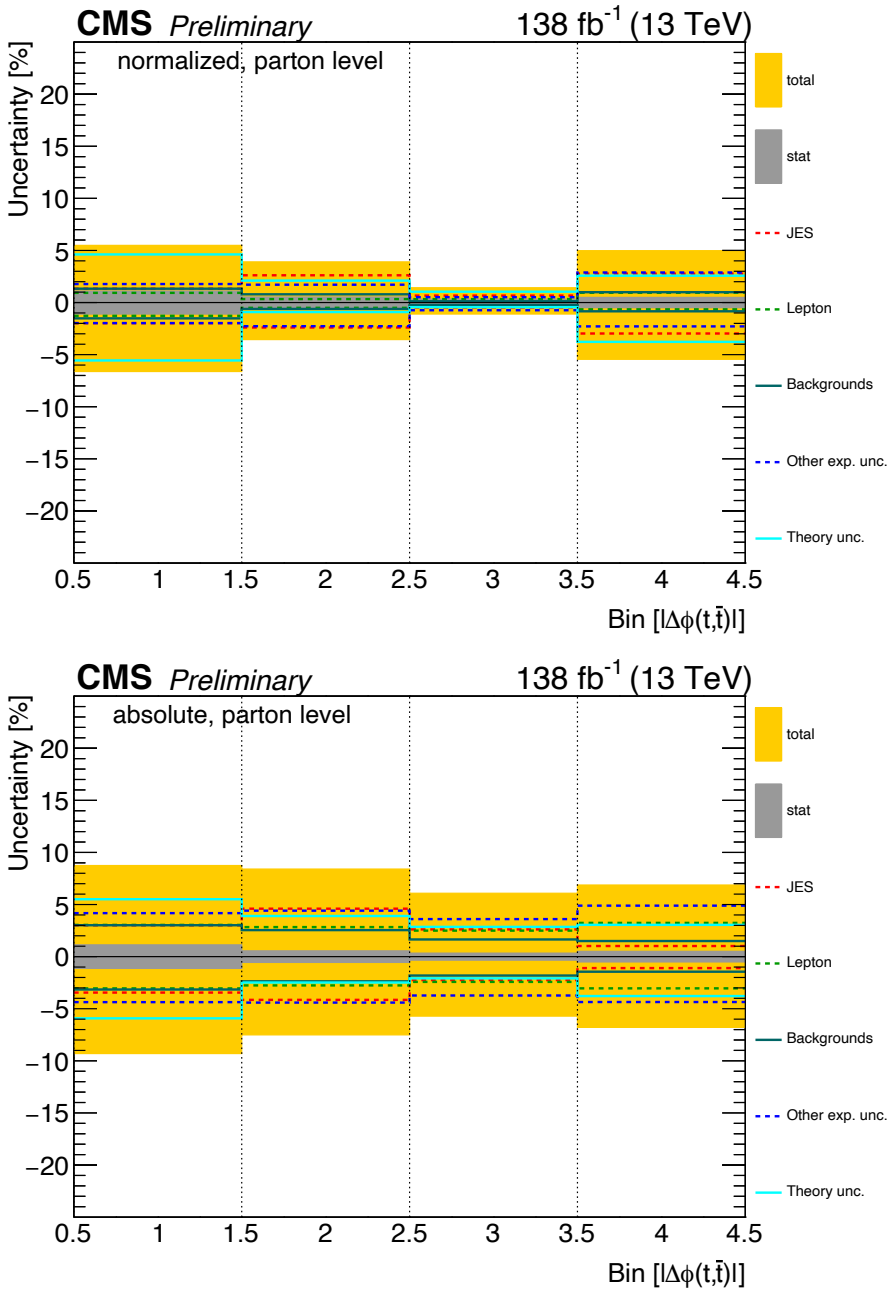

Figure J.6: The figure shows the uncertainty contributions of the differential $t\bar{t}$ cross section measured as a function of the absolute value of the azimuthal angle (ϕ) between the top and the anti-top, $|\Delta\phi(t,\bar{t})|$, for both normalized (top) and absolute (bottom) measurements performed in the full phase space at parton level.

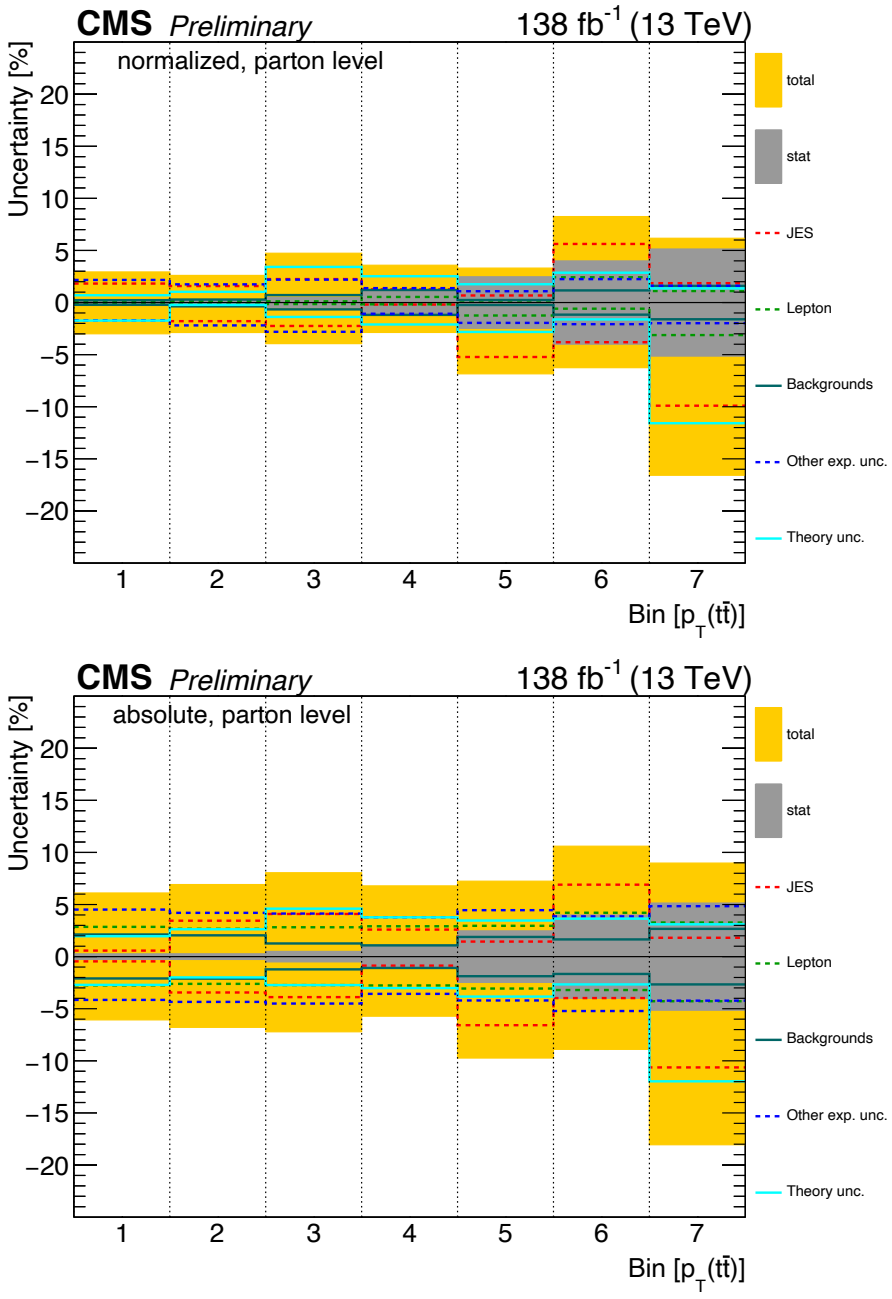

Figure J.7: The figure shows the uncertainty contributions of the differential $t\bar{t}$ cross section measured as a function of the transverse momentum of the $t\bar{t}$ system, $p_{\mathrm{T}}(t\bar{t})$, for both normalized (top) and absolute (bottom) measurements performed in the full phase space at parton level.

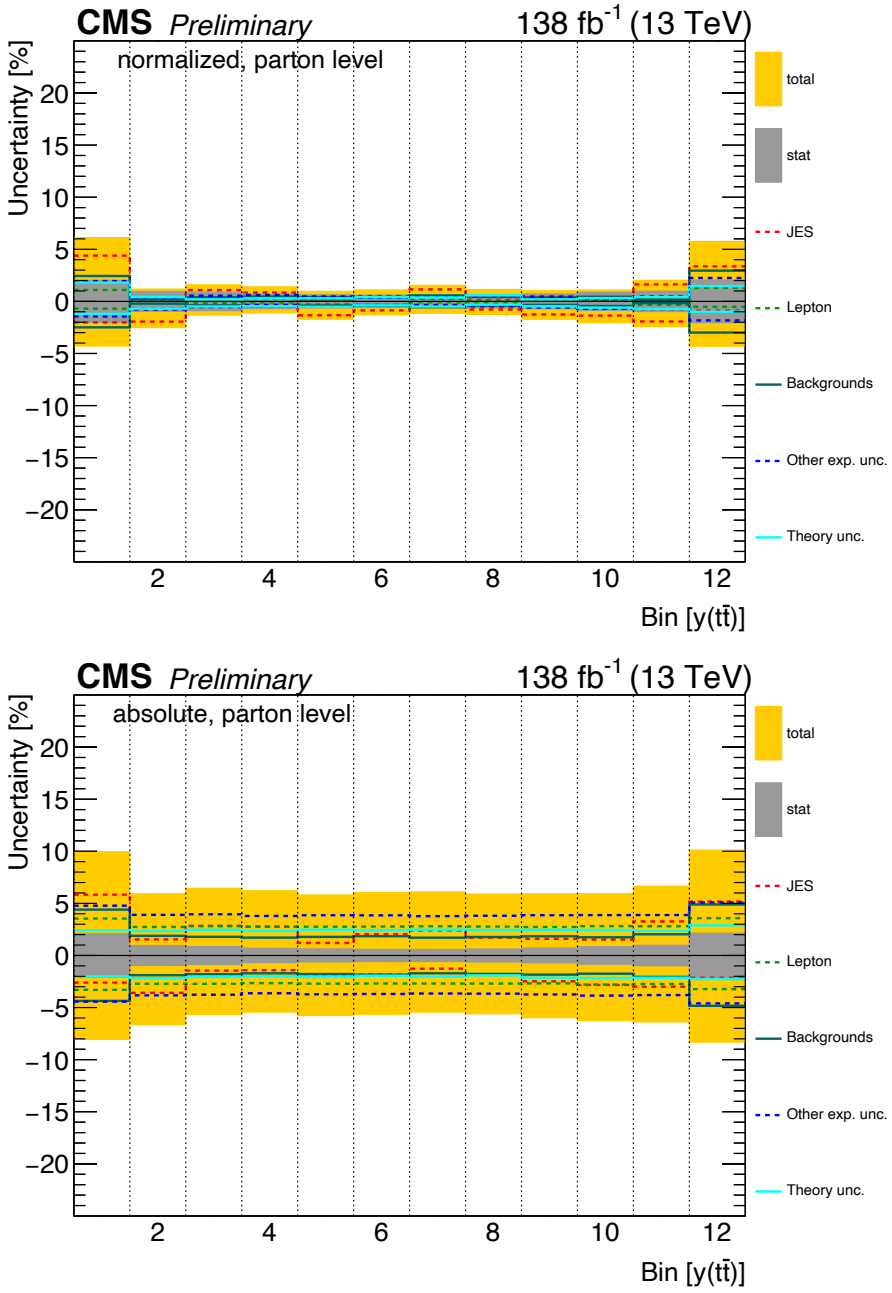

Figure J.8: The figure shows the uncertainty contributions of the differential $t\bar{t}$ cross section measured as a function of the rapidity of the $t\bar{t}$ system, $y(t\bar{t})$, for both normalized (top) and absolute (bottom) measurements performed in the full phase space at parton level.

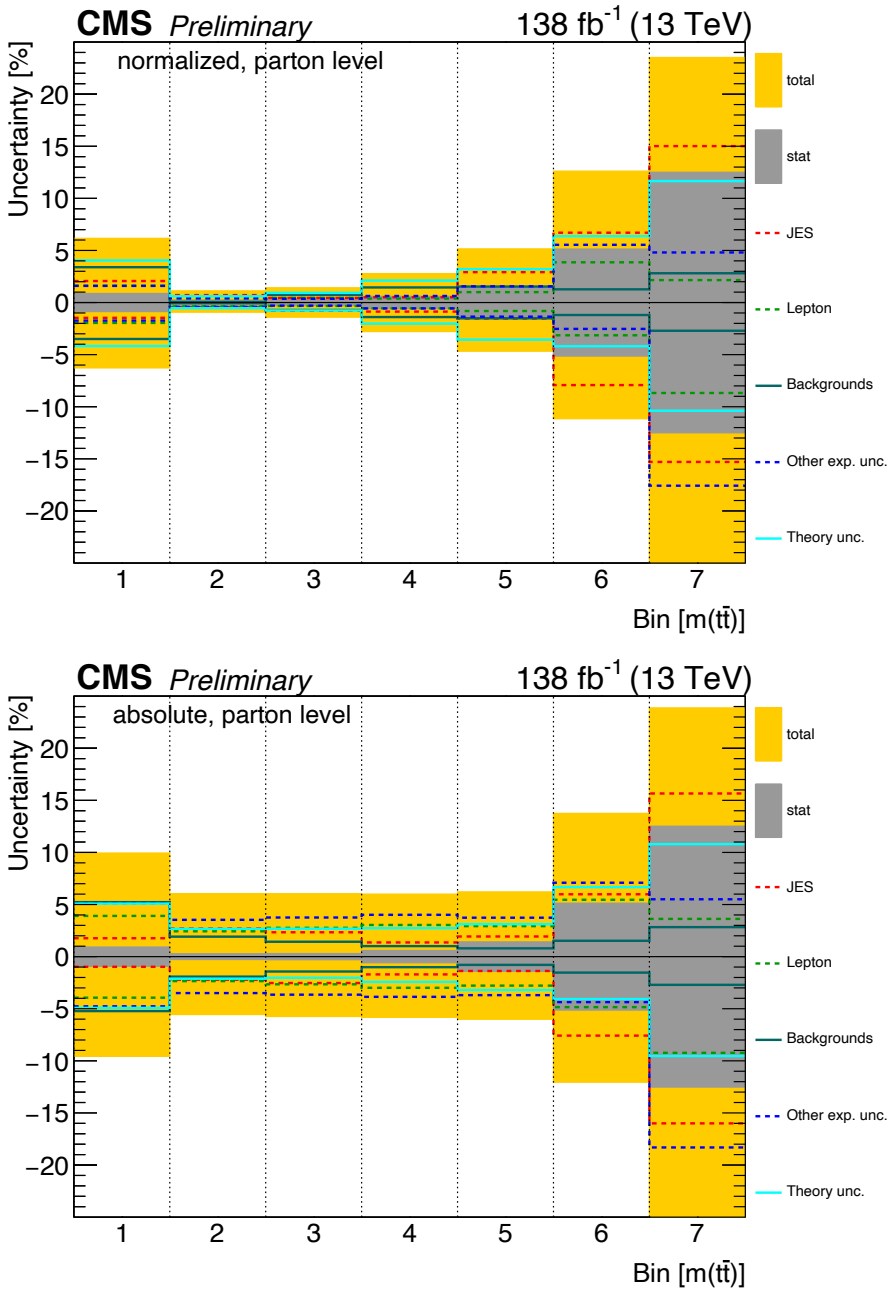

Figure J.9: The figure shows the uncertainty contributions of the differential $t\bar{t}$ cross section measured as a function of the invariant mass of the $t\bar{t}$ system, $m(t\bar{t})$, for both normalized (top) and absolute (bottom) measurements performed in the full phase space at parton level.

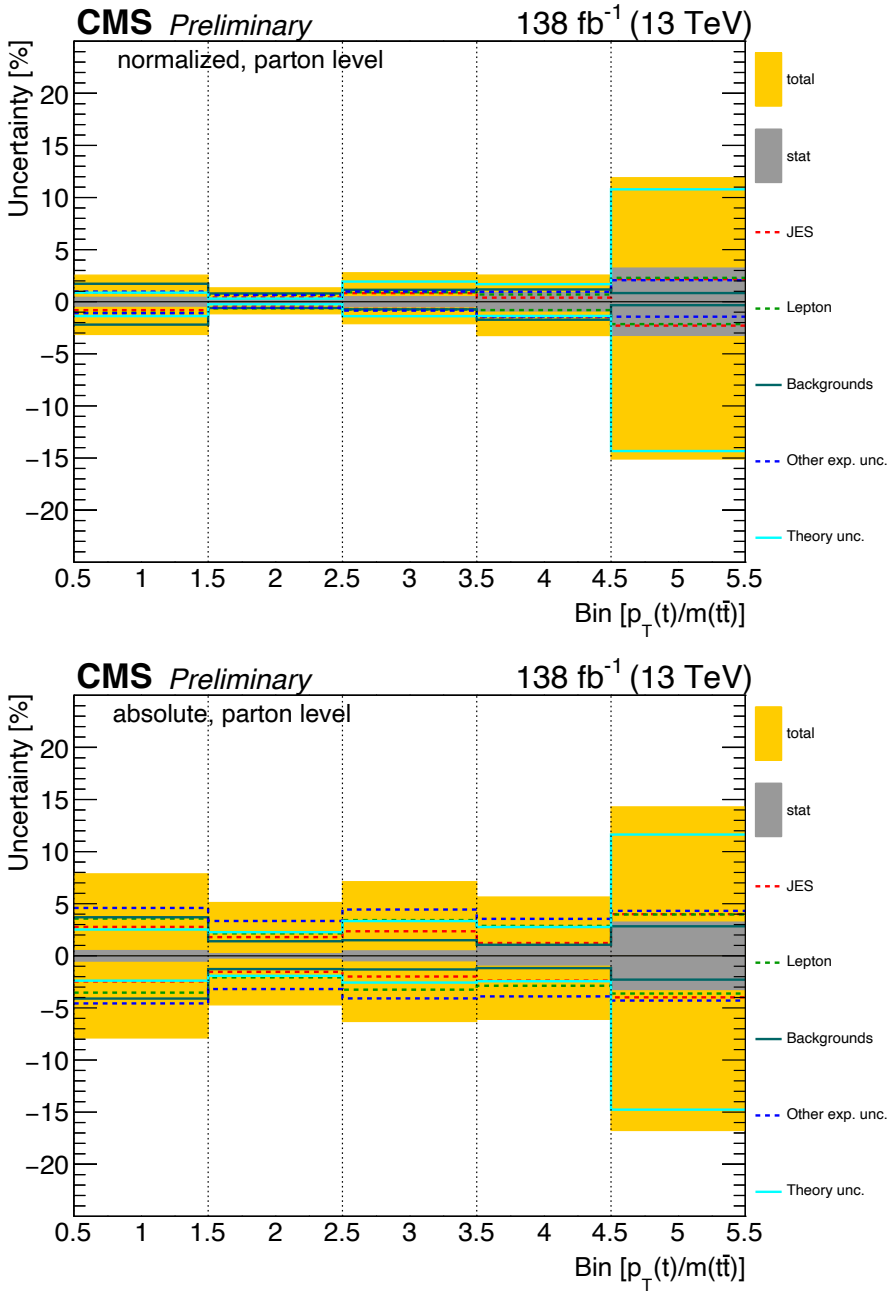

Figure J.10: The figure shows the uncertainty contributions of the differential $t\bar{t}$ cross section measured as a function of the ratio of the transverse momentum of the top quark over the invariant mass of the $t\bar{t}$ system, $p_{\mathrm{T}}(t)/m(t\bar{t})$, for both normalized (top) and absolute (bottom) measurements performed in the full phase space at parton level.

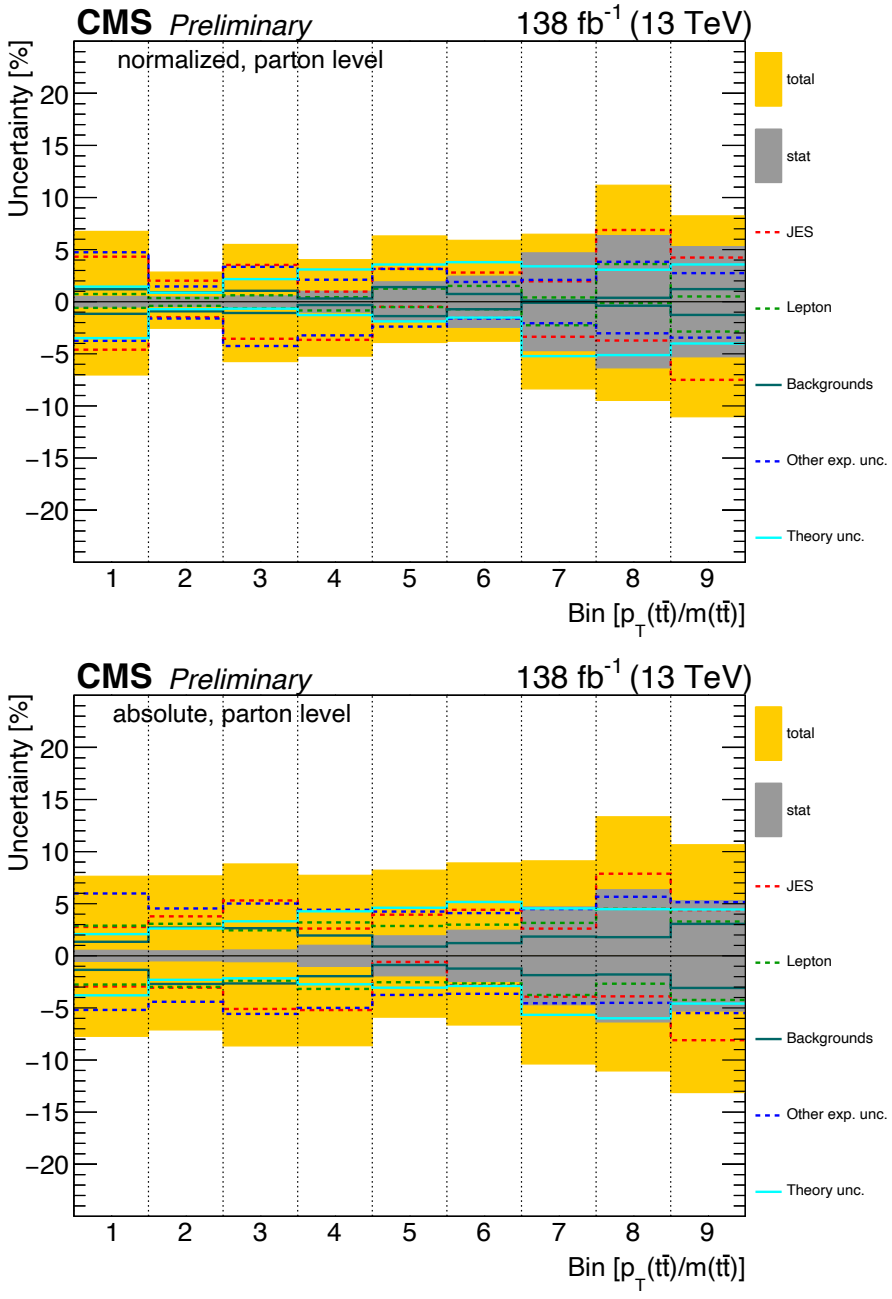

Figure J.11: The figure shows the uncertainty contributions of the differential $t\bar{t}$ cross section measured as a function of the ratio of the transverse momentum of the $t\bar{t}$ system over the invariant mass of the $t\bar{t}$ system, $p_{\mathrm{T}}(t\bar{t})/m(t\bar{t})$, for both normalized (top) and absolute (bottom) measurements performed in the full phase space at parton level.

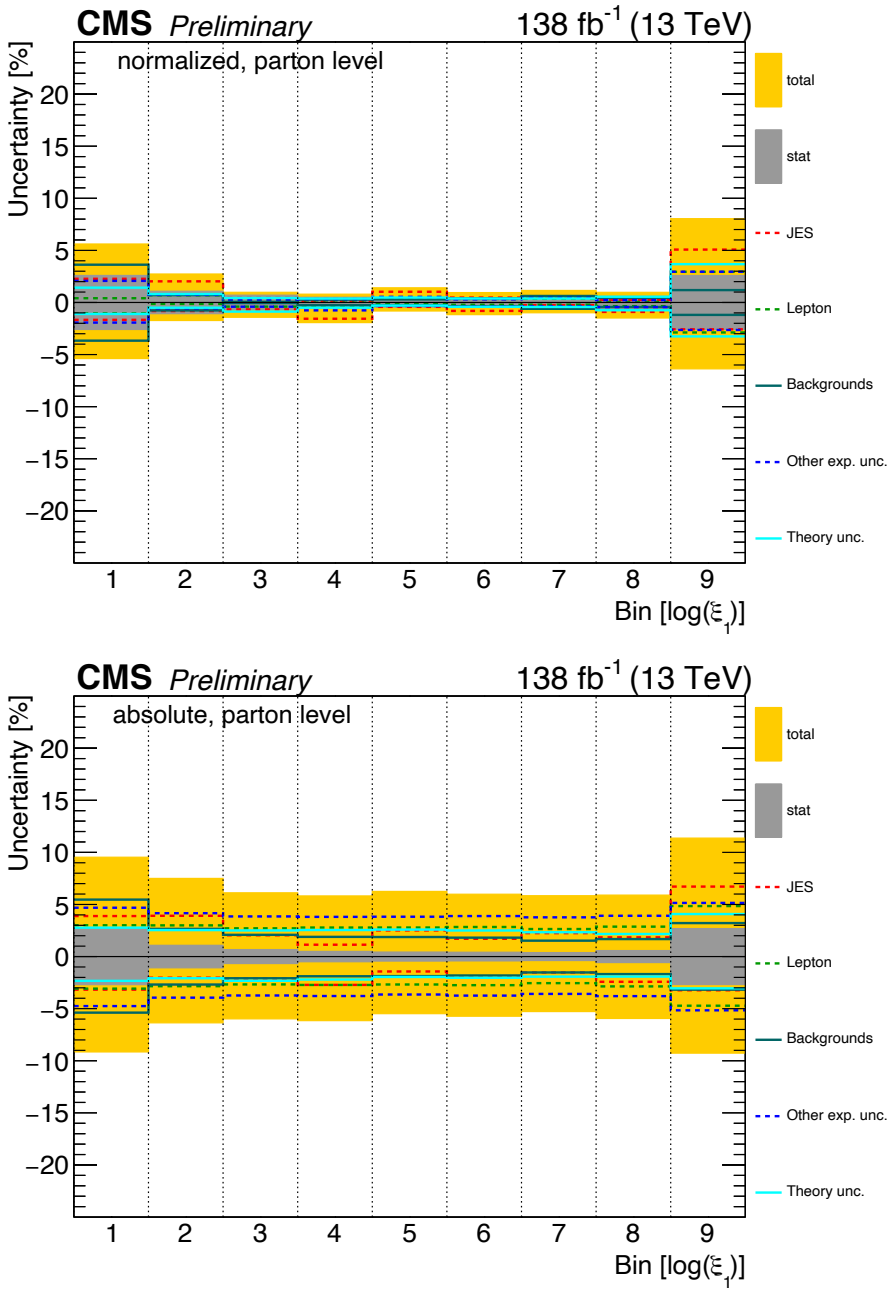

Figure J.12: The figure shows the uncertainty contributions of the differential $t\bar{t}$ cross section measured as a function of $\log(\xi_1)$, which is equivalent to the momentum fraction of the incoming parton from one of the protons in the leading order QCD picture, for both normalized (top) and absolute (bottom) measurements performed in the full phase space at parton level.

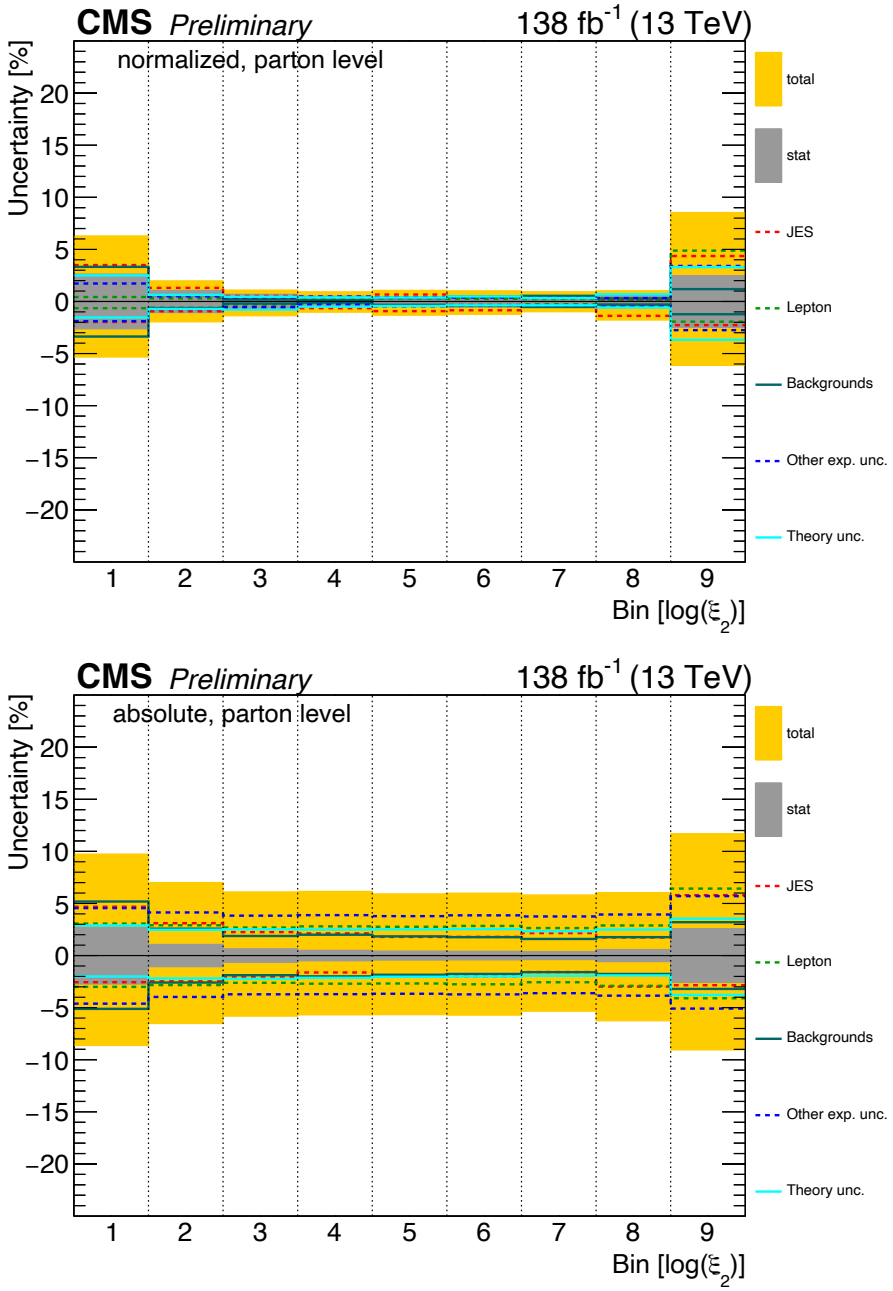

Figure J.13: The figure shows the uncertainty contributions of the differential $t\bar{t}$ cross section measured as a function of $\log(\xi_2)$, which is equivalent to the momentum fraction of the incoming parton from one of the protons in the leading order QCD picture, for both normalized (top) and absolute (bottom) measurements performed in the full phase space at parton level.

J.1.2 Particle level

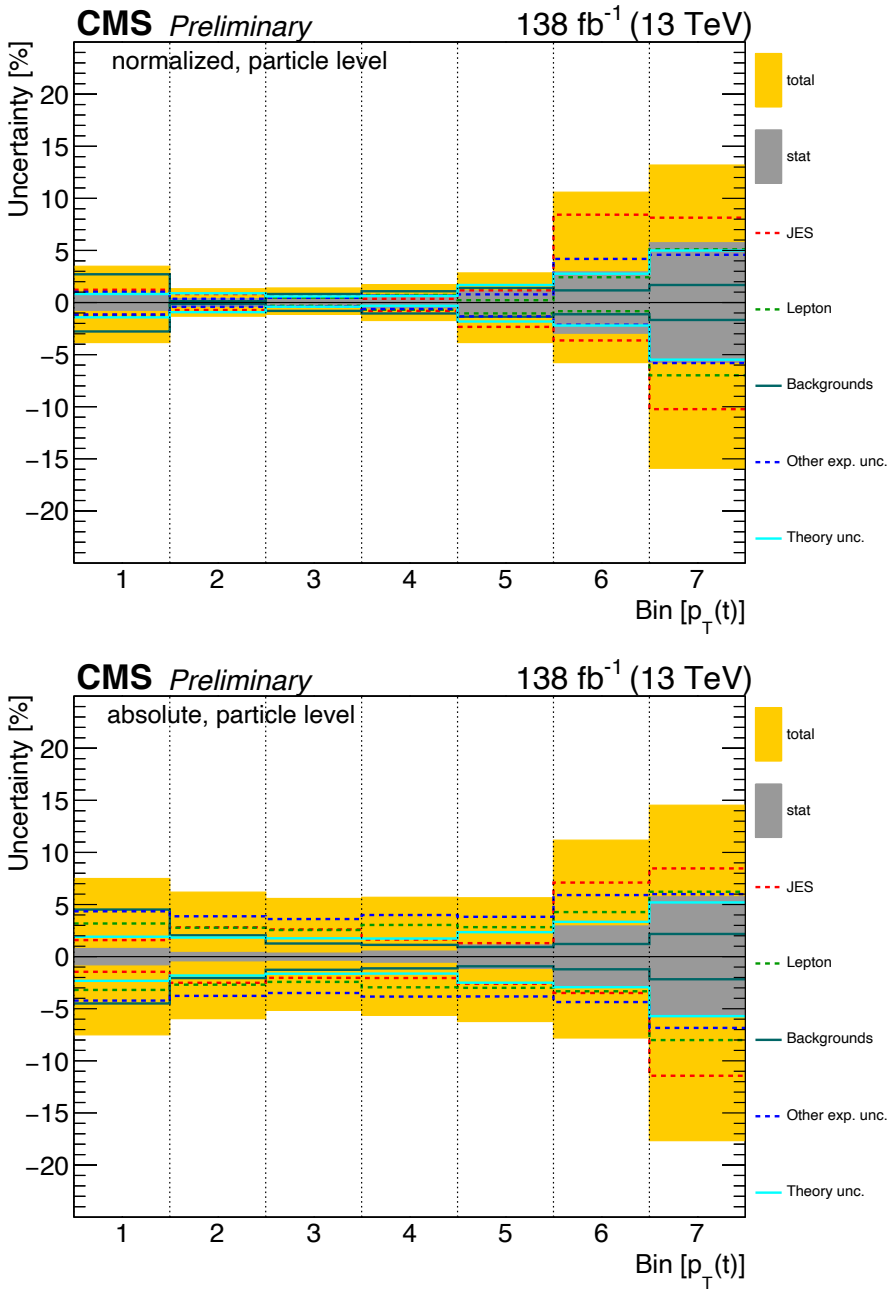

Figure J.14: The figure shows the uncertainty contributions of the differential $t\bar{t}$ cross section measured as a function of the transverse momentum of the top, $p_{\mathrm{T}}(t)$, for both normalized (top) and absolute (bottom) measurements performed in the fiducial phase space at particle level.

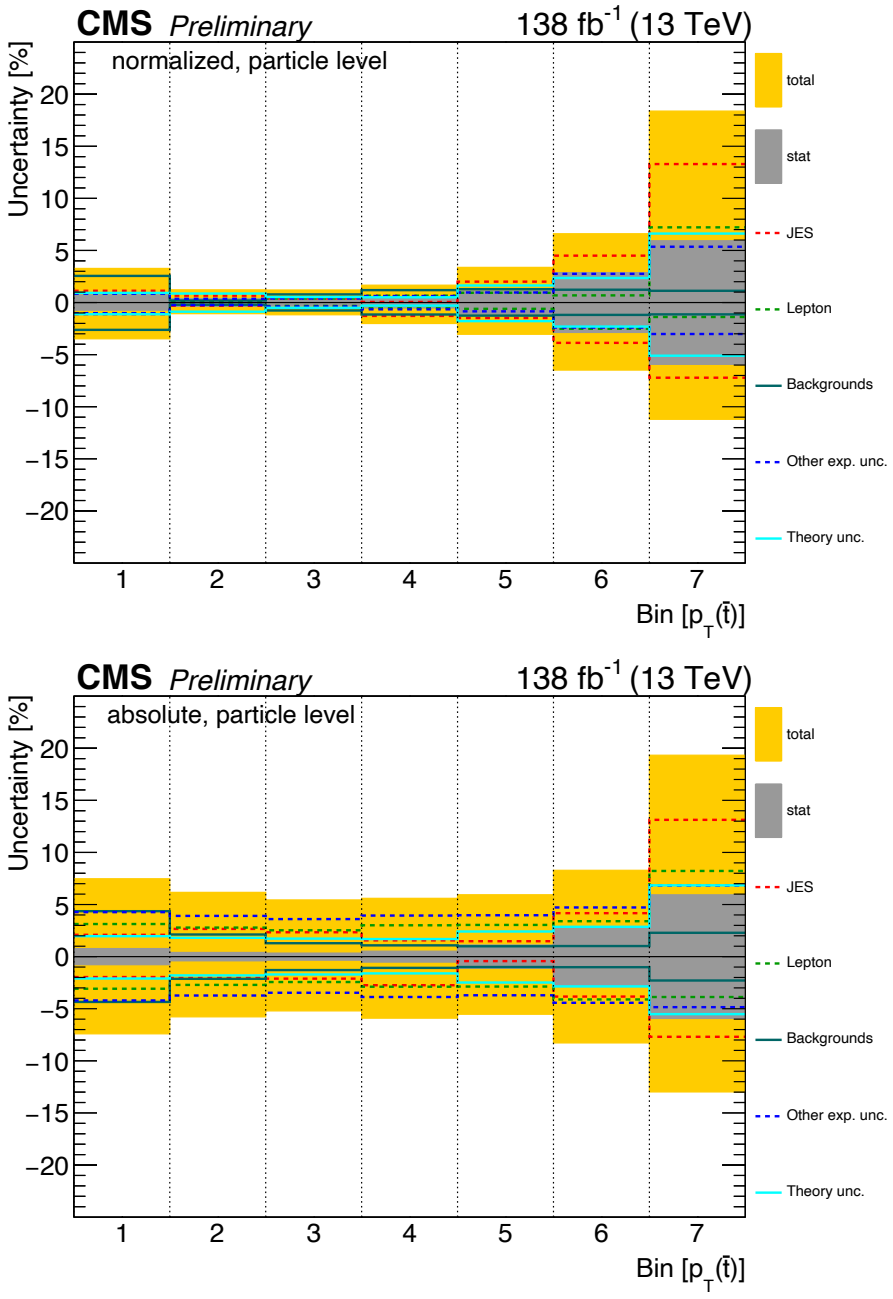

Figure J.15: The figure shows the uncertainty contributions of the differential $t\bar{t}$ cross section measured as a function of the transverse momentum of the anti-top, $p_{\mathrm{T}}(\bar{t})$, for both normalized (top) and absolute (bottom) measurements performed in the fiducial phase space at particle level.

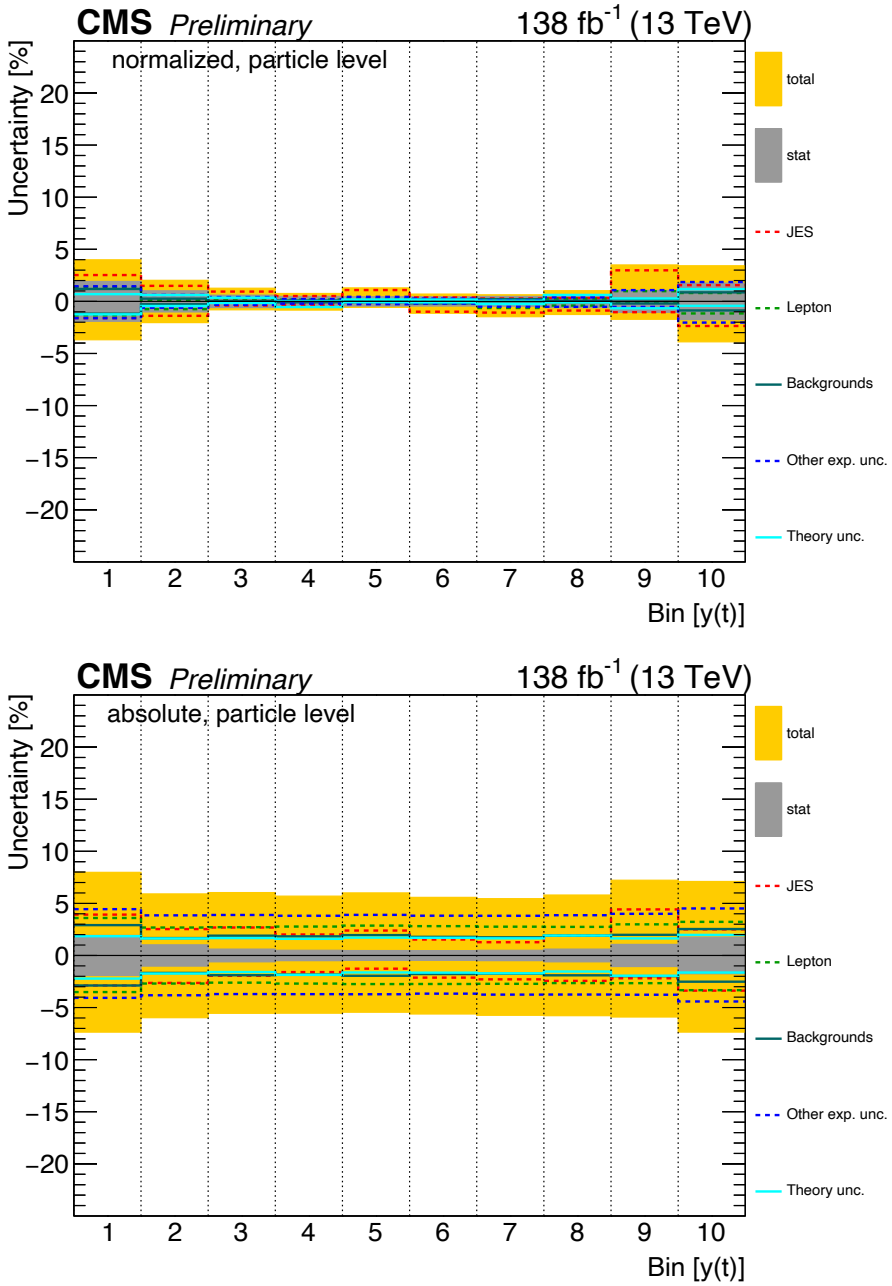

Figure J.16: The figure shows the uncertainty contributions of the differential $t\bar{t}$ cross section measured as a function of the rapidity of the top, $y(t)$, for both normalized (top) and absolute (bottom) measurements performed in the fiducial phase space at particle level.

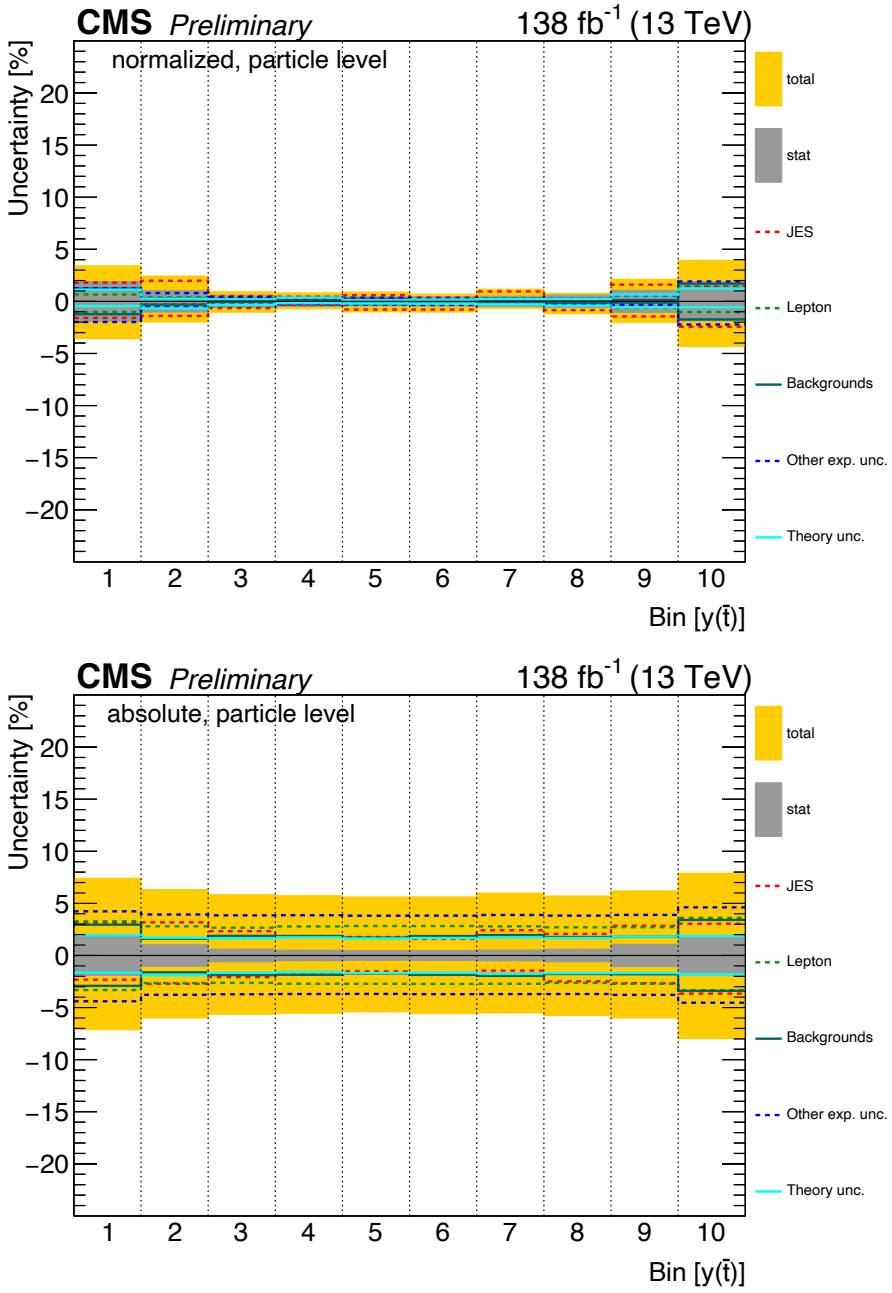

Figure J.17: The figure shows the uncertainty contributions of the differential $t\bar{t}$ cross section measured as a function of the rapidity of the anti-top, $y(\bar{t})$, for both normalized (top) and absolute (bottom) measurements performed in the fiducial phase space at particle level.

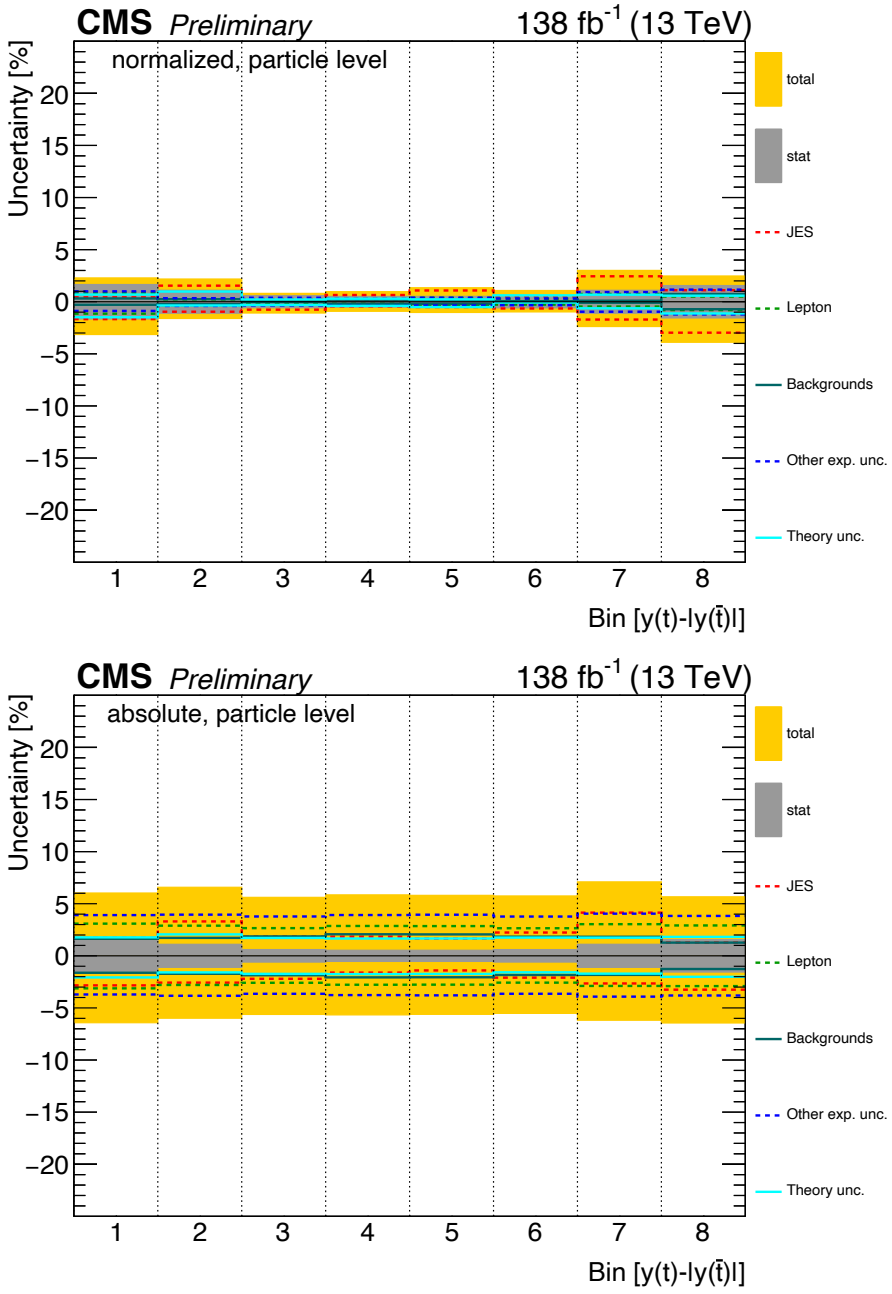

Figure J.18: The figure shows the uncertainty contributions of the differential $t\bar{t}$ cross section measured as a function of the difference in absolute value of rapidity of the top and absolute value of rapidity of the anti-top, $|y(t)| - |y(\bar{t})|$, for both normalized (top) and absolute (bottom) measurements performed in the fiducial phase space at particle level.

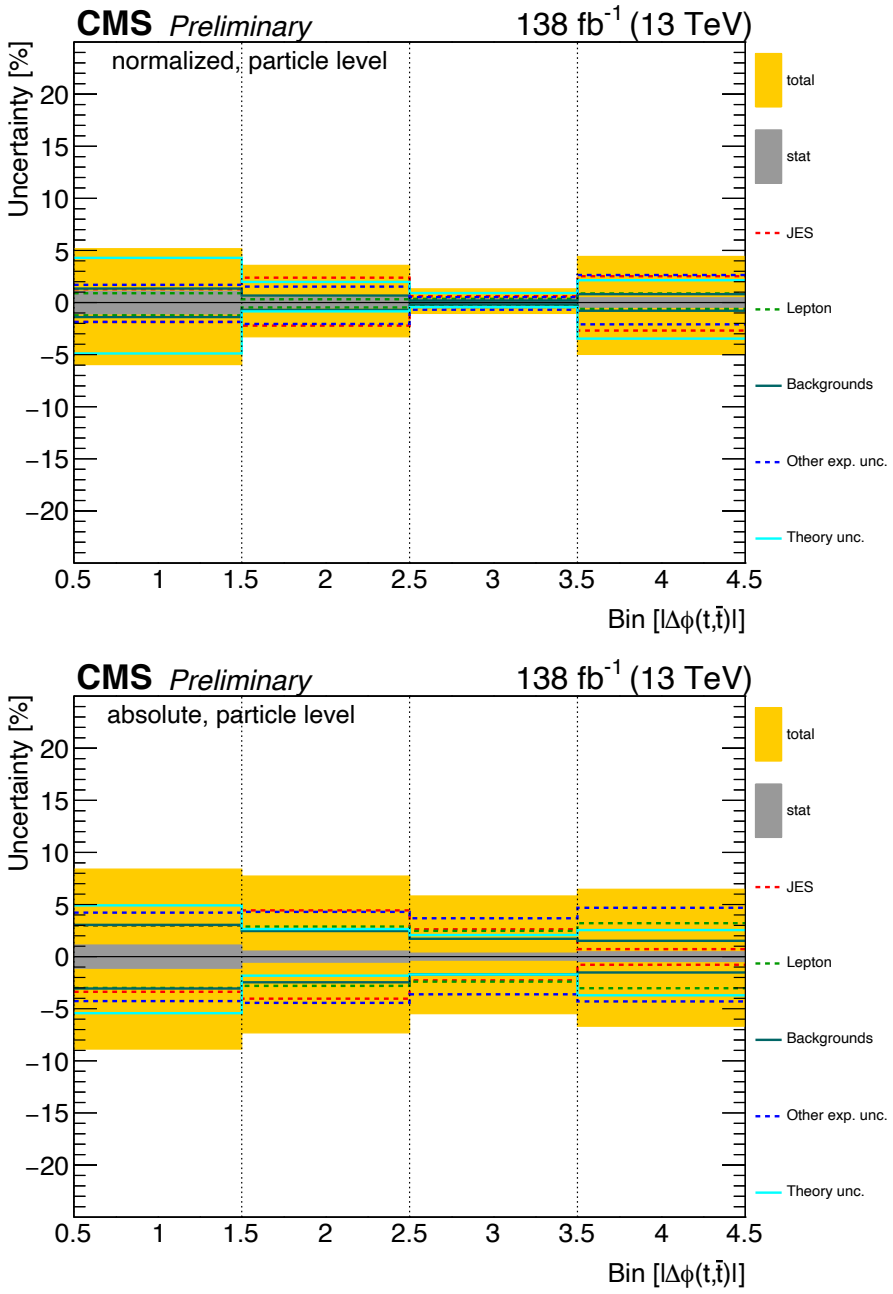

Figure J.19: The figure shows the uncertainty contributions of the differential $t\bar{t}$ cross section measured as a function of the absolute value of the azimuthal angle (ϕ) between the top and the anti-top, $|\Delta\phi(t,\bar{t})|$, for both normalized (top) and absolute (bottom) measurements performed in the fiducial phase space at particle level.

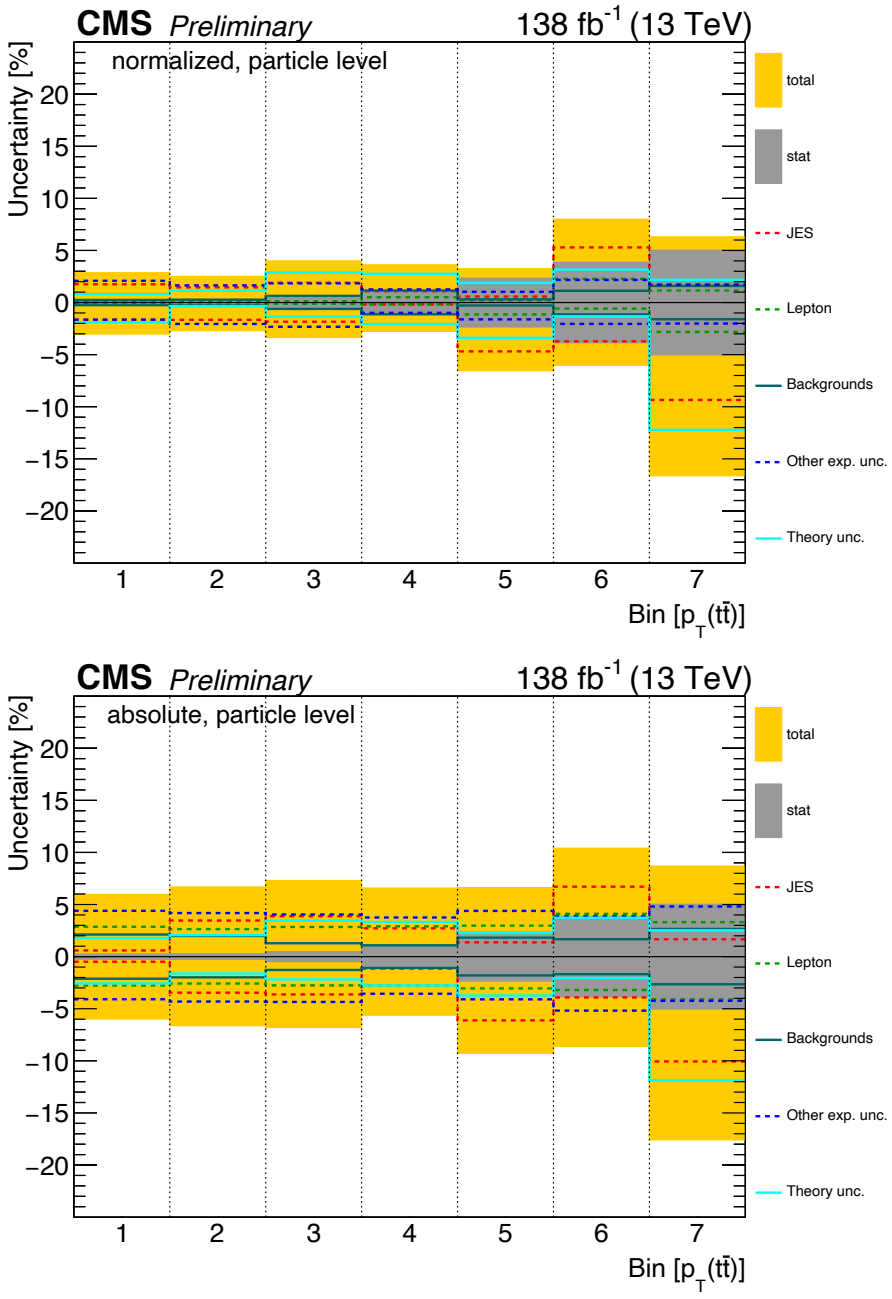

Figure J.20: The figure shows the uncertainty contributions of the differential $t\bar{t}$ cross section measured as a function of the transverse momentum of the $t\bar{t}$ system, $p_{\mathrm{T}}(t\bar{t})$, for both normalized (top) and absolute (bottom) measurements performed in the fiducial phase space at particle level.

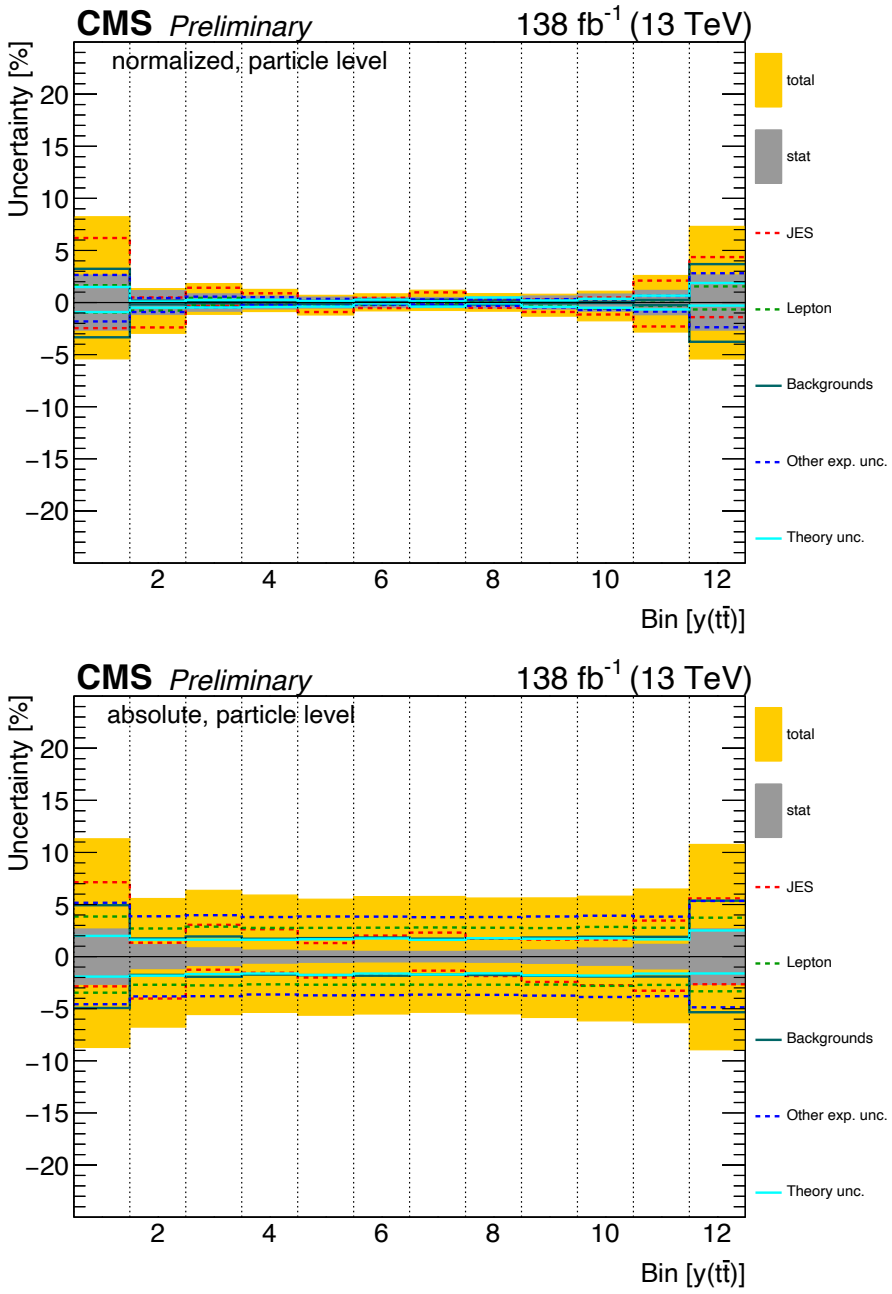

Figure J.21: The figure shows the uncertainty contributions of the differential $t\bar{t}$ cross section measured as a function of the rapidity of the $t\bar{t}$ system, $y(t\bar{t})$, for both normalized (top) and absolute (bottom) measurements performed in the fiducial phase space at particle level.

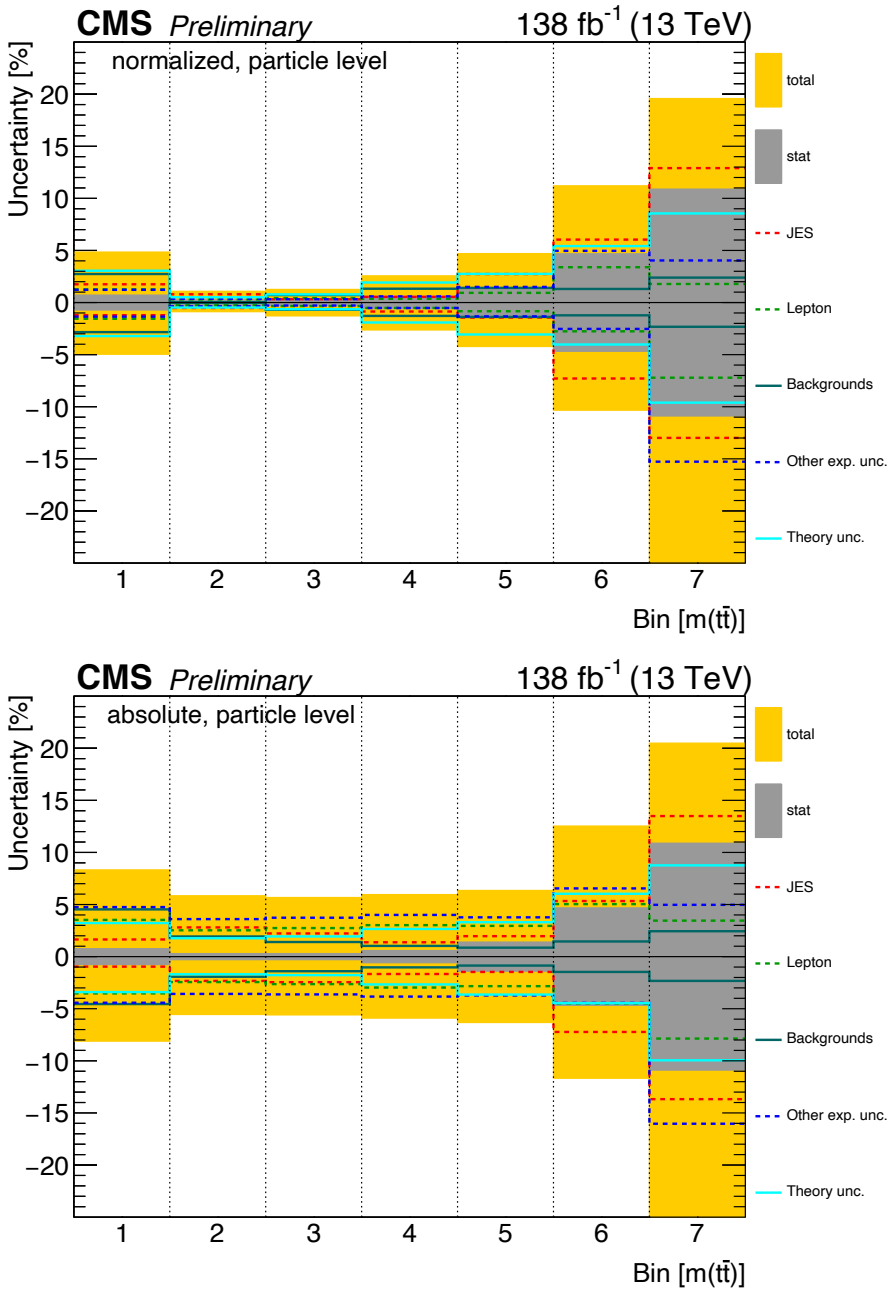

Figure J.22: The figure shows the uncertainty contributions of the differential $t\bar{t}$ cross section measured as a function of the invariant mass of the $t\bar{t}$ system, $m(t\bar{t})$, for both normalized (top) and absolute (bottom) measurements performed in the fiducial phase space at particle level.

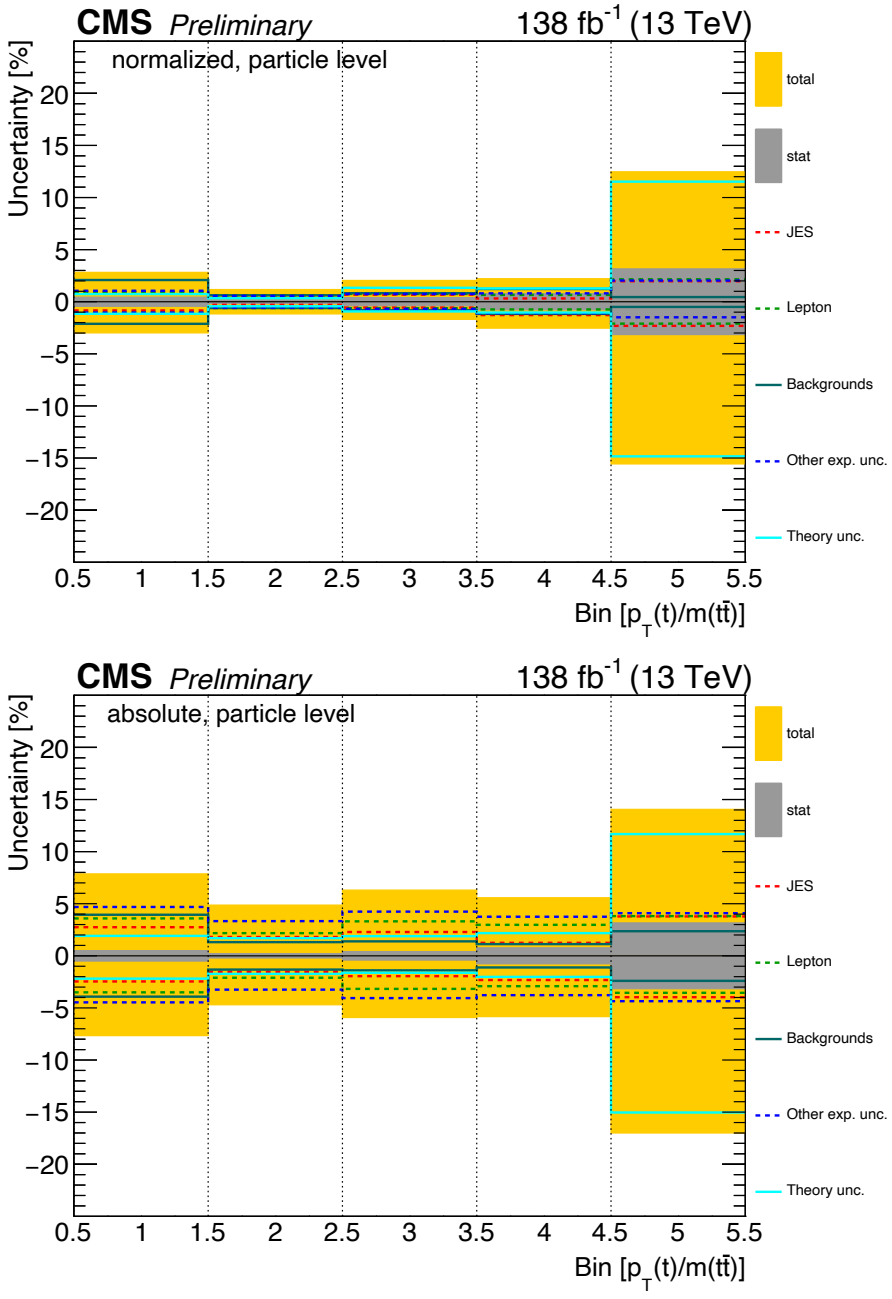

Figure J.23: The figure shows the uncertainty contributions of the differential $t\bar{t}$ cross section measured as a function of the ratio of the transverse momentum of the top quark over the invariant mass of the $t\bar{t}$ system, $p_{\mathrm{T}}(t)/m(t\bar{t})$, for both normalized (top) and absolute (bottom) measurements performed in the fiducial phase space at particle level.

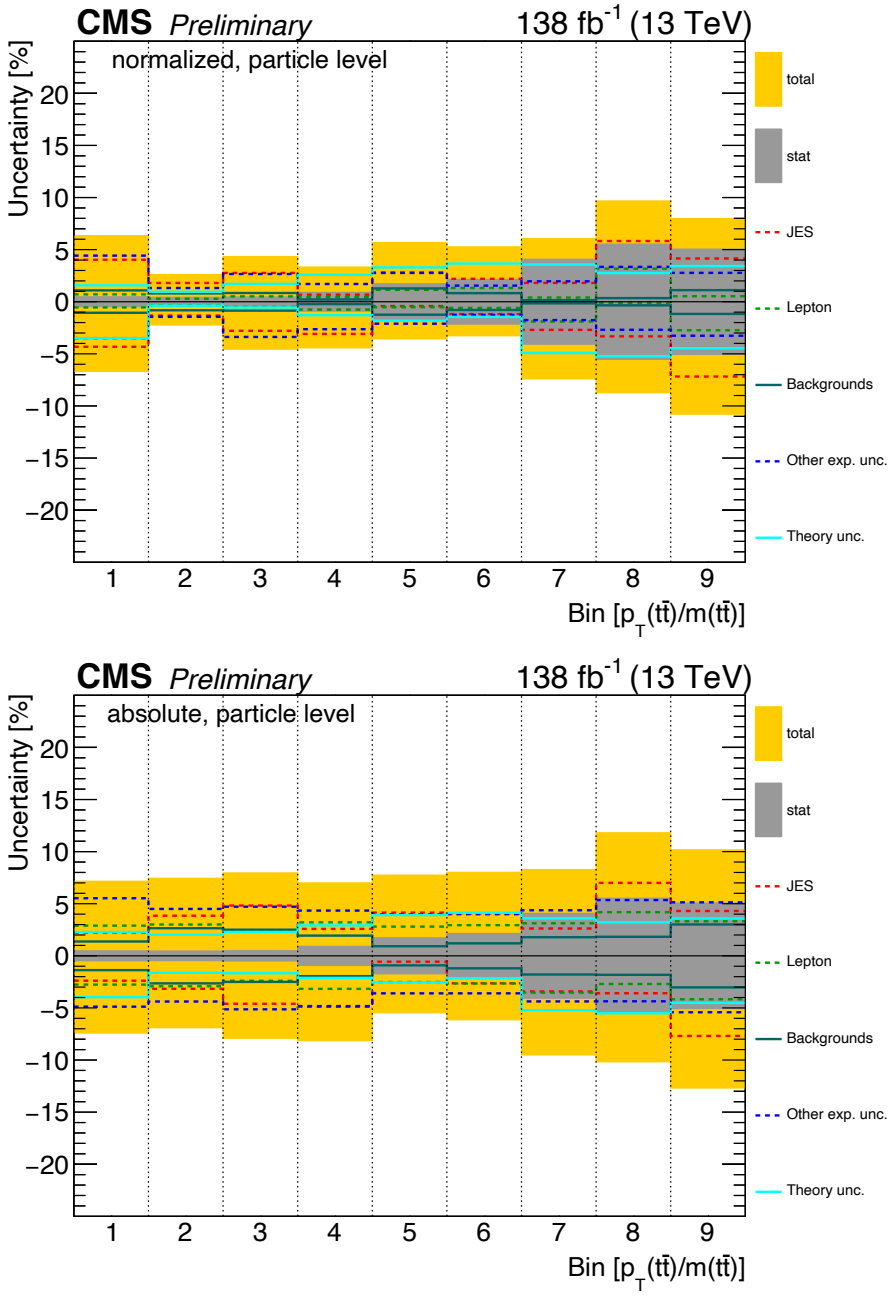

Figure J.24: The figure shows the uncertainty contributions of the differential $t\bar{t}$ cross section measured as a function of the ratio of the transverse momentum of the $t\bar{t}$ system over the invariant mass of the $t\bar{t}$ system, $p_{\mathrm{T}}(t\bar{t})/m(t\bar{t})$, for both normalized (top) and absolute (bottom) measurements performed in the fiducial phase space at particle level.

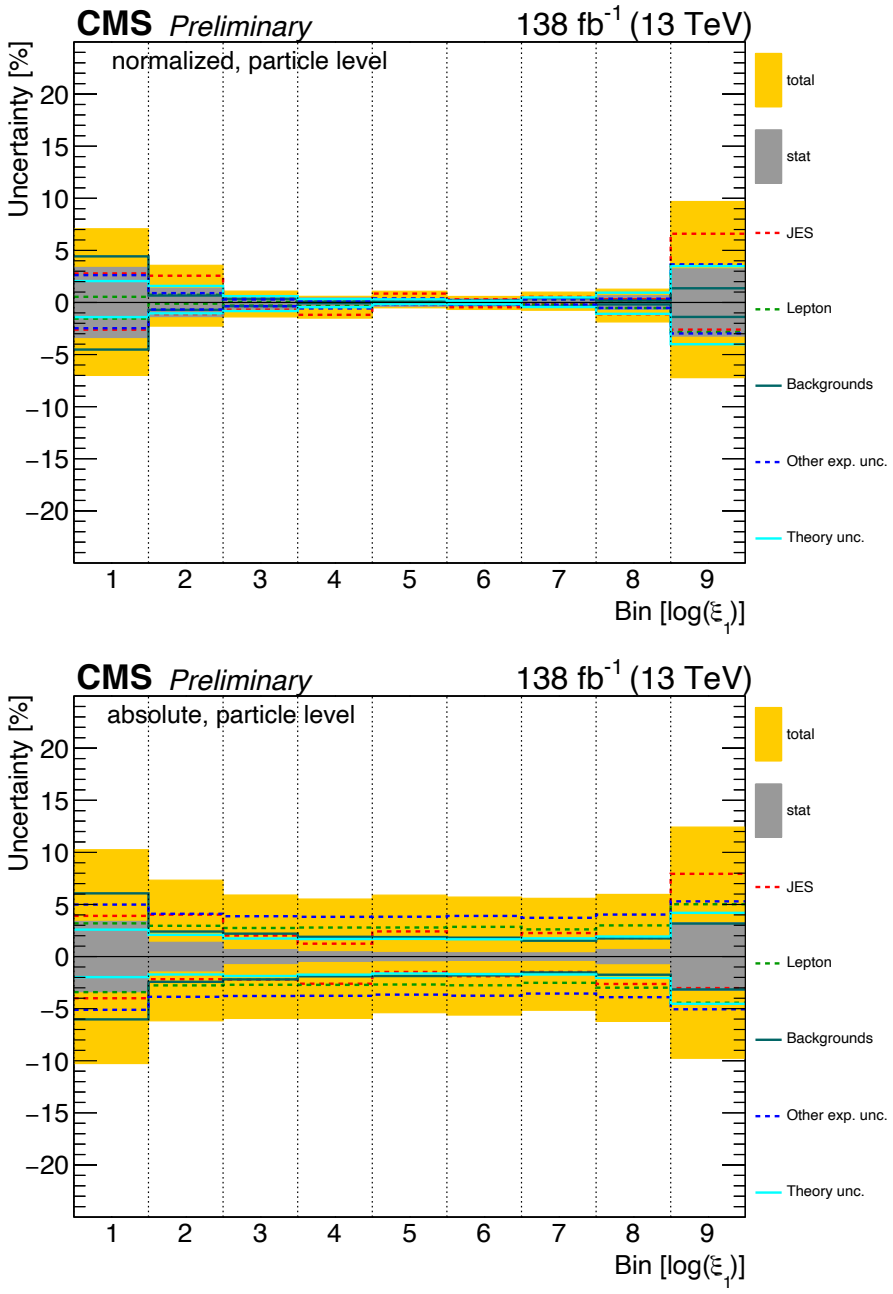

Figure J.25: The figure shows the uncertainty contributions of the differential $t\bar{t}$ cross section measured as a function of $\log(\xi_1)$, which is equivalent to the momentum fraction of the incoming parton from one of the protons in the leading order QCD picture, for both normalized (top) and absolute (bottom) measurements performed in the fiducial phase space at particle level.

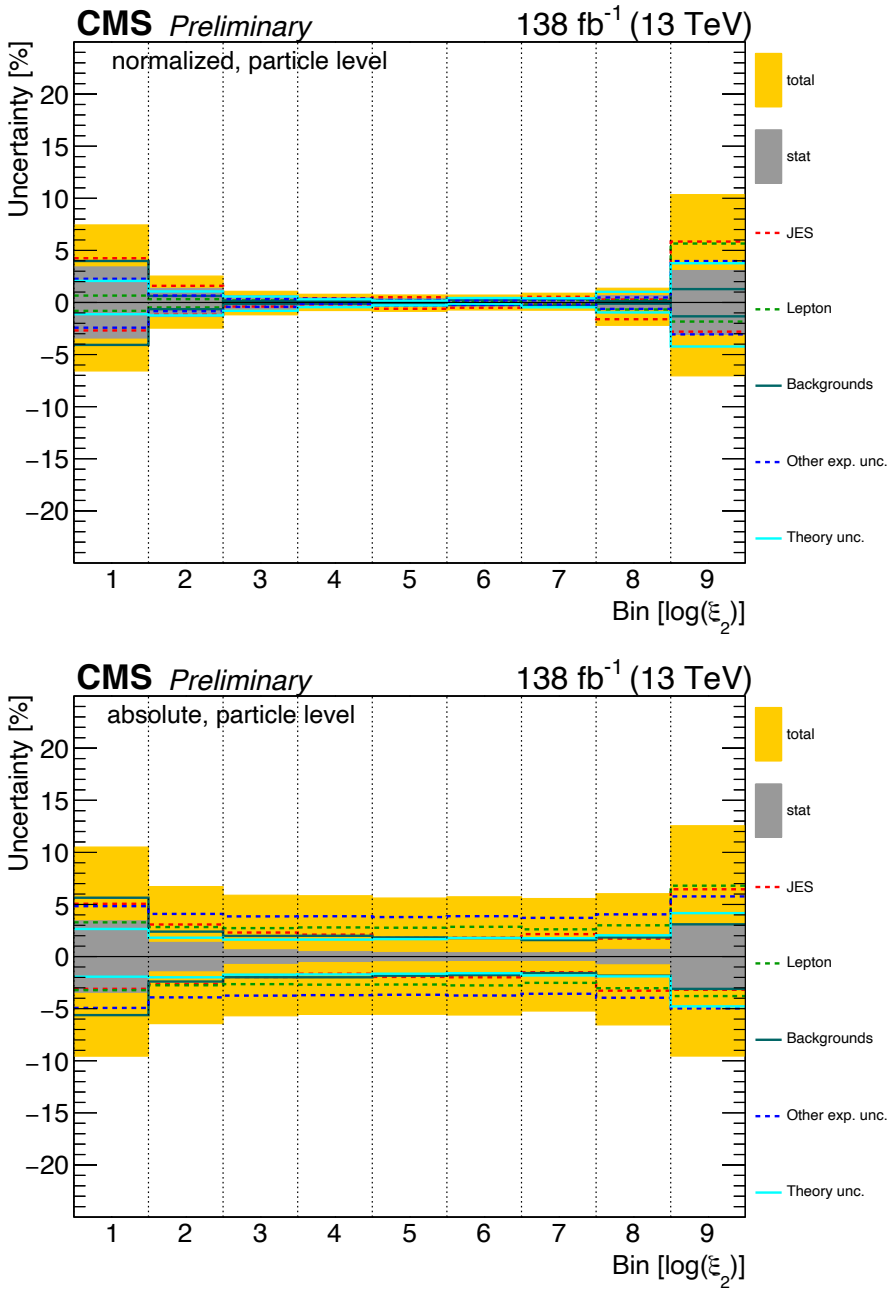

Figure J.26: The figure shows the uncertainty contributions of the differential $t\bar{t}$ cross section measured as a function of $\log(\xi_2)$, which is equivalent to the momentum fraction of the incoming parton from one of the protons in the leading order QCD picture, for both normalized (top) and absolute (bottom) measurements performed in the fiducial phase space at particle level.

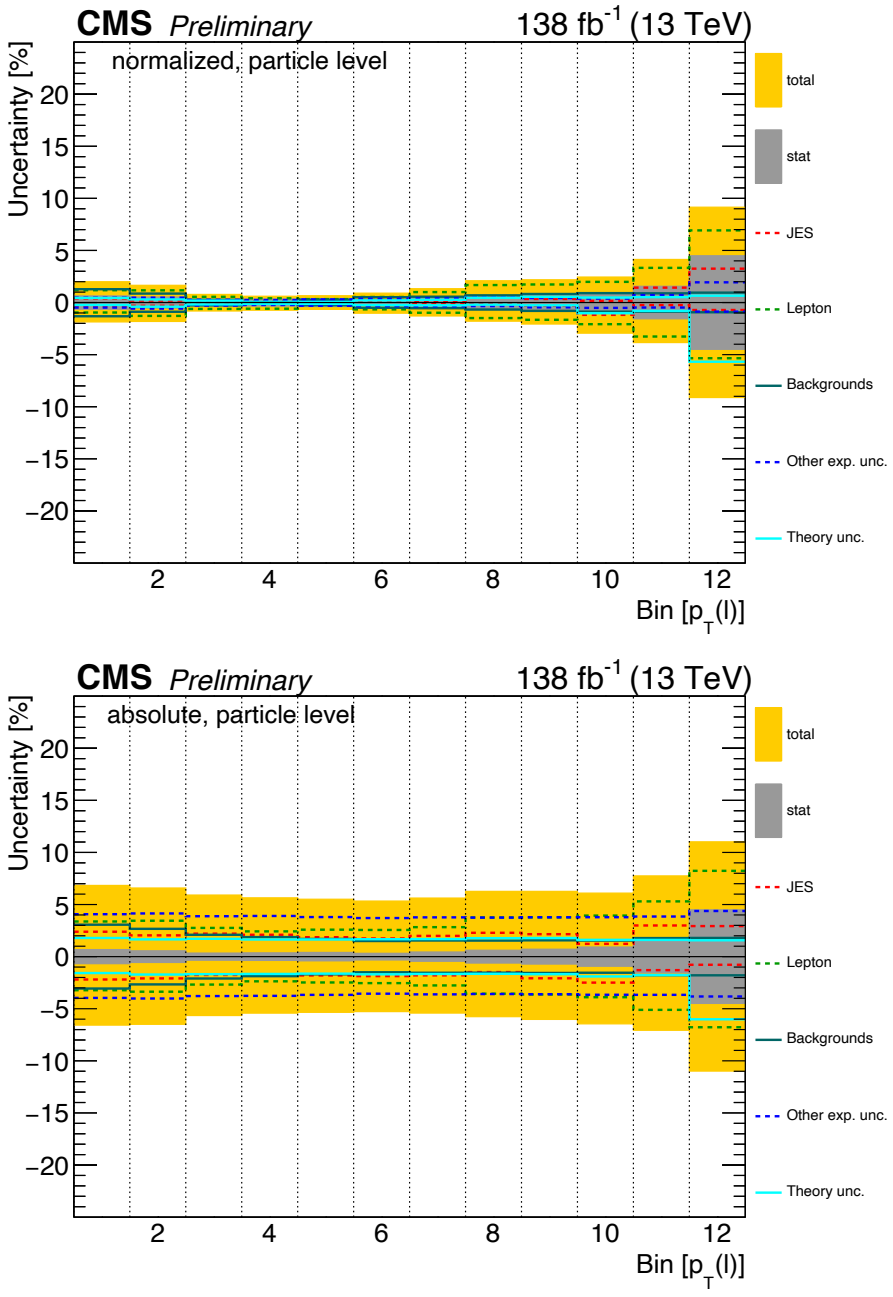

Figure J.27: The figure shows the uncertainty contributions of the differential $t\bar{t}$ cross section measured as a function of the transverse momentum of the lepton, $p_{\mathrm{T}}(\ell)$, for both normalized (top) and absolute (bottom) measurements performed in the fiducial phase space at particle level.

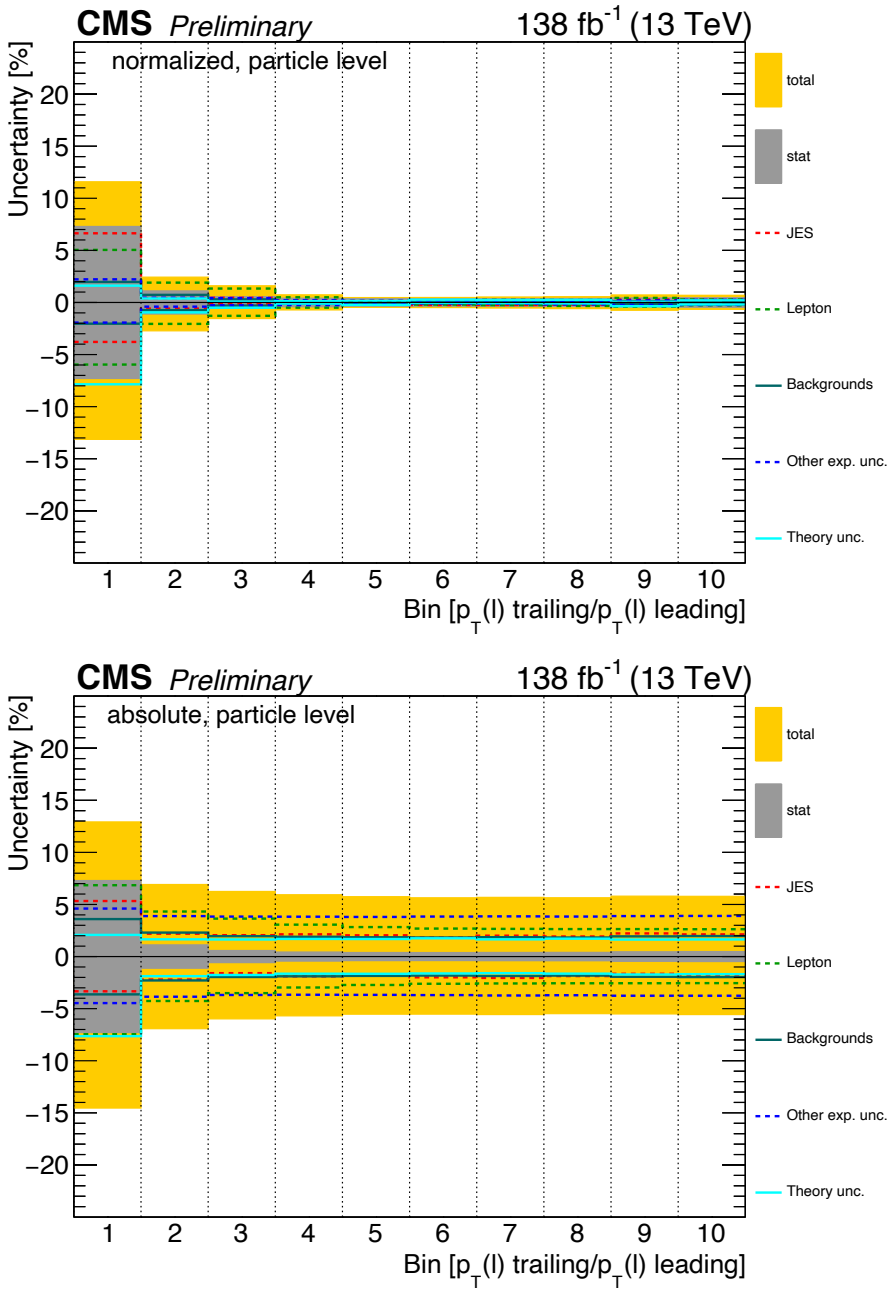

Figure J.28: The figure shows the uncertainty contributions of the differential $t\bar{t}$ cross section measured as a function of the ratio of the transverse momentum of the trailing lepton over the transverse momentum of the leading lepton, $p_{\mathrm{T}}(\ell)$ trailing/$p_{\mathrm{T}}(\ell)$ leading, for both normalized (top) and absolute (bottom) measurements performed in the fiducial phase space at particle level.

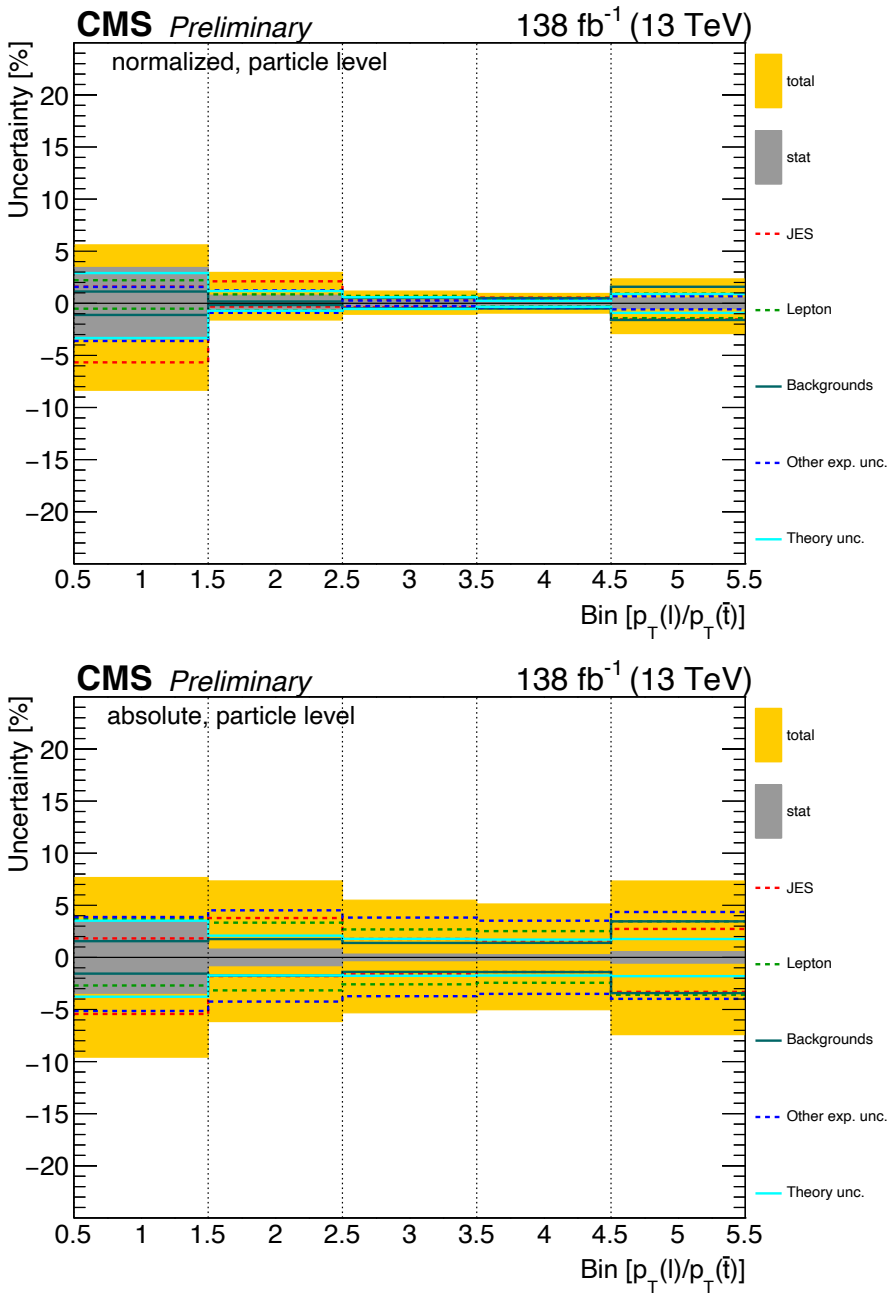

Figure J.29: The figure shows the uncertainty contributions of the differential $t\bar{t}$ cross section measured as a function of the ratio of the transverse momentum of the lepton over the transverse momentum of the anti-top quark, $p_{\mathrm{T}}(\ell)/p_{\mathrm{T}}(\bar{\mathrm{t}})$, for both normalized (top) and absolute (bottom) measurements performed in the fiducial phase space at particle level.

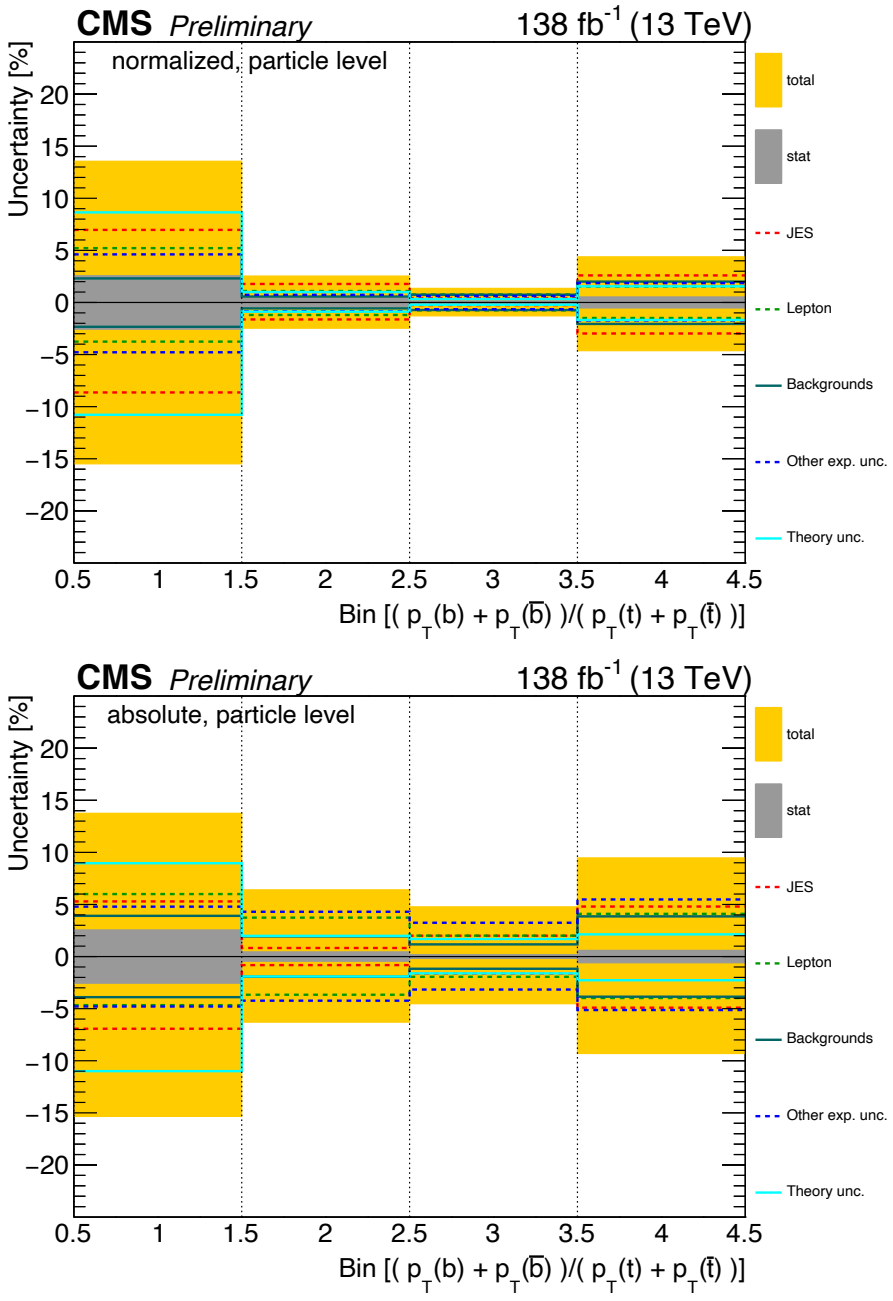

Figure J.30: The figure shows the uncertainty contributions of the differential $t\bar{t}$ cross section measured as a function of the ratio of the scalar sum of p_{T} of b and p_{T} of anti-b over the scalar sum of p_{T} of top and p_{T} of anti-top, $(p_{\mathrm{T}}(\mathrm{b}) + p_{\mathrm{T}}(\bar{\mathrm{b}}))/(p_{\mathrm{T}}(\mathrm{t}) + p_{\mathrm{T}}(\bar{\mathrm{t}}))$, for both normalized (top) and absolute (bottom) measurements performed in the fiducial phase space at particle level.

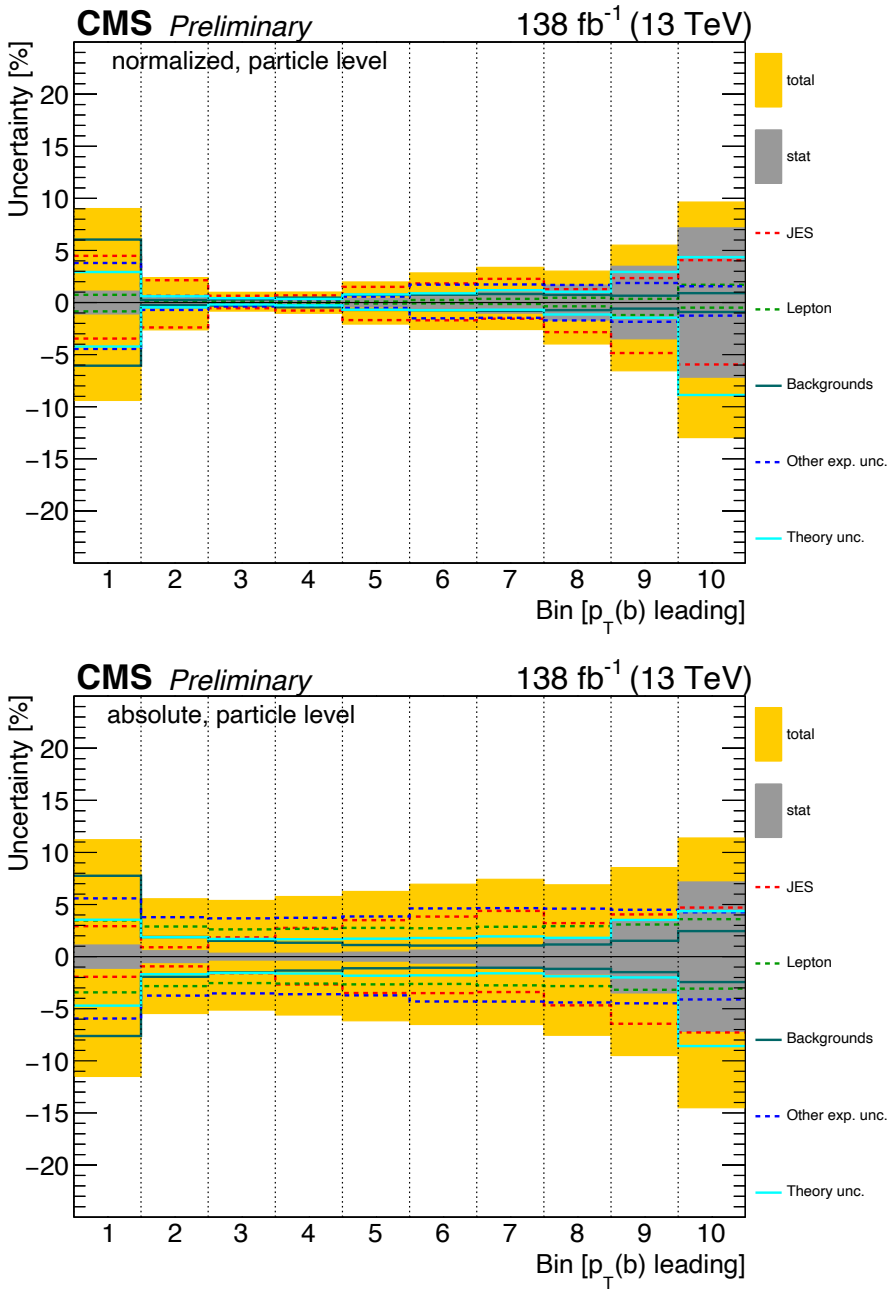

Figure J.31: The figure shows the uncertainty contributions of the differential $t\bar{t}$ cross section measured as a function of the transverse momentum of the leading b quark, p_{T}(b) leading, for both normalized (top) and absolute (bottom) measurements performed in the fiducial phase space at particle level.

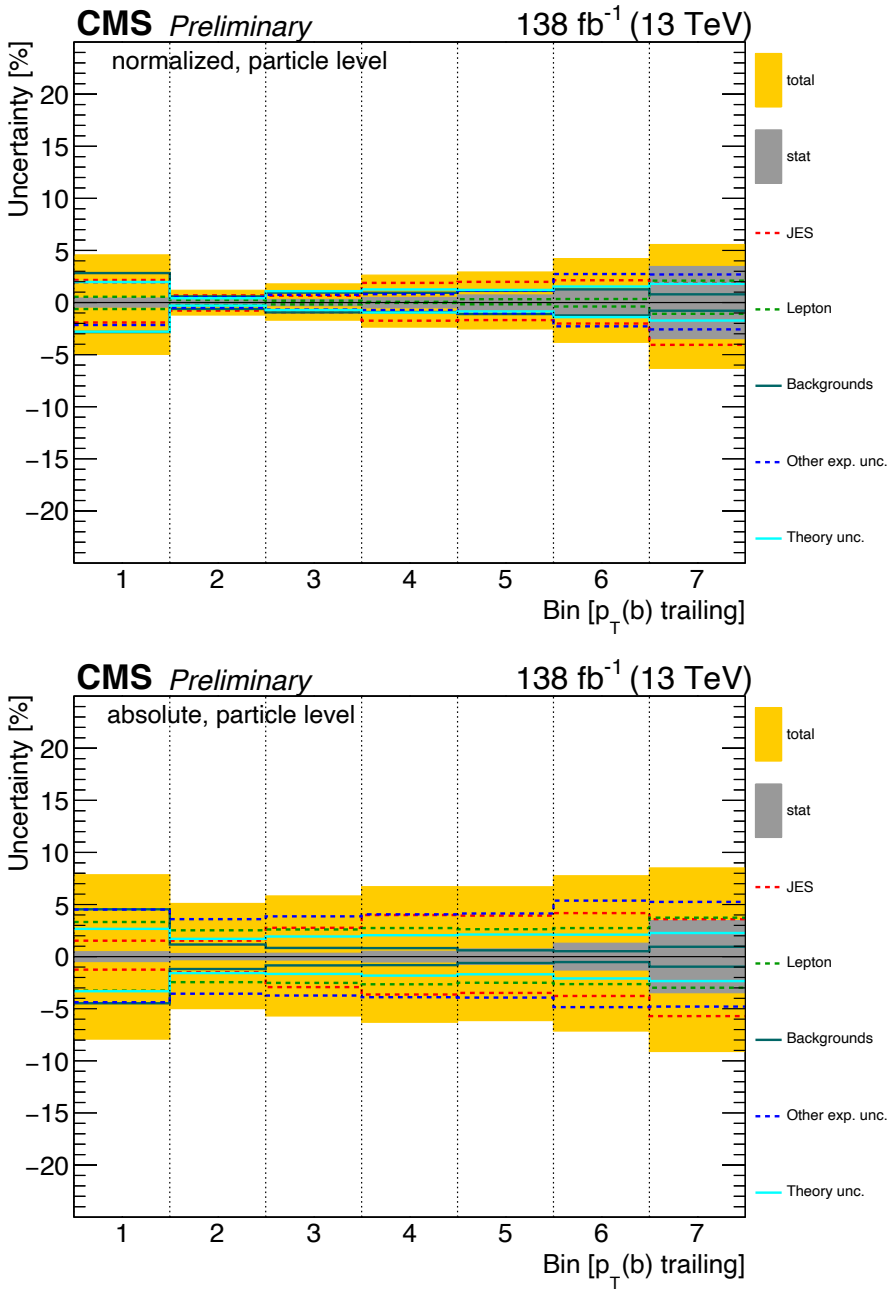

Figure J.32: The figure shows the uncertainty contributions of the differential $t\bar{t}$ cross section measured as a function of the transverse momentum of the trailing b quark, p_{T}(b) trailing, for both normalized (top) and absolute (bottom) measurements performed in the fiducial phase space at particle level.

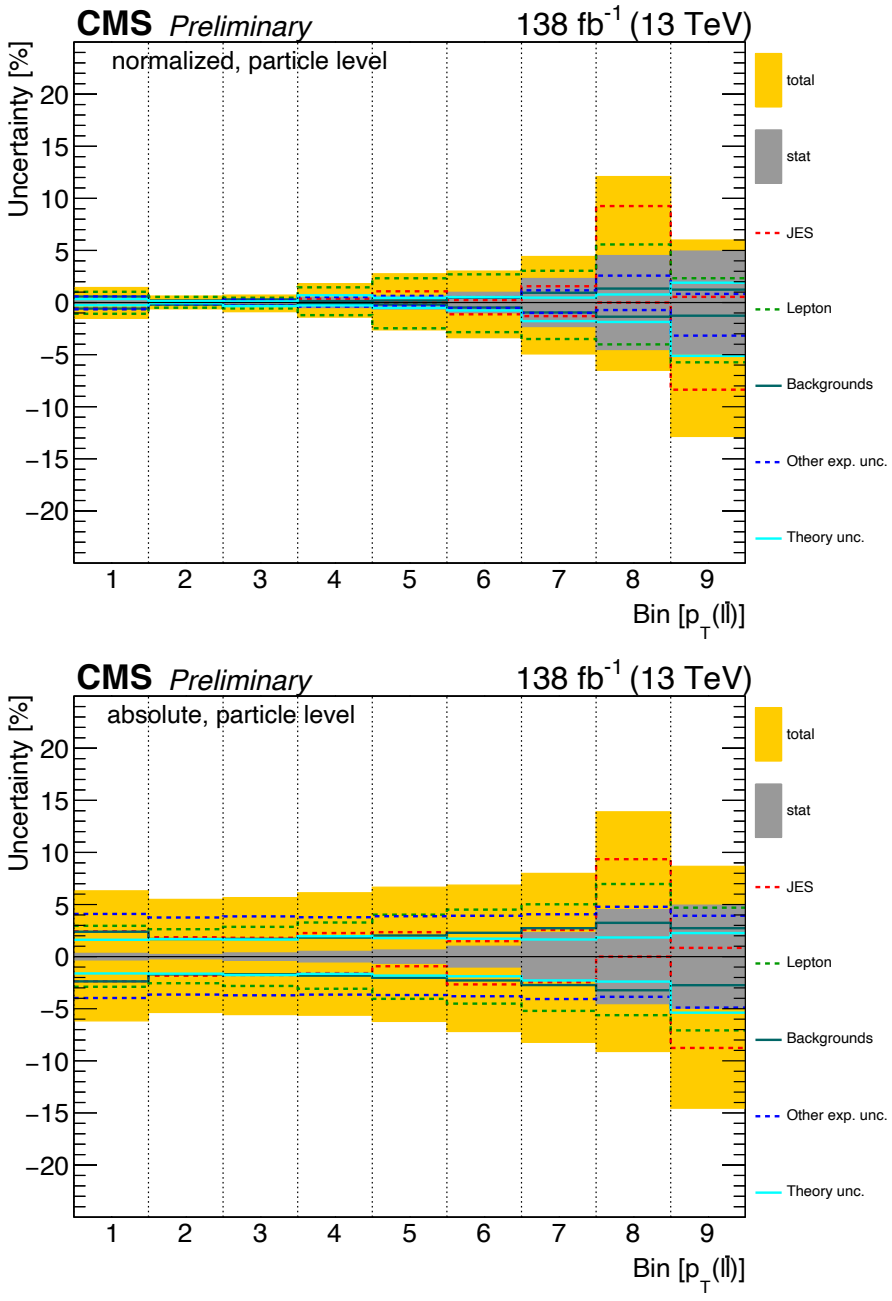

Figure J.33: The figure shows the uncertainty contributions of the differential $t\bar{t}$ cross section measured as a function of the transverse momentum of the $\ell\bar{\ell}$ system, $p_{\mathrm{T}}(\ell\bar{\ell})$, for both normalized (top) and absolute (bottom) measurements performed in the fiducial phase space at particle level.

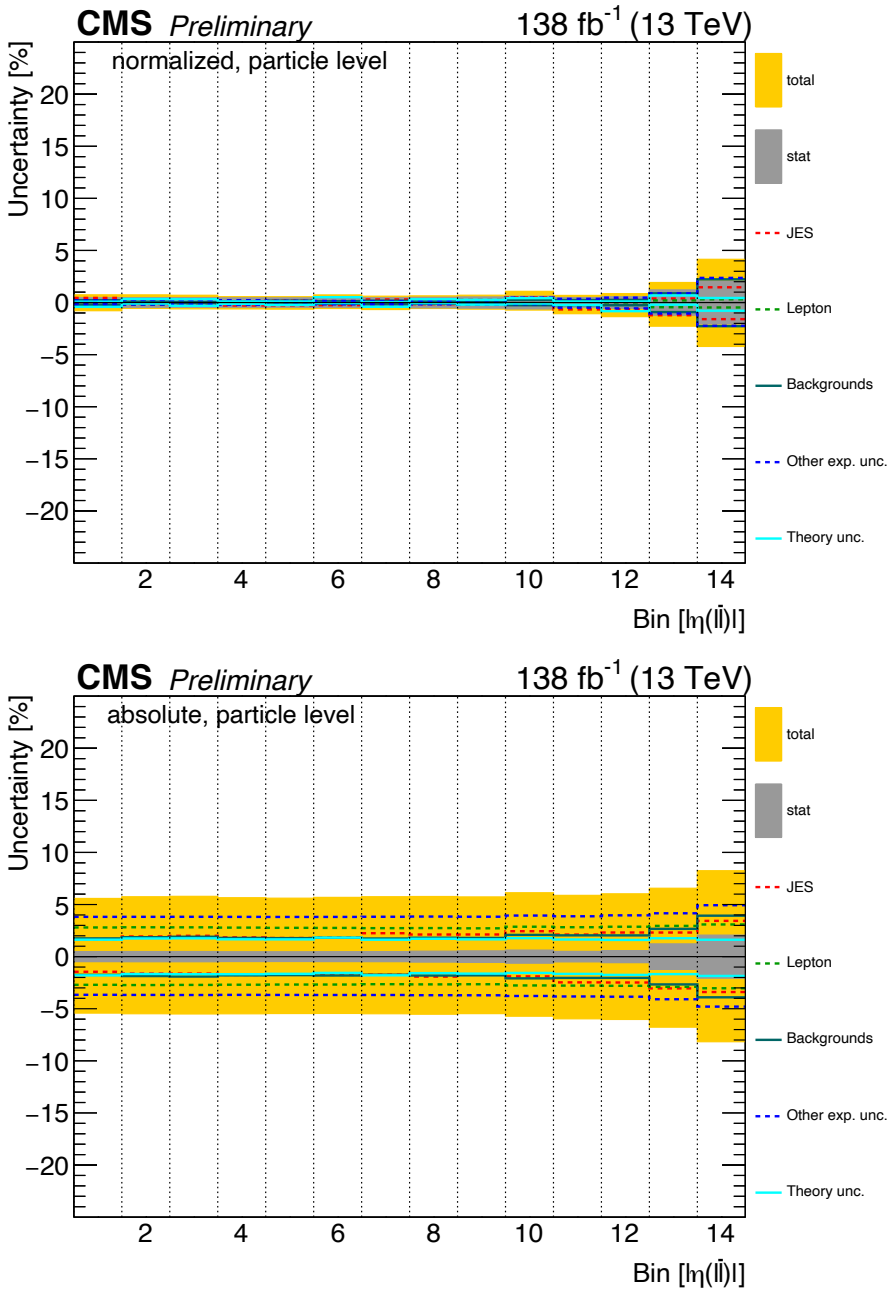

Figure J.34: The figure shows the uncertainty contributions of the differential $t\bar{t}$ cross section measured as a function of the absolute pseudorapidity of the $\ell\bar{\ell}$ system, $|\eta(\ell\bar{\ell})|$, for both normalized (top) and absolute (bottom) measurements performed in the fiducial phase space at particle level.

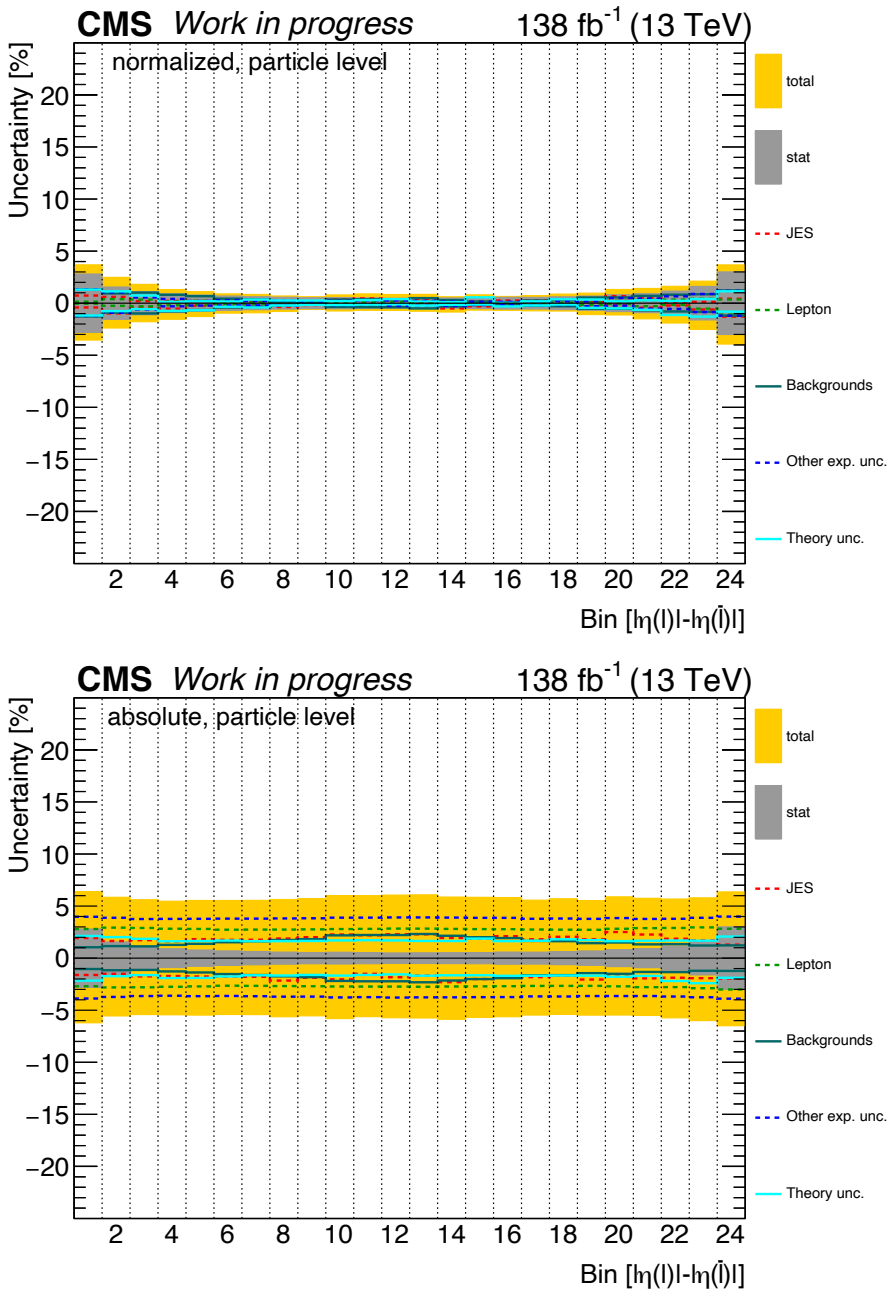

Figure J.35: The figure shows the uncertainty contributions of the differential $t\bar{t}$ cross section measured as a function of the difference in absolute pseudorapidity of the lepton and absolute pseudorapidity of the anti-lepton, $|\eta(\ell)| - |\eta(\bar{\ell})|$, for both normalized (top) and absolute (bottom) measurements performed in the fiducial phase space at particle level.

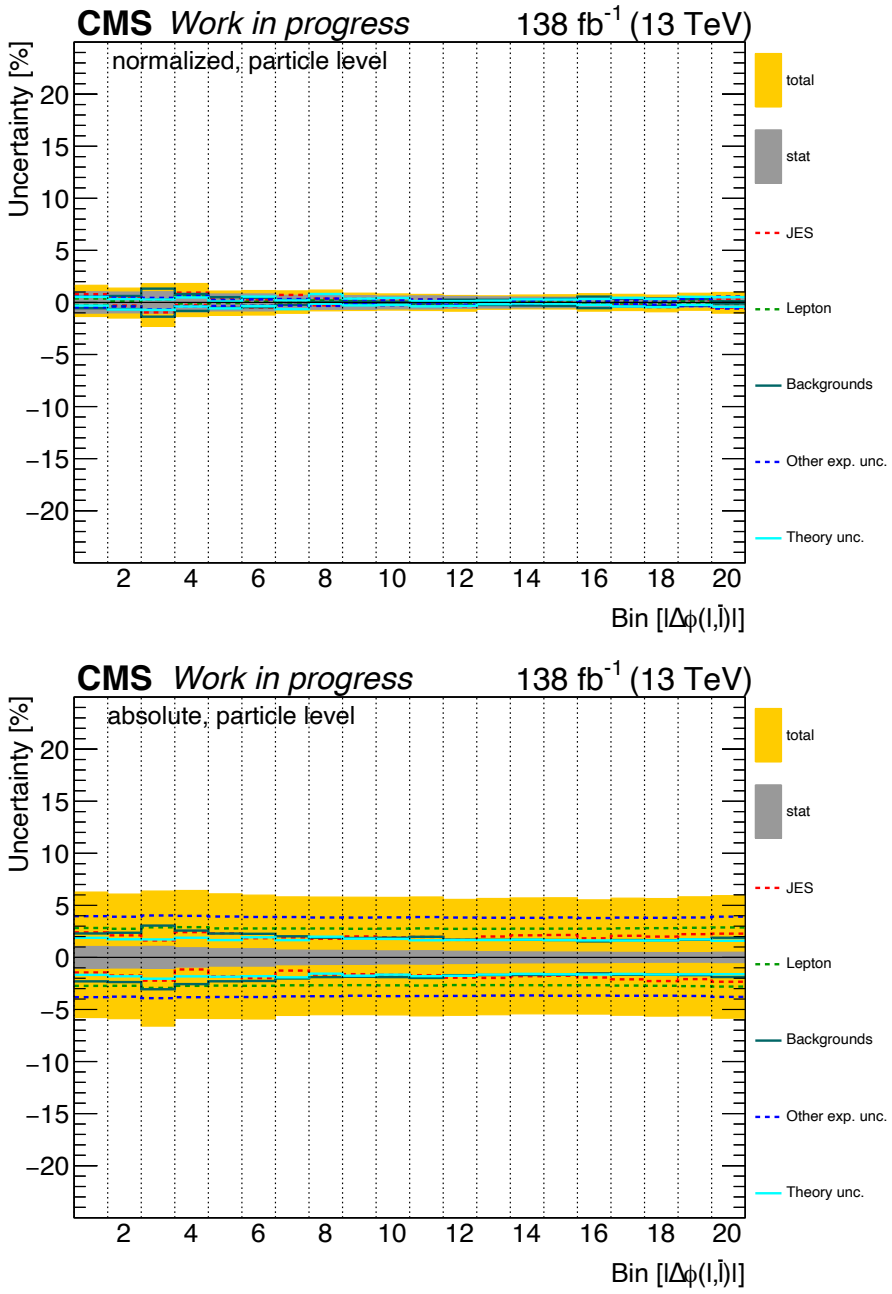

Figure J.36: The figure shows the uncertainty contributions of the differential $t\bar{t}$ cross section measured as a function of the absolute value of the azimuthal angle (ϕ) between the lepton and the anti-lepton, $|\Delta\phi(\ell,\bar{\ell})|$, for both normalized (top) and absolute (bottom) measurements performed in the fiducial phase space at particle level.

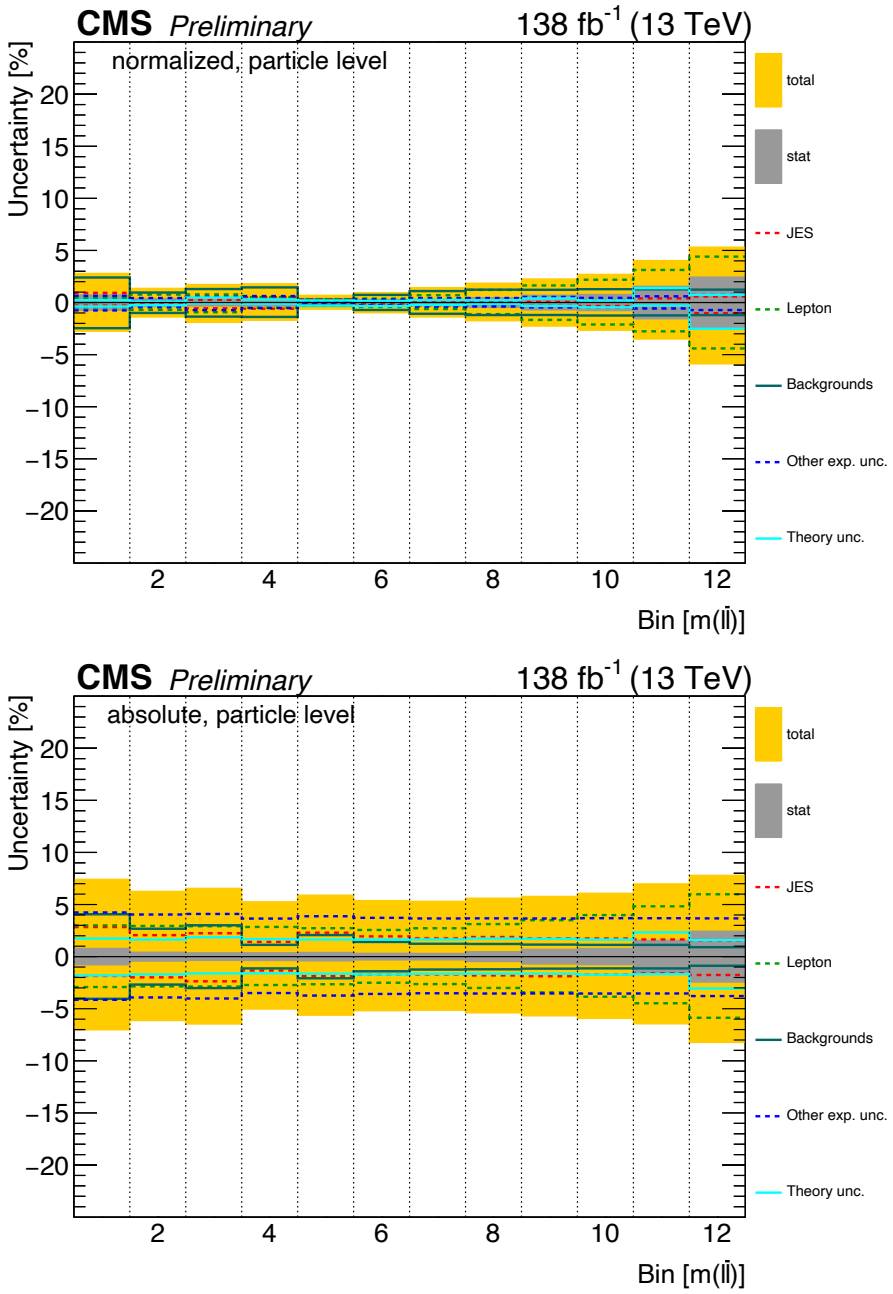

Figure J.37: The figure shows the uncertainty contributions of the differential $t\bar{t}$ cross section measured as a function of the invariant mass of the $\ell\bar{\ell}$ system, $m(\ell\bar{\ell})$, for both normalized (top) and absolute (bottom) measurements performed in the fiducial phase space at particle level.

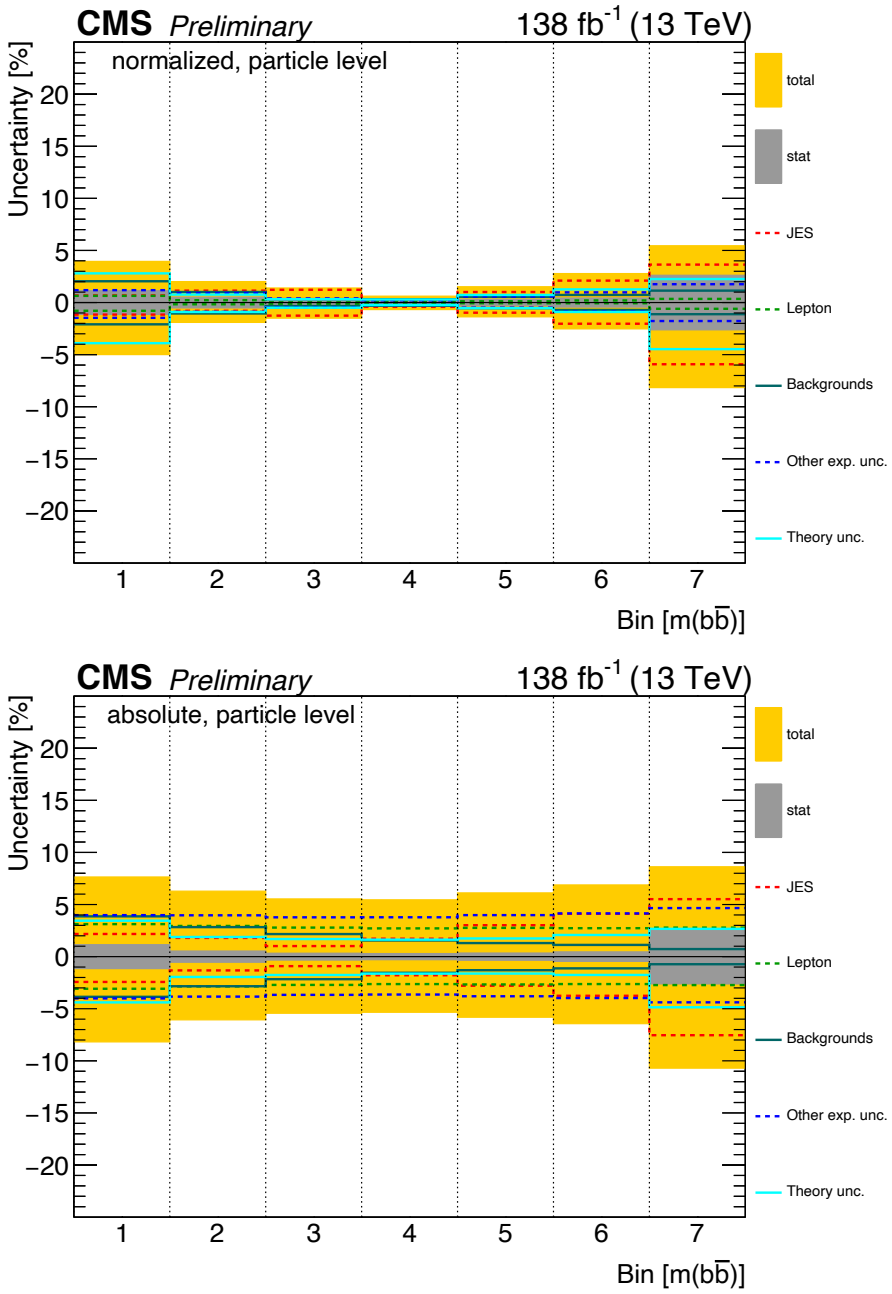

Figure J.38: The figure shows the uncertainty contributions of the differential $t\bar{t}$ cross section measured as a function of the invariant mass of the $b\bar{b}$ system, $m(b\bar{b})$, for both normalized (top) and absolute (bottom) measurements performed in the fiducial phase space at particle level.

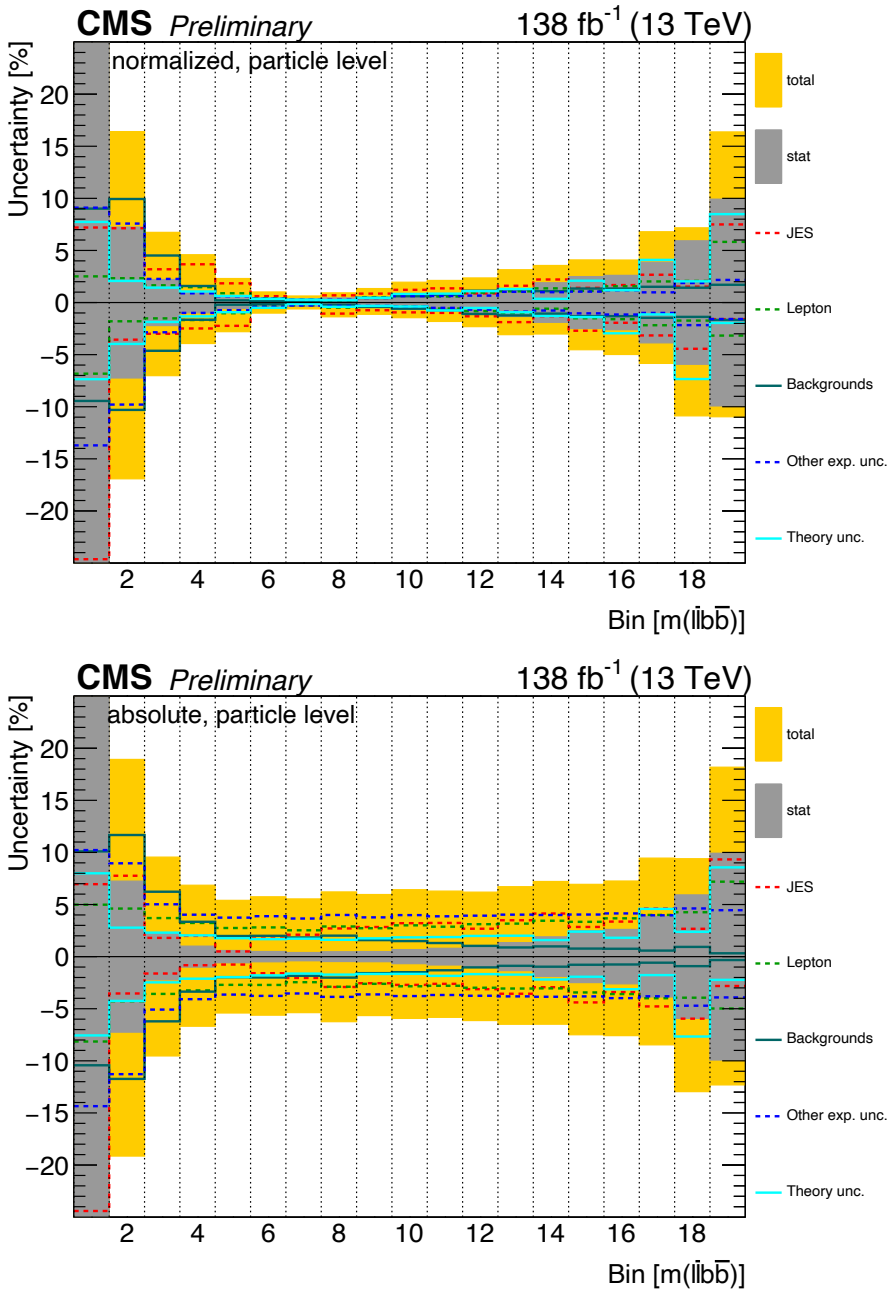

Figure J.39: The figure shows the uncertainty contributions of the differential $t\bar{t}$ cross section measured as a function of the invariant mass of the $l\bar{l}b\bar{b}$ system, $m(\ell\bar{\ell}\mathrm{b}\bar{\mathrm{b}})$, for both normalized (top) and absolute (bottom) measurements performed in the fiducial phase space at particle level.

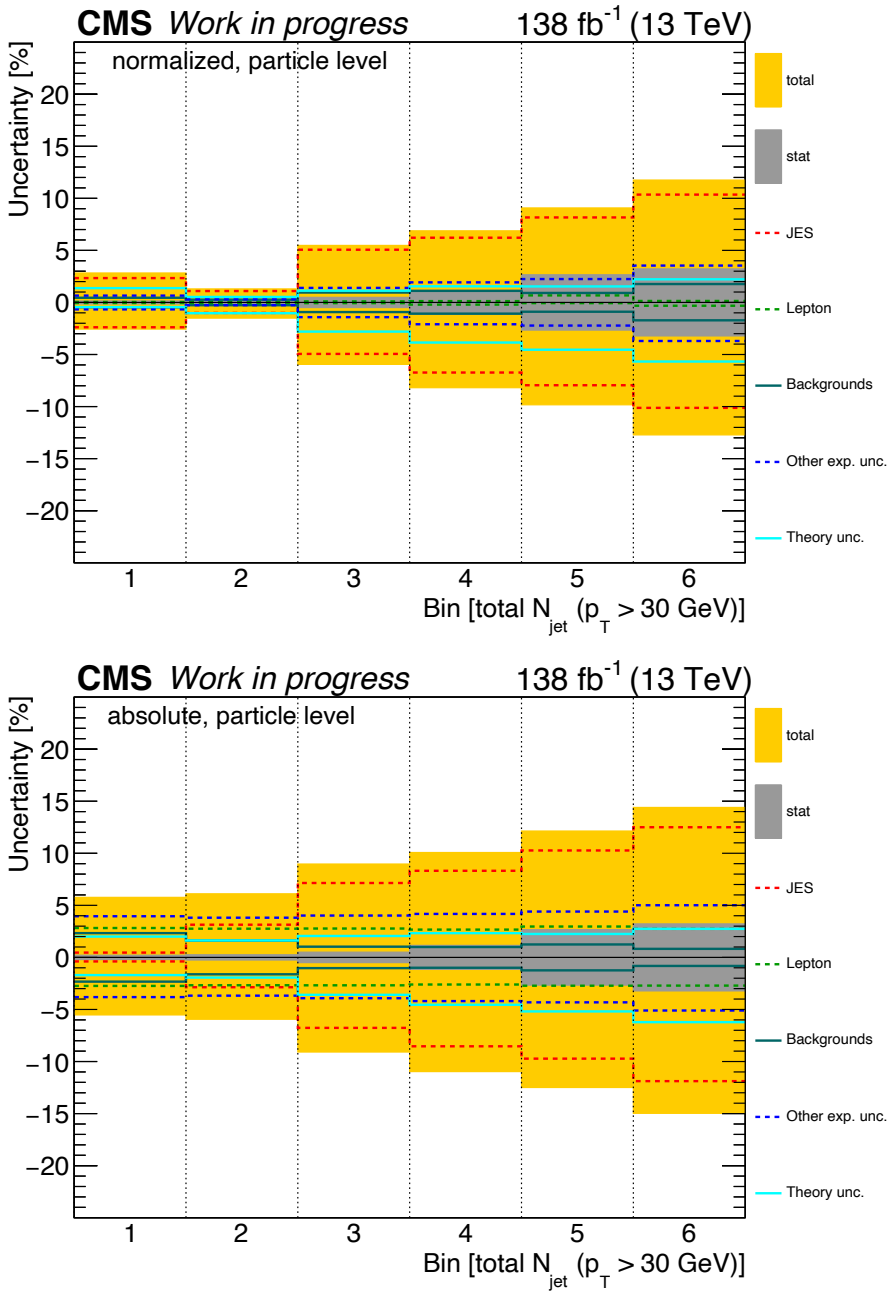

Figure J.40: The figure shows the uncertainty contributions of the differential $t\bar{t}$ cross section measured as a function of the total jet multiplicity, N_{jet} (the last bin is inclusive for ≥ 7), for both normalized (top) and absolute (bottom) measurements performed in the fiducial phase space at particle level.

J.2 Double-differential measurements

J.2.1 Particle level

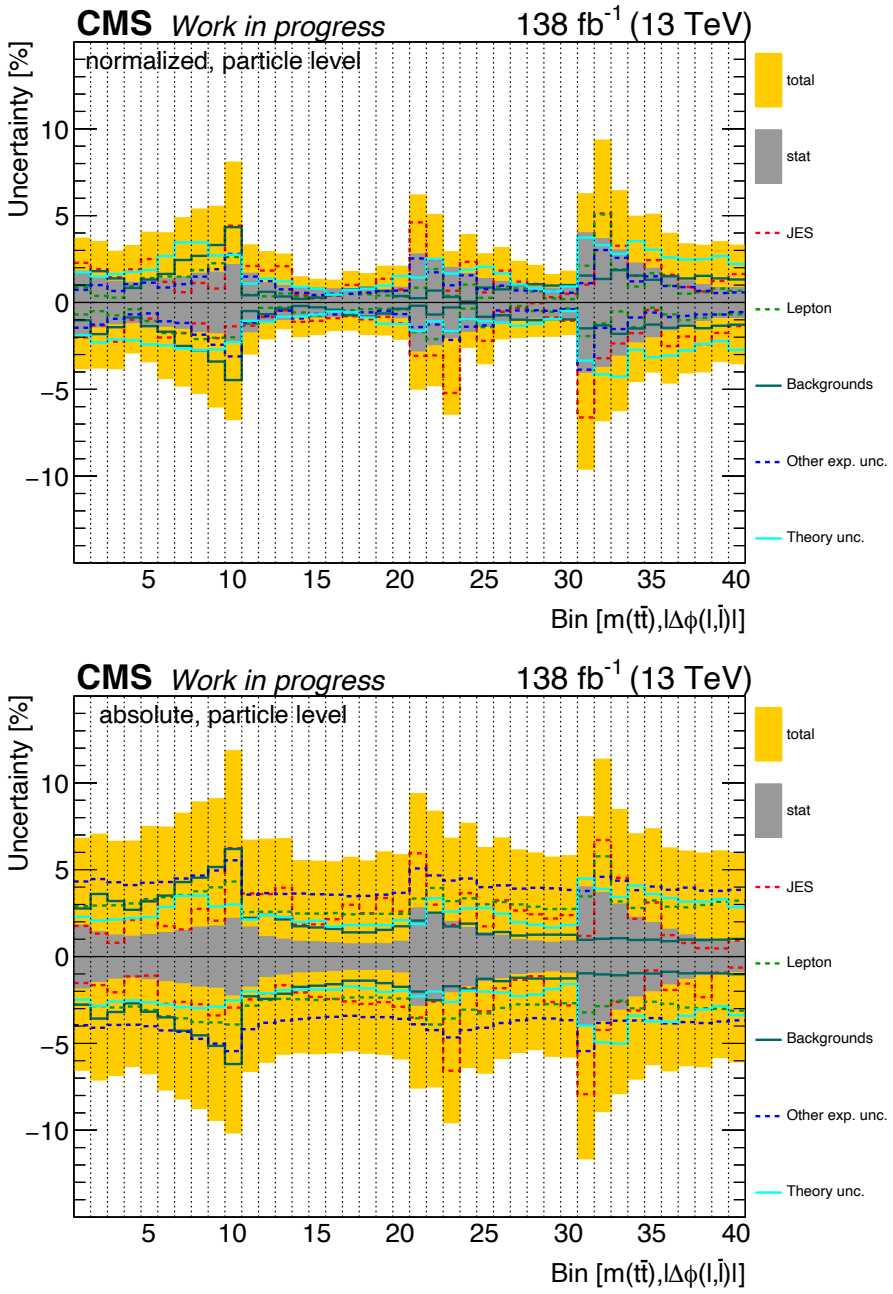

Figure J.41: The figure shows the uncertainty contributions of the differential $t\bar{t}$ cross section measured as a function of the absolute value of the azimuthal angle between the lepton and the anti-lepton, $|\Delta\phi(\ell,\bar{\ell})|$, in ranges of the invariant mass of the $t\bar{t}$ system, $m(t\bar{t})$, for both normalized (top) and absolute (bottom) measurements performed in the fiducial phase space at particle level.

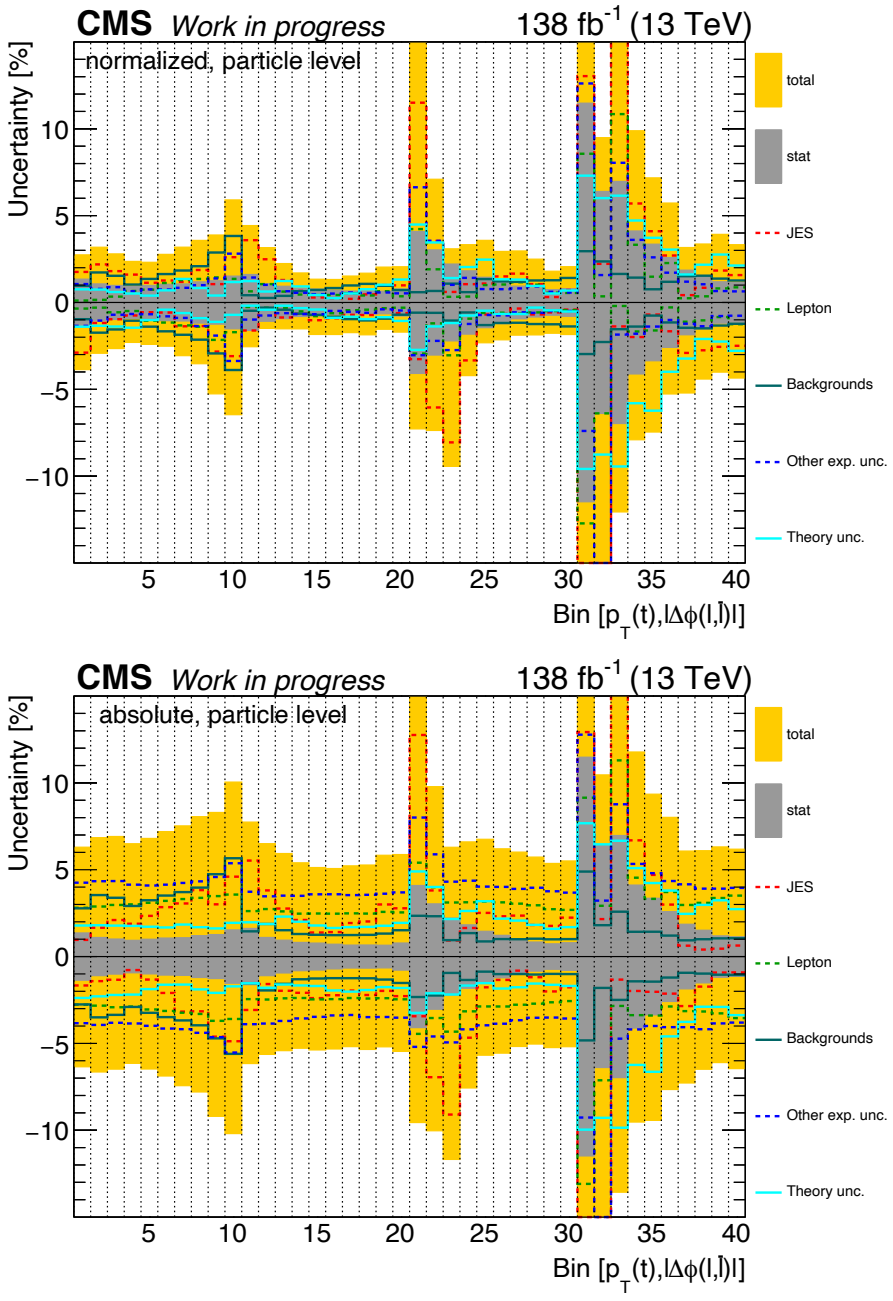

Figure J.42: The figure shows the uncertainty contributions of the differential $t\bar{t}$ cross section measured as a function of the absolute value of the azimuthal angle between the lepton and the anti-lepton, $|\Delta\phi(\ell,\bar{\ell})|$, in ranges of the transverse momentum of the top, $p_{\mathrm{T}}(t)$, for both normalized (top) and absolute (bottom) measurements performed in the fiducial phase space at particle level.

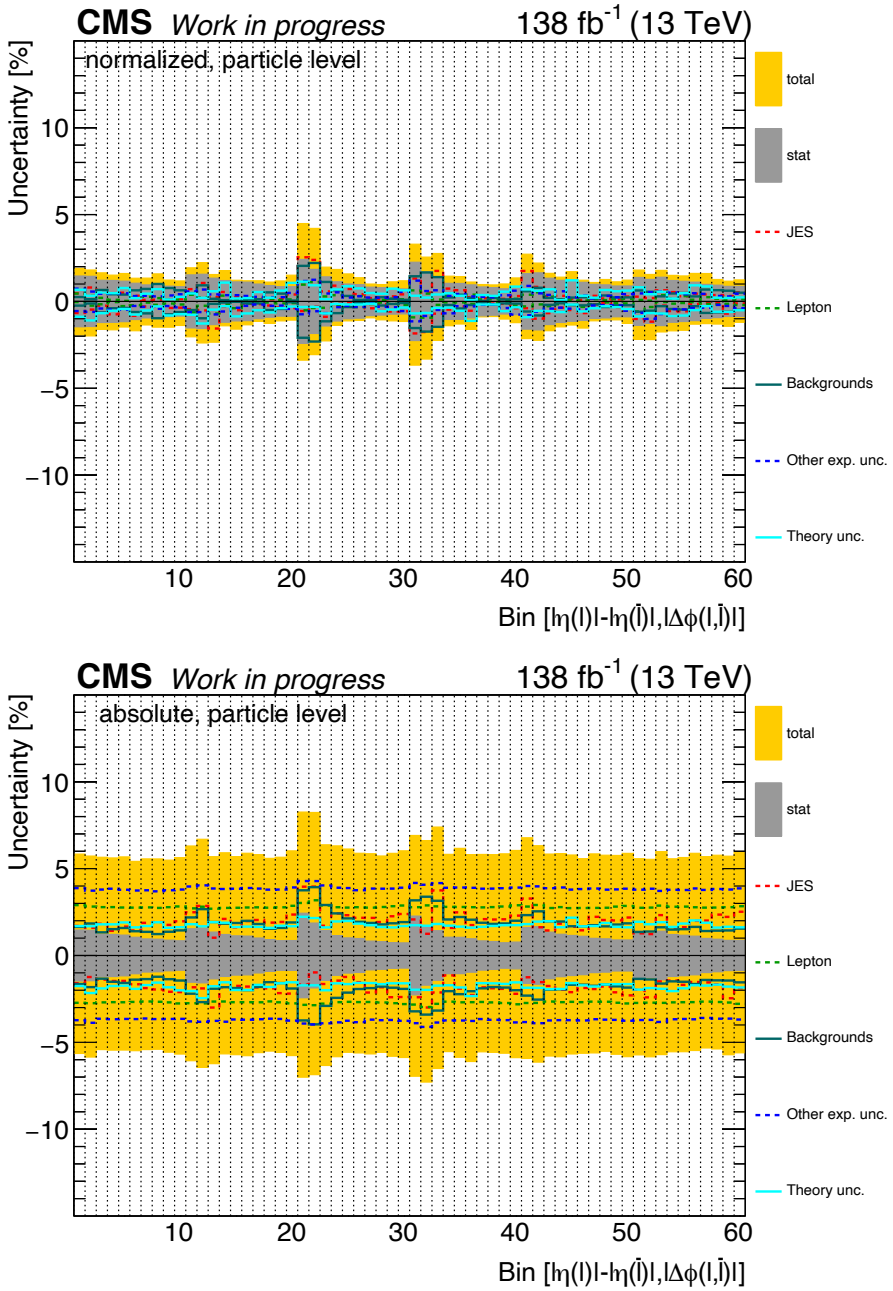

Figure J.43: The figure shows the uncertainty contributions of the differential $t\bar{t}$ cross section measured as a function of the absolute value of the azimuthal angle between the lepton and the anti-lepton, $|\Delta\phi(\ell,\bar{\ell})|$, in ranges of the difference in absolute value of pseudorapidity of the lepton and absolute value of pseudorapidity of the anti-lepton, $|\eta(\ell)| - |\eta(\bar{\ell})|$, for both normalized (top) and absolute (bottom) measurements performed in the fiducial phase space at particle level.

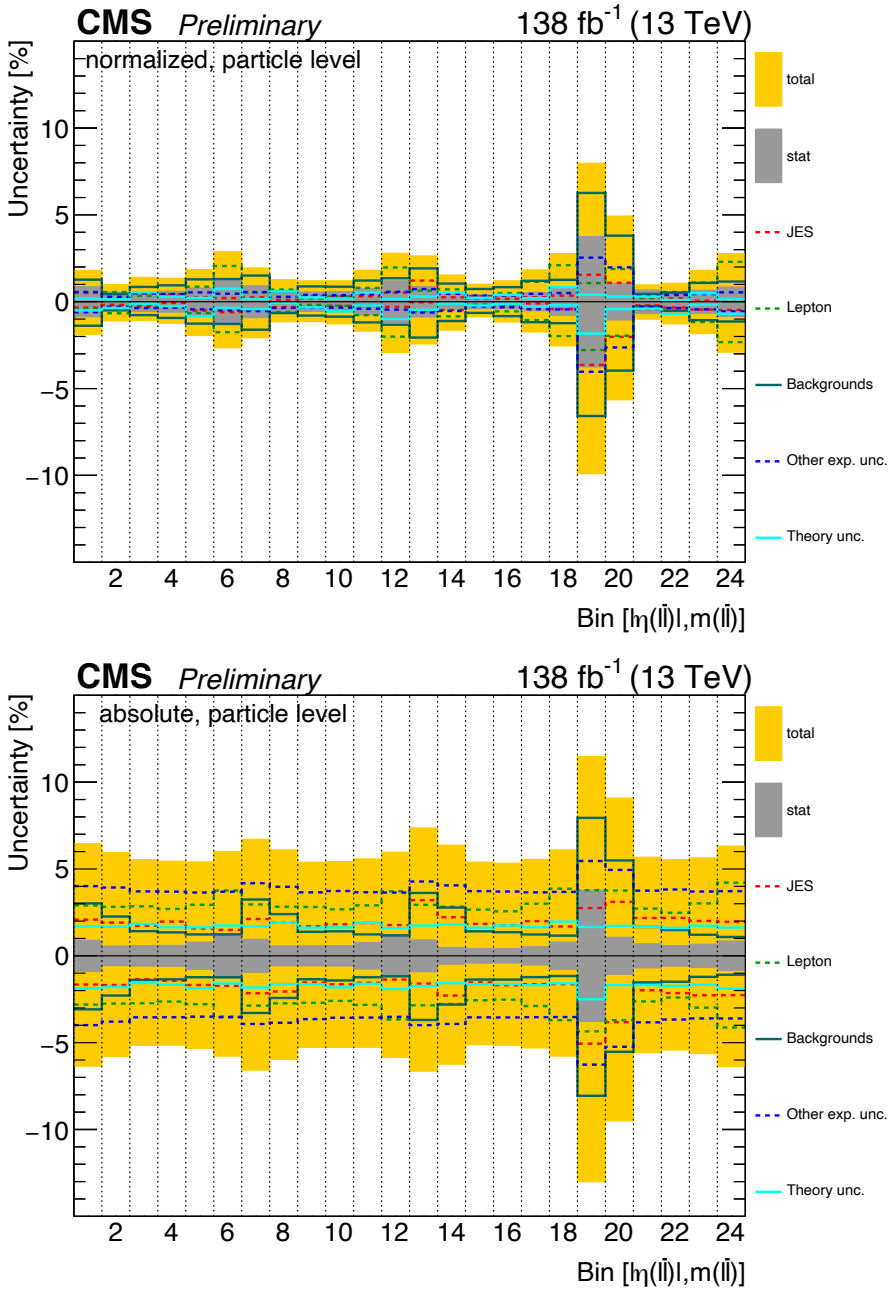

Figure J.44: The figure shows the uncertainty contributions of the differential $t\bar{t}$ cross section measured as a function of the invariant mass of the $\ell\bar{\ell}$ system, $m(\ell\bar{\ell})$, in ranges of the absolute pseudorapidity of the $\ell\bar{\ell}$ system, $|\eta(\ell\bar{\ell})|$, for both normalized (top) and absolute (bottom) measurements performed in the fiducial phase space at particle level.

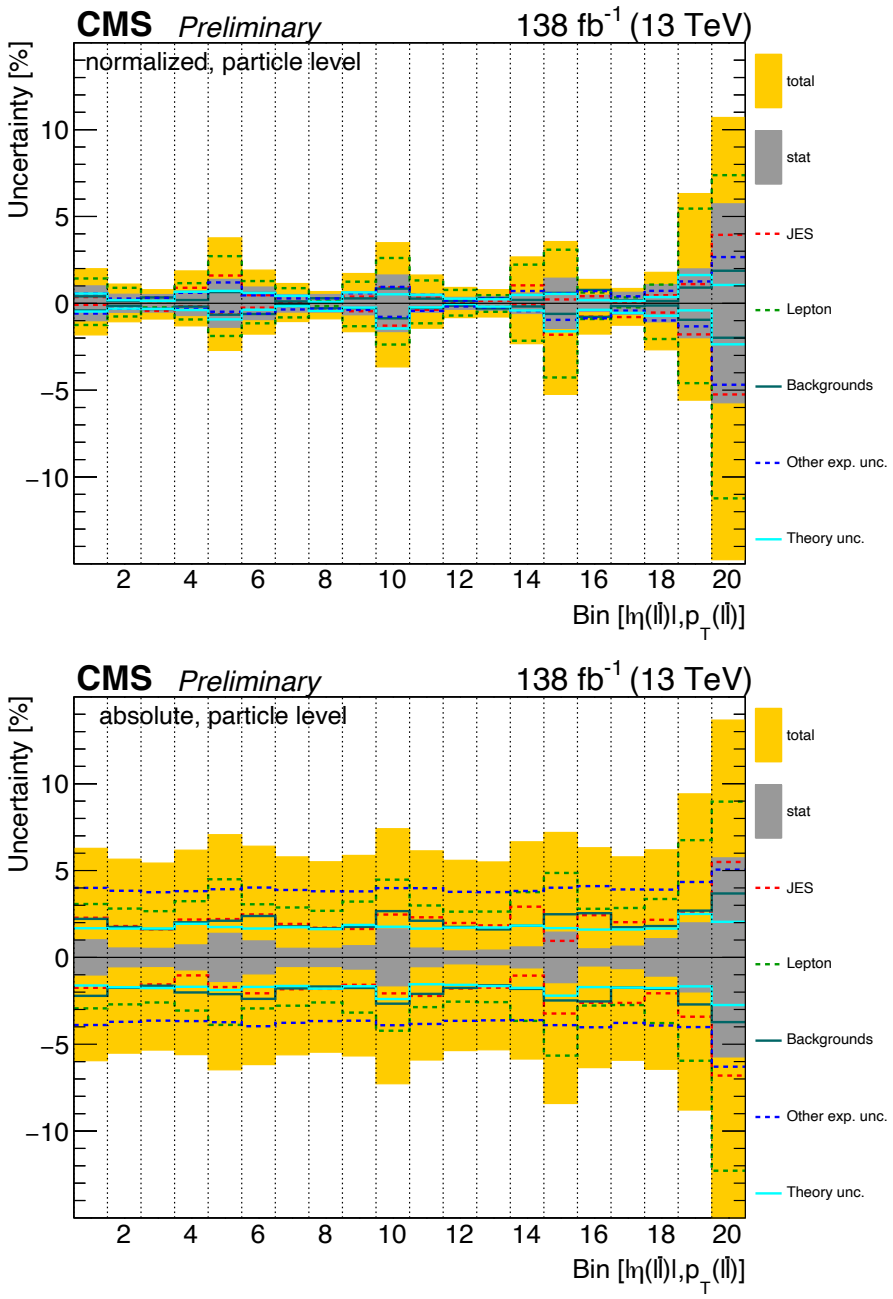

Figure J.45: The figure shows the uncertainty contributions of the differential $t\bar{t}$ cross section measured as a function of the transverse momentum of the $\ell\bar{\ell}$ system, $p_{\mathrm{T}}(\ell\bar{\ell})$, in ranges of the absolute pseudorapidity of the $\ell\bar{\ell}$ system, $|\eta(\ell\bar{\ell})|$, for both normalized (top) and absolute (bottom) measurements performed in the fiducial phase space at particle level.

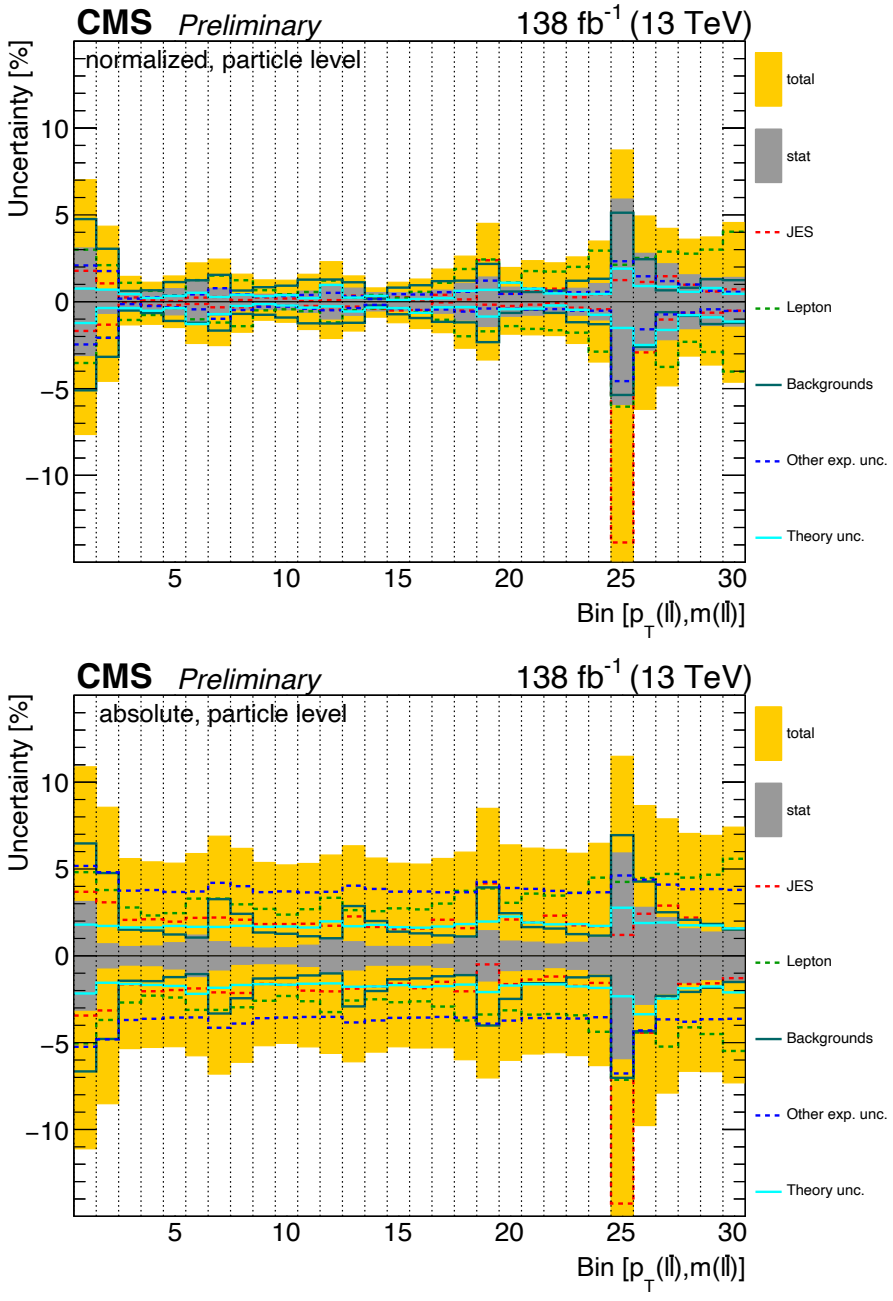

Figure J.46: The figure shows the uncertainty contributions of the differential $t\bar{t}$ cross section measured as a function of the invariant mass of the $\ell\bar{\ell}$ system, $m(\ell\bar{\ell})$, in ranges of the transverse momentum of the $\ell\bar{\ell}$ system, $p_{\mathrm{T}}(\ell\bar{\ell})$, for both normalized (top) and absolute (bottom) measurements performed in the fiducial phase space at particle level.

Appendix K

Numerical cross sections and uncertainties

K.1 Single-differential measurements

K.1.1 Parton level

Table K.1: Numerical values are shown for the normalized differential $t\bar{t}$ cross section measured as a function of the transverse momentum of the top, $p_{\mathrm{T}}(t)$, in the full phase space at parton level. Corresponding statistical and systematic uncertainties are also shown in percent.

p_{T}(t) [GeV]	$\frac{1}{\sigma(t\bar{t})}\frac{\mathrm{d}\sigma}{\mathrm{d}p_{\mathrm{T}}(\mathrm{t})}$[GeV^{-1}]	stat. [%]	syst. [%]	bin
0.0–55.0	3.635×10^{-3}	0.8	$^{+3.6}_{-4.1}$	1
55.0–100.0	6.273×10^{-3}	0.4	$^{+1.3}_{-1.2}$	2
100.0–165.0	4.638×10^{-3}	0.4	$^{+1.7}_{-1.3}$	3
165.0–240.0	1.935×10^{-3}	0.6	$^{+2.0}_{-1.9}$	4
240.0–330.0	5.762×10^{-4}	1.4	$^{+3.2}_{-4.6}$	5
330.0–440.0	1.364×10^{-4}	3.6	$^{+12.4}_{-6.2}$	6
440.0–600.0	2.719×10^{-5}	7.3	$^{+15.6}_{-19.0}$	7

Table K.2: Numerical values are shown for the normalized differential $t\bar{t}$ cross section, measured as a function of the transverse momentum of the anti-top, $p_{\mathrm{T}}(\bar{t})$, in the full phase space at parton level. Corresponding statistical and systematic uncertainties are also shown in percent.

$p_{\mathrm{T}}(\bar{t})$ [GeV]	$\frac{1}{\sigma(t\bar{t})}\frac{\mathrm{d}\sigma}{\mathrm{d}p_{\mathrm{T}}(\bar{t})}$[GeV^{-1}]	stat. [%]	syst. [%]	bin
0.0–55.0	3.651×10^{-3}	0.8	$^{+3.4}_{-3.7}$	1
55.0–100.0	6.252×10^{-3}	0.4	$^{+1.2}_{-1.0}$	2
100.0–165.0	4.616×10^{-3}	0.4	$^{+1.5}_{-1.3}$	3
165.0–240.0	1.948×10^{-3}	0.6	$^{+1.9}_{-2.3}$	4
240.0–330.0	5.778×10^{-4}	1.4	$^{+4.0}_{-3.5}$	5
330.0–440.0	1.402×10^{-4}	3.5	$^{+7.1}_{-7.2}$	6
440.0–600.0	2.687×10^{-5}	7.6	$^{+22.7}_{-12.6}$	7

Table K.3: Numerical values are shown for the normalized differential $t\bar{t}$ cross section measured as a function of the rapidity of the top, $y(t)$, in the full phase space at parton level. Corresponding statistical and systematic uncertainties are also shown in percent.

y(t)	$\frac{1}{\sigma(t\bar{t})}\frac{\mathrm{d}\sigma}{\mathrm{d}y(\mathrm{t})}$	stat. [%]	syst. [%]	bin
−2.6–−1.8	8.067×10^{-2}	1.6	$^{+2.9}_{-2.6}$	1
−1.8–−1.4	1.645×10^{-1}	0.9	$^{+1.7}_{-1.6}$	2
−1.4–−0.9	2.268×10^{-1}	0.6	$^{+1.2}_{-0.6}$	3
−0.9–−0.5	2.768×10^{-1}	0.5	$^{+0.7}_{-0.8}$	4
−0.5–0.0	2.993×10^{-1}	0.5	$^{+1.4}_{-0.5}$	5
0.0–0.5	2.996×10^{-1}	0.5	$^{+0.7}_{-1.2}$	6
0.5–0.9	2.773×10^{-1}	0.5	$^{+0.6}_{-1.6}$	7
0.9–1.4	2.232×10^{-1}	0.7	$^{+0.8}_{-1.2}$	8
1.4–1.8	1.601×10^{-1}	0.9	$^{+3.0}_{-1.3}$	9
1.8–2.6	8.505×10^{-2}	1.5	$^{+2.5}_{-2.9}$	10

Table K.4: Numerical values are shown for the normalized differential $t\bar{t}$ cross section measured as a function of the rapidity of the anti-top, $y(\bar{t})$, in the full phase space at parton level. Corresponding statistical and systematic uncertainties are also shown in percent.

$y(\bar{t})$	$\frac{1}{\sigma(t\bar{t})}\frac{\mathrm{d}\sigma}{\mathrm{d}y(\bar{t})}$	stat. [%]	syst. [%]	bin
−2.6–−1.8	8.075×10^{-2}	1.6	$^{+2.4}_{-2.5}$	1
−1.8–−1.4	1.636×10^{-1}	0.9	$^{+2.0}_{-1.5}$	2
−1.4–−0.9	2.275×10^{-1}	0.6	$^{+0.7}_{-1.0}$	3
−0.9–−0.5	2.768×10^{-1}	0.5	$^{+0.8}_{-0.6}$	4
−0.5–0.0	3.073×10^{-1}	0.5	$^{+1.0}_{-1.1}$	5
0.0–0.5	2.992×10^{-1}	0.5	$^{+0.7}_{-1.1}$	6
0.5–0.9	2.728×10^{-1}	0.5	$^{+1.2}_{-0.5}$	7
0.9–1.4	2.277×10^{-1}	0.6	$^{+0.6}_{-1.1}$	8
1.4–1.8	1.605×10^{-1}	0.9	$^{+1.6}_{-1.7}$	9
1.8–2.6	8.064×10^{-2}	1.6	$^{+2.9}_{-3.4}$	10

Table K.5: Numerical values are shown for the normalized differential $t\bar{t}$ cross section measured as a function of the difference in absolute value of rapidity of the top and absolute value of rapidity of the anti-top, $|y(t)| - |y(\bar{t})|$, in the full phase space at parton level. Corresponding statistical and systematic uncertainties are also shown in percent.

$\|y(t)\| - \|y(\bar{t})\|$	$\frac{1}{\sigma(t\bar{t})} \frac{d\sigma}{d\|y(t)\|-\|y(\bar{t})\|}$	stat. [%]	syst. [%]	bin
−2.6–−1.4	5.481×10^{-2}	1.6	$^{+1.5}_{-2.5}$	1
−1.4–−0.9	1.947×10^{-1}	1.1	$^{+1.9}_{-1.2}$	2
−0.9–−0.4	3.235×10^{-1}	0.6	$^{+0.7}_{-0.9}$	3
−0.4–0.0	4.309×10^{-1}	0.6	$^{+1.1}_{-1.0}$	4
0.0–0.4	4.319×10^{-1}	0.6	$^{+1.5}_{-1.1}$	5
0.4–0.9	3.245×10^{-1}	0.6	$^{+1.0}_{-0.8}$	6
0.9–1.4	1.966×10^{-1}	1.1	$^{+2.9}_{-2.1}$	7
1.4–2.6	5.785×10^{-2}	1.5	$^{+1.8}_{-3.6}$	8

Table K.6: Numerical values are shown for the normalized differential $t\bar{t}$ cross section measured as a function of the absolute value of the azimuthal angle (ϕ) between the top and the anti-top, $|\Delta\phi(t,\bar{t})|$, in the full phase space at parton level. Corresponding statistical and systematic uncertainties are also shown in percent.

$\|\Delta\phi(\mathrm{t},\bar{\mathrm{t}})\|$	$\frac{1}{\sigma(t\bar{t})} \frac{d\sigma}{d\|\Delta\phi(\mathrm{t},\bar{\mathrm{t}})\|}$	stat. [%]	syst. [%]	bin
0.0–1.6	6.353×10^{-2}	1.1	$^{+5.4}_{-6.5}$	1
1.6–2.7	2.183×10^{-1}	0.5	$^{+3.9}_{-3.5}$	2
2.7–3.0	1.010×10^{0}	0.3	$^{+1.4}_{-1.1}$	3
3.0–3.1	2.521×10^{0}	0.5	$^{+5.0}_{-5.4}$	4

Table K.7: Numerical values are shown for the normalized differential $t\bar{t}$ cross section measured as a function of the transverse momentum of the $t\bar{t}$ system, $p_{\mathrm{T}}(t\bar{t})$, in the full phase space at parton level. Corresponding statistical and systematic uncertainties are also shown in percent.

$p_{\mathrm{T}}(\mathrm{t\bar{t}})$ [GeV]	$\frac{1}{\sigma(t\bar{t})}\frac{\mathrm{d}\sigma}{\mathrm{d}p_{\mathrm{T}}(\mathrm{t\bar{t}})}$[GeV^{-1}]	stat. [%]	syst. [%]	bin
0–40	1.214×10^{-2}	0.2	$^{+2.9}_{-3.0}$	1
40–100	5.260×10^{-3}	0.2	$^{+2.6}_{-2.9}$	2
100–200	1.421×10^{-3}	0.5	$^{+4.7}_{-3.9}$	3
200–310	3.646×10^{-4}	1.1	$^{+3.4}_{-2.7}$	4
310–420	9.906×10^{-5}	2.5	$^{+2.2}_{-6.4}$	5
420–570	2.662×10^{-5}	4.0	$^{+7.2}_{-4.8}$	6
570–1000	3.459×10^{-6}	5.1	$^{+3.4}_{-15.8}$	7

Table K.8: Numerical values are shown for the normalized differential $t\bar{t}$ cross section measured as a function of the rapidity of the $t\bar{t}$ system, $y(t\bar{t})$, in the full phase space at parton level. Corresponding statistical and systematic uncertainties are also shown in percent.

$y(\mathrm{t\bar{t}})$	$\frac{1}{\sigma(t\bar{t})}\frac{\mathrm{d}\sigma}{\mathrm{d}y(\mathrm{t\bar{t}})}$	stat. [%]	syst. [%]	bin
-2.6–-1.6	6.051×10^{-2}	2.0	$^{+5.8}_{-3.8}$	1
-1.6–-1.2	1.754×10^{-1}	1.0	$^{+0.7}_{-2.3}$	2
-1.2–-0.9	2.435×10^{-1}	0.9	$^{+1.3}_{-1.0}$	3
-0.9–-0.6	2.987×10^{-1}	0.7	$^{+1.2}_{-0.9}$	4
-0.6–-0.3	3.360×10^{-1}	0.6	$^{+0.7}_{-1.6}$	5
-0.3–0.0	3.568×10^{-1}	0.6	$^{+0.9}_{-1.1}$	6
0.0–0.3	3.608×10^{-1}	0.6	$^{+1.4}_{-1.0}$	7
0.3–0.6	3.340×10^{-1}	0.6	$^{+1.0}_{-1.1}$	8
0.6–0.9	2.934×10^{-1}	0.7	$^{+0.7}_{-1.6}$	9
0.9–1.2	2.444×10^{-1}	0.9	$^{+0.6}_{-1.9}$	10
1.2–1.6	1.723×10^{-1}	1.0	$^{+1.8}_{-2.2}$	11
1.6–2.6	6.017×10^{-2}	2.0	$^{+5.4}_{-3.8}$	12

Table K.9: Numerical values are shown for the normalized differential $t\bar{t}$ cross section measured as a function of the invariant mass of the $t\bar{t}$ system, $m(t\bar{t})$, in the full phase space at parton level. Corresponding statistical and systematic uncertainties are also shown in percent.

$m(\mathrm{t\bar{t}})$ [GeV]	$\frac{1}{\sigma(t\bar{t})}\frac{\mathrm{d}\sigma}{\mathrm{d}m(\mathrm{t\bar{t}})}$ [GeV^{-1}]	stat. [%]	syst. [%]	bin
300–380	1.771×10^{-3}	0.9	$^{+7.9}_{-8.3}$	1
380–470	4.077×10^{-3}	0.3	$^{+1.0}_{-0.9}$	2
470–620	2.026×10^{-3}	0.3	$^{+1.9}_{-1.8}$	3
620–820	6.395×10^{-4}	0.6	$^{+2.6}_{-2.6}$	4
820–1100	1.611×10^{-4}	1.5	$^{+2.8}_{-2.9}$	5
1100–1500	2.944×10^{-5}	4.0	$^{+4.3}_{-6.1}$	6
1500–2500	2.735×10^{-6}	8.4	$^{+17.6}_{-7.4}$	7

Table K.10: Numerical values are shown for the normalized differential $t\bar{t}$ cross section measured as a function of the ratio of the transverse momentum of the top quark over the invariant mass of the $t\bar{t}$ system, $p_{\mathrm{T}}(t)/m(t\bar{t})$, in the full phase space at parton level. Corresponding statistical and systematic uncertainties are also shown in percent.

$p_{\mathrm{T}}(\mathrm{t})/m(\mathrm{t\bar{t}})$	$\frac{1}{\sigma(t\bar{t})}\frac{\mathrm{d}\sigma}{\mathrm{d}p_{\mathrm{T}}(\mathrm{t})/m(\mathrm{t\bar{t}})}$	stat. [%]	syst. [%]	bin
0.0–0.1	1.916×10^{0}	0.4	$^{+2.5}_{-3.1}$	1
0.1–0.3	3.152×10^{0}	0.2	$^{+1.3}_{-1.1}$	2
0.3–0.4	1.722×10^{0}	0.5	$^{+2.7}_{-2.1}$	3
0.4–0.6	3.084×10^{-1}	0.9	$^{+2.4}_{-3.1}$	4
0.6–1.0	1.456×10^{-2}	3.2	$^{+11.5}_{-14.7}$	5

Table K.11: Numerical values are shown for the normalized differential $t\bar{t}$ cross section measured as a function of the ratio of the transverse momentum of the $t\bar{t}$ system over the invariant mass of the $t\bar{t}$ system, $p_{\mathrm{T}}(t\bar{t})/m(t\bar{t})$, in the full phase space at parton level. Corresponding statistical and systematic uncertainties are also shown in percent.

$p_{\mathrm{T}}(\mathrm{t\bar{t}})/m(\mathrm{t\bar{t}})$	$\frac{1}{\sigma(t\bar{t})}\frac{\mathrm{d}\sigma}{\mathrm{d}p_{\mathrm{T}}(\mathrm{t\bar{t}})/m(\mathrm{t\bar{t}})}$	stat. [%]	syst. [%]	bin
0.0–0.1	6.598×10^{0}	0.5	$^{+6.7}_{-7.0}$	1
0.1–0.1	4.756×10^{0}	0.5	$^{+2.8}_{-2.5}$	2
0.1–0.2	2.281×10^{0}	0.6	$^{+5.5}_{-5.7}$	3
0.2–0.3	9.804×10^{-1}	1.0	$^{+3.9}_{-5.1}$	4
0.3–0.4	4.887×10^{-1}	1.9	$^{+6.0}_{-3.4}$	5
0.4–0.6	2.178×10^{-1}	2.5	$^{+5.4}_{-2.9}$	6
0.6–0.7	9.116×10^{-2}	4.7	$^{+4.5}_{-6.9}$	7
0.7–0.9	3.413×10^{-2}	6.3	$^{+9.2}_{-7.0}$	8
0.9–1.5	6.886×10^{-3}	5.3	$^{+6.3}_{-9.7}$	9

Table K.12: Numerical values are shown for the normalized differential $t\bar{t}$ cross section measured as a function of $\log(\xi_1)$, which is equivalent to the momentum fraction of the incoming parton from one of the protons in the leading order QCD picture, in the full phase space at parton level. Corresponding statistical and systematic uncertainties are also shown in percent.

$log(\xi_1)$	$\frac{1}{\sigma(t\bar{t})}\frac{\mathrm{d}\sigma}{\mathrm{d}log(\xi_1)}$	stat. [%]	syst. [%]	bin
-3.0–-2.2	6.431×10^{-2}	2.6	$^{+5.0}_{-4.7}$	1
-2.2–-2.0	3.177×10^{-1}	1.1	$^{+2.5}_{-1.4}$	2
-2.0–-1.8	4.912×10^{-1}	0.7	$^{+0.7}_{-1.2}$	3
-1.8–-1.6	6.601×10^{-1}	0.5	$^{+0.6}_{-1.9}$	4
-1.6–-1.4	7.659×10^{-1}	0.4	$^{+1.3}_{-0.7}$	5
-1.4–-1.2	7.871×10^{-1}	0.4	$^{+0.8}_{-1.1}$	6
-1.2–-0.9	6.908×10^{-1}	0.4	$^{+1.1}_{-0.9}$	7
-0.9–-0.7	4.408×10^{-1}	0.6	$^{+0.8}_{-1.4}$	8
-0.7–0.0	7.441×10^{-2}	2.6	$^{+7.6}_{-5.8}$	9

Table K.13: Numerical values are shown for the normalized differential $t\bar{t}$ cross section measured as a function of $\log(\xi_2)$, which is equivalent to the momentum fraction of the incoming parton from one of the protons in the leading order QCD picture, in the full phase space at parton level. Corresponding statistical and systematic uncertainties are also shown in percent.

$log(\xi_2)$	$\frac{1}{\sigma(t\bar{t})}\frac{\mathrm{d}\sigma}{\mathrm{d}log(\xi_2)}$	stat. [%]	syst. [%]	bin
−3.0–−2.2	6.394×10^{-2}	2.6	$^{+5.7}_{-4.6}$	1
−2.2–−2.0	3.221×10^{-1}	1.1	$^{+1.7}_{-1.6}$	2
−2.0–−1.8	4.995×10^{-1}	0.7	$^{+0.9}_{-1.2}$	3
−1.8–−1.6	6.590×10^{-1}	0.5	$^{+0.8}_{-0.9}$	4
−1.6–−1.4	7.678×10^{-1}	0.4	$^{+1.0}_{-1.2}$	5
−1.4–−1.2	7.830×10^{-1}	0.4	$^{+0.9}_{-1.2}$	6
−1.2–−0.9	6.829×10^{-1}	0.4	$^{+0.8}_{-0.9}$	7
−0.9–−0.7	4.362×10^{-1}	0.6	$^{+0.8}_{-1.7}$	8
−0.7–0.0	7.683×10^{-2}	2.5	$^{+8.2}_{-5.6}$	9

K.1.2 Particle level

Table K.14: Numerical values are shown for the normalized differential $t\bar{t}$ cross section measured as a function of the transverse momentum of the top, $p_{\mathrm{T}}(t)$, in the fiducial phase space at particle level. Corresponding statistical and systematic uncertainties are also shown in percent.

p_{T}(t) [GeV]	$\frac{1}{\sigma(t\bar{t})}\frac{\mathrm{d}\sigma}{\mathrm{d}p_{\mathrm{T}}(\mathrm{t})}$[GeV^{-1}]	stat. [%]	syst. [%]	bin
0.0–55.0	3.336×10^{-3}	0.7	$^{+3.4}_{-3.8}$	1
55.0–100.0	5.924×10^{-3}	0.4	$^{+1.3}_{-1.3}$	2
100.0–165.0	4.591×10^{-3}	0.3	$^{+1.4}_{-1.1}$	3
165.0–240.0	2.134×10^{-3}	0.5	$^{+1.6}_{-1.6}$	4
240.0–330.0	7.244×10^{-4}	1.1	$^{+2.6}_{-3.7}$	5
330.0–440.0	1.864×10^{-4}	2.9	$^{+10.2}_{-5.0}$	6
440.0–600.0	3.643×10^{-5}	5.7	$^{+11.9}_{-14.8}$	7

Table K.15: Numerical values are shown for the normalized differential $t\bar{t}$ cross section measured as a function of the transverse momentum of the anti-top, $p_{\mathrm{T}}(\bar{t})$, in the fiducial phase space at particle level. Corresponding statistical and systematic uncertainties are also shown in percent.

$p_{\mathrm{T}}(\bar{t})$ [GeV]	$\frac{1}{\sigma(t\bar{t})}\frac{\mathrm{d}\sigma}{\mathrm{d}p_{\mathrm{T}}(\bar{t})}$[GeV^{-1}]	stat. [%]	syst. [%]	bin
0.0–55.0	3.350×10^{-3}	0.7	$^{+3.2}_{-3.4}$	1
55.0–100.0	5.902×10^{-3}	0.4	$^{+1.2}_{-1.0}$	2
100.0–165.0	4.570×10^{-3}	0.3	$^{+1.2}_{-1.1}$	3
165.0–240.0	2.145×10^{-3}	0.5	$^{+1.6}_{-1.9}$	4
240.0–330.0	7.272×10^{-4}	1.1	$^{+3.2}_{-2.8}$	5
330.0–440.0	1.909×10^{-4}	2.9	$^{+5.9}_{-5.8}$	6
440.0–600.0	3.625×10^{-5}	5.9	$^{+17.4}_{-9.5}$	7

Table K.16: Numerical values are shown for the normalized differential $t\bar{t}$ cross section measured as a function of the rapidity of the top, $y(t)$, in the fiducial phase space at particle level. Corresponding statistical and systematic uncertainties are also shown in percent.

y(t)	$\frac{1}{\sigma(t\bar{t})}\frac{\mathrm{d}\sigma}{\mathrm{d}y(\mathrm{t})}$	stat. [%]	syst. [%]	bin
−2.6–−1.8	3.415×10^{-2}	1.9	$^{+3.5}_{-3.1}$	1
−1.8–−1.4	1.488×10^{-1}	1.0	$^{+1.7}_{-1.8}$	2
−1.4–−0.9	2.458×10^{-1}	0.6	$^{+1.1}_{-0.6}$	3
−0.9–−0.5	3.140×10^{-1}	0.5	$^{+0.6}_{-0.7}$	4
−0.5–0.0	3.436×10^{-1}	0.5	$^{+1.2}_{-0.4}$	5
0.0–0.5	3.438×10^{-1}	0.4	$^{+0.5}_{-1.0}$	6
0.5–0.9	3.145×10^{-1}	0.5	$^{+0.4}_{-1.4}$	7
0.9–1.4	2.425×10^{-1}	0.6	$^{+0.8}_{-1.1}$	8
1.4–1.8	1.444×10^{-1}	1.1	$^{+3.3}_{-1.4}$	9
1.8–2.6	3.612×10^{-2}	1.7	$^{+2.9}_{-3.5}$	10

Table K.17: Numerical values are shown for the normalized differential $t\bar{t}$ cross section measured as a function of the rapidity of the anti-top, $y(\bar{t})$, in the fiducial phase space at particle level. Corresponding statistical and systematic uncertainties are also shown in percent.

$y(\bar{t})$	$\frac{1}{\sigma(t\bar{t})}\frac{\mathrm{d}\sigma}{\mathrm{d}y(\bar{t})}$	stat. [%]	syst. [%]	bin
−2.6–−1.8	3.403×10^{-2}	1.9	$^{+2.8}_{-3.0}$	1
−1.8–−1.4	1.471×10^{-1}	1.0	$^{+2.2}_{-1.7}$	2
−1.4–−0.9	2.458×10^{-1}	0.6	$^{+0.7}_{-0.8}$	3
−0.9–−0.5	3.136×10^{-1}	0.5	$^{+0.7}_{-0.5}$	4
−0.5–0.0	3.518×10^{-1}	0.4	$^{+0.8}_{-0.9}$	5
0.0–0.5	3.435×10^{-1}	0.4	$^{+0.5}_{-0.9}$	6
0.5–0.9	3.092×10^{-1}	0.5	$^{+1.0}_{-0.4}$	7
0.9–1.4	2.462×10^{-1}	0.6	$^{+0.5}_{-1.0}$	8
1.4–1.8	1.439×10^{-1}	1.0	$^{+1.8}_{-1.7}$	9
1.8–2.6	3.415×10^{-2}	1.9	$^{+3.5}_{-3.9}$	10

Table K.18: Numerical values are shown for the normalized differential $t\bar{t}$ cross section measured as a function of the difference in absolute value of rapidity of the top and absolute value of rapidity of the anti-top, $|y(t)|-|y(\bar{t})|$, in the fiducial phase space at particle level. Corresponding statistical and systematic uncertainties are also shown in percent.

$\|y(t)\| - \|y(\bar{t})\|$	$\frac{1}{\sigma(t\bar{t})}\frac{d\sigma}{d\|y(t)\|-\|y(\bar{t})\|}$	stat. [%]	syst. [%]	bin
−2.6–−1.4	2.973×10^{-2}	1.7	$^{+1.6}_{-2.7}$	1
−1.4–−0.9	1.823×10^{-1}	1.1	$^{+1.9}_{-1.2}$	2
−0.9–−0.4	3.508×10^{-1}	0.6	$^{+0.6}_{-0.9}$	3
−0.4–0.0	4.908×10^{-1}	0.5	$^{+0.8}_{-0.8}$	4
0.0–0.4	4.917×10^{-1}	0.5	$^{+1.2}_{-0.9}$	5
0.4–0.9	3.515×10^{-1}	0.6	$^{+0.9}_{-0.8}$	6
0.9–1.4	1.834×10^{-1}	1.1	$^{+2.8}_{-2.1}$	7
1.4–2.6	3.112×10^{-2}	1.6	$^{+1.9}_{-3.6}$	8

Table K.19: Numerical values are shown for the normalized differential $t\bar{t}$ cross section measured as a function of the absolute value of the azimuthal angle (ϕ) between the top and the anti-top, $|\Delta\phi(t,\bar{t})|$, in the fiducial phase space at particle level. Corresponding statistical and systematic uncertainties are also shown in percent.

$\|\Delta\phi(t,\bar{t})\|$	$\frac{1}{\sigma(t\bar{t})}\frac{d\sigma}{d\|\Delta\phi(t,\bar{t})\|}$	stat. [%]	syst. [%]	bin
0.0–1.6	6.002×10^{-2}	1.1	$^{+5.1}_{-5.9}$	1
1.6–2.7	2.166×10^{-1}	0.5	$^{+3.5}_{-3.2}$	2
2.7–3.0	1.031×10^{0}	0.3	$^{+1.3}_{-1.0}$	3
3.0–3.1	2.521×10^{0}	0.5	$^{+4.4}_{-5.0}$	4

Table K.20: Numerical values are shown for the normalized differential $t\bar{t}$ cross section measured as a function of the transverse momentum of the $t\bar{t}$ system, $p_{\mathrm{T}}(t\bar{t})$, in the fiducial phase space at particle level. Corresponding statistical and systematic uncertainties are also shown in percent.

$p_{\mathrm{T}}(\mathrm{t\bar{t}})$ [GeV]	$\frac{1}{\sigma(t\bar{t})}\frac{\mathrm{d}\sigma}{\mathrm{d}p_{\mathrm{T}}(\mathrm{t\bar{t}})}$[GeV^{-1}]	stat. [%]	syst. [%]	bin
0–40	1.165×10^{-2}	0.2	$^{+2.9}_{-3.0}$	1
40–100	5.456×10^{-3}	0.2	$^{+2.5}_{-2.7}$	2
100–200	1.471×10^{-3}	0.5	$^{+4.0}_{-3.3}$	3
200–310	3.811×10^{-4}	1.0	$^{+3.5}_{-2.6}$	4
310–420	1.077×10^{-4}	2.3	$^{+2.2}_{-6.1}$	5
420–570	2.892×10^{-5}	3.9	$^{+7.0}_{-4.6}$	6
570–1000	3.486×10^{-6}	5.0	$^{+3.8}_{-15.9}$	7

Table K.21: Numerical values are shown for the normalized differential $t\bar{t}$ cross section measured as a function of the rapidity of the $t\bar{t}$ system, $y(t\bar{t})$, in the fiducial phase space at particle level. Corresponding statistical and systematic uncertainties are also shown in percent.

$y(\mathrm{t\bar{t}})$	$\frac{1}{\sigma(t\bar{t})}\frac{\mathrm{d}\sigma}{\mathrm{d}y(\mathrm{t\bar{t}})}$	stat. [%]	syst. [%]	bin
−2.6–−1.6	1.587×10^{-2}	2.6	$^{+7.8}_{-4.7}$	1
−1.6–−1.2	1.310×10^{-1}	1.1	$^{+0.7}_{-2.7}$	2
−1.2–−0.9	2.432×10^{-1}	0.8	$^{+1.6}_{-0.8}$	3
−0.9–−0.6	3.407×10^{-1}	0.6	$^{+1.1}_{-0.6}$	4
−0.6–−0.3	4.103×10^{-1}	0.5	$^{+0.4}_{-1.1}$	5
−0.3–0.0	4.484×10^{-1}	0.5	$^{+0.7}_{-0.6}$	6
0.0–0.3	4.525×10^{-1}	0.5	$^{+1.1}_{-0.6}$	7
0.3–0.6	4.080×10^{-1}	0.5	$^{+0.7}_{-0.6}$	8
0.6–0.9	3.348×10^{-1}	0.6	$^{+0.5}_{-1.1}$	9
0.9–1.2	2.442×10^{-1}	0.8	$^{+0.7}_{-1.5}$	10
1.2–1.6	1.282×10^{-1}	1.2	$^{+2.3}_{-2.6}$	11
1.6–2.6	1.583×10^{-2}	2.6	$^{+6.8}_{-4.7}$	12

Table K.22: Numerical values are shown for the normalized differential $t\bar{t}$ cross section measured as a function of the invariant mass of the $t\bar{t}$ system, $m(t\bar{t})$, in the fiducial phase space at particle level. Corresponding statistical and systematic uncertainties are also shown in percent.

$m(\mathrm{t\bar{t}})$ [GeV]	$\frac{1}{\sigma(t\bar{t})}\frac{\mathrm{d}\sigma}{\mathrm{d}m(\mathrm{t\bar{t}})}$[GeV^{-1}]	stat. [%]	syst. [%]	bin
300–380	1.991×10^{-3}	0.7	$^{+5.9}_{-6.1}$	1
380–470	3.896×10^{-3}	0.3	$^{+0.8}_{-0.8}$	2
470–620	2.038×10^{-3}	0.3	$^{+1.5}_{-1.4}$	3
620–820	6.475×10^{-4}	0.6	$^{+2.4}_{-2.3}$	4
820–1100	1.541×10^{-4}	1.5	$^{+2.8}_{-2.8}$	5
1100–1500	2.504×10^{-5}	3.9	$^{+3.5}_{-6.2}$	6
1500–2500	1.745×10^{-6}	8.2	$^{+15.3}_{-7.6}$	7

Table K.23: Numerical values are shown for the normalized differential $t\bar{t}$ cross section measured as a function of the ratio of the transverse momentum of the top quark over the invariant mass of the $t\bar{t}$ system, $p_{\mathrm{T}}(t)/m(t\bar{t})$, in the fiducial phase space at particle level. Corresponding statistical and systematic uncertainties are also shown in percent.

$p_{\mathrm{T}}(\mathrm{t})/m(\mathrm{t\bar{t}})$	$\frac{1}{\sigma(t\bar{t})}\frac{\mathrm{d}\sigma}{\mathrm{d}p_{\mathrm{T}}(\mathrm{t})/m(\mathrm{t\bar{t}})}$	stat. [%]	syst. [%]	bin
0.0–0.1	1.663×10^{0}	0.4	$^{+2.8}_{-3.0}$	1
0.1–0.3	3.121×10^{0}	0.2	$^{+1.2}_{-1.2}$	2
0.3–0.4	1.984×10^{0}	0.4	$^{+2.0}_{-1.6}$	3
0.4–0.6	3.873×10^{-1}	0.8	$^{+2.1}_{-2.4}$	4
0.6–1.0	1.656×10^{-2}	3.2	$^{+12.1}_{-15.2}$	5

Table K.24: Numerical values are shown for the normalized differential $t\bar{t}$ cross section measured as a function of the ratio of the transverse momentum of the $t\bar{t}$ system over the invariant mass of the $t\bar{t}$ system, $p_{\mathrm{T}}(t\bar{t})/m(t\bar{t})$, in the fiducial phase space at particle level. Corresponding statistical and systematic uncertainties are also shown in percent.

$p_{\mathrm{T}}(\mathrm{t\bar{t}})/m(\mathrm{t\bar{t}})$	$\frac{1}{\sigma(t\bar{t})}\frac{\mathrm{d}\sigma}{\mathrm{d}p_{\mathrm{T}}(\mathrm{t\bar{t}})/m(\mathrm{t\bar{t}})}$	stat. [%]	syst. [%]	bin
0.0–0.1	6.010×10^{0}	0.5	$^{+6.3}_{-6.7}$	1
0.1–0.1	4.879×10^{0}	0.4	$^{+2.6}_{-2.2}$	2
0.1–0.2	2.404×10^{0}	0.5	$^{+4.3}_{-4.5}$	3
0.2–0.3	1.032×10^{0}	0.9	$^{+3.2}_{-4.3}$	4
0.3–0.4	5.119×10^{-1}	1.7	$^{+5.4}_{-3.1}$	5
0.4–0.6	2.315×10^{-1}	2.1	$^{+4.8}_{-2.5}$	6
0.6–0.7	9.713×10^{-2}	4.1	$^{+4.5}_{-6.2}$	7
0.7–0.9	3.665×10^{-2}	5.5	$^{+7.9}_{-6.8}$	8
0.9–1.5	6.952×10^{-3}	5.1	$^{+6.2}_{-9.5}$	9

Table K.25: Numerical values are shown for the normalized differential $t\bar{t}$ cross section measured as a function of $\log(\xi_1)$, which is equivalent to the momentum fraction of the incoming parton from one of the protons in the leading order QCD picture, in the fiducial phase space at particle level. Corresponding statistical and systematic uncertainties are also shown in percent.

$log(\xi_1)$	$\frac{1}{\sigma(t\bar{t})}\frac{\mathrm{d}\sigma}{\mathrm{d}log(\xi_1)}$	stat. [%]	syst. [%]	bin
−3.0–−2.2	1.661×10^{-2}	3.4	$^{+6.2}_{-6.1}$	1
−2.2–−2.0	2.335×10^{-1}	1.4	$^{+3.3}_{-1.8}$	2
−2.0–−1.8	4.945×10^{-1}	0.6	$^{+0.9}_{-1.2}$	3
−1.8–−1.6	7.603×10^{-1}	0.4	$^{+0.4}_{-1.4}$	4
−1.6–−1.4	9.406×10^{-1}	0.4	$^{+1.0}_{-0.4}$	5
−1.4–−1.2	9.839×10^{-1}	0.3	$^{+0.5}_{-0.6}$	6
−1.2–−0.9	7.966×10^{-1}	0.3	$^{+0.9}_{-0.7}$	7
−0.9–−0.7	3.411×10^{-1}	0.7	$^{+1.1}_{-1.7}$	8
−0.7–0.0	1.661×10^{-2}	3.2	$^{+9.1}_{-6.5}$	9

Table K.26: Numerical values are shown for the normalized differential $t\bar{t}$ cross section measured as a function of $\log(\xi_2)$, which is equivalent to the momentum fraction of the incoming parton from one of the protons in the leading order QCD picture, in the fiducial phase space at particle level. Corresponding statistical and systematic uncertainties are also shown in percent.

$log(\xi_2)$	$\frac{1}{\sigma(t\bar{t})}\frac{\mathrm{d}\sigma}{\mathrm{d}log(\xi_2)}$	stat. [%]	syst. [%]	bin
−3.0–−2.2	1.663×10^{-2}	3.4	$^{+6.6}_{-5.6}$	1
−2.2–−2.0	2.371×10^{-1}	1.3	$^{+2.1}_{-2.1}$	2
−2.0–−1.8	5.033×10^{-1}	0.6	$^{+0.9}_{-1.0}$	3
−1.8–−1.6	7.612×10^{-1}	0.4	$^{+0.6}_{-0.6}$	4
−1.6–−1.4	9.432×10^{-1}	0.4	$^{+0.6}_{-0.8}$	5
−1.4–−1.2	9.792×10^{-1}	0.3	$^{+0.6}_{-0.6}$	6
−1.2–−0.9	7.898×10^{-1}	0.3	$^{+0.8}_{-0.7}$	7
−0.9–−0.7	3.376×10^{-1}	0.7	$^{+1.2}_{-2.1}$	8
−0.7–0.0	1.718×10^{-2}	3.1	$^{+9.9}_{-6.3}$	9

Table K.27: Numerical values are shown for the normalized differential $t\bar{t}$ cross section measured as a function of the transverse momentum of the lepton, $p_{\mathrm{T}}(\ell)$, in the fiducial phase space at particle level. Corresponding statistical and systematic uncertainties are also shown in percent.

$p_{\mathrm{T}}(l)$ [GeV]	$\frac{1}{\sigma(t\bar{t})}\frac{\mathrm{d}\sigma}{\mathrm{d}p_{\mathrm{T}}(l)}$[GeV^{-1}]	stat. [%]	syst. [%]	bin
20.0–25.0	1.731×10^{-2}	0.6	$^{+1.9}_{-1.7}$	1
25.0–30.0	1.909×10^{-2}	0.5	$^{+1.6}_{-1.7}$	2
30.0–40.0	1.840×10^{-2}	0.3	$^{+0.7}_{-0.8}$	3
40.0–50.0	1.574×10^{-2}	0.3	$^{+0.5}_{-0.7}$	4
50.0–60.0	1.239×10^{-2}	0.4	$^{+0.5}_{-0.5}$	5
60.0–80.0	8.185×10^{-3}	0.3	$^{+0.9}_{-1.0}$	6
80.0–100.0	4.372×10^{-3}	0.4	$^{+1.3}_{-1.2}$	7
100.0–120.0	2.272×10^{-3}	0.6	$^{+2.0}_{-1.7}$	8
120.0–150.0	1.047×10^{-3}	0.7	$^{+2.1}_{-1.9}$	9
150.0–200.0	3.554×10^{-4}	0.9	$^{+2.3}_{-2.8}$	10
200.0–300.0	6.275×10^{-5}	1.6	$^{+3.8}_{-3.5}$	11
300.0–400.0	7.894×10^{-6}	4.5	$^{+8.0}_{-7.9}$	12

Table K.28: Numerical values are shown for the normalized differential $t\bar{t}$ cross section measured as a function of the ratio of the transverse momentum of the trailing lepton over the transverse momentum of the leading lepton, $p_{\mathrm{T}}(\ell)$ trailing/$p_{\mathrm{T}}(\ell)$ leading, in the fiducial phase space at particle level. Corresponding statistical and systematic uncertainties are also shown in percent.

$p_{\mathrm{T}}(l)$ trailing/$p_{\mathrm{T}}(l)$ leading	$\frac{1}{\sigma(t\bar{t})}\frac{\mathrm{d}\sigma}{\mathrm{d}p_{\mathrm{T}}(l)\text{ trailing}/p_{\mathrm{T}}(l)\text{ leading}}$	stat. [%]	syst. [%]	bin
0.0–0.1	5.496×10^{-3}	7.3	$^{+9.0}_{-10.9}$	1
0.1–0.2	1.735×10^{-1}	1.1	$^{+2.2}_{-2.5}$	2
0.2–0.3	6.455×10^{-1}	0.6	$^{+1.5}_{-1.4}$	3
0.3–0.4	1.085×10^{0}	0.4	$^{+0.6}_{-0.6}$	4
0.4–0.5	1.335×10^{0}	0.4	$^{+0.3}_{-0.3}$	5
0.5–0.6	1.450×10^{0}	0.4	$^{+0.3}_{-0.3}$	6
0.6–0.7	1.435×10^{0}	0.4	$^{+0.4}_{-0.4}$	7
0.7–0.8	1.389×10^{0}	0.4	$^{+0.4}_{-0.5}$	8
0.8–0.9	1.294×10^{0}	0.4	$^{+0.6}_{-0.6}$	9
0.9–1.0	1.188×10^{0}	0.5	$^{+0.5}_{-0.5}$	10

Table K.29: Numerical values are shown for the normalized differential $t\bar{t}$ cross section measured as a function of the ratio of the transverse momentum of the lepton over the transverse momentum of the anti-top quark, $p_{\mathrm{T}}(\ell)/p_{\mathrm{T}}(\bar{t})$, in the fiducial phase space at particle level. Corresponding statistical and systematic uncertainties are also shown in percent.

$p_{\mathrm{T}}(l)/p_{\mathrm{T}}(\bar{t})$	$\frac{1}{\sigma(t\bar{t})}\frac{\mathrm{d}\sigma}{\mathrm{d}p_{\mathrm{T}}(l)/p_{\mathrm{T}}(\bar{t})}$	stat. [%]	syst. [%]	bin
0.0–0.1	1.030×10^{-1}	3.4	$^{+4.4}_{-7.6}$	1
0.1–0.2	9.026×10^{-1}	0.8	$^{+2.9}_{-1.4}$	2
0.2–0.4	1.461×10^{0}	0.3	$^{+1.1}_{-1.0}$	3
0.4–0.8	9.550×10^{-1}	0.2	$^{+0.9}_{-0.9}$	4
0.8–3.0	1.023×10^{-1}	0.5	$^{+2.3}_{-2.9}$	5

Table K.30: Numerical values are shown for the normalized differential $t\bar{t}$ cross section measured as a function of the ratio of the scalar sum of p_{T} of b and p_{T} of anti-b over the scalar sum of p_{T} of top and p_{T} of anti-top, $(p_{\mathrm{T}}(\mathrm{b})+p_{\mathrm{T}}(\bar{\mathrm{b}}))/(p_{\mathrm{T}}(\mathrm{t})+p_{\mathrm{T}}(\bar{\mathrm{t}}))$, in the fiducial phase space at particle level. Corresponding statistical and systematic uncertainties are also shown in percent.

$(p_{\mathrm{T}}(b)+p_{\mathrm{T}}(\bar{b}))/(p_{\mathrm{T}}(\mathrm{t})+p_{\mathrm{T}}(\bar{t}))$	$\frac{1}{\sigma(t\bar{t})}\frac{\mathrm{d}\sigma}{\mathrm{d}(p_{\mathrm{T}}(b)+p_{\mathrm{T}}(\bar{b}))/(p_{\mathrm{T}}(\mathrm{t})+\ p_{\mathrm{T}}(\bar{t}))}$	stat. [%]	syst. [%]	bin
0.0–0.2	6.786×10^{-2}	2.6	$^{+13.3}_{-15.3}$	1
0.2–0.5	7.726×10^{-1}	0.4	$^{+2.5}_{-2.4}$	2
0.5–1.0	1.150×10^{0}	0.2	$^{+1.3}_{-1.3}$	3
1.0–3.0	1.075×10^{-1}	0.5	$^{+4.3}_{-4.6}$	4

Table K.31: Numerical values are shown for the normalized differential $t\bar{t}$ cross section measured as a function of the transverse momentum of the leading b quark, $p_{\mathrm{T}}(\mathrm{b})$ leading, in the fiducial phase space at particle level. Corresponding statistical and systematic uncertainties are also shown in percent.

$p_{\mathrm{T}}(b)$ leading [GeV]	$\frac{1}{\sigma(t\bar{t})}\frac{\mathrm{d}\sigma}{\mathrm{d}p_{\mathrm{T}}(b)\text{ leading}}$[GeV^{-1}]	stat. [%]	syst. [%]	bin
30.0–50.0	3.336×10^{-3}	1.1	$^{+9.0}_{-9.3}$	1
50.0–65.0	9.475×10^{-3}	0.5	$^{+2.3}_{-2.6}$	2
65.0–85.0	1.162×10^{-2}	0.3	$^{+0.9}_{-0.8}$	3
85.0–110.0	9.269×10^{-3}	0.3	$^{+1.0}_{-1.0}$	4
110.0–140.0	5.438×10^{-3}	0.4	$^{+1.9}_{-2.0}$	5
140.0–180.0	2.447×10^{-3}	0.6	$^{+2.8}_{-2.5}$	6
180.0–230.0	8.694×10^{-4}	1.0	$^{+3.2}_{-2.4}$	7
230.0–300.0	2.450×10^{-4}	1.7	$^{+2.5}_{-3.6}$	8
300.0–400.0	4.344×10^{-5}	3.5	$^{+4.3}_{-5.5}$	9
400.0–800.0	2.640×10^{-6}	7.2	$^{+6.5}_{-10.8}$	10

Table K.32: Numerical values are shown for the normalized differential $t\bar{t}$ cross section measured as a function of the transverse momentum of the trailing b quark, p_{T}(b) trailing, in the fiducial phase space at particle level. Corresponding statistical and systematic uncertainties are also shown in percent.

$p_{\mathrm{T}}(b)$ trailing [GeV]	$\frac{1}{\sigma(t\bar{t})}\frac{\mathrm{d}\sigma}{\mathrm{d}p_{\mathrm{T}}(b)\,\mathrm{trailing}}$[GeV^{-1}]	stat. [%]	syst. [%]	bin
30.0–40.0	2.266×10^{-2}	0.4	$^{+4.6}_{-5.0}$	1
40.0–55.0	1.981×10^{-2}	0.3	$^{+1.1}_{-1.2}$	2
55.0–75.0	1.211×10^{-2}	0.3	$^{+1.8}_{-1.7}$	3
75.0–100.0	5.382×10^{-3}	0.5	$^{+2.6}_{-2.3}$	4
100.0–140.0	1.796×10^{-3}	0.7	$^{+2.8}_{-2.4}$	5
140.0–210.0	3.422×10^{-4}	1.3	$^{+4.0}_{-3.6}$	6
210.0–600.0	9.571×10^{-6}	3.5	$^{+4.4}_{-5.3}$	7

Table K.33: Numerical values are shown for the normalized differential $t\bar{t}$ cross section measured as a function of the transverse momentum of the $\ell\bar{\ell}$ system, $p_{\mathrm{T}}(\ell\bar{\ell})$, in the fiducial phase space at particle level. Corresponding statistical and systematic uncertainties are also shown in percent.

$p_{\mathrm{T}}(l\bar{l})$ [GeV]	$\frac{1}{\sigma(t\bar{t})}\frac{\mathrm{d}\sigma}{\mathrm{d}p_{\mathrm{T}}(l\bar{l})}$[GeV^{-1}]	stat. [%]	syst. [%]	bin
0.0–40.0	5.307×10^{-3}	0.3	$^{+1.4}_{-1.5}$	1
40.0–80.0	1.098×10^{-2}	0.2	$^{+0.6}_{-0.6}$	2
80.0–100.0	8.072×10^{-3}	0.3	$^{+0.6}_{-0.8}$	3
100.0–120.0	4.711×10^{-3}	0.5	$^{+1.7}_{-1.3}$	4
120.0–150.0	1.993×10^{-3}	0.6	$^{+2.7}_{-2.6}$	5
150.0–200.0	5.038×10^{-4}	1.0	$^{+2.9}_{-3.2}$	6
200.0–250.0	1.071×10^{-4}	2.3	$^{+3.8}_{-4.4}$	7
250.0–300.0	3.100×10^{-5}	4.5	$^{+11.2}_{-4.7}$	8
300.0–400.0	8.133×10^{-6}	4.9	$^{+3.4}_{-11.9}$	9

Table K.34: Numerical values are shown for the normalized differential $t\bar{t}$ cross section measured as a function of the absolute pseudorapidity of the $\ell\bar{\ell}$ system, $|\eta(\ell\bar{\ell})|$, in the fiducial phase space at particle level. Corresponding statistical and systematic uncertainties are also shown in percent.

$\lvert\eta(l\bar{l})\rvert$	$\frac{1}{\sigma(t\bar{t})}\frac{\mathrm{d}\sigma}{\mathrm{d}\lvert\eta(l\bar{l})\rvert}$	stat. [%]	syst. [%]	bin
0.0–0.2	4.415×10^{-1}	0.5	$^{+0.6}_{-0.6}$	1
0.2–0.4	4.404×10^{-1}	0.5	$^{+0.6}_{-0.3}$	2
0.4–0.6	4.462×10^{-1}	0.5	$^{+0.5}_{-0.4}$	3
0.6–0.8	4.539×10^{-1}	0.5	$^{+0.3}_{-0.4}$	4
0.8–1.0	4.500×10^{-1}	0.4	$^{+0.3}_{-0.4}$	5
1.0–1.2	4.452×10^{-1}	0.5	$^{+0.6}_{-0.3}$	6
1.2–1.4	4.309×10^{-1}	0.5	$^{+0.4}_{-0.5}$	7
1.4–1.6	3.988×10^{-1}	0.5	$^{+0.4}_{-0.3}$	8
1.6–1.8	3.570×10^{-1}	0.5	$^{+0.5}_{-0.3}$	9
1.8–2.0	2.980×10^{-1}	0.6	$^{+0.9}_{-0.4}$	10
2.0–2.4	2.076×10^{-1}	0.5	$^{+0.5}_{-1.0}$	11
2.4–3.0	9.592×10^{-2}	0.6	$^{+0.6}_{-1.2}$	12
3.0–3.6	3.161×10^{-2}	1.2	$^{+1.5}_{-1.9}$	13
3.6–5.0	5.731×10^{-3}	2.1	$^{+3.6}_{-3.7}$	14

Table K.35: Numerical values are shown for the normalized differential $t\bar{t}$ cross section measured as a function of the difference in absolute pseudorapidity of the lepton and absolute pseudorapidity of the anti-lepton, $|\eta(\ell)| - |\eta(\bar{\ell})|$, in the fiducial phase space at particle level. Corresponding statistical and systematic uncertainties are also shown in percent.

$\|\eta(l)\| - \|\eta(\bar{l})\|$	$\frac{1}{\sigma(t\bar{t})} \frac{\mathrm{d}\sigma}{\mathrm{d}\|\eta(l)\|-\|\eta(\bar{l})\|}$	stat. [%]	syst. [%]	bin
−2.4–−2.2	8.283×10^{-3}	2.8	$^{+2.4}_{-2.2}$	1
−2.2–−2.0	2.740×10^{-2}	1.6	$^{+1.9}_{-1.8}$	2
−2.0–−1.8	5.384×10^{-2}	1.1	$^{+1.4}_{-1.4}$	3
−1.8–−1.6	8.507×10^{-2}	0.9	$^{+1.0}_{-1.3}$	4
−1.6–−1.4	1.240×10^{-1}	0.8	$^{+0.8}_{-1.0}$	5
−1.4–−1.2	1.692×10^{-1}	0.7	$^{+0.6}_{-0.7}$	6
−1.2–−1.0	2.160×10^{-1}	0.6	$^{+0.6}_{-0.7}$	7
−1.0–−0.8	2.692×10^{-1}	0.6	$^{+0.4}_{-0.6}$	8
−0.8–−0.6	3.261×10^{-1}	0.5	$^{+0.3}_{-0.3}$	9
−0.6–−0.4	3.708×10^{-1}	0.5	$^{+0.6}_{-0.5}$	10
−0.4–−0.2	4.087×10^{-1}	0.5	$^{+0.7}_{-0.5}$	11
−0.2–0.0	4.456×10^{-1}	0.5	$^{+0.7}_{-0.5}$	12
0.0–0.2	4.420×10^{-1}	0.5	$^{+0.7}_{-0.6}$	13
0.2–0.4	4.119×10^{-1}	0.5	$^{+0.4}_{-0.7}$	14
0.4–0.6	3.720×10^{-1}	0.5	$^{+0.6}_{-0.4}$	15
0.6–0.8	3.236×10^{-1}	0.6	$^{+0.3}_{-0.4}$	16
0.8–1.0	2.710×10^{-1}	0.6	$^{+0.5}_{-0.5}$	17
1.0–1.2	2.158×10^{-1}	0.6	$^{+0.6}_{-0.4}$	18
1.2–1.4	1.678×10^{-1}	0.7	$^{+0.7}_{-0.8}$	19
1.4–1.6	1.220×10^{-1}	0.8	$^{+1.0}_{-0.8}$	20
1.6–1.8	8.315×10^{-2}	0.9	$^{+1.1}_{-1.2}$	21
1.8–2.0	5.188×10^{-2}	1.2	$^{+1.1}_{-1.5}$	22
2.0–2.2	2.690×10^{-2}	1.6	$^{+1.4}_{-1.9}$	23
2.2–2.4	7.729×10^{-3}	3.0	$^{+2.1}_{-2.5}$	24

Table K.36: Numerical values are shown for the normalized differential $t\bar{t}$ cross section measured as a function of the absolute value of the azimuthal angle (ϕ) between the lepton and anti-lepton, $|\Delta\phi(\ell,\overline{\ell})|$, in the fiducial phase space at particle level. Corresponding statistical and systematic uncertainties are also shown in percent.

$\lvert\Delta\phi(l,\bar{l})\rvert$	$\frac{1}{\sigma(t\bar{t})}\frac{\mathrm{d}\sigma}{\mathrm{d}\lvert\Delta\phi(l,\bar{l})\rvert}$	stat. [%]	syst. [%]	bin
0.0–0.1	1.851×10^{-1}	1.0	$^{+1.3}_{-0.9}$	1
0.1–0.3	1.991×10^{-1}	1.0	$^{+0.9}_{-1.1}$	2
0.3–0.5	2.173×10^{-1}	1.0	$^{+1.5}_{-2.1}$	3
0.5–0.6	2.460×10^{-1}	0.9	$^{+1.6}_{-1.0}$	4
0.6–0.8	2.638×10^{-1}	0.8	$^{+0.7}_{-0.9}$	5
0.8–0.9	2.705×10^{-1}	0.8	$^{+0.8}_{-0.9}$	6
0.9–1.1	2.839×10^{-1}	0.7	$^{+0.9}_{-0.8}$	7
1.1–1.3	2.905×10^{-1}	0.7	$^{+1.0}_{-0.5}$	8
1.3–1.4	2.989×10^{-1}	0.7	$^{+0.6}_{-0.4}$	9
1.4–1.6	3.115×10^{-1}	0.6	$^{+0.5}_{-0.4}$	10
1.6–1.7	3.230×10^{-1}	0.6	$^{+0.4}_{-0.5}$	11
1.7–1.9	3.384×10^{-1}	0.6	$^{+0.3}_{-0.6}$	12
1.9–2.0	3.534×10^{-1}	0.5	$^{+0.3}_{-0.4}$	13
2.0–2.2	3.667×10^{-1}	0.5	$^{+0.5}_{-0.3}$	14
2.2–2.4	3.770×10^{-1}	0.5	$^{+0.5}_{-0.4}$	15
2.4–2.5	3.918×10^{-1}	0.5	$^{+0.7}_{-0.7}$	16
2.5–2.7	3.989×10^{-1}	0.5	$^{+0.6}_{-0.6}$	17
2.7–2.8	4.130×10^{-1}	0.5	$^{+0.5}_{-0.8}$	18
2.8–3.0	4.166×10^{-1}	0.5	$^{+0.8}_{-0.6}$	19
3.0–3.1	4.194×10^{-1}	0.5	$^{+0.8}_{-0.9}$	20

Table K.37: Numerical values are shown for the normalized differential $t\bar{t}$ cross section measured as a function of the invariant mass of the $\ell\bar{\ell}$ system, $m(\ell\bar{\ell})$, in the fiducial phase space at particle level. Corresponding statistical and systematic uncertainties are also shown in percent.

$m(l\bar{l})$ [GeV]	$\frac{1}{\sigma(t\bar{t})}\frac{\mathrm{d}\sigma}{\mathrm{d}m(l\bar{l})}$[GeV^{-1}]	stat. [%]	syst. [%]	bin
20.0–40.0	4.115×10^{-3}	0.7	$^{+2.7}_{-2.7}$	1
40.0–60.0	6.593×10^{-3}	0.4	$^{+1.3}_{-1.3}$	2
60.0–80.0	7.934×10^{-3}	0.3	$^{+1.7}_{-1.9}$	3
80.0–100.0	7.385×10^{-3}	0.3	$^{+1.8}_{-1.7}$	4
100.0–120.0	6.048×10^{-3}	0.4	$^{+0.6}_{-0.5}$	5
120.0–150.0	4.360×10^{-3}	0.3	$^{+0.9}_{-0.9}$	6
150.0–200.0	2.395×10^{-3}	0.3	$^{+1.4}_{-1.4}$	7
200.0–250.0	1.102×10^{-3}	0.5	$^{+1.8}_{-1.7}$	8
250.0–300.0	5.177×10^{-4}	0.7	$^{+2.2}_{-2.1}$	9
300.0–400.0	1.940×10^{-4}	0.8	$^{+2.6}_{-2.6}$	10
400.0–500.0	5.351×10^{-5}	1.6	$^{+3.7}_{-3.1}$	11
500.0–650.0	1.513×10^{-5}	2.4	$^{+4.7}_{-5.4}$	12

Table K.38: Numerical values are shown for the normalized differential $t\bar{t}$ cross section measured as a function of the invariant mass of the $b\bar{b}$ system, $m(b\bar{b})$, in the fiducial phase space at particle level. Corresponding statistical and systematic uncertainties are also shown in percent.

$m(b\bar{b})$ [GeV]	$\frac{1}{\sigma(t\bar{t})}\frac{\mathrm{d}\sigma}{\mathrm{d}m(b\bar{b})}$[GeV^{-1}]	stat. [%]	syst. [%]	bin
0.0–50.0	7.926×10^{-4}	1.1	$^{+3.8}_{-4.9}$	1
50.0–85.0	3.589×10^{-3}	0.5	$^{+1.9}_{-1.8}$	2
85.0–130.0	5.191×10^{-3}	0.3	$^{+1.4}_{-1.5}$	3
130.0–190.0	4.438×10^{-3}	0.3	$^{+0.6}_{-0.6}$	4
190.0–280.0	2.299×10^{-3}	0.3	$^{+1.5}_{-1.3}$	5
280.0–630.0	3.524×10^{-4}	0.4	$^{+2.7}_{-2.5}$	6
630.0–1000.0	1.264×10^{-5}	2.6	$^{+4.8}_{-7.7}$	7

Table K.39: Numerical values are shown for the normalized differential $t\bar{t}$ cross section measured as a function of the invariant mass of the $l\bar{l}b\bar{b}$ system, $m(\ell\bar{\ell}\mathrm{b}\bar{\mathrm{b}})$, in the fiducial phase space at particle level. Corresponding statistical and systematic uncertainties are also shown in percent.

$m(l\bar{l}b\bar{b})$ [GeV]	$\frac{1}{\sigma(t\bar{t})}\frac{\mathrm{d}\sigma}{\mathrm{d}m(l\bar{l}b\bar{b})}$[GeV^{-1}]	stat. [%]	syst. [%]	bin
20.0–125.0	6.606×10^{-6}	26.9	$^{+16.8}_{-31.4}$	1
125.0–150.0	1.686×10^{-4}	7.2	$^{+14.7}_{-15.3}$	2
150.0–180.0	6.910×10^{-4}	2.2	$^{+6.4}_{-6.7}$	3
180.0–210.0	1.896×10^{-3}	1.0	$^{+4.5}_{-3.8}$	4
210.0–240.0	3.536×10^{-3}	0.6	$^{+2.2}_{-2.7}$	5
240.0–270.0	4.398×10^{-3}	0.5	$^{+0.9}_{-0.9}$	6
270.0–310.0	4.288×10^{-3}	0.4	$^{+0.5}_{-0.5}$	7
310.0–350.0	3.441×10^{-3}	0.4	$^{+0.8}_{-1.3}$	8
350.0–400.0	2.496×10^{-3}	0.5	$^{+1.3}_{-1.0}$	9
400.0–450.0	1.639×10^{-3}	0.7	$^{+1.8}_{-1.3}$	10
450.0–510.0	1.033×10^{-3}	0.8	$^{+2.0}_{-1.6}$	11
510.0–580.0	6.019×10^{-4}	1.0	$^{+2.1}_{-2.1}$	12
580.0–660.0	3.303×10^{-4}	1.3	$^{+2.9}_{-2.8}$	13
660.0–750.0	1.707×10^{-4}	1.9	$^{+3.0}_{-2.3}$	14
750.0–850.0	8.471×10^{-5}	2.5	$^{+3.2}_{-3.8}$	15
850.0–1000.0	3.817×10^{-5}	2.6	$^{+3.1}_{-4.2}$	16
1000.0–1200.0	1.172×10^{-5}	3.9	$^{+5.6}_{-4.4}$	17
1200.0–1500.0	2.949×10^{-6}	5.9	$^{+4.0}_{-9.1}$	18
1500.0–2500.0	2.415×10^{-7}	9.9	$^{+13.0}_{-4.7}$	19

Table K.40: Numerical values are shown for the normalized differential $t\bar{t}$ cross section measured as a function of the total jet multiplicity, N_{jet} (the last bin is inclusive for $\geq$ 7), in the fiducial phase space at particle level. Corresponding statistical and systematic uncertainties are also shown in percent.

total N_{jet}	$\frac{1}{\sigma(t\bar{t})}\frac{\mathrm{d}\sigma}{\mathrm{d}\,\mathrm{total}\,N_{\mathrm{jet}}}$	stat. [%]	syst. [%]	bin
2	5.331×10^{-1}	0.1	$^{+2.8}_{-2.6}$	1
2.5–3.5	2.997×10^{-1}	0.2	$^{+1.3}_{-1.5}$	2
3.5–4.5	1.150×10^{-1}	0.5	$^{+5.5}_{-5.9}$	3
4.5–5.5	3.686×10^{-2}	1.1	$^{+6.8}_{-8.1}$	4
5.5–6.5	1.107×10^{-2}	2.7	$^{+8.7}_{-9.5}$	5
6.5–7.5	4.251×10^{-3}	3.2	$^{+11.3}_{-12.3}$	6

K.2 Double-differential measurements

K.2.1 Particle level

Table K.41: Part 1: Numerical values are shown for the normalized differential $t\bar{t}$ cross section measured as a function of the absolute value of the azimuthal angle between the lepton and the anti-lepton, $|\Delta\phi(\ell,\bar{\ell})|$, in ranges of the invariant mass of the $t\bar{t}$ system, $m(t\bar{t})$, in the fiducial phase space at particle level. Corresponding statistical and systematic uncertainties are also shown in percent.

$m(\mathrm{t\bar{t}})$ [GeV]	$\lvert\Delta\phi(l,\bar{l})\rvert$	$\frac{1}{\sigma(t\bar{t})}\frac{\mathrm{d}\sigma}{\mathrm{d}\lvert\Delta\phi(l,\bar{l})\rvert}$	stat. [%]	syst. [%]	bin
300–400	0.0–0.3	7.073×10^{-2}	1.8	$^{+3.2}_{-3.4}$	1
300–400	0.3–0.6	8.689×10^{-2}	1.4	$^{+3.2}_{-3.5}$	2
300–400	0.6–0.9	9.749×10^{-2}	1.2	$^{+2.7}_{-3.6}$	3
300–400	0.9–1.3	9.519×10^{-2}	1.2	$^{+3.1}_{-2.7}$	4
300–400	1.3–1.6	8.811×10^{-2}	1.3	$^{+3.8}_{-3.2}$	5
300–400	1.6–1.9	8.294×10^{-2}	1.4	$^{+3.8}_{-4.2}$	6
300–400	1.9–2.2	7.451×10^{-2}	1.5	$^{+4.6}_{-4.6}$	7
300–400	2.2–2.5	6.799×10^{-2}	1.7	$^{+5.1}_{-5.0}$	8
300–400	2.5–2.8	6.483×10^{-2}	1.7	$^{+5.3}_{-5.8}$	9
300–400	2.8–3.1	6.238×10^{-2}	2.2	$^{+7.8}_{-6.4}$	10
400–500	0.0–0.3	6.811×10^{-2}	1.7	$^{+2.9}_{-2.4}$	11
400–500	0.3–0.6	8.455×10^{-2}	1.1	$^{+2.7}_{-1.8}$	12
400–500	0.6–0.9	9.932×10^{-2}	1.0	$^{+2.6}_{-1.1}$	13
400–500	0.9–1.3	1.083×10^{-1}	0.9	$^{+1.2}_{-1.8}$	14
400–500	1.3–1.6	1.151×10^{-1}	0.8	$^{+1.0}_{-1.6}$	15
400–500	1.6–1.9	1.226×10^{-1}	0.8	$^{+1.0}_{-1.4}$	16
400–500	1.9–2.2	1.299×10^{-1}	0.7	$^{+1.6}_{-1.4}$	17

Table K.42: Part 2: Numerical values are shown for the normalized differential $t\bar{t}$ cross section measured as a function of the absolute value of the azimuthal angle between the lepton and the anti-lepton, $|\Delta\phi(\ell,\bar{\ell})|$, in ranges of the invariant mass of the $t\bar{t}$ system, $m(t\bar{t})$, in the fiducial phase space at particle level. Corresponding statistical and systematic uncertainties are also shown in percent.

$m(\mathrm{t\bar{t}})$ [GeV]	$\lvert\Delta\phi(l,\bar{l})\rvert$	$\frac{1}{\sigma(t\bar{t})}\frac{\mathrm{d}\sigma}{\mathrm{d}\lvert\Delta\phi(l,\bar{l})\rvert}$	stat. [%]	syst. [%]	bin
400–500	2.2–2.5	1.327×10^{-1}	0.7	$^{+1.5}_{-1.7}$	18
400–500	2.5–2.8	1.309×10^{-1}	0.7	$^{+2.0}_{-1.7}$	19
400–500	2.8–3.1	1.287×10^{-1}	0.9	$^{+1.9}_{-1.9}$	20
500–650	0.0–0.3	3.700×10^{-2}	2.8	$^{+5.5}_{-4.1}$	21
500–650	0.3–0.6	4.019×10^{-2}	2.4	$^{+4.4}_{-4.1}$	22
500–650	0.6–0.9	4.779×10^{-2}	2.0	$^{+2.1}_{-6.1}$	23
500–650	0.9–1.3	5.550×10^{-2}	1.7	$^{+3.5}_{-2.0}$	24
500–650	1.3–1.6	6.848×10^{-2}	1.4	$^{+2.4}_{-3.2}$	25
500–650	1.6–1.9	8.025×10^{-2}	1.2	$^{+2.9}_{-1.7}$	26
500–650	1.9–2.2	9.717×10^{-2}	1.0	$^{+2.2}_{-1.8}$	27
500–650	2.2–2.5	1.087×10^{-1}	0.9	$^{+1.9}_{-1.7}$	28
500–650	2.5–2.8	1.183×10^{-1}	0.8	$^{+1.4}_{-1.8}$	29
500–650	2.8–3.1	1.238×10^{-1}	0.9	$^{+1.6}_{-1.6}$	30
650–1500	0.0–0.3	1.642×10^{-2}	4.0	$^{+4.8}_{-8.7}$	31
650–1500	0.3–0.6	1.897×10^{-2}	3.7	$^{+8.6}_{-5.7}$	32
650–1500	0.6–0.9	2.170×10^{-2}	3.0	$^{+5.7}_{-5.4}$	33
650–1500	0.9–1.3	2.751×10^{-2}	2.3	$^{+4.4}_{-3.9}$	34
650–1500	1.3–1.6	3.367×10^{-2}	2.0	$^{+4.7}_{-3.5}$	35
650–1500	1.6–1.9	4.525×10^{-2}	1.6	$^{+3.7}_{-4.4}$	36
650–1500	1.9–2.2	5.868×10^{-2}	1.2	$^{+3.1}_{-3.9}$	37
650–1500	2.2–2.5	7.577×10^{-2}	1.0	$^{+3.1}_{-3.9}$	38
650–1500	2.5–2.8	9.287×10^{-2}	0.9	$^{+3.4}_{-3.3}$	39
650–1500	2.8–3.1	1.032×10^{-1}	0.9	$^{+3.2}_{-3.4}$	40

Table K.43: Part 1: Numerical values are shown for the normalized differential $t\bar{t}$ cross section measured as a function of the absolute value of the azimuthal angle between the lepton and the anti-lepton, $|\Delta\phi(\ell,\bar{\ell})|$, in ranges of the transverse momentum of the top, $p_{\mathrm{T}}(t)$, in the fiducial phase space at particle level. Corresponding statistical and systematic uncertainties are also shown in percent.

p_{T}(t) [GeV]	$\lvert\Delta\phi(l,\bar{l})\rvert$	$\frac{1}{\sigma(t\bar{t})}\frac{\mathrm{d}\sigma}{\mathrm{d}\lvert\Delta\phi(l,\bar{l})\rvert}$	stat. [%]	syst. [%]	bin
0.0–80.0	0.0–0.3	9.926×10^{-2}	1.3	$^{+2.4}_{-3.6}$	1
0.0–80.0	0.3–0.6	1.134×10^{-1}	1.1	$^{+3.0}_{-2.7}$	2
0.0–80.0	0.6–0.9	1.238×10^{-1}	1.0	$^{+2.6}_{-2.5}$	3
0.0–80.0	0.9–1.3	1.219×10^{-1}	0.9	$^{+2.2}_{-2.1}$	4
0.0–80.0	1.3–1.6	1.137×10^{-1}	1.0	$^{+2.1}_{-2.2}$	5
0.0–80.0	1.6–1.9	1.075×10^{-1}	1.0	$^{+2.6}_{-2.3}$	6
0.0–80.0	1.9–2.2	1.006×10^{-1}	1.1	$^{+3.0}_{-2.9}$	7
0.0–80.0	2.2–2.5	9.325×10^{-2}	1.2	$^{+3.4}_{-3.3}$	8
0.0–80.0	2.5–2.8	8.758×10^{-2}	1.2	$^{+3.7}_{-5.1}$	9
0.0–80.0	2.8–3.1	8.621×10^{-2}	1.5	$^{+5.7}_{-6.3}$	10
80.0–150.0	0.0–0.3	6.703×10^{-2}	1.6	$^{+4.1}_{-2.0}$	11
80.0–150.0	0.3–0.6	8.278×10^{-2}	1.1	$^{+3.0}_{-1.0}$	12
80.0–150.0	0.6–0.9	9.821×10^{-2}	0.9	$^{+2.0}_{-1.2}$	13
80.0–150.0	0.9–1.3	1.096×10^{-1}	0.8	$^{+1.5}_{-1.3}$	14
80.0–150.0	1.3–1.6	1.190×10^{-1}	0.8	$^{+1.1}_{-1.7}$	15
80.0–150.0	1.6–1.9	1.294×10^{-1}	0.7	$^{+1.1}_{-1.7}$	16
80.0–150.0	1.9–2.2	1.365×10^{-1}	0.7	$^{+1.4}_{-1.6}$	17
80.0–150.0	2.2–2.5	1.408×10^{-1}	0.7	$^{+1.6}_{-1.7}$	18

Table K.44: Part 2: Numerical values are shown for the normalized differential $t\bar{t}$ cross section measured as a function of the absolute value of the azimuthal angle between the lepton and the anti-lepton, $|\Delta\phi(\ell,\bar{\ell})|$, in ranges of the transverse momentum of the top, $p_{\mathrm{T}}(t)$, in the fiducial phase space at particle level. Corresponding statistical and systematic uncertainties are also shown in percent.

p_{T}(t) [GeV]	$\lvert\Delta\phi(l,\bar{l})\rvert$	$\frac{1}{\sigma(t\bar{t})}\frac{\mathrm{d}\sigma}{\mathrm{d}\lvert\Delta\phi(l,\bar{l})\rvert}$	stat. [%]	syst. [%]	bin
80.0–150.0	2.5–2.8	1.409×10^{-1}	0.7	$^{+1.9}_{-1.4}$	19
80.0–150.0	2.8–3.1	1.383×10^{-1}	0.8	$^{+1.9}_{-1.5}$	20
150.0–250.0	0.0–0.3	2.138×10^{-2}	4.1	$^{+14.7}_{-6.0}$	21
150.0–250.0	0.3–0.6	2.806×10^{-2}	3.0	$^{+6.4}_{-6.7}$	22
150.0–250.0	0.6–0.9	3.719×10^{-2}	2.2	$^{+2.2}_{-9.2}$	23
150.0–250.0	0.9–1.3	4.440×10^{-2}	1.8	$^{+2.8}_{-3.8}$	24
150.0–250.0	1.3–1.6	5.851×10^{-2}	1.5	$^{+3.3}_{-1.8}$	25
150.0–250.0	1.6–1.9	7.299×10^{-2}	1.2	$^{+2.7}_{-1.8}$	26
150.0–250.0	1.9–2.2	9.207×10^{-2}	0.9	$^{+2.8}_{-1.6}$	27
150.0–250.0	2.2–2.5	1.083×10^{-1}	0.8	$^{+2.4}_{-1.7}$	28
150.0–250.0	2.5–2.8	1.227×10^{-1}	0.7	$^{+1.6}_{-1.6}$	29
150.0–250.0	2.8–3.1	1.297×10^{-1}	0.8	$^{+1.9}_{-1.7}$	30
250.0–600.0	0.0–0.3	4.226×10^{-3}	11.5	$^{+21.5}_{-24.0}$	31
250.0–600.0	0.3–0.6	6.675×10^{-3}	6.4	$^{+7.0}_{-35.3}$	32
250.0–600.0	0.6–0.9	6.637×10^{-3}	7.0	$^{+27.4}_{-9.8}$	33
250.0–600.0	0.9–1.3	1.018×10^{-2}	4.1	$^{+9.0}_{-6.8}$	34
250.0–600.0	1.3–1.6	1.399×10^{-2}	3.4	$^{+6.3}_{-6.7}$	35
250.0–600.0	1.6–1.9	2.071×10^{-2}	2.6	$^{+5.1}_{-4.6}$	36
250.0–600.0	1.9–2.2	3.120×10^{-2}	1.9	$^{+2.6}_{-4.9}$	37
250.0–600.0	2.2–2.5	4.302×10^{-2}	1.5	$^{+3.0}_{-4.1}$	38
250.0–600.0	2.5–2.8	5.600×10^{-2}	1.2	$^{+3.7}_{-3.8}$	39
250.0–600.0	2.8–3.1	6.457×10^{-2}	1.1	$^{+3.1}_{-4.2}$	40

Table K.45: Part 1: Numerical values are shown for the normalized differential $t\bar{t}$ cross section measured as a function of the absolute value of the azimuthal angle between the lepton and the anti-lepton, $|\Delta\phi(\ell,\bar{\ell})|$, in ranges of the difference in absolute value of pseudorapidity of the lepton and absolute value of pseudorapidity of the anti-lepton, $|\eta(\ell)| - |\eta(\bar{\ell})|$, in the fiducial phase space at particle level. Corresponding statistical and systematic uncertainties are also shown in percent.

$\lvert\eta(l)\rvert - \lvert\eta(\bar{l})\rvert$	$\lvert\Delta\phi(l,\bar{l})\rvert$	$\frac{1}{\sigma(t\bar{t})}\frac{\mathrm{d}\sigma}{\mathrm{d}\lvert\Delta\phi(l,\bar{l})\rvert}$	stat. [%]	syst. [%]	bin
−2.4–−1.0	0.0–0.3	3.289×10^{-2}	1.5	$^{+1.2}_{-1.3}$	1
−2.4–−1.0	0.3–0.6	3.334×10^{-2}	1.4	$^{+1.1}_{-1.4}$	2
−2.4–−1.0	0.6–0.9	3.609×10^{-2}	1.2	$^{+1.1}_{-1.1}$	3
−2.4–−1.0	0.9–1.3	3.781×10^{-2}	1.2	$^{+0.9}_{-1.1}$	4
−2.4–−1.0	1.3–1.6	3.984×10^{-2}	1.2	$^{+1.1}_{-0.9}$	5
−2.4–−1.0	1.6–1.9	4.449×10^{-2}	1.0	$^{+0.8}_{-1.3}$	6
−2.4–−1.0	1.9–2.2	4.798×10^{-2}	0.9	$^{+0.9}_{-1.0}$	7
−2.4–−1.0	2.2–2.5	5.119×10^{-2}	0.9	$^{+1.3}_{-1.2}$	8
−2.4–−1.0	2.5–2.8	5.479×10^{-2}	0.9	$^{+0.9}_{-1.2}$	9
−2.4–−1.0	2.8–3.1	5.715×10^{-2}	0.8	$^{+0.8}_{-1.1}$	10
−1.0–−0.5	0.0–0.3	3.782×10^{-2}	1.5	$^{+1.2}_{-1.4}$	11
−1.0–−0.5	0.3–0.6	3.842×10^{-2}	1.6	$^{+1.6}_{-1.8}$	12
−1.0–−0.5	0.6–0.9	4.131×10^{-2}	1.3	$^{+0.8}_{-1.9}$	13
−1.0–−0.5	0.9–1.3	4.330×10^{-2}	1.2	$^{+1.3}_{-0.7}$	14
−1.0–−0.5	1.3–1.6	4.661×10^{-2}	1.1	$^{+0.5}_{-1.1}$	15
−1.0–−0.5	1.6–1.9	4.953×10^{-2}	1.1	$^{+0.4}_{-0.8}$	16
−1.0–−0.5	1.9–2.2	5.396×10^{-2}	1.0	$^{+0.6}_{-0.6}$	17
−1.0–−0.5	2.2–2.5	5.816×10^{-2}	0.9	$^{+0.6}_{-0.9}$	18
−1.0–−0.5	2.5–2.8	6.173×10^{-2}	0.8	$^{+0.8}_{-0.7}$	19
−1.0–−0.5	2.8–3.1	6.279×10^{-2}	0.9	$^{+1.2}_{-0.7}$	20
−0.5–0.0	0.0–0.3	2.590×10^{-2}	2.4	$^{+3.8}_{-2.4}$	21
−0.5–0.0	0.3–0.6	4.316×10^{-2}	1.8	$^{+3.8}_{-2.4}$	22
−0.5–0.0	0.6–0.9	5.779×10^{-2}	1.4	$^{+1.4}_{-1.8}$	23
−0.5–0.0	0.9–1.3	6.203×10^{-2}	1.1	$^{+1.5}_{-0.8}$	24
−0.5–0.0	1.3–1.6	6.662×10^{-2}	1.0	$^{+1.2}_{-0.5}$	25
−0.5–0.0	1.6–1.9	7.161×10^{-2}	1.0	$^{+1.0}_{-0.5}$	26
−0.5–0.0	1.9–2.2	7.767×10^{-2}	0.8	$^{+0.6}_{-0.5}$	27
−0.5–0.0	2.2–2.5	8.324×10^{-2}	0.8	$^{+0.6}_{-0.7}$	28

Table K.46: Part 2: Numerical values are shown for the normalized differential $t\bar{t}$ cross section measured as a function of the absolute value of the azimuthal angle between the lepton and the anti-lepton, $|\Delta\phi(\ell,\bar{\ell})|$, in ranges of the difference in absolute value of pseudorapidity of the lepton and absolute value of pseudorapidity of the anti-lepton, $|\eta(\ell)| - |\eta(\bar{\ell})|$, in the fiducial phase space at particle level. Corresponding statistical and systematic uncertainties are also shown in percent.

$\lvert\eta(l)\rvert - \lvert\eta(\bar{l})\rvert$	$\lvert\Delta\phi(l,\bar{l})\rvert$	$\frac{1}{\sigma(t\bar{t})}\frac{\mathrm{d}\sigma}{\mathrm{d}\lvert\Delta\phi(l,\bar{l})\rvert}$	stat. [%]	syst. [%]	bin
−0.5–0.0	2.5–2.8	8.734×10^{-2}	0.7	$^{+0.9}_{-0.8}$	29
−0.5–0.0	2.8–3.1	8.937×10^{-2}	0.7	$^{+0.9}_{-0.9}$	30
0.0–0.5	0.0–0.3	2.624×10^{-2}	2.3	$^{+2.4}_{-2.9}$	31
0.0–0.5	0.3–0.6	4.487×10^{-2}	1.7	$^{+1.9}_{-2.9}$	32
0.0–0.5	0.6–0.9	5.649×10^{-2}	1.4	$^{+2.4}_{-1.8}$	33
0.0–0.5	0.9–1.3	6.321×10^{-2}	1.0	$^{+1.0}_{-0.9}$	34
0.0–0.5	1.3–1.6	6.571×10^{-2}	1.0	$^{+1.0}_{-0.8}$	35
0.0–0.5	1.6–1.9	7.207×10^{-2}	1.0	$^{+0.6}_{-1.3}$	36
0.0–0.5	1.9–2.2	7.823×10^{-2}	0.8	$^{+0.5}_{-0.3}$	37
0.0–0.5	2.2–2.5	8.252×10^{-2}	0.8	$^{+0.5}_{-0.4}$	38
0.0–0.5	2.5–2.8	8.738×10^{-2}	0.7	$^{+0.7}_{-0.7}$	39
0.0–0.5	2.8–3.1	8.886×10^{-2}	0.8	$^{+1.1}_{-1.0}$	40
0.5–1.0	0.0–0.3	3.660×10^{-2}	1.6	$^{+2.2}_{-1.4}$	41
0.5–1.0	0.3–0.6	3.804×10^{-2}	1.6	$^{+1.5}_{-1.5}$	42
0.5–1.0	0.6–0.9	4.071×10^{-2}	1.3	$^{+0.9}_{-1.0}$	43
0.5–1.0	0.9–1.3	4.341×10^{-2}	1.2	$^{+0.7}_{-0.8}$	44
0.5–1.0	1.3–1.6	4.683×10^{-2}	1.1	$^{+1.3}_{-0.7}$	45
0.5–1.0	1.6–1.9	5.062×10^{-2}	1.1	$^{+0.5}_{-1.1}$	46
0.5–1.0	1.9–2.2	5.491×10^{-2}	1.0	$^{+0.5}_{-0.5}$	47

Table K.47: Part 3: Numerical values are shown for the normalized differential $t\bar{t}$ cross section measured as a function of the absolute value of the azimuthal angle between the lepton and the anti-lepton, $|\Delta\phi(\ell,\bar{\ell})|$, in ranges of the difference in absolute value of pseudorapidity of the lepton and absolute value of pseudorapidity of the anti-lepton, $|\eta(\ell)| - |\eta(\bar{\ell})|$, in the fiducial phase space at particle level. Corresponding statistical and systematic uncertainties are also shown in percent.

$\lvert\eta(l)\rvert - \lvert\eta(\bar{l})\rvert$	$\lvert\Delta\phi(l,\bar{l})\rvert$	$\frac{1}{\sigma(t\bar{t})}\frac{\mathrm{d}\sigma}{\mathrm{d}\lvert\Delta\phi(l,\bar{l})\rvert}$	stat. [%]	syst. [%]	bin
0.5–1.0	2.2–2.5	5.790×10^{-2}	1.0	$^{+0.8}_{-0.5}$	48
0.5–1.0	2.5–2.8	6.059×10^{-2}	0.9	$^{+0.7}_{-0.6}$	49
0.5–1.0	2.8–3.1	6.318×10^{-2}	0.9	$^{+0.8}_{-0.9}$	50
1.0–2.4	0.0–0.3	3.262×10^{-2}	1.4	$^{+1.2}_{-1.7}$	51
1.0–2.4	0.3–0.6	3.457×10^{-2}	1.3	$^{+0.9}_{-1.8}$	52
1.0–2.4	0.6–0.9	3.463×10^{-2}	1.4	$^{+1.1}_{-1.1}$	53
1.0–2.4	0.9–1.3	3.739×10^{-2}	1.2	$^{+0.9}_{-1.2}$	54
1.0–2.4	1.3–1.6	3.976×10^{-2}	1.2	$^{+0.9}_{-1.2}$	55
1.0–2.4	1.6–1.9	4.245×10^{-2}	1.1	$^{+1.2}_{-0.7}$	56
1.0–2.4	1.9–2.2	4.697×10^{-2}	1.0	$^{+1.3}_{-0.8}$	57
1.0–2.4	2.2–2.5	5.100×10^{-2}	0.9	$^{+0.8}_{-0.9}$	58
1.0–2.4	2.5–2.8	5.394×10^{-2}	0.9	$^{+0.8}_{-1.1}$	59
1.0–2.4	2.8–3.1	5.652×10^{-2}	0.9	$^{+0.9}_{-0.8}$	60

Table K.48: Numerical values are shown for the normalized differential $t\bar{t}$ cross section measured as a function of the invariant mass of the $\ell\bar{\ell}$ system, $m(\ell\bar{\ell})$, in ranges of the absolute pseudorapidity of the $\ell\bar{\ell}$ system, $|\eta(\ell\bar{\ell})|$, in the fiducial phase space at particle level. Corresponding statistical and systematic uncertainties are also shown in percent.

$\lvert\eta(l\bar{l})\rvert$	$m(l\bar{l})$ [GeV]	$\frac{1}{\sigma(t\bar{t})}\frac{\mathrm{d}\sigma}{\mathrm{d}m(l\bar{l})}$[GeV^{-1}]	stat. [%]	syst. [%]	bin
0.0–0.5	20.0–50.0	1.485×10^{-3}	0.9	$^{+1.6}_{-1.7}$	1
0.0–0.5	50.0–80.0	1.901×10^{-3}	0.5	$^{+0.8}_{-1.0}$	2
0.0–0.5	80.0–120.0	1.401×10^{-3}	0.6	$^{+1.3}_{-0.9}$	3
0.0–0.5	120.0–170.0	7.203×10^{-4}	0.6	$^{+1.2}_{-1.1}$	4
0.0–0.5	170.0–250.0	2.449×10^{-4}	0.8	$^{+1.7}_{-1.8}$	5
0.0–0.5	250.0–650.0	1.880×10^{-5}	1.3	$^{+2.6}_{-2.3}$	6
0.5–1.0	20.0–50.0	1.345×10^{-3}	0.9	$^{+1.7}_{-1.9}$	7
0.5–1.0	50.0–80.0	1.884×10^{-3}	0.6	$^{+1.1}_{-1.0}$	8
0.5–1.0	80.0–120.0	1.492×10^{-3}	0.6	$^{+1.1}_{-1.0}$	9
0.5–1.0	120.0–170.0	7.701×10^{-4}	0.6	$^{+1.1}_{-1.1}$	10
0.5–1.0	170.0–250.0	2.688×10^{-4}	0.8	$^{+1.6}_{-1.5}$	11
0.5–1.0	250.0–650.0	2.193×10^{-5}	1.2	$^{+2.5}_{-2.7}$	12
1.0–2.0	20.0–50.0	1.688×10^{-3}	0.9	$^{+2.5}_{-2.3}$	13
1.0–2.0	50.0–80.0	2.932×10^{-3}	0.5	$^{+1.5}_{-1.6}$	14
1.0–2.0	80.0–120.0	2.660×10^{-3}	0.4	$^{+0.9}_{-0.8}$	15
1.0–2.0	120.0–170.0	1.513×10^{-3}	0.4	$^{+1.1}_{-1.1}$	16
1.0–2.0	170.0–250.0	5.658×10^{-4}	0.5	$^{+1.8}_{-1.7}$	17
1.0–2.0	250.0–650.0	5.026×10^{-5}	0.8	$^{+2.7}_{-2.4}$	18
2.0–5.0	20.0–50.0	2.271×10^{-4}	3.8	$^{+7.0}_{-9.2}$	19
2.0–5.0	50.0–80.0	9.725×10^{-4}	1.0	$^{+4.8}_{-5.5}$	20
2.0–5.0	80.0–120.0	1.164×10^{-3}	0.7	$^{+0.7}_{-0.7}$	21
2.0–5.0	120.0–170.0	8.011×10^{-4}	0.6	$^{+0.9}_{-1.1}$	22
2.0–5.0	170.0–250.0	3.604×10^{-4}	0.7	$^{+1.7}_{-1.7}$	23
2.0–5.0	250.0–650.0	4.118×10^{-5}	0.8	$^{+2.6}_{-2.8}$	24

Table K.49: Numerical values are shown for the normalized differential $t\bar{t}$ cross section measured as a function of the transverse momentum of the $\ell\bar{\ell}$ system, $p_{\mathrm{T}}(\ell\bar{\ell})$, in ranges of the absolute pseudorapidity of the $\ell\bar{\ell}$ system, $|\eta(\ell\bar{\ell})|$, in the fiducial phase space at particle level. Corresponding statistical and systematic uncertainties are also shown in percent.

$\lvert\eta(l\bar{l})\rvert$	$p_{\mathrm{T}}(l\bar{l})$ [GeV]	$\frac{1}{\sigma(t\bar{t})}\frac{\mathrm{d}\sigma}{\mathrm{d}p_{\mathrm{T}}(l\bar{l})}$[GeV^{-1}]	stat. [%]	syst. [%]	bin
0.0–0.5	0.0–40.0	5.698×10^{-4}	1.0	$^{+1.7}_{-1.5}$	1
0.0–0.5	40.0–70.0	2.398×10^{-3}	0.5	$^{+1.0}_{-0.9}$	2
0.0–0.5	70.0–100.0	2.381×10^{-3}	0.5	$^{+0.6}_{-0.8}$	3
0.0–0.5	100.0–150.0	8.869×10^{-4}	0.7	$^{+1.7}_{-1.1}$	4
0.0–0.5	150.0–400.0	4.205×10^{-5}	1.4	$^{+3.5}_{-2.3}$	5
0.5–1.0	0.0–40.0	6.618×10^{-4}	0.9	$^{+1.7}_{-1.5}$	6
0.5–1.0	40.0–70.0	2.519×10^{-3}	0.5	$^{+1.0}_{-0.9}$	7
0.5–1.0	70.0–100.0	2.358×10^{-3}	0.5	$^{+0.4}_{-0.7}$	8
0.5–1.0	100.0–150.0	8.681×10^{-4}	0.7	$^{+1.6}_{-1.5}$	9
0.5–1.0	150.0–400.0	3.719×10^{-5}	1.6	$^{+3.1}_{-3.3}$	10
1.0–2.0	0.0–40.0	1.795×10^{-3}	0.5	$^{+1.5}_{-1.3}$	11
1.0–2.0	40.0–70.0	4.608×10^{-3}	0.3	$^{+0.8}_{-0.7}$	12
1.0–2.0	70.0–100.0	3.531×10^{-3}	0.4	$^{+0.7}_{-0.7}$	13
1.0–2.0	100.0–150.0	1.168×10^{-3}	0.6	$^{+2.6}_{-2.3}$	14
1.0–2.0	150.0–400.0	4.713×10^{-5}	1.4	$^{+3.2}_{-5.0}$	15
2.0–5.0	0.0–40.0	2.279×10^{-3}	0.5	$^{+1.3}_{-1.7}$	16
2.0–5.0	40.0–70.0	1.581×10^{-3}	0.6	$^{+0.6}_{-1.1}$	17
2.0–5.0	70.0–100.0	6.534×10^{-4}	1.1	$^{+1.4}_{-2.5}$	18
2.0–5.0	100.0–150.0	1.581×10^{-4}	2.0	$^{+6.0}_{-5.2}$	19
2.0–5.0	150.0–400.0	5.015×10^{-6}	5.7	$^{+9.0}_{-13.6}$	20

Table K.50: Numerical values are shown for the normalized differential $t\bar{t}$ cross section measured as a function of the invariant mass of the $\ell\bar{\ell}$ system, $m(\ell\bar{\ell})$, in ranges of the transverse momentum of the $\ell\bar{\ell}$ system, $p_{\mathrm{T}}(\ell\bar{\ell})$, in the fiducial phase space at particle level. Corresponding statistical and systematic uncertainties are also shown in percent.

$p_{\mathrm{T}}(l\bar{l})$ [GeV]	$m(l\bar{l})$ [GeV]	$\frac{1}{\sigma(t\bar{t})}\frac{\mathrm{d}\sigma}{\mathrm{d}m(l\bar{l})}$[GeV^{-1}]	stat. [%]	syst. [%]	bin
0.0–40.0	20.0–50.0	3.552×10^{-4}	3.1	$^{+6.3}_{-7.0}$	1
0.0–40.0	50.0–80.0	1.921×10^{-3}	0.7	$^{+4.3}_{-4.5}$	2
0.0–40.0	80.0–120.0	1.749×10^{-3}	0.5	$^{+1.4}_{-1.2}$	3
0.0–40.0	120.0–170.0	8.659×10^{-4}	0.6	$^{+1.0}_{-1.2}$	4
0.0–40.0	170.0–250.0	2.837×10^{-4}	0.8	$^{+1.3}_{-1.3}$	5
0.0–40.0	250.0–650.0	2.172×10^{-5}	1.2	$^{+1.9}_{-2.1}$	6
40.0–70.0	20.0–50.0	1.922×10^{-3}	0.8	$^{+2.3}_{-2.4}$	7
40.0–70.0	50.0–80.0	2.648×10^{-3}	0.5	$^{+1.5}_{-1.7}$	8
40.0–70.0	80.0–120.0	2.253×10^{-3}	0.4	$^{+1.2}_{-1.0}$	9
40.0–70.0	120.0–170.0	1.196×10^{-3}	0.5	$^{+1.1}_{-1.1}$	10
40.0–70.0	170.0–250.0	4.131×10^{-4}	0.6	$^{+1.5}_{-1.5}$	11
40.0–70.0	250.0–650.0	3.257×10^{-5}	1.0	$^{+2.1}_{-1.9}$	12
70.0–100.0	20.0–50.0	1.662×10^{-3}	0.8	$^{+1.3}_{-1.5}$	13
70.0–100.0	50.0–80.0	2.017×10^{-3}	0.5	$^{+0.6}_{-0.7}$	14
70.0–100.0	80.0–120.0	1.671×10^{-3}	0.5	$^{+1.0}_{-1.1}$	15
70.0–100.0	120.0–170.0	9.701×10^{-4}	0.5	$^{+1.2}_{-1.5}$	16
70.0–100.0	170.0–250.0	3.624×10^{-4}	0.7	$^{+1.8}_{-1.7}$	17
70.0–100.0	250.0–650.0	3.146×10^{-5}	1.1	$^{+2.4}_{-2.5}$	18
100.0–150.0	20.0–50.0	7.260×10^{-4}	1.4	$^{+4.3}_{-3.0}$	19
100.0–150.0	50.0–80.0	9.724×10^{-4}	0.8	$^{+1.8}_{-1.7}$	20
100.0–150.0	80.0–120.0	9.048×10^{-4}	0.8	$^{+2.2}_{-1.7}$	21
100.0–150.0	120.0–170.0	6.327×10^{-4}	0.7	$^{+2.1}_{-1.8}$	22
100.0–150.0	170.0–250.0	2.882×10^{-4}	0.8	$^{+2.5}_{-2.3}$	23
100.0–150.0	250.0–650.0	3.031×10^{-5}	1.0	$^{+3.3}_{-3.3}$	24
150.0–400.0	20.0–50.0	7.772×10^{-5}	5.9	$^{+6.4}_{-16.8}$	25
150.0–400.0	50.0–80.0	1.287×10^{-4}	2.8	$^{+4.1}_{-5.5}$	26
150.0–400.0	80.0–120.0	1.400×10^{-4}	2.2	$^{+3.6}_{-4.3}$	27
150.0–400.0	120.0–170.0	1.409×10^{-4}	1.6	$^{+3.3}_{-2.7}$	28
150.0–400.0	170.0–250.0	9.304×10^{-5}	1.4	$^{+3.5}_{-3.4}$	29
150.0–400.0	250.0–650.0	1.610×10^{-5}	1.4	$^{+4.3}_{-4.4}$	30